RILEM Bookseries

Carlos Chastre · José Neves · Diogo Ribeiro · Fernando F. S. Pinho · Hugo Biscaia · Maria Graça Neves · Paulina Faria · Rui Micaelo *Editors*

Testing and Experimentation in Civil Engineering

From Current to Smart Technologies

rilem

Springer

Testing and Experimentation in Civil Engineering

RILEM BOOKSERIES

Volume 41

RILEM, The International Union of Laboratories and Experts in Construction Materials, Systems and Structures, founded in 1947, is a non-governmental scientific association whose goal is to contribute to progress in the construction sciences, techniques and industries, essentially by means of the communication it fosters between research and practice. RILEM's focus is on construction materials and their use in building and civil engineering structures, covering all phases of the building process from manufacture to use and recycling of materials. More information on RILEM and its previous publications can be found on www.RILEM.net.

Indexed in SCOPUS, Google Scholar and SpringerLink.

Carlos Chastre · José Neves · Diogo Ribeiro ·
Fernando F. S. Pinho · Hugo Biscaia ·
Maria Graça Neves · Paulina Faria · Rui Micaelo
Editors

Testing and Experimentation in Civil Engineering

From Current to Smart Technologies

Springer

Editors
Carlos Chastre
CERIS and Department of Civil Engineering, NOVA School of Science and Technology
Universidade NOVA de Lisboa
Caparica, Portugal

Diogo Ribeiro
CONSTRUCT and Department of Civil Engineering, School of Engineering
Polytechnic of Porto
Porto, Portugal

Hugo Biscaia
UNIDEMI and Department of Mechanical and Industrial Engineering, NOVA School of Science and Technology
Universidade NOVA de Lisboa
Caparica, Portugal

Paulina Faria
CERIS and Department of Civil Engineering, NOVA School of Science and Technology
Universidade NOVA de Lisboa
Caparica, Portugal

José Neves
CERIS and Department of Civil Engineering, Architecture and Georesources
Instituto Superior Técnico
Universidade de Lisboa
Lisboa, Portugal

Fernando F. S. Pinho
CERIS and Department of Civil Engineering, NOVA School of Science and Technology
Universidade NOVA de Lisboa
Caparica, Portugal

Maria Graça Neves
CERIS and Department of Civil Engineering, NOVA School of Science and Technology
Universidade NOVA de Lisboa
Caparica, Portugal

Rui Micaelo
CERIS and Department of Civil Engineering, NOVA School of Science and Technology
Universidade NOVA de Lisboa
Caparica, Portugal

ISSN 2211-0844 ISSN 2211-0852 (electronic)
RILEM Bookseries
ISBN 978-3-031-29190-6 ISBN 978-3-031-29191-3 (eBook)
https://doi.org/10.1007/978-3-031-29191-3

This Springer imprint is published by the registered company Springer Nature Switzerland AG
The registered company address is: Gewerbestrasse 11, 6330 Cham, Switzerland

Preface

The 3rd Conference on Testing and Experimentation in Civil Engineering (TEST&E 2022) was held in Almada, Portugal, at NOVA School of Science & Technology (FCT NOVA) during June 21–23, 2022. This series of conferences began in 2016 under the auspices of the Association of Accredited Laboratories of Portugal (RELACRE) and the Instituto Superior Técnico of the University of Lisbon (IST).

The focus of the conference was the smart technologies that nowadays have a significant impact on the development of Civil Engineering. Smart technologies assume an increasingly important role in the planning, design, construction, operation, and maintenance of the built environment. The continuous evolution of testing and experimentation also contributes to integrating new technologies. We believe the conference gave an important contribution to promoting smart technologies in testing and experimentation in Civil Engineering.

Participants from 15 nationalities attended the conference. A total of 110 extended abstracts were accepted for oral presentation, and a dedicated volume was published. In addition, presenters were invited to submit full papers and to undergo a review process by a minimum of two reviewers. This volume contains the final 40 papers covering the most recent and innovative scientific and technological developments in the following topics:

- 3D modelling and printing
- Biomaterials, nanomaterials, and new materials
- Destructive and non-destructive tests
- Inspection, monitoring, and automatic damage identification
- Modelling (calibration, simulation) and validation of models
- New sensors and technologies (photogrammetry, laser scanning, drones, and wireless).

The editors thank the authors for their participation in this volume and the members of the Scientific Committee for their contribution to the peer-review process. Finally, the editors would also like to acknowledge Springer Nature for the edition of this volume and the special conference support provided by RILEM—International Union of Laboratories and Specialists in Building Materials, Systems and Structures.

Caparica, Portugal	Carlos Chastre
Lisboa, Portugal	José Neves
Porto, Portugal	Diogo Ribeiro
Caparica, Portugal	Fernando F. S. Pinho
Caparica, Portugal	Hugo Biscaia
Caparica, Portugal	Maria Graça Neves
Caparica, Portugal	Paulina Faria
Caparica, Portugal	Rui Micaelo

Acknowledgments

The editors would like to express their sincere gratitude to professionals and organizations that directly or indirectly contributed to the realization of this book; to the Springer RILEM Book Series for accepting this book proposal on the challenging and innovative thematic of smart technologies on testing and experimentation in Civil Engineering; to the Springer Editor, Dr. Pierpaolo Riva, for all the support in addressing all the questions during the book preparation; to the educational institutions NOVA School of Science and Technology (FCT NOVA), Instituto Superior Técnico (IST), and School of Engineering of Polytechnic of Porto (ISEP), as well as the Civil Engineering Research and Innovation for Sustainability (CERIS), Research and Development Unit in Mechanical and Industrial Engineering (UNIDEMI), and Institute of R&D in Structures and Construction (CONSTRUCT), which are financed by Foundation for Science and Technology (Portugal) through UIDB/04625/2020, UIDB/00667/2020, and UIDB/04708/2020, respectively, for providing the necessary conditions for the development of the book edition; to all the authors of the book chapters, for their remarkable commitment to the objectives of the publication and their enthusiasm to be part of this project. Finally, the co-editors would like to thank all the readers of this book for their interest and passion in the most recent smart technologies and innovations in testing and experimentation in Civil Engineering.

Contents

RILEM Publications

The following list is presenting the global offer of RILEM Publications, sorted by series. Each publication is available in printed version and/or in online version.

RILEM Proceedings (PRO)

PRO 1: Durability of High Performance Concrete (ISBN: 2-912143-03-9; e-ISBN: 2-351580-12-5; e-ISBN: 2351580125); *Ed. H. Sommer*

PRO 2: Chloride Penetration into Concrete (ISBN: 2-912143-00-04; e-ISBN: 2912143454); *Eds. L.-O. Nilsson and J.-P. Ollivier*

PRO 3: Evaluation and Strengthening of Existing Masonry Structures (ISBN: 2-912143-02-0; e-ISBN: 2351580141); *Eds. L. Binda and C. Modena*

PRO 4: Concrete: From Material to Structure (ISBN: 2-912143-04-7; e-ISBN: 2351580206); *Eds. J.-P. Bournazel and Y. Malier*

PRO 5: The Role of Admixtures in High Performance Concrete (ISBN: 2-912143-05-5; e-ISBN: 2351580214); *Eds. J. G. Cabrera and R. Rivera-Villarreal*

PRO 6: High Performance Fiber Reinforced Cement Composites—HPFRCC 3 (ISBN: 2-912143-06-3; e-ISBN: 2351580222); *Eds. H. W. Reinhardt and A. E. Naaman*

PRO 7: 1st International RILEM Symposium on Self-Compacting Concrete (ISBN: 2-912143-09-8; e-ISBN: 2912143721); *Eds. Å. Skarendahl and Ö. Petersson*

PRO 8: International RILEM Symposium on Timber Engineering (ISBN: 2-912143-10-1; e-ISBN: 2351580230); *Ed. L. Boström*

PRO 9: 2nd International RILEM Symposium on Adhesion between Polymers and Concrete ISAP ’99 (ISBN: 2-912143-11-X; e-ISBN: 2351580249); *Eds. Y. Ohama and M. Puterman*

PRO 10: 3rd International RILEM Symposium on Durability of Building and Construction Sealants (ISBN: 2-912143-13-6; e-ISBN: 2351580257); *Ed. A. T. Wolf*

PRO 11: 4th International RILEM Conference on Reflective Cracking in Pavements (ISBN: 2-912143-14-4; e-ISBN: 2351580265); *Eds. A. O. Abd El Halim, D. A. Taylor and El H. H. Mohamed*

PRO 12: International RILEM Workshop on Historic Mortars: Characteristics and Tests (ISBN: 2-912143-15-2; e-ISBN: 2351580273); *Eds. P. Bartos, C. Groot and J. J. Hughes*

PRO 13: 2nd International RILEM Symposium on Hydration and Setting (ISBN: 2-912143-16-0; e-ISBN: 2351580281); *Ed. A. Nonat*

PRO 14: Integrated Life-Cycle Design of Materials and Structures—ILCDES 2000 (ISBN: 951-758-408-3; e-ISBN: 235158029X); (ISSN: 0356-9403); *Ed. S. Sarja*

PRO 15: Fifth RILEM Symposium on Fibre-Reinforced Concretes (FRC)—BEFIB'2000 (ISBN: 2-912143-18-7; e-ISBN: 291214373X); *Eds. P. Rossi and G. Chanvillard*

PRO 16: Life Prediction and Management of Concrete Structures (ISBN: 2-912143-19-5; e-ISBN: 2351580303); *Ed. D. Naus*

PRO 17: Shrinkage of Concrete—Shrinkage 2000 (ISBN: 2-912143-20-9; e-ISBN: 2351580311); *Eds. V. Baroghel-Bouny and P.-C. Aïtcin*

PRO 18: Measurement and Interpretation of the On-Site Corrosion Rate (ISBN: 2-912143-21-7; e-ISBN: 235158032X); *Eds. C. Andrade, C. Alonso, J. Fullea, J. Polimon and J. Rodriguez*

PRO 19: Testing and Modelling the Chloride Ingress into Concrete (ISBN: 2-912143-22-5; e-ISBN: 2351580338); *Eds. C. Andrade and J. Kropp*

PRO 20: 1st International RILEM Workshop on Microbial Impacts on Building Materials (CD 02) (e-ISBN 978-2-35158-013-4); *Ed. M. Ribas Silva*

PRO 21: International RILEM Symposium on Connections between Steel and Concrete (ISBN: 2-912143-25-X; e-ISBN: 2351580346); *Ed. R. Eligehausen*

PRO 22: International RILEM Symposium on Joints in Timber Structures (ISBN: 2-912143-28-4; e-ISBN: 2351580354); *Eds. S. Aicher and H.-W. Reinhardt*

PRO 23: International RILEM Conference on Early Age Cracking in Cementitious Systems (ISBN: 2-912143-29-2; e-ISBN: 2351580362); *Eds. K. Kovler and A. Bentur*

PRO 24: 2nd International RILEM Workshop on Frost Resistance of Concrete (ISBN: 2-912143-30-6; e-ISBN: 2351580370); *Eds. M. J. Setzer, R. Auberg and H.-J. Keck*

PRO 25: International RILEM Workshop on Frost Damage in Concrete (ISBN: 2-912143-31-4; e-ISBN: 2351580389); *Eds. D. J. Janssen, M. J. Setzer and M. B. Snyder*

PRO 26: International RILEM Workshop on On-Site Control and Evaluation of Masonry Structures (ISBN: 2-912143-34-9; e-ISBN: 2351580141); *Eds. L. Binda and R. C. de Vekey*

PRO 27: International RILEM Symposium on Building Joint Sealants (CD03; e-ISBN: 235158015X); *Ed. A. T. Wolf*

PRO 28: 6th International RILEM Symposium on Performance Testing and Evaluation of Bituminous Materials—PTEBM'03 (ISBN: 2-912143-35-7; e-ISBN: 978-2-912143-77-8); *Ed. M. N. Partl*

PRO 29: 2nd International RILEM Workshop on Life Prediction and Ageing Management of Concrete Structures (ISBN: 2-912143-36-5; e-ISBN: 2912143780); *Ed. D. J. Naus*

PRO 30: 4th International RILEM Workshop on High Performance Fiber Reinforced Cement Composites—HPFRCC 4 (ISBN: 2-912143-37-3; e-ISBN: 2912143799); *Eds. A. E. Naaman and H. W. Reinhardt*

PRO 31: International RILEM Workshop on Test and Design Methods for Steel Fibre Reinforced Concrete: Background and Experiences (ISBN: 2-912143-38-1; e-ISBN: 2351580168); *Eds. B. Schnütgen and L. Vandewalle*

PRO 32: International Conference on Advances in Concrete and Structures 2 vol. (ISBN (set): 2-912143-41-1; e-ISBN: 2351580176); *Eds. Ying-shu Yuan, Surendra P. Shah and Heng-lin Lü*

PRO 33: 3rd International Symposium on Self-Compacting Concrete (ISBN: 2-912143-42-X; e-ISBN: 2912143713); *Eds. Ó. Wallevik and I. Níelsson*

PRO 34: International RILEM Conference on Microbial Impact on Building Materials (ISBN: 2-912143-43-8; e-ISBN: 2351580184); *Ed. M. Ribas Silva*

PRO 35: International RILEM TC 186-ISA on Internal Sulfate Attack and Delayed Ettringite Formation (ISBN: 2-912143-44-6; e-ISBN: 2912143802); *Eds. K. Scrivener and J. Skalny*

PRO 36: International RILEM Symposium on Concrete Science and Engineering—A Tribute to Arnon Bentur (ISBN: 2-912143-46-2; e-ISBN: 2912143586); *Eds. K. Kovler, J. Marchand, S. Mindess and J. Weiss*

PRO 37: 5th International RILEM Conference on Cracking in Pavements—Mitigation, Risk Assessment and Prevention (ISBN: 2-912143-47-0; e-ISBN: 2912143764); *Eds. C. Petit, I. Al-Qadi and A. Millien*

PRO 38: 3rd International RILEM Workshop on Testing and Modelling the Chloride Ingress into Concrete (ISBN: 2-912143-48-9; e-ISBN: 2912143578); *Eds. C. Andrade and J. Kropp*

PRO 39: 6th International RILEM Symposium on Fibre-Reinforced Concretes—BEFIB 2004 (ISBN: 2-912143-51-9; e-ISBN: 2912143748); *Eds. M. Di Prisco, R. Felicetti and G. A. Plizzari*

PRO 40: International RILEM Conference on the Use of Recycled Materials in Buildings and Structures (ISBN: 2-912143-52-7; e-ISBN: 2912143756); *Eds. E. Vázquez, Ch. F. Hendriks and G. M. T. Janssen*

PRO 41: RILEM International Symposium on Environment-Conscious Materials and Systems for Sustainable Development (ISBN: 2-912143-55-1; e-ISBN: 2912143640); *Eds. N. Kashino and Y. Ohama*

PRO 42: SCC'2005—China: 1st International Symposium on Design, Performance and Use of Self-Consolidating Concrete (ISBN: 2-912143-61-6; e-ISBN: 2912143624); *Eds. Zhiwu Yu, Caijun Shi, Kamal Henri Khayat and Youjun Xie*

PRO 43: International RILEM Workshop on Bonded Concrete Overlays (e-ISBN: 2-912143-83-7); *Eds. J. L. Granju and J. Silfwerbrand*

PRO 44: 2nd International RILEM Workshop on Microbial Impacts on Building Materials (CD11) (e-ISBN: 2-912143-84-5); *Ed. M. Ribas Silva*

PRO 45: 2nd International Symposium on Nanotechnology in Construction, Bilbao (ISBN: 2-912143-87-X; e-ISBN: 2912143888); *Eds. Peter J. M. Bartos, Yolanda de Miguel and Antonio Porro*

PRO 46: Concrete Life'06—International RILEM-JCI Seminar on Concrete Durability and Service Life Planning: Curing, Crack Control, Performance in Harsh Environments (ISBN: 2-912143-89-6; e-ISBN: 291214390X); *Ed. K. Kovler*

PRO 47: International RILEM Workshop on Performance Based Evaluation and Indicators for Concrete Durability (ISBN: 978-2-912143-95-2; e-ISBN: 9782912143969); *Eds. V. Baroghel-Bouny, C. Andrade, R. Torrent and K. Scrivener*

PRO 48: 1st International RILEM Symposium on Advances in Concrete through Science and Engineering (e-ISBN: 2-912143-92-6); *Eds. J. Weiss, K. Kovler, J. Marchand, and S. Mindess*

PRO 49: International RILEM Workshop on High Performance Fiber Reinforced Cementitious Composites in Structural Applications (ISBN: 2-912143-93-4; e-ISBN: 2912143942); *Eds. G. Fischer and V. C. Li*

PRO 50: 1st International RILEM Symposium on Textile Reinforced Concrete (ISBN: 2-912143-97-7; e-ISBN: 2351580087); *Eds. Josef Hegger, Wolfgang Brameshuber and Norbert Will*

PRO 51: 2nd International Symposium on Advances in Concrete through Science and Engineering (ISBN: 2-35158-003-6; e-ISBN: 2-35158-002-8); *Eds. J. Marchand, B. Bissonnette, R. Gagné, M. Jolin and F. Paradis*

PRO 52: Volume Changes of Hardening Concrete: Testing and Mitigation (ISBN: 2-35158-004-4; e-ISBN: 2-35158-005-2); *Eds. O. M. Jensen, P. Lura and K. Kovler*

PRO 53: High Performance Fiber Reinforced Cement Composites—HPFRCC5 (ISBN: 978-2-35158-046-2; e-ISBN: 978-2-35158-089-9); *Eds. H. W. Reinhardt and A. E. Naaman*

PRO 54: 5th International RILEM Symposium on Self-Compacting Concrete (ISBN: 978-2-35158-047-9; e-ISBN: 978-2-35158-088-2); *Eds. G. De Schutter and V. Boel*

PRO 55: International RILEM Symposium Photocatalysis, Environment and Construction Materials (ISBN: 978-2-35158-056-1; e-ISBN: 978-2-35158-057-8); *Eds. P. Baglioni and L. Cassar*

PRO 56: International RILEM Workshop on Integral Service Life Modelling of Concrete Structures (ISBN 978-2-35158-058-5; e-ISBN: 978-2-35158-090-5); *Eds. R. M. Ferreira, J. Gulikers and C. Andrade*

PRO 57: RILEM Workshop on Performance of cement-based materials in aggressive aqueous environments (e-ISBN: 978-2-35158-059-2); *Ed. N. De Belie*

PRO 58: International RILEM Symposium on Concrete Modelling—CONMOD'08 (ISBN: 978-2-35158-060-8; e-ISBN: 978-2-35158-076-9); *Eds. E. Schlangen and G. De Schutter*

PRO 59: International RILEM Conference on On Site Assessment of Concrete, Masonry and Timber Structures—SACoMaTiS 2008 (ISBN set: 978-2-35158-061-5; e-ISBN: 978-2-35158-075-2); *Eds. L. Binda, M. di Prisco and R. Felicetti*

PRO 60: Seventh RILEM International Symposium on Fibre Reinforced Concrete: Design and Applications—BEFIB 2008 (ISBN: 978-2-35158-064-6; e-ISBN: 978-2-35158-086-8); *Ed. R. Gettu*

PRO 61: 1st International Conference on Microstructure Related Durability of Cementitious Composites 2 vol., (ISBN: 978-2-35158-065-3; e-ISBN: 978-2-35158-084-4); *Eds. W. Sun, K. van Breugel, C. Miao, G. Ye and H. Chen*

PRO 62: NSF/ RILEM Workshop: In-situ Evaluation of Historic Wood and Masonry Structures (e-ISBN: 978-2-35158-068-4); *Eds. B. Kasal, R. Anthony and M. Drdácký*

PRO 63: Concrete in Aggressive Aqueous Environments: Performance, Testing and Modelling, 2 vol., (ISBN: 978-2-35158-071-4; e-ISBN: 978-2-35158-082-0); *Eds. M. G. Alexander and A. Bertron*

PRO 64: Long Term Performance of Cementitious Barriers and Reinforced Concrete in Nuclear Power Plants and Waste Management—NUCPERF 2009 (ISBN: 978-2-35158-072-1; e-ISBN: 978-2-35158-087-5); *Eds. V. L'Hostis, R. Gens and C. Gallé*

PRO 65: Design Performance and Use of Self-consolidating Concrete—SCC'2009 (ISBN: 978-2-35158-073-8; e-ISBN: 978-2-35158-093-6); *Eds. C. Shi, Z. Yu, K. H. Khayat and P. Yan*

PRO 66: 2nd International RILEM Workshop on Concrete Durability and Service Life Planning—ConcreteLife'09 (ISBN: 978-2-35158-074-5; ISBN: 978-2-35158-074-5); *Ed. K. Kovler*

PRO 67: Repairs Mortars for Historic Masonry (e-ISBN: 978-2-35158-083-7); *Ed. C. Groot*

PRO 68: Proceedings of the 3rd International RILEM Symposium on ‘Rheology of Cement Suspensions such as Fresh Concrete (ISBN 978-2-35158-091-2; e-ISBN: 978-2-35158-092-9); *Eds. O. H. Wallevik, S. Kubens and S. Oesterheld*

PRO 69: 3rd International PhD Student Workshop on ‘Modelling the Durability of Reinforced Concrete (ISBN: 978-2-35158-095-0); *Eds. R. M. Ferreira, J. Gulikers and C. Andrade*

PRO 70: 2nd International Conference on ‘Service Life Design for Infrastructure’ (ISBN set: 978-2-35158-096-7, e-ISBN: 978-2-35158-097-4); *Eds. K. van Breugel, G. Ye and Y. Yuan*

PRO 71: Advances in Civil Engineering Materials—The 50-year Teaching Anniversary of Prof. Sun Wei’ (ISBN: 978-2-35158-098-1; e-ISBN: 978-2-35158-099-8); *Eds. C. Miao, G. Ye and H. Chen*

PRO 72: First International Conference on ‘Advances in Chemically-Activated Materials—CAM’2010’ (2010), 264 pp., ISBN: 978-2-35158-101-8; e-ISBN: 978-2-35158-115-5; *Eds. Caijun Shi and Xiaodong Shen*

PRO 73: 2nd International Conference on ‘Waste Engineering and Management—ICWEM 2010’ (2010), 894 pp., ISBN: 978-2-35158-102-5; e-ISBN: 978-2-35158-103-2, *Eds. J. Zh. Xiao, Y. Zhang, M. S. Cheung and R. Chu*

PRO 74: International RILEM Conference on ‘Use of Superabsorbent Polymers and Other New Additives in Concrete’ (2010) 374 pp., ISBN: 978-2-35158-104-9; e-ISBN: 978-2-35158-105-6; *Eds. O.M. Jensen, M.T. Hasholt, and S. Laustsen*

PRO 75: International Conference on ‘Material Science—2nd ICTRC—Textile Reinforced Concrete—Theme 1’ (2010) 436 pp., ISBN: 978-2-35158-106-3; e-ISBN: 978-2-35158-107-0; *Ed. W. Brameshuber*

PRO 76: International Conference on ‘Material Science—HetMat—Modelling of Heterogeneous Materials—Theme 2’ (2010) 255 pp., ISBN: 978-2-35158-108-7; e-ISBN: 978-2-35158-109-4; *Ed. W. Brameshuber*

PRO 77: International Conference on ‘Material Science—AdIPoC—Additions Improving Properties of Concrete—Theme 3’ (2010) 459 pp., ISBN: 978-2-35158-110-0; e-ISBN: 978-2-35158-111-7; *Ed. W. Brameshuber*

PRO 78: 2nd Historic Mortars Conference and RILEM TC 203-RHM Final Workshop—HMC2010 (2010) 1416 pp., e-ISBN: 978-2-35158-112-4; *Eds. J. Válek, C. Groot and J. J. Hughes*

PRO 79: International RILEM Conference on Advances in Construction Materials Through Science and Engineering (2011) 213 pp., ISBN: 978-2-35158-116-2, e-ISBN: 978-2-35158-117-9; *Eds. Christopher Leung and K.T. Wan*

PRO 80: 2nd International RILEM Conference on Concrete Spalling due to Fire Exposure (2011) 453 pp., ISBN: 978-2-35158-118-6; e-ISBN: 978-2-35158-119-3; *Eds. E.A.B. Koenders and F. Dehn*

PRO 81: 2nd International RILEM Conference on Strain Hardening Cementitious Composites (SHCC2-Rio) (2011) 451 pp., ISBN: 978-2-35158-120-9; e-ISBN: 978-2-35158-121-6; *Eds. R.D. Toledo Filho, F.A. Silva, E.A.B. Koenders and E.M.R. Fairbairn*

PRO 82: 2nd International RILEM Conference on Progress of Recycling in the Built Environment (2011) 507 pp., e-ISBN: 978-2-35158-122-3; *Eds. V.M. John, E. Vazquez, S.C. Angulo and C. Ulsen*

PRO 83: 2nd International Conference on Microstructural-related Durability of Cementitious Composites (2012) 250 pp., ISBN: 978-2-35158-129-2; e-ISBN: 978-2-35158-123-0; *Eds. G. Ye, K. van Breugel, W. Sun and C. Miao*

PRO 84: CONSEC13—Seventh International Conference on Concrete under Severe Conditions—Environment and Loading (2013) 1930 pp., ISBN: 978-2-35158-124-7; e-ISBN: 978-2- 35158-134-6; *Eds. Z.J. Li, W. Sun, C.W. Miao, K. Sakai, O.E. Gjorv and N. Banthia*

PRO 85: RILEM-JCI International Workshop on Crack Control of Mass Concrete and Related issues concerning Early-Age of Concrete Structures—ConCrack 3—Control of Cracking in Concrete Structures 3 (2012) 237 pp., ISBN: 978-2-35158-125-4; e-ISBN: 978-2-35158-126-1; *Eds. F. Toutlemonde and J.-M. Torrenti*

PRO 86: International Symposium on Life Cycle Assessment and Construction (2012) 414 pp., ISBN: 978-2-35158-127-8, e-ISBN: 978-2-35158-128-5; *Eds. A. Ventura and C. de la Roche*

PRO 87: UHPFRC 2013—RILEM-fib-AFGC International Symposium on Ultra-High Performance Fibre-Reinforced Concrete (2013), ISBN: 978-2-35158-130-8, e-ISBN: 978-2-35158-131-5; *Eds. F. Toutlemonde*

PRO 88: 8th RILEM International Symposium on Fibre Reinforced Concrete (2012) 344 pp., ISBN: 978-2-35158-132-2, e-ISBN: 978-2-35158-133-9; *Eds. Joaquim A.O. Barros*

PRO 89: RILEM International workshop on performance-based specification and control of concrete durability (2014) 678 pp., ISBN: 978-2-35158-135-3, e-ISBN: 978-2-35158-136-0; *Eds. D. Bjegović, H. Beushausen and M. Serdar*

PRO 90: 7th RILEM International Conference on Self-Compacting Concrete and of the 1st RILEM International Conference on Rheology and Processing of Construction Materials (2013) 396 pp., ISBN: 978-2-35158-137-7, e-ISBN: 978-2-35158-138-4; *Eds. Nicolas Roussel and Hela Bessaies-Bey*

PRO 91: CONMOD 2014—RILEM International Symposium on Concrete Modelling (2014), ISBN: 978-2-35158-139-1; e-ISBN: 978-2-35158-140-7; *Eds. Kefei Li, Peiyu Yan and Rongwei Yang*

PRO 92: CAM 2014—2nd International Conference on advances in chemically-activated materials (2014) 392 pp., ISBN: 978-2-35158-141-4; e-ISBN: 978-2-35158-142-1; *Eds. Caijun Shi and Xiadong Shen*

PRO 93: SCC 2014—3rd International Symposium on Design, Performance and Use of Self-Consolidating Concrete (2014) 438 pp., ISBN: 978-2-35158-143-8; e-ISBN: 978-2-35158-144-5; *Eds. Caijun Shi, Zhihua Ou and Kamal H. Khayat*

PRO 94 (online version): HPFRCC-7—7th RILEM conference on High performance fiber reinforced cement composites (2015), e-ISBN: 978-2-35158-146-9; *Eds. H.W. Reinhardt, G.J. Parra-Montesinos and H. Garrecht*

PRO 95: International RILEM Conference on Application of superabsorbent polymers and other new admixtures in concrete construction (2014), ISBN: 978-2-35158-147-6; e-ISBN: 978-2-35158-148-3; *Eds. Viktor Mechtcherine and Christof Schroefl*

PRO 96 (online version): XIII DBMC: XIII International Conference on Durability of Building Materials and Components (2015), e-ISBN: 978-2-35158-149-0; *Eds. M. Quattrone and V.M. John*

PRO 97: SHCC3—3rd International RILEM Conference on Strain Hardening Cementitious Composites (2014), ISBN: 978-2-35158-150-6; e-ISBN: 978-2-35158-151-3; *Eds. E. Schlangen, M.G. Sierra Beltran, M. Lukovic and G. Ye*

PRO 98: FERRO-11—11th International Symposium on Ferrocement and 3rd ICTRC—International Conference on Textile Reinforced Concrete (2015), ISBN: 978-2-35158-152-0; e-ISBN: 978-2-35158-153-7; *Ed. W. Brameshuber*

PRO 99 (online version): ICBBM 2015—1st International Conference on Bio-Based Building Materials (2015), e-ISBN: 978-2-35158-154-4; *Eds. S. Amziane and M. Sonebi*

PRO 100: SCC16—RILEM Self-Consolidating Concrete Conference (2016), ISBN: 978-2-35158-156-8; e-ISBN: 978-2-35158-157-5; *Ed. Kamal H. Kayat*

PRO 101 (online version): III Progress of Recycling in the Built Environment (2015), e-ISBN: 978-2-35158-158-2; *Eds I. Martins, C. Ulsen and S. C. Angulo*

PRO 102 (online version): RILEM Conference on Microorganisms-Cementitious Materials Interactions (2016), e-ISBN: 978-2-35158-160-5; *Eds. Alexandra Bertron, Henk Jonkers and Virginie Wiktor*

PRO 103 (online version): ACESC'16—Advances in Civil Engineering and Sustainable Construction (2016), e-ISBN: 978-2-35158-161-2; *Eds. T.Ch. Madhavi, G. Prabhakar, Santhosh Ram and P.M. Rameshwaran*

PRO 104 (online version): SSCS'2015—Numerical Modeling—Strategies for Sustainable Concrete Structures (2015), e-ISBN: 978-2-35158-162-9

PRO 105: 1st International Conference on UHPC Materials and Structures (2016), ISBN: 978-2-35158-164-3; e-ISBN: 978-2-35158-165-0

PRO 106: AFGC-ACI-fib-RILEM International Conference on Ultra-High-Performance Fibre-Reinforced Concrete—UHPFRC 2017 (2017), ISBN: 978-2-35158-166-7; e-ISBN: 978-2-35158-167-4; *Eds. François Toutlemonde and Jacques Resplendino*

PRO 107 (online version): XIV DBMC—14th International Conference on Durability of Building Materials and Components (2017), e-ISBN: 978-2-35158-159-9; *Eds. Geert De Schutter, Nele De Belie, Arnold Janssens and Nathan Van Den Bossche*

PRO 108: MSSCE 2016—Innovation of Teaching in Materials and Structures (2016), ISBN: 978-2-35158-178-0; e-ISBN: 978-2-35158-179-7; *Ed. Per Goltermann*

PRO 109 (2 volumes): MSSCE 2016—Service Life of Cement-Based Materials and Structures (2016), ISBN Vol. 1: 978-2-35158-170-4; Vol. 2: 978-2-35158-171-4; Set Vol. 1&2: 978-2-35158-172-8; e-ISBN : 978-2-35158-173-5; *Eds. Miguel Azenha, Ivan Gabrijel, Dirk Schlicke, Terje Kanstad and Ole Mejlhede Jensen*

PRO 110: MSSCE 2016—Historical Masonry (2016), ISBN: 978-2-35158-178-0; e-ISBN: 978-2-35158-179-7; *Eds. Inge Rörig-Dalgaard and Ioannis Ioannou*

PRO 111: MSSCE 2016—Electrochemistry in Civil Engineering (2016); ISBN: 978-2-35158-176-6; e-ISBN: 978-2-35158-177-3; *Ed. Lisbeth M. Ottosen*

PRO 112: MSSCE 2016—Moisture in Materials and Structures (2016), ISBN: 978-2-35158-178-0; e-ISBN: 978-2-35158-179-7; *Eds. Kurt Kielsgaard Hansen, Carsten Rode and Lars-Olof Nilsson*

PRO 113: MSSCE 2016—Concrete with Supplementary Cementitious Materials (2016), ISBN: 978-2-35158-178-0; e-ISBN: 978-2-35158-179-7; *Eds. Ole Mejlhede Jensen, Konstantin Kovler and Nele De Belie*

PRO 114: MSSCE 2016—Frost Action in Concrete (2016), ISBN: 978-2-35158-182-7; e-ISBN: 978-2-35158-183-4; *Eds. Marianne Tange Hasholt, Katja Fridh and R. Doug Hooton*

PRO 115: MSSCE 2016—Fresh Concrete (2016), ISBN: 978-2-35158-184-1; e-ISBN: 978-2-35158-185-8; *Eds. Lars N. Thrane, Claus Pade, Oldrich Svec and Nicolas Roussel*

PRO 116: BEFIB 2016—9th RILEM International Symposium on Fiber Reinforced Concrete (2016), ISBN: 978-2-35158-187-2; e-ISBN: 978-2-35158-186-5; *Eds. N. Banthia, M. di Prisco and S. Soleimani-Dashtaki*

PRO 117: 3rd International RILEM Conference on Microstructure Related Durability of Cementitious Composites (2016), ISBN: 978-2-35158-188-9; e-ISBN: 978-2-35158-189-6; *Eds. Changwen Miao, Wei Sun, Jiaping Liu, Huisu Chen, Guang Ye and Klaas van Breugel*

PRO 118 (4 volumes): International Conference on Advances in Construction Materials and Systems (2017), ISBN Set: 978-2-35158-190-2; Vol. 1: 978-2-35158-193-3; Vol. 2: 978-2-35158-194-0; Vol. 3: ISBN:978-2-35158-195-7; Vol. 4: ISBN:978-2-35158-196-4; e-ISBN: 978-2-35158-191-9; *Ed. Manu Santhanam*

PRO 119 (online version): ICBBM 2017—Second International RILEM Conference on Bio-based Building Materials, (2017), e-ISBN: 978-2-35158-192-6; *Ed. Sofiane Amziane*

PRO 120 (2 volumes): EAC-02—2nd International RILEM/COST Conference on Early Age Cracking and Serviceability in Cement-based Materials and Structures, (2017), Vol. 1: 978-2-35158-199-5, Vol. 2: 978-2-35158-200-8, Set: 978-2-35158-197-1, e-ISBN: 978-2-35158-198-8; *Eds. Stéphanie Staquet and Dimitrios Aggelis*

PRO 121 (2 volumes): SynerCrete18: Interdisciplinary Approaches for Cement-based Materials and Structural Concrete: Synergizing Expertise and Bridging Scales of Space and Time, (2018), Set: 978-2-35158-202-2, Vol.1: 978-2-35158-211-4, Vol.2: 978-2-35158-212-1, e-ISBN: 978-2-35158-203-9; *Eds. Miguel Azenha, Dirk Schlicke, Farid Benboudjema, Agnieszka Knoppik*

PRO 122: SCC'2018 China—Fourth International Symposium on Design, Performance and Use of Self-Consolidating Concrete, (2018), ISBN: 978-2-35158-204-6, e-ISBN: 978-2-35158-205-3; *Eds. C. Shi, Z. Zhang, K. H. Khayat*

PRO 123: Final Conference of RILEM TC 253-MCI: Microorganisms-Cementitious Materials Interactions (2018), Set: 978-2-35158-207-7, Vol.1: 978-2-35158-209-1, Vol.2: 978-2-35158-210-7, e-ISBN: 978-2-35158-206-0; *Ed. Alexandra Bertron*

PRO 124 (online version): Fourth International Conference Progress of Recycling in the Built Environment (2018), e-ISBN: 978-2-35158-208-4; *Eds. Isabel M. Martins, Carina Ulsen, Yury Villagran*

PRO 125 (online version): SLD4—4th International Conference on Service Life Design for Infrastructures (2018), e-ISBN: 978-2-35158-213-8; *Eds. Guang Ye, Yong Yuan, Claudia Romero Rodriguez, Hongzhi Zhang, Branko Savija*

PRO 126: Workshop on Concrete Modelling and Material Behaviour in honor of Professor Klaas van Breugel (2018), ISBN: 978-2-35158-214-5, e-ISBN: 978-2-35158-215-2; *Ed. Guang Ye*

PRO 127 (online version): CONMOD2018—Symposium on Concrete Modelling (2018), e-ISBN: 978-2-35158-216-9; *Eds. Erik Schlangen, Geert de Schutter, Branko Savija, Hongzhi Zhang, Claudia Romero Rodriguez*

PRO 128: SMSS2019—International Conference on Sustainable Materials, Systems and Structures (2019), ISBN: 978-2-35158-217-6, e-ISBN: 978-2-35158-218-3

PRO 129: 2nd International Conference on UHPC Materials and Structures (UHPC2018-China), ISBN: 978-2-35158-219-0, e-ISBN: 978-2-35158-220-6

PRO 130: 5th Historic Mortars Conference (2019), ISBN: 978-2-35158-221-3, e-ISBN: 978-2-35158-222-0; *Eds. José Ignacio Álvarez, José María Fernández, Íñigo Navarro, Adrián Durán, Rafael Sirera*

PRO 131 (online version): 3rd International Conference on Bio-Based Building Materials (ICBBM2019), e-ISBN: 978-2-35158-229-9; *Eds. Mohammed Sonebi, Sofiane Amziane, Jonathan Page*

PRO 132: IRWRMC'18—International RILEM Workshop on Rheological Measurements of Cement-based Materials (2018), ISBN: 978-2-35158-230-5, e-ISBN: 978-2-35158-231-2; *Eds. Chafika Djelal, Yannick Vanhove*

PRO 133 (online version): CO2STO2019—International Workshop CO2 Storage in Concrete (2019), e-ISBN: 978-2-35158-232-9; *Eds. Assia Djerbi, Othman Omikrine-Metalssi, Teddy Fen-Chong*

PRO 134: 3rd ACF/HNU International Conference on UHPC Materials and Structures—UHPC'2020, ISBN: 978-2-35158-233-6, e-ISBN: 978-2-35158-234-3; *Eds.Caijun Shi & Jiaping Liu*

PRO 135: Fourth International Conference on Chemically Activated Materials (CAM2021), ISBN: 978-2-35158-235-0, e-ISBN: 978-2-35158-236-7; *Eds. Caijun Shi & Xiang Hu*

RILEM Reports (REP)

Report 19: Considerations for Use in Managing the Aging of Nuclear Power Plant Concrete Structures (ISBN: 2-912143-07-1); *Ed. D. J. Naus*

Report 20: Engineering and Transport Properties of the Interfacial Transition Zone in Cementitious Composites (ISBN: 2-912143-08-X); *Eds. M. G. Alexander, G. Arliguie, G. Ballivy, A. Bentur and J. Marchand*

Report 21: Durability of Building Sealants (ISBN: 2-912143-12-8); *Ed. A. T. Wolf*

Report 22: Sustainable Raw Materials—Construction and Demolition Waste (ISBN: 2-912143-17-9); *Eds. C. F. Hendriks and H. S. Pietersen*

Report 23: Self-Compacting Concrete state-of-the-art report (ISBN: 2-912143-23-3); *Eds. Å. Skarendahl and Ö. Petersson*

Report 24: Workability and Rheology of Fresh Concrete: Compendium of Tests (ISBN: 2-912143-32-2); *Eds. P. J. M. Bartos, M. Sonebi and A. K. Tamimi*

Report 25: Early Age Cracking in Cementitious Systems (ISBN: 2-912143-33-0); *Ed. A. Bentur*

Report 26: Towards Sustainable Roofing (Joint Committee CIB/RILEM) (CD 07) (e-ISBN 978-2-912143-65-5); *Eds. Thomas W. Hutchinson and Keith Roberts*

Report 27: Condition Assessment of Roofs (Joint Committee CIB/RILEM) (CD 08) (e-ISBN 978-2-912143-66-2); *Ed. CIB W 83/RILEM TC166-RMS*

Report 28: Final report of RILEM TC 167-COM ‘Characterisation of Old Mortars with Respect to Their Repair (ISBN: 978-2-912143-56-3); *Eds. C. Groot, G. Ashall and J. Hughes*

Report 29: Pavement Performance Prediction and Evaluation (PPPE): Interlaboratory Tests (e-ISBN: 2-912143-68-3); *Eds. M. Partl and H. Piber*

Report 30: Final Report of RILEM TC 198-URM ‘Use of Recycled Materials’ (ISBN: 2-912143-82-9; e-ISBN: 2-912143-69-1); *Eds. Ch. F. Hendriks, G. M. T. Janssen and E. Vázquez*

Report 31: Final Report of RILEM TC 185-ATC ‘Advanced testing of cement-based materials during setting and hardening’ (ISBN: 2-912143-81-0; e-ISBN: 2-912143-70-5); *Eds. H. W. Reinhardt and C. U. Grosse*

Report 32: Probabilistic Assessment of Existing Structures. A JCSS publication (ISBN 2-912143-24-1); *Ed. D. Diamantidis*

Report 33: State-of-the-Art Report of RILEM Technical Committee TC 184-IFE ‘Industrial Floors’ (ISBN 2-35158-006-0); *Ed. P. Seidler*

Report 34: Report of RILEM Technical Committee TC 147-FMB ‘Fracture mechanics applications to anchorage and bond’ Tension of Reinforced Concrete Prisms—Round Robin Analysis and Tests on Bond (e-ISBN 2-912143-91-8); *Eds. L. Elfgren and K. Noghabai*

Report 35: Final Report of RILEM Technical Committee TC 188-CSC ‘Casting of Self Compacting Concrete’ (ISBN 2-35158-001-X; e-ISBN: 2-912143-98-5); *Eds. Å. Skarendahl and P. Billberg*

Report 36: State-of-the-Art Report of RILEM Technical Committee TC 201-TRC ‘Textile Reinforced Concrete’ (ISBN 2-912143-99-3); *Ed. W. Brameshuber*

Report 37: State-of-the-Art Report of RILEM Technical Committee TC 192-ECM ‘Environment-conscious construction materials and systems’ (ISBN: 978-2-35158-053-0); *Eds. N. Kashino, D. Van Gemert and K. Imamoto*

Report 38: State-of-the-Art Report of RILEM Technical Committee TC 205-DSC ‘Durability of Self-Compacting Concrete’ (ISBN: 978-2-35158-048-6); *Eds. G. De Schutter and K. Audenaert*

Report 39: Final Report of RILEM Technical Committee TC 187-SOC ‘Experimental determination of the stress-crack opening curve for concrete in tension’ (ISBN 978-2-35158-049-3); *Ed. J. Planas*

Report 40: State-of-the-Art Report of RILEM Technical Committee TC 189-NEC ‘Non-Destructive Evaluation of the Penetrability and Thickness of the Concrete Cover’ (ISBN 978-2-35158-054-7); *Eds. R. Torrent and L. Fernández Luco*

Report 41: State-of-the-Art Report of RILEM Technical Committee TC 196-ICC 'Internal Curing of Concrete' (ISBN 978-2-35158-009-7); *Eds. K. Kovler and O. M. Jensen*

Report 42: 'Acoustic Emission and Related Non-destructive Evaluation Techniques for Crack Detection and Damage Evaluation in Concrete'—Final Report of RILEM Technical Committee 212-ACD (e-ISBN: 978-2-35158-100-1); *Ed. M. Ohtsu*

Report 45: Repair Mortars for Historic Masonry—State-of-the-Art Report of RILEM Technical Committee TC 203-RHM (e-ISBN: 978-2-35158-163-6); *Eds. Paul Maurenbrecher and Caspar Groot*

Report 46: Surface delamination of concrete industrial ffioors and other durability related aspects guide—Report of RILEM Technical Committee TC 268-SIF (e-ISBN: 978-2-35158-201-5); *Ed. Valerie Pollet*

3D Modelling and Printing

Use of Automated Control Machining Tools for Design, Construction, and Testing with Hydraulic Physical Models

António Muralha, Sílvia Amaral, Nuno Aido, Ricardo Jónatas, Solange Mendes, José F. Melo, and Teresa Viseu

Abstract To the present day, hydraulic physical models are essential for hydraulic structures design validation and optimization. 'Traditional' modeling methods for hydraulic physical experimentation present some limitations and challenges. These have been overcome and dealt with at LNEC by adopting new constructive technologies and innovative automation methods, such as 3D printing, CNC cutting, and automatic measurement systems. These new technologies reduce the time needed to perform studies by increasing the ability for faster building, making easier any modifications of model components, and reducing construction waste upon model demolition. This work presents different studies performed at LNEC where 3D printed and CNC cut pieces were used: two 3D print pieces used in a spillway model; a large-scale 3D print of a scaled failing dam; a large head orifice spillway reproduced using CNC machining; and an entire physical model constructed fully based on new building technologies. These 'Novel' constructive technologies evidenced that they fulfill the needs of physical model studies, ensuring adequate structural behavior and appropriately reproducing the flow conditions.

A. Muralha (✉) · S. Amaral · N. Aido · R. Jónatas · J. F. Melo · T. Viseu
Laboratório Nacional de Engenharia Civil, Lisbon, Portugal
e-mail: amuralha@lnec.pt

S. Amaral
e-mail: samaral@lnec.pt

N. Aido
e-mail: npereira@lnec.pt

R. Jónatas
e-mail: rjonatas@lnec.pt

J. F. Melo
e-mail: jfmelo@lnec.pt

T. Viseu
e-mail: tviseu@lnec.pt

S. Mendes
CERIS, Instituto Superior Técnico, Lisbon, Portugal
e-mail: svmendes@lnec.pt

C. Chastre et al. (eds.), *Testing and Experimentation in Civil Engineering*,
RILEM Bookseries 41, https://doi.org/10.1007/978-3-031-29191-3_1

Keywords CNC cut · 3D printing · Automation techniques · Hydraulic physical modeling

1 Introduction

Several methodologies are used to support the design of hydraulic structures, as numerical and physical modeling, empirical tools, or in situ measurements. Although each approach encompasses its advantages and limitations, physical modeling stands out as it allows a very close representation of the complex physical processes involved in hydraulic structures flows.

In Portugal, this activity has been carried out mostly at the National Laboratory for Civil Engineering (LNEC) since 1951. Having several experimental facilities and a laboratory dedicated to the exploration of reduced hydraulic models of river structures and hydraulic works, LNEC has been playing a key role in Portuguese hydraulic engineering. The methodologies applied until recently, have efficiently enabled the analysis of design solutions for hydraulic structures, dams and for protection against erosion and floods, as well as in the study of solutions for river requalification and rehabilitation, such as fish passages or other measures.

Compared to other approaches, as numerical modeling or analytical analysis, physical modeling can be particularly expensive and time-consuming. However, it allows the simulation of particularly complex flows and their interaction with solid boundaries such as sedimentary beds, rock or hydro-mechanical equipment, or air/water interaction in free surface flows. Physical modeling is essential for the development of empirical methods, calibration and/or validation of numerical models allowing to validate studies of hydraulic structures involving complex flows.

Traditionally, this activity has been carried out by materializing the physical models by means of common civil construction materials, such as plaster, cement, mortar, reinforced concrete, and masonry, and based on molding processes involving high precision work to produce the models respecting the intended scale roughness (i.e., with very smooth surfaces). Due to its artisanal nature, this physical model's constructive way is characterized by high execution times and manufacturing costs, not allowing an optimization of the manufacturing process. It adds a growing difficulty for attracting and/or training technicians to perform the involved skilled tasks. Another drawback derives from the fact that, once the physical model studies are completed, the waste material resulting from demolition is not reusable or presents a very reduced possibility for recycling.

Considering the importance of physical modeling studies at LNEC, several steps have been taken in recent years to overcome the limitations of the 'traditional' construction and molding methods, namely by moving towards new construction technologies and innovative automation methods, such as 3D printing and computer numerical control (CNC) cutting technique. Also, the automation of measurement systems efficiency and accuracy and level of human intervention has been progressively improved, by introducing linear positioners for velocity or pressure measurements on a georeferenced point mesh.

This paper presents the recent advances in physical models' construction and testing currently being adopted at LNEC.

2 'Traditional' Constructive Methods

Physical models of hydraulic structures were traditionally built by erecting masonry and/or concrete reservoirs and filling them with sand and gravel for topography reproduction. The hydraulic structures themselves were modeled by the artisans that built plaster molds to be filled with cement mortar or resins, or sometimes, carving the complex geometries of the structures in wood (Fig. 1).

The artisanal approach normally begins with marking a reference grid on the floor, in which the projection of the model limits, involved structures' axes and terrain contour lines are drawn, Fig. 1a. Once the implantation area is duly, the confining walls of the model are erected in masonry or concrete, thus creating a reservoir.

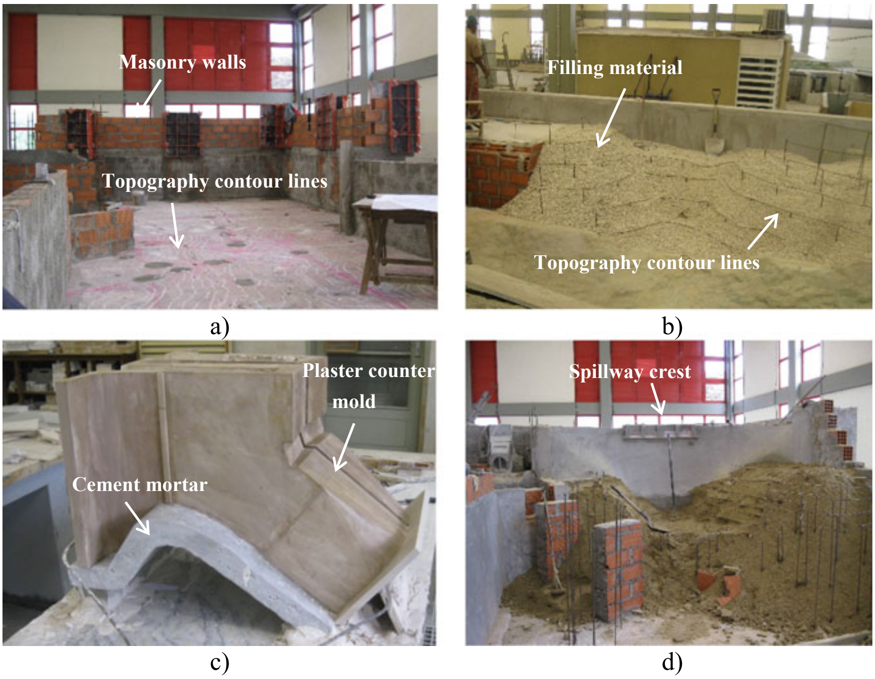

Fig. 1 Traditional construction process of different physical models at LNEC: **a** boundaries and contour lines; **b** reproduction of contour lines and filling; **c** materialization of a flood spillway; **d** spillway installation

Fig. 2 Physical model of Salamonde Dam built using the traditional method, [1]

Contour lines are materialized with small diameter steel bars (6 mm), Fig. 1b. Then, the model can be filled with gravel or sand up to the limit created by the contour lines, the surface of which is coated with cement mortar, the result representing the topography of the study area with an impervious and resistant surface to withstand the loads to perform the tests. The components that materialize the hydraulic structures are reproduced off-site using molds and counter-molds techniques, usually in cement mortar, and sometimes using resins or transparent Poly(methyl methacrylate) material, acrylic, Fig. 1c. Once the scale models of the hydraulic structures are finished, they are duly placed in the model based on previously marked reference points, Fig. 1d.

The final phase of the physical model building process involves the construction of the water barrier structure (dam, weir, levee, …) which is generally built of masonry or concrete. After completing all the construction phases described above, the final details of the physical model are carried out, involving painting, placing measurement marks, or installing walkways or structures to install measurement equipment, being then ready for the experimental works (see the final appearance of Salamonde Dam physical model built with the traditional method, Fig. 2).

The construction processes of the described physical models require significant personnel and time resources, namely for the construction, the usually needed modifications, and, upon completion of the study, demolition once the space is required for new studies. The increasing demands in terms of complexity of the physical models and decreasing deadlines to produce results have highlighted the need of using time-saving and expedited construction and molding methods to reduce the construction time, to facilitate the study of optimized or alternative solutions and also to reduce the demolition effort and waste as well as enabling reuse of materials. On the other hand, the previous traditional construction methods did not favor flow visualization, namely in tunnels or hydroelectric circuits, and did not facilitate the placement of sensors in many locations of the modeled area, having these to be foreseen during the design phase of the model. Under this context, measurements were performed mainly manually and without automation.

3 'Novel' Constructive Technologies

3.1 Framework

Considering the recent progress in materials and production processes, new solutions for the construction of physical models are becoming increasingly available. A process for identifying strategic partners with the appropriate capabilities has been initiated and a progressive introduction of new approaches and techniques for building physical models has been carried out.

The first case in which these new techniques were adopted involved the reproduction of a specific hydraulic structure by means of 3D printing, which was used as an alternative to the initial shapes of a flood spillway of Alto Tâmega Dam, [2], aiming at optimizing its hydraulic performance. It followed the integral reproduction of a complex-shaped flood spillway of Cahora Bassa Dam, [3], using transparent material by means of through computerized cutting techniques automatically controlled (CNC). More recently, models of the inlet structures of the tunnels of Plano Geral de Drenagem de Lisboa with relevant dimensions were entirely made adopting the new construction techniques, minimizing the use of brick masonry walls, with CNC machining and reproducing the hydraulic structures by combining a judicious combination of CNC machining and 3D printing.

The reproduction process of a hydraulic structure or any other part of the physical model is preceded by its detailed 3D conception in CAD, enabling a direct transfer of the model components into 3D printing or CNC cutting. Conception also involves a judicious selection of the materials, taking into account their roughness, transparency, flexibility, imperviousness and resistance to the hydraulic and mechanic actions they will be subjected to during construction and testing.

3.2 CNC Cutting—Subtracting Manufacturing

CNC machining is a subtractive manufacturing technique based on the removal of material using cutting, drilling, milling and engraving tools, respectively: knife, drill, cutter and laser. An example of the inlet structures of the tunnels of Plano Geral de Drenagem de Lisboa models whose main structures were developed based CNC machining can be found in Fig. 3. The CNC cutting machine has a minimum of two axes, x and y, as in most cutting machines, such as the film cutting machine (typically paper or vinyl) or the laser cutting and engraving machine. The CNC machine used to manufacture the hydraulic structures used in the physical models presented here has three axes (x, y, z) and a working area of 190 × 90 × 8 cm, so that it can reproduce elements using both 2D or 3D processes. In 2D machining, CAD drawings define the cutting lines and pockets into a plate with a depth defined by the operator. For the 3D case, the CAD drawing detail is fully reproduced in a block of material by the CNC.

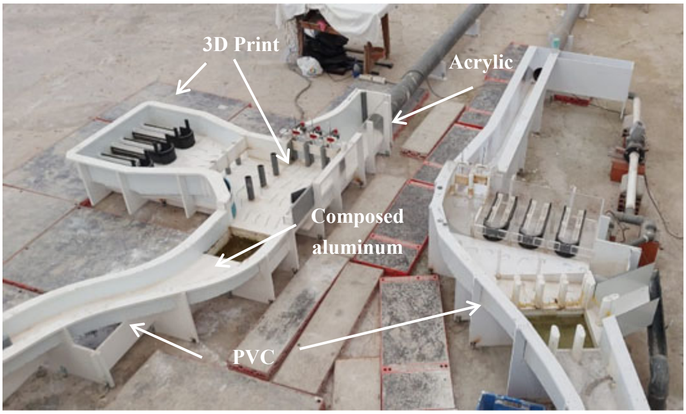

Fig. 3 Inlet structures of the tunnels of Plano Geral de Drenagem de Lisboa models obtained through CNC Machining

The preparatory work is always detailed, in both 2D or 3D machining operations, since none waives the need to obtain a 3D drawing of the element to reproduce. But the 3D machining is usually more time-consuming than the correspondent 2D because it results from successive passes of the cutting tool at several depths or dimensions of the material. For the reproduction of the hydraulic structures through this process, it is normally used acrylic and polycarbonate materials, because of their ease of use in the CNC machine, but mainly for their transparency, strength, and flexibility. The latter also presents good adequacy to mold to sharp curvatures. Expanded PVC material is also used in CNC machining because it does not absorb water, which enables its immersion for long periods. As expanded PVC behaves similarly to plywood, it can also be cut and screwed, having the advantage of being lighter (density between 0.5 and 0.7 g/cm^3) and more resistant to water. However, due to its low density (lower than that of water), it has the drawback of being subjected to water impulse when submerged, requiring a support structure to avoid unintended displacements.

The last materials that were used in CNC machining were polyethylene and high-density polystyrene, their softness enabling fast machining processes and good surface finishing. The 3D machining of this type of materials allows an easy and fast reproduction of topography in physical models. After machining all the elements composing the physical model its assembly is fast and only requires an adequate surface coating to ensure strength and water tightness during the experimental tests. Note that both polyethylene and polystyrene have low densities which is a disadvantage for the element's stability. The use of these materials is hence conditioned to the non-existence of water on their lower surface or to a proper fixation that prevents its displacement with the water impulse.

The major constraint of 3-axis CNC machining is the need to manually reposition the block of material in case machining is required on the opposite side or on the top part of the block. The use of cut tools with different diameters or specific characteristics also contributes to increasing the model manufacturing time. Intrinsic to this subtractive manufacturing technique (CNC), there is a high waste of material coming from the cutting and removal of the surplus in the slabs or blocks to be machined. Thus, when preparing the elements for CNC machining, their arrangement should be optimized to reduce material waste. Finally, due to the large diameter of the cutting tools, the reproduction of interior angles may be less accurate, which must be considered during the preparation of the workpiece and will allow complementary measures to be implemented whenever required.

3.3 3D Modeling and Printing—Additive Manufacturing

3D printing is an additive manufacturing technique with several processes available such as: Fused Filament Fabrication (FFF) which is characterized by the deposition of thermoplastic filament; Stereolithography Apparatus (SLA) which is based on the photosensitization of polymers/resins; and Selective Laser Sintering (SLS) which corresponds to the sintering of powdered material, typically polyamide or metal in the Direct Metal Laser Sintering (DMLS) variant.

3D printing allows the reproduction of practically any part or model, as complex as it may be, with the detail required for the reproduction of hydraulic structures, without requiring human intervention during the printing process, an example of a 3D printed model being presented in Fig. 4. The most time-consuming phase of the process is the preparation of 3D printing digital model, that must assure the closure of the polygon mesh.

Since the ability to 3D printing by the common FFF processes is typically limited to a 30.5 cm of side cubic volume, and the large-scale 3D printing is still very difficult and expensive, the hydraulic structure printing involves a preparatory phase to allow

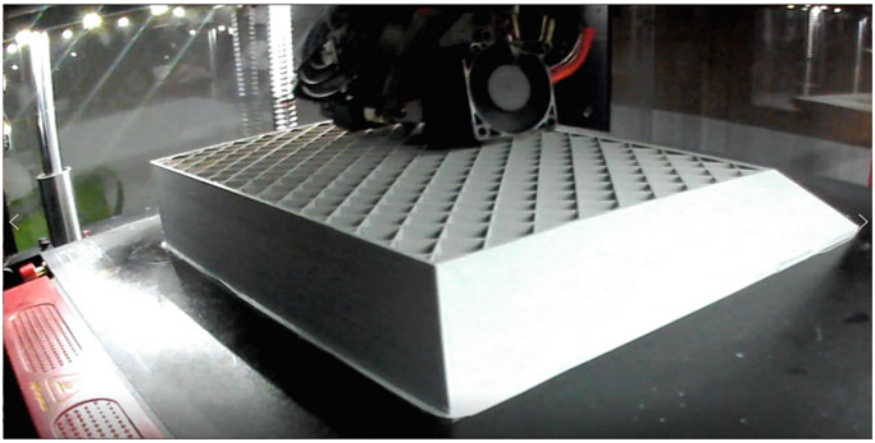

Fig. 4 3D printing through FFF process. Part of the reproduction of failed dam

fractioning of the structure to be modeled into various subsets to be separately printed and duly joined afterwards. The FFF process builds the models by superimposed layers requiring that spans and cavities be shored up with provisional support material to be removed in a finishing phase of the manufacturing process.

3D printing in the physical modeling was introduced at LNEC selecting the filament deposition technique (FFF) using thermoplastic ABS, copolymer of acrylonitrile, butadiene, and styrene. Both the FFF technique and the adopted materials met the models' requirements, namely adequate robustness, and surface smoothness, despite the unavoidable anisotropy of the surface roughness caused by the layered material deposition involved in the printing process. This feature has been overcome by polishing the surfaces whenever smoothness features are not met directly from the printing process.

3.4 Automation for Experimental Measurements and Control

Characterizing the flow conditions in physical model studies can be time-consuming. If, for example, the aim of the study is to characterize the flow at twenty different points with ten different flow conditions by taking two minutes in each data acquisition and requiring four minutes to position the probe manually, the whole process will take more than twenty hours of measurements. However, this time can be significantly reduced by using a linear positioner that allows the automatic displacement of the probes between measuring positions, has the advantage of minimizing the positioning errors between measurements and frees up the personnel that would have to be allocated for carrying out the measurements manually. If the probe is manually placed at the measuring point, the positioning errors are significantly higher than by using computer-controlled linear positioning systems with known accuracy features. The attenuation of positioning errors combined with a higher velocity of data acquisition led LNEC to adopt automatic linear positioners for this purpose. Although a wide range of this type of equipment is available on the market, they are usually quite expensive, this had led to the option of conceiving and building linear positioners for internal use, enabling this option increased flexibility to adapt this equipment to case-specific needs. The first linear positioner was built considering partial automation, i.e., including only one, then two-axis, and presently, with the acquired experience and a thoughtful dimensioning, robust three-axis linear positioners are being successfully produced and explored.

Figure 5a presents one of the first automatic positioners with a single axis developed at LNEC, which then enabled a significant evolution in flow characteristics measurements. The first positioner was built using commercially acquired parts as. Once 3D printing capability was achieved, an increased autonomy capability for producing custom-made components to be incorporated into the linear positioners was achieved. The red components of Fig. 5b are such LNEC's custom-made 3D printed elements. That brought numerous advantages to the conception and production of this equipment. Presently, they are designed in a modular way with the

a) b) c)

Fig. 5 Linear positioners: **a** one-axis model; **b** three-axis model; **c** sluice gates of Cahora Bassa spillway [3]

main purpose of simplifying their use in facilities with different characteristics and dimensions.

Automation processes are granting the access to more complex experimental setups in physical modeling, a path that LNEC is already on. Take as example the computationally controlled operation of floodgates, allowing to act on the degrees and speeds of opening and closing of the gates, Fig. 5c.

4 Examples of Application of 'Novel' Constructive Technologies

4.1 3D Printing of a Complex-Shaped Flip Bucket

The modifications on the design shapes of the Alto Tâmega Dam spillway flip bucket studied in a physical model at LNEC were accomplished by producing two 3D printed parts in ABS plastic, [2]. Given the geometric complexity of the modifications to be implemented and the incompatible deadlines associated to produce them considering the traditional method as described in Sect. 2, it was decided to resort to 3D printing for the more complex components to be then inserted in a larger and simpler component produced traditionally in cement mortar. Figure 6 shows the printed parts placed on the model, which, using this technique, significantly reduced the time needed to reproduce the changes in the outlet structure of the spillway model. During the production process of the spillway flip bucket, it was kept in mind the possibility that further changes might be required. Thus, the larger cement mortar component was conceived in such a manner that accommodating alternative 3D printed parts with different geometries would be easy and would not involve any modifications it. Additionally, in the 3D printing design phase, required features to allow the placement of measuring instruments for pressure measurements were easily included without

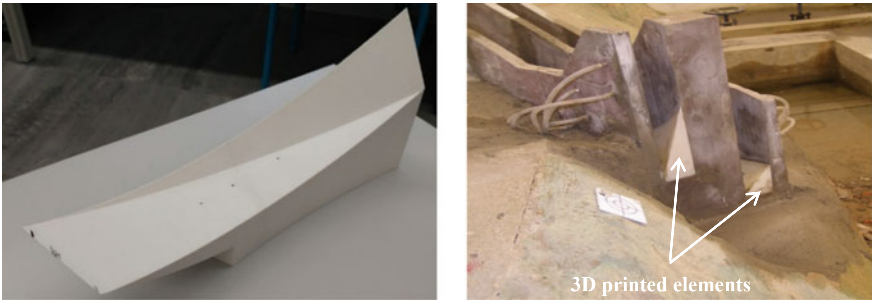

a) b)

Fig. 6 Outlet structure of Alto Tâmega Dam physical model of a flood spillway structure with the 3D printed parts included: **a** 3D printed element detail; **b** 3D printed element placed in the outlet structure, [2]

leading to additional production costs, as it is normally the case with the traditional production approaches.

During the tests, it was verified that the 3D printed elements performed well regarding the intense hydrodynamic actions of the water flow, fulfilling the function for which they were conceived.

4.2 3D Printing of a Failed Dam with PLC Material

To better study the physical processes occurring in the effluent flow below a breached dam it is necessary to freeze a time instant of the failure evolution in which several measurements can be done without the interference of the eroded material. Regarding this type of application two different types of tests were performed, for which different failed dams had to be 3D printed.

Regarding the first type, the goal was to reproduce a particular time instant of the failure in which a block of soil falls from the dam to characterize in detail the flow hydrodynamics near the breach as well as the influence block before, during and after its falls. Both the failed dam and the block of soil that falls are entirely represented through 3D printing in PLA (Fig. 7). These 3D printed structures were then placed in a rectangular channel assuring all boundaries were properly sealed before the experiments.

The second type regards the detailed measurements of the velocity field in several sections of the breach through PIV (Particles Image Velocimetry). For this goal only half of a failed dam in some time instants are necessary to be implemented in the experimental channel. Three different time instants corresponding to three half-failed dams were 3D printed in PLA with about 30 cm height. An example of one-time instant reproduced can be found in Figs. 7 and 8.

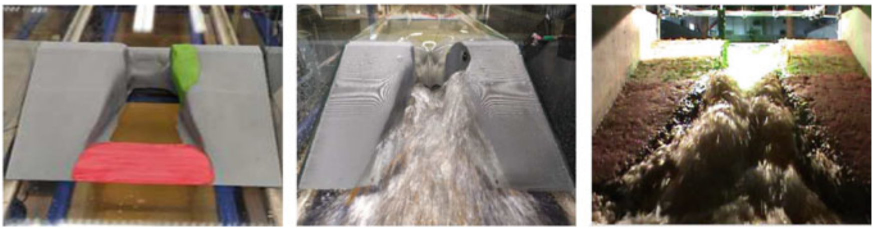

a) b) c)

Fig. 7 Frontal view of the failed dam (in grey) with the soil block (in green). Left; center—3D printed model with and with the block of soil; right—base dam breach test

a) b) c)

Fig. 8 Representation of one time instant of the failure process of an embankment dam: **a** 3D print in PLA of half model; **b** 3D print placed in the experimental channel; detail of the printed breach near the channel wall

Being able to reproduce several time instants of an embankment dam during the failure process with a non-erodible dam body allows a broad characterization of the flow in several sections with high resolution. Printing only half a dam allows optical access to the breach section through the transparent side wall of the main channel and also makes it available to describe the flow on the erosion cavities near the toe of the dam that would not be possible by other means.

4.3 CNC Machining of a Mid-Bottom Spillway

In the second phase of the implementation of novel construction processes for the physical models, a mid-bottom spillway of Cahora Bassa Dam [3], was built using 3D printing and CNC machining techniques. Thus, a transparent acrylic and polycarbonate spillway was built by CNC machining, allowing the visualization of the flow, Fig. 9a. During the preparation process, all instrumentation expected to be used was carefully considered, and the base holes required for the introduction of pressure

Fig. 9 **a** Mid-bottom flood spillway of Cahora Bassa Dam reproduced in acrylic and polycarbonate; **b** sluice gate cofferdam, [3].

transducers and piezometers were drilled into the walls of the spillway. In addition to the spillway walls the upstream flow conveyance structures were obtained by CNC machining of high-density polyurethane slices that were subsequently glued together. This procedure allowed to produce complex structures in a faster and less costly way. The elements reproduced with a polyurethane material required a waterproofing treatment after being machined, as well as a fastening system implementation to prevent them from being displaced due to the water impulse, Fig. 9b.

The physical model of this mid-bottom spillway also involved the representation of a sluice gate cofferdam, characterized by a complex truss-type structure that, if produced by traditional methods, would require a significant effort and time, incompatible with the imposed deadlines. 3D printing was selected among the available options to reproduce this port, Fig. 9b since, the structures obtained through this method present suitable strength and roughness characteristics.

As demonstrated in the previous case, after starting the tests, the used materials and processes perfectly meet the physical model requirements, both in terms of behavior of the surfaces in contact with the flow and in structural strength. It should be noted that the printed part of the spillway is subjected to considerable tensile/compression stresses during the tests, as well as to a withstanding pressure of approximately 24.5 kPa when fully closed.

4.4 Producing an Entire Physical Model Based on 'Novel' Technologies

Based on the experience that has been acquired at LNEC, physical models are now being developed with 'novel' constructive technologies. Take as example the physical models presented in Fig. 3. Its entire design was based on 'novel' technologies, namely 3D modeling, 3D printing and CNC cutting. In a further addition to these 'novel' technologies, automatic operation of floodgates is also currently being installed in the physical models' tests, Fig. 5c.

Presently, the support structures and the base of the models are being materialized with CNC cutting of PVC plates, Fig. 3. 4 mm thick composite aluminum and acrylic plates are typically used to represent the walls of the model. Small elements like piles, gates, and screeners are produced through 3D printing.

Using these techniques, the assembly of the model with the produced elements is completed in a shorter time than it would be required with the traditional construction techniques. During the flow characterization process, it is usually verified that the flow conditions can be improved by changing the geometry of some parts of the model. The 3D printing allows to test several changes in the physical model allowing to improve the flow conditions in a more efficient and faster way and hence, reducing the time required for the optimization of the hydraulic structures under study.

At the end, these 'novel' technologies translate in a faster and more natural way to perform physical modeling of hydraulic structures allowing better all involvement of participating entities in all phases of the model, namely in the design, production, assembly, initial tests, alternative solutions for improvement, and final testing.

5 Conclusions

Based on the presented examples of the application of the 'novel' construction technologies, it can be concluded that hydraulic physical models' traditional building processes can be adequately replaced by innovative approaches that take advantage of some fast-evolving technologies and materials. Consequently, the construction deadlines and the timings to introduce and test modified designs can be, respectively, shortened and optimized, allowing better and faster responses to the studies involving physical models.

3D printing technique allows the production of elements with adequate accuracy, even when high geometrical complexity is involved. The model elements, if properly conceived, produced and finished, present good characteristics both in terms of roughness, imperviousness, and mechanical resistance.

CNC machining allows to produce elements of considerable dimensions with proper accuracy and shorter timings when compared with the traditional construction processes. By means of CNC machining, the general use of transparent materials becomes much easier in situations where, adopting traditional approaches, would be very complex and/or very expensive.

The implemented workflow involving measurement automation and control systems significantly reduces the errors associated with the positioning of the measuring probes and the time needed to perform the cumbersome measurement campaigns.

The novel construction processes and materials currently in use are a considerable added value in the process of building, exploring, and demolishing physical models, which enables the continuity, whilst improving, experimental hydraulics, namely the use of physical models.

References

1. Muralha, A., Couto, L., Oliveira, M., Dias da Silva, J., Alvarez, T., Sardinha, R.: Salamonde Dam complementary spillway. Design, hydraulic model and ongoing works. In: 2nd International Dam World Conference. Lisbon (2015)
2. Muralha, A., Alves, E., Ramirez, M., Hermano, F.: Ensaios Hidráulicos em Modelo Reduzido dos Descarregadores de Cheias da Barragem de Alto Tâmega. In: 14º Congresso da Água, Évora (2018)
3. Melo, J.F., Carvalho, E.F., Meireles, I., Pinotes, P., Malauene, C.: Cahora Bassa Dam spillway rehabilitation. Emergency stoplog operation and regulating gates instrumentation. In: 88th Annual Meeting, International Commission on Large Dams and Symposium on Sustainable Development of Dams and River Basins. New Delhi, India (2021)

3D Modelling and Printing for the Design of the Wooden Structure of the Church of San Martín de Plasencia, Spain

José-Carlos Salcedo

Abstract This paper exposes the methodology with 3D modelling and 3D printing for the design of the wooden structure of the church of San Martín in Plasencia, which is rebuilt after a fire. This experimental method provides advantages both to document and to be able to recover the correct architectural form in wooden structures of the historical heritage, as well as for the structural check and construction of the wooden assemblies.

Keywords Smart technologies · 3D modelling · 3D printing · Wooden structures

1 Introduction

This work exposes the methodology with 3D modelling and 3D printing carried out for the architectural-structural design, verification and construction in a woodworking workshop of a real wooden structure in an important historical-patrimonial building.

It is the wooden roof structure of the church of San Martín, located in the historical city center of Plasencia (Cáceres, Spain), declared of cultural interest. This church suffered a major fire in August 2020, which severely damaged both its structure and the movable artistic heritage it houses.

An extraordinary project has been carried out, because reconstructions in historic buildings are not common.[1] In this case, it has been authorized thanks to the historical documentation prepared and because, although the structure did not collapse after the fire, there was an irreversible loss of wooden transversal sections, which endangered its structural safety and made it impossible to use this heritage asset.

[1] National regulations, that transposes international agreements on heritage, do not usually allow reconstructions, so as not to falsify historical authenticity, except in exceptional cases.

J.-C. Salcedo (✉)
University of Extremadura, Cáceres, Spain
e-mail: jcsalcedo@unex.es

C. Chastre et al. (eds.), *Testing and Experimentation in Civil Engineering*,
RILEM Bookseries 41, https://doi.org/10.1007/978-3-031-29191-3_2

The concept of this type of historic timber structures is often not understood, due to today's widespread use of rigid node structures (steel and concrete) for building roofs, based on trusses, space grids, rigid frames, etc., which have a different behavior.

1.1 The Wooden Structure of the San Martíns' Church

The church of San Martín has a historical structure from the thirteenth century with later reforms:

The load-bearing structure is made of granite stone masonry walls with lime mortar, with stonework carved from the same granite in the corners, buttresses, jambs and arches. With this system, three naves are formed (central nave and two side naves), the chancel and a lateral sacristy (Fig. 1). The walls where this arches are situated are 20.5 m long (behind transversal walls), 10.5 m high and only 0.55 m thick. This is very slenderness (very high in relation to its thickness), so the arches on this walls -to reach the open space of the church floor- are very vulnerable to horizontal forces out of plan. This historic building has never had vaults, its walls were not designed to withstand horizontal thrusts, only for the weight of light wooden roofs.

The three naves are covered with a wooden structure, in a classic Spanish carpentry system [1]:

- The two lateral naves (minors) are covered with a pitch by the system known as "a la molinera", by means of a framework of a single order of inclined beams bearing from wall to wall.
- The central nave is covered with an imposing cable-stayed wooden structure of pairs, knuckle ("nudillo") and row, of 8 m span, which makes it an extreme case of those described in the Spanish historical treatise by Diego López de Arenas [2], hence its structural importance. Said wooden structure has seven equal modules or "sets" and all of them, in turn, are built with only seven exactly equal pieces (it is therefore a prefabricated historical construction that is made by manufacturing

Fig. 1 General and detail images of the state after the fire of the church of San Martín (2020). *Image source* OCR-Extremadura

pieces in series to later be assembled in situ). Each set has 4 cantilever supports ("ménsulas"), 2 tie-rods (on the right side), 2 tie-rods (on the left side), 2 brackets ("estribos"), 8 × 2 pairs, 8 knuckles and a row.

1.2 Modifications in the '60 s of the Twentieth Century and Fire in 2020

However, the wooden structure described (currently existing and damaged by the fire) is not the original, because in the '60 s of the twentieth century -due to the pathology of roof dampness suffered by the building- the wood must has suffered severe damage (surely rot and attack by xylophages), so the intervention that was carried out then could nowadays be considered unfortunate and aggressive, because it structurally altered both its way of functioning and its structural design.

There is evidence of a project [3] to replace the roof structures with steel trusses, but it was not carried out at the end. Finally it was intervened in the following way:

- Replacing the wooden roof structures "a la molinera" of the lateral naves with inclined slabs of reinforced concrete joists with interaxes of small timbrel vaults built with bricks.
- The wooden structure of the central nave, which originally should have been a Mudejar structure "de lazo", was partially replaced by a new one with several structural and heritage anomalies. Therefore, at the time of carrying out the project that is currently being intervened in 2022, drafted by the architect Natalia Hernández [4], it is taking place a historic opportunity to rebuild it correctly, having the agents of the work the technical support from the University of Extremadura [5] using new 3D techniques.

Figure 1 shows two images of the timber structure of the central nave, after the fire in 2020. The structure bridges the 8.0 m separation of the two walls with arches ("arquerías") of the central nave (measured on the interior face), by means of a cable-stayed structure (called "asiento"), in which each set of structure has two tie-rods (visibles) and two brackets (embedded in the crown of the walls). To this cable-stayed structure are attached the two inclined roofs, based on pairs, knuckles ("en almizate") and a row on the top.

The fire has caused severe damage to the wooden, which are irreversibly afected and cannot be recovered.

1.3 Objective

The aim of this research work is twofold:

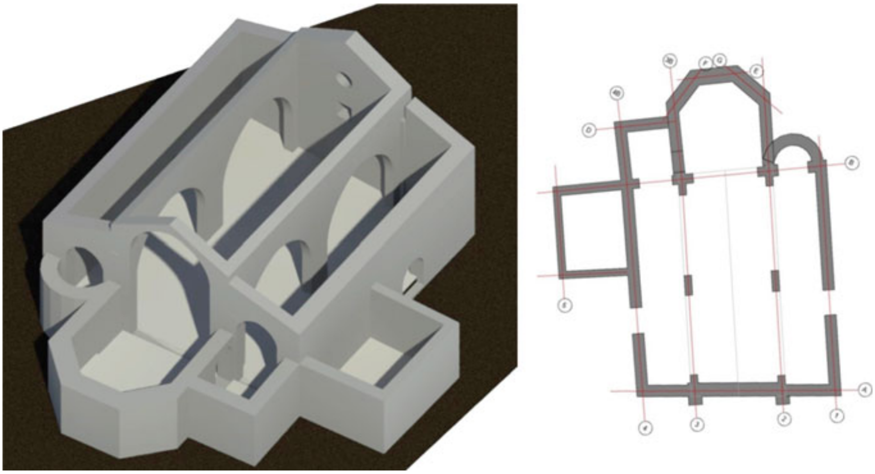

Fig. 2 On the left, Autodesk®REVIT® model of the load-bearing wall structure of St. Martín's Church. On the right, floor plan sketch

– On the one hand, to synthesize for publication the technical assistance [5] provided to the architectural project and to the restoration work [4], which has allowed: documenting the recovery of the original structural form of the truss (article 33 of the Historical Heritage Law) [7], justifying the structure that is projected [5] [4] and providing the technical data for its construction by a carpenter.
– On the other hand, to expose the used method of 3D modelling and 3D printing, which can be applied to other cases of wooden trusses.

2 Use of the 3D Model for Checking the Structural Design

2.1 Digital Model of the Supporting Structure

Figure 2 shows the digital model of the load-bearing structure of this church. In the investigation, only the wooden structure of the central nave has been treated. The vaults of the chancel and the lateral sacristy are not the object of study and therefore their lower walls are represented without the vaults that cover them. It can be appreciated, both in the 3D image and in the attached plan scheme, the extreme slenderness of the walls (thickness is one twentieth of their height) and their arches that form the central nave and are the support for the framework under study.

This geometry is characteristic of Spanish structural carpentry "de armar" [1, 2] because, thanks to the cable-stayed[2] structure, the roofs transmit to the walls

[2] For a better graphical understanding of this timber frame, consulting the works of Javier de Mingo is recommended [6].

exclusively vertical actions (weight), without thrusts. This is the structural reason why the walls can be so slender. The absence of thrust and lightness are therefore the structural basis of this system.

2.2 Detection of Previous Structural Anomalies

Apart from the damage caused by the fire, the structural anomalies that the framework of the central nave has had since the 1960s, when it was intervened, are the following:

– Small structural transversal sections, which are smaller than those of the historical treatise by López de Arenas [2]. See Table 2. They are probably due to the lack of adequate tree transversal sections at that date.
– A slope of the roofs of “cartabón de a ocho” (22.5º or 41.42%), which is not typical of a traditional cable-stayed structure of pairs, but smaller (typical of “a la molinera” roofs). It has been possible to determinate that the original cable-stayed structure had a bigger slope because the original slope (about 30º) of the gable on the façade at the foot of the church is still preserved today.
– An abnormally high position of the knuckle “nudillo” (Fig. 3): It has been assumed that by reducing the slope of the roof and consequently lowering the ridge height, it was decided to keep the horizontal plane of the knuckle at its original height so as not to cover a pre-existing arch that separates the central nave from the main chapel of the church.
– A 3 cm thick layer of cement mortar with steel wire mesh was placed on top of the roofs, following a widespread custom at that time. This is considered completely inadequate because it duplicates the dead loads to the walls that support it. In other words, the central pillars of the building are working at twice the stress originally foreseen.
– Furthermore, through pits on the walls it has been possible to know that certain connections, such as those of the tie-rods to the brackets, were made in an anomalous way, not following the classical treatise and without structural safety.

2.3 Digital and Physical Models to Justify the Optimal Structural Form

For the present research, three polylactic acid plastic (PLA) models of a set of cable stayed wooden structure have been made, following the methodology described below. The analysis of these three models has allowed to decide the most suitable architectural and structural form, recovering with objective data the original structure, as well as documenting its reconstruction.

– Model 1, of the current pathological state after the fire.

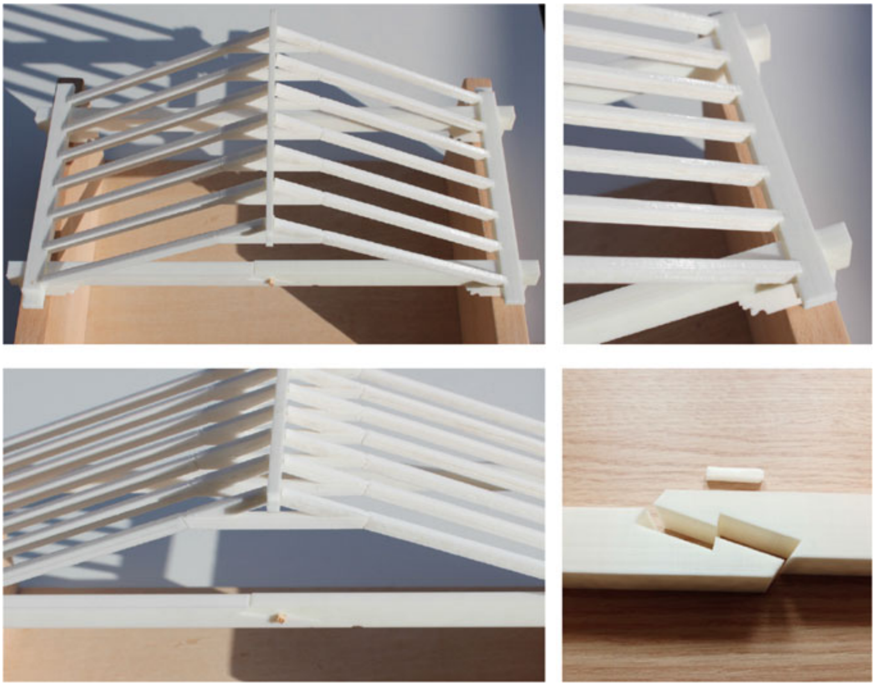

Fig. 3 General and detailed images of the realized model 2 of the structure, 3D printed at 1/33 (a complete set) and 1/10 (detail of assemblies) scales. It has the "cartabón de a ocho" slopes and the abnormally high knuckle, as it is found currently

– Model 2, from the preliminary project [4], with the same geometric pattern as the current one (slopes, knuckle position and number of pairs), but with the sections resized [5] to comply with the structural code [8, 9].
– Model 3, proposed by the technical assistance in April 2021, with the original geometric design recovered [4].

2.4 *Structural Basis*

Of the four existing essential requirements of any structure: balance, stability, strength and stiffness, the balance is the key in this type of timber cable-stayed structure, since experience shows that timber trusses do not fail due to limit strength but rather collapse due to dislocation of their parts by the assemblies, either due to poor workmanship or pathological conditions caused by fire, rot or xylophages.

All conventional analytical calculations are based on the assumption that the assemblies are correct and there are no eccentricities, but this assumption is, in practice, impossible to guarantee in the calculation of a timber structure, due to the way it is built. The currently used numerical models, based on finite elements, cannot simulate the model of a wooden structure of this type (where the pieces are insetted into each other but as spare parts), so it is convenient to complete the study by simulating the structure through scale models that replicate the real constructive behavior.

The methodology presented here has limited this problem since it provides computer files that are first materialized in a plastic model built on a reduced scale that allows the analysis of the assemblies and, subsequently, these same files are used for the material execution in the workshop of the cuts for the assemblies (by numerical control cutting techniques), eliminating the execution error.

The dimensioning of the wood elements, which for reasons of space is not explained in detail, was carried out [5] according to the Spanish structural [10, 11] and fire safety codes [12]:

– The tie-rods have been dimensioned to the axial tension produced by the horizontal thrust of the brackets. The top chords in pairs ("pares") have been dimensioned to flexo-compression.
– The knuckles ("nudillos") to compression.
– The brackets (along the walls) to the deflected bending produced by the top chords.

The critical sections (those notched by the assemblies) have been checked. And the assemblies have been previously designed following Lopez de Arenas' treatise on Spanish carpentry [2].

Structural material: following the supervision of the technical office of Regional Government (historical heritage), the owner and the project manager´s decision, was not to use laminated wood,[3] but pine sawn timber (carpentry "de lo blanco"). At the time the work was being carried out, the supply of wood for carpentry was very limited and finally the best wood that the contractor could find according to his contract is *silvestre pine* (Soria pine) which, after the controls carried out [5] corresponds to a resistant class C27.

2.5 Dimensioning and Checking of Timber Transversal Sections

In contrast to concrete structural systems, in the calculation of timber structures, the resistant sections resulting from the calculation must be checked at the end with the real available sections, which come from the dimensions (length and trunk) of the trees. In the present case, the available timber transversal-sections for testing were those shown in Table 1.

The dimensioning carried out has accredited compliance with all limit states [11] according to the evaluation of loads carried out on the basis of the Spanish Technical Code [10] and the excess in the transversal sections has been translated into

[3] The most common practice in this kind of restoration of heritage assets is to use laminated wood to allow the identification of the added elements (article 33 of the Historical Heritage Law).

Table 1 Commercially available C27 class pine wood ("pino Soria") transversal sections

Structural elements of the cable stayed wooden structure	Transversal sections	
	Before squaring	After squaring
Tie-rods ("tirantes")	25 × 30 cm	24 × 29 cm
Brackets ("estribos")	30 × 30 cm	29 × 29 cm
Top chords in pairs and knucless ("nudillos")	12 × 16 cm	11,5 × 15,5 cm
Cantilever supports ("ménsulas")	25 × 30 cm	24 × 29 cm
Supports along the walls ("soleras")	Recovered	Recovered

Table 2 Comparison of wood transversal sections

Elements of the structure	Transv. section	Treatise "Núñez de Arenas"	Model 1	Model 2	Model 3
			Current	Preliminary project	Proposed for the work
Top chords in pairs and knucless	Width (cm)	10,4	8,0	12,0	11,5
	Height (cm)	14,8	12,0	17,0	15,5
	t-FR (min)	–	–	50,0	45,0 (**)
Tie-rods	Width (cm)	20,8	18,0	24,0	24,0
	Height (cm)	29,6	25,0	34,0	29,0
	t-FR (min)	–	–	120,0	125,0
Brackets	Width (cm)	20,8	(*)	24,0	29,0
	Height (cm)	29,6	(*)	34,0	29,0
	t-FR (min)	–	–	Protected	Protected

fire resistance time (minutes for structural stability in case of fire, t-FR), calculated according to the fire safety standard [12].

Table 2 gives the sections of the three models made (compared with the sections of the treatise by López de Arenas [2] for this Plasencia´s structure with 8 m span). Note:

– That the wooden structure of the current state (damaged by the fire) has transversal sections lower than those of the historical treatise.
– That the transversal sections of model 2 (of the preliminary project) are higher than those of the current state and those of the treatise, in order to comply with the structural code and the fire standard. The calculations were made with the same geometry of the existing structure ("cartabón de a ocho").
– The verification of the available pine transversal sections in model 3 (proposed for the work and final result of the technical support carried out), after taking the decisions to recover the original slope of the roof (slope of the top chords in pairs) and to put the knuckle in its correct position.

In order for the existing sections for the pairs (12 × 16 cm before squaring, resulting in 11.5 × 15.5 cm after squaring) to comply with the calculations, it was necessary to increase the number of top chords ("pares") in the set (and their consequent reduction of the interaxis). In the existing structure (model 1) and in the preliminary project (model 2), the pairs were 50 cm apart; however, in model 3, the pairs were placed closer together, at 35 cm.

(*) They were badly executed, so they do not serve as a reference. (**) As the fire resistance time (t-FR) is 5 min less than the design time, additional measures have been proposed.

The structural advantages offered by model 3 with respect to model 2 are evident by contrasting:

– By having increased the slope of the top chords, the bending moment to which they are subjected is reduced, and the thrusts they transmit are also reduced, resulting in less tension on the tie-rods.
– As the knuckle is put at 2/3 of the height, the brackets are less stressed.
– Having reduced the interaxis of the top chords, the gravitational loads to which they are subjected are less.

In addition to the historical contributions of recovering the original architectural form, with the original roof slope and the position of the knuckle at 2/3.

2.6 Structural-Legal Justification

The structural justification of interventions in historical heritage is very complex, only for specialists. It is a legal and technical exercise. The international structural codes do not specifically contemplate these kind of wooden structures. Furthermore, as they are logically later than this historical construction, they are not of obligatory application (emanated from the principle of legal security). The Spanish Technical Code [10] has a chapter called "Annex D" that allows the qualitative and quantitative evaluation of the safety of these existing buildings.

This is why it is necessary to study in the architectural project the patrimonial incompatibilities of the regulations. In the technical assistance carried out [5], the structure has been justified following the "structural safety requirement" of art. 3 of the Ley de Ordenación de la Edificación [8], also in its development, articles 2 and 10 of part I of the CTE [9] and, only where they are applicable due to compatibility: 1-The calculation bases of DB-SE [10], 2-the actions of DB-SE-AE, 3-the limit states of DB-SE-M [11] and 4-the fire test of DB-SI [12], have been used. Eurocode-5 for the design of timber structures [13], also does not consider this kind of historical heritage.

3 Method Carried Out for 3D Modelling and 3D Printing

In the present case, for the geometrical design of the wooden structure, the starting point was the historical treatise on Spanish carpentry by López de Arenas [2].

Figure 4 shows how to draw geometrically several angles based on this treatise: starting from a circle in which a polygon is inscribed with the number of sides that gives it its name, in this way angles are formed that will be used by the carpenter for the execution of the assemblies of the wooden structure.

Figure 5 shows CAD drawings of the design of the structure in elevation-section:

(a) Alternative patterns, from the bevel-6 “cartabón de a seis” to the bevel-11 “cartabón de a once”. The two drawings in red correspond to the current state of the Plasencia timber structure (with bevel-8 “cartabón de a ocho” and anomalous knuckle above the level of an existing arch) and to the final project (which recovers the original slope of bevel-6 “cartabón de a seis” and with knuckle at 2/3 of the height).

(b) Elements of the timber structure: Tensile tie-rods, flexocompression top chords in pairs, brackets, which receive the top chords and transmit their stress to the tie-rods (working at skewed bending), knuckle at 2/3 of the height following the criteria of the Spanish timber carpentry “de Lo Blanco”, row, which braces the top chords in pairs at the ridge and cantilever supports, which keep the wooden structure elevated on the load bearing structure protecting the wood from humidity. For security reasons, the decision was taken to build the tie-rods in a single piece, without the assembly known in Spanish carpentry as “rayo de Júpiter”, to avoid the structural failure in case of imbalance.

(c) Measurements, as a result of a span of 8.30 m (at the axis of the supports in the load bearing structure of walls “soleras”) and the aforementioned angle of “cartabón de a seis” with the knuckle at 2/3.

Figure 6 shows a detail of the previous figure, which specifies the form of support of the timber structure on the walls. From this definition it is possible to draw in

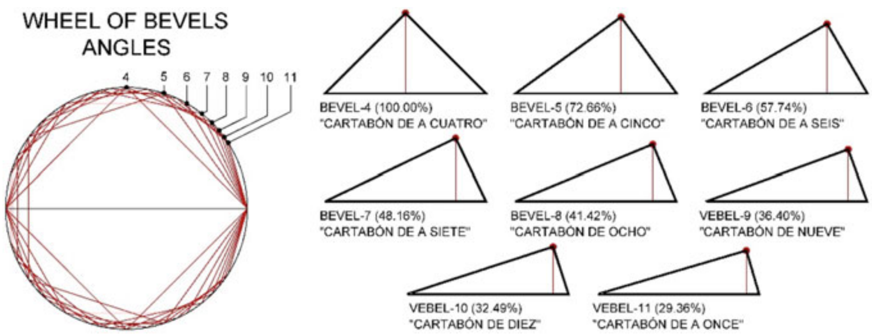

Fig. 4 Geometric pattern of various angles for the structure, from the bevel-4 “cartabón de a cuatro”, with a slope of 45º (or 100%), to the bevel-11, with a slope of 29.36% (or 16.36%)

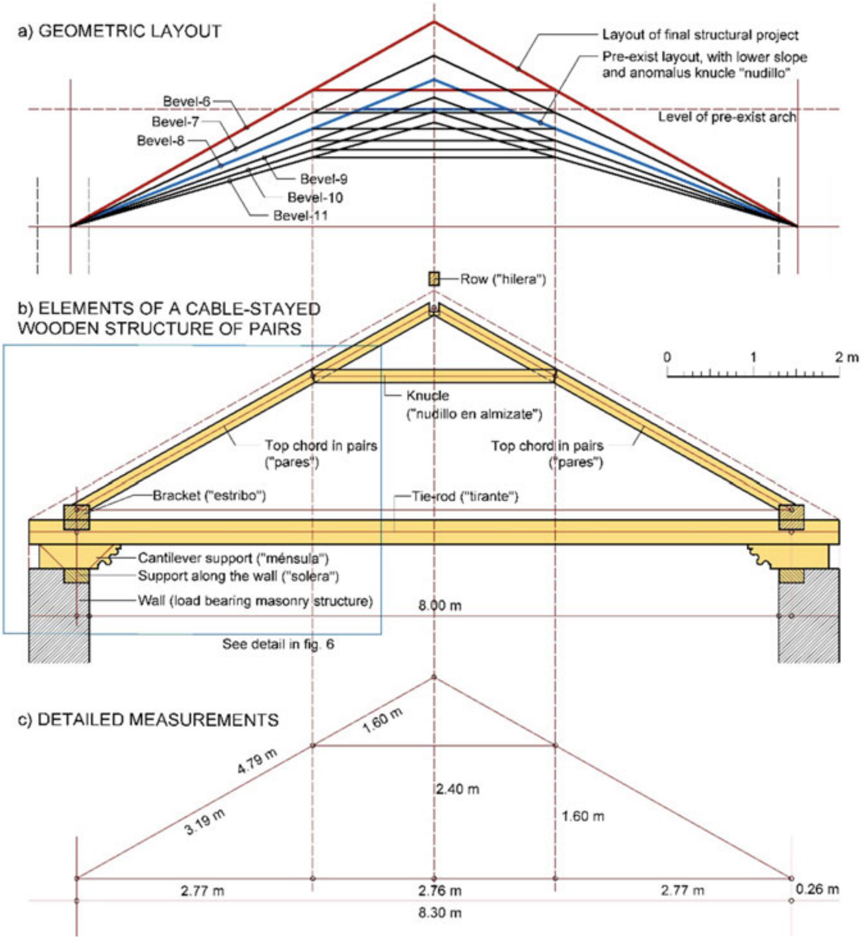

Fig. 5 Design of the wood structure: pattern, structural elements with their names and dimensions

CAD the seven pieces of the wooden structure in 3D. As can be seen, the bracket ("estribo") must be on axis with the "solera", in turn, to the internal face of the wall. The maximum end tie-rods ("cogote") that physically fits in the wall is 41 cm. This measurement must be checked with the calculation of the shear stress in this area of the tie-rods (the most critical point due to the anisotropy of the wood), in order to constructively resolve the resistance and durability of the wood.

Figure 7 shows the CAD drawing of the pieces in two dimensions and the CAD work to go from 2 to 3D, extruding the planar geometric shapes, to create the seven pieces of this wooden structure.

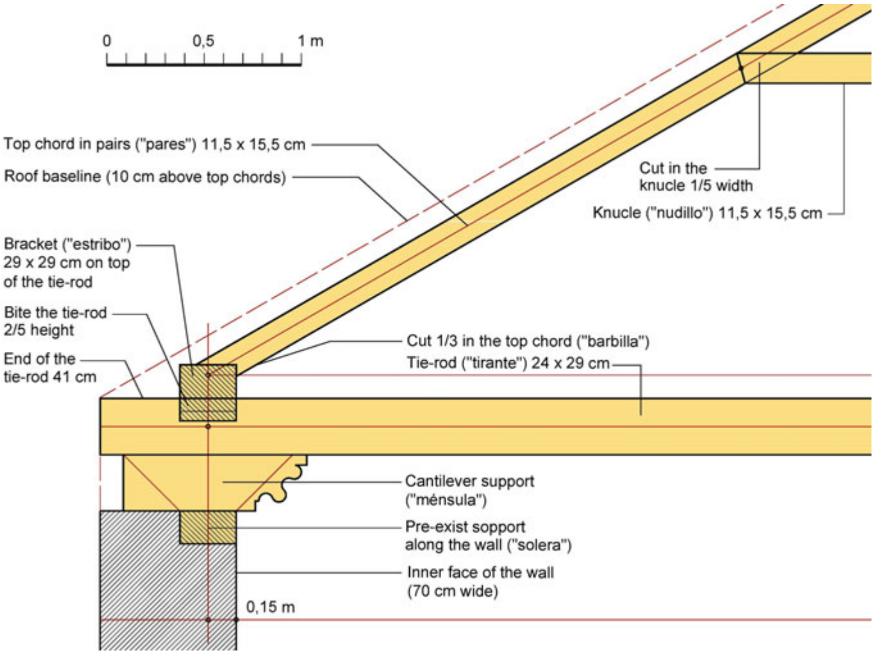

Fig. 6 Detail of the support of the structure on the bearing wall. It is important that the end of the tie-rods "cogote" be as large as possible and, in this configuration, it cannot be larger than 41 cm

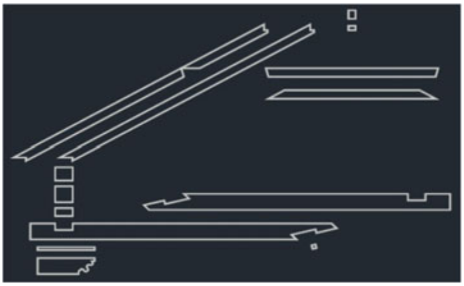

Fig. 7 Left: CAD drawing of the geometric figures for the pieces of which the structure is composed. Right: Extrusion of each of the figures that make up the pieces

Figure 8 (left) shows the seven pieces already assembled. Each of these pieces are exported to an STL format file[4] that allows both its 3D printing in plastic and its construction in a wood shop by means of industrial computerized manufacturing.

The STL files for each of the seven parts were delivered to an external company that was commissioned to "3D print" them at a scale of 1/33 for the complete model and 1/10 for the details of the assemblies, choosing white PLA plastic. Figure 3

[4] The STL file format is the industry standard data transmission format for rapid prototyping.

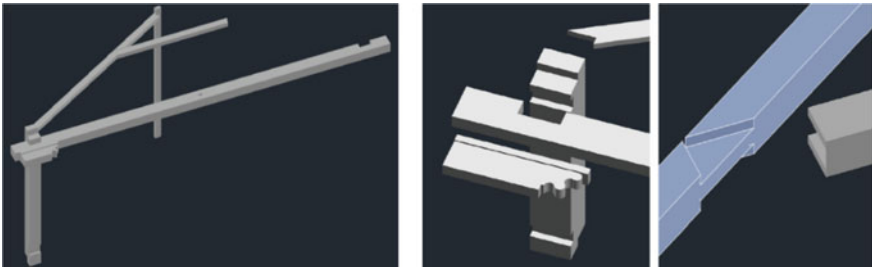

Fig. 8 Left: Each of the 7 pieces of the structure created in 3D CAD. Centre and right: Detail of the assemblies, which can be analyzed before printing

showed several photographs of one of the three models made during the process. These same files also have been used to produce all the full-scale parts in wood, in a carpentry workshop with industrial computerized manufacturing, with the safety that their assemblies would coincide exactly with the models, with no execution errors.

Figure 8 (Centre and right) shows details of the assemblies. By means of these pieces the correct fit can be checked, to verify its future execution in real scale wood.

4 Conclusions

It has been exposed the research work of technical assistance to the project and construction of the wooden structure of the church of *San Martín* de Plasencia (declared of cultural interest). This church suffered in 2020 a fire that damaged irreversibly the wooden structure, so the Bishopric of Plasencia has promoted its restoration, rebuilding the structure with wood with its original structural form.

For the technical assistance, a 3D modelling and 3D printing methodology has been used, which is not a mere graphic representation, but provides insight into how the structure works, the knowledge and documentation for the recovery of the original form, and the conservation of the heritage asset.

The realization of up to three physical models in PLA plastic at 1/33 scale has allowed to study the optimal architectural form: one with the current state to study its previous structural anomalies, other with the geometric shape of the current state and the resized transversal sections and finally, the proposed structure for its construction (recovering the original angle of the roof of bevel-6 "cartabón de a seis" and knuckle at 2/3) verifying the available wood sections with respect to the structural and fire regulations.

The 3D modelling and printing method used serves both to verify the architectural-structural design and to check the assembly joints in the physical model in PLA plastic. The STL files created are also used for the actual workshop construction of the full-scale wooden structural elements with their assemblies. Therefore, it is considered a method of interest to be repeated in other cases.

Acknowledgements To the architect Natalia Hernández and the company OCR-Extremadura for their confidence in this technical assistance. To the construction manager Esther Arroyo, for the facilities in the work and because I am proud, as her former professor, to see her work on this complex construction work.

Funding This research has been carried out by means of the research contract SGTRI-148/22 subscribed between OCR-Extremadura S. L. and the University of Extremadura, by procedure of art. 83-LOU.

References

1. NUERE, Enrique: La Carpintería de Armar Española. Spanish Institute of Architecture and University of Alcalá de Henares. Ed. Munilla-Lería. Madrid (2003)
2. López De Arenas, D.: Breve compendio de la carpintería de lo blanco y Tratado de alarifes. Sevilla. National Library of Spain 1/65901-R/31812. (1633). Accessible in the Selection of Spanish architecture and construction teatrises 19–20th century. Ed. Juan de Herrera Institute, Madrid, 2005. (CD-Rom facsímil)
3. Martínez Lebrato, L.: Proyecto de reforma de la iglesia de San Martín filial de San Esteban (Plasencia). Unpublished (1966)
4. Hernández, N.: Proyecto de restauración de la iglesia de San Martín, Plasencia. Unpublished. Commisioned by regional government of Extremadura (2021)
5. Salcedo, J.-C.: Asistencia técnica a la ejecución de la restauración de la estructura de madera de la iglesia de San Martín (Plasencia). Technical document. University of Extremadura. Ref. SGTRI-148/22. Last date: March 8 (2022)
6. Mingo, J. de: Albanécar, Bitácora sobre la Carpintería de Lo Blanco (2021). https://www.albanecar.es/
7. Law 2/1999, March 29, de Patrimonio Histórico y Cultural de Extremadura. Regional government of Extremadura. DOE nº 59, May 22 1999
8. Law 38/1999, November 5, de Ordenación de la Edificación. Kingdom of Spain. BOE nº 266, November 6, 1999
9. CTE: Código Técnico de la Edificación. R.D. 314/2006, March 17. Ministry of Housing. Madrid. B.O.E. nº 74, March 28, 2006. Modified document R.D. 732/2019 (2016)
10. DB-SE: Código Técnico de la Edificación. Documento Básico de Seguridad Estructural. Bases de Cálculo. Ministry of Housing. Madrid. Modified document R.D. 732/2019 (2019)
11. DB-SE-M: Código Técnico de la Edificación. Documento Básico de Seguridad Estructural. Madera. Ministry of Housing. Madrid. Modified document R.D. 732/2019 (2019)
12. DB-SI: Código Técnico de la Edificación. Documento Básico de Seguridad en caso de Incendio. Ministry of Housing. Madrid (2019)
13. Eurocode-5 Design of Wooden Structures. European Committee of Standardization. European Union (1995)

Biomaterials, Nanomaterials, and New Materials

Thermal Properties of Polymer Adhesive Modified with TiO_2 Used for Structural Strengthening

Kamil Krzywiński, Carlos Chastre, Katarzyna Fedoruk, Adam Sieradzki, and Łukasz Sadowski

Abstract The study presents the results of thermal analysis of epoxy resin coating modified with titanium dioxide obtained using differential scanning calorimetry. The analysis shows an improvement in the glass transition temperature of modified specimens.

Keywords Epoxy resin · Adhesive · Titanium dioxide · Thermal properties

1 Introduction

The need to increase bridge capacity encourages engineers to use different strengthening methods. One of these methods uses carbon fiber reinforcement polymer (CFRP), which could dramatically increase the mechanical capacity of elements [1–3]. The asset of this method is also the low weight of used materials. Epoxy resin as an adhesive connect carbon fiber and strengthening element. It is responsible for transmitting stress [4, 5] from elements to carbon fiber [6]. All the materials are exposed to the external environment (sunlight, air temperature). The curing process is responsible for the properties of the adhesive. The epoxy resin cured at air temperature achieves a lower glass transition temperature (T_g) than post-cured specimens [7]. To reduce the effect of low T_g, it is possible to modify epoxy resin with titanium dioxide TiO_2 [8]. The additive increases the pull-off strength of modified epoxy resin to the concrete substrate. Also, it could increase glass transition temperature T_g,

K. Krzywiński (✉) · Ł. Sadowski
Department of Materials Engineering and Construction Processes, Wroclaw University of Science and Technology, Wroclaw, Poland
e-mail: kamil.krzywinski@pwr.edu.pl

C. Chastre
CERIS and Department of Civil Engineering, NOVA School of Science and Technology, Universidade NOVA de Lisboa, Lisbon, Portugal

K. Fedoruk · A. Sieradzki
Department of Experimental Physics, Wroclaw University of Science and Technology, Wroclaw, Poland

C. Chastre et al. (eds.), *Testing and Experimentation in Civil Engineering*,
RILEM Bookseries 41, https://doi.org/10.1007/978-3-031-29191-3_3

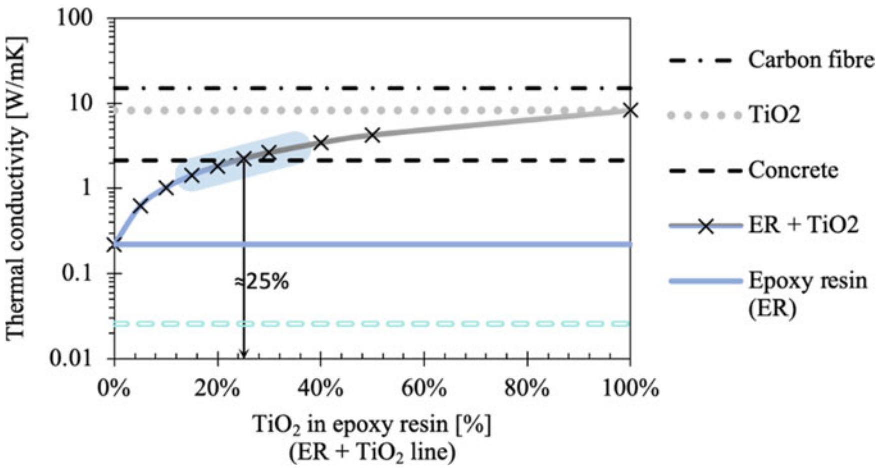

Fig. 1 Thermal conductivity of different materials

which could be described as a temperature above which the mechanical properties of epoxy resin decrease.

Figure 1 presents the mean thermal conductivity of materials used in the strengthening method mentioned above. The epoxy resin exposed to high air temperature or sunlight could reduce its mechanical properties. The low thermal conductivity of epoxy resin does not allow to transfer heat quickly to concrete with high thermal capacity. The epoxy resin should be modified to obtain thermal conductivity closer to concrete to achieve satisfying results. This will result in better thermal protection of epoxy adhesive. Song and Zhang [9] presented an exemplary increment of polymer composite thermal conductivity by adding Al_2O_3.

It is visible from Fig. 1 that to achieve a polymer-cementitious composite with proper thermal conductivity, it is necessary to modify epoxy resin to increase its thermal conductivity. Therefore, the authors decided to modify epoxy resin with titanium dioxide powder which has higher thermal conductivity. The polymer was modified with 15–30% of TiO_2. In this range, the thermal conductivity of polymer composite is close to the concrete.

The thermal conductivity of concrete was estimated using Eq. (1) proposed by Asadi et al. [10]. The assumed density ρ is 2350 kg/m^3.

$$k = 0.0625e^{0.0015p} \tag{1}$$

2 Materials and Methods

2.1 Epoxy Resin and Granite Powder

A commercially available epoxy was used in this study. The epoxy resin was prepared using components A and B with a weight ratio of 100:25. The components were mechanically mixed using a ribbon impeller for 3 min to obtain a uniform consistency. After 7 days of curing, specimens obtained designed strength.

In this research, white titanium dioxide TiO_2 particles were used. The TiO_2 particles (Grupa Azoty Tytanpol, Kuznica, Poland) had a rutile crystallographic structure. The particle size was around 301 nm. To each sample, 15, 20, 25, and 30% weight of the epoxy resin was added to the mixture.

2.2 Thermal Analysis

The thermal properties of modified epoxy resin were studied using differential scanning calorimetry according to Sect. 2.4 presented in [8]. To achieve reliable results, specimens were prepared to obtain a weight close to 20 mg. Based on the results the glass transition temperature was calculated using trend lines estimated for each thermal state (glassy state, glass transition, and rubbery state). The mid-point of the glass transition state represents glass transition temperature T_g, as it is presented in Fig. 2.

3 Results and Discussion

Figure 3 presents the specific heat capacity of epoxy resin modified with titanium dioxide TiO_2. The specific heat capacity (c) of the reference sample and epoxy resin with 15, 20, 25, and 30% of TiO_2 in $T = 25$ °C is 1538, 1365, 1273, 1248, and 1224 J/kgK, respectively. It is visible that TiO_2 changes the thermal properties of epoxy resin. As a result, specific heat capacity c is reduced, and the glass transition stage differs for each specimen. Curves of c have a similar shape.

In comparison to previous studies [8], only reference sample and epoxy resin with 20% of TiO_2 have similar specific heat capacity. It was noticed in [8] that some specimens do not contain uniformly distributed particles in the epoxy resin matrix. It was visible by obtaining large TiO_2 clusters. To avoid this problem in the current study, specimens were mixed using different impeller (ribbon instead of turbine—based on nomenclature presented in Chap. 7 by Peker and Helvaci [11]).

Figure 4 was created based on Fig. 3 using trend lines for glassy state, glass transition, and rubbery state, respectively. Based on calculated trend line equations, summarized in Table 1, it was possible to estimate glass transition temperature T_g as it

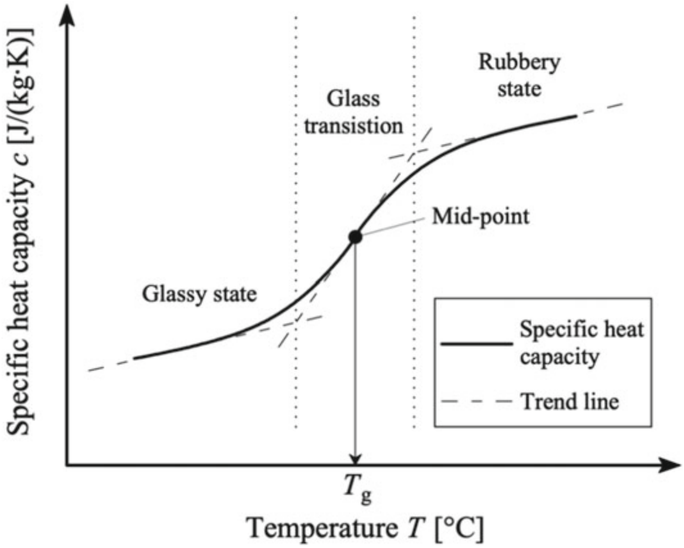

Fig. 2 Schematic illustration of the temperature dependence of the specific heat capacity of amorphous polymers

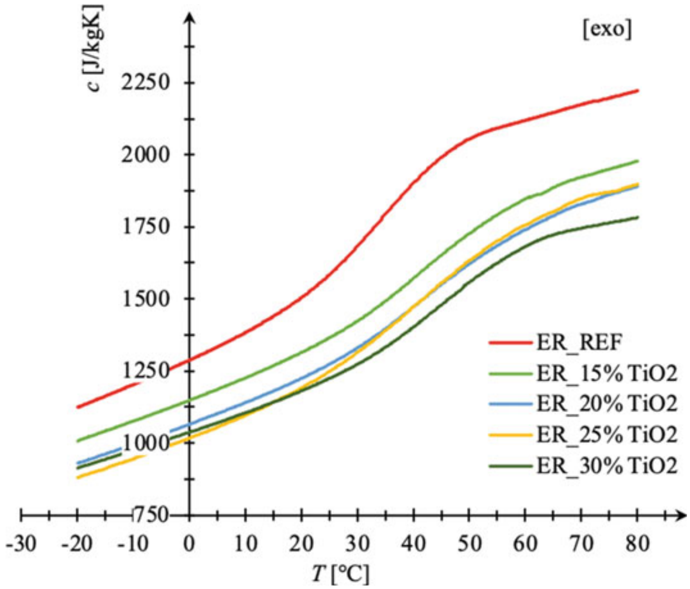

Fig. 3 Mean specific heat capacity of epoxy resin modified with TiO_2

is also presented in Fig. 2. It is visible that all three states (glassy state, glass transition, and rubbery state) moved to the higher temperatures. It means that the border between glassy state-glass transition and glass transition-rubbery state is observed in higher temperatures for specimen with titanium dioxide compared to reference specimen. The glass transition temperature T_g of epoxy composites also increases. It can be noticed that T_g depends on the volume fraction of titanium dioxide TiO_2 added to the epoxy resin matrix.

The glass transition temperatures T_g for each specimen are presented in Fig. 5. The use of titanium dioxide significantly increased T_g. The growth of T_g, in comparison

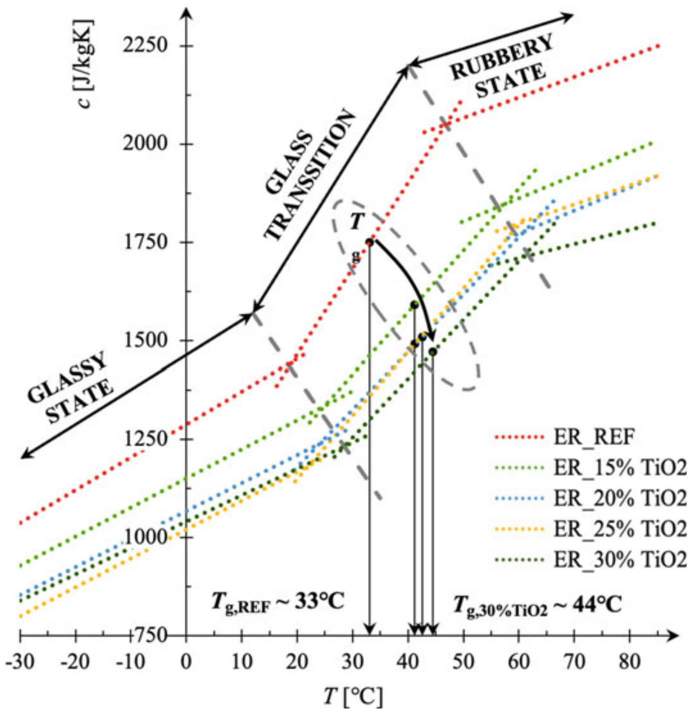

Fig. 4 Trend lines of specific heat capacity for three different stages

Table 1 The trend line equations for three temperature stages

Specimen	Glassy state	Glass transition	Rubbery state
ER_REF	y = 8.34x + 1287	y = 21.8x + 1028	y = 5.22x + 1806
ER_15% TiO_2	y = 7.37x + 1150	y = 15.7x + 941	y = 5.87x + 1509
ER_20% TiO_2	y = 7.13x + 1067	y = 14.5x + 888	y = 5.88x + 1419
ER_25% TiO_2	y = 7.35x + 1020	y = 16.1x + 826	y = 4.85x + 1506
ER_30% TiO_2	y = 6.69x + 1041	y = 14.9x + 807	y = 3.60x + 1493

to the reference sample, is 8.2, 9.5, 8.2, and 11.5 °C for specimens with 15, 20, 25, and 30% of TiO_2, respectively. The behavior of modified epoxy resin is different compared to specimens measured by Goyat et al. [12]. Those specimens occurred reduction of glass transition temperature above 10 percentage by weight (wt%) of TiO_2. The difference in the results obtained by Goyat et al. [12] compared to this study may be caused by great TiO_2 cluster size created by a stirring impeller used during mixing. Goyat et al. [12] observed a significant increase in cluster size for specimens with TiO_2 above 7 wt%. Nevertheless, the results also show improvement of the glass transition temperature for all modified specimens.

Using titanium dioxide reduces the specific heat capacity of the polymer composite. It also affects the glass transition temperature. Figure 6 presents the relation between c and T_g. It is visible that lower specific heat capacity is related to the higher glass transition temperature. This relationship can be described by Eq. (2). Where x is T_g temperature and y specific heat capacity. It can be concluded that the reduction of c extends the glassy state in natural temperatures. That can significantly improve epoxy resin's mechanical properties and durability in a broader range of temperatures.

$$y = 2893e^{-0.015x} \tag{2}$$

Figure 7 shows the relation of specific heat capacity in glass transition temperature and wt% of TiO_2 added to epoxy resin. The c decreases with a higher amount of TiO_2. This behavior is natural when epoxy resin is filled with TiO_2 with lower specific heat capacity. Equation (3) can describe the relationship between c in T_g temperature and wt% of TiO_2, where x is wt% of TiO_2 and y specific heat capacity in T_g temperature.

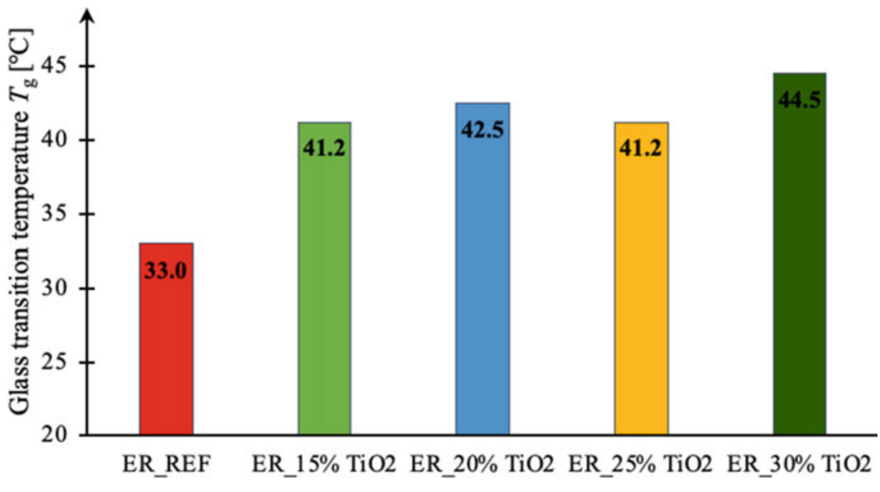

Fig. 5 Glass transition temperature T_g of specimens modified with titanium dioxide

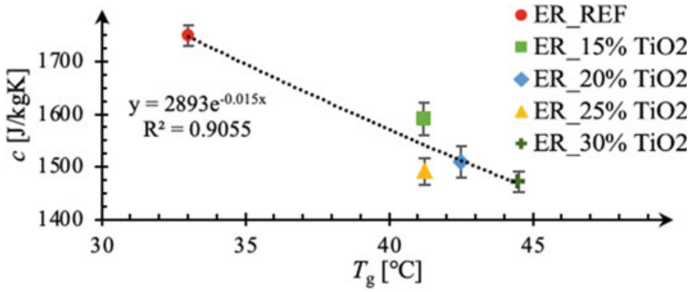

Fig. 6 The relationship between glass transition temperature T_g and specific heat capacity c

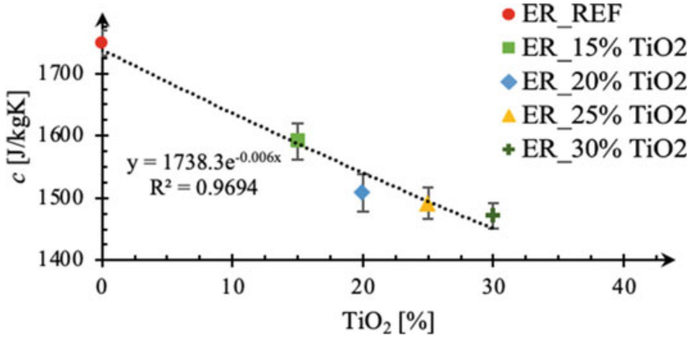

Fig. 7 The relationship between TiO_2 added to epoxy resin and specific heat capacity c in glass transition temperature T_g

$$y = 1738.3e^{-0.006x} \tag{3}$$

Titanium dioxide can change the mechanical properties of epoxy resin. It can also improve glass transition temperature T_g, which for this study can be described using Eq. (4). Where x is wt% of TiO_2 and y glass transition temperature. It is visible from Fig. 8 that a higher amount of titanium dioxide increases the glass transition temperature of epoxy resin. The improvement of T_g can result from the decrease in the chain segments' mobility, which was either caused by a higher interaction between the TiO_2 particles and the epoxy matrix [13]. It can also result from the impeded chain mobility due to a high amount of particles [12].

$$y = 34.023e^{0.0094x} \tag{4}$$

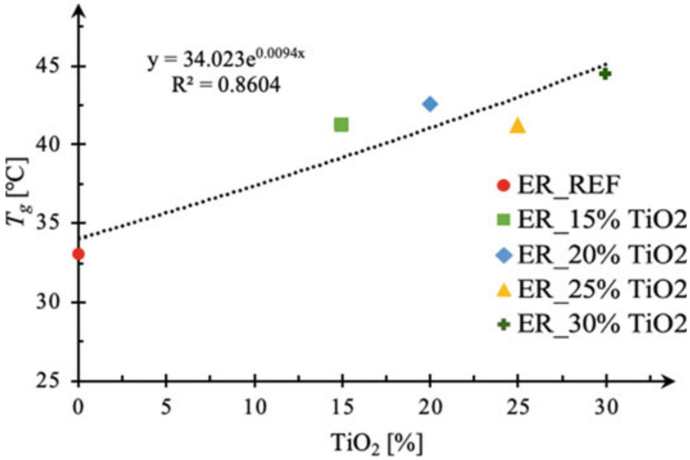

Fig. 8 The relationship between TiO_2 added to epoxy resin and glass transition temperature T_g

4 Conclusions

Obtained results show that modification of epoxy resin with TiO_2 can increase glass transition temperature T_g of composite. As a result, modified epoxy resin has extended glassy state in which epoxy resin has stable mechanical properties. Therefore, it can be stated that modification of the epoxy resin with TiO_2 improves the durability of the adhesive exposed to the temperatures up to the T_g temperature of analyzed specimens. Moreover, TiO_2 reduces the specific heat capacity of composite and might significantly increase thermal conductivity.

It was confirmed that modification of epoxy resin with TiO_2 has a desirable effect on the composite. Change of thermal properties protects epoxy resin much better in the external environment. A thin layer of modified adhesive can more effectively transfer heat from itself to the concrete substrate instead of collecting it. In comparison, a pure epoxy resin layer works as thermal insulation with low thermal conductivity. The use of TiO_2 has an additional advantage. The viscosity of epoxy increased with a higher amount of the filler, which helps to apply it to the bottom part of strengthened elements.

Acknowledgements This work was supported by the Ministry of Education and Science (MEiN, Poland) [grant no. 0151/DIA/2020/49].

References

1. Cardoso, R.: Strengthening load-bearing wall openings using concrete beams and CFRP: case study. Pract. Period. Struct. Des. Constr. **25**(2), 06020002 (2020)
2. Biscaia, H.C., Chastre, C., Borba, I.S., Silva, C., Cruz, D.: Experimental evaluation of bonding between CFRP laminates and different structural materials. J. Compos. Constr. **20**(3), 04015070 (2016)
3. Biscaia, H.C., Chastre, C., Cruz, D., Franco, N.: Flexural strengthening of old timber floors with laminated carbon fiber-reinforced polymers. J. Compos. Constr. **21**(1), 04016073 (2017)
4. El Awad, S.: The Inference of the Mechanical Properties of Materials at Micro and Meso-Scale via the Micro-Bending Technique (Doctoral dissertation, University of Houston, 2020).
5. El Awad, S., Stefaniuk, D., Krakowiak, K.J.: Determination of elastic and flexural strength properties of multi-scale materials via indentation assisted micro-bending experiment and inverse analysis. Mech. Mater. **158**, 103889 (2021)
6. Silva, M.A., Biscaia, H.: Degradation of bond between FRP and RC beams. Compos. Struct. **85**(2), 164–174 (2008)
7. Carbas, R.J.C., Marques, E.A.S., Da Silva, L.F.M., Lopes, A.M.: Effect of cure temperature on the glass transition temperature and mechanical properties of epoxy adhesives. J. Adhes. **90**(1), 104–119 (2014)
8. Krzywiński, K., Sieradzki, A., Sadowski, Ł, Królicka, A., Chastre, C.: Thermal wear of epoxy composite modified with rutile titanium dioxide. Compos. Struct. **282**, 115127 (2022)
9. Song, J., Zhang, Y.: Effect of an interface layer on thermal conductivity of polymer composites studied by the design of double-layered and triple-layered composites. Int. J. Heat Mass Transf. **141**, 1049–1055 (2019)
10. Asadi, I., Shafigh, P., Hassan, Z.F.B.A., Mahyuddin, N.B.: Thermal conductivity of concrete–a review. J. Build. Eng. **20**, 81–93 (2018)
11. Peker, S.M., Helvaci, S.S.: Solid-Liquid Two Phase Flow. Elsevier (2011)
12. Goyat, M.S., Rana, S., Halder, S., Ghosh, P.K.: Facile fabrication of epoxy-TiO_2 nanocomposites: a critical analysis of TiO_2 impact on mechanical properties and toughening mechanisms. Ultrason. Sonochem. **40**, 861–873 (2018)
13. Chen, K.H., Yang, S.M.: Synthesis of epoxy–montmorillonite nanocomposite. J. Appl. Polym. Sci. **86**(2), 414–421 (2002)

Production and Characterization of Polymeric Capsules Containing Rejuvenators for Asphalt Mixtures Self-healing Purposes

Rui Micaelo, Andreia Caeiro, Luís Baltazar, and João P. Borges

Abstract Pavement distresses are a result of loading and natural ageing, though asphalt mixtures have self-healing capacity because the asphalt binder is a self-healing material. It has been demonstrated before that the asphalt binder drains to the cracks, closing it, if sufficient time and adequate temperature conditions are given. In practice, this mechanism is highly inefficient because traffic is not interrupted, and in-service temperatures are not high enough. Self-healing can be accelerated with capsules containing rejuvenators. The released rejuvenator modifies locally the rheology of the binder to drain faster to the crack. This paper investigates the effect of fabrication conditions of polymeric capsules, containing sunflower oil, to the morphological, geometrical, thermal, and mechanical characteristics of capsules. Capsules were produced by ionotropic gelation of sodium alginate and calcium chloride, using extrusion and air-atomization methods. The effect of supplementary high temperature conditioning and cross-linking with glutaraldehyde were investigated. The results showed that the amount of oil encapsulated in capsules depends on the sodium alginate and calcium chloride concentrations. Thus, these concentration values affect the size and mechanical properties of capsules. The mechanical strength increases substantially with the supplementary treatment. Finally, the

R. Micaelo (✉)
CERIS, Department of Civil Engineering, School of Science and Technology, Universidade Nova de Lisboa, Campus de Caparica, 2829-516 Caparica, Portugal
e-mail: ruilbm@fct.unl.pt

A. Caeiro
School of Science and Technology, Universidade Nova de Lisboa, Campus de Caparica, 2829-516 Caparica, Portugal

J. P. Borges
CENIMAT/I3N, Department of Materials Science, School of Science and Technology, Universidade Nova de Lisboa, Campus de Caparica, 2829-516 Caparica, Portugal
e-mail: jpb@fct.unl.pt

L. Baltazar
CENIMAT|i3N, Department of Civil Engineering, School of Science and Technology, Universidade Nova de Lisboa, Campus de Caparica, 2829-516 Caparica, Portugal
e-mail: luis.baltazar@fct.unl.pt

C. Chastre et al. (eds.), *Testing and Experimentation in Civil Engineering*, RILEM Bookseries 41, https://doi.org/10.1007/978-3-031-29191-3_4

capsules showed to significantly improve the self-healing ability of bituminous mastic beams.

Keywords Self-healing materials · Microcapsules · Rejuvenator · Bituminous mastic

1 Introduction

Global spending on road infrastructure is very high (estimated \$1 trillion in 2018), however many roads in high GDP countries are in poor condition. The road agencies' budget for maintenance is insufficient (e.g. in the USA, the estimated deficit is \$92bn [1]), and even with adequate planning of maintenance works the performance of current materials limits the required reduction in budget needs [2]. In future, road vehicle automation (truck fleets) is also likely to speed up damage due to increasing traffic and less variation in traffic patterns. Self-healing, mechanomutable additives and other technologies are being now investigated to improve long-term durability [3]. Thus, innovative solutions are needed to steer the digital and green transitions planned in transport infrastructures.

Asphalt mixture, which consists of mineral aggregates (90% v/v) with size ranging from a few microns to 25 mm and bitumen (10% v/v), is the most widely used road surfacing material. Aggregates give structural stability to asphalt, while bitumen, a fluid with temperature-dependent viscosity, binds the aggregates together. After several years, the effects of traffic load, oxygen, UV radiation, thermal cycling and ambient moisture result in oxidation of the bitumen and microcracking in the mastic [4–6]. Moisture impregnates bitumen by diffusion [7] and reduces adhesion to the aggregates. Mechanical loads then create interfacial cracks [8], which accelerates the water penetration and therefore the material's deterioration.

Two methods have been investigated in last decades to reverse material's damage: internal heating and rejuvenation [9]. Bitumen has self-healing properties [10], however, with ageing the effectiveness of wetting and inter-diffusion mechanisms is largely reduced. Due to the high viscosity at ambient temperatures the bitumen drains very slowly to the crack tip. Internal heating of asphalt with conductive additives via induction energy melts the bitumen and close cracks fast. However, high temperature cycles also speed up ageing, and it is not known when to apply heating [11]. Different oils, rich in maltene constituents, can be used as rejuvenators to provide the bitumen with its original properties. The pointed advantages of using embedded capsules containing rejuvenators, when compared with spreading rejuvenators onto the pavement surface, are the application of the rejuvenator to the entire material, not only the part near the surface, when it is naturally required, and the protection of the environment [12]. These capsules will remain inactive in the asphalt road for several years until an external factor, e.g. loading, triggers their breakage and the rejuvenators dissolve the bitumen around the microcapsules. Then, the binder can easily flow into the cracks and self-healing is accelerated. However, the development of capsules for this purpose is still at an early stage [13, 14].

In the literature many microencapsulation methods and techniques are found. This paper investigates the effect of fabrication conditions of polymeric capsules, containing sunflower oil, to the morphological, geometrical, thermal, and mechanical characteristics of capsules. Capsules were produced by ionotropic gelation of sodium alginate and calcium chloride, using the extrusion drop-wise and air-atomization methods. In addition, it was evaluated the self-healing ability of bituminous mastic beams with these capsules.

2 Experiments

2.1 Materials

The materials used in the fabrication of microcapsules were: sodium alginate ($NaC_6H_7O_6$), obtained from PanReac AppliChen; calcium chloride dihydrate ($CaCl_2H_4O_2$), obtained from Carl Roth; glutaraldehyde ($C_5H_8O_2$), obtained from Sigma Aldrich; sunflower oil, obtained from Auchan. The sunflower oil was the rejuvenator encapsulated in alginate beads.

To evaluate the effect of microcapsules containing rejuvenator on the self-healing properties of bituminous materials, bituminous mastic specimens were fabricated and tested. Mastic was fabricated with neat asphalt binder (penetration grade 35/50) and limestone filler.

2.2 Preparation of Microcapsules

The ionotropic gelation technique was used in this study to encapsulate sunflower oil. In this method polyelectrolytes (alginate) are cross linked in the presence of counter ions (calcium) to form hydrogels, which entrap the encapsulated agent (sunflower oil) [15]. Thus, the hydrogels are formed by dropping the polymeric and encapsulated agent emulsion into the aqueous solution of polyvalent cations. This is a simple method of microencapsulation that has been largely used in different fields [16].

An emulsion of sunflower oil and sodium alginate in water, at room temperature, was prepared using a mechanical stirrer (400 rpm). The concentration of sunflower oil was 10% (v/v), whereas various concentrations (w/w) of sodium alginate were used (0.50, 0.75, 1.00 and 1.50%). The calcium chloride solution in ultrapure water was prepared with various concentrations: 1.70, 3.40, 5.30, 6.60 and 7.30%. These formulations were aimed at evaluating the effect of formulation on the microcapsules' properties. The preparation of the alginate beads containing sunflower oil was carried out with two different schemes (see Fig. 1): extrusion drop-wise using a syringe;

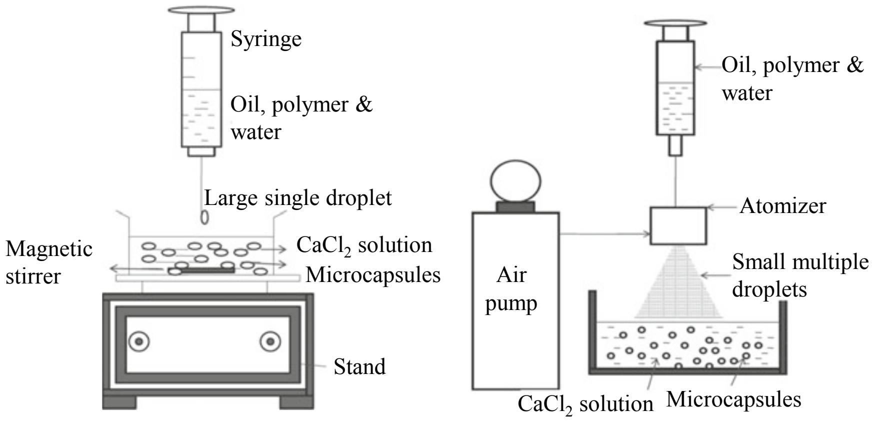

Fig. 1 Microencapsulation: **a** extrusion drop-wise; **b** air atomization (adapted from [17])

and air atomization. To investigate the effect of formulation on the microcapsules' properties the first method was used. Then, the air atomization method was used to prepare smaller microcapsules with a specific formulation.

Two extrusion rates (10 and 40 ml/h) were used in the extrusion drop-wise method. With the air atomization scheme the extrusion rate was 5 ml/h and the air pressure 5.49 l/min.

After the preparation of the alginate beads, they were kept in the calcium chloride solution for 24 h under constant stirring. The microcapsules were then harvested and put in ethanol for 24 h to remove the oil from the surface. Finally, they were placed on top of filter paper and allowed to dry at room temperature.

In addition, it was investigated the effect of additional cross-linking, by temperature and chemically with glutaraldehyde, on the mechanical strength of microcapsules [18]. A solution of 1 ml of glutaraldehyde in 25 ml of calcium chloride solution was prepared. The alginate beads were harvested after the preparation and put in the glutaraldehyde and calcium chloride solution, which was then heated in a water bath at 85 °C for 20 min. The recipient was allowed to cool at room temperature, and then the capsules were filtered and dried in a ventilated oven at 40 °C.

2.3 Testing Methods

The microcapsules were characterized in terms of their morphological, geometrical, thermal and mechanical properties. In addition, it was evaluated the self-healing ability of bituminous mastic beams with and without capsules.

Microcapsules were inspected under an optical microscope (OLYMPUS BX51) to evaluate their morphology and size. The inner microstructure was evaluated under the scanning electron microscope (SEM). The mechanical strength of microcapsules was measured by means of uniaxial compression test in a universal testing machine. Testing was performed under displacement control (0.7 mm/min). Thermogravimetric analysis (TGA) of microcapsules and constituents was performed to evaluate the effect of temperature on capsules and to determine their composition by analysis of characteristic decomposition patterns. Testing was performed in a NETZSCH 449 F3 Jupiter, under conditions as following: sample mass 11 mg; heating rate 10 K/min; range of temperature 25–600 ºC; inert gas N2 at 50 ml/min.

Bituminous mastic specimens were fabricated with and without capsules, and tested to determine the effect of capsules on self-healing. The bituminous mastic was fabricated with bitumen 35/50 and limestone filler, using a filler-to-bitumen (w/w) ratio of 2.0. The content of capsules was 5% of bitumen (w/w). Beam specimens (80 mm $\times$ 20 mm $\times$ 20 mm) were produced using PE500 molds. The beams had a notch in the middle of the bottom surface to obtain failure through a single crack in test. The specimens were kept at -20 ºC after demolding, and before testing. The healing ability (H) of mastic beams was defined as:

$$H = \frac{P^{2nd}}{P^{1st}} \tag{1}$$

where P^{1st} and P^{2nd} are the peak loads (flexural strength values) of the first and second tests, respectively. The flexural strength was measured by means of three-point bending (3 PB) testing at -20 ºC. An universal testing machine, Zwick Z050, was used under displacement control (3 mm/min). After the first test, the two pieces of the broken specimen were assembled in the mold and stored in a room at 18 ºC. The specimens were kept in the room for 2, 24 and 48 h, and then they were put in the freezer at -20 ºC. Then the specimens were reloaded under 3 PB. A minimum of two replicates were tested for every material/test condition.

3 Results and Discussions

3.1 Characterization of Microcapsules

Microcapsules prepared with the extrusion drop-wise method were approximately spherical with a rough external surface (see Fig. 2a). This can be related with the method used to form the particles (syringe dropping), and with the use of a polymer and encapsulated agent emulsion in the preparation of microcapsules. In addition, the size of microcapsules varied between 0.82 mm and 2.18 mm. Table 1 lists the average size of microcapsules from different formulations.

The size varied with both the alginate and calcium chloride concentrations and the syringe flow rate, however, the effect of each variable is not simple. For 40 ml/h of flow, the effect of sodium alginate concentration was not relevant for 0.75% and 1.0% but smaller or larger microcapsules were obtained with 0.5 and 1.5%. In general, the

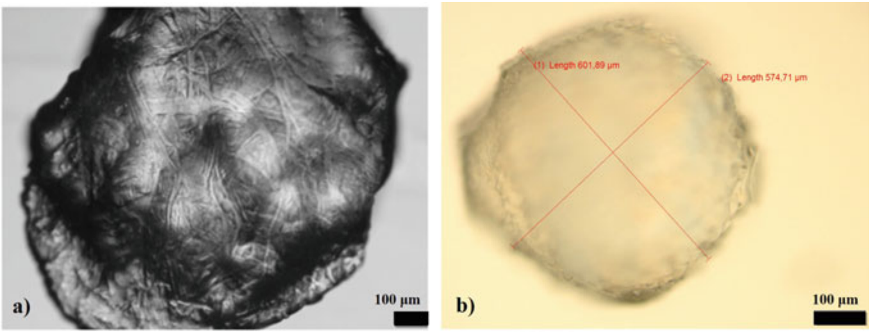

Fig. 2 Microcapsules prepared by **a** extrusion drop-wise; and **b** air atomization

Table 1 Size (average diameter) of microcapsules fabricated by extrusion drop-wise

Syringe flow rate	40 ml/h	40 ml/h	40 ml/h	40 ml/h	10 ml/h
Alginate	0.5% (mm)	0.75% (mm)	1.0% (mm)	1.5% (mm)	1.0% (mm)
1.7% $CaCl_2$	0.82	0.82	0.95	1.77	1.97
3.4% $CaCl_2$	1.42	0.96	1.08	1.68	2.04
5.3% $CaCl_2$	1.54	1.05	1.09	1.02	2.09
6.6% $CaCl_2$	1.14	1.15	1.39	1.85	2.18
7.3% $CaCl_2$	1.43	1.56	1.57	1.74	2.13

size increased with the calcium chloride concentration, however, using a low flow rate in the syringe the variation in size of microcapsules with the calcium chloride concentration was rather small. As expected, the size can be significantly reduced with air atomization, which also improves the surface smoothness. Air pressure forces the emulsion to pass through small openings, forming small uniform droplets. The average size of microcapsules with 1.0% alginate and 7.3% $CaCl_2$ was 0.71, 0.68 and 0.57 mm for air pressure of, respectively, 5.18, 5.49 and 6.09 l/min.

Microcapsules to incorporate in asphalt mixtures must have sufficient mechanical strength to survive harsh mixing and compaction conditions, and to release the rejuvenator only when significant damage had occurred. The microcapsules did not show a peak in the load-deformation curve, instead the load increases continuously till the end because the oil is forced outside the capsule due to internal pressure and the load increase rate changes to a very high value when almost only the polymer is being compressed between the steel plates. The strength value was defined when the initial curve slope ended. Table 2 lists the compressive strength of microcapsules with different formulations prepared by extrusion drop-wise. Strength values varied between 0.7 N and 3.0 N. The calcium chloride concentration did not have a significant effect on strength. Actually, the strength was more affected by the extrusion rate. This suggests that even the lowest concentration solution had sufficient calcium ions for cross-linking the alginate. In literature [12, 14, 15] are indicated higher values for similar purpose capsules, but they were larger. Also, the ratio of sodium alginate to oil is low (0.1 w/w) and they were not fully dry as is showed in the next section. Polymeric capsules have a very ductile behavior, and when mixed with rigid elements they are deformed to adapt their shape to existing voids in the primary elements structure.

In addition, the resistance of microcapsules to high temperature conditions used in asphalt mixtures fabrication is very important. TGA testing to microcapsules (alginate 1.00% and calcium chloride 5.30%) showed low mass loss up to 140 ºC, and substantial from 180 ºC. In the literature is indicated that high temperatures cause degradation of the polymer structure and cross-linking points [19]. Based on the TGA test results, these capsules can be incorporated in traditional hot-mix asphalt.

Table 3 shows the composition of microcapsules prepared with different formulations. Composition was determined from the TGA test results following the method described in [15]. The content of rejuvenator varied significantly (15.2–69.1%) with formulation used in preparation. In general, the rejuvenator content increased with the concentration of calcium chloride, whereas the opposite trend of variation was found for the sodium alginate concentration. The "egg structure" formed by polymer cross-linking was made less permeable to the rejuvenator when more calcium ions were available. Moreover, microcapsules retained some water at the end of the drying procedure. Because alginate is highly hydrophilic, some absorbed/adsorbed water was not removed with air drying.

To improve the mechanical strength of capsules, additional cross-link of the alginate beads was implemented. Cross-linking was promoted by temperature and chemically by glutaraldehyde. For microcapsules prepared with sodium alginate 1.00 and 7.30% calcium chloride, the strength increased to 3.4 N and the average size was.

Table 2 Mechanical strength of microcapsules prepared by extrusion drop-wise

Sodium alginate (%)	Calcium chloride (%)	10 ml/h (N)	40 ml/h (N)
1.00	1.70	1.5	2.6
	3.40	1.3	2.2
	5.30	1.3	3.0
	6.60	1.4	2.0
	7.30	1.3	0.7

Table 3 Composition of microcapsules fabricated by extrusion drop-wise

Calcium chloride	1.7%	5.3%				7.3%
Sodium alginate	1.0%	0.5%	0.75%	1.0%	1.5%	1.0%
Polymer (%)	60.0	30.5	68.0	61.7	81.1	53.3
Rejuvenator (%)	34.1	69.1	28.4	37.2	15.2	45.7
Water (%)	4.8	0.4	3.6	1.2	3.5	1.0

1.65 mm. These values are compared with 1.3 N and 2.13 mm (see Tables 1 and 2). SEM technique was used to investigate the effect of additional cross-linking on microstructure. Figure 3 shows that the most superficial layer of microcapsules was modified by the implemented procedure. In addition, it was evaluated the effect of the additional cross-link in the encapsulation capacity (Table 4). The content of rejuvenator in microcapsules increased significantly. Thus, it is concluded that additional cross-linking should be used for the proposed purpose, incorporation in asphalt mixtures.

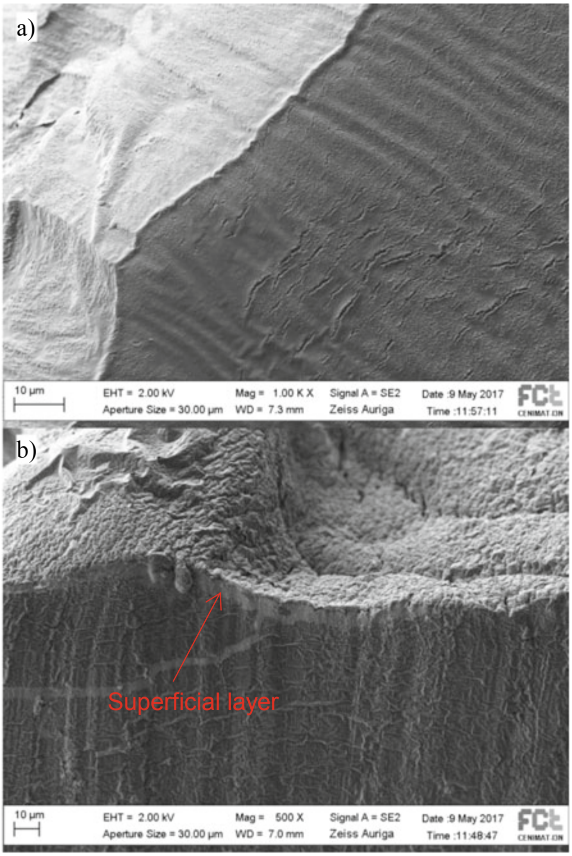

Fig. 3 SEM images of microcapsules surface: **a** original; and **b** extra cross-link

Table 4 Composition of microcapsules

	Extrusion	Air atomization
Polymer (%)	29.3	23.5
Rejuvenator (%)	64.0	69.0
Water (%)	6.7	7.5

Table 5 Strength recovery values of bituminous mastic beams

Resting time (h)	No microcapsules (%)	With microcapsules (%)
2	17.5	42.5
24	40.0	69.7
48	62.7	88.0

3.2 Self-healing of Bituminous Mastic

The effect of microcapsules containing sunflower oil on the self-healing ability of bituminous mastic was evaluated as described in Sect. 2.2. Table 5 shows the strength recovery (healing ability H, Eq. (1)) of bituminous mastic at 18 ºC for three different resting times. Strength recovery was significantly greater in mastic specimens with microcapsules. It is considered that this gain was promoted by the sunflower oil released from capsules. The sunflower oil diffused into the binder, modifying its rheological behavior. The oil reduced binder's stiffness and the softer the binder the faster it flows.

However, the high strength recovery values of mastic specimens without microcapsules are related to the large binder content in specimens. In conventional asphalt mixtures the binder content is significantly smaller, with only a thin film covering the aggregate particles, and consequently the strength recovery capacity is much lower. Also, the test method used imposes a single large cracking surface, which is let to rest without intermittent loading. In field, cracking occurs for broad temperature conditions, cracking surfaces are broken up by air voids and aggregate particles and traffic loading is not interrupted.

4 Conclusions

This paper investigated the effect of fabrication conditions of polymeric capsules, containing sunflower oil, to the morphological, geometrical, thermal, and mechanical characteristics of capsules. Microcapsules prepared by ionotropic gelation of sodium alginate with calcium ions encapsulated moderate amounts of rejuvenator and had adequate resistance to high temperatures. However, they were fairly soft. Additional cross-link by temperature exposition and chemically by glutaraldehyde significantly increased the encapsulation efficiency and the mechanical strength. Moreover, microcapsules can be made smaller with the air atomization method. Finally, these microcapsules showed to significantly improve the self-healing ability of bituminous mastic beams. In following studies, the effect of the test conditions on self-healing of bituminous mastic and asphalt mixtures will be investigated.

Acknowledgments The authors gratefully acknowledge the FCT—Fundação para a Ciência e a Tecnologia, I.P., for its financial support via the projects LA/P/0037/2020, UIDP/50025/2020 and

UIDB/50025/2020 of the Associate Laboratory Institute of Nanostructures, Nanomodelling and Nanofabrication—i3N, and project UIDB/04625/2020 of the CERIS—Civil Engineering Research and Innovation for Sustainability.

References

1. ASCE: Infrastructure Report Card. American Society of Civil Engineers (2017)
2. Ferreira, A., Micaelo, R., Souza, R.: Cracking models for use in pavement maintenance management. In: Cracking Models for Use in Pavement Maintenance Management (2012)
3. Segundo, I.R., Freitas, E., Branco, V.T.F.C., et al.: Review and analysis of advances in functionalized, smart, and multifunctional asphalt mixtures. Renew. Sustain. Energy Rev. **151**, 111552 (2021). https://doi.org/10.1016/j.rser.2021.111552
4. Crucho, J., Picado-Santos, L., Neves, J., et al.: Tecnico accelerated ageing (TEAGE)—a new laboratory approach for bituminous mixture ageing simulation. Int. J. Pavement Eng. **21**, 753–765 (2020). https://doi.org/10.1080/10298436.2018.1508845
5. Carl, C., Lopes, P., Sá da Costa, M., et al.: Comparative study of the effect of long-term ageing on the behaviour of bitumen and mastics with mineral fillers. Constr. Build. Mater. **225**, 76–89 (2019). https://doi.org/10.1016/j.conbuildmat.2019.07.150
6. Pereira, A., Micaelo, R., Quaresma, L., Cidade, M.T.: Evaluation of different methods for the estimation of the bitumen fatigue life with DSR testing. In: Canestrari, F., Partl, M.N. (eds.) 8th RILEM International Symposium on Testing and Characterization of Sustainable and Innovative Bituminous Materials, pp. 1017–1028. Springer, Netherlands, Dordrecht (2016)
7. Apeagyei, A.K., Grenfell, J.R.A., Airey, G.D.: Application of Fickian and non-Fickian diffusion models to study moisture diffusion in asphalt mastics. Mater Struct **48**, 1461–1474 (2015). https://doi.org/10.1617/s11527-014-0246-2
8. Pereira, A., Micaelo, R., Quaresma, L., Cidade, M.T, Canestrari, F., Partl M.N.: 8th RILEM international symposium on testing and characterization of sustainable and innovative bituminous materials evaluation of different methods for the estimation of the bitumen fatigue life with DSR testing. Springer. Neth. Dordrecht. 1017–1028 (2016)
9. Liang, B., Lan, F., Shi, K., et al.: Review on the self-healing of asphalt materials: mechanism, affecting factors, assessments and improvements. Constr. Build. Mater. **266**, 120453 (2021). https://doi.org/10.1016/j.conbuildmat.2020.120453
10. Qiu, J., van de Ven, M., Wu, S., et al.: Evaluating self healing capability of bituminous mastics. Exp. Mech. **52**, 1163–1171 (2012). https://doi.org/10.1007/s11340-011-9573-1
11. Garcia, A., Salih, S., Gómez-Meijide, B.: Optimum moment to heal cracks in asphalt roads by means electromagnetic induction. Construct. Build. Mater. **238**,117627 (2020). https://doi.org/10.1016/j.conbuildmat.2019.117627
12. García, Á., Schlangen, E., van de Ven, M., Sierra-Beltrán, G.: Preparation of capsules containing rejuvenators for their use in asphalt concrete. J. Hazard. Mater. **184**, 603–611 (2010). https://doi.org/10.1016/j.jhazmat.2010.08.078
13. Su, J.-F., Yang, P., Wang, Y.-Y., et al.: Investigation of the self-healing behaviors of microcapsules/bitumen composites by a repetitive direct tension test. Materials **9**, 600 (2016). https://doi.org/10.3390/ma9070600
14. Micaelo, R., Freire, A.C., Pereira, G.: Asphalt self-healing with encapsulated rejuvenators: effect of calcium-alginate capsules on stiffness, fatigue and rutting properties. Mater. Struct. **53**, 20 (2020). https://doi.org/10.1617/s11527-020-1453-7
15. Micaelo, R., Al-Mansoori, T., Garcia, A.: Study of the mechanical properties and self-healing ability of asphalt mixture containing calcium-alginate capsules. Construct. Build. Mater. **123**, 734–744 (2016). https://doi.org/10.1016/j.conbuildmat.2016.07.095

16. Patil, J.S., Kamalapur, M.V., Marapur, S.C., Kadam, D.V.: Ionotropic gelation and polyelectrolyte complexation: the novel techniques to design hydrogel particulate sustained, modulated drug delivery system: a review. Dig. J. Nanomater. Biostruct. **5**, 8 (2010)
17. Patil, J.S., Marapur, S.C., Gurav, P.B., Banagar, A.V.: Ionotropic gelation and polyelectrolyte complexation technique: novel approach to drug encapsulation. In: Handbook of Encapsulation and Controlled Release. CRC Press (2015)
18. Rosenberg, M., Lee, S.J.: Calcium-alginate coated, whey protein-based microspheres: preparation, some properties and opportunities. J. Microencapsul. **21**, 263–281 (2004). https://doi.org/10.1080/02652040410001673937
19. Leo, W.J., McLoughlin, A.J., Malone, D.M.: Effects of sterilization treatments on some properties of alginate solutions and gels. Biotechnol. Prog.0 **6**, 51–53 (1990). https://doi.org/10.1021/bp00001a008

A Review of Laboratory Tests to Evaluate Agro-Industrial Wastes Properties as Building Materials

Eleonora Cintura, Lina Nunes, and Paulina Faria

Abstract The current research trend is finding out feasible solutions to guarantee sustainable building practices. Among the studied possibilities, the production of eco-friendly materials is widely investigated. To propose efficient building products the proper evaluation of their properties is extremely important. The present work considers some laboratory tests to analyse building materials, focusing on agro-industrial wastes (bio-wastes of floriculture and forest management, agricultural practices and agro-industrial processes). It considers hygrothermal performance and biological susceptibility of agro-industrial wastes both individually and in composites. Several past studies addressed this topic by using different laboratory tests and mainly considering composites. Although bio-susceptibility is one of the main drawbacks of bio-based building materials, it is not so commonly assessed. However, many laboratory tests can be carried out, due to the different bio agents and critical conditions. The present work aims at collecting this information to give a summarised list of methods that could be a simplified starting point to study agro-industrial wastes and agro-industrial waste-based composites for building practices.

Keywords Bio-based · Bio-susceptibility · Bio-waste · Composites · Hygroscopicity · Thermal properties · Raw material

E. Cintura (✉) · P. Faria
CERIS, Department of Civil Engineering, NOVA School of Science and Technology, NOVA University of Lisbon, 2829-516 Caparica, Portugal
e-mail: e.cintura@fct.unl.pt

E. Cintura · L. Nunes
Structures Department, National Laboratory for Civil Engineering, Avenida Do Brasil 101, 1700-066 Lisbon, Portugal

L. Nunes
CE3C, Centre for Ecology, Evolution and Environmental Changes, University of the Azores, 9700-042 Angra Do Heroísmo, Portugal

C. Chastre et al. (eds.), *Testing and Experimentation in Civil Engineering*, RILEM Bookseries 41, https://doi.org/10.1007/978-3-031-29191-3_5

1 Introduction

It is widely known that the building sector is one of the human activities most responsible for environmental impact, requiring about 40% of the total energy use [1, 2]. Eco-efficient solutions to moderate this problem have been studied. Among them, the possibility of using agro-industrial wastes (from forest management and floriculture, agricultural practices and agro-industrial processes) to produce building composites with thermal insulation properties. These composites can improve the energy performance of the building stock, moderate the environmental impact, and reduce the volumes of wastes disposal [3–5].

Several past studies investigated the hygrothermal properties of composites made up of agro-industrial wastes considering different methods. Brás et al. [6] analysed the thermal performance of cement-based mortars with expanded cork granulate, a by-product derived from cutting and trimming operations, by using the transient method. They demonstrated that cork improves mortar's thermal insulation capacity. La Gennusa et al. [1] combined several agro-industrial wastes with hydraulic lime and evaluated their thermal performance by heat flow meter. They demonstrated that the most uniform samples made up of the lightest aggregates had better insulation properties, although all the considered materials showed promising performance. Furthermore, they concluded that thermal conductivity was widely influenced by samples' composition, density and temperature during the tests. Czajkowski et al. [7] analysed the thermal properties of commercial insulating panels made up of cereal straw by considering the transient method and the inverse method. The researchers demonstrated that both methods were effective and that considering the temperature's influence guaranteed higher accuracy of the thermal conductivity measurements.

Even though most of the past studies focused on composites, also the properties of the raw materials are extremely important, as they are closely linked [8]. Past research assessed this topic mainly considering the recommendations given by Amziane et al. [9]. This document reported the outcome of a RILEM technical committee, proposing how to evaluate some properties of bio-aggregates. However, many other different methods could be considered, too. Knowing the several possibilities to evaluate hygrothermal properties of agro-industrial wastes allows selecting the most suitable ones for each type of application.

Even if the employment of agro-industrial wastes for building practices guarantees many benefits, there are also several drawbacks, such as lowering fire resistance, lowering durability and increasing bio-susceptibility [10, 11], while increasing hygroscopicity. Laboratory tests have to be focused on the analysis of these problems too, to guarantee a complete evaluation. Knowing the drawbacks helps to moderate and solve them, making agro-industrial waste-based composites more efficient. Biological susceptibility is one of the biggest drawbacks; it affects the durability of the materials, human health, and internal comfort. It depends on different factors, such as chemical composition (e.g. cellulose, hemicellulose, lignin contents), environmental conditions (temperature and relative humidity), surface texture, or pH [12–15]. For this reason, many laboratory tests could be carried out. This allows finding out solutions to moderate biological attacks, e.g. by specific treatments of the agro-industrial wastes, combining different materials, or using specific techniques to produce composites. Santos et al. [16] used air lime to improve resistance to mould growth of earth-based plasters. De Carvalho et al. [17] produced panels made up of sunflower stalks and gypsum, adding potassium benzoate to inhibit fungal proliferation. Brambilla and Sangiorgio [12] reported strategies to lower bio-susceptibility in buildings: the reduction of thermal bridges and the increase of air changes or ventilation rates to control indoor relative humidity.

The feasibility of using agro-industrial wastes for building practices could be evaluated by considering several laboratory tests. The present work aims at summarizing some already used, focusing on hygrothermal performance and biological susceptibility. It considers both agro-industrial wastes and agro-industrial wastes-based composites. The outcome is a summarised list of information that could be a starting point to improve the already known laboratory tests and develop new ones.

2 Testing Agro-Industrial Wastes and Composites

2.1 Agro-Industrial Wastes

Since raw materials' properties are linked to the ones of the final products [8], the analysis of agro-industrial wastes individually secures a more conscious use of them. Several recent past studies [18–21] reported that there are no unified standards to evaluate the properties of agro-industrial wastes. Therefore, the same standards of conventional materials may be considered. However, many past studies referred to RILEM Technical Committee 236-BBM "Bio-aggregate-based building materials" recommendations [9]. The document described guidelines for evaluating loose bulk density, particle size, thermal conductivity, water content, water absorption and hygroscopicity of bio-aggregates, reporting hemp shiv as an example.

Laborel-Préneron et al. [18] referenced recommendations of RILEM TC 236-BBM [9] to study the properties of barley straw, corn cob and hemp shiv. They evaluated particle size distribution (by image analysis method), loose bulk density, thermal conductivity (by hot plate method) and water absorption. For sorption and desorption behaviour they considered Dynamic Vapour Sorption (DVS) method. Cintura et al. [22] analysed loose bulk density and particle size distribution (by sieving method) of grape and olive press wastes, hazelnut shells, spent coffee grounds and Maritime pine (*Pinus pinaster* Ait.) chips by using the same recommendations [9]. Loose bulk density was evaluated also according to EN 1097–3 [23], while thermal conductivity was assessed by the transient method, by using the Modified Transient Plane Source sensor (ISOMET).

Different methods from the recommendations of RILEM TC 236-BBM could be considered to evaluate bio-aggregates' properties. For example, Brouard et al. [24] analysed rape straw and sunflower steam and described a different method to evaluate water absorption. The researchers immersed the aggregates in water for 1 h at different temperatures and considered their mass at specific times. They also evaluated microstructure, to investigate aggregates' pore size, by using Scanning Electron Microscopy (SEM). Ansell et al. [20] referred to RILEM TC 236-BBM [9] to characterize hemp, flax, rape and wheat straw, and corn cob only for loose bulk density. Microstructural morphological properties were evaluated by SEM, porosity by mercury intrusion porosimeter (MIP), thermal conductivity by heat flow meter, and moisture buffering value (MBV) by the NORDTEST method [25]. Liuzzi et al. [26] considered olive leaves and olive branches. They analysed porosity and density by using helium gas pycnometer and microstructural morphological properties by SEM.

As these past studies demonstrated, there is not one specific and unified method to characterize agro-industrial wastes. This allows selecting the most suitable laboratory tests, according to the considered materials. On the other side, only using the same methods could guarantee an effective comparison between different materials.

2.2 Composites

Building composites have been more studied than raw materials [11]. Depending on the type (i.e., particleboards, plasters, mortars, etc.), there are suitable standardized and non-standardized assessment methods used.

Binici et al. [27] produced composites of corn stalks and epoxy resin (Araldite-LY-554), gypsum and Portland cement (CEM I 42.5) as binders. The researchers evaluated water absorption according to ASTM 67 [28] and thermal conductivity according to ASTM C1113 [29]. The results demonstrated that the composites could be considered thermal insulation materials.

Lima and Faria [30] used the German standard DIN 18,947 [31] to evaluate density, thermal conductivity and hygroscopicity of plastering mortars made up of clayish earth and siliceous sand and different percentages of oat straw and typha fibre-wool. As the researchers reported, DIN standards are known as an important reference for earth-based materials. The results demonstrated that natural fibres improved the thermal insulation properties though depending on the fibres and content.

Liuzzi et al. [26] considered European standards to study the hygrothermal properties of a clay plaster with olive fibres (leaves and branches). Water vapour permeability was evaluated according to EN 1015–19 [32], and hygroscopicity properties by using EN 12571 [33]. Porosity was evaluated by helium gas pycnometer. As for thermal properties, the researchers used the transient method (ISOMET); for MBV, the NORDTEST protocol [25] was used. They demonstrated that olive fibres improved the insulation performance of the composite. NORDTEST [25] is a widely used method to determine the MBV [34]. It can be applied to different composites. For example, it was considered for panels made up of rice husk and earth, stabilised with hemihydrated gypsum and air lime [35]; for panels made up of hemp shiv and a bio-based binder of starch derivative and a crosslinking agent [20]; for hemp-lime (hemp shiv, hydraulic lime and a rapid setting additive) [36].

Monteiro et al. [37], Farag et al. [38] and Nunes et al. [39] considered European standards for particleboards. They analysed particleboards composited of cardoon particles and a cassava starch-based binder, panels made up of olive stones and unsaturated polyester liquid resin (Jet sealer), and cement-bonded particleboards with banana pseudosteam, respectively. Bulk density was evaluated according to EN 323 [40]; moisture content according to EN 322 [41].

Palumbo et al. [42] considered EN 12664 [43] to study the thermal conductivity of samples of different bio-based insulation materials: hemp-lime, hemp fibre, wood wool, wood fibre, barley straw-starch and corn pith-alginate. As for the hygroscopicity properties, ISO 24353 [44] was referenced.

As this data collection shows, there are many different methods already known and used to evaluate bio-waste-based composites and a great number of past studies that addressed this topic.

2.3 Bio-Susceptibility

Several laboratory tests are already used to evaluate biological susceptibility, but this property is not so commonly considered, neither for agro-industrial wastes individually nor for composites. As previously anticipated, this is a known drawback of agro-industrial wastes, hence it should be further assessed.

Table 1 collects examples of information from past studies that evaluated biological susceptibility to some of the relevant biodeterioration agents.

In addition to the assessment of biological susceptibility, some past studies investigated the possibilities to moderate and solve it. Considering the ones in Table 1, Indrayani et al. [54] reported that citric acid avoided degradation by termites; Palumbo et al. [10] demonstrated that boric acid could improve resistance to mould growth.

3 Discussion

This collection of information demonstrates that there are many different methods to evaluate hygrothermal properties and bio susceptibility of agro-industrial wastes, both as raw materials and included in composites.

Agro-industrial wastes' properties as raw materials are commonly evaluated according to the recommendations of RILEM Technical Committee 236-BBM [9]. This is a useful and important guideline, also considering the relevance that bio-aggregates are taking in the last years. It is in step with the times and answers to the current research's requirements. Nevertheless, this document does not assess some important properties that could improve the evaluation of the performance

Table 1 Examples of past studies that evaluated bio-susceptibility of agro-industrial waste, individually and in composites

Biological attack	Bio agents	Standard/Method	Composites/Materials[a]	Ref
Brown rot fungi	*Gloeophyllum trabeum* (Pers.) Murrill	"Mini-block method" [45]	Particleboards with cardoon particles and a cassava starch-based binder	[37]
	Brunneoporus malicola (Pers.) Murr. (≈*Gleophyllum trabeum*) and *Trametes versicolor* (L., Fr.) Quél	Adapted from AWPA E-10 [46] and AWPA E-30 [47]	Particleboards with papaya stalk, macadamia nut carpel, coffee husks, eucalypt sawdust and urea–formaldehyde as a binder	[13]
Moulds	*Aspergillus niger*	Adapted from ASTM D5590-17 [48]	Earth-based mortars with siliceous sand, oat fibres and hydrated air lime	[16]
	Aspergillus niger and *Penicillium funiculosum*	Adapted from ASTM D5590-17 [48] and ASTM C1338-19 [49]	ETICS with expanded cork thermal insulation and lime-based coating	[14]
	Aspergillus niger and *Penicillium funiculosum*	Adapted from ASTM D5590-17 [48] and ASTM C1338-19 [49]	Cement-bonded particleboards with banana fibres, maritime pine (*Pinus pinaster*) chips and Portland cement	[39]
	Aspergillus niger and *Penicillium funiculosum*	Adapted from ASTM D5590-17 [48]	Grape press waste, olive press waste, hazelnut shells, spent coffee grounds and wood chips as raw materials	[8]
	No inoculation	Johansson et al. [50]	Insulation composites with corn pith bonded with sodium alginate and calcium sulphate dihydrate	[10]
	–	Viel et al. [51]; assessment according to ISO 846 [52]	Panels with hemp shiv and rape straw, with and without starch derivate binders additives and solvents	[51]
Termites	*Cryptotermes brevis* Walker, Isoptera: Kalotermitidae	Maistrello [53]	Particleboards with papaya stalk, macadamia nut carpel, coffee husks, eucalypt sawdust and urea–formaldehyde as a binder	[13]

(continued)

Table 1 (continued)

Biological attack	Bio agents	Standard/Method	Composites/Materials[a]	Ref
	Coptotermes formosanus	Mass loss and survival rates of termite	Boards with pineapple leaves and a mix of citric acid and sucrose as a binder	[54]
	Reticulitermes grassei	Cintura et al. [8]	Grape press waste, olive press waste, hazelnut shells, spent coffee grounds and wood chips as raw materials	[8]
	Reticulitermes grassei Clément	Adaptation of EN 117 [55]	Particleboards with cardoon particles and a cassava starch-based binder	[37]

[a]*Note* only bio-based composites are reported

of bio-aggregates. Some information could be further detailed or deepened [8]. For example, as Brouard et al. [24] described, water absorption could be evaluated considering the influence of temperature. As for the particle size analysis by the sieving method, the sieving time could be specified according to the type of bio-aggregates [8]. The thermal conductivity could be related to hygroscopic capacity. Other important information could be added, namely the evaluation of biological susceptibility by considering different bio-deterioration agents. However, all these are considerations to improve a cutting-edge document and an important reference to study bio-aggregates by a unified method. Finally, it is important to underline that the lack of a specific standard to evaluate agro-industrial wastes' properties could be both an advantage (flexibility in the choice of the methods) and a disadvantage (difficult comparison between the results and different studies).

As for composites, several standardized methods could be considered. Many of them are not specific for agro-industrial wastes, as they were drawn up for conventional materials. Considering the research trend of using bio-based materials, these methods could be updated. Specific standards can be proposed too, as, for example, the German standard for earth plasters, considered by Lima and Faria [30]. Nevertheless, the presence of many different methods already used has some benefits. First, it is possible to choose the most suitable one for the considered composites. Then, the same property could be evaluated by different laboratory tests that could enrich the discussions of the results and allow reaching important conclusions. Finally, since many past studies used the same methods, there are also many results. This makes easier the comparison between different materials and the discussions and validation of the results.

As regards the resistance to biological attack, many different methods and standards guarantee the evaluation of bio-susceptibility after inoculation [51], depending on the biodeterioration agents, the exposure method and the considered conditions.

Table 1 presents, as an example, only a small set of past studies that addressed the topic of bio susceptibility of agro-industrial wastes. The bibliographic research carried out for this work demonstrated that, even if the biological attack is one of the main drawbacks of agro-industrial wastes, is not so commonly addressed [16]. It has to be further evaluated since it can cause radical changes to materials' properties, compromise durability and affect human health [10, 51, 56]. The analysis of biological susceptibility could guarantee better use of agro-industrial wastes, as biological vulnerability could be prevented or moderated. Research should further investigate this topic, and studies related to the use of agro-industrial waste should always consider it. The already known methods to evaluate biological susceptibility could be improved and new laboratory tests proposed. Some of the already known and used could be collected to define a guideline to investigate this property. A greater number of studies that assess this property would also allow easier comparisons between different materials therefore an easier understanding of the results.

4 Conclusions

The present work reports laboratory tests to evaluate hygrothermal properties and biological susceptibility of agro-industrial wastes, considered as raw materials and in composites. It aims at providing a first review to be used as support for future research works. This work allows reaching the following conclusions:

- There are no specific standards to analyse agro-industrial wastes as raw materials. Past studies evaluated hygrothermal properties and bio susceptibility according to different methods.
- Past research usually analysed composites made up of agro-industrial wastes according to the standards used for conventional materials. This facilitates the comparison between them but can be complemented.
- Biological susceptibility is not so commonly assessed. Being one of the main drawbacks of using agro-industrial wastes, it should be further investigated.

References

1. La Gennusa, M., Marino, C., Nucara, A., Panzera, M.F., Pietrafesa, M.: Insulating building components made from a mixture of waste and vegetal materials: thermal characterization of nine new products. Sustainability **13**, 13820 (2021). https://doi.org/10.3390/su132413820
2. Posani, M., Veiga, R., de Freitas, V.P.: Retrofitting historic walls: feasibility of thermal insulation and suitability of thermal mortars. Heritage **4**, 2009–2022 (2021). https://doi.org/10.3390/heritage4030114
3. Liuzzi, S., Sanarica, S.: Stefanizzi, P: Use of agro-wastes in building materials in the Mediterranean area: a review. Energy Procedia **126**, 242–249 (2017). https://doi.org/10.1016/j.egypro.2017.08.147

4. Posani, M., Veiga, M.D.R., Peixoto de Freitas, V., Kompatscher, K., Schellen, H.: Dynamic hygrothermal models for monumental, historic buildings with HVAC systems: complexity shown through a case study. In: E3S Web of Conference, vol. 172, p. 15007 (2020). https://doi.org/10.1051/e3sconf/202017215007.
5. Ranesi, A., Faria, P., Correia, R., Freire, M.T., Veiga, R., Gonçalves, M.: Gypsum Mortars with acacia dealbata biomass waste additions: effect of different fractions and contents. Buildings **12**, 339 (2022). https://doi.org/10.3390/buildings12030339
6. Brás, A., Leal, M., Faria, P.: Cement-cork mortars for thermal bridges correction. Comparison with cement-EPS mortars performance. Constr. Build. Mater. **49**, 315–327 (2013). https://doi.org/10.1016/j.conbuildmat.2013.08.006
7. Czajkowski, Ł., Kocewicz, R., Weres, J., Olek, W.: Estimation of thermal properties of straw-based insulating panels. Materials (Basel) **15**, 1073 (2022). https://doi.org/10.3390/ma15031073
8. Cintura, E., Faria, P., Duarte, M., Nunes, L.: Bio-wastes as aggregates for eco-efficient boards and panels: screening tests of physical properties and bio-susceptibility. Infrastructures **7**, 26 (2022). https://doi.org/10.3390/infrastructures7030026
9. Amziane, S., Collet, F., Lawrence, M., Magniont, C., Picandet, V., Sonebi, M.: Recommendation of the RILEM TC 236-BBM: characterisation testing of hemp shiv to determine the initial water content, water absorption, dry density, particle size distribution and thermal conductivity. Mater. Struct. **50**, 167 (2017). https://doi.org/10.1617/s11527-017-1029-3
10. Palumbo, M., Lacasta, A.M., Navarro, A., Giraldo, M.P., Lesar, B.: Improvement of fire reaction and mould growth resistance of a new bio-based thermal insulation material. Constr. Build. Mater. **139**, 531–539 (2017). https://doi.org/10.1016/j.conbuildmat.2016.11.020
11. Cintura, E., Nunes, L., Esteves, B., Faria, P.: Agro-industrial wastes as building insulation materials: a review and challenges for Euro-Mediterranean countries. Ind. Crops Prod. **171**, 113833 (2021). https://doi.org/10.1016/j.indcrop.2021.113833
12. Brambilla, A., Sangiorgio, A.: Mould growth in energy efficient buildings: causes, health implications and strategies to mitigate the risk. Renew. Sustain. Energy Rev. **132**, 110093 (2020). https://doi.org/10.1016/j.rser.2020.110093
13. Gonçalves, F.G., Paes, J.B., Lopez, Y.M., Segundinho, P.G. de A., de Oliveira, R.G.E., Fassarella, M.V., Brito, A.S., Chaves, I.L.S., Martins, R.S.F.: Resistance of particleboards produced with ligno-cellulosic agro-industrial wastes to fungi and termites. Int. Biodeterior. Biodegrad. **157**, 105159 (2021). https://doi.org/10.1016/j.ibiod.2020.105159
14. Parracha, J.L., Borsoi, G., Flores-Colen, I., Veiga, R., Nunes, L., Dionísio, A., Gomes, M.G., Faria, P.: Performance parameters of ETICS: correlating water resistance, bio-susceptibility and surface properties. Constr. Build. Mater. **272**, 121956 (2021). https://doi.org/10.1016/j.conbuildmat.2020.121956
15. Echeverria, C.A., Ozkan, J., Pahlevani, F., Willcox, M., Sahajwalla, V.: Effect of hydrothermal hot-compression method on the antimicrobial performance of green building materials from heterogeneous cellulose wastes. J. Clean. Prod. **280**, 124377 (2021). https://doi.org/10.1016/j.jclepro.2020.124377
16. Santos, T., Nunes, L., Faria, P.: Production of eco-efficient earth-based plasters: influence of composition on physical performance and bio-susceptibility. J. Clean. Prod **167**, 55–67 (2017). https://doi.org/10.1016/j.jclepro.2017.08.131
17. de Carvalho, P.S., Nora, M.D., da Rosa, L.C.: Development of an acoustic absorbing material based on sunflower residue following the cleaner production techniques. J. Clean. Prod. **270**, 122478 (2020). https://doi.org/10.1016/j.jclepro.2020.122478
18. Laborel-Préneron, A., Magniont, C., Aubert, J.-E.: Characterization of barley straw, hemp shiv and corn cob as resources for bioaggregate based building materials. Waste Biomass Valorization **9**, 1095–1112 (2017). https://doi.org/10.1007/s12649-017-9895-z
19. Brás, A., Antunes, A., Laborel-Préneron, A., Ralegaonkar, R., Shaw, A., Riley, M., Faria, P.: Optimisation of bio-based building materials using image analysis method. Constr. Build. Mater. **223**, 544–553 (2019). https://doi.org/10.1016/j.conbuildmat.2019.06.148

20. Ansell, M.P., Lawrence, M., Jiang, Y., Shea, A., Hussain, A., Calabria-Holley, J., Walker, P.: Natural plant-based aggregates and bio-composite panels with low thermal conductivity and high hygrothermal efficiency for applications in construction. In: Nonconventional and Vernacular Construction Materials, pp. 217–245. Elsevier (2020). https://doi.org/10.1016/B978-0-08-102704-2.00010-X
21. Ratsimbazafy, H.H., Laborel-Préneron, A., Magniont, C., Evon, P.: Comprehensive characterization of agricultural by-products for bio-aggregate based concrete. Bio-Based Build. Mater. 77–84 (2022). https://doi.org/10.4028/www.scientific.net/CTA.1.77
22. Cintura, E., Nunes, L., Faria, P.: Characterization of agro-wastes to be used as aggregates for eco-efficient insulation boards. In: Proceedings of CEES 2021-1st International Conference on Construction, Energy, Environment and Sustainability. Coimbra, Portugal (2021). ISBN: 978-989-54499-1-0
23. EN 1097–3: Tests for mechanical and physical properties of aggregates Part 3: Determination of loose bulk density and voids. European Committee for Standardization, Brussels, Belgium (1998)
24. Brouard, Y., Belayachi, N., Hoxha, D., Ranganathan, N., Méo, S.: Mechanical and hygrothermal behavior of clay–Sunflower (*Helianthus annuus*) and rape straw (*Brassica napus*) plaster bio-composites for building insulation. Constr. Build. Mater. **161**, 196–207 (2018). https://doi.org/10.1016/j.conbuildmat.2017.11.140
25. Rode, C., Peuhkuri, R.H., Mortensen, L.H., Hansen, K.K., Time, B., Gustavsen, A., Ojanen, T., Ahonen, J., Svennberg, K., Arfvidsson, Jesper TotalRode, C., Peuhkuri, R.H., Mortensen, L.H., Hansen, K.K., Time, B., Gustavsen, A., Ojanen, T., Ahonen, J., Svennberg, K., Arfvidsson, J.T.: Moisture Buffering of Building Materials (BYG Report No. R-127). Technical University of Denmark, Department of Civil Engineering: Lyngby, Denmark (2005). ISBN 8778771951
26. Liuzzi, S., Rubino, C., Stefanizzi, P., Petrella, A., Boghetich, A., Casavola, C., Pappalettera, G.: Hygrothermal properties of clayey plasters with olive fibers. Constr. Build. Mater. **158**, 24–32 (2018). https://doi.org/10.1016/j.conbuildmat.2017.10.013
27. Binici, H., Aksogan, O., Demirhan, C.: Mechanical, thermal and acoustical characterizations of an insulation composite made of bio-based materials. Sustain. Cities Soc. **20**, 17–26 (2016). https://doi.org/10.1016/j.scs.2015.09.004
28. ASTM C67–03: Standard test methods for sampling and testing brick and structural clay tile. ASTM International: Pennsylvania, PA, USA (2017)
29. ASTM C1113/C1113M-09: Standard Test Method for Thermal Conductivity of Refractories by Hot Wire (Platinum Resistance Thermometer Technique). ASTM International: Pennsylvania, PA, USA (2019)
30. Lima, J., Faria, P.: Eco-efficient earthen plasters: the influence of the addition of natural fibers. In: Fangueiro, R., Rana, S. (eds.) RILEM Bookseries, pp. 315–327. Springer Netherlands, Dordrecht (2016). https://doi.org/10.1007/978-94-017-7515-1_24
31. DIN 18947: Earth plasters–Terms and definitions, requirements, test methods. Deutsches Institut fur Normung. Berlin, Germany (2013)
32. EN 1015–19: Methods of test for mortar for masonry–determination of water vapour permeability of hardened rendering and plastering mortars. European Committee for Standardization. Brussels, Belgium (1998)
33. EN 12571: Hygrothermal performance of building materials and products–Determination of hygroscopic sorption properties. International Standards Organization. Geneva, Switzerland (2013)
34. Ranesi, A., Veiga, M.R.V., Faria, P.: Laboratory characterization of relative humidity dependent properties for plasters : a systematic review. Constr. Build. Mater. **304**, 124595 (2021). https://doi.org/10.1016/j.conbuildmat.2021.124595
35. Antunes, A., Faria, P., Silva, V., Brás, A.: Rice husk-earth based composites: a novel bio-based panel for buildings refurbishment. Constr. Build. Mater. **221**, 99–108 (2019). https://doi.org/10.1016/j.conbuildmat.2019.06.074
36. Latif, E., Lawrence, M., Shea, A., Walker, P.: Moisture buffer potential of experimental wall assemblies incorporating formulated hemp-lime. Build. Environ. **93**, 199–209 (2015). https://doi.org/10.1016/j.buildenv.2015.07.011

37. Monteiro, S., Nunes, L., Martins, J., Magalhães, F.D., Carvalho, L.: Low-density cardoon (*Cynara cardunculus* L.) particleboards bound with potato starch-based adhesive. Polymers (Basel) **12**, 1–16 (2020). https://doi.org/10.3390/polym12081799
38. Farag, E., Alshebani, M., Elhrari, W., Klash, A., Shebani, A.: Production of particleboard using olive stone waste for interior design. J. Build. Eng. **29**, 101119 (2020). https://doi.org/10.1016/j.jobe.2019.101119
39. Nunes, L., Cintura, E., Parracha, J.L., Fernandes, B., Silva, V., Faria, P.: Cement-bonded particleboards with banana pseudostem waste: physical performance and bio-susceptibility. Infrastructures **6**, 86 (2021). https://doi.org/10.3390/infrastructures6060086
40. EN 323: Wood-based panels. Determination of density. European Committee for Standardization. Brussels, Belgium (1993)
41. EN 322: Wood-based panels. Determination of moisture content. European Committee for Standardization. Brussels, Belgium (1993)
42. Palumbo, M., Lacasta, A.M., Holcroft, N., Shea, A., Walker, P.: Determination of hygrothermal parameters of experimental and commercial bio-based insulation materials. Constr. Build. Mater. **124**, 269–275 (2016). https://doi.org/10.1016/j.conbuildmat.2016.07.106
43. EN 12664: Thermal performance of building materials and products. Determination of thermal resistance by means of guarded hot plate and heat flow meter methods. Dry and moist products of medium and low thermal resistance. European Committee for Standardization. Brussels, Belgium (2001)
44. ISO 24353: Hygrothermal performance of building materials and products-Determination of moisture adsorption/desorption properties in response to humidity variation. International Standards Organization. Geneva, Switzerland (2008)
45. Bravery, A.F.: A miniaturized wood-block test for rapid evaluation of wood preservative fungicides. In: Proc. IRG Annu. Meet. IRG/WP 2113, pp. 57–66. Peebles, Scotland, (1978)
46. AWPA E-10: Laboratory Method for Evaluating the Decay Resistance of Wood-Based Materials against Pure Basidiomycete Cultures: Soil/block Test, pp. 406–417. American Wood Protection Association (2016)
47. AWPA E-30: Standard Method for Evaluating Natural Decay Resistance of Woods Using Laboratory Decay Tests, pp. 494–498. American Wood Protection Association (2016).
48. ASTM D5590–17: Standard Test Method for Determining the Resistance of Paint Films and Related Coatings to Fungal Defacement by Accelerated Four-Week Agar Plate Assay. ASTM International, Pennsylvania, PA, USA (2021)
49. ASTM C1338–19: Standard test method for determining fungi resistance of insulation materials and facings. ASTM International, Pennsylvania, PA, USA (2019)
50. Johansson, P., Ekstrand-Tobin, A., Svensson, T., Bok, G.: Laboratory study to determine the critical moisture level for mould growth on building materials. Int. Biodeterior. Biodegrad. **73**, 23–32 (2012). https://doi.org/10.1016/j.ibiod.2012.05.014
51. Viel, M., Collet, F., Lecieux, Y., François, M.L.M., Colson, V., Lanos, C., Hussain, A., Lawrence, M.: Resistance to mold development assessment of bio-based building materials-Compos. Part B Eng. **158**, 406–418 (2019). https://doi.org/10.1016/j.compositesb.2018.09.063
52. ISO 846: Plastics—Evaluation of the action of microorganisms. International Standards Organization. Geneva, Switzerland (2019)
53. Maistrello, L.: Termites and standard norms in wood protection: a proposal targeting drywood termites. In: Aslam, M.K., Ahmad, W. (eds.) Termites and Sustainable Management, pp. 261–287. Springer, Berlin (2018). https://doi.org/10.1007/978-3-319-68726-1_12
54. Indrayani, Y., Setyawati, D., Munawar, S.S., Umemura, K., Yoshimura, T.: Evaluation of termite resistance of Medium Density Fiberboard (MDF) manufacture from agricultural fiber bonded with citric acid. Procedia Environ. Sci. **28**, 778–782 (2015). https://doi.org/10.1016/j.proenv.2015.07.091
55. EN 117: Durability of wood and wood-based products. European Committee for Standardization. Brussels, Belgium (2012)

56. Stefanowski, B.K., Curling, S.F., Ormondroyd, G.A.: A rapid screening method to determine the susceptibility of bio-based construction and insulation products to mould growth. Int. Biodeterior. Biodegradation **116**, 124–132 (2017). https://doi.org/10.1016/j.ibiod.2016.10.025

Geotechnical Characterization of Vegetal Biomass Ashes Based Materials for Liner Production

Leonardo Marchiori, Andre Studart, Maria Vitoria Morais, António Albuquerque, and Victor Cavaleiro

Abstract This paper aims to evaluate geotechnically, chemically, mechanically, and hydraulically parameters of vegetal-based biomass ashes (VBA) and its soil incorporation with different ratios as potential liner material and soils strengthening. Composites were developed for testing with different ratios of VBA: soil, following 05:95, 10:90, 15:85, and 20:80%. All laboratorial testing program followed European standards. For geotechnical characterization, the following tests were performed for all mixtures, the soil and VBA: granulometric distribution, specific gravity and Atterberg limits. Chemical characterization was done by collecting pH values and energy-dispersive X-ray spectroscopy (EDS) parameters for elemental and oxides analysis. Also, x-ray diffraction (XRD) was done to evaluate all sample's mineralogical description. In addition, mechanical analysis was conducted by analyzing expansibility, one-dimension consolidation through oedometer, and consolidated undrained (CU) triaxial test, along with falling head permeability for additional permeability analysis. Results have shown a finer granulometry and decrease of plasticity, 5% to non-plastic behavior, as higher amounts of VBA are introduced, exposing a filling-material behavior. EDS and XRD analysis indicate quartz, muscovite, orthoclase and calcite composition, and VBA could possibly have pozzolanic properties due to high silica-alum-ferric oxides amount. Mechanical parameters have shown a stabilization of VBA within the analyzed soil, exposing a slight reduction on settlements while increasing friction angle, 25–30º, and decreasing cohesion, 5–0 kPa. Permeability values have shown their feasibility for liners application, as found values characterizes all mixtures as low-permeability materials, especially introducing 5% of the residue into soil which values were below 10^{-9} m/s. Thus, the incorporation of VBA into soils paves a solid alternative for reusing this material in varied applications, as the analyzed soft soil has been geotechnically enhanced. Additional analysis, mainly pozzolanicity levels and leachability tests, can contribute for this on-going study to stablish VBA as a feasible material for the industry.

L. Marchiori (✉) · A. Studart · M. V. Morais · A. Albuquerque · V. Cavaleiro
Civil Engineering and Architecture Department, University of Beira Interior, FibEnTech and Geobiotec, Covilha, Portugal
e-mail: leonardo.marchiori@ubi.pt

C. Chastre et al. (eds.), *Testing and Experimentation in Civil Engineering*,
RILEM Bookseries 41, https://doi.org/10.1007/978-3-031-29191-3_6

Keywords Geotechnical characterization · Biomass ashes · Liner material · Soil reinforcement · Earthworks

1 Introduction

Vegetal biomass ashes (VBA) are by-products from combustion, pyrolysis, and incineration of varied type of vegetal biomass, mainly composed by tree ashes. Their combustion is mainly used for energy production, already representing a significant 10% of energy supply around the world [1]. To enhance the fuels' calorific value, it can be associated to coal powered plants as a co-combustion product, this activity produces filter, bottom, and fly biomass ashes as by-products, which present different physical–chemical characteristics compared to the original biomass [1], due to high temperatures and different furnaces processes. Also, although there is a belief that biomass is renewable—as the released CO_2 is the same used in the nature—this claim is not correct for biomass ashes, as the combustion processes alter the original biomass, transforming into a residue that could contaminate waters and soils [3]. Therefore, researching new applications for VBA are necessary to avoid general contamination, [3] indicated possible replacement of gravel in road construction while also feasible for fine-grained clays and soils' replacement in the construction of landfill liners due to its latent hydraulic properties. Thus, to mitigate environmental impacts, research around their reuse through soil's amendment in different ratios is needed looking to ameliorate soft soils' geomechanical characteristics, making feasible for varied earthworks, such as liners applications.

Waterproofing liners are normally based in clays or geomembranes. Clays are generally weak soils, normally stabilized with cement, lime and other industrial products that are not environmentally friendly and could represent an environmental hazard. Geosynthetics, although an effective material, is still a costly solution [4, 5] and can impact the general cost–benefit value of an earthwork. Therefore, these stablished methodologies could be improved through new methodologies and greener approaches, such as through the valorization of biomass ashes. Bagasse ash, rice husk ash, and palm oil fuel ash are prominent examples of such residues; cellulose and paper mill sludge, for example, consist mainly of fibbers and fillers can have low hydraulic conductivity (k) when properly compacted [6]. Leme and Miguel [7] analyzed the industrial potential for VBA and concluded the main advantage is the concentration and recovery of valuable components—SiO_2, Al_2O_3, CaO—which could indicate their feasibility for soft soil reinforcement, increasing effective friction angle while reducing voids and settlement, along with low permeability for liner production. A deeper investigation over chemical and mechanical parameters can also provide data to better understand and assess VBA's properties and its interaction with soils [7–9].

Therefore, understanding the characteristics of the analyzed VBA when introduced into soils could provide a better understanding for earthworks' application and contribute for its valorization, leading to an approach of production within the scope of circular economy. Thus, this paper aims to investigate and characterize geomechanically a VBA mainly based on biomass pine and olive ashes, and mixtures of VBA and a weak soil for evaluating their feasibility for application as liner material.

2 Methodology

VBA were collected at the industrial park of VALAMB, Castelo Branco, Portugal, and the soil was collected from the same region. Four mixtures of VBA:SOIL were developed based on dried masses in temperatures of 60–65 °C, with the following ratios:

Materials	VBA (%)	Soil (%)
Soil	0	100
VBA	100	0
05:95%	05	95
10:90%	10	90
15:85%	15	85
20:80%	20	80

All the materials, individually and the mixtures, were characterized for the determination of specific gravity (G_S), granulometry distribution (D_{10}, D_{50} and D_{90}) by sieves procedure, and consistency limits (W_L, W_P, PI) according to European standard ISO 17982 [10–12]. Normal Proctor compaction tests followed the procedure in BS1377-4 [13] for optimal characteristics ($\rho_{d,\,opt}$ and w_{opt}). Chemical compositions were determined through energy-dispersive X-ray spectroscopy (EDS) and scanning electrons microscopy (SEM) images by S-2700 Hitachi, Rontec, USA, and mineralogical analysis through X-ray diffraction (XRD), using a Phillips Analytical X-Ray B. V. from Rigaku, model DMAXIII, USA. EDS and XRD were also carried out for samples of the raw vegetal material (RVM) to compare the values with the ones for VBA.

Settlements during the oedometer tests were measured by an automatic LCR transducer strain gauge, through MPE with maximum strain of 25.8 mm and precision of 0.001 mm, connected to a data logger MPX3000, VJ Technology. Readings were performed on a logarithmic time scale, following the load scale of 1-30-150–300-600-1200 kPa, and the unload for 1200-300-1 kPa, based on [14].

For the triaxial compression tests, the equipment from GDSLab was used. Several series of consolidated undrained triaxial compression tests (CU) with pore water pressure and axial strain measurements were carried out. Saturation was interrupted when Skempton parameter B reached 0.95, and consolidation, when there was no difference in the volume for a certain period. The tests were ended when the axial strain reached 22%. For each material, three CU tests were performed, with confining pressures of 100, 200, and 300 kPa.

Falling-head permeability tests were performed in replicates for each material, with initial hydraulic gradients (i) of 25 and 100, based on [15].

Mechanical and hydraulic tests were not performed for VBA by itself due to very bad workability.

3 Results and Discussion

3.1 Geotechnical Characterization

Geotechnical parameters results are presented in Table 1 and show that VBA granulometry is finer than the soil, possibly indicating good filling properties, as it would fill voids within analyzed mixtures. A non-plastic (NP) behavior is observed for the mixtures with 10–20% of VBA, although 5% of VBA:SOIL remained just as plastic as the soil, a low-plasticity material. The literature review showed variable results, [17] found ashes with around 2.0 while [26] 2.6 of specific gravity, and as plasticity results, most studies found no plasticity for VBA.

Compaction parameters revealed an increasing of optimum water content (w_{opt}) and decrease in optimum dry density ($\rho_{d,\,opt}$) when VBA was increased up to 20%, providing a lighter material and a clay similar performance. Soil amendment with VBA is providing a finer granulometry as higher introduced VBA's portions are. Therefore, this result is an initial positive result, as the decrease of the soil's plasticity while decreasing specific gravity (G_S) could indicate VBA filling properties and weight reduction capacity, both being desirable characteristics, as better logistics due to easier material transport. Further mechanical analysis will be discussed to evaluate the impact of such characteristics in the resistance and consolidation parameters.

Table 1 Geotechnical parameters for soil, VBA e mixtures

Material	Particle size				Density	Plasticity			Compaction	
	Fines	D_{10}	D_{50}	D_{90}	G_S	W_L	W_P	PI	w_{opt}	$\rho_{d,\,opt}$
	%	µm	µm	µm	–	%	%	%	%	g/cm^3
Soil	11	80	850	2000	2.7	40	35	5	19	1.70
VBA	10	75	600	1500	1.9	NL	NP	NP	25	0.90
05:95%	10	75	750	1800	2.6	41	33	8	16	1.65
10:90%	12	80	550	1700	2.5	44	NP	NP	18	1.60
15:85%	11	80	500	1750	2.5	43	NP	NP	21	1.55
20:80%	12	80	500	1600	2.4	42	NP	NP	25	1.50

D_{10}, D_{50}, D_{90}: particle size below 10, 50 or 90% of all particles; Gs: specific gravity; W_L: liquid limit; W_P: plastic limit; PI: plastic index; NL: non-liquid; NP: non-plastic; w_{opt}: optimum water content; $\rho_{d,\,opt}$: optimum dry density

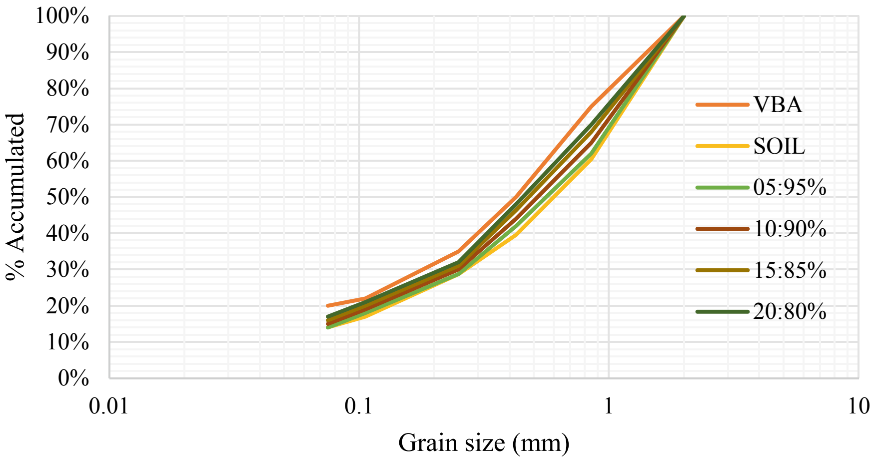

Fig. 1 Granulometric distributions for all samples

According to Unified Soil Classification System (USCS) in ASTM D2467, all tested materials are well-graded sand (SW), as exposed in Fig. 1, particle size distributions are very similar, the orange line and the yellow line show VBA and soil, respectively, being VBA finer than soil, therefore the mixtures are in between those curves, it is difficult to perceive due to the scale of granulometric distribution, however the material behaves as finer with greater VBA introductions. In the classification and compaction characteristics context, VBA around several studies [17–23, 26] behave like a typical sandy soil with silt.

3.2 Mechanical Performance

Mechanical parameters results are presented in Table 2 and show that VBA's feasibility for both enhancing soil's resistance and slightly reducing its consolidation. Although expansibility parameter (S) has not decreased, VBA's introduction has not significantly impacted the original soil's expansibility, exposing their possible introduction without altering some original parameters of the soil. S was not performed to RVM due to its coarse particle size distribution, being unable to sieve the amount required for the test.

One-dimensional oedometric consolidation samples were remoulded compacting a Normal Proctor mould and extruded from it in laboratory, for the test there were only the initial consolidation due to the pore stone and top cap, then the loads were applied. Initial void ratios distinguished in between 50 and 65% due to rearrange of particles within different VBA introduction ratios, possibly filling the voids for 05–10% and for 15–20% increasing the size of the pores. Figure 2 exposes oedometer curves, the chosen loads for oedometer were mainly to evaluate the compressibility

Table 2 Mechanical parameters

Material	Expansibility	Consolidation				Triaxial	
	S (%)	e_0 (%)	C_C (–)	C_S (–)	C_R (–)	c' (kPa)	φ' (º)
Soil	22	55	0.100	0.015	0.015	10	25
VBA	18	–	–	–	–	–	–
05:95%	20	50	0.100	0.024	0.013	0	25
10:90%	22	52	0.090	0.021	0.017	0	25
15:85%	22	59	0.080	0.018	0.018	0	30
20:80%	20	65	0.070	0.017	0.021	0	25

coefficient (C_c) progressively from 30 to 1200 kPa, exposing a slight Cc reduction, which indicate lower settlement which could eventually minimize damage within civil structures, such as fissures. S values fluctuated in 20% with a little reduction when introducing VBA, also stabilizing the composites. For liner, it can help prevent residues and heavy metals to percolate and infiltrate into subsoil and groundwater. Consolidation behaviour for VBA:SOIL mixtures do not change significantly the soil's performance, which can be seen as a positive characteristic, as the residue's introduction did not worsen the soil. Corroborating with [26–29] long-term data which consolidated VBA as a stabilizer for many types of soils, as expansive, soft, and organic ones.

Consolidated undrained triaxial specimens were recompacted inside a triaxial mould using similar energy to Normal Proctor compaction, they followed the procedure of firstly saturate the sample with a confining stress of 100 kPa and then consolidate until there was no pore volume change. Stress path curves are presented in Fig. 3, in accordance with the results presented in Table 2, 15:85% composites seem to be the most susceptible reinforcement, with high effective friction angle (*φ*') of 30º and no cohesion (c') making the composite susceptible for varied earthworks, such as

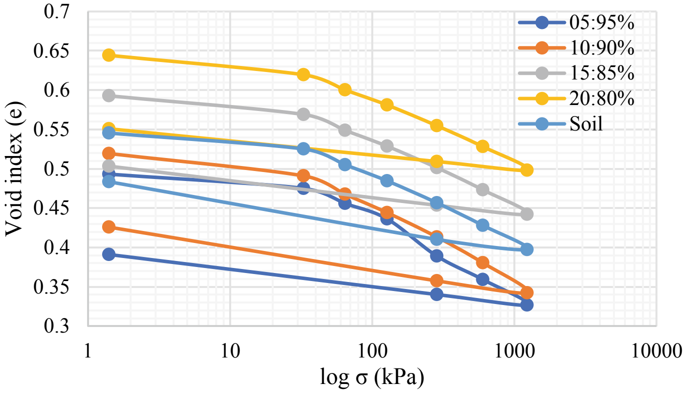

Fig. 2 Oedometric curves for soil, and mixtures

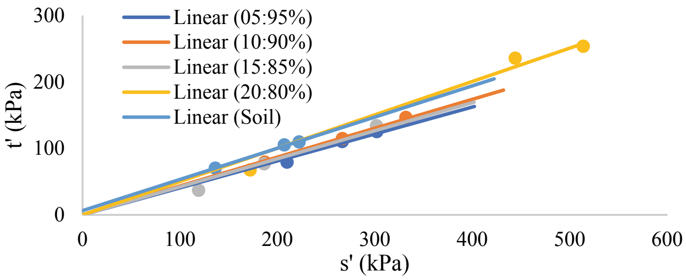

Fig. 3 Stress paths envelops for soil and mixtures

retaining structures or liners [16, 17]. Other mixtures presented the same behaviour, c' = 0 and the no interference in φ' of the soil, stabilizing the soil. Previous studies have presented VBA's successful introduction into soils, enhancing some parameters, such as shear resistance increase, or maintaining soils' original values, such as plasticity indexes and consolidation parameters [18, 19]. Thus, found results corroborate to the VBA's successful introduction ameliorating geomechanical parameters of soils.

Oedometric and triaxial tests were not performed for the VBA by itself because the materials do not have workability for moulding, and the main objective is to incorporate the by-product into soils.

3.3 Hydraulic Conductivity

Hydraulic conductivity is the main parameter for analyzing a materials' susceptibility for liners application. Low permeability is highly recommended for soils and materials in such applications [20]. Found k values are summarized in Table 3. The same sampling procedure of the oedometer consolidation tests were done for the permeability, although introduced in a permeameter with the same diameter, and as the specimens had 2.0 cm height, the rest of the permeameter were filled with water.

Presented data states the soil is a low permeability material and a proper material for liner applications. When introducing VBA, k values had an impact on the average of a magnitude order of 10x, indicating a behavior closer to a granular material,

Table 3 Permeability results for soil and mixtures

Material	k (m/s)
Soil	6×10^{-11}–3×10^{-9}
05:95%	6×10^{-10}–1×10^{-9}
10:90%	6×10^{-10}–1×10^{-8}
15:85%	1×10^{-9}–2×10^{-8}
20:80%	1×10^{-9}–2×10^{-8}

although generally maintaining low permeability characteristics. Regarding 05:95% mixtures, found results were close to the limit for liners making feasible for this application. Although unsatisfactory values were also obtained for the 10–15–20% mixtures, exposing a necessity of treatment for the sample.

Osinubi and Eberemu [21] tested residual compacted granite soil treated with 0–15% biomass ash, which should behave like VBA due to combustion, to assess its hydraulic conductivity for use in landfills and resulted in an improvement in soil plasticity, also showed for the 05:95% sample, although differs for the others mixtures, while $\rho_{d,\,opt}$ and w_{opt} decreased and increased, respectively, increasing biomass ash content. In general, k decreased to a 10% biomass ash content, for which k was around 10^{-9} m/s, but with 15% increased to k around 10^{-7} cm/s, unsuitable for liners. [21] also tested on a reddish-brown lateritic soil treated with up to 12% of biomass ash to assess its suitability in applications of waste containment barriers and in the 4–12% range of residue into composite material, compacted samples recorded hydraulic conductivity values below 10^{-9} m/s, making it suitable for use in barrier applications of waste containment.

Abovementioned works on VBA:SOIL composite had shown great impact on permeability up to 10% of residue's incorporation, corroborating with Table 3 results, and concluding that for granular soils, VBA can decrease k, and for clayey, increase k, although not very significantly, making possible a controlled introduction of VBA into soils for geotechnical purposes.

Analyzing collected data, the 05:85% seems to be the optimal mixture, as it managed to reach values below 10^{-9} cm/s in all tests, characterizing itself as a possible liner material. In addition, the 20:80% mixture has suffered a drop on the hydraulic performance, which can be due to an excess of granular material behavior without plasticity, allowing greater water percolation and, therefore, k values above the limit.

3.4 Chemical and Mineralogical Composition

Chemical analysis were conducted to evaluate all samples' composition and investigate their origins and a larger understanding of their behaviour, in addition, the raw vegetal material (RVM) of the combusted VBA was analysed to possibly trace some elements. Therefore, EDS oxides are in Table 4. [1, 8, 9] made a comprehensive and extensive study around biomass ashes chemical composition aligned with the raw material, and concluded that it can vary in oxides percentages mainly due to raw material typology, incineration or industrial processes and location of the culture or the power plant because of weathering effect.

As stated in [18], VBA is considerably different from RVM, having higher amounts of Na, Si, Ca, S and Fe and a crystalline structure as there are many minor peaks hard to characterize apart from the above-mentioned. Also, a generally amorphous structure is also present, mostly due to physic-chemical alterations as calcination through incineration process occur. These elements' enrichment has different and varied causes as the incineration process of RVM involves different

Table 4 EDS results for soil, VBA and RVM

Material	Soil	VBA	RVM	05:95%	10:90%	15:85%	20:80%
Na_2O (%)	0.6	1.2	0.4	0.8	0.9	1.0	1.1
MgO (%)	2.3	4.2	7.6	2.6	2.9	3.4	3.6
Al_2O_3 (%)	27	18	34	26	25	24	23
SiO_2 (%)	56	45	4.6	54	53	52	51
CaO (%)	–	15	3.3	2.4	3.6	6	8
K_2O (%)	4.5	7.1	8.8	4.8	5.2	5.4	5.7
SO_3 (%)	–	1.8	0.5	–	–	–	–
Fe_2O_3 (%)	8.3	5.8	0.1	8	7.7	7.6	7.5
TiO_2 (%)	0.9	0.7	0.8	0.9	0.8	0.7	0.7
MnO (%)	–	–	27	–	–	–	–
Others (%)	0,4	0,2	12,9	–	–	–	–

methodologies and chemical products. Different type of coals can be used as fuel while granular materials, such as silicious sand, are also commonly used within fluidized bed methodology [22]. Silica, for example, was the element that suffered the highest increase, probably due to the use of silicious sand during the fluidized bed combustion process of RVM.

Followed by the silica, calcium suffered high enhancement, which although hard to precisely explain the reason, several studies have also stated this behaviour on pine-based biomass and could trace it back to thermal-conversions happening from 500 ºC, being more pronounced on carbonated minerals, such as Calcite's ($CCaO_3$) disintegration that releases CO_2 and forms CaO [8, 9]. In addition, coals' varied composition and generally high amount of alkali metals [23] could also induce the conversion of some elements to new composites through the iteration of the coals' reactive part with released gases during incineration, such as sulphur.

Mineralogical composition were conducted for VBA, RVM, and the soil, and RVM, XRD were not done for the mixtures due to supposed no mineralogical change. Table 5 shows found mineralogy for VBA, RVM, and SOIL, respectively, along with XRD diffractograms shown in Figs. 4, 5 and 6.

Although similar minerals were found among their composition, the quantities vary considerably, while also being hard to identify every peak through VBA's sample as there are many minor peaks hard to trace back. In addition, all samples have shown mineralogy compatible with the collection location—Castelo Branco's region—which is mostly corresponded by metamorphic schists, feldspars, and granites [24]. Therefore, although presenting mostly similar mineralogy, the chemical number of oxides and the structure itself change considerably to the point of being basically a new material. This new material is also characterized by having the sum of Si + Al + Fe content around 70%, indicating pozzolanic properties, as [25] defines this amount for possibly having good levels of pozzolanicity, creating a silica-gel that could minimize voids while enhancing resistance.

Table 5 Mineralogical results for soil, VBA and RVM

Mineral	RVM	VBA	SOIL
Quartz	X	X	X
Muscovite	X	X	X
Orthoclase	X	X	
Calcite	X	X	
Kaolinite	X		X

Quartz (SiO_2); Muscovite (Al_2.8Fe0.1H_2K0.6Mg0.04Na0.37O12Si_3.04Ti0.0_2); Orthoclase (AlKO8Si_3); Calcite ($CCaO_3$); Kaolinite ($Al_2H_4O_9Si_2$)

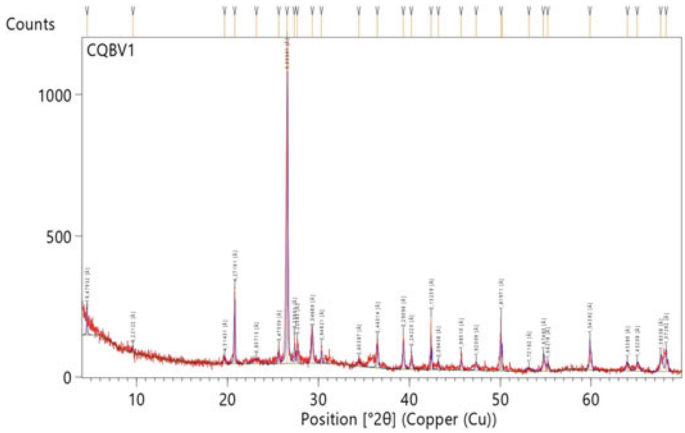

Fig. 4 XRD results for VBA

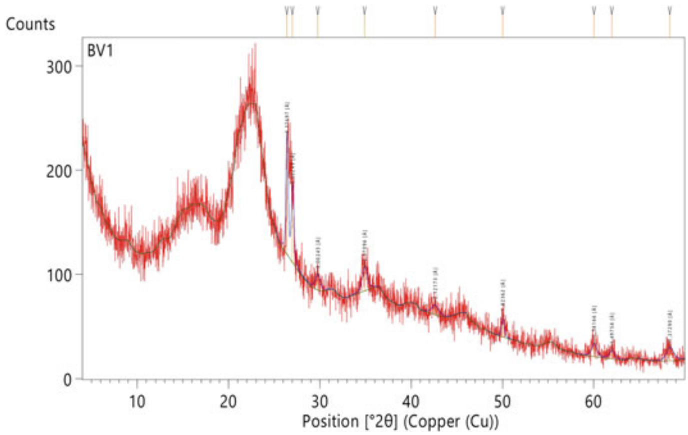

Fig. 5 XRD results for RVM

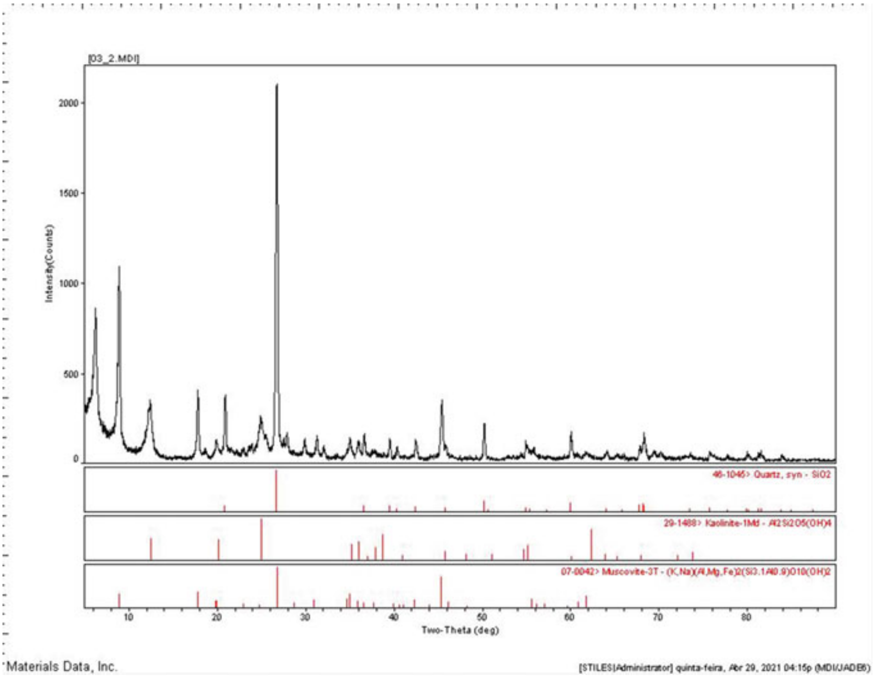

Fig. 6 XRD results the soil

To complement, SEM evaluation on a magnification of 300 × was conducted for VBA, soil, and mixtures, and due to bigger particle size, 50 × for RVM. Results can be observed through Figs. 7, 8, 9, 10, 11, 12 and 13 for RVM, VBA, soil, and mixtures, respectively. Although RVM has a coarse granulometry comparing with other even with lower magnification images. VBA presents a finer granulometry compared to RVM and soil, corroborating with previous analysis of void-filling capacity, as it can also be stated throughout analysed mixtures. This decrease in particle size can be attributed to combustion processes which disintegrated the raw material and deeply impacted their physic-chemical characteristics.

4 Conclusion

The analysed biomass ashes seem to be a feasible soil substitute for liners applications on the 05:95% proportion due to hydraulic conductivity and geotechnical characteristics. It can mitigate the utilization of clayey soil, a scarce raw material, and geosynthetics which are still a costly solution.

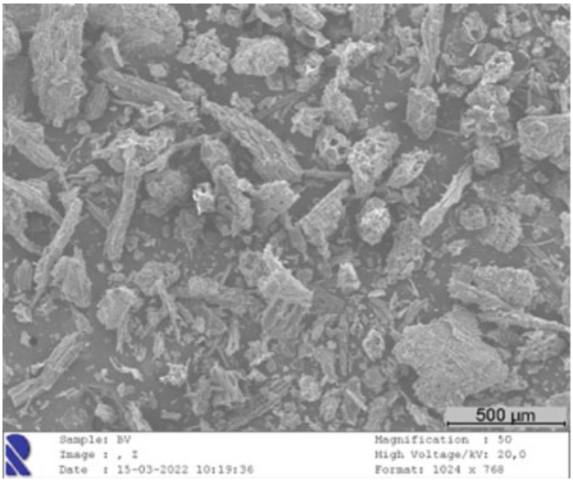

Fig. 7 SEM image for RVM

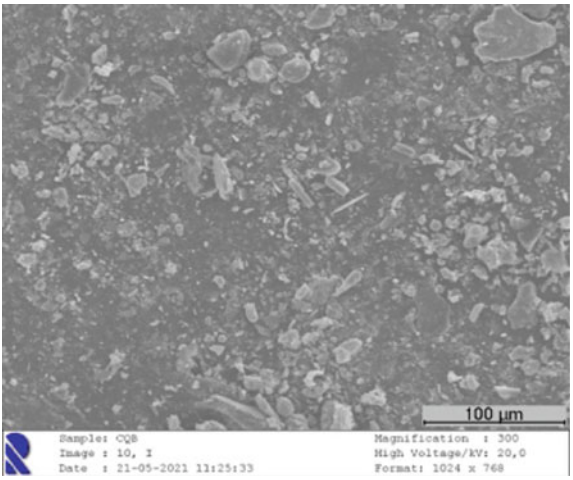

Fig. 8 SEM image for VBA

Although other mixtures could possibly be used through samples' treatment, lowering permeability values. Furthermore, the conclusions of this research towards the valorisation of residues within the scope of circular economy were:

- Granulometry distribution generated finer materials within VBA incorporation.
- Resistance and consolidation were ameliorated by VBA's filling properties and lowering plasticity characteristic.
- All samples showed soil's strengthening, principally the 15:85% and 20:80% ratios due to an increase on friction angle and decrease of cohesion.
- Results have shown enhancement of the analysed soil' geomechanical characteristics and, mostly, conserving soil's parameters.

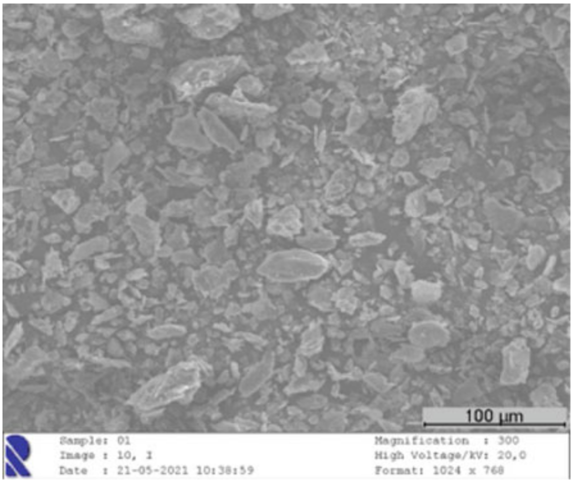

Fig. 9 SEM image for Soil

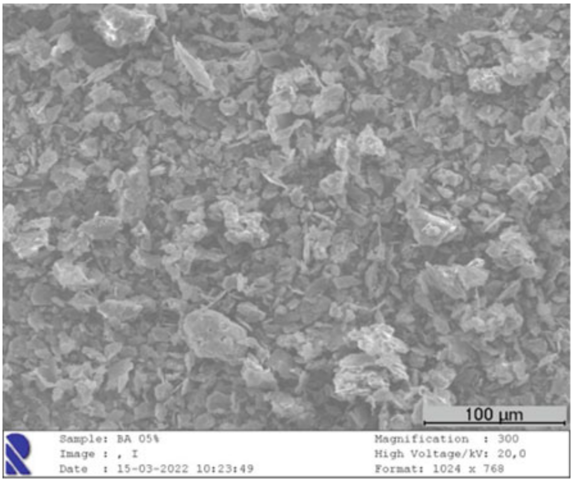

Fig. 10 SEM image for 05:95%

- Chemical analysis indicated a possible pozzolanic activity, which could also be useful, principally if associated to leachability and FTIR tests, needing this future evaluation.
- 05:95% ratio of VBA within soil as composite material seems to be an alternative liner material, reaching required k values, not changing consolidation, plasticity, and shearing performance of the soil.

Fig. 11 SEM image for 10:90%

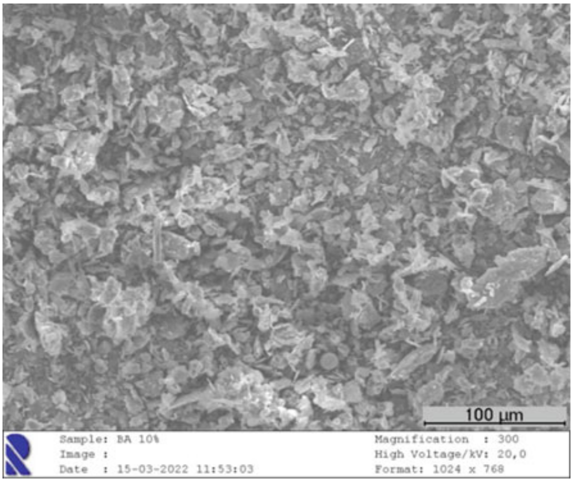

Fig. 12 SEM image for 15:85%

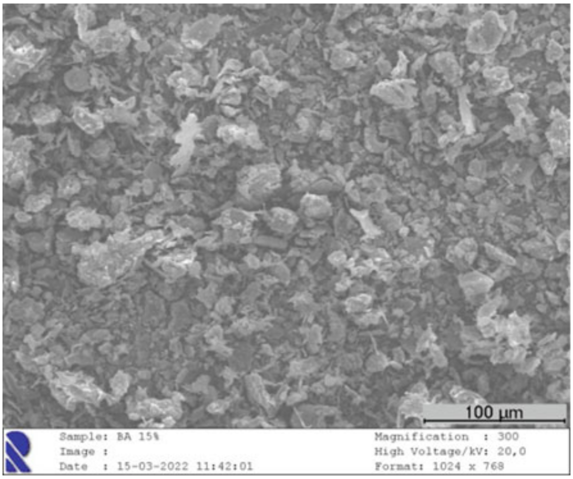

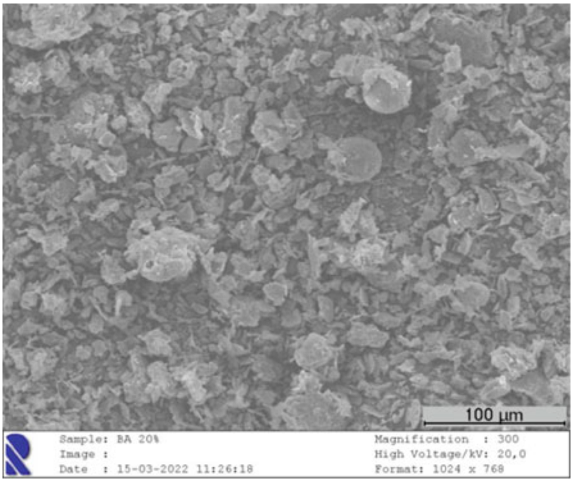

Fig. 13 SEM image for 20:80%

Acknowledgements The authors are grateful to the Foundation for Science and Technology (FCT, Portugal) for financial support by national funds through the projects UIDB/00195/2020 (FibEn-Tech) and UIDB/04035/2020 (GeoBioTec). The authors are also grateful to João Dias das Neves, VALAMB—Grupo Razão, who provided the biomass ashes' material, and Dra. Ana Gomes, from UBI's Optical Center with the EDS, XRD and SEM analysis.

References

1. Vassilev, S.V., Baxter, D., Andersen, L.K., Vassileva, C.G.: An overview of the chemical composition of biomass. Fuel **89**(5), 913–933 (2010). https://doi.org/10.1016/j.fuel.2009.10.022
2. van Loo, S., Koppejan, J.: The Handbook of Biomass Combustion and Co-Firing. Earthscan (2008)
3. Obernberger I, Supancic K: Possibilities of ash utilisation from biomass combustion plants. (2009).
4. Duffy, D.P.: Landfill Economics—Part 1—Getting Down to Business. MSW Management (2015)
5. Duffy, D.P.: Landfill Economics—Part 2—Getting Down to Business. MSW Management (2016)
6. Vassilev, S.V., Baxter, D., Andersen, L.K., Vassileva, C.G.: An overview of the composition and application of biomass ash. Fuel **105**, 19–39 (2013). https://doi.org/10.1016/j.fuel.2012.10.001
7. Alves de Godoy Leme, M., Gonçalves Miguel, M.: Permeability and retention to water and leachate of a compacted soil used as liner. Water, Air, Soil Pollut. **229**(11) (2018). https://doi.org/10.1007/s11270-018-4001-0
8. Vamvuka, D., Zografos, D.: Predicting the behaviour of ash from agricultural wastes during combustion. Fuel **83**(14–15), 2051–2057 (2004). https://doi.org/10.1016/j.fuel.2004.04.012
9. Vamvuka, D., Pitharoulis, M., Alevizos, G., Repouskou, E., Pentari, D.: Ash effects during combustion of lignite/biomass blends in fluidized bed. Renew. Energy **34**(12), 2662–2671 (2009). https://doi.org/10.1016/j.renene.2009.05.005

10. ISO17892–3: Geotechnical investigation and testing—Laboratory testing of soil—Part 3: Determination of particle density (2015)
11. ISO17892–4: Geotechnical investigation and testing—Laboratory testing of soil—Part 4: Determination of particle size distribution (2016)
12. ISO17892–12: Geotechnical investigation and testing—Laboratory testing of soil—Part 12: Determination of liquid and plastic limits (2018)
13. BS 1377–4: Methods of test for Soils for civil engineering purposes—Part 4: Compaction-related tests. British Standards Institution, UK (1990)
14. ISO17892–5: Geotechnical investigation and testing—Laboratory testing of soil—Part 5: Incremental loading oedometer test. (2017)
15. ISO17892–11; Geotechnical investigation and testing—Laboratory testing of soil—Part 11: Permeability tests. (2019)
16. Rubinos, D.A., Spagnoli, G.: Utilization of waste products as alternative landfill liner and cover materials–a critical review. Crit. Rev. Environ. Sci. Technol. **48**(4), 376–438 (2018). https://doi.org/10.1080/10643389.2018.1461495
17. Marchiori, L., Albuquerque, A.: Critical review of industrial solid wastes as barrier material for impermeabilization of storage waste facilities. In: SUM2020—5th Symposium on Urban Mining and Circular Economy (2020)
18. Studart, A., Marchiori, L., Morais, M.V., Albuquerque, A., Almeida, P.G., Cavaleiro, V.: Chemical and mineralogical characterization of biomass ashes for soil reinforcement and liner material. In: 1st International FibEnTech Congress (FibEnTech21) New Opportunities for Fibrous Materials in the Ecological Transition, pp. 1–7, Covilhã (2021)
19. Marchiori, L. et al.: Geotechnical characterization of biomass ashes for soil reinforcement and liner material. In: 1st International FibEnTech Congress (FibEnTech21) New Opportunities for Fibrous Materials in the Ecological Transition, pp. 1–6, Covilhã (2021)
20. Khalid, N., Mukri, M., Fadzil Arshad, M., Sidek, N., Kamarudin, F.: Effect on Salak Tinggi residual soil mixed Bentonite as compacted clay liner. IOP Conf. Ser. Mater. Sci. Eng. **513**(1), 012024 (2019). https://doi.org/10.1088/1757-899X/513/1/012024
21. Osinubi, K.J., Eberemu, A.O.: Hydraulic conductivity of compacted lateritic soil treated with bagasse ash. Int. J. Environ. Waste Manag. **11**(1), 38–58 (2013). https://doi.org/10.1504/IJEWM.2013.050522
22. Pinto, J.C.F.: Características da cinza de combustão de biomassa em leito fluidizado. Universidade de Aveiro (2011)
23. Vassilev, S.V., Vassileva, C.G.: A new approach for the classification of coal fly ashes based on their origin, composition, properties, and behaviour. Fuel **86**(10–11), 1490–1512 (2007). https://doi.org/10.1016/j.fuel.2006.11.020
24. Cunha, P.: Evolução tectono-sedimentar terciária da região de Sarzedas (Portugal). Comunicação Serviço de Geologia Portugal **73**(1/2), 67–84 (1987)
25. ASTM C618: 12a Standard Specification for Coal Fly Ash and Raw or Calcined Natural Pozzolan for Use in Concrete". https://doi.org/10.1520/C0618-12a
26. Edil, T.B., Berthouex, P.M., Vesperman, K.D.: Fly ash as a potential waste liner. In: Geotechnical Practice for Waste Disposal 87', GSP13 (1987)
27. Li, L., Benson, C.H., Edil, T.B., Hatipoglu, B.: Sustainable construction case history: fly ash stabilization of recycled asphalt pavement material. Geotech. Geol. Eng. **26**(2), 177–187 (2008). https://doi.org/10.1007/s10706-007-9155-2
28. Tastan, E.O., Edil, T.B., Benson, C.H., Aydilek, A.H.: Stabilization of organic soils with fly ash. J. Geotech. Geoenviron. Eng. **137**(9), 819–833 (2011). https://doi.org/10.1061/(ASCE)GT.1943-5606.0000502
29. Senol, A., Bin-Shafique, M.S., Edil, T.B., Benson, C.H.: Use of class c fly ash for stabilization of soft subgrade. In: Fidth Internation Congress on Advances in Civil Engineering (2002)

An Input in the Asian Wasp Nest (AWN) Study

Jorge Pinto, Mário Ginja, Miguel Nepomuceno, and Sandra Pereira

Abstract The Asian Wasp Nest (AWN) is an impressive and robust natural construction built by an insect. The building process occurs during spring and summer. This type of nest is not reused. The scale size between the Asian wasp and the AWN is substantial. In Portugal, we can find AWN on trees, roofs, balconies, chimneys, and other possibilities. When the AWN is built on trees, the tree's branches work as support. The complexity of this natural construction in terms of shape motivated this research work. Therefore, an AWN sample was used in order to obtain some information concerning this technical aspect. In this context, X-ray tests were performed to give guidance about the internal structure of the AWN without damaging it. The obtained experimental results show the richness of this type of construction. Understating the AWN may guide new building processes, different structural shapes, alternative natural building materials, and passive building technics, among other constructive fields.

Keywords Asian Wasp Nest · Biomimetic · Smart building · X-ray · Natural construction · Test

J. Pinto (✉) · M. Ginja · S. Pereira
University of Trás-os-Montes e Alto Douro (UTAD), Vila Real, Portugal
e-mail: tiago@utad.pt

M. Ginja
e-mail: mginja@utad.pt

S. Pereira
e-mail: spereira@utad.pt

J. Pinto · M. Nepomuceno · S. Pereira
CMADE—Centre of Materials and Building Technologies, UBI, Covilhã, Portugal
e-mail: mcsn@ubi.pt

M. Ginja
Centre for Animal Sciences and Veterinary Studies (CECAV), UTAD, Vila Real, Portugal

M. Nepomuceno
University of Beira Interior (UBI), Covilhã, Portugal

Lab2PT, Landscape, Heritage and Territory Laboratory, Guimarães, Portugal

C. Chastre et al. (eds.), *Testing and Experimentation in Civil Engineering*,
RILEM Bookseries 41, https://doi.org/10.1007/978-3-031-29191-3_7

1 Introduction

Several examples of earth construction mimic nature functions, called biomimetic [1–3]. Other natural models were also applied in the building construction and as a sustainable option [2–7].

The study of nests of birds and insects can give valuable knowledge to the building industry [8–11], in particular, the earth construction. This research team has already done some works related to swallow nests (Portuguese andorinha-dos-beirais) [12–16].

That knowledge encouraged this group to embrace other challenges in this area which is the study of the Asian wasp nests (AWN).

Some studies on the wasp nests have focused on the colonies' behaviour [17–23] rather than the construction perspective.

In this context, this paper's main objective is to contribute to the study of the AWN as a natural construction. In particular, are presented some AWN examples, indicating some possibilities of the supports of the nest, delivering some approximate dimensions of the nest and describing its form. For this last purpose, X-ray tests were performed to obtain information without damaging the AWN, which is a novelty.

In this paper, some information concerning the building process of the Awn is presented. Some technical aspects related to the shape and the size of this type of nest are also introduced. The results of the X-ray test of the AWN are also shown and described.

2 Context

There are several wildlife constructions. The African anthill, the wasp nest (Fig. 1a), the termite mud tube (Fig. 1b) and the swallow nest (Fig. 1c) are some of these examples. Each one may have its specific architecture, material and building technique. There is a scale proportion between the construction and its builder in the mentioned example and in general. The shape of the structure may be related to its function and the shape of the builder. The building material is natural. The building technique seems to be a progressive process resulting in monolithic construction. The building material appears to be applied with certain plasticity that gets hard by drying.

According to the examples shown in Fig. 1, it is also possible to realize that may exist a direct connection between these natural constructions and the industrialized construction. For instance, the termite mud tube shown in Fig. 1b is built on a granite masonry wall. On the other hand, the swallow nest of Fig. 1c is built on the pipes.

The examples in Fig. 1 indicate that natural and industrialized constructions may interact in harmony.

The AWN is also one of these types of natural construction, and it is the focus of this research work.

a) Wasp nest b) Termite mud tube c) Swallow nest

Fig. 1 Examples of natural constructions

a) Egg box b) Lightened fungiform reinforced concrete slab

Fig. 2 Alveolar structural examples

For instance, based on the idea of the wasp nest alveolar shape (Fig. 1a), Fig. 2 shows two examples of current applications in which the alveolar structural shape is also applied. These two examples are egg boxes (Fig. 2a) and lightened fungiform reinforced concrete slabs (Fig. 2b).

At the same time, Fig. 3 shows other organic shape structural elements similar to natural organic constructions.

3 Some Highlights About AWN

AWN can be built in urban or rural areas, Fig. 4. The trees tend to be deciduous type such as chestnut (castanea sativa), oak (quercus), poplar (populus), hazel (corylus avellana), among other species. They are generally constructed on the top of the tree and orientated south.

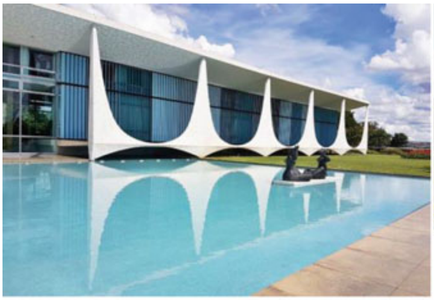

a) Reinforced concrete columns b) Pedestrian GLULAM bridge

c) Bamboo columns d) Bamboo roof

Fig. 3 Some examples of organic shape structural elements

a) Rural area b) Urban area

Fig. 4 Two examples of AWN

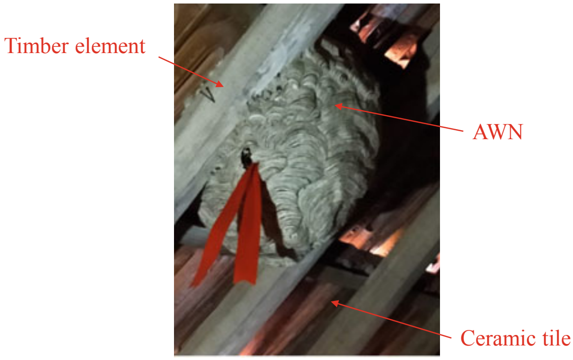

Fig. 5 An AWN built in a roof

At the same time, AWN may also be built-in buildings, as mentioned above and such as the one presented in Fig. 5, which was built on the roof. In this case, the AWN is mainly supported on the ceramic tile.

4 The AWN Used as the Study Case

The AWN used as a study case was on the tree shown in Fig. 6, a poplar tree (*populus*). It was picked up in December of 2021. From Fig. 6, it is possible to figure out the impressive size of this AWN. The nest is supported on branches of the tree. The water drop shape of the nest is also observed in this figure. In addition, there is a red ribbon attached to the nest that indicates that the nest was deactivated.

The AWN was removed from the tree by cutting the main branch. Figure 7 shows this AWN in the lab where it has been kept from December 2021 under controlled temperature and humidity. The nest has a length of 0.75 m and a wide of 0.40 m, approximately. Its weight is 2.40 kg, including the weight of the branches. Therefore, it indicates that the density of the building material of the AWN seems to have a low density. In addition, the colour of the AWN is quite similar to the colour of the branch of the tree.

Before the removal of this AWN from the tree, it seems that it had been exposed to climate exposure such as temperature variation and the direct impact of rain during a certain time. It may explain the level of deterioration of the surface of this AWN, as shown in Fig. 7. In contrast, the AWN of Fig. 5 presents an intact surface. It is also protected from direct exposure to UV and rain. In this situation, the AWN was formed in the spring of 2021 and deactivated in July of 2021.

a) Overview b) Detailed view

Fig. 6 AWN used as a study case on the tree

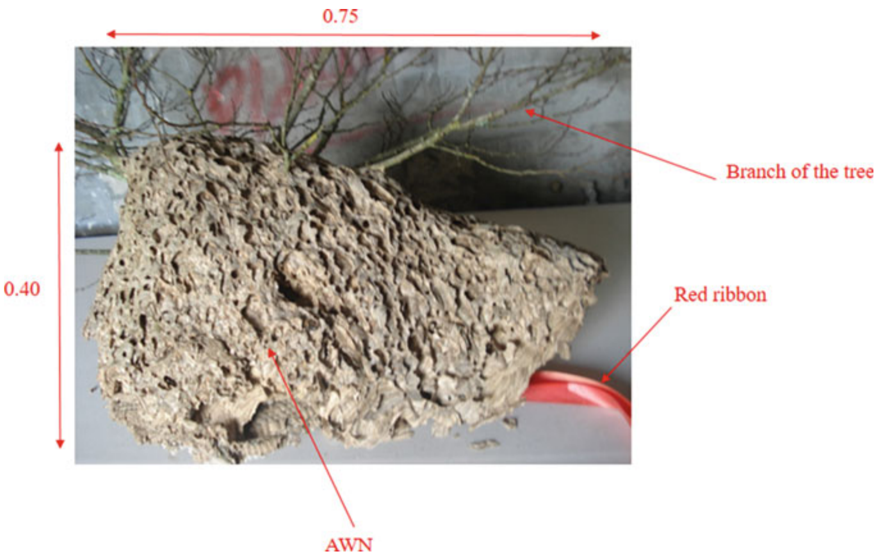

Fig. 7 Some dimensions of the AWN used as study (m)

5 X-ray Test of the AWN

An X-ray test was performed in the AWN in order to understand the interior structure of this construction. This test was done in the Veterinary Hospital of UTAD.

The AWN was tested in two positions, 1 and 2, according to Figs. 8, 9 and 10, respectively.

The radiographic of the nest in positions 1 and 2 are shown in Figs. 9 and 11, respectively.

In these radiographs, the high intensity of white colour corresponds to high density. Therefore, it is possible to differentiate quite clear the branches of the tree (higher density of white colour) from the walls of the nest (medium-density white colour) and the empty spaces of the nest (dark colour).

In terms of position 1, the radiography of the left side of the nest (Fig. 9a) indicates that the nest is lighter in terms of construction density because there are bigger open spaces between the walls. In contrast, the right side of the nest (Fig. 9b) is more heavily built. In fact, the amount of white colour is significantly more considerable.

Based on the obtained results, it seems that the left side of the nest and the outer part of the nest is more related to the circulation of the wasps, to the natural ventilation,

Fig. 8 X-ray test of the AWN (position 1)

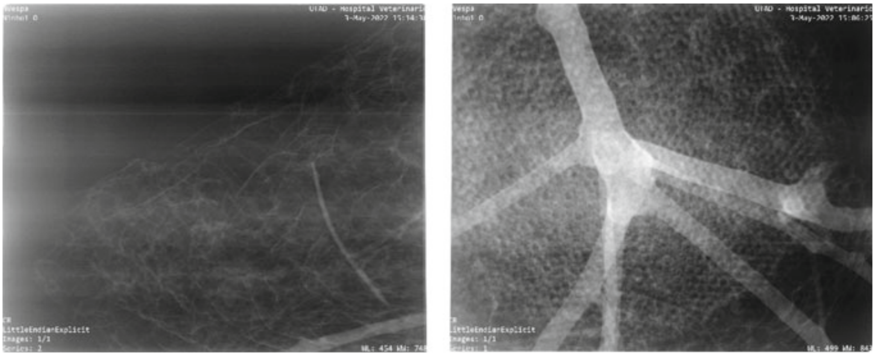

a) Left side b) Right side

Fig. 9 Radiographs of the AWN (position 1)

Fig. 10 R-ray of the AWN (position 2)

to the protection from UV radiation and from the water of the rain. At the same time, the right side of the nest seems to be more related to the wasps' accommodation and the breeding process. This information may indicate that there are different areas of the nest related to various functions such as circulation, ventilation, and lodging, among other purposes.

In this Fig. 9b, it is also apparent that the branches of the tree correspond to brighter white colour because they have a more significant density. In particular, these X-ray results, Fig. 9b, also show how the AWN braces the branch tree. The nest is supported on these branches. The connection between the nest material and the branch of the tree and the length of connection are two important aspects that deserve to be researched. Meanwhile, the existing compatibility between the nest material and the timber is evident.

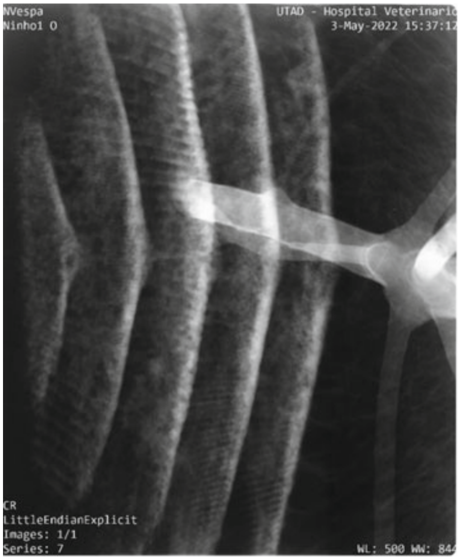

Fig. 11 Radiography of the AWN (position 2)

From Fig. 9a, it is also evident the alveolar shape type of the internal structure of the AWN is more noticeable on the right side of the nest.

The X-ray results obtained in position 2 of the nest (Fig. 10) are also relevant. In this case, the existing heterogeneity of the nest is evident, which corroborates the above description.

On the right side of the AWN, there is a nuclear part of the nest built with layers of circular alveolar slabs concentric and connected by a set of columns. These aspects can be observed in Figs. 10 and 11. In this particular AWN, there are five circular alveolar slabs (Fig. 11). The space between slabs is approximately similar and according to Fig. 11.

On the other hand, according to Fig. 10, it is possible to figure out the other part of the nest (the left side of the nest and the top covering of the nuclear region of the nest). In these nest parts, the structure seems to be more irregular. There are a set of thin layers overlapped with each other. The layers connect by columns. The space between layers is not uniform, and it is bigger than the nuclear part of the nest. The alveolar pattern is not applied in these parts of the nest.

In order to complement the above description of the AWN, Fig. 12 shows a portion of the first layer of the circular alveolar slab (Fig. 12a) and it also shows some Asian wasps almost reaching the adult size. Each Asian wasp is created in one alveolar unit and the size of the alveolar is proportionally to the size of the Asian wasp. In this case, the length of the Asian wasp is 0.025 m, approximately, Fig. 12b.

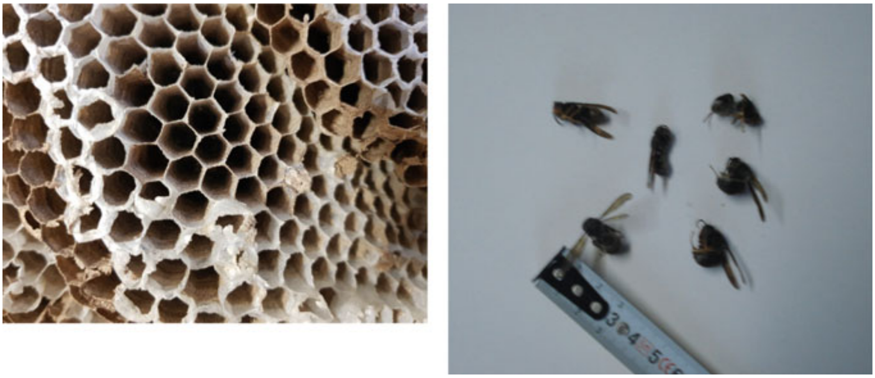

a) Detail of the alveolar slab b) Size of Asian wasp

Fig. 12 Size relation between the alveolar unit of the slab and Asian wasp

6 Conclusions

It was concluded that a lot of the AWN in the North part of Portugal could be located in rural or urban areas.

In general, AWN can be built on deciduous tree types or buildings.

In addition, AWN can reach an impressive size. This type of nest can also be robust and can present good durability.

The X-ray test was proper to give guidance on the internal structure of the AWN. It was able to identify this structure without being intrusive. There was no damage in terms of material or terms of structure.

The radiographic indicates that the AWN is not uniformly built. There is a part of the nest more heavily built corresponding to the area of the nest devoted to breeding. The X-ray tests also show that the internal structure of the AWN is in general alveolar shape.

The complexity of the AWN in terms of shape and structure may be considered a natural smart construction.

Acknowledgements This work was partially supported by the FCT (Portuguese Foundation for Science and Technology) through the projects UIDB/04082/2020 (CMADE), UIDB/CVT/00772/2020 (CECAV) and LA/P/0059/2020 (AL4AnimalS). The collaboration of the Veterinary Hospital of UTAD was also priceless.

References

1. Reddi, S., Jain, A.K., Yun, H.B., et al.: Biomimetics of stabilized earth construction: challenges and opportunities. Energy Build. **55**, 452–458 (2012)
2. Oguntona, O.A., Aigbavboa, C.O.: Promoting biomimetic materials for a sustainable construction industry. Bioinspired, Biomim. Nanobiomater. **6**, 122–130 (2017)
3. Arbabzadeh, M., Etesam, I., Mofidi, S.M.: Biomimetic and vernacular building design in connection with environment. Eur. Asian J. Biosci. **11**, 37–44 (2017)
4. Di Salvo, S.: Advances in research for biomimetic materials. Adv. Mater. Res. **1149**, 28–40 (2018)
5. Oguntona, O.A., Aigbavboa, C.O.: Biomimetic reinvention of the construction industry: energy management and sustainability. Energy Procedia **142**, 2721–2727 (2017)
6. Shah, K.W., Huseien, G.F.: Biomimetic self-healing cementitious construction materials for smart buildings. Biomimetics **5**, 1–22 (2020)
7. Al-Tabbaa, A., Lark, R., Jefferson, T., et al. : Smart biomimetic construction materials for next generation infrastructure. In: International Symposium for Next Generation Infrastructure, pp. 28–37 (2017)
8. Papoulis, D., Tzortzakaki, O., Avramidis, P., et al.: Mineralogical and textural characteristics of nest building geomaterials used by three sympatric mud-nesting hirundine species. Sci. Rep. **8**, 11050 (2018)
9. Jung, Y., Jung, S., Lee, S.I., et al.: Avian mud nest architecture by self-secreted saliva. In: Proceedings of the National Academy of Sciences of the United States of America; 118. Epub ahead of print 19 January 2021. https://doi.org/10.1073/pnas.2018509118
10. Turner, J.S., Soar, R.C.: Beyond biomimicry: what termites can tell us about realizing the living building. In: First International Conference on Industrial Intelligence Construction, pp. 14–16 (2008)
11. French, J.R.J., Ahmed, B.M.: Biomimicry of termite social cohesion and design to inspire and create sustainable systems. In: On Biomimetics. InTech. Epub ahead of print 29 August 2011. https://doi.org/10.5772/19350
12. Silva, B., Nunes, F., Correia, J., et al.: Aprender a construir com terra através da andorinha-dos-beirais. Digit - Rev Digit Arqueol Arquit e Artes. Epub ahead of print 6 December 2012. https://doi.org/10.14195/2182-844x_1_11
13. Silva, B., Correia, J., Nunes, F., et al.: Bird Nest Construction: Lessons for Building with Earth. In: WSEAS Transactions on Environment and Development, pp. 83–92
14. Silva, B., Correia, J., Nunes, F., et al.: Earth construction - Bird teaching. In: Proceedings of the 2nd WSEAS International Conference on Natural Hazards, NAHA '09, Climate Changes, Global Warming, Biological Problems, CGB '09, Urban Rehabilitation and Sustainability, URES '09, pp. 72–78 (2009)
15. Silva, B., Nunes, F., Pinto, A., et al.: Perspectiva biomimética do ninho da andorinha-dos-beirais. In: VIII° Seminario Iberoamericano de Construcción con Tierra II° Seminario Argentino de Arquitectura y Construcción con Tierra "Arquitectura de Tierra y Hábitat Sostenible". https://www.researchgate.net/publication/235965700_Perspectiva_biomimetica_do_ninho_da_andorinha-dos-beirais (2009, accessed 28 May 2021)
16. Cristelo, N., Pinto, J., Morais, A., et al.: Sugar components as a natural reinforcement of earth based construction materials. Building 225–230 (2008)
17. Perveen, F., Shah, M.: Nest architectural patterns by three wasp species (Vespa velutina, Polistes flavus and Sceliphron formosum) with reference to their behavior. Int. J. Insect Sci. **5**, IJIS.S10737 (2013)
18. Downing, H.A., Jeanne, R.L.: Nest construction by the paper wasp, Polistes: a test of stigmergy theory. Anim. Behav. **36**, 1729–1739 (1988)
19. Sánchez, X.F., Charles, R.J.: Notes on the nest architecture and colony composition in winter of the yellow-legged asian hornet, vespa velutina lepeletier 1836 (Hym.: Vespidae), in its introduced habitat in galicia (NW Spain). Insects, 10. Epub ahead of print 1 August 2019. https://doi.org/10.3390/insects10080237

20. Karsai, I., Wenzel, J.W.: Organization and regulation of nest construction behavior in Metapolybia wasps. J. Insect Behav. **13**, 111–140 (2000)
21. Jeanne, R.L.: The adaptiveness of social wasp nest architecture. Q. Rev. Biol. **50**, 267–287 (1975)
22. Klingner, R., Richter, K., Schmolz, E., et al.: The role of moisture in the nest thermoregulation of social wasps. Naturwissenschaften **92**, 427–430 (2005)
23. Pilat, M.: Wasp-inspired construction algorithms. Masters coursework (CSPC 607) University of Calgary, pp. 1–14 (2006)

Destructive and Non-destructive Testing

Moisture Buffering Value of Plasters: The Influence of Two Different Test Methods

Alessandra Ranesi, Paulina Faria, and Rosário Veiga

Abstract The moisture buffering value (MBV) is considered nowadays an easy way to classify building materials when the purpose is assessing their potential passive contribution to indoor comfort and energy saving. In literature different test methods, and relative MBVs calculated on the basis of these, are found. Hence, a study was conducted to confirm the comparability of results. Eight different plastering mortars and finishing pastes underwent the two most common test methods—the ISO 24353 and the NORDTEST protocol—and the related MBVs were calculated. It was observed that the MBV is different when different test methods are followed, although results are proportional. The values obtained following the NORDTEST method are found always higher that the values obtained following the ISO 24353 and, therefore, it is concluded that MBV is affected by the test procedures and can only be directly compared when the same procedure is used.

Keywords Mortar · Building material · Indoor wall coating · Indoor comfort · Moisture passive regulation · Hygroscopic behaviour

1 Introduction

Interior ceilings and walls are big surfaces of exposure to the indoor environment and are commonly covered by plasters, applied in systems composed by one or more

A. Ranesi (✉)
CERIS, NOVA School of Science and Technology, Universidade NOVA de Lisboa and National Laboratory for Civil Engineering, Lisbon, Portugal
e-mail: a.ranesi@campus.fct.unl.pt

P. Faria
CERIS, NOVA School of Science and Technology, Universidade NOVA de Lisboa, Lisbon, Portugal
e-mail: paulina.faria@fct.unl.pt

R. Veiga
Buildings Department, National Laboratory for Civil Engineering, Lisbon, Portugal
e-mail: rveiga@lnec.pt

C. Chastre et al. (eds.), *Testing and Experimentation in Civil Engineering*,
RILEM Bookseries 41, https://doi.org/10.1007/978-3-031-29191-3_8

layers of mortars. The plasters outer layer can be left in direct contact with the indoor air or covered by a complementary finishing system, such as a paint system. Thus, without considering the effect of furniture in the room [1, 2], the plasters can represent the biggest surface of interaction with the indoor air. Moreover, due to the large time spent by people inside buildings (around 90%) [3] the indoor environmental quality is getting more and more attention. In this context, the hygrothermal behaviour of building materials is rising increasing interest due to their potential contribution to passive regulation, with all its benefits both in terms of energy saving [4–6] and occupants' comfort and health [7–11].

The hygrothermal comfort involves several factors which mostly depend on the users, such as natural ventilation, occupancy or type of activity, that are difficult to control. However, building materials can play an important role for passive designs of new buildings or rehabilitation of existing ones. For instance, indoor thermal insulation can be pursued by the application of thermal plasters in the interior surface of facade walls, even though an external solution would always be more efficient preventing thermal bridges. Moreover, on thermal plasters and renders, mortars can be applied as a single-layer material or as part of an insulation system, despite potential differences in performance [12]. According to an adaptive thermal comfort model [13], the indoor relative humidity level influences the thermal sensation of users and, therefore, their comfort. Since some hygroscopic coating materials can contribute to relative humidity passive regulation, the possibility of quantifying their moisture storage and potential as relative humidity passive regulators has been pursued in the last decades [14].

Porous building materials, like mortars, are generally very sensitive to environmental hygrothermal conditions. The pore structure (number, size, shape, connection of pores) has big impact on the hygrothermal behaviour of the porous materials [13]. Furthermore, the combination of coupled air temperature and relative humidity can modify some of their intrinsic properties (i.e. thermal conductivity, water vapour permeability), making more challenging the construction of a theoretical model.

The laboratory characterization of moisture storage capacity of building materials has been systematized only in recent years and for this reason some uncertainties still exist about the test methods to be applied [14–18]. The NORDTEST protocol [19] and the ISO 24353 [20] standard test procedures are the test methods most found in literature. In a previous paper [21], it was observed that among sixteen studies on moisture buffering of plasters, approximately 72% were run according to the NORDTEST protocol [19] and about 16% followed the ISO 24353 [20]. Nevertheless, the two test procedures show some methodological differences, presented in Sect. 2, which can jeopardize results and affect their comparison.

2 Moisture Buffering Value

The moisture buffering value (MBV) quantifies the capacity of one material to capture (adsorb) and release (desorb) water vapour from the air.

The experimental determination of MBV quantifies the moisture uptaken and released by the material when exposed to specific conditions. It is commonly accepted to evaluate the property at a fixed temperature, to avoid triggering other mechanisms. Moreover, generally, each cycle (adsorption plus desorption) lasts 24 h, split as 8/16 or 12/12 h. To ensure reliable results it is also important that the material reaches the quasi-steady state, so the number of cycles to run differs from one material to another, but never set below four. The practical MBV is calculated as the average of the last three adsorption and desorption values, each calculated as the mass variation per square meter divided by the amplitude of the RH step.

However, it is possible to calculate the ideal MBV as a prediction of the surface water vapour flux during the time of exposure. In this case the equation will consider the period of exposure and the moisture effusivity (which depends on the intrinsic properties of the material and the saturation water pressure given by the test conditions). If the material is heterogeneous and the thickness of the specimen higher than the material moisture penetration depth, this value will be similar to the practical one.

The so far presented theory was introduced by Rode et al. [19], together with an evaluation scale, a simple 5 levels–classification from negligible to excellent, with the purpose of simplifying the comparison between different materials.

2.1 NORDTEST Protocol

The method developed within the NORDTEST Project [19] is widely used to evaluate moisture buffering of a building material or product. The most common condition is the 33–75% RH step, with a fixed temperature of 23 °C, which simulates the daily use of a bedroom in Northern Europe countries. The MBV is therefore calculated on the basis of the quasi-steady state conditions reached after multiple cyclic steps of 8 h at 75% and 16 h at 33% RH.

2.2 ISO 24353

The standard ISO 24353 [20] introduced loading and unloading phases of the same duration (12 h each) and, when cyclic tests are run, three possible relative humidity scenarios are defined: low (30–55% RH), middle (50–75% RH) and high (70–95% RH). The middle relative humidity conditions are the most chosen [21] and, from a previous study [22], they were found also to be the closest to monitored real conditions in unheated or intermittently heated bedrooms in Southern Europe.

3 Tested Plasters

The NORDTEST method [19] (33–75% RH) was applied to eight plastering mortars and pastes which can be used for plaster finishing layers, as described in Sect. 2.1. A climatic chamber FITOCLIMA 700EDTU was used. The ISO 24353 method [20] was applied to the same eight plastering materials, according to its middle range humidity condition (50–75% RH) as described in Sect. 2.2, using the same climatic chamber.

The tested plastering materials were the following:

- a clayey earth-based plastering mortar (E);
- two air lime plus gypsum finishing pastes (CL_G) with increasing content of gypsum, namely CL70_G20 and CL50_G50;
- a gypsum finishing paste (G);
- a natural hydraulic lime plastering mortar (NHL);
- two cement plastering mortars (C) with increasing water/binder ratio, namely C_0.9 and C_1.3.

The samples were obtained from prismatic standard specimens, cut into slices of approximately 40 mm × 40 mm × 20 mm. Five specimens for each material were tested, with only one 40 mm × 40 mm surface left in direct contact with the environment and the other 5 surfaces sealed with aluminum tape (Fig. 1).

The complete characterization of the presented plastering mortars and finishing pastes was discussed in a previous study [23] and some of their RH dependent properties are synthesized in Table 1.

4 Results

Results of MBV obtained using both the methodologies are presented in Fig. 2 and compared with ranges for MBV classes proposed by Rode et al. [19].

Both methods showed the same ranking of materials: the plaster with the best buffering performance is the earth-based one followed by the pastes obtained by the combination of air lime and gypsum, the plasters based on hydraulic binders and, finally, the air lime mortar and the gypsum paste. The results are largely in agreement with data on equilibrium moisture content (showed in Table 1) with exception of the air lime-gypsum finishing pastes. In fact, their equilibrium moisture content at 80% RH is higher than for the earth mortar but it is also evident that, from 70 to 80%, they show different response. The earth-based plaster keeps the slope of the adsorption curve slightly increasing with the RH level, whereas for the air lime-gypsum pastes, instead, a sharp rise is observed after 70% RH and even sharper above 80% RH. This behaviour, already discussed elsewhere [23], was found responsible for an important hysteresis in desorption and, thereby, for a large residual moisture content at the end of desorption. When daily cycles are applied, thus the final value of

(a) (c)

(b) (d)

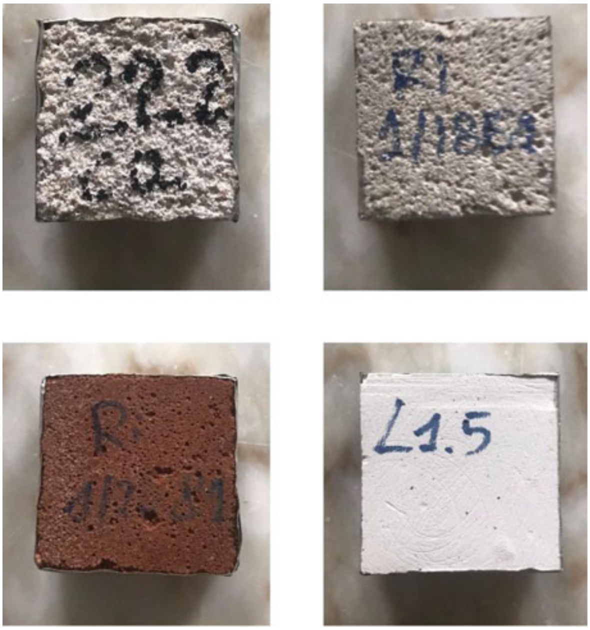

Fig. 1 Specimens 40 mm × 40 mm × 20 mm based on **a** air lime, **b** cement, **c** earth and **d** air lime-gypsum, sealed by aluminum tape and ready to be tested

Table 1 Synthesis of hygroscopic characterization of plasters from a previous study [23]

	E	CL	NHL	C_1.3	C_0.9	G	CL_{50}_G_{50}	CL_{70}_G_{20}
μ [−]	9.1	7.4	9.3	14.5	20.4	5.5	5.2	5.2
MC_{30}	0.04	0.02	0.03	0.03	0.03	0.02	0.02	0.03
MC_{50}	0.19	0.04	0.07	0.09	0.12	0.06	0.10	0.11
MC_{70}	0.44	0.08	0.15	0.19	0.26	0.14	0.24	0.28
MC_{80}	0.64	0.12	0.21	0.27	0.38	0.21	0.74	0.80

Notation: μ—water vapour resistance factor; MC—equilibrium moisture content at absorption stages expressed in % of weight

moisture buffering would be influenced by this residual moisture content, reducing the amplitude of the moisture exchange, lowering down the MBV. MBV also pointed out a high standard deviation of the gypsum finishing paste. The five specimens of gypsum paste underwent multiple tests in a previous campaign [23] and always showed differences of hygroscopic response between them in a coherent way. For this reason, the high standard deviation was already related to a heterogeneity of the prismatic original specimen, from which the five samples were obtained, and results were all considered reliable [23].

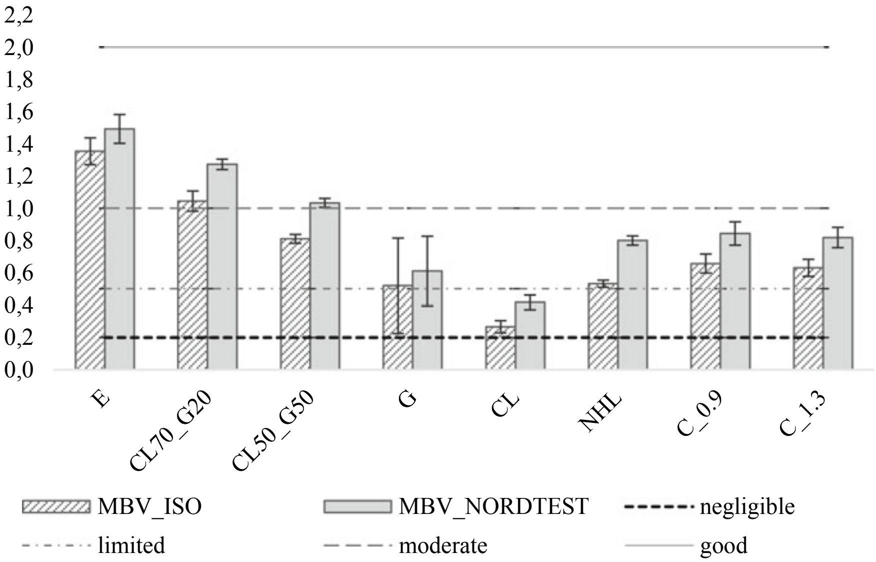

Fig. 2 MBV results of the earth-based plaster (E), air lime and gypsum pastes (CL_G), gypsum paste (G), natural hydraulic lime (NHL) and cement (C) plasters with different water/binder ratio, tested according to NORDTEST and ISO 24353 conditions. Results are compared to the NORDTEST classification limits [19]

Overall, results from ISO 24353 [20] middle level humidity conditions are slightly lower than the ones from NORDTEST protocol [19], but the plastering mortars and finishing pastes mainly still belong to the same classes (Fig. 2) either if tested according to one method or the other. The clay earth-based plaster (E) and paste CL70_G20, based on air lime (CL) with addition of gypsum (G), are classified as *good* when tested by both test methods. Also the gypsum paste (G) and the plastering mortars based on natural hydraulic lime (NHL) and cement (C_0.9 and C_1.3) obtained the same MBV class (*moderate*) whether tested by both methods. The *limited* moisture buffering behaviour of the air lime plaster (CL) is also confirmed by both methods. Finally, the paste CL50_G50 is the only material that showed an MBV falling in the upper class if tested by NORDTEST. Considering that the NORDTEST applies 8 h of adsorption and 16 h of desorption (instead of 12 h/12 h) to the tested materials, for a RH step way higher (33–75%) than the ISO standard (50–75%), results agree with expectations. Thus, one method could be overestimating real materials behaviours or the other underestimating these same, depending on exposure conditions.

To better understand the difference of results, the NHL plaster was taken as example for quantifying the moisture stored, according to one or the other method, during the last cycle of adsorption.

The ISO 24353 [20] result indicates that for 1 m^2 of plaster applied with two centimeters of thickness, around 12 g of moisture are adsorbed after 12 h of high RH

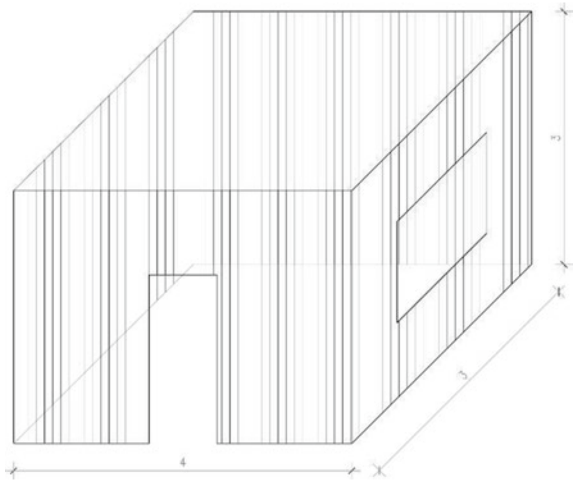

Fig. 3 Schematic representation of the room

Table 2 Values resulting from calculation

	Volume (m^3)	Surface (m^2)	Plastered (m^2)	Moisture uptaken NORDTEST (g)—8 h	Moisture uptaken ISO24353 (g)—12 h
Room	36	66	26.6	824.6	319.2

exposure (75%RH). Instead, 8 h of exposure to the NORDTEST high RH condition (75%RH), corresponds to approx. 31 g/m^2 of moisture adsorbed. Indeed, if the plaster based on natural hydraulic lime is applied on the walls of a common room with 3 m × 4 m × 3 m volume, represented in Fig. 3, with a door of 0.8 m × 2.0 m and a window of 1.2 m × 1.5 m (26.6 m^2 of plaster exposed surface, without the ceiling which could also be plastered), the moisture adsorbed could be either 319.2 g (12 h) or 824.6 g (8 h), using the ISO or the NORDTEST procedures, respectively (values are resumed in Table 2).

The calculation evidences the strong influence of the starting condition (33% RH rather than 50% RH, for the NORDTEST and the ISO, respectively) and, thus, the wider RH step the plaster would be exposed to according to the NORDTEST method, together with the importance of the exposure duration.

5 Conclusions

The passive contribution plasters can have to energy saving, occupants comfort and health, rely on their moisture balance ability. It is well-known that avoiding extreme relative humidity values contributes to occupants' health and thermal comfort sensation and can have direct and indirect effects on energy savings (heating and cooling).

Thus, the passive regulation of indoor RH can contribute to turn buildings greener. The moisture buffering value (MBV) is a quantification of this mechanism and can be obtained following different test methods.

Hence, in the study, two widespread test methods have been applied to eight plastering mortars and finishing pastes and results were found slightly different. The highest MBV were obtained by the NORDTEST as expected, considering that the RH step applied is wider and every cycle applies adsorption for half of the time of desorption. A longer time for desorbing would mitigate the hysteretic response that sometimes porous materials, as plasters, present. However, the ratio between each material is kept the same wether if tested according to one method or the other.

Moreover, most of the analyzed mortars belong to the same class when tested according to the Northern protocol or the ISO standard. Nevertheless, a difference in the absolute value of MBV is observed and can result in significantly different quantities of moisture exchange, as it was shown by calculation.

There is no doubt that the main inconsistencies between the two test methods are represented by test settings, such as time of exposure and relative humidity levels. The starting and final RH conditions, the width of the step and the exposure time are responsible for the response, especially for porous materials.

For the former reasons, direct comparability in terms of absolute MBV should be excluded unless the same test procedure was used. Hence, the classification and characterization by MBV is justified if the test method is specified.

Funding Information This research was funded by Portuguese Foundation for Science and Technology: Alessandra Ranesi Doctoral Training Programme EcoCoRe grant number PD/BD/150399/2019 and Civil Engineering Research and Innovation for Sustainability (CERIS) project UIDB/04625/2020.

References

1. Svennberg, K., Hedegaard, L.G., Rode, C.: Moisture buffer performance of a fully furnished room. In: Moisture Buffer Performance of a Fully Furnished Room (2004)
2. Yang, X., Fazio, P., Ge, H., Rao, J.: Evaluation of moisture buffering capacity of interior surface materials and furniture in a full-scale experimental investigation. Build. Environ. **47**, 188–196 (2012). https://doi.org/10.1016/j.buildenv.2011.07.025
3. Sundell, J.: On the history of indoor air quality and health. Indoor Air **14** (Suppl 7): 51–58 (2004). ISSN: 0905–6947.
4. Legros, C., Cosnier, M., Piot, A., Pailha, M., Woloszyn, M.: Impact of moisture by using for improving summer comfort in buildings. In: The 16th IBPSA International Conference and Exhibition, 2–4 September, Rome (2019)
5. Osayintola, O.F., Simonson, C.J.: Moisture buffering capacity of hygroscopic building materials: experimental facilities and energy impact. Energy Build. **38**, 1270–1282 (2006)
6. Yu, S., Cui, Y., Shao, Y., Han, F.: Simulation research on the effect of coupled heat and moisture transfer on the energy consumption and indoor environment of public buildings. Energies **12**, 141 (2019). https://doi.org/10.3390/en12010141

7. Arundel, A.V., Sterling, E.M., Biggin, J.H., Sterling, T.D.: Indirect health effects of relative humidity in indoor environments. Environ. Health Perspect. **65**, 351 (1986). https://doi.org/10.1289/ehp.8665351
8. Davis, R.E., McGregor, G.R., Enfield, K.B.: Humidity: a review and primer on atmospheric moisture and human health. Environ. Res. **144**, 106–116 (2016). https://doi.org/10.1016/j.envres.2015.10.014
9. Sato, M., Fukayo, S., Yano, E.: Adverse environmental health effects of ultra-low relative humidity indoor air. J. Occup. Health **45**, 133–136 (2003)
10. Psomas, T., Teli, D., Langer, S., Wahlgren, P., Wargocki, P.: Indoor humidity of dwellings and association with building characteristics, behaviors and health in a northern climate. Build. Environ. **198**, 107885 (2021). https://doi.org/10.1016/j.buildenv.2021.107885
11. Wolkoff, P.: Indoor air humidity, air quality, and health—An overview. Int. J. Hyg. Environ. Health **221**(3), 376–390 (2018). https://doi.org/10.1016/j.ijheh.2018.01.015
12. Posani, M., Veiga, R., de Freitas, V.: Thermal mortar-based insulation solutions for historic walls: An extensive hygrothermal characterization of materials and systems. Constr. Build. Mater. **315**, 125640 (2022). https://doi.org/10.1016/j.conbuildmat.2021.125640
13. Vellei, M., Herrera, M., Fosas, D., Natarajan, S.: The influence of relative humidity on adaptive thermal comfort. Build. Environ. **24**, 171–185 (2017). https://doi.org/10.1016/j.buildenv.2017.08.005
14. Padfield, T.: Humidity buffering of the indoor climate by absorbent walls. In: The 5th Symposium on Building Physics in the Nordic Countries, 2 (1999)
15. Ferroukhi, M.Y., Belarbi, R., Limam, K., Si Larbi, A., Nouviaire, A.: Assessment of the effects of temperature and moisture content on the hygrothermal transport and storage properties of porous building materials. Heat Mass Transf. **55**, 1607–1617 (2019). https://doi.org/10.1007/s00231-018-02550-5
16. Kreiger, B.K., Srubar, W.V., III.: Moisture buffering in buildings: a review of experimental and numerical methods. Energy Build. **202**, 109394 (2019). https://doi.org/10.1016/j.enbuild.2019.109394
17. Cascione, V., Maskell, D., Shea, A., Walker, P.: A review of moisture buffering capacity: from laboratory testing to full-scale measurement. Constr. Build. Mater. **200**, 333–343 (2019). https://doi.org/10.1016/J.CONBUILDMAT.2018.12.094
18. Roels, S., Janssen, H.: A comparison of the nordtest and japanese test methods for the moisture buffering performance of building materials. J. Build. Phys. **30**(2), 137–161 (2006)
19. Rode, C., Peuhkuri, R.H., Mortensen, L.H., Hansen, K.K., Time, B., Gustavsen, A., Ojanen, T., Ahonen, J., Svennberg, K., Harderup, L.E., Arfvidsson, J.: Moisture buffering of building materials. Technical University of Denmark, Department of Civil Engineering. BYG Report, R-127 (2005)
20. ISO 24353 (2008): Hygrothermal performance of building materials and products—Determination of moisture adsorption/desorption properties in response to humidity variation., ISO, Geneva, Switzerland
21. Ranesi, A., Faria, P., Veiga, R.: Laboratory characterization of relative humidity dependant properties for plasters: a systematic review. Constr. Build. Mater. **304**, 124595 (2021). https://doi.org/10.1016/j.conbuildmat.2021.124595
22. Ranesi, A., Posani, M., Veiga, R.: Faria P (2022) A discussion on winter indoor hygrothermal conditions and hygroscopic behaviour of plasters in southern Europe. Infrastructures **7**(3), 38 (2022). https://doi.org/10.3390/infrastructures7030038
23. Ranesi, A., Veiga, R., Faria, P.: Traditional and modern plasters for built heritage: suitability and contribution for passive relative humidity regulation. Heritage **4**, 2337–2355 (2021). https://doi.org/10.3390/heritage4030132

Study on the Effect of the Bedding Mortar Composition on the Shear and Compression Behavior of Old Brick Masonry Walls

Armando Demaj, Ana I. Marques, João Gomes Ferreira, and António Sousa Gago

Abstract The aim of this study was to investigate the influence of the bedding mortar characteristics on the shear and compression behavior of brick masonry walls typical of old buildings. For this purpose, two different mortar compositions were considered, namely a cement mortar and a lime-cement mortar with composition ratios of 1:0:5 and 1:3:12 (ce-ment:hydrated lime:sand), respectively. The initial part of the study consisted of experimentally determining the main mortars' characteristics. Then, their effect on the shear and compression behavior of solid clay brick masonry was experimentally assessed. For this purpose, di-agonal compression tests and axial compression tests were performed on masonry specimens made with both types of bedding mortars. The results show that the mortar characteristics have a significant influence both on the shear and compressive behavior. The average shear strength values of the cement mortar walls were six times higher than that of the cement-lime mortar walls. The average compressive strength values of the cement mortar walls were two times higher than that of the cement-lime mortar walls. This shows that the mortar characteristics have a greater influence on the shear behavior when com-pared to compressive behavior.

Keywords Cement · Lime · Mortar · Masonry · Shear · Compression

A. Demaj · J. G. Ferreira (✉) · A. S. Gago
IST, ULisboa, CERIS, Lisbon, Portugal
e-mail: joao.gomes.ferreira@tecnico.ulisboa.pt

A. Demaj
Epoka University, Tirana, Albania

A. I. Marques
LNEC, Lisbon, Portugal
e-mail: aimarques@lnec.pt

C. Chastre et al. (eds.), *Testing and Experimentation in Civil Engineering*,
RILEM Bookseries 41, https://doi.org/10.1007/978-3-031-29191-3_9

1 Introduction

The in-plane shear behavior of a load-bearing brick masonry wall is expected to strongly depend on the properties of its bedding mortar. In the case of shear loading, if the mortar is too weak when compared to the bricks, premature shear collapse occurs, normally characterized by a stepped crack. In this case, diagonal cracking develops through the horizontal and vertical mortar joints, without crossing the bricks, that remain apparently intact. On the other hand, if the mortar is too strong, the wall behaves monolithically, and the diagonal cracking develops continuously, crossing both the mortar and the bricks without visible change in its direction.

Also, in the case of compressive loading, it was seen that, as expected, the mortar characteristics have a significant role in the wall strength although not as much in its rupture mode.

In the framework of the project RESIST-2020—"Seismic Rehabilitation of Old Ma-sonry-Concrete Buildings", walls with two different bedding mortars were investigat-ed: (i) a cement-based mortar with a ratio by volume of 1:0:5 (cement:hydrated lime:sand), with 1/3 of sandpit sand and 2/3 of river sand (by volume); (ii) a lime-cement mortar with a ratio by volume of 1:3:12 (cement:hydrated lime:sand), in which only river sand was used. The lime selected for the preparation of the mixes was calicitic hydrated lime CL 90, manufactured by Lusical, whereas the cement used was CEM II/B—L 32.5 N from the manufacturer Secil.

The mortars were experimentally characterized to obtain their main mechanical characteristics.

For assessing the shear and compression behavior of walls, diagonal compression tests were performed on small wall specimens—*wallettes*—made with the two bedding mortar compositions previously characterized. The bricks used in both *wallettes* were similar, in order to limit the varying parameters and allow for the analysis of the role of the mortar type only. The bricks were solid with dimensions of 25 × 11 × 7 (cm) and average compressive strength of about 25 MPa.

2 Mechanical Properties of the Mortars

Both mortars were tested, in prismatic specimens of dimensions 40 × 40 × 160 mm^3, at 28, 90, and 180 days for (i) unit weight; (ii) flexural strength; (iii), and compressive strength [1]; and (iv) dynamic modulus of elasticity through resonance frequency [2]. Figures 1, 2, 3 and 4 present these values obtained for both types of mortar at the three different ages. For each type of test and for each age, three specimens were tested. The result presented represents the average value obtained for a set of three specimens tested.

The results presented in Fig. 1 show that the unit mass of cement mortar is only slightly higher than that of cement-lime mortar (about 1900 kg/m^3 against 1800 kg/m^3 at 180 days). Unlikely, the flexural and compressive strengths of both types of mortar

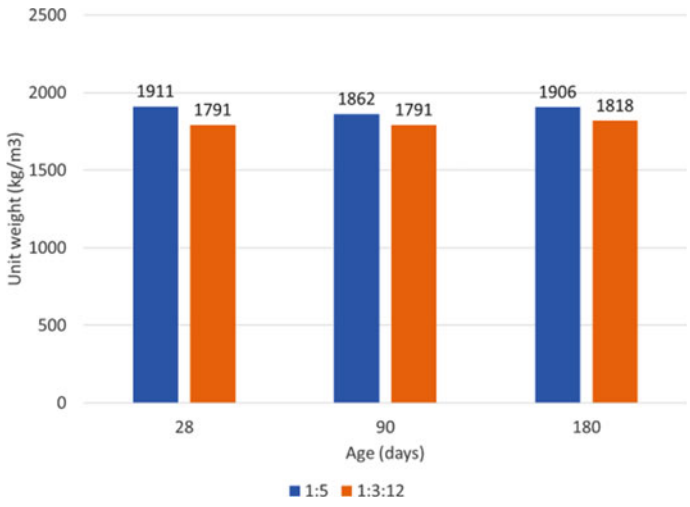

Fig. 1 Unit weight of the two different types of mortars at the ages of 28, 90, and 180 days

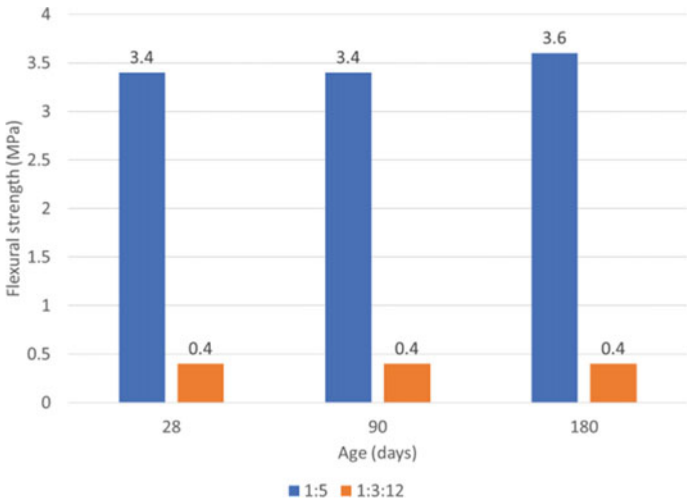

Fig. 2 Flexural strength of the two different types of mortars at the ages of 28, 90, and 180 days

are significantly different. At 180 days, the flexural and compressive strengths of cement mortar are about 3.6 MPa and 13.7 MPa, respectively, whereas the corresponding values for the cement-lime mortar are approximately 0.4 MPa (9 times lower) and 0.8 MPa (17 times lower).

The dynamic elastic modulus of the bedding mortar (obtained by the resonance frequency tests) are also clearly dependent on the type of binder used. While the

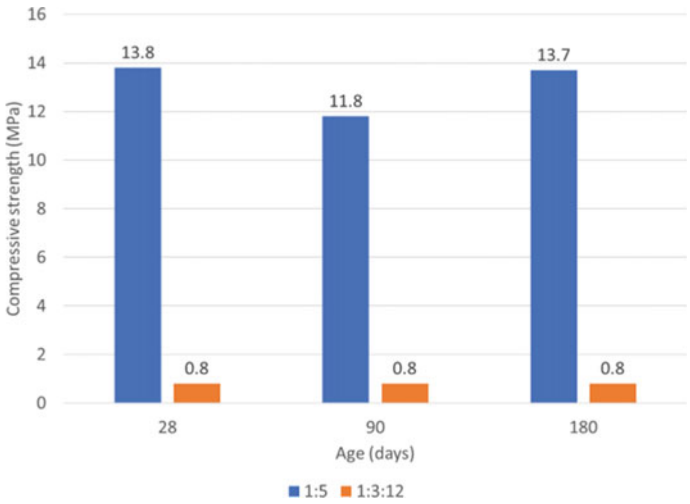

Fig. 3 Compression strength of the two different types of mortars at the ages of 28, 90, and 180 days

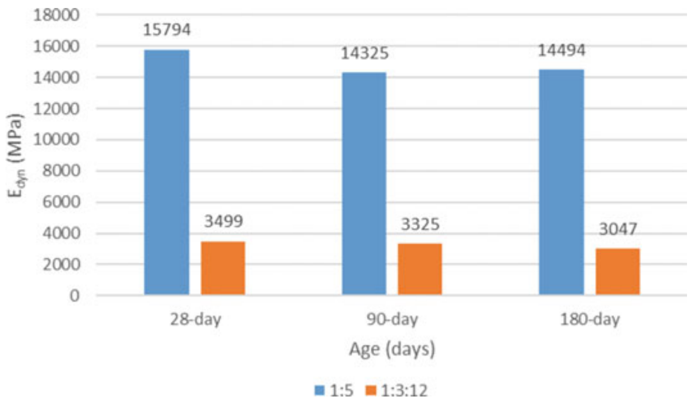

Fig. 4 Dynamic elastic modulus by resonance frequency of the two different types of mortars at the ages of 28, 90, and 180 days

cement mortar presents values of about 15 GPa, the cement-lime mortar presents values of about 3 GPa (about 5 times lower).

3 Diagonal Compression Tests

Six unreinforced masonry *wallettes* were constructed, three of them with 1:0:5 (cement:lime:sand) ratio bedding mortar, and the other three with 1:3:12 ratio. The test was carried out in accordance with the standard ASTM 519-10 [3]. The *wallettes*' dimensions were approximately 25 × 80 × 80 (cm) All specimens were instrumented using 6 Linear Variable Differential Transformer (LVDT) to measure the respective deformations (2 vertical and horizontal LVDT in each face and two others measuring the press head displacement).

Figures 5 and 6 show the shear stress—shear strain diagrams of the *wallettes* of each type tested, respectively with cement-sand and cement-lime-sand mortar.

Table 1 presents the individual and average shear strength values for both types of *wallettes* tested.

The maximum shear stress values of the 1:5 mortar *wallettes* were 1.47 MPa, 1.40 MPa and 1.00 MPa—average value of 1.29 MPa. The corresponding values of the cement-lime mortar *wallettes* were 0.29 MPa, 0.20 MPa and 0.13 MPa—average value of 0.21 MPa. In terms of shear strength, on average, the cement-sand mortar *wallettes* present a value more than 6 times higher than that of the cement-lime-sand mortar *wallettes*. Figures 7 and 8 show the rupture mode of the three *wallettes* of each type tested.

As seen in Figs. 7 and 8, the strong mortar *wallettes* behave practically as a monolithic element, with diagonal (vertical) cracking developing continuously without a change in direction in the mortar joints' locations. The weak mortar *wallettes* rupture,

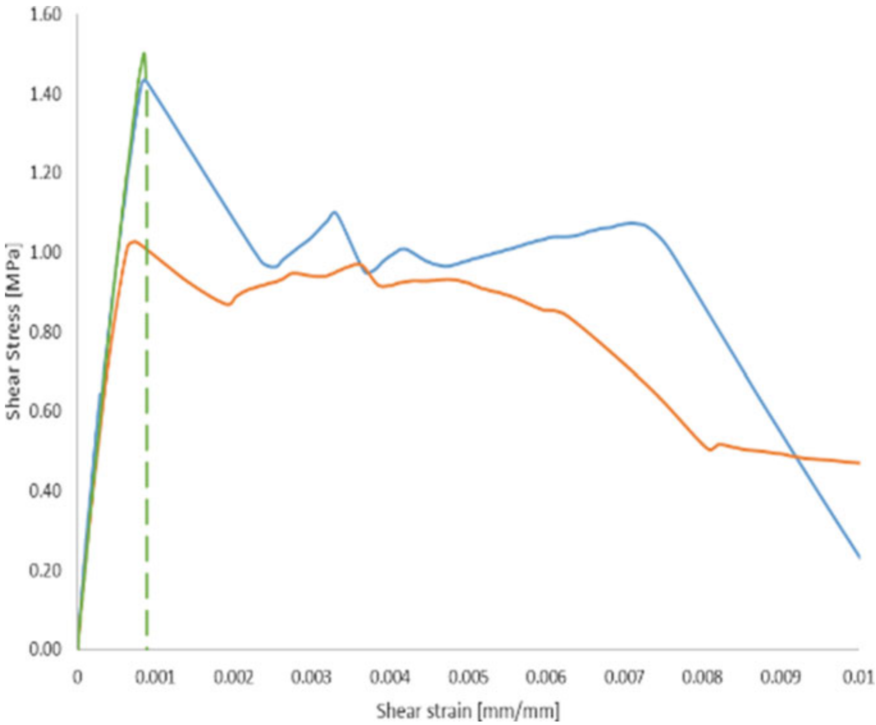

Fig. 5 Shear stress—shear strain diagrams of 1:5 mortar *wallettes*

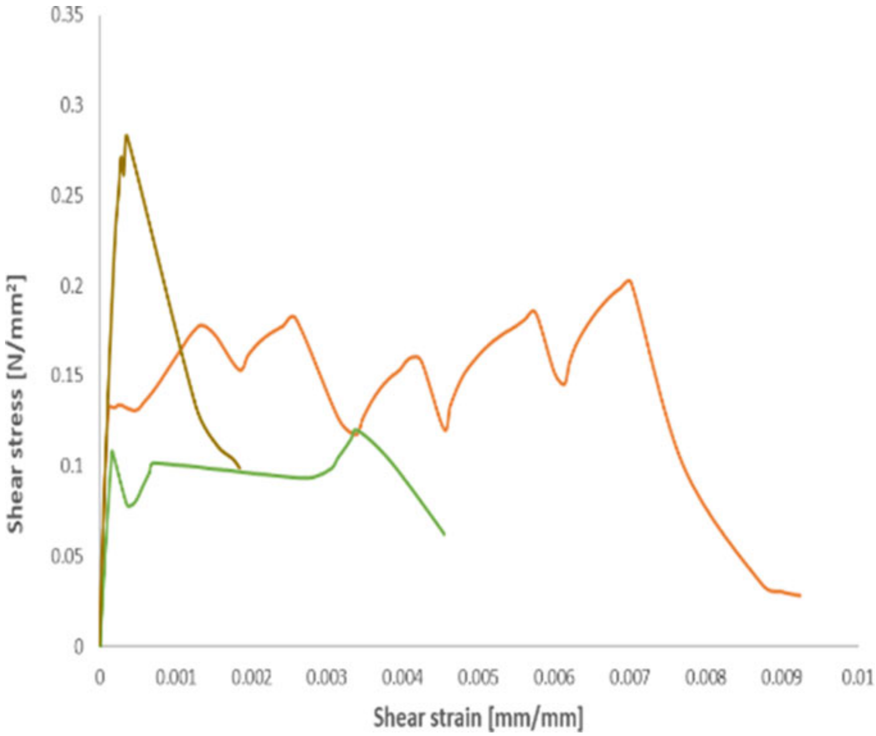

Fig. 6 Shear stress—shear strain diagrams of 1:3:12 mortar *wallettes*

Table 1 Shear strength tests results (MPa)

Wallettes with mortar 1:0:5				*Wallettes* with mortar 1:3:12			
WAS-1	WAS-2	WAS-3	Average	WBS-1	WBS-2	WBS-3	Average
1.47	1.40	1.00	**1.29**	0.29	0.20	0.13	**0.21**

Fig. 7 Rupture mode of 1:5 cement-sand mortar *wallettes*

Fig. 8 Rupture mode of 1:3:12 cement-lime-sand mortar *wallettes*

in turn, occurs with stepped cracking that develops through the mortar joints while the bricks practically do not show any cracking. These rupture modes are compatible with the different bedding mortars and show the importance of their composition on the shear behaviour of old masonry walls made with clay bricks.

4 Axial Compression Tests

Besides the diagonal compression tests performed on masonry *wallettes*, also axial compression tests were performed in three *wallettes* of each type, based on the standard ASTM C1314-21 [4]. All tests were instrumented using 8 LVDT's to measure the respective vertical (2 LVDT in each face) and horizontal (1 LVDT in each face) deformations and also the press head displacement (2 LVDT).

Table 2 presents the individual and average compressive strength values for both types of *wallettes* tested.

The maximum compressive stress values of the 1:0:5 mortar *wallettes* were 12.8 MPa, 11.9 MPa and 11.8 MPa—average value of 12.2 MPa. The corresponding values of the cement-lime mortar *wallettes* were 6.2 MPa, 6.2 MPa and 6.3 MPa—average value of 6.2 MPa. In terms of compressive strength, on average, the cement-sand mortar *wallettes* present a value which is about 2 times higher than that of the cement-lime-sand mortar *wallettes*. Figures 9 and 10 show the compressive rupture mode of the *wallettes* of each type.

Figures 9 and 10 show that the rupture mode of the two different types of *wallettes* is similar, characterized essentially by vertical or sub-vertical cracking through the

Table 2 Compressive strength tests results (MPa)

Wallettes with mortar 1:0:5				*Wallettes* with mortar 1:3:12			
WAC-1	WAC-2	WAC-3	Average	WB-C1	WB-C2	WB-C3	Average
12.8	11.9	11.8	**12.2**	6.2	6.2	6.3	**6.2**

WAC-1 WAC-2 WAC-3

Fig. 9 Compressive rupture mode of 1:0:5 cement-sand mortar *wallettes*

WBC-1 WBC-2 WBC-3

Fig. 10 Compressive rupture mode of 1:3:12 cement-lime-sand mortar *wallettes*

ele-ment depth. In some cases, cracking also developed parallel to the wall plane, ap-proximately in its middle depth.

5 Conclusion

Two types of bedding mortars used in the fabrication of solid clay brick *wallettes*, which were experimentally characterized. The mortars had a composition (cement:hydrated lime:sand) of 1:0:5 (“strong” mortar) and 1:3:12 (“weak” mortar).

Three *wallettes* of each type were subjected to diagonal compression (shear) tests and three others were subjected to axial compression tests.

The “strong” mortar *wallettes* have achieved a shear strength that was 6 times higher than that of the “weak” mortar *wallettes*. The “strong” mortar *wallettes* behaved as monolithic whereas the "weak" mortar *wallettes* behaved as a set of bricks barely connected by their bedding mortar.

In what regard compressive strength, the effect of the mortar has the same tendency but is less accentuated, with the "strong" mortar *wallettes* showing "only" twice as strong when compared with the "weak" mortar *wallettes.* This seems to be due to the lower "weak" mortar cohesion that has naturally a more accentuated effect on slippage than on compression, especially for low thicknesses, as in the case of mortar bedding joints.

Through the obtained collapse mechanisms, it is possible to observe that the adherence between the brick units and the mortar greatly influences the shear resistance and the configuration of the masonry collapse mechanism. This aspect was clearly evidenced in the 1:3:12 cement-lime-sand mortar *wallettes*, where shear failures occurred at the brick and mortar interface. Adhesion can be controlled through the workability of the mortar and the wetness of the bricks, which were taken into account in this work, during the construction of the *wallettes.*

Acknowledgements The authors gratefully acknowledge the financial support of the FCT (Fundação para a Ciência e a Tecnologia) for the project PTDC/ECI-EGC/30567/2017, "RESIST-2020 – Seismic Rehabilitation of Old Masonry-Concrete Buildings".

LNEC—Laboratório Nacional de Engenharia Civil, Lisbon, Portugal, is acknowledge by hosting the experimental tests presented here.

References

1. EN 1015-11:2019. Methods of test for mortar for masonry - Part 11: Determination of flexural and compressive strength of hardened mortar. Brussels, Belgium: European Committee for Standardization (2019)
2. EN 14146:2004 - Natural stone test methods - Determination of the dynamic modulus of elasticity (by measuring the fundamental resonance frequency). Brussels, Belgium: European Committee for Standardization (2004)
3. ASTM E519-10. Standard test method for diagonal tension (shear) in masonry assemblages. s.l. American Society for Testing and Materials, West Conshohocken, PA (2010)
4. ASTM C1314-21. Standard Test Method for Compressive Strength of Masonry Prisms, American Society for Testing and Materials, West Conshohocken, PA (2021)

New Methodology for Rocks' Geomechanical Characterization with Schmidt Sclerometer

Victor Cavaleiro, Leonardo Marchiori, Maria Vitoria Morais, Gabriel Marchi, and Marcela Cocchiarale

Abstract Hardness is a parameter that gives information about the behavior of rocks when subjected to certain deformations. Various non-destructive tests are available for hardness quantification, the use of the Schmidt Sclerometer is the most used due its expedition, among existing sclerometers, the Schmidt rebound hammer, type N-34, with an impact energy equal to 2,207 N.m (0.225 Kgm) was selected for experimental tests. Schmidt's hardness index (R) obtained were related to other physical parameters of the rock, namely uniaxial compressive strength (UCS), elasticity modulus (Ɛ), specific gravity and granularity. For comparison purpose, several literature's methodologies are present focused on improving procedures and developing correlations for different rock types. In this sense, to assess the methodology that best suits granitic rocks' characterization, several laboratorial and "in situ" tests from the literature were performed. Additionally, the paper proposes a new methodology based on the analysis of the results and a good relation between R and UCS parameters, concluding reliability on the methodology for values of non-porphyroid granitic rocks, predominantly biotitic and from medium to fine granularity, in a precise and consistent way.

Keywords Schmidt sclerometer · Rock's hardness · Rock's characterization · Methodology

V. Cavaleiro (✉) · L. Marchiori · M. V. Morais · G. Marchi · M. Cocchiarale
Civil Engineering and Architecture Department, Universidade Beira Interior (UBI), Covilhã, Portugal
e-mail: victorc@ubi.pt

L. Marchiori
e-mail: leonardo.marchiori@ubi.pt

V. Cavaleiro · L. Marchiori · M. V. Morais
GeoBioTec, Universidade Beira Interior (UBI), Covilhã, Portugal

L. Marchiori · M. V. Morais
FibEnTech, Universidade Beira Interior (UBI), Covilhã, Portugal

M. Cocchiarale
Civil Engineering Department, Universidade Federal do Rio de Janeiro (UFRJ), Rio de Janeiro, Brazil

C. Chastre et al. (eds.), *Testing and Experimentation in Civil Engineering*, RILEM Bookseries 41, https://doi.org/10.1007/978-3-031-29191-3_10

1 Introduction

Hardness has proved to be an important parameter in rock massif's characterization for most applications [1]. This work aims to propose a new methodology based on hardness ratio of Schmidt (R) intending to reduce inaccuracies and making correlations with uniaxial compressive strength (UCS).

The Schmidt hardness of a given material is obtained by measuring the rebound of a mass of steel, which happens when the hammer is struck against a surface. The piston that is incorporated in the Sclerometer, which is attached to a load spring, is automatically released from its chamber. Thus, a part of the piston's energy is dissipated by absorption and transformed, the remaining energy is the one which returns the penetration impact resistance of a given structural surface [2]. In this way, the lower the energy released, the greater the resistance of the rocky surface, and, in turn, time, the greater the piston bounce. The Schmidt hardness is represented by the value of R. This value can be related to the uniaxial compressive strength (σ_c) of the constituent rock of the surface tested or with its elasticity modulus ($\mathcal{E}_t$), according to the value of its specific weight [2, 3]. However, the evaluation of rock hardness through the Schmidt hardness index is influenced by several factors, such as the type of Schmidt sclerometer used, the procedure adopted for the test, and the specifications of the sample [4]. This fact has led to the publication of several works where different methodologies are presented focused on improving procedures for collecting data, and development of new correlations for different rock types. In this sense, to assess the most appropriate methodology to obtain hardness of granite rocks for ornamental purposes, several tests were carried out according to methodologies presented in the literature.

2 Materials and Methods

Three types of Portuguese's fine-to-medium-grained non-porphyroid granites with different degrees of alteration were considered: the fine-grained "Golden Yellow" granites from Figueira (FIG), the "Blue-Grey" granites from Ruvina (RUV), and the "Medium Grain" from Rochoso (ROC) granite. These granites are from Guarda region, chosen based on more than a hundred tests carried out by the working group, making a representative number for the region. "In situ" tests followed methodologies from Table 3, and laboratorial R used the new methodology proposed by this work, also, UCS were obtained with hydraulic press Seidner D-1740 Reidlingen.

For laboratorial R tests, 10 representative samples of each type of granite were collected from the same sites selected for the in-situ tests for results' validation, by the proposed methodology. The samples were prepared in specimens with dimensions of 150 × 150 mm. A square with dimensions of 120 × 120 mm was drawn in the central part of the specimen with a mesh of 20 × 20 mm, as shown in Fig. 1, and seven impacts were randomly distributed in this mesh, with the specimens confined in the

Fig. 1 Laboratorial specimens

hydraulic press. From the readings obtained, the smallest value and the maximum value are eliminated, and the final admissible value of R is the average of the five readings with a standard deviation (σ_R) value never greater than three (3). The result is a dimensionless number that is considered as the hardness index of the tested material that varies in a linear scale from 10 to 100.

It is important to emphasize that the calibrated Schmidt Sclerometer must always be placed perpendicular to the tested surface, avoiding variations in the readings, values acquired in directions other than the horizontal are subject to gravitational action and should be normalized using to the correction curves provided by the manufacturer. Petrographically, these granites are non-porphyroids of two micas, predominantly biotitic, make part of the great granitic batholith of Beira region. These are monzonitic granites, with great uniformity in terms of chemical and textural composition, exposed in Table 1.

Table 2 summarizes essential physical parameters for the analyzed rocks, RUV and ROC materials being very similar to each other, and FIG differing, having lower specific gravity, and higher water absorption and open porosity. The "Golden Yellow" granite from FIG is a homogeneously textured and fine-grained rock, the average

Table 1 Chemical composition

Granite	SiO_2	TiO_2	Al_2O_3	Fe_2O_3	MnO	MgO	CaO	Na_2O	K_2O
FIG	71.03	0.23	14.55	2.35	–	0.46	0.63	3.33	5.46
RUV	72.52	0.43	14.76	1.82	0.03	0.0.32	1.09	3.51	4.82
ROC	73.10	0.15	14.41	1.53	0.04	0.28	0.59	2.99	5.27

Table 2 Physical characteristics

Granite	Specific gravity (−)	Water absorption (%)	Open porosity (%)
FIG	2.55	1.74	4.41
RUV	2.60	0.68	1.78
ROC	2.61	0.55	1.44

value of open porosity (4.40%) confirms its greater degree of alteration compared to the other granites. And Table 3 summarizes literature's methodologies.

According to Aydin [4] the Type N hammer is less sensitive to uneven surfaces and should preferably be used in applications in field. From Table 3, it is seen that the number of readings performed in each method varies substantially. If on the one hand Deere and Miller [6] and Ege et al. [7] suggest the execution of 24 and 25 readings, Hucka [5] and Poole and Farmer [13] observed that the R values obtained by repeated readings (ten and five impacts respectively) at individual points are more consistent than the values of one individual impact, and, Shorey et al. [14] defends the realization of a single impact because seems to be more reliable for estimating uniaxial compression.

Table 3 Schmidt sclerometer methodologies

Authors	Methodologies for R determination
[5]	Performance of 10 tests, considering as R the highest value
[6]	Execution of at least 24 tests, considering R as the average value
[7]	Execution of 25 tests, where R is the average of the 13 readings that record higher values
[8]	Run 25 tests, where R is the average of the values
[9]	Execution of 15 tests in locations not more than 25 mm and takes the value of R as the average of the 10 highest results, since that the maximum deviation does not exceed 2.5
[10]	Carry out 10 tests, on a surface of at least 100 cm^2 and obtaining R as the average of all readings, after eliminating the tests whose results deviate ± 5 from the mean
[11]	Carry out 20 tests, in places with a distance equal to or greater than the diameter of the Schmidt sclerometer, R is determined by averaging 50% of the trials recorded with higher values
[11]	R is obtained by calculating the average of 5 trials that recorded higher values raised for a total of 10
[12]	Performance of 8 tests, with R being the average value
[13]	R is the maximum value assigned during the performance of 5 tests
[14]	Advocates obtaining R from the execution of a single test
[15]	R is obtained by averaging the results recorded in 5 trials

3 Results and Discussion

A linear relation was developed between R and UCS parameters in Eq. (1) following Table 4 author's experimental tests results.

$$\sigma_c = 20.91 + 0.33 * R \tag{1}$$

Figure 2 correlates the average of other methodologies applied in situ following Table 3 methodologies; and laboratorial values of R, using author's methodology, for 10 tests performed for FIG, RUV and ROC granites. And Fig. 3 shows laboratorial R values with UCS.

When analyzing the results, it appears that the granite FIG has R lower than the other granites, this one also presenting a higher standard deviation, these values may be related to the greater degree of alteration presented by these granites due to its open porosity of 4.1%, this physical property is linked to the existence of networks of interconnected cracks and pores. Open porosity affects the strength and mechanical characteristics, and it is inversely proportional to the strength mechanics, specific density, and porosity, resulting in void areas, increasing weakness.

Comparing the values of R obtained by the different methods, it seems that there is a slight inconsistency in results, this fact is to be expected considering the specificities of each method and in particular the number of readings considered. It is verified,

Table 4 Schmidt sclerometer results

Methodologies for R determination	FIG		RUV		ROC	
	R	σ_R	R	σ_R	R	σ_R
[5]	44.0	–	54.0	–	65.0	–
[6]	33.3	6.3	47.5	4.5	65.5	3.7
[7]	40.1	6.1	50.6	3.8	62.2	2.9
[8]	35.2	6.5	46.8	4.3	59.4	2.9
[9]	38.7	6.3	50.5	4.8	62.2	3.4
[10]	31.3	6.5	45.5	4.8	57.8	2.1
[11]	38.4	5.9	52.6	4.4	63.4	3.2
[11]	39.2	5.6	50.8	4.7	62.4	2.6
[12]	32.5	5.2	47.4	3.5	59.6	3.7
[13]	32.7	3.9	50.3	5.4	63.3	3.3
[13]	38.0	3.5	51.0	2.7	58.2	2.6
[14]	29.0	–	46.0	–	60.0	–
[15]	31.6	4.9	46.8	5.4	61.8	2.8
Author's	35.6	2.9	49.2	2.8	61.2	2.6
UCS,med (MPa)	52.9		96.4		1339	
σ_c (MPa)	7.5		2.5		1.0	

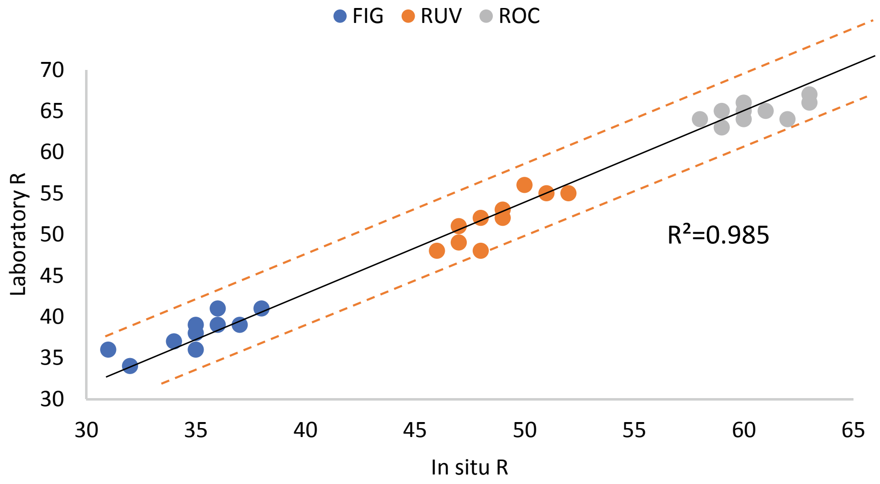

Fig. 2 In situ and laboratorial R values correlation

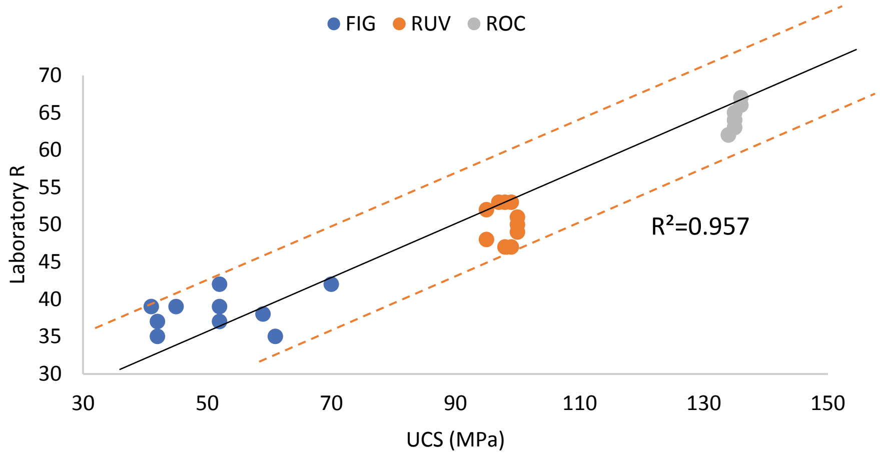

Fig. 3 UCS and laboratorial R correlation

however, that the value of R obtained by method proposed here is very close to the average of the values of R obtained by all the methods rehearsed, and that in general it has a smaller standard deviation.

To minimize reading errors caused by microfractures or other discontinuities near the points of impact on the rock mass, and to test the validity of the values obtained in situ by the proposed methodology, 10 tests were performed with the Schmidt Sclerometer according to the proposed methodology in 10 different specimens for each type of granite. Subsequently and since the Schmidt hammer is a non-destructive method, the same methods were used to the same samples to determine the values of uniaxial compression, and thus, establish a direct relationship with Schmidt hardness values. All results were treated statistically, to understand if this method can be considered valid for the determination of hardness in granites, in such a way that it is a value representative of the resistance in question.

From the analysis of the graph in Fig. 3, for a confidence interval of 95%, it appears that the coefficient of determination between the variables tested is $R^2 = 0.957$, so it is evident that there is a strong relationship, indicating a good degree of precision in the use of this equation to determine the compression value uniaxial from the Schmidt hardness value. Comparing the values of R obtained in situ and in the laboratory, for the method proposed here, it appears that the values obtained in the laboratory are higher. This situation was to be expected since in situ tests, for most cases, the average of the R values decreases and the degree of dispersion between the R value increases [15]. As for the uniaxial compression values, it appears that granites with a higher degree of alteration have a lower σ_c value, this fact had also been described by [16]. These were related to the R values obtained in the laboratory.

4 Conclusions

1. The proposed methodology is presented:
2. A smooth, flat, and clean surface with an area of 15 cm^2 of the rock is selected and prepared. It is verified that this area is free from cracks or any discontinuity in the rock mass, to a depth of about 6 cm. In cases where this is not the case, another area is chosen to be not influenced by these conditions.
3. Seven (7) impacts are carried out with a calibrated Schmidt type N-34 rebound hammer, with an impact energy equal to 2,207 N.m, randomly distributed on the surface of the selected area.
4. From these 7 readings, the smallest value and the maximum value are eliminated, with the final R value being the average of the remaining five readings, with a standard deviation value never greater than three.

The result is a dimensionless number that is considered as the hardness index of the tested material that varies in a linear scale from 10 to 100. Schmidt hardness values obtained in situ are closer to the average of the values obtained comparing to other methodologies; R values from Table 1 obtained in situ and in the laboratory showed good correlation ($R^2 = 0.985$), for a confidence interval of 95%, and R values, in general, had a smaller dispersion in relation to the mean, with a standard deviation of less than 3; Schmidt hardness index, in addition to providing information about the surface hardness of the rock, provides a good correlation with the UCS ($R^2 = 0.957$).

Acknowledgements The authors are grateful to the Foundation for Science and Technology (FCT, Portugal) for financial support by national funds through the projects UIDB/00195/2020—FibEn-Tech—and UIDB/04035/2020—GeoBioTec.

References

1. Cavaleiro, V.: Contribuição para o conhecimento de recursos não metálicos da região da Guarda. Universidade de Lisboa, Lisboa, Faculdade de Ciências (1994)
2. Schmidt, E.: Rebound hammer for concrete testing (Der Beton-Prüfhammer). Schweiz, Bauztg. **15**, 378–379 (1950)
3. Katz, O., Reches, Z., Roegiers, J.C.: Evaluation of mechanical rock properties using a Schmidt hammer. Int. J. Rock Mech. Min. Sci. **37**(4), 723–728 (2000)
4. Aydin, A., Basu, A.: The Schmidt hammer in rock material characterization. Eng. Geol. **41**, 1211–1214 (2005)
5. Hucka, V.: A rapid method of determining the strength of rocks in situ. Int. J. Rock Mech., Min. Sci. Geomech. Abstracts. **2**(2), 127–134 (1965)
6. Deere, D.U., Miller, R.P.: Engineering classification and index properties for intact rock. Illinois University at Urbana Department of Civil Engineering (1966)
7. Ege, J.R., Miller, D.R., Danilchik, W.: Schmidt hammer test method for field determination of physical properties of zeolitized tuff. ES Geology Survey Open-File Report 70–117 (1970)
8. BS 4408-4: Recommendations for non-destructive methods of test for concrete. Surface hardness methods. BSI (1971)
9. Soiltest Inc: Operating instructions—concrete test hammer. Soiltest Inc (1976)
10. Proceq, S.A.: Operating Instructions, Concrete Test Hammer, Types N and Nr. Riesbachstrasse 57, Postfach 491, CH-8034, Zurich, Switzerland (1977)
11. Barton, N.: Suggested methods for the quantitative description of discontinuities in rock masses, ISRM Int. J. Rock Mech., Min. Sci. Geomech. Abstracts **15**(6) (1978)
12. Irfan, T.Y., Dearman, W.R.: Engineering classification and index properties of a weathered granite. Bull. Int. Assoc. Eng. Geol. **17**(1), 79–90 (1978)
13. Poole, R.W., Farmer, I.W.: Consistency and repeatability of Schmidt Hammer rebound data during field testing. Int. J. Rock Mech., Min. Sci. Geomech. Abstracts **17**(3), 167–171 (1980)
14. Sheorey, P.R., Barat, D., Das, M.N., Mukherjee, K.P., Singh, B.: Schmidt hammer rebound data for estimation of large scale in situ coal strength. Int. J. Rock Mech., Min. Sci. Geomech. Abstracts **21**(1), 39–42 (1984)
15. RILEM: Essais recommandés pour mesurer l'altération des peirres et évaluer l'efficacité des méthodes de traitemente. Matériaux et Constructions **75**, 175–253 (1980)
16. Antão, A.M.M.C., Quinta Ferreira, M.: Efeito da alteração da resistência e nocomportamento da deformação do granito da Gurada. Actas do 9º Congresso Nacional de Geotecnia **1**, 189–198 (2004)

Experimental Analysis of Traditional Stone Masonry Walls Under Blast Loadings

Bruno Joaquim, João Conceição, and Fernando F. S. Pinho

Abstract This paper presents results obtained in a MSc thesis (1st author) developed in NOVA School of Science and Technology (FCT NOVA) (Joaquim, in Behaviour of traditional stone masonry walls subjected to blast loading. Master Thesis, Civil Engineering. FCT NOVA, Lisbon, 2021) regarding the blast behavior of traditional stone masonry walls. In order to understand this phenomenon, two types of tests were performed, using two traditional stone masonry specimens (M1 and M2) with dimensions 1.20 m × 1.20 m × 0.40 m (length × width × thickness), produced by Pinho (Ordinary masonry walls—Experimental study with unstrengthened and strengthened specimens. Ph.D Thesis, Civil Engineering. FCT NOVA, Lisbon, 17/out/07, 2007). Firstly, the specimens (walls) were subjected to unconfined explosions—without physical barriers between the explosion and the target/wall. Secondly, after the explosions, the axial compressive strengths of the two walls were evaluated. In this paper, the results and discussion of the first kind of tests are presented.

Keywords Traditional stone masonry walls · Blast · Incident pressure · Reflected pressure · Axial compressive strength

1 Experimental Work

Traditional stone masonry walls are usually (external) "resistant walls". Thus, a testing system was developed to apply a pre-load of 0.25 MPa to each wall, which

B. Joaquim (✉)
Civil Engineering Department, FCT NOVA, Lisbon, Portugal
e-mail: b.joaquim@campus.fct.unl.pt

J. Conceição
CINAMIL, Military Academy, FCT NOVA, Lisbon, Portugal
e-mail: joaofilipemelro@gmail.com

F. F. S. Pinho
CERIS, Civil Engineering Department, FCT NOVA, Lisbon, Portugal

C. Chastre et al. (eds.), *Testing and Experimentation in Civil Engineering*, RILEM Bookseries 41, https://doi.org/10.1007/978-3-031-29191-3_11

in turn may simulate a lower floor wall of a traditional Portuguese ancient stone building.

Field tests took place at Campo Militar de Santa Margarida (CMSM), which has safety and optimal and operational conditions to perform this experimental procedure.

Due to the lack of bibliography and knowledge concerning the expected results, the ideal approach would be to reproduce perfect airbursts, firstly, in order to facilitate the study and create data regarding traditional stone masonry walls' blast resistance.

It was not possible to test the walls in the horizontal position, similarly to tests previously performed [1, 2] under the Project PTDC/ECI-EST/31046/2017—PROTEDES, due to their constitution, weight and pre-load applied. Therefore, a different testing system was used, Fig. 1, allowing three types of unconfined explosions on two masonry specimens: perfect aerial, near-surface and surface explosions. Making this system closer to reality also adds difficulty in recording and processing data.

The testing facility of Competence Centre for Infrastructure Protection (CCPI), located in CMSM, comprises a foundation and reinforced concrete walls (0.35 m thick), 1.65 m apart. Additionally, the test system has several steel parts (e.g. brackets and beams) to ensure the assembly of different support systems.

In order to keep the wall perpendicularly to the blast action direction, two UNP300 metal beams were used, with the upper one supported on two metal brackets and the lower one 15 cm off the ground, Fig. 2.

A metallic tripod with a rope weas used to place the explosive and adjust the height and distance to the target.

Two incident pressure transducers and one reflected pressure transducer [(×2) PCB 137B24 and PCB 137B24, respectively] were used.

In order to evaluate the explosion's effects on the wall, transversal displacements of each wall were measured using an expedite system consisting of steel tubes filled

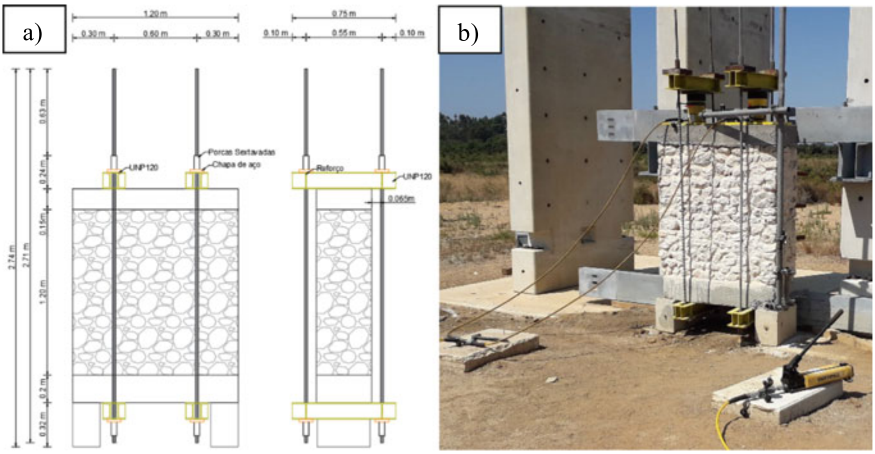

Fig. 1 **a** Schematic representation of the tested specimens (M1 and M2) [3]; **b** Application of vertical pre-load of 0.25 MPa to the specimens [3], before the explosive actions

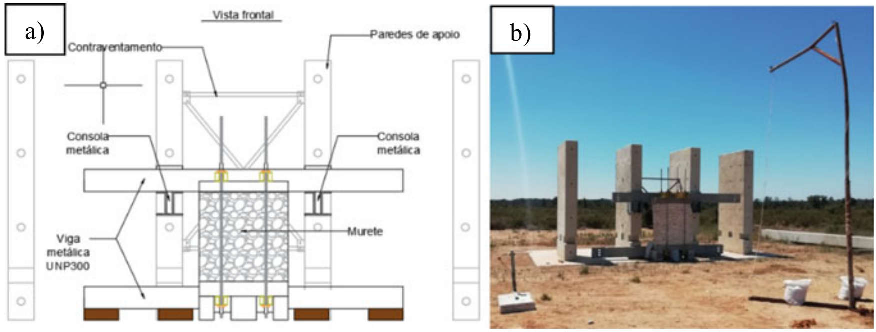

Fig. 2 **a** Schematic representation of the testing system; **b** Testing setup

Table 1 Distance and charge of the explosive in each test

Test	R (m)	W (kg)
1st (M2)	5	2.0
2nd (M2)	1	1.3
3rd (M1)	1	4.0

with foam. This measurement system was positioned behind the wall, placing six metal bars in contact with the back of the wall, wrapped in foam inside the metal tubes.

Explosive *EurodynTM* was used in the experimental tests, with 75% of TNT's detonation power. The quantity of explosive used, presented in Table 1, was determined through numerical simulations.

The distances and loads of the first test (specimen M2) were based on previous works performed under the project PTDC/ECI-EST/31046/2017—PROTEDES, allowing future comparisons regarding different constructive solutions. For the second test, using specimen M2 again, it was kept approximately the same incident impulse, varying the distance and the amount of explosive. These variations were performed to cause more damage and analyze the difference between reflected pressures. In the third test (specimen M1), to allow data extraction and axial compression test execution, the explosive quantity was defined to create more damage without leading the rampart to collapse.

For safety reasons, the handling of the explosive was carried out by the EOD (Explosive Ordnance Disposal) team from the 1st Engineering Regiment based in Tancos.

2 Visual Damage Assessment

The first test used 20 kg of explosive at a distance of 5.0 m from the target (M2), and there was no visible damage except a small crack on the face exposed to the blast.

In the second test (M2, again), the incident impulse was kept approximately the same as in the first test, varying the distance and amount of explosive (1.0 m and 1.3 kg, respectively) to cause more damage and analyze the difference between reflected pressures. In this test, the following damage was observed—several cracks (higher width crack of 1.4 mm) and some craters on the face exposed to the blast and the side of the wall; on the face opposite to the blast, there was no visible damage.

In the third test (specimen M1), there was an increase in the amount of explosive relative to the second test, and the damage acquired a greater dimension, with the wall showing cracks (maximum 0.8 mm) on the face opposite to the explosion. However, the wall did not collapse, and there was no spalling on this face. On the other hand, a large part of the mortar on the face exposed to the blast was disintegrated.

3 Results

Firstly, a filtering of the data obtained from the incident and reflected pressures was performed to allow an evaluation by comparing the positive phase of the explosion between the shock wave profiles obtained in the experimental tests and the theoretical profiles obtained through Friedlander's equation. In Eq. (1), where t is the value of time recorded since the arrival to the positive phase, where the incident peak pressure occurs (P_{S0}), and b is a shape constant.

$$P_{(t)} = P_{S0} \cdot \left(1 - \frac{t}{t_0}\right) \cdot e^{\frac{bt}{t_0}} \tag{1}$$

Subsequently, a comparison was made between the values of incident peak pressure (P_{S0}) and reflected peak pressure (P_r) (2) of Kinney and Graham [4], Eq. (3) of Rankine-Hugoniot [5] and the "KINGERY_master" calculation sheetsmaster".

$$P_{S0}[MPa] = \frac{808 \cdot \left[1 + \left(\frac{Z}{4{,}5}\right)^2\right] \cdot P_0}{\left[1 + \left(\frac{Z}{0{,}048}\right)^2\right]^{\frac{1}{2}} \cdot \left[1 + \left(\frac{Z}{0{,}32}\right)^2\right]^{\frac{1}{2}} \cdot \left[1 + \left(\frac{Z}{1{,}35}\right)^2\right]^{\frac{1}{2}}} \tag{2}$$

$$\mathrm{P_r} = 2 \cdot \mathrm{P_{S0}} \times \left(\frac{7 \cdot \mathrm{P_0} + 4 \cdot \mathrm{P_{S0}}}{7 \cdot \mathrm{P_0} + \mathrm{P_{S0}}}\right) \tag{3}$$

Parameters given in Eqs. (2) and (3) if it is a surface explosion, the comparative analysis of experimental data used in UFC 3-340-02 [6], reveal that W must be corrected by a multiplication factor of 1.8. Z is the reduced distance obtained by Eq. (4) and P_0 is the atmospheric pressure.

$$Z = \frac{R}{\sqrt[3]{W}} \tag{4}$$

Finally, we compared the values of the incident pulses (P_{S0}) and reflected impulses (P_r), obtained in the experimental tests, by numerical integration of the shock wave profiles recorded by the transducers and the theoretical incidents and reflected impulses by Eq. (6) of Kinney and Graham [4], Eq. (7) and the "KINGERY_master" spreadsheets.

$$i_s[MPa.ms] = \frac{0,0067\sqrt{1+\left(\frac{Z}{0,23}\right)^4}}{Z^2\sqrt{1+\left(\frac{Z}{1,55}\right)^3}} \tag{6}$$

$$i_r[MPa.ms] = \frac{i_s.P_r}{P_{S0}} \tag{7}$$

3.1 Comparison of Experimental and Theoretical Shock Wave Profiles

In order to study the shock wave profiles obtained experimentally, a comparison was made between these and the curves that would be obtained using Eq. (1).

The values of the curves obtained from each incident pressure transducer were averaged to standardize the values and obtain a global perception of the events in each test. Only the values referring to the positive phase were considered, ignoring the negative phase.

Finally, to obtain the theoretical curve suitable to the profile obtained, some variables were calculated: shape constant (b); positive phase time (t_0) and incident peak pressure (P_{so}). Those were obtained as a function of the minimum value of the sum of the standard deviations (S.D.) between the values obtained by the description of Eq. (2) and the experimental values.

With the results of the first test (wall M2) it was possible to approximate the incident pressure curve, Fig. 3, based on Eq. (1), having been obtained the values b = 0.92; t_0 = 2.91 ms and P_{so} = 0.56 MPa.

Regarding the reflective pressure curve, Fig. 4, due to successive reflections and interference in the sensor reading, it was not possible to obtain the entire curve, only the peak reflected pressure.

In the second test (specimen M2), due to the reflections evidenced in Figs. 5 and 6, the wave prolongation did not allow for a good fit based on Eq. (1). The

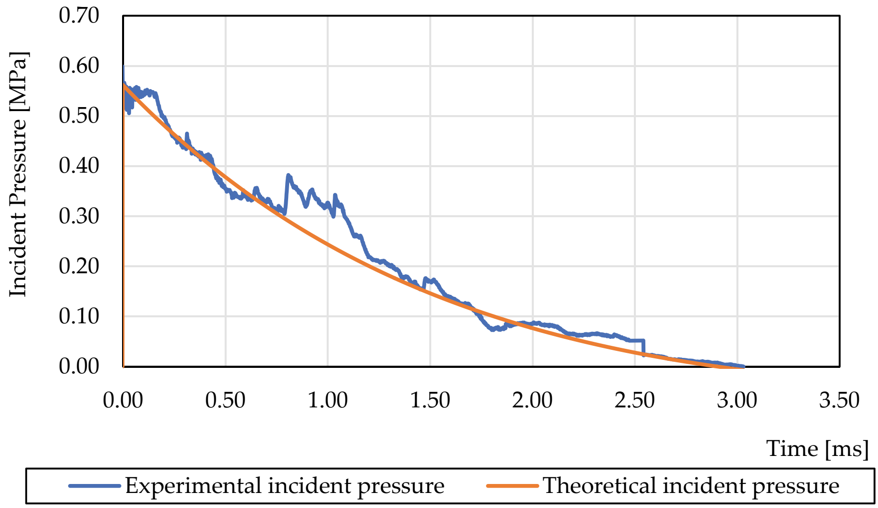

Fig. 3 Comparison of incident shock wave profiles from the 1st test (M2)

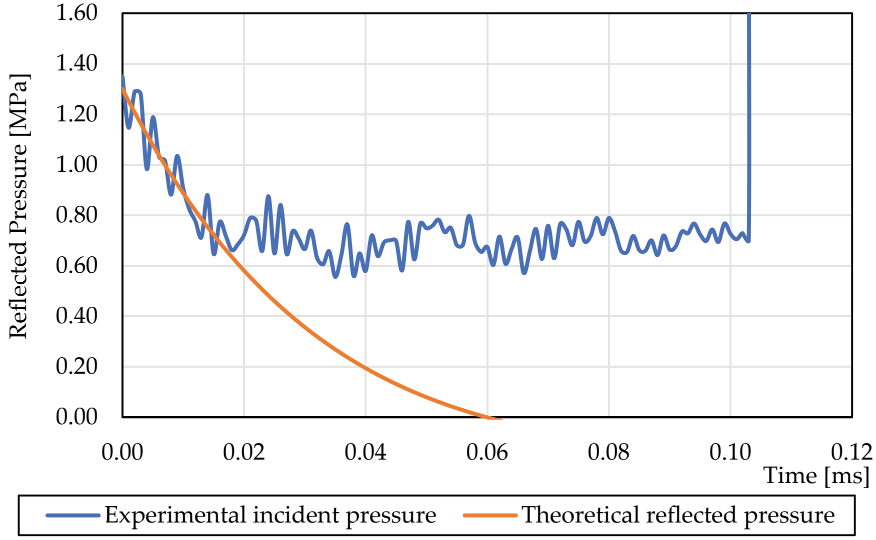

Fig. 4 Comparison of shock wave profiles reflected from the 1st test (M2)

quick decrease of the peak pressure also contributes decisively to the lack of a better approximation of the profiles. For the minimum value of S.D. (best approximation to the experimental curve) the parameters are not coherent, as shown in Table 2. These reflections occurred due to the proximity of the sensors to the wall and test system, being only 1.00 m away.

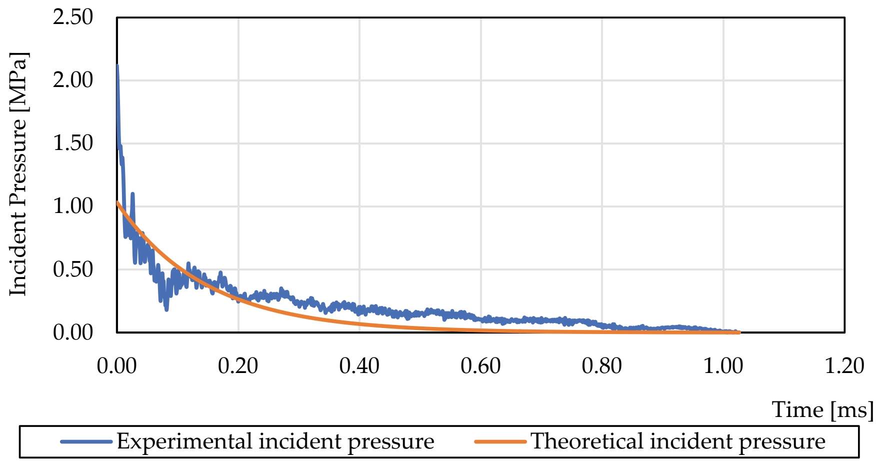

Fig. 5 Comparison of incident shock wave profiles from the 2nd test (M2)

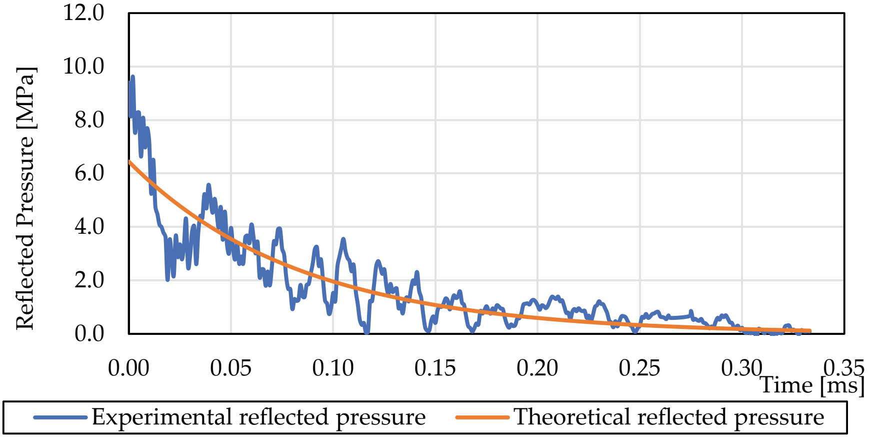

Fig. 6 Comparison of the reflected shock wave profiles of the 2nd test (M2)

Table 2 Comparison of parameters describing the positive phase of the shock wave profile (2nd Test)

Wave profile	b	t_0 (ms)	P_{S0} (MPa)	SD
Incident	286.67	42.27	1.03	8.90
Reflected	359.40	30.23	6.44	200.34

Similarly, to the second test, in the third test (specimen M1), the explosive was placed at a distance of 1.00 m from the wall, causing reflections. These reflections did not allow a good approximation of the theoretical and experimental curves for the incident and reflected pressures. The profiles of the shock wave curves of the incident and reflected pressures are represented in Figs. 7 and 8 respectively, as presented in Table 3.

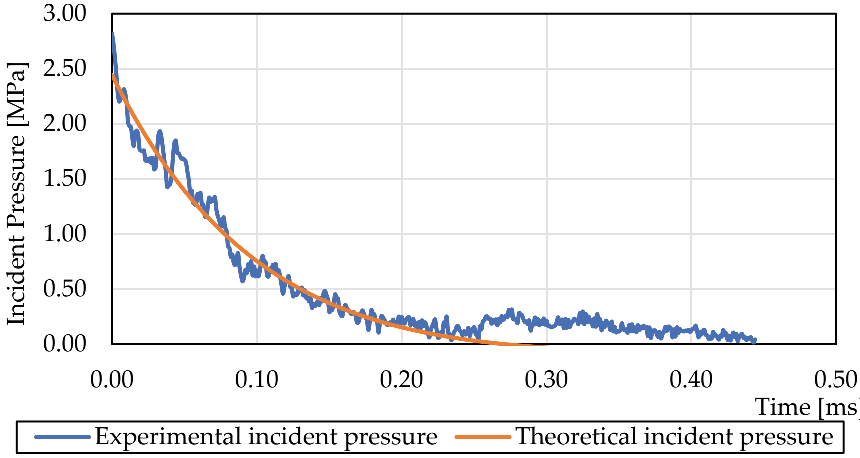

Fig. 7 Comparison of incident shock wave profiles from the 3rd test (M1)

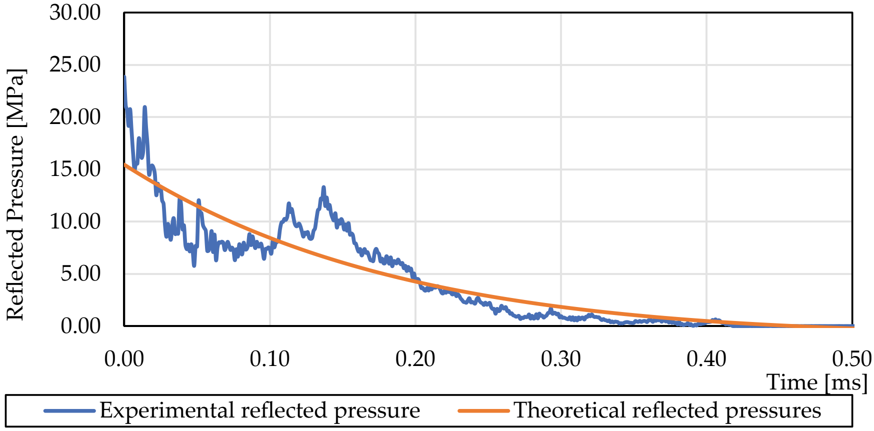

Fig. 8 Comparison of the reflected shock wave profiles of the 3rd test (M1)

Table 3 Comparison of parameters describing the positive phase of the shockwave profile (3rd Test)

Wave profile	b	t_0 (ms)	P_{S0} (MPa)	SD
Incident	1.92	0.27	2.44	11.60
Reflected	1.65	0.46	15.45	1737.53

Table 4 Incident and reflected pressures obtained experimentally and theoretically

Values (MPa)	1st test (M2)		2nd test (M2)		3rd test (M1)	
	P_{S0}	P_r	P_{S0}	P_r	P_{S0}	P_r
Experimental	0.60	1.35	2.12	9.40	2.82	23.85
Theoretical air blast	0.20	0.67	0.99	5.43	2.15	14.01
Theoretical surface explosion	0.32	1.22	1.50	9.09	3.14	20.64
Aerial calculation sheet	0.19	0.62	0.92	4.89	2.05	13.74
Surface calculation sheet	0.26	1.01	1.33	7.96	2.80	20.13

3.2 Comparison of Incident Peak and Reflected Pressures

By comparing the experimental values with theoretical formulations, it can be seen that formers are closer to a surface explosion.

The most significant discrepancies are for the incident pressure, with an error of 87.5% observed in the first test and 41.4% in the second test; however, the error decreases in the third test, observing a value of 10.2%. This can be justified by the experimental test conditions in natural conditions outside the laboratory. In the case of the second test, a sensor recorded a higher peak of 2.58 MPa, and the other one of 1.65 MPa which is closer to the theoretical values.

Regarding the reflected pressure, it has a minor error between its theoretical values and spreadsheets being respectively 10.4%, 3.4% and 15.5% in the first, second and third tests. It is also possible to observe that the values of the positive phase duration and impulses are in greater agreement with the "KINGERY_master" calculation sheets of RD Willcox of CESO(N) (1993).

In Table 4, we can see the results obtained through the experimental tests and compare them with theoretical calculations (Eqs. 2 and 3 and spreadsheet results).

3.3 Comparison of Incident and Reflected Impulses

Impulses, namely the reflected ones, are fundamental in analyzing the blast action because it is the force that effectively acts on the wall, resulting from the incident and reflected pressures, Table 5.

Table 5 Incident and reflected impulses obtained experimentally and theoretically

Values (MPa.ms)	1st test (M2)		2nd test (M2)		3rd test (M1)	
	I_s	I_r	I_s	I_r	I_s	I_r
Experimental	0.62	–	0.21	0.56	0.21	2.16
Theoretical air blast	0.09	0.29	0.12	0.64	0.12	0.81
Theoretical surface explosion	0.10	0.37	0.12	0.74	0.13	0.87
Aerial calculation sheet	0.22	0.57	0.17	0.55	0.25	1.32
Surface calculation sheet	0.33	0.88	0.23	0.87	0.26	2.12

In the first test, it was impossible to experimentally quantify the action reproduced on the wall (reflected impulse) due to an incorrect transducer measurement. Regarding the second and third tests, errors of 24.3% and 148%, respectively, were found by comparing the experimental and the theoretical values of the surface explosion.

On the other hand, comparing the experimental values with the values obtained through the spreadsheet, for the surface explosion, errors of 35.6% and 1.9% are registered, respectively, in the second and third tests.

It can be seen that relevant errors were obtained, probably due to the proximity between the explosive and the wall (only 1.0 m, almost contact blast).

4 Conclusions

For these explosive loads, there was no collapse and projection of aggregates. Thus, it is essential to continue the study, increasing the explosive loads, in order to really know the ultimate load and failure mechanisms, with the purpose of adopting the best strengthening solutions for this constructive solution.

Moreover, concerning studies in the field of out-of-plane actions in traditional stone masonry walls, the information is relatively scarce, so it would be necessary to understand the stiffness, ultimate loads and maximum deflections of this type of wall, in order to obtain more accurate results in the description of the events and effects by an explosion.

The tests performed at a distance of 1.0 m from the target, due to the high proximity, show similar behaviour to the contact explosions, exhibiting localized damage. This distance also leads to the registration of reflections by the sensors, which hinders a good fit to the theoretical curve. This may show that these formulations may not be suitable for short distances.

References

1. Nabais, D.: Development of an innovative system for the protection of concrete structures against explosions. Master Thesis, Military Engineering. Lisbon, Military Academy/Instituto Superior Técnico (2016). (in Portuguese)
2. Pereira, V.: Innovative system for explosion protection of buildings—Reinforced concrete facade panels with thin walled steel connectors. Master Thesis, Military Engineering. Lisbon, Military Academy/Instituto Superior Técnico (2017). (in Portuguese)
3. Pinho, F.F.S.: Ordinary masonry walls—Experimental study with unstrengthened and strengthened specimens. Ph.D Thesis, Civil Engineering. FCT NOVA, Lisbon, 17/out/07 (2007). (in Portuguese)
4. Kinney, G.F., Graham, K.J.: Explosive Shocks in Air. Springer. ISBN: 978-3-642-86682-1 (1985)
5. Gomes, G.: Reuse of current buildings for operational purposes—Blast assesment. Collection "ARES", 13. Lisbon; Instituto Universitário Militar (2016)
6. UFC 3-340-02 (2008): Structures to resist the effects of accidental explosions; U.S Department of Defense
7. Joaquim, B.: Behaviour of traditional stone masonry walls subjected to blast loading. Master Thesis, Civil Engineering. FCT NOVA, Lisbon (2021). (in Portuguese)

Dynamic Behavior of a Two-Storey Cross Laminated Timber Mockup

Matteo Salvalaggio, Filippo Lorenzoni, and Maria Rosa Valluzzi

Abstract Timber constructions have gained an increasing attention in the last years, due to the limited installation time and the reduced expertise in manpower required, since panels assemblage is mainly based on dry mounting techniques. Among these, Cross Laminated Timber (CLT) products are extensively used in constructions, as they allow to overcome the main weaknesses of hardwood artifacts. Moreover, CLT components are also being tested within the restoration and re-use of existing buildings. Since these timber products are relatively new in the construction market, experimental data and site investigations are still limited and some aspects still unknown. Among the many, dynamic characterization of CLT structures, and related model updating, is rare in literature. In such a context, an experimental campaign aimed at assessing the linear dynamic behavior of CLT structures was carried out. A building-scale specimen (mockup) was constructed; it was made of C24 CLT walls and diaphragms (floor and roof) with 10- and 14-cm thick panels, respectively, connected through steel brackets and screws. The mockup was investigated via dynamic identification tests, by implementing 12 piezoelectric accelerometers, i.e., 4 on the first floor and 8 on the roof. The experimental characterization was aimed at: (i) assessing the structural dynamic behavior and identifying the role of structural details on it; (ii) evaluating the experimental stiffness, compared to analytical predictions. At last, a finite element (FE) model was implemented and updated based on the experimental outcomes.

Keywords Cross laminated timber CLT · Dynamic characterization · Modal analysis · Finite element modeling FEM

M. Salvalaggio (✉) · M. R. Valluzzi
Department of Cultural Heritage, University of Padova, 35139 Padova, Italy
e-mail: matteo.salvalaggio@unipd.it

M. R. Valluzzi
e-mail: mariarosa.valluzzi@unipd.it

F. Lorenzoni
Department of Geosciences, University of Padova, 35131 Padova, Italy
e-mail: filippo.lorenzoni@unipd.it

C. Chastre et al. (eds.), *Testing and Experimentation in Civil Engineering*,
RILEM Bookseries 41, https://doi.org/10.1007/978-3-031-29191-3_12

1 Introduction

The structural behavior of CLT structures is strictly connected to the properties of massive panels and, especially in the nonlinear field, joints [3].

Since CLT panels and structures constitute new technologies, the amount of unknows about their structural characterization is still relevant. Hence, the increase of related knowledge is necessary.

The dynamic characterization of CLT assemblages has been scarcely investigated (i.e., dynamic identification and model updating). For the best of the authors knowledge, the studies conducted are reported in [1, 6]. They concerned the application of Operational Modal Analysis (OMA) to multi-story CLT buildings (with finished works) and the following numerical model updating procedure. However, case studies also focused on the contributions of materials other than timber and non-structural weights.

In this work, to improve the knowledge on the dynamic behavior of timber structures, OMA was applied to a two-story CLT specimen (hereafter, mockup).

This paper reports the outcomes of Ambient Vibration Tests (AVT) performed on the mockup, the construction of a FE model, some parametric analyses and the model updating procedure. The main aims consist of: (i) the identification of the dynamic behavior of the CLT structure, and (ii) the characterization of the influence of the mechanical parameters (i.e., timber-to-timber and steel-to-timber joints) on the overall behavior.

2 Materials and Method

The mockup consisted of a two-story structure of $4 \times 9 \times 6$ m size (Fig. 1a), made with 10 cm-thick CLT walls and roof, while the floor was 14 cm thick. Such structural components were made of jointed 1.2 m-wide panels. Traditional hold-down and angle bracket elements (produced by Rhotoblaas) were used to prevent rocking and sliding phenomena, respectively. The mockup was connected to the foundation reinforced concrete beam through 16 WHTPLATE440 and 21 TCP200 plate-type brackets, whereas 44 WHT440 and 21 TTF240 elements were used for inter-story connections. Full-threaded steel screws Ø5 × 60 mm were used for the fastening of such brackets; partially threaded screws Ø8 × 200 mm timber-to-timber joints (i.e., wall-to-wall, wall-to-diaphragm).

Dynamic identification tests were performed using 12 PCB Piezotronics 393 B12 accelerometers connected via coaxial wires to the National Instruments PXI 4472 acquisition system. Accelerometers were placed at diaphragms level, 4 on the floor and 8 on the roof, according to the layout shown in Fig. 1b.

The proprietary software IRS StructuralX was used for the management of signal acquisition. Ambient vibrations were acquired with a 200 Hz sample frequency in record files of about 10 min duration (120’000 points).

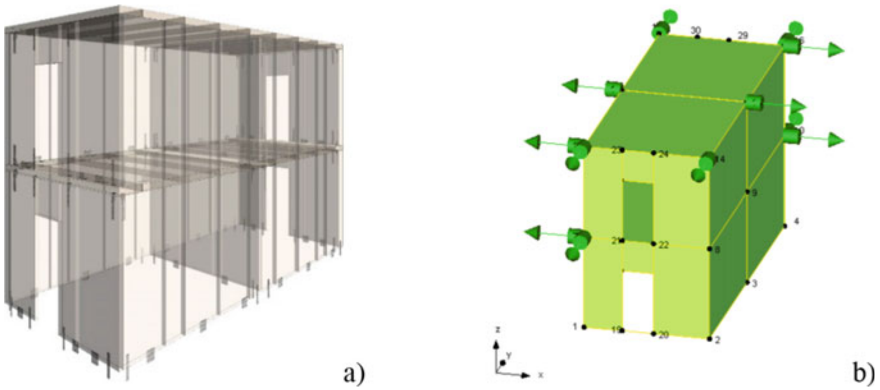

Fig. 1 CLT mockup: **a** 3D model; **b** scheme of accelerometers setup

The processing of signals was done by the Frequency Domain Decomposition technique (FDD [2]), in the Artemis software [8]. Eight records were analyzed, and outcomes were cross-checked by calculating frequency discrepancy Df (Eq. (1)) and Modal Assurance Criterion MAC (Eq. (2)) between two modes, *r* and *s*:

$$D_f = 100\left|\frac{f^r - f^s}{f^r}\right| \tag{1}$$

$$MAC = \frac{\left|\sum_{i=1}^{n} \varphi_i^r \varphi_i^s\right|^2}{\sum_{i=1}^{n} \left(\varphi_i^r\right)^2 \sum_{i=1}^{n} \left(\varphi_i^s\right)^2} \tag{2}$$

where f^r and f^s, ${\varphi_i}^r$ and ${\varphi_i}^s$ are the frequencies and shapes of *r* and *s* modes, respectively, *n* the nodes of the model.

Once validated, the experimental mode frequencies and shapes were used for the updating of the mockup's numerical model.

The FE model was constructed in the Strand7 R2.4.6 environment [7] through 2-D 4-noded plate elements of 20 cm in size for the CLT panels, 2-noded spring elements for the steel brackets (hold-downs and angle brackets), and 2-noded connection elements for timber-to-timber connections. The final model was composed of 2920 plate elements, and 456 springs and connections elements.

Diaphragms were assumed rigid, hence 298 link elements (149 per slab) were used to constrain all walls upper nodes to the floors mass centers (Fig. 2).

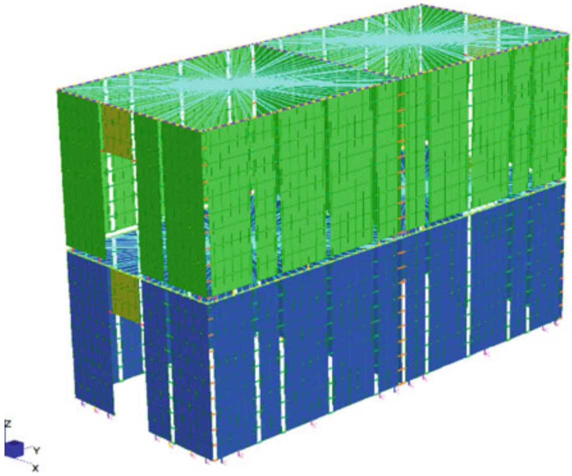

Fig. 2 Finite element model of the mockup in Strand7 environment

3 Ambient Vibration Test and Modal Identification

Ambient vibration tests (AVT) and application of FDD allowed main modal parameters of the structure to be extracted, i.e., natural frequencies, mode shapes and damping ratios.

Table 1 summarizes the outcomes of the analyses. Figure 3 shows the mode shapes. Frequency values were significant compared to analytical estimation for first mode equal to 5.22 Hz, according to EN 1995-1-1 [5]. The former transversal bending mode was detected at 8.73 Hz. After that, a torsional shape and a longitudinal bending shape were found at 10.87 and 16.34 Hz, respectively. Beyond these, also a second-order transverse bending shape was detected at 20.97 Hz. Shapes were regular and did not show any unexpected deviance.

Table 1 Modal parameters of the mockup extracted by FDD technique

Mode n°	Mode shape	Frequency *f*		
		Average value [Hz]	St. Dev. [Hz]	COV [%]
1	Transv. bending	8.73	0.08	0.97
2	Torsional	10.87	0.11	0.99
3	Long. bending	16.34	1.10	6.74
4	II Transv. bending	20.97	0.39	1.85

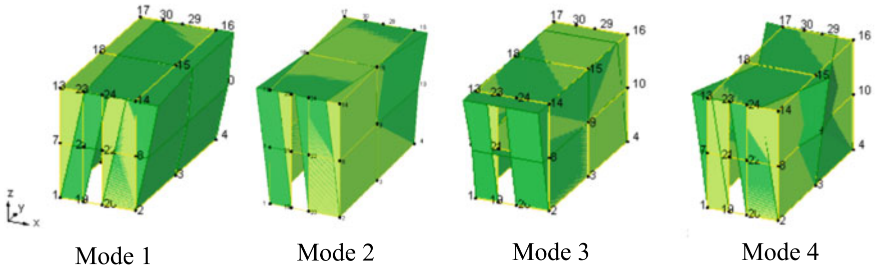

Fig. 3 Experimental mode shapes of the mockup

4 Numerical Modeling

The finite element model, as described in Sect. 2, was composed of shell elements for CLT panels and spring ones for connections. Diaphragms (floor and roof) were considered rigid; masses lumped at such heights, with a point mass connected to related walls nodes.

Panels orthotropic linear properties (i.e., Young's moduli E_x and E_y, shear modulus G_{xy}) were derived by the *Laminate* assumption in Strand7, with plies constituted by the CLT layers, as $E_x = 7010$ MPa, $E_y = 3856$ MPa and $G_{xy} = 690$ MPa. Connections stiffnesses (i.e., k_{ser}) for timber-to-timber and steel-to-timber joints were derived from [5]. Wall-to-diaphragm joints were considered rigid. Table 2 reports the main mechanical parameters adopted in the model.

Prior to the calibration of the finite element model based on OMA outcomes, some parametric analyses were carried out. According to [4], modeling uncertainties can be subdivided into (i) epistemic and (ii) aleatory categories. Therefore, the parametric analyses were based on such distinction.

Table 2 Mechanical parameters of joints according to EN 1995-1-1 [5]

Joint type	Connectors	Shear stiffness [N/mm]	Tensile stiffness [N/mm]
Hold-down	WHTPLATE 440	8892	88,920
Angle bracket	Titan TCP 200	74,100	74,100
Hold-down	WHT440	14,820	148,200
Angle bracket	Titan TTN240	88,920	88,920
Joint type	Connectors	Shear stiffness [kN/m/m]	Tensile stiffness [kN/m/m]
In-plane wall-to-wall	2 x Ø5 × 60 mm screws/150 mm	50,996	50,996
L- and T-type wall-to-wall joints	Ø8 × 200 mm screws/200 mm	31,122	31,122
L- and T-type wall-to-diaphragm joints	Ø8 × 200 mm screws/200 mm	Rigid	Rigid

Epistemic unknows of the CLT mockup model consisted of the connection degree between CLT components. Thus, it was assessed how the assumption of rigid connections (i.e., continuum mesh without discrete springs) for (i) L, T and (ii) in-plane wall-to-wall joints could affect the overall dynamic behavior of the mockup model.

Once fixed the epistemic uncertainties, the aleatory ones, i.e., the quantification of joints mechanical linear properties, were evaluated.

4.1 Parametric Analyses on Epistemic Uncertainties

The influence of connection degree was assessed through an incremental approach, starting from a model with all wall-to-wall joints deformable (i.e., discretized by springs with finite stiffness values). Two further models were analyzed: one with rigid L and T wall-to-wall joints and deformable in-plane wall-to-wall joints; the other one with all wall-to-wall joints deformable. Figure 4 shows the results of the analysis.

The in-plane connections constituted the most affecting parameter due to their high number. As an example, the former transverse mode moved from 6.42 − 9.71 Hz. The further addition of L and T deformable connections did not significantly alter the outcomes.

Hence, it was chosen to adopt the model with all deformable joints, to consider each wall-to-wall joint property.

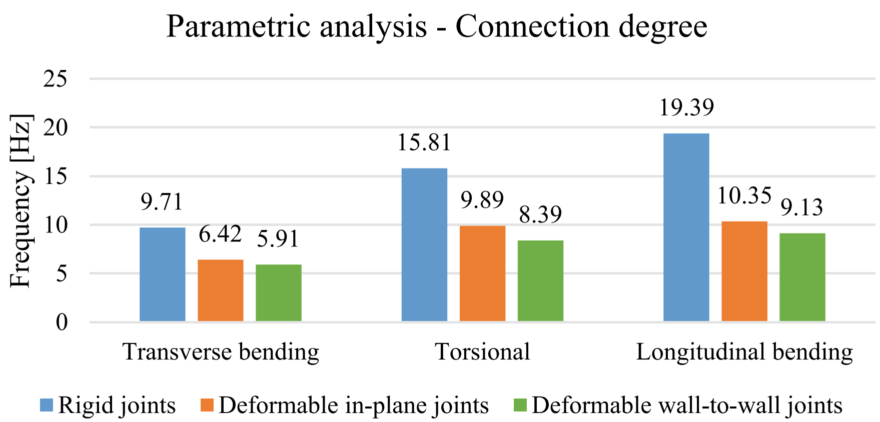

Fig. 4 Mode frequency values in function of wall-to-wall connection degrees

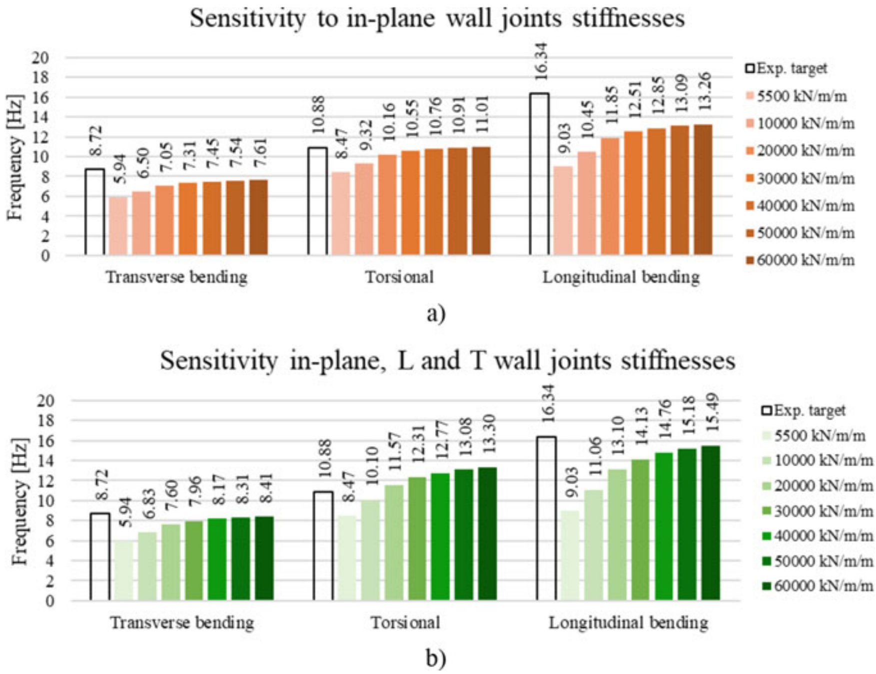

Fig. 5 Mode frequency values in function of wall-to-wall stiffness value

4.2 *Parametric Analyses on Aleatory Uncertainties*

Aleatory unknows consisted of the normal and shear stiffnesses of in-plane, T and L wall-to-wall joints. Such values were made vary, keeping constant the others (i.e., steel brackets and CLT panels). Two parametric analyses were performed, based on (i) in-plane joints and (ii) in-plane, L and T joints. Figure 5 shows the values of mode frequencies in function of joint stiffnesses variation. L and T joints appeared more influential than in-plane ones, especially for the torsional mode. However, to approach experimental target frequencies, all the joints stiffnesses had to be considered.

4.3 *Calibration*

To update the numerical model, all wall-to-wall joints were considered deformable, i.e., discretized by spring elements. The calibration was controlled by Frequency Discrepancy Df (Eq. (1)) and MAC (Eq. (2)) indexes. Based on the parametric analyses presented in Sect. 4.2, stiffness values of in-plane, L, T wall-to-wall joints were considered equal to 60,000 kN/m/m. Table 3 summarizes the updated values for wall-to-wall joints.

Table 3 Mechanical parameters of joints after model updating procedure (bolded the ones changed after calibration)

Joint type	Connectors	Shear stiffness [kN/m/m]	Tensile stiffness [kN/m/m]
In-plane wall-to-wall	2 x Ø5 × 60 mm screws/150 mm	60,000	60,000
L- and T-type wall-to-wall joints	Ø8 × 200 mm screws/200 mm	60,000	60,000
L- and T-type wall-to-diaphragm joints	Ø8 × 200 mm screws/200 mm	Rigid	Rigid

Table 4 Results of FE model calibration: comparison between modal and numerical parameters: f_{EXP} and f_{NUM} are the experimental and numerical frequencies

Mode	f_{EXP}	f_{NUM}	D_f [%]	MAC
1	8.71	8.41	3	0.97
2	10.88	13.30	22	0.87
3	16.28	15.49	5	0.97

Table 4 reports the results of calibration procedure, i.e., the comparison between experimental and numerical (FEM) outputs. The matching of the first and third mode shapes (the transverse and longitudinal bending, respectively) was very good: MAC values were both equal to 0.97 and frequency discrepancy below 5%. Torsional mode calibration showed some weaknesses: the 0.87 MAC value was acceptable, although the frequency discrepancy of 22% was still significant. However, the model updating procedure can be considered successful overall. Figure 6 shows the final numerical mode shapes.

5 Conclusions

The performance of AVT on the mockup provided further data on the dynamic behavior of CLT timber structures. The following conclusions can be drawn from this study:

- CLT assemblages provide a consistent stiffness (i.e., high natural frequency value), that is usually underestimated by the analytical equation reported in [5];
- L and T joints are more influential than in-plane ones, especially for the torsional mode, which appeared as relying on corner connection degree;
- the assumptions of rigid connections for jointed walls can significantly affect the overall stiffness (i.e., frequency values) and should be carefully considered in the design of massive timber structures;

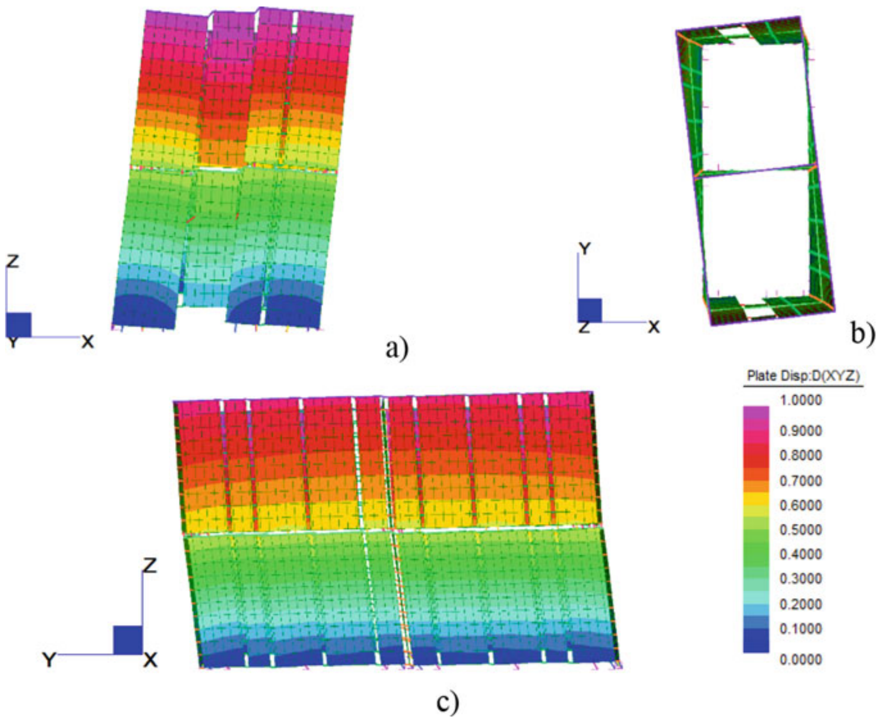

Fig. 6 Mode shapes of finite element model: **a** X bending mode; **b** torsional mode; **c** Y bending mode

- model updating procedure permitted to obtain a good matching of mode shapes, especially for bending ones;
- analytical values of joints presented in [5] could underestimate the dynamic stiffness of joints. The calibration of the model required approximately doubling those values for L and T joints;
- the assumption of rigid diaphragms and wall-to-floor connections seems an acceptable choice for obtaining a satisfactory model calibration.

Acknowledgements This study was supported by the CORE-WOOD (Competitive Repositioning of WOOD sector) Italian project, in the framework of POR-FESR 2014-2020 Line 1 Action 1.1.4 of the Veneto Region. Authors thank Bozza Legnami for providing the structural material and workmanship; the Master students A. Zenari and F. Zanotto are also acknowledged for their contribution in the research activities.

References

1. Aloisio, A., Pasca, D., Tomasi, R., Fragiacomo, M.: Dynamic identification and model updating of an eight-storey CLT building. Eng. Struct. **213**, 110593 (2020). https://doi.org/10.1016/j.engstruct.2020.110593
2. Brincker, R., Zhang, L., Andersen, P.: Modal identification of output-only systems using frequency domain decomposition. Smart Mater. Struct. **10**, 441–445 (2001). https://doi.org/10.1088/0964-1726/10/3/303
3. Casagrande, D., Rossi, S., Sartori, T., Tomasi, R.: Proposal of an analytical procedure and a simplified numerical model for elastic response of single-storey timber shear-walls. Constr. Build. Mater. **102**, 1101–1112 (2016). https://doi.org/10.1016/j.conbuildmat.2014.12.114
4. Cattari, S., Degli Abbati, S., Alfano, S., Brunelli, A., Lorenzoni, F., da Porto, F.: Dynamic calibration and seismic validation of numerical models of URM buildings through permanent monitoring data. Earthq. Eng. Struct. Dyn. **50**, 2690–2711 (2021). https://doi.org/10.1002/eqe.3467
5. EN 1995-1-1:2004+A2:2014: Eurocode 5 - Design of timber structures. Comité Européen de Normalisation (2014)
6. Mugabo, I., Barbosa, A.R., Riggio, M.: Dynamic characterization and vibration analysis of a four-story mass timber building. Front. Built Environ. **5**, (2019). https://doi.org/10.3389/fbuil.2019.00086
7. Strand7 Pty Ltd: Strand7 2.4.6 (2013)
8. Structural Vibration Solutions: ARTeMIS Extractor Pro (2006)

Shear Capacity Assessment of Steel-To-CLT Connectors

Matteo Salvalaggio, Enrico Garbin, and Maria Rosa Valluzzi

Abstract In modern prefabricated wooden buildings, CLT elements (Cross Laminated Timber, also known as Xlam, CrossLam or BSP) are assembled into macro elements (e.g., walls and slabs) and anchored by means of steel brackets and fasteners. A wide variety of such elements, in the shape of nails, screws and bolts, has been used in the construction market in recent years. Both the novelty of the construction technique and the wide number of fastener types imply that the knowledge about timber (CLT) joints is still limited. Under seismic shocks, steel-to-timber joints can prevent timber panels from overturning but, due to their high stiffness and low ductility, seismic energy dissipation occurs by damaging the timber elements over the fastening area. Hence, the sizing of such joints is a key factor in the design of a timber building. To improve the knowledge on the behavior of fastened steel-to-timber joints an experimental campaign was carried out. The paper discusses the testing of steel-to-CLT specimens, at changing of fasteners (i) type (i.e., 60 mm-length Anker nails and screws) and (ii) number (i.e., 2, 10, 18). The research aimed at characterizing the strength and stiffness of the compound element and at estimating the potential redistribution of loads at increasing number of fasteners (i.e., group effect).

Keywords Cross laminated timber · Steel fasteners · Slip modulus · Experimental test

M. Salvalaggio (✉) · M. R. Valluzzi
Department of Cultural Heritage, University of Padova, 35139 Padova, Italy
e-mail: matteo.salvalaggio@unipd.it

M. R. Valluzzi
e-mail: mariarosa.valluzzi@unipd.it

E. Garbin
Inter-Departmental Research Centre for the Study of Cement Materials and Hydraulic Binders (CIRCe Centre), University of Padova, 35131 Padova, Italy
e-mail: enrico.garbin@unipd.it

C. Chastre et al. (eds.), *Testing and Experimentation in Civil Engineering*,
RILEM Bookseries 41, https://doi.org/10.1007/978-3-031-29191-3_13

1 Introduction

One of the advantages of CLT constructions, beyond their structural and energy performances, concerns the assembling easiness and speed, due to dry mounting technique. Timber-to-timber and steel-to-timber connections rule the behavior of massive timber structures, as pointed out by [1]. Among these, fastened plate junctions (i.e., nails and screws) provide adequate stiffness and strength to satisfy the design requirements of new constructions. One of the main drawbacks in the implementation of such structural details concerns the arise of the pinching effect, which occurs while cyclic loads act (e.g., seismic action), due to low embedment strength of wooden component and yielding of steel fasteners. The main consequences of this phenomenon regard: (i) the damage at wood-to-steel interface, which then requires the shift of brackets position or the substitution of the wooden substrate and (ii) the reduction of potential dissipative capacity of connections, due to the fastener-wood pinching gap.

Hence, the design of junctions within a timber building plays a key role in the definition of its structural robustness and safety. Indeed, joints constitute one of the major reasons for damage arousing among timber structures subjected to winds and earthquakes, when poorly designed [10].

Since timber characteristics and fasteners production have a wide variability, the performances of steel plate connections can vary according to wood types (e.g., solid wood, glulam, CLT); connector types, size, slenderness, and number. Analytical equations were derived over the years, mainly based on the Johansen's theory [9], as widely discussed in [8]. EN 1995-1-1 [5] and the Italian guidelines DT 206-R1/2018 [2] provide some design rules commonly used for connections sizing in professional practice.

Failure of fastened connections occurs mainly for (i) connectors load capacity loss; (ii) the so-called block shear, i.e., the detachment of the timber portion surrounding the fasteners, (iii) row shear out failure, or (iv) splitting of wood. The study herein described aims at characterizing the steel-to-timber behavior in the (i) case.

Estimations base on the assumptions of rigid-plastic behaviors for both timber and steel fasteners, due to embedment capacity and yielding limit, respectively. Failure modes due to load capacity loss of fastening, according to EN 1995-1-1 [5], can be divided into three categories (I, II and III), based on the failure modes of the steel fastener, i.e., rigid rotation, and arise of one or two plastic hinges, respectively.

Crocetti et al. [3] carried out an extensive testing campaign on nailed steel-to-timber connections, varying some main parameters, i.e., steel plate thickness, nail length, pattern (number and layout), wood density and category, and moisture content. Many new insights were found out by this study. Among these, it was proven that EN 1995-1-1 [5] formulations generally tend to underestimate the fasteners shear strength; the thickness of steel plates (i.e., 2.5 or 5 mm) and the spacing do not affect significantly the shear capacity, while a single fastener bears significantly more load until failure than grouped ones. Nail length and wood moisture content can significantly affect mechanical performances. It was also reported that analytical formulations can significantly differ from experimental outcomes.

Jockwer and Jorissen [8] discussed the outcomes of several investigations performed on dowel-type fastened connections and found out that stiffness values have a large variability (i.e., coefficient of variation of about 45% and 30%, for stiffness K_s and elastic stiffness K_e, respectively). Moreover, it was found that EN 1995-1-1 [5] analytical estimations are not adequate to predict such values, due to large differences with experimental results and the neglection of some key factors (e.g., moisture content). Number of dowels per row and rows of fasteners have a nonlinear impact on the overall connection. At last, Jockwer and Jorissen [8] suggested to deepen the research about connections stiffness, in function of different types and connectors.

An experimental testing campaign was carried out to extend the knowledge about such elements. Tests aimed at characterizing the shear behavior of steel plates fastened to CLT components by nails and screws, and at detecting the shear load-carrying capacity of steel fasteners and their potential 'group effect'.

This paper discusses the performances of steel-to-CLT specimens, at changing of fasteners (i) type (i.e., 60 mm-length Anker nails and screws) and (ii) number (i.e., 2, 10, 18), to characterize the strength and stiffness of the compound element and to estimate the potential redistribution of loads at increasing number of fasteners (i.e., 'group effect'). Based on [3], the specimens were composed of 3 mm-thick S355 steel plates fastened to a 3-layer CLT element.

2 Materials and Method

2.1 Theory

The design and testing of specimens was based on the analytical equations given in [5] for steel plate connections. Noteworthy, a subdivision about the thickness of the plate in function of the fastener diameter *d* is suggested. If plate thickness is minor or equal to *0.5·d*, it is considered 'thin', if higher or equal to *d*, it is considered 'thick'. The design shear load carrying capacity for nails, bolts, dowels, screws, per fastener, are defined as function of thin or thick plate and the possible yielding mechanism as per Eqs. (1) and (2).

$$F_{v,Rd,thin} = min\left\{\begin{array}{ll} 0.4 f_{h,d} t_1 d & \text{(a)} \\ 1.15\sqrt{2M_{y,Rd} f_{h,d} d} + \frac{F_{ax,Rd}}{4} & \text{(b)} \end{array}\right\} \tag{1}$$

$$F_{v,Rd,thick} = min\left\{\begin{array}{ll} f_{h,d} t_1 d & \text{(c)} \\ 2.3\sqrt{M_{y,Rd} f_{h,d} d} + \frac{F_{ax,Rd}}{4} & \text{(d)} \\ f_{h,d} t_1 d\left[\sqrt{2 + \frac{4M_{y,Rd}}{f_{h,d} {t_1}^2 d}} - 1\right] + \frac{F_{ax,Rd}}{4} & \text{(e)} \end{array}\right\} \tag{2}$$

where t_1 is the smaller between timber member or fastener penetration depth, d is the fastener diameter, $F_{ax,Rd}$ is the axial withdrawal capacity, $M_{y,Rd}$ is the fastener yield bending moment, $f_{h,d}$ is the embedment strength in the timber member. According to [5], the latter one (in N/mm^2) can be calculated as per Eq. (3), in case holes are not predrilled (as common practice for diameters smaller than 8 mm):

$$f_{h,k} = 0.082\rho_k d^{-0.3} \tag{3}$$

with ρ_k being the characteristic density of wood, in kg/m^3, and d the fastener diameter, in mm. In case the plate relative thickness is between *0.5* and $1{\cdot}d$, the load-carrying value is the result of the interpolation between $F_{v,Rd,thick}$ and $F_{v,Rd,thin}$. Eqs. (1) and (2) include a contribute by Johansen's theory [9] in the first addend, and a contribute for the rope effect related to fastener withdrawal capacity in the second one. The latter has an upper bound equal to 25% of the first (Johansen contribute) in case of nails, and 100% in case of screws.

The group-effect of fasteners should also be considered, adopting the effective number of fasteners ratio n_{ef}, calculated as per Eq. (4):

$$n_{ef} = n^{k_{ef}} \tag{4}$$

where n_{ef} is the effective number of nails in the row parallel to the grain, n is the number of nails in the row, k_{ef} is equal to 1, if the spacing a_1 is bigger than $14{\cdot}d$, 0.85 if $a_1 = 10{\cdot}d$, 0.7 if $a_1 = 7{\cdot}d$.

2.2 Description of Specimens and Testing Procedure

Six types of specimens were built, by varying fastener (i) type and (ii) number. For each case, four samples were assembled, for a total of 24 elements. Within each type, one sample classified as '*_T' was used to pre-assess the parameters that rule the test according to EN 26891 [6]; the average experimental value was derived by the subsequent three tests. Table 1 reports the characteristics of the specimens; Fig. 1 shows their layout, according to spacing between fasteners and timber element edges, and fasteners themselves, given by [5]. The spacing of fasteners parallel to the load direction was equal to 40 mm.

A tensile displacement-controlled loading history, according to [6], was applied by a Galdabini SUN 60 electro-mechanic universal testing machine, varying load speed within 1−2 mm/min, so that tests could be ended between 15 and 20 min.

The setup (Fig. 2a) consisted of a retaining system made of two parallel 50 mm-thick steel plates, whose bottom one was fastened to the lower moving head of the testing machine. The wooden piece of the specimen was placed between the two plates and kept compressed by four bolted steel bars. The free upper part of the fastened plate was clamped within the top moving head of the testing machine, by which load was applied and recorded. The relative displacements between the

Table 1 Fastened steel-to-timber specimens details

Specimen	Fastener type	Fasteners number	Timber characteristics	Steel plate characteristics
19_B30_N	Nail (Ø4 × 60 mm)	2	100 mm-thick 3-layer C24 CLT (w × h, 120 × 300 mm) [7]	3 mm-thick S355 [4]
543_B30H30_N		10		
977_B30H30_N		18		
19_B30_S	Screws (Ø5 × 60 mm)	2		
543_B30H30_S		10		
977_B30H30_S		18		

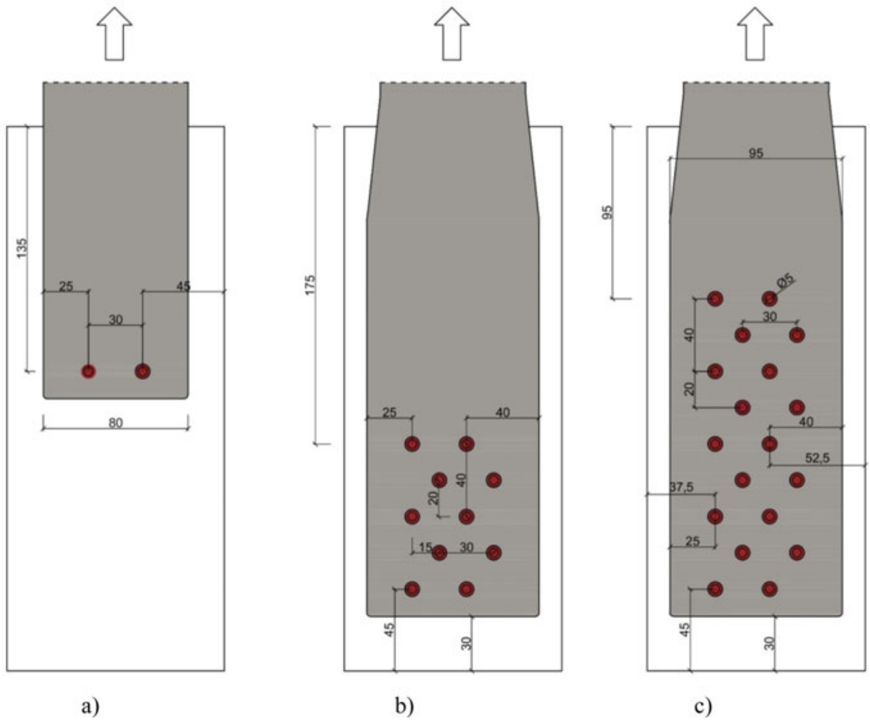

Fig. 1 Layout of fastened steel plate joints (measures in mm): **a** 19_B30; **b** 543_B30H30; **c** 977_B30H30

steel plate and the timber substrate were measured by HBM WA 50 Linear Variable Displacement Transducers (LVDT).

Results of tests were elaborated in terms of load-slip curves, and main parameters, i.e., load capacity (maximum load F_{max}) and slip modulus k_s, according to [6], as:

$$k_s = 0.4F_{est}/\upsilon_i \tag{5}$$

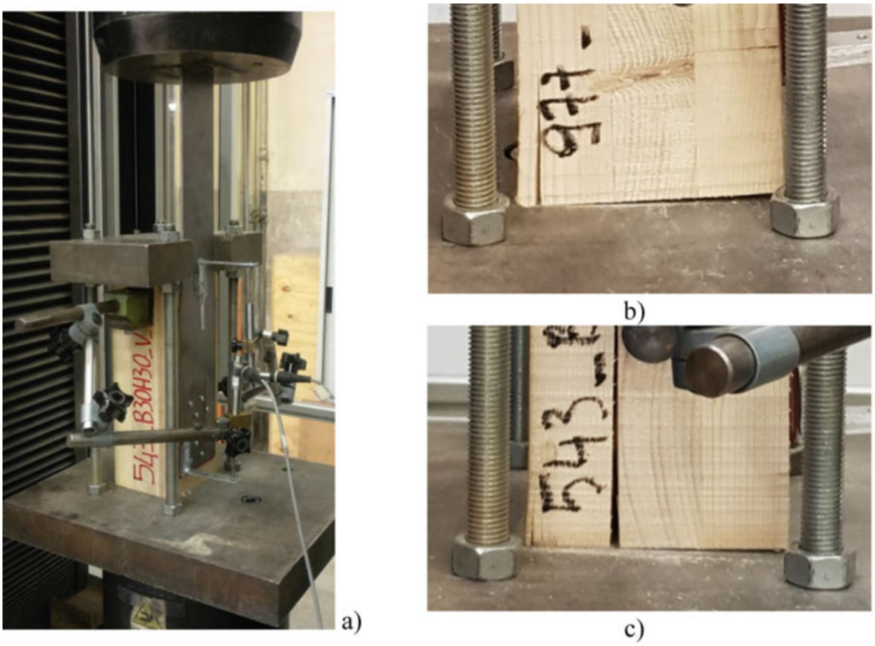

Fig. 2 **a** Testing setup of fastened joints; details of timber specimen **b** uplifting due to asymmetric loading, **c** debonding of CLT layers due to screws rope effect

where F_{est} is the estimated maximum load, υ_i the initial slip, i.e., the slip at achievement of 40% of F_{est} during the first load step.

3 Results

3.1 Characterization of Shear Strength and Stiffness

Figure 3 and Table 2 shows the load–displacement curves and the main parameters of the specimens, respectively. The behavior of 2-fasteners specimens (19_B30_N_*) showed the most variable results, whereas the 10-fasteners (543_B30H30_*) outcomes appeared to be the most consistent ones.

The outcomes are aligned to the findings of [3]. The shear load-carrying capacities of nails were close to the ones discussed in that paper (in the case of 60 mm-long nails), as well as the performances of single nails compared to grouped ones. Screws performances were globally higher, although the Coefficient of Variation (CoV) was substantially large (especially for 18-fasteners group, about 60%), as noticed also in [8]; moreover, no systematic decrease was found at increasing number of screws. The rope effect (due to axial strength of fasteners) was clear in the testing of screws,

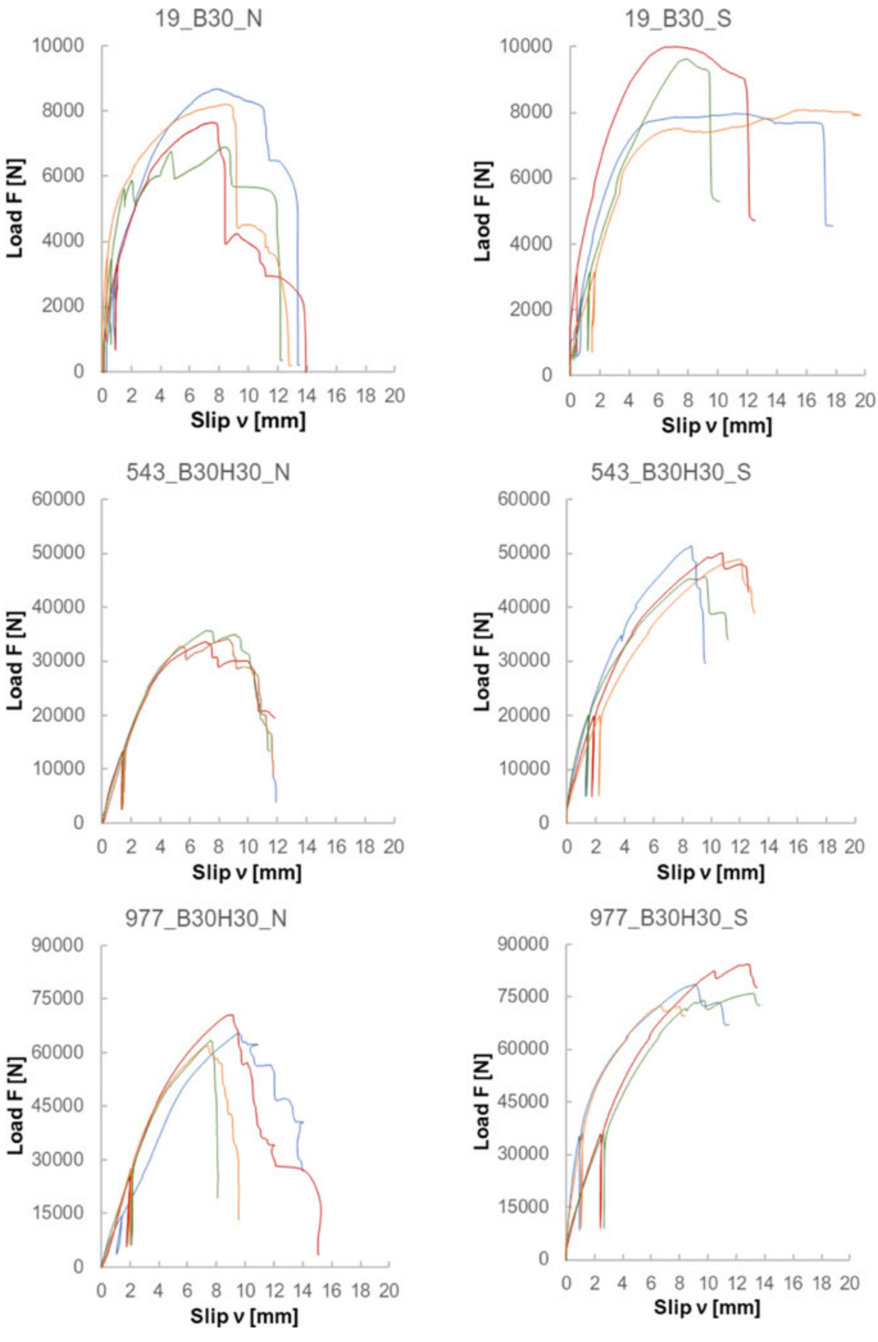

Fig. 3 Load-slip curves of nailed (N) and screwed (S) steel-timber specimens: T, in blue; 1, in red; 2, in green; 3, in orange. Load refers to global number of fasteners

Table 2 Global and normalized (per fastener) parameters values of fastened steel-timber connections. (Avg = Average; SD = Standard Deviation; CoV = Coefficient of Variation)

Specimen	Parameter	Nails			Full-threaded screws		
		Avg	SD	CoV (%)	Avg	SD	CoV (%)
19_B30 (2 fasteners)	F_{max} [N]	7585	769	10.1	9236	1039	11.2
	$v_{\boldsymbol{u}}$ [mm]	8.22	0.62	7.5	10.0	4.13	41.0
	$F_{0,4}$ [N]	3034	307	10.1	3694	415.78	11.2
	v_i [mm]	0.61	0.39	63.4	1.45	0.50	34.8
	k_i [N/mm]	6111	2926	47.9	3011	1452	48.2
	k_s [N/mm]	5497	2297	41.8	2447	974.91	39.8
	$F_{max,fastener}$ [N]	3792	384	10.1	4618	519	11.2
	$F_{0,4,\ fastener}$ [N]	1517	153	10.1	1847	207	11.2
	$k_{i,\ fastener}$ [N/mm]	3055	1463	47.9	1505	726	48.2
	$k_{s,\ fastener}$ [N/mm]	2748	1148	41.8	1223	487	39.8
543_B30H30 (10 fasteners)	F_{max} [N]	36,429	2907	7.9	48,237	2432	5.0
	$v_{\boldsymbol{u}}$ [mm]	7.88	1.07	13.6	10.79	1.46	13.5
	$F_{0,4}$ [N]	14,571	1162	7.9	19,294	973	5.0
	v_i [mm]	1.67	0.22	13.1	1.75	0.41	23.7
	k_i [N/mm]	8770	564	6.4	11,597	2690	23.2
	k_s [N/mm]	8446	265	3.2	9421	1992	21.1
	$F_{max,fastener}$ [N]	3642	290	7.9	4823	243	5.0
	$F_{0,4,\ fastener}$ [N]	1457	116	7.9	1929	97	5.0
	$k_{i,\ fastener}$ [N/mm]	877	56	6.4	1159	269	23.2
	$k_{s,\ fastener}$ [N/mm]	844	26	3.1	942	199	21.1
977_B30H30 (18 fasteners)	F_{max} [N]	65,261	3815	5.8	77,554	4990	6.4
	$v_{\boldsymbol{u}}$ [mm]	8.04	1.06	13.1	10.86	3.09	28.4
	$F_{0,4}$ [N]	26,104.5	1526.03	5.8	31,021	1996	6.4
	v_i [mm]	2.09	0.46	21.9	1.69	0.78	46.3
	k_i [N/mm]	12,552.1	1956.87	15.5	21,949	13,950	63.5
	k_s [N/mm]	13,074.2	2989.66	22.8	18,423	12,017	65.2
	$F_{max,fastener}$ [N]	3625.63	211.95	5.8	4308	277	6.4
	$F_{0,4,\ fastener}$ [N]	1450.25	84.78	5.8	1723	110	6.4
	$k_{i,\ fastener}$ [N/mm]	697.34	108.72	15.6	1219	775	63.5
	$k_{s,\ fastener}$ [N/mm]	726.34	166.09	22.9	1023	667	65.2

as an out-of-plane moment aroused due to asymmetric loading (Fig. 2b), which led to the delamination of the timber layers composing the CLT substrate in one case (Fig. 2c).

3.2 Discussion of Results

The analysis of results contributed to improve the knowledge about fasteners characteristics. Figure 4 shows the average of slip modulus and load values per each specimen. Figure 5 analyzes the outcomes distribution in function of moisture content, maximum load and slip modulus.

The decrease of slip modulus values, at number of fasteners increasing, among nails is clear (Fig. 4a), especially if compared to screws tendency. The load-carrying capacity is less affected by the group effect, since a trend can be defined for nails, whereas it cannot be found for screws.

The influence of samples MC versus the load capacity was also assessed. Three measures per sample were taken by Logica H&S LG 43 resistance pin-type moisture meter. Figure 5a shows the relation between maximum load and moisture content. A trend of data was not detected. However, it must be noted that MC ranges between 10 and 13.5%, which can be assumed as a good condition for structural performances (i.e., 12% is the reference for timber construction components in Italy).

The evaluation of the influence of the so-called ‘group-effect’ was carried out by plotting maximum loads F_{max} (Fig. 5b) and slip moduli k_s (Fig. 5c) per each fastener

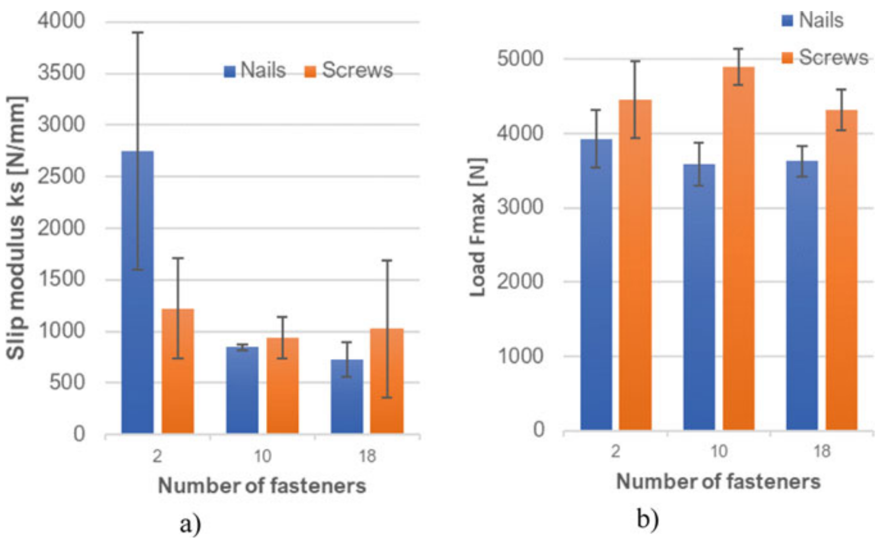

Fig. 4 Slip modulus (**a**) and maximum load (**b**) versus number of fasteners, with related standard deviation

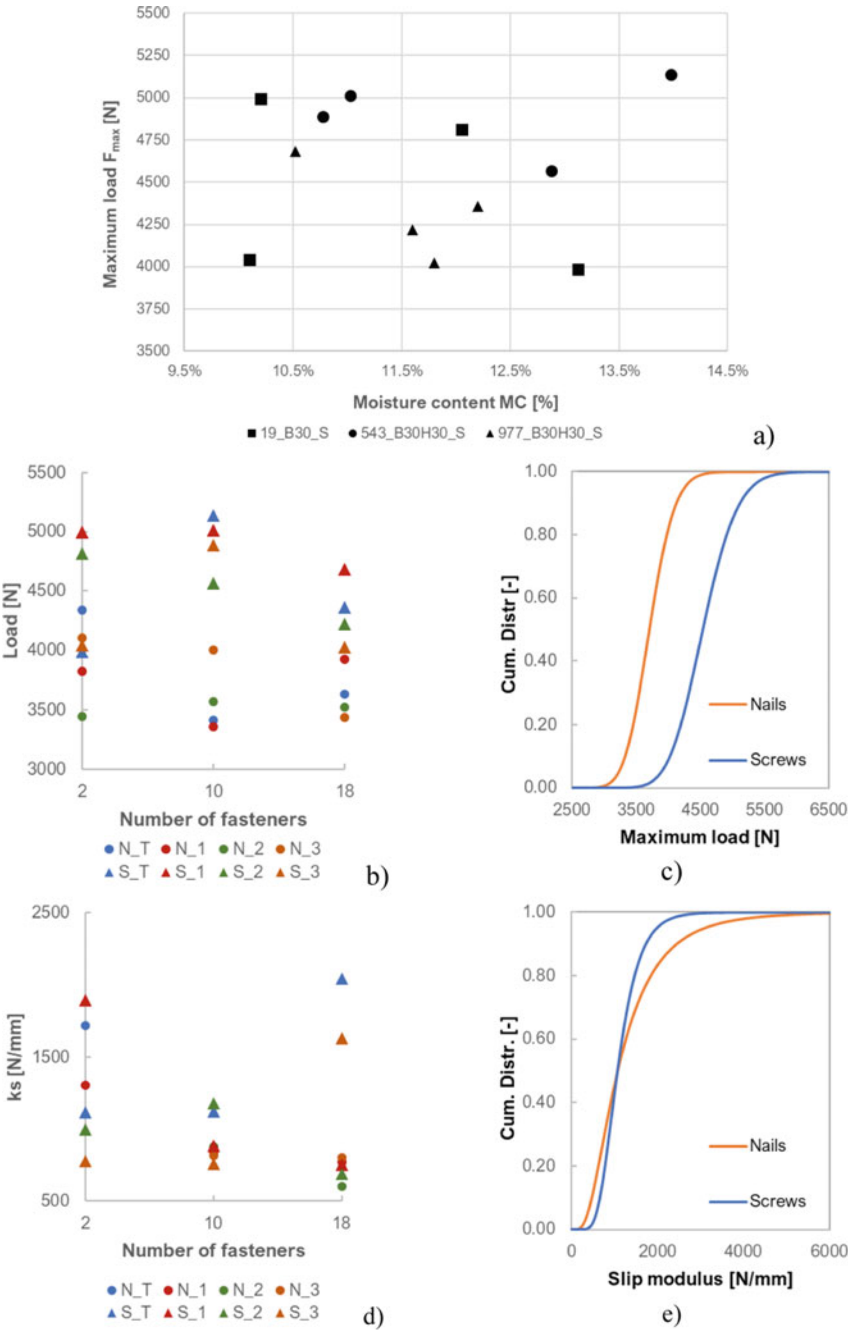

Fig. 5 **a** Maximum load values versus Moisture Content (MC) variation; influence of number of fasteners per joints on **b, d** maximum load-capability F_{max} (**b** and **c**, respectively) and on slip modulus k_s (**d** and **e**, respectively). The cumulative distribution of maximum load and slip modulus follows a lognormal distribution

versus the group number variation. No significant trends were found in the recorded load values. Nails showed a slight decrease in the average load value, whereas screws showed the highest value in the case of ten connectors. The influence of group effect was clearer on the slip modulus, the values distribution of which suggests a decrease in the number of fasteners growing. Once again, this is particularly true for nails, whereas screws had a more irregular trend (e.g., two of four values at 18 connectors diverged significantly from the others). The percentile values of maximum loads and stiffnesses were also calculated (Fig. 5c, e) based on the entire number of tested samples (i.e., 12 for nails and 12 for screws). Although the number of samples has a limited statistical meaning, it is still comparable to the ones by [3]. The 5%-quintiles resulted in 3225 and 3893 N for maximum load, 373 and 586 N/mm for slip modulus, for nails and screws, respectively. The corresponding analytical values, according to [5] avoiding any group effect, are equal to 2612 and 2460 N for maximum load, 1029 and 1772 N/mm, for slip modulus.

4 Conclusions

The experimental investigation on the shear load capability of steel-timber joints contributed to explore the validity of some analytical assumptions, as follows:

- The load-carrying capacity of screws was confirmed to be higher than nails one, thanks to the rope effect, which could be considered according to [5]. However, probably due to such consistent effect with a noticeable moment arising, the variability of both load and stiffness performances is high. In addition, the 60 mm-long fasteners are placed for one half among the external layers of CLT (grain parallel to load direction) and for the other half (a bit less due to steel plate 3 mm thickness, indeed) among the inner ones (grain perpendicular to load direction). These latter fibers can be subjected to local deficiency related to the presence of wood knots, which can induce failure or crack surfaces, especially in a small size wood element with no confinement, such the ones tested herein.
- Moisture content, although limited in a narrow variation (10–13.5%), showed no systematic influence on load capacity of fasteners.
- The number of fasteners showed to slightly affect the load capacity of the joints, in particular of nails, whereas the screws behavior was less predictable. Similar estimations were drawn for slip modulus. Single nail stiffness (i.e., slip modulus) is clearly higher than grouped ones (k_s equals to 2748, 845 and 726 N/mm for 1, 10, 18 fasteners, respectively); however large variability of results (i.e., CoV) interferes with the construction of a prediction law for screws. This was also found by [8], who found that significant CoV percentages were related to experimental tests on dowel-type connections, i.e., 45.8 and 30.9%, comparable to those found in this study.

These results contributed to extend the database of fasteners characterization, since the wide variability of timber properties (wooden species, CLT layers, MC) and steel plates (thickness, layout of holes) obstructs the possibility of a univocal characterization. As discussed by [3], analytical estimations by [5] showed to underestimate experimental resistance of such connections, whereas slip modulus does not take into account factors that should be instead, as observed by [8].

Acknowledgements This study was supported by the CORE-WOOD (Competitive Repositioning of WOOD sector) Italian project, in the framework of POR-FESR 2014-2020 Line 1 Action 1.1.4 of the Veneto Region, and by the BIRD163979 'Optimization of dissipative connections for structures in seismic prone areas' research study funded by the University of Padova.

References

1. Casagrande, D., Rossi, S., Sartori, T., Tomasi, R.: Proposal of an analytical procedure and a simplified numerical model for elastic response of single-storey timber shear-walls. Constr. Build. Mater. **102**, 1101–1112 (2016). https://doi.org/10.1016/j.conbuildmat.2014.12.114
2. CNR—Consiglio Nazionale delle Ricerche: Istruzioni per la Progettazione, l'Esecuzione ed il Controllo di Strutture di legno. (2018)
3. Crocetti, R., Gustafsson, P.J., Girhammar, U.A., Costa, L., Asimakidis, A.: Nailed steel plate connections: strength and ductile failure modes. Structures. (2016). https://doi.org/10.1016/j.istruc.2016.07.003
4. EN 10025–2:2004: Hot rolled products of structural steels. (2004)
5. EN 1995:2014+A2:2014: Eurocode 5 - Design of timber structures. Comité Européen de Normalisation (2014)
6. EN 26891:1991: Timber structures—Joints made with mechanical fasteners—General principles for the determination of strength and deformation characteristics. (1991)
7. EN 338:2016: Structural timber—Strength classes. (2016)
8. Jockwer, R., Jorissen, A.: Stiffness and deformation of connections with dowel-type fasteners. In: Sandhaas, C., Munch-Andersen, J., Dietsch, P. (eds.) Design of connections in timber structures. A state-of-the-art report by COST Action FP1402 / WG3. pp. 95–126 (2018)
9. Johansen, K.W.: Theory of timber connections. In: International association of bridge and structural engineering,vol. 9. pp. 249–262. Bern (1949)
10. Smith, I., Foliente, G.: Load and resistance factor design of timber joints: international practice and future direction. J. Struct. Eng. **128**, 48–59 (2002)

Test Procedures for the Characterization of Earth Plastering Mortars: Necessary Adaptations

Tânia Santos and Paulina Faria

Abstract Earth mortars present advantages, especially when applied to plasters. To evaluate the behavior of earth plastering mortars, some adaptations can be made to the test procedures defined for current mortars—capillary absorption and drying—or earth blocks—water erosion by dripping action. However, specific tests for earth mortars—linear shrinkage and cracking, dry abrasion resistance, adsorption and desorption by hygroscopicity—can also be applied to evaluate the behavior of current mortars. It is considered important to assess the surface cohesion of earth plasters, as to current mortar plasters. In this way, it is possible to complement the characterization and, thus, be able to make a more efficient comparison between current and earth plastering mortars, depending on the intended applications. The type of specimens—with or without the influence of the substrate—as well as their dimensions, may also influence the correct analysis of the characteristics of the mortar samples produced in the laboratory, exposed in situ or extracted from case studies.

Keywords Characterization · Clayish earth · Mortar · Test procedure

1 Introduction

Earth is one of the oldest building materials, and despite having fall into disuse with the emergence of current binders, as lime and cement, its interest is reappearing on the scientific community due to several advantages. In fact, earth is a natural composite, composed by different types and fractions of clay, silt, sand and coarser particles, such as gravel. It is non-toxic, has high hygroscopicity, conferred by clay, is a reusable material (if it is not chemically stabilized) and is easily recycled [1]. For use in earth plastering mortars, it only needs to be disaggregated and sieved to

T. Santos · P. Faria (✉)
CERIS, NOVA School of Science and Technology, NOVA University Lisbon, Caparica, Portugal
e-mail: paulina.faria@fct.unl.pt

T. Santos
e-mail: tr.santos@campus.fct.unl.pt

C. Chastre et al. (eds.), *Testing and Experimentation in Civil Engineering*, RILEM Bookseries 41, https://doi.org/10.1007/978-3-031-29191-3_14

remove the coarser sand and gravel. The earth from the excavation site (to build the foundations and underground floors of buildings or other underground works) can be used. Therefore, the earth needs less energy for its preparation compared to current binders that need heat treatments and frequently milling [2].

When the earth is too clayey, additional aggregate or plant fibers can be added. When the earth has very low clay content, low content of other binder (gypsum, air lime) can be added. In that case the earth mortar is called stabilized. The addition of binder may also be used to provide resistance to the action of water, so that the mortar can be used for rendering [3] or plastering areas with water. To improve earth renders resistance to water, a surface protection can also be applied [2].

Earth plasters have advantages for comfort and indoor air quality, conferred by the hygroscopic capacity of the clay, and the properties of earth mortars are greatly influenced by the type of clay used [4, 5].

To the authors' knowledge there is only one standard specifically defining requirements, classification and testing procedures for earth plastering mortars: the German standard DIN 18947 [6], which is specific for earth plasters without addition of common binders. This standard refers to several parts of the EN 1015 standards for different test procedures, although these standards refer to mortars with lime and cement, which have some different characteristics from earth mortars. For this reason, it is considered that it is necessary to make some adaptations to the test procedures to characterize the earth plastering mortars in a more correct way.

On the other hand, the DIN 18947 [6] standard defines some specific test procedures for earth plastering mortars, which may be beneficial to apply for the characterization of other plastering mortars. Furthermore, to better compare the characteristics of earth-based and other mortars, it would be beneficial to standardize test procedures.

Finally, the type of specimen used in the characterization tests of plastering mortars may not be the most representative of real plasters and that may bring some variability to the characteristics obtained in the laboratory and in situ.

In the present study, it is intended to make a compilation of the test procedures applied to lime and cement plastering mortars which are adapted to earth mortars, as well as the test procedures for the characterization of earth plasters that can also be applied to other plastering mortars. Furthermore, an evaluation of the variability of the use of different specimens in the characteristics of the plastering mortars is made, analyzed together with some results obtained by different authors for different types of mortars and/or specimens.

2 Adaptation of Tests to Characterize Earth Mortars

2.1 Specimens and Samples

Most of the mortar characterization tests are carried out with specimens produced in impermeable metallic molds with 40 mm × 40 mm × 160 mm, which are not representative of in situ plasters or bedding masonry mortars. The exception are specimens for capillary absorption under low pressure (by Karsten tubes) and adhesion tests, which are produced in contact with a substrate.

The authors and other researchers [7, 8] consider that, to evaluate a mortar with a microstructure similar to the one it will present in situ, the tests should be carried out on specimens molded in contact with a porous substrate and with a thickness of 2 cm (or similar).

That can be performed applying a mesh (namely a glass fiber one) on top of a porous substrate, such as a hollow brick, and plastering the brick surface. After hardening, the mesh facilitates the separation of the mortar specimen from the brick [7, 8]. The mortar specimen, after having hardened in contact with the substrate, will have a microstructure closer to a real case. Therefore, it can be cut in samples with sizes adequate for testing. All the samples will have the thickness of the plaster (≈ 20 mm); for flexural strength, samples will be cut to have an area of 40 mm × 160 mm; the half samples could be used for compression, with 40 mm × 40 mm area although with low thickness. Samples of rendering mortar could also be cut for capillarity and drying (test procedure to be addressed ahead, like the one used for samples extracted from case studies), and for water vapor permeability tests.

2.2 Capillary Absorption and Drying

Given the susceptibility of unstabilized earth mortars when in contact with liquid water, this type of mortar should not be applied in damp areas or outdoors without stabilization or surface protection. For this reason, the capillary absorption of earth mortars is not a requirement and, therefore, the DIN standard [6] does not defines the test procedures for this property. However, in some cases this property should be considered. For example (situation 1), when the plaster is intended to be applied on a wall which presents a problem of capillary rise of water from the soil, the mortar needs to resist this action. On the other hand (situation 2), when comparing the influence of stabilizers on earth mortars, the analysis of the capillary absorption and drying capacity of the mortar is also important.

The EN 15801 [9] and EN 1015–18 [10] define the requirements and the test procedure for determining the capillarity absorption of mortars applied in the conservation of cultural heritage, and produced with lime and cement as binders, respectively.

Different authors have evaluated the capillary absorption and drying capacity of earth mortars based on the mentioned standards, considering some adaptations due to the specific characteristics of earth mortars [5, 11, 12]. It was concluded that the necessary adaptations are [5]: the samples to be tested must be taken from specimens made in contact with the substrate or, at the limit, cubic samples with 40 mm to reduce the time in contact with water until saturation; the exposed surface of the plaster must be placed in contact with water when situation 2 is simulated; the surface once in contact with the substrate most be placed in contact with the water when situation 1 is simulated; the sides of the sample must be waterproofed with a product applied by a painting; a very fine mesh of polyethylene, without water absorption but which allows the absorption of water by the mortar, should be placed at the base of each sample to minimize the loss of fine particles from the mortar; this mesh can be laterally stuck with an elastic band; as earth mortars without stabilization in contact with water become plastic in a short time, samples should be placed and handled in a basket specially designed, to minimize the amount of water retained in the basket during the consecutive weighing process and keep it as constant as possible [5].

Due to the rapid capillary water absorption of earth mortars, the time between initial weighings must also be adapted [5]: during the first 5 min of testing the samples must be weighed at 1 min intervals; then every 5 min, extending the period between weighings thereafter, depending on the type of samples tested. In the saturation phase, there must be 2 weighings 24 h apart to complete the capillary absorption test. After the last weighing of the capillary absorption test, the samples must be removed from the water, as well as the elastic and mesh, and the first weighing of the drying test must be carried out, following the EN 16322 [13] standard.

For drying, the position of the sample must be inverted, considering that the drying area corresponds to the one previously in contact with water, while the opposite one must be in contact with an impermeable surface, such as a Petri dish.

Different researchers analyzed the capillary absorption and drying with a similar test procedure [5, 11, 14]. Lima et al. [5] analyzed the capillary absorption and drying of earth mortars with different clay mineralogy (illitic, kaolinitic and montmorillonitic clays) and concluded that: montmorillonitic earth mortar presents significantly higher capillary water absorption coefficient (AC) and higher total absorbed water (asymptotic value) comparing with illitic and kaolinitic earth mortars. When drying, the illitic and montmorillonitic mortars present similar behavior, while the kaolinitic mortars present a slightly lower drying rate during the first phase.

On the other hand, Gomes et al. [14] analyzed the capillary absorption and drying of earth-based mortars with local and commercial earth, with 0, 5, 10 and 15% of air lime, hydraulic lime, Portland cement and natural cement and with 0 or 5% of hemp fibers. These researchers concluded that: mortars with local earth have the lowest AC; the greater the percentage of binder added, the greater the AC of the mortars and the amount of water absorbed, which is an undesirable effect; mortars with the addition of Portland cement are those that present the greatest amount of absorbed water; the addition of fibers increases the amount of water absorbed. The fibers and binders' addition retard drying.

2.3 Water Erosion by Dripping Action

Water erosion can be an important characteristic when dripping situations on the plaster, such as splashes during cleaning and access of water by an open window when it rains, are foreseeable. To assess water erosion by dripping action, the Geelong method is used, defined by the New Zealand standard NZS 4298/A1 [15], developed to characterize specimens of rammed earth, adobe or compressed earth blocks. Since the plasters are thinner than those construction products, it is necessary to make some adaptations to the test procedure [5]: the amount of dripping water must be reduced proportionally to the thickness of the specimen (from 100 to 12 ml); the drip time should be reduced to a range of 2.4–3.0 min, corresponding to a water flow range of 4–5 ml/min (similar to the maximum flow allowed by the standard); the specimen slop should be increased to 2/1 (≈ 63º) to emphasize the material lost by the sample due to the "run-off" effect of water erosion; the lost material can be collected and dried for quantification. Figure 1 shows a scheme of the apparatus for the determination of water erosion by dripping water in mortars.

The test result can be expressed by the mass loss, the water absorbed by the specimen during the test, the area of the impact zone caused by the "splash" effect of dripping water, and by the maximum depth of the impact zone [5].

By the analysis of earth mortars with different clay mineralogy, Lima et al. [5] concluded that: the kaolinitic mortar lost almost twice the mass lost by the illitic and montmorillonitic mortars; the kaolinitic and montmorillonitic mortars present similar water absorption and a little superior to that obtained by the illitic mortar;

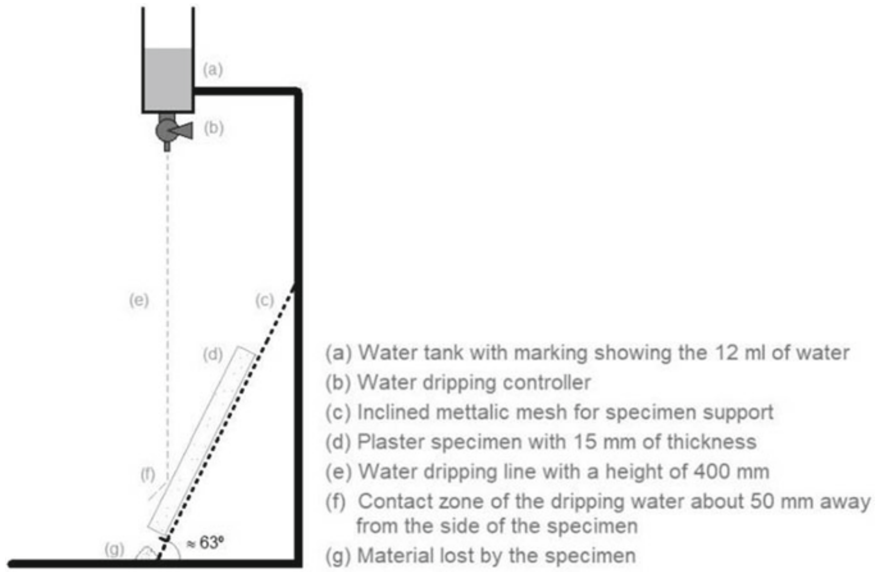

Fig. 1 Water erosion by dripping test apparatus, adapted from NZS 4298/A1 [15] and Lima et al. [5]

finally, as for the area and depth of erosion, the montmorillonitic mortar presents the highest results and the illitic mortar presents better behavior.

In another study, Pinto et al. [16] analyzed the water erosion by dripping action of an earth-based render of *tabique* walls (partition walls produced with a lightweight timber structure, filled and plastered with earth mortars) with the same test procedure but with some differences: the distance between the galling drop and the contact zone of the dripping water is 1.0 m; the inclination of the specimen to the horizontal is 45º; the test result is expressed by the test duration and the number of drops. These researchers obtained better behavior on earth mortars with air lime addition (≈ 24 h and ≈ 173,000 drops) compared with unstabilized earth mortars (≈ 40 min and ≈ 5000 drops). Stazi et al. [17] also analyzed the water erosion of earth-based mortars with some differences: dripping of 100 ml of water on the specimen for 20−60 min and 50º inclination of the specimen.

The need to standardize this test procedure is evident, since at least three different studies performed the test under different conditions, some of them measuring different characteristics, which compromises the comparison of results between mortars from different studies.

3 Characterization Tests of Earth Plasters that Can be Carried Out on Other Mortars

The DIN 18947 [6] defines simple tests to characterize earth plasters that may be of interest to perform on common binder renders and plasters: linear shrinkage in the mold, dry abrasion resistance and hygroscopicity. In addition to these tests defined by the standard, it is considered that it is an asset to assess the surface cohesion of earth plasters, evaluating in some way their surface resistance.

3.1 Linear Shrinkage

Linear shrinkage in the mold is determined by the difference in length of the fresh and dry specimen in prismatic mold of 40 mm × 40 mm × 160 mm [6]; in the case of plasters, it can also be evaluated using the planar specimens of 500 mm × 200 mm × 15 mm presented ahead to evaluate the hygroscopicity of the mortars. In this way, the free linear shrinkage is determined. Nevertheless, in none of the cases, there is the effect of the substrate, so it may be more efficient to assess the susceptibility to shrinkage through the observation of plaster specimens applied on a substrate, such as a brick, block, slab, or experimental wallette, with the largest possible area to be representative. In this case, the restrained shrinkage is determined, observing the eventual occurrence of cracking by shrinkage of the mortar adhered to the support.

Lima et al. [5] analyzed the linear shrinkage in prismatic and planar specimens, with 40 mm × 40 mm × 160 mm and 500 mm × 200 mm × 15 mm, respectively, and concluded that: the different specimens presented similar linear shrinkage tendency; kaolinitic and montmorillonitic mortars presented lower (0.22–0.38%) and higher (3.03–3.30%) linear shrinkage, respectively, and illitic mortar presented intermediate behavior (0.85–0.89%). These researchers also analyzed the influence of the substrate in the shrinkage of mortars through the specimen of 20 mm of plaster layer applied over hollow bricks and concluded that the tested montmorillonitic, illitic and kaolinitic earth plasters presented significant, rare and absent cracking, respectively. It is considered that the evaluation of shrinkage in plaster specimens applied on a substrate is more representative of the reality compared to prismatic specimens of 40 mm × 40 mm × 160 mm molded in impermeable metallic molds, with different microstructure. Emiroğlu et al. [18], Santos et al. [19], Stazi et al. [17] and Pinto et al. [16] also evaluated the influence of the substrate on the cracking behavior of plasters.

On the other hand, Santos et al. [1] analyzed the linear shrinkage of three earth-based mortars compared with gypsum and cement-based mortars in prismatic specimens of 40 mm × 40 mm × 160 mm. Most mortars were pre-mixed and their complete composition was unknown. The earth mortar with air lime presented higher linear shrinkage (1.4%) and the earth mortar with different particle size sand and fibers, and the gypsum and cement mortars presented similar behavior (0.1–0.2%).

3.2 *Dry Abrasion Resistance*

The dry abrasion resistance is determined through the loss of material from the surface of a plaster specimen by 20 rotations applied for 15–25 s of a rotating circular brush of defined hardness with 65 mm of diameter, applied with a constant vertical contact force of 20 N [5, 6]. The test results can be expressed by the mass loss of the specimen and the groove produced in the surface. The hardness of circular brush influences the results obtained for the same mortar, as demonstrated by Faria et al. [20] who evaluated the influence of three brushes with different hardness.

Lima et al. [5] analyzed the dry abrasion of earth mortars with different clay mineralogy and concluded that illitic mortar presented the best resistance to dry abrasion (with a mass loss of 1.1 g), montmorillonitic mortar presented intermediate resistance (5.8 g) and kaolinitc mortar presented the worst behavior (8.8 g).

Comparing earth-based with gypsum and cement-based pre-mixed mortars, Santos et al. [1] concluded that earth mortars with a different particle size of sand and with fibers presented higher mass loss by dry abrasion (0.63–0.87 g), earth mortar with air lime additions and cement had an intermediate mass loss (0.20 g) and gypsum mortar had the best behavior with 0.0 g of mass loss.

3.3 Adsorption and Desorption

Hygroscopicity is a property that can be very important for plasters. According to DIN 18947 [6], the adsorption by hygroscopicity is determined through the mass variation that occurs by exposing planar plaster specimens in metallic molds, to ensure that vapor adsorption occurs only on the upper exposed surface. This set (specimen and mold) is stabilized in a climatic chamber with a temperature of 23 ºC and relative humidity (RH) of 50%. Afterwards, the chamber conditions are changed, and the specimens are exposed to 80% of RH and 23 ºC temperature for 12 h, with weighings at defined time intervals of 0.5, 1, 3, 6 and 12 h.

Some adaptations to the test procedure may be implemented to improve the results obtained [5]: suppression of the weighing at 0.5 h to minimize the interference of the stabilization time of the climatic chamber in the weighing process; the test should also be extended from 12 to 24 h for a better understanding of the adsorption behavior of the plasters under analysis. It is considered important that this test must be complemented with the water vapor desorption test, carried out by the inverse procedure [5]: after the adsorption test, the specimens are weighed and the climatic chamber conditions are changed to 50% of RH, maintaining the temperature; specimens are weighed at the same defined time intervals.

Lima et al. [5] analyzed the adsorption and desorption for 24 h of earth mortars with different clay type and with planar specimens of 500 mm × 200 mm × 15 mm in metallic molds and concluded that: montmorillonitic mortar presented very high adsorption and desorption capacity (110 g/m^2 after 12 h), kaolinitic mortar presented the lowest capacity ≈ 30 g/m^2(after 12 h) and illitic mortar presented the intermediate capacity (≈ 60 g/m^2 after 12 h).

Santos et al. [1], when analyzing the adsorption and desorption of earth-based mortars compared with gypsum and cement-based pre-mixed mortars, also with planar specimens of 500 mm × 200 mm × 15 mm, concluded that: the earth mortar with fibers presented higher adsorption capacity (≈ 80 g/m^2 after 12 h), followed by the earth mortar with different particle size (≈ 60 g/m^2 after 12 h); the cement-based mortar presented intermediate capacity (≈ 40 g/m^2 after 12 h); finally, the earth mortar with air lime and the gypsum mortar presented the worst behavior (≈ 20 g/m^2 after 12 h).

Faria et al. [20] analyzed the influence of the size of the specimens in the adsorption and desorption test, testing the same mortar with planar specimens of 500 mm × 200 mm × 15 mm in metallic molds and circular specimens with 90 mm in diameter and 15 and 20 mm of thickness, waterproofed in all faces except the upper one so that the adsorption and desorption of water vapor only take place on that surface. These researchers concluded that circular specimens, with a lower area exposed to adsorption, adsorbed less water vapor per surface compared to planar specimens, with a higher exposed area, most probably due to border effect. However, they shown the same tendency over the test period of time, as far as the results obtained with planar and circular specimens are comparable.

3.4 Surface Cohesion

A high or weak bonding between the particles of the mortars confer a good or bad cohesion to the mortar, respectively. The evaluation of the surface cohesion of a mortar makes it possible to assess whether or not to apply a surface treatment as a consolidant to the plaster [21].

Earth plasters generally present adequate cohesion [22], although it should be tested. Drdácky et al. [23] defined a test procedure for surface cohesion determination and some adaptations were considered necessary by Faria et al. [20] and Santos et al. [1]: the surface cohesion was determined by the variation of mass of an adhesive tape with the dimension of 50 × 70 mm, pressed for 1 min with a constant intensity of 4 kg weight applied on top of a resilient material placed on the surface of specimens. After peeling the adhesive tape, the surface lack of cohesion was defined by the increase of mass of the adhesive tape [1].

Santos et al. [1] analyzed the surface cohesion of earth, gypsum and cement-based plasters and concluded that, as expected, the unstabilized earth plasters presented the lower surface cohesion (the higher mass loss by lack of surface cohesion, 0.07 g) and the gypsum plaster presented the higher surface cohesion (with 0.00 g of mass loss by lack of surface cohesion). The earth plaster with air lime addition also analyzed by Santos et al. [1] presented mass loss by lack of surface cohesion of 0.03 g. These results can be justified by the higher bonding strength between the particles of earth with air lime plaster and gypsum plaster in comparison with the earth plaster.

4 Conclusions

The present study intends to contribute to a better understanding of the possibilities for the characterization of plastering and rendering mortars. The necessary adaptations to the defined test procedures for the characterization of mortars of current binders or earth blocks are compiled for the characterization of earth mortars. In parallel, the test procedures for the characterization of earth mortars that can be used to characterize mortars with current binders were also discussed, so it is possible to complement the characterization of different mortars.

The standardization of test procedures for the characterization of earth-based plasters allows for a more efficient comparison between these plasters.

The adsorption and desorption capacity as well as dry abrasion resistance are characteristics that are only standardized for earth plasters. However, it is considered that they should be determined, through the same test procedure, for plasters of common binders. Therefore, it is possible to evaluate the efficiency of different types of plasters, as well as the comparison of their characteristics, which allows the choice of the best solution according to the intended application.

Finally, the specimens used for the characterization of plastering and rendering mortars should be revised to be more representative of the real in situ microstructure of those mortars.

Acknowledgements The authors acknowledge the Portuguese Foundation for Science and Technology (FCT) for the support given to CERIS, through the strategic project UIDB/04625/2020. Tânia Santos also thanks FCT for their PhD fellowship SFRH/BD/147428/2019.

References

1. Santos, T., Gomes, M.I., Santos Silva, A., Ferraz, E., Faria, P.: Comparison of mineralogical, mechanical and hygroscopic characteristic of earthen, gypsum and cement-based plasters. Constr. Build. Mater. **254**, 119222 (2020). https://doi.org/10.1016/j.conbuildmat.2020.119222
2. Faria, P., Lima, J.: Earth plasters. Earth construction notebooks 3 (in Portuguese). Argumentum, Lisbon, Portugal (2018). ISBN: 978–989–8885–04–3.
3. EN 998–1: Specification for mortar for masonry—Part 1: Rendering and plastering mortar. CEN, Brussels (2016)
4. Schroeder, H.: Sustainable building with earth. Springer International Publishing, Cham, Switzerland (2016). https://doi.org/10.1007/978-3-319-19491-2
5. Lima, J., Faria, P., Santos Silva, A.: Earth plasters: the influence of clay mineralogy in the plasters' properties. Int. J. Archit. Herit. **14**, 948–963 (2020). https://doi.org/10.1080/15583058.2020.1727064
6. DIN 18947: Earth plasters—Terms and definitions, requirements, test methods (in German). DIN, Berlin (2018)
7. Travincas, R., Bellei, P., Torres, I., Flores-Colen, I., Matias, G., Silveira, D.: The use of fibreglass mesh in the experimental characterisation of applied coating mortars. Coatings **12**, 1091 (2022). https://doi.org/10.3390/coatings12081091
8. Bellei, P., Arromba, J., Flores-Colen, I., Veiga, R., Torres, I.: Influence of brick and concrete substrates on the performance of renders using in-situ testing techniques. J. Build. Eng. **43**, 102871 (2021). https://doi.org/10.1016/j.jobe.2021.102871
9. EN 15801: Conservation of cultural property. Test methods. Determination of water absorption by capillarity. CEN, Brussels (2009)
10. EN 1015–18: Methods of test for mortar for masonry—Part 18: Determination of water absorption coefficient due to capillary action of hardened mortar. CEN, Brussels (2002)
11. Santos, T., Nunes, L., Faria, P.: Production of eco-efficient earth-based plasters: Influence of composition on physical performance and bio-susceptibility. J. Clean. Prod. **167**, 55–67 (2017). https://doi.org/10.1016/j.jclepro.2017.08.131
12. Gomes, M.I., Gonçalves, T.D., Faria, P.: Hydric behavior of earth materials and the effects of their stabilization with cement or lime: study on repair mortars for historical rammed earth structures. J. Mater. Civ. Eng. **28**, 04016041 (2016). https://doi.org/10.1061/(ASCE)MT.1943-5533.0001536
13. EN 16322: Conservation of cultural heritage. Test method. Determination of drying properties. CEN, Brussels (2013)
14. Gomes, M.I., Faria, P., Gonçalves, T.D.: Earth-based mortars for repair and protection of rammed earth walls. Stabilization with mineral binders and fibers. J. Clean. Prod. **172**, 2401–2414 (2018). https://doi.org/10.1016/j.jclepro.2017.11.170
15. NZS 4298/A1: Materials and workmanship for earth buildings. NZS: Wellington (1998/2000)
16. Pinto, J., Cunha, S., Soares, N., Soares, E., Cunha, V.M.C.F., Ferreira, D., Sá, A.B.: Earth-based render of tabique walls – An experimental work contribution. Int. J. Archit. Herit. **11**, 185–197 (2017). https://doi.org/10.1080/15583058.2015.1020459

17. Stazi, F., Nacci, A., Tittarelli, F., Pasqualini, E., Munafò, P.: An experimental study on earth plasters for earthen building protection: The effects of different admixtures and surface treatments. J. Cult. Herit. **17**, 27–41 (2016). https://doi.org/10.1016/j.culher.2015.07.009
18. Emiroğlu, M., Yalama, A., Erdoğdu, Y.: Performance of ready-mixed clay plasters produced with different clay/sand ratios. Appl. Clay Sci. **115**, 221–229 (2015). https://doi.org/10.1016/j.clay.2015.08.005
19. Santos, T., Faria, P., Santos Silva, A.: Eco-efficient earth plasters: The effect of sand grading and additions on fresh and mechanical properties. J. Build. Eng. **33**, 101591 (2021). https://doi.org/10.1016/j.jobe.2020.101591
20. Faria, P., Santos, T., Aubert, J.E.: Experimental characterization of an earth eco-efficient plastering mortar. J. Mater. Civ. Eng. **28**, 04015085 (2016). https://doi.org/10.1061/(ASCE)MT.1943-5533.0001363
21. Röhlen, U., Ziegert, C.: Earth Building Practice—Planning, Design, Building, 1st edn. Bauwerk, Beuth Verlag GmbH, Berlin, German (2011). ISBN: 978-3-410-21737-4
22. Vissac, A., Bourgès, A., Gandreau, D., Anger, R., Fontaine, L.: Clays & Biopolymers. Natural stabilizers for earthen construction (in french), CRAterre, Villefontaine, France (2017). ISBN: 978–2–906901–88–9
23. Drdácký, M., Lesák, J., Niedoba, K., Valach, J.: Peeling tests for assessing the cohesion and consolidation characteristics of mortar and render surfaces. Mater. Struct. **48**, 1947–1963 (2015). https://doi.org/10.1617/s11527-014-0285-8

Large Static Testing Equipment: Design and Testing of a Settlement Facility

Nathanaël Savalle, Marco Francesco Funari, Luciano Fernandes, Carla Colombo, Simon Szabó, Sajad Hussaini, Shaghayegh Karimzadeh, and Paulo B. Lourenço

Abstract Masonry structures are highly vulnerable to climate change effects. In particular, over the last few decades, the effects of global warming have caused wetter winters and drier summers. Such phenomenon has produced variations in soil saturation that, in the long term, may trigger consolidation-induced differential settlements. Therefore, the experimental replication of settlement actions is essential for developing appropriate numerical tools and understanding their consequences on masonry structures. This paper describes the installation of a $1.5 \times 1\text{m}^2$ settlement table at the University of Minho. Practical issues and first tests on masonry shear walls are also discussed.

N. Savalle (✉)
Université Clermont Auvergne, Clermont Auvergne INP, CNRS, Institut Pascal, 63000 Clermont-Ferrand, France
e-mail: nathanael.savalle@uca.fr

N. Savalle · M. F. Funari · L. Fernandes · C. Colombo · S. Szabó · S. Hussaini · S. Karimzadeh · P. B. Lourenço
University of Minho, ISISE, ARISE, Department of Civil Engineering, Guimarães, Portugal
e-mail: m.funari@surrey.ac.uk

L. Fernandes
e-mail: luciano@civil.uminho.pt

C. Colombo
e-mail: carla.colombo95@gmail.com

S. Szabó
e-mail: simon.szabo117@gmail.com

S. Hussaini
e-mail: hussaini@civil.uminho.pt

S. Karimzadeh
e-mail: shaghkn@civil.uminho.pt

P. B. Lourenço
e-mail: pbl@civil.uminho.pt

M. F. Funari
Department of Civil and Environmental Engineering, University of Surrey, Guilford GU2 7XH, UK

C. Chastre et al. (eds.), *Testing and Experimentation in Civil Engineering*,
RILEM Bookseries 41, https://doi.org/10.1007/978-3-031-29191-3_15

Keywords Static tests · Settlement tests · Masonry · Dry-joint · Large-scale testing

1 Introduction

Masonry is one of the oldest construction materials and currently constitutes a significant part of our built heritage. As Historical Masonry Structures (HMS) hold both economic and cultural values, their structural integrity must be preserved. In particular, they significantly contribute to the touristic attractiveness of many historical centres, especially in Europe, being critical assets of many countries and cities. However, as extensively reported in the literature, HMS are prone to be damaged when subjected to soil settlements [1–5].

From the experimental standpoint, tilting tests are commonly adopted to simulate mass proportional horizontal actions and identify the associated collapse mechanisms [6–13]. On the other hand, the response of HMS subjected to differential soil settlement must be tackled by adopting a general framework that includes soil-structure interaction [14, 15]. However, from an experimental perspective, given the complexity of tests replicating the whole system [16–19], the structures' behaviour is simply investigated by imposing a predefined vertical displacement (settlement) at the structure's foundation [5, 20–24]. The effect of settlements on HMS is often simplified to the behaviour of 2D shear walls (with or without openings). In this case, the wall response depends on its proportion subjected to settlement [22]. However, the literature survey reveals that the influence of the proportion of walls subjected to settlement has not yet been qualitatively and quantitatively unveiled.

This paper presents the new settlement table at the University of Minho. In the following, Sect. 2 describes the table's design and installation, while Sect. 3 reports the first tests conducted on the settlement table. Finally, Sect. 4 presents the drawn conclusions.

2 Experimental Facility Description

The design of the settlement table considers a twofold configuration. In particular, in the settlement experimental setup, the existent tilting table facility is used at the rest position, reproducing the foundation part that does not settle, whereas the integrated designed part aims to simulate the vertical foundation movement.

The tilting table is 1.5 m square-shaped and comprises a 10 mm thick steel plate, which ensures a perfectly flat surface welded to IPE80 steel profiles (Fig. 1a). On one side, the table is connected to a steel beam through four 8 mm steel hinges (Fig. 1b). When used alone, an 8 mm steel wire lifts the other end to allow high tilting angles, up to more than 45º [25]. An example of its use on dry-joint single-leaf masonry structures can be found in [9].

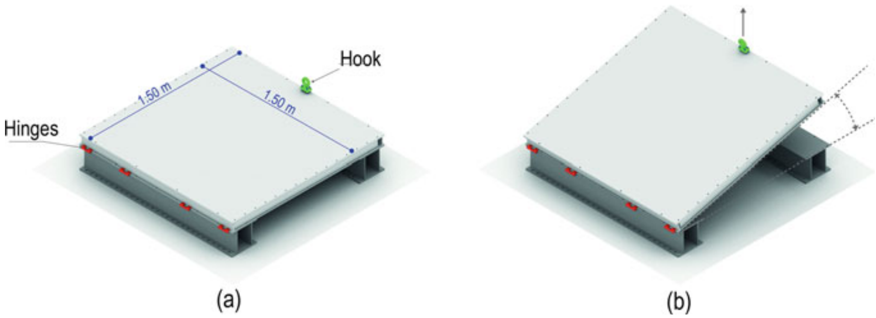

Fig. 1 3D model of the tilting table facility installed at the University of Minho: **a** rest position and **b** inclined configuration

The settlement setup is composed of two tables placed next to each other. The first one consists of the 1.5 m squared tilting table, fixed at a horizontal inclination. In this configuration, the tilting table is supported by four steel profiles fixed to the ground (Fig. 2). The second table (settlement table) is connected to an actuator and thus can move vertically, simulating the foundation settlement. The settlement table consists of a 10 mm sheet welded to HEA120 steel profiles. The whole system is connected to three linear guides through intermediate steel elements. The three guides ensure that the table has only one degree of freedom, i.e. the vertical translation.

Finally, the actuator load cell (200 kN) and LVDT allow to monitor the force imposed by the actuator and the displacement of the settlement table. When the actuator moves downwards, the specimen placed on top is subjected to a differential

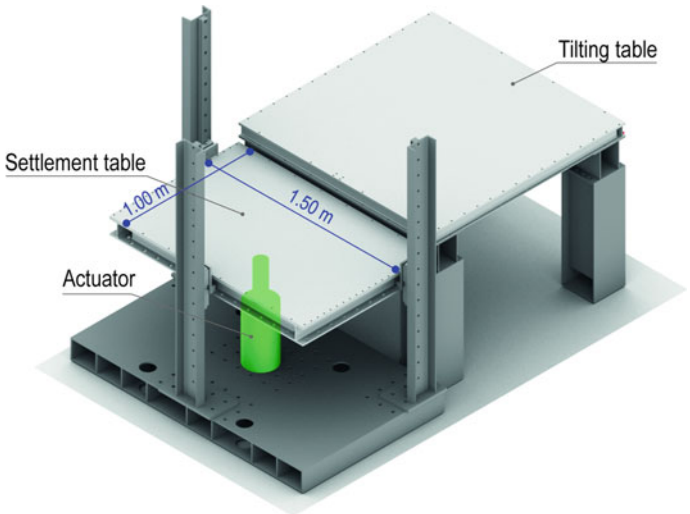

Fig. 2 Settlement table installed at the University of Minho

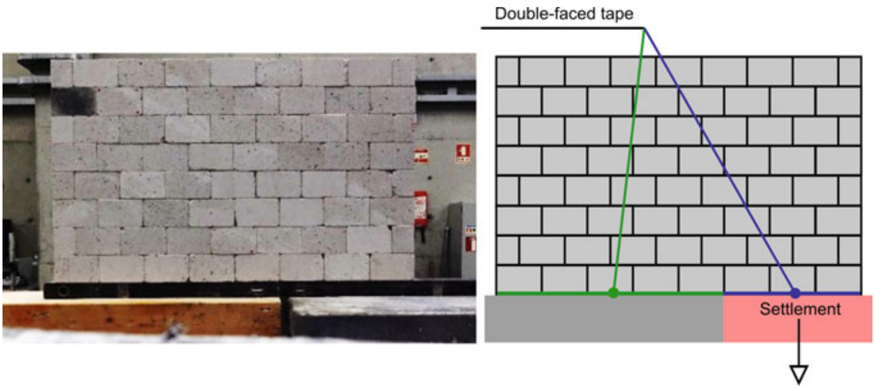

Fig. 3 Settlement experimental setup at the initial stage

settlement with respect to the part of the structure standing on the tilting table (Fig. 3). It is worth highlighting that the actuator and the three guides are attached to a rigid base connected to the laboratory's floor.

3 Settlement Tests on Masonry Shear Walls

The experimental setup has been used to conduct settlement test on single-leaf dry-joint masonry structures. They are presented in the following. The masonry units adopted in the experimental campaign are provided by the Xella Company [26]: their complete characterisation process is presented in [9]. For the sake of brevity, Table 1 reports dimensions, density and friction coefficient arising from the mechanical characterisation tests.

Shear walls made of eight masonry courses have been investigated (Fig. 3). The specimens comprise units arranged in a regular bond pattern, resulting in a wall height of 562 mm high, 574 mm wide and 57.3 mm thick. As depicted in Fig. 3, the specimens stand on both tables to create the differential settlement. For the tests conducted in this work, the settlement procedure consists of three steps; in the first one, the table moves downwards at a speed of 0.02 mm/s for fifty seconds. The second step lasts eighty-three additional seconds with a rate of 0.06 mm/s. Finally, in the third step, the speed is kept equal to 0.2 mm/s up to the end of the test. This procedure aims at precisely capture the initial part of the settlement, where the load decreases very quickly. Concerning the acquisition system, a digital camera records the tests with a picture taken each ten seconds.

Table 1 Principal characteristics of the masonry units considered

Dimensions	Density	Friction angle
(114.9· 70.3· 57.3) mm^3	1876 kg/m^3	33.4°

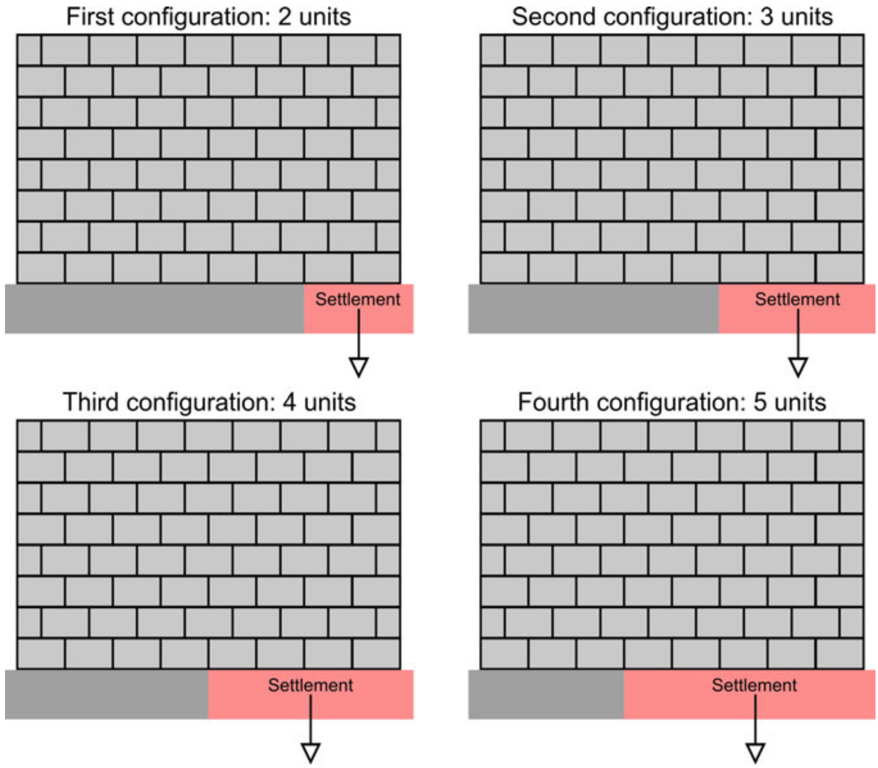

Fig. 4 The four configurations tested on the settlement table

Four different configurations have been tested (Fig. 4):

- Two units subjected to settlement;
- Three units subjected to settlement;
- Four units subjected to settlement;
- Five units subjected to settlement.

Concerning the boundary conditions, the first course of the masonry wall has always been fixed to the table through double-faced tape strips (Fig. 3).

For each configuration, at least three specimens have been tested in order to ensure repeatability. In an attempt to complement the actuator load cell and check its reliability, a weighing scale has been placed below the settling part of the shear walls to monitor the vertical load of each test. Hence, as an illustrative example, Fig. 5 compares the load recorded by the scale and the actuator load cell for the three tests of the third configuration (4 units settling). While the scale gives similar results for the three tests, the load cell provides divergent responses. In addition, the values given by the load cell are unrealistic. Out of the results, the load cell appears unreliable, justifying the need to measure the load through a scale. Actually,

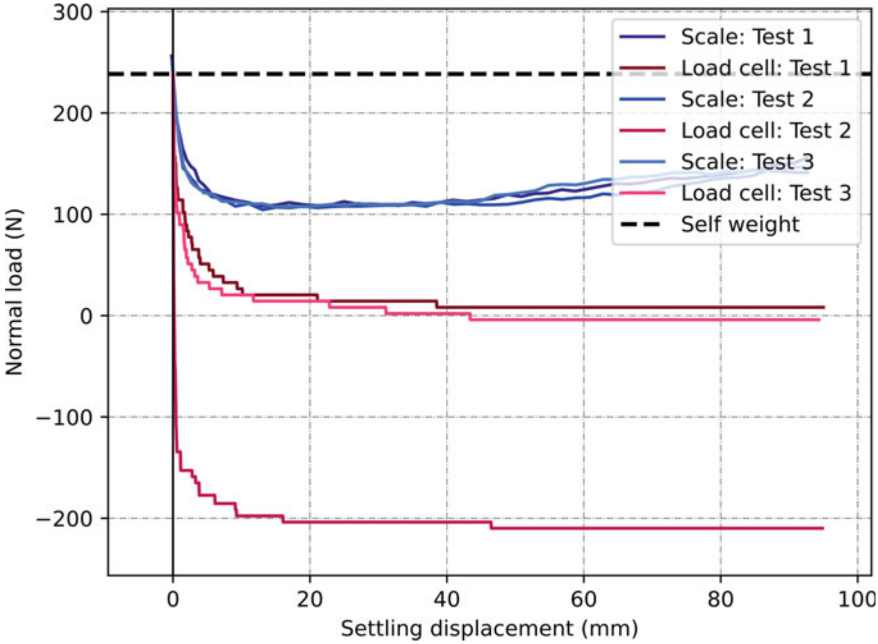

Fig. 5 Comparison of the loads measured by the scale and the actuator load cell

the linear guides are not only preventing the bending of the actuator but also carry vertical loads through friction. Therefore, the settlement table will be stiffened for future tests, and the linear guides will be softened to allow reliable measures of the weight through the actuator load cell.

Figures 6, 7, 8 and 9 show the responses of the four investigated configurations when subjected to settlement. For each repeated test, the load is monitored only through the weighing scale, as a direct outcome of the pre-mentioned investigation (Fig. 5). From Figs. 6, 7, 8 and 9, one can observe similarities and differences in the four studied configurations. These are developed hereafter.

First of all, the responses detected by the experimental apparatus have been post-processed, and the curves have been shifted to a zero-reference displacement (i.e. initial configuration), which coincides with a vertical load equivalent to the self-weight of the settling part. One should note that the vertical load in the y-axis of the figures excludes the weight of the setup and the first fixed row of masonry units, as they do not play any role. The first outcome concerns the very high repeatability of the experiments. Then, one can observe three different phases for each configuration: (i) load decrease, (ii) constant load and (iii) load increase. However, it is important to highlight that the thresholds delimiting these phases vary between the tested configurations. More in detail, it is observed that the four configurations display a similar first phase (Phase I), characterised by a sharp decrease in the vertical load associated

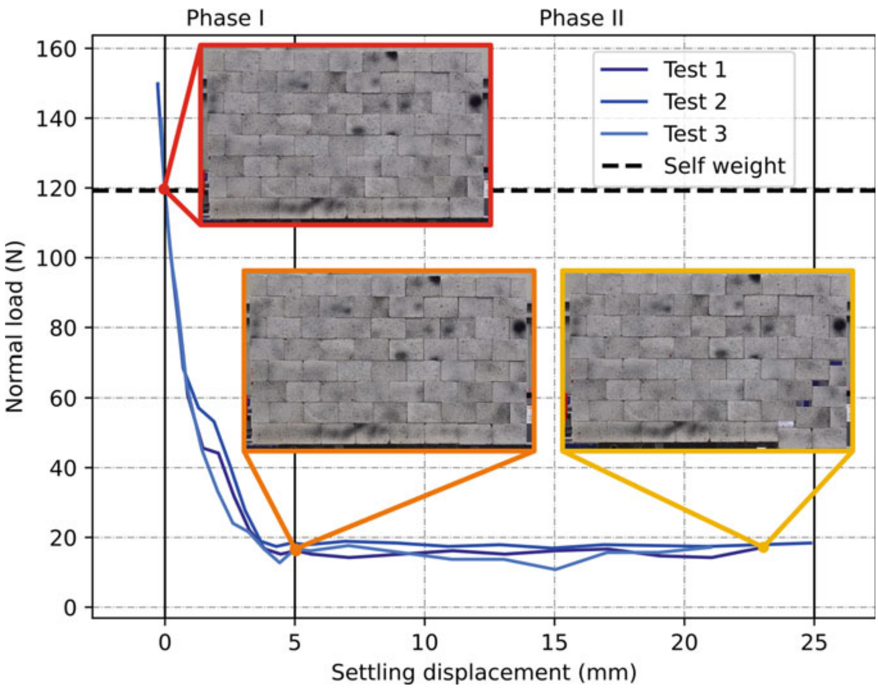

Fig. 6 Load–displacement responses of the repeated tests of the first configuration (two units settling). Some pictures of the mechanisms at critical instants are also displayed

with meagre vertical settlements (maximum equal to 5, 10, 12 and 15 mm for the 1st, 2nd, 3rd and 4th configuration, respectively).

Compared to the initial mechanism, at the end of phase I, some cracks are observable. In particular, the one following the path "UP-RIGHT-UP-RIGHT" starting from the discontinuity in the bottom boundary condition. After, Phase II corresponds to a plateau in the vertical load while the settling displacement increases. However, from this point on, the similarities between the specimens end. Indeed, one can note that the plateau (Phase II) lasts until the end of the test for the first configuration (Fig. 6), resulting in a final mechanism that is entirely mechanically stable for any settlement. On the contrary, for the three other cases (Figs. 7, 8 and 9), Phase II ends approximately after 30 mm of vertical settlement with a smooth transition to phase III, where the load increases again with the vertical settlement, yet with a much smaller slope compared to Phase I. At the end of Phase II, the mechanism has already evolved compared to the previous step. For the second and third configurations (Figs. 7 and 8), the main crack (path "UP-RIGHT-UP-RIGHT") becomes

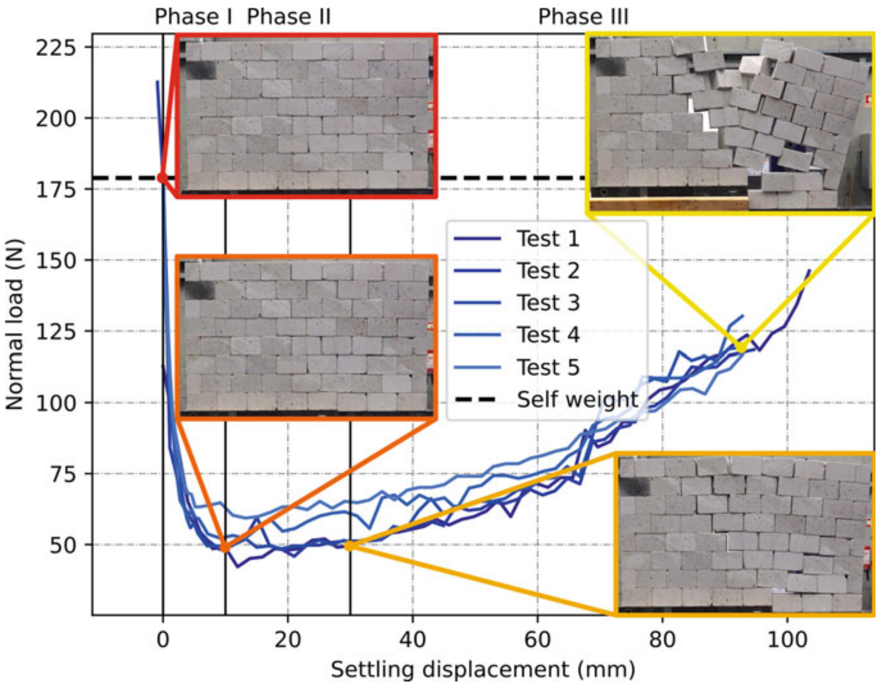

Fig. 7 Load–displacement responses of the repeated tests of the second configuration (three units settling). Some pictures of the mechanisms at critical instants are also displayed

more visible. However, secondary cracks are also propagating in the rest of the walls. These cracks are distributed almost everywhere up to the path "UP-LEFT-UP-LEFT", starting from the discontinuity in the bottom boundary condition. In addition, one can notice the beginning of a rocking motion about the right toe of the walls leading to marked cracks in that area. On the contrary, at the end of Phase II, the fourth configuration (Fig. 9) mainly displays a marked "UP-RIGHT-UP-RIGHT" path cracks, while small cracks are hardly visible in the rest of the wall. As depicted in Fig. 10, at the end of the settlement (90–100 mm), the last three configurations end with a similar mechanism, i.e., the rocking motion of a macro-block composed of the right pier (Part 3) and a central triangular part (Part 4). It leaves a stable triangle on the settlement table (Part 2). Additionally, frictional dissipations (grey areas) occur between the central triangular part (Part 4) and the left stable part (Part 1). Similarly, frictional interactions also develop between the rocking right pier (Part 3), the stable settling part (Part 2) and the central triangular part (Part 4) due to the geometrical incompatibility of their rigid motions.

Finally, one should remark that the final vertical load of the last three configurations (Figs. 7, 8 and 9) is different. While the second configuration almost reaches the initial vertical load at the end of the settlement test (Fig. 7), the other two are still very far from their initial loads (Figs. 8 and 9). Actually, it is observable that

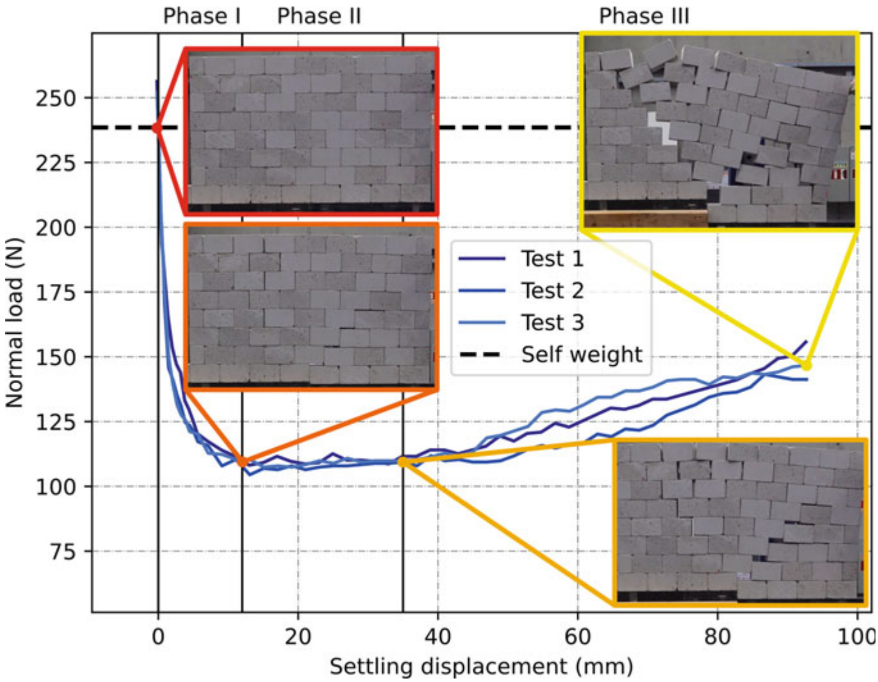

Fig. 8 Load–displacement responses of the repeated tests of the third configuration (four units settling). Some pictures of the mechanisms at critical instants are also displayed

the second configuration is much closer to the structure's collapse than the third and fourth configurations. It also means that the more significant the proportion of a shear wall subjected to settlement is, the more ductile its response becomes. However, this gain could not be quantified here since no complete collapse was reached in order to prevent damaging the masonry units.

4 Conclusions

The present work describes large-scale testing equipment, namely a $1 \times 1.5\ m^2$ settlement table, laid next to a 1.5 m squared tilting table, which can also be used autonomously to pseudo-statically reproduce seismic actions. The settlement setup comprises a moving part (one degree of freedom represented by the vertical translation) and a fixed part consisting of the tilting table placed at rest. Specimens stand on both tables, while the downward movement of the settlement table reproduces a differential soil settlement.

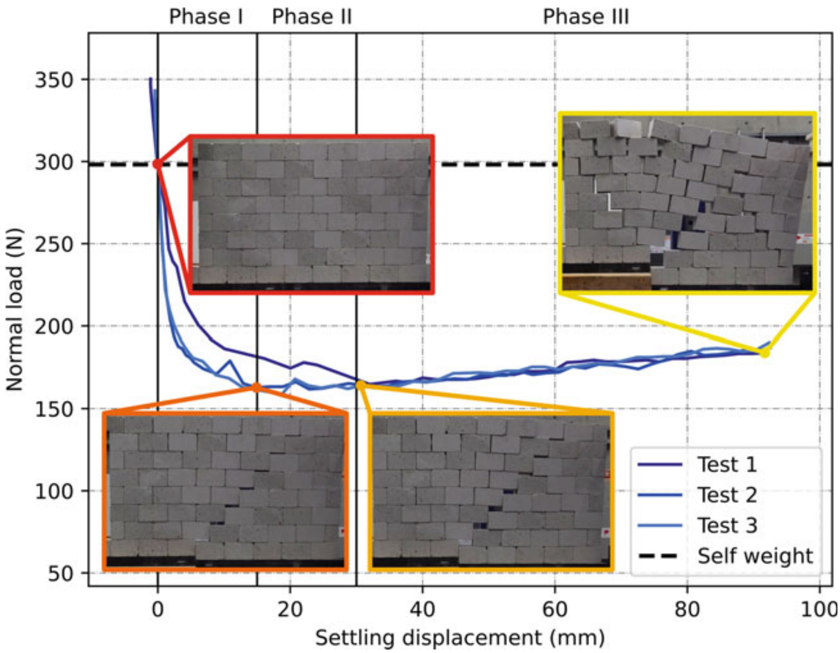

Fig. 9 Load–displacement responses of the repeated tests of the fourth configuration (five units settling). Some pictures of the mechanisms at critical instants are also displayed

The experimental facility allows the testing of masonry prototypes at a large scale, up to 2.5×1.5 m^2, while supporting up to approximately one-ton specimens. Therefore, it enables the investigation of the behaviour of both dry-joint and mortared masonry specimens.

The present paper focuses on the response of dry-joint masonry shear walls to settlement. It is shown that the behaviour (vertical load response and collapse mechanism) is significantly affected by the proportion of a shear wall subjected to settlement. Additionally, the testing procedure is found highly repeatable, confirming the quality of the experimental campaign, that can serve as an experimental validation framework for analytical and numerical models. In conclusion, this work is envisioned as preliminary phase towards the understanding of how 3D masonry structures are affected by vertical differential settlements.

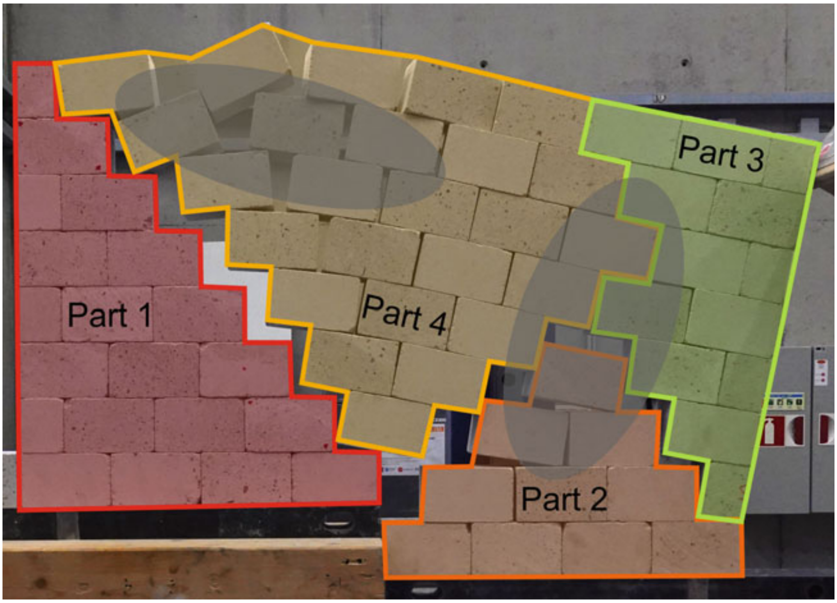

Fig. 10 Representative collapse mechanism obtained at the end of the settlement on the third configuration. Similar mechanisms are observable for the second and the fourth configurations. The shear wall is divided into four parts with frictional dissipations between them

References

1. Peduto, D., Korff, M., Nicodemo, G., Marchese, A., Ferlisi, S.: Empirical fragility curves for settlement-affected buildings: analysis of different intensity parameters for seven hundred masonry buildings in The Netherlands. Soils Found. **59**(2), 380–397 (2019). https://doi.org/10.1016/j.sandf.2018.12.009
2. Foraboschi, P.: Specific structural mechanics that underpinned the construction of Venice and dictated Venetian architecture. Eng. Fail. Anal. **78**, 169–195 (2017). https://doi.org/10.1016/j.engfailanal.2017.03.004
3. DeJong, M.J.: Settlement effects on masonry structures. In: Structural Analysis of Historical Constructions: Anamnesis, Diagnosis, Therapy, Controls. Proceedings of the 10th International Conference on Structural Analysis of Historical Constructions, SAHC 2016, pp. 449–456
4. Gagliardo, R., et al.: Rigid block and finite element analysis of settlement-induced failure mechanisms in historic masonry walls. Frattura ed Integrità Strutturale **51**, 517–533 (2020). https://doi.org/10.3221/IGF-ESIS.51.39
5. Portioli, F., Cascini, L.: Large displacement analysis of dry-jointed masonry structures subjected to settlements using rigid block modelling. Eng. Struct. **148**, 485–496 (2017). https://doi.org/10.1016/j.engstruct.2017.06.073
6. Vaculik, J., Griffith, M.C., Magenes, G.: Dry stone masonry walls in bending—part II: analysis. Int. J. Arch. Herit. **8**(1), 29–48 (2014). https://doi.org/10.1080/15583058.2012.663060
7. Casapulla, C., Maione, A.: Experimental and analytical investigation on the corner failure in masonry buildings: interaction between rocking-sliding and horizontal flexure. Int. J. Arch. Herit. **14**(2), 208–220 (2020). https://doi.org/10.1080/15583058.2018.1529206

8. Savalle, N., Vincens, E., Hans, S.: Pseudo-static scaled-down experiments on dry stone retaining walls: preliminary implications for the seismic design. Eng. Struct. **171**, 336–347 (2018). https://doi.org/10.1016/j.engstruct.2018.05.080
9. Colombo, C., Savalle, N., Mehrotra, A., Funari, M.F., Lourenço, P.B.: Experimental, numerical and analytical investigations of masonry corners: influence of the horizontal pseudo-static load orientation. Constr. Build. Mater. **344**, 127969 (2022). https://doi.org/10.1016/j.conbuildmat.2022.127969
10. Casapulla, C., Argiento, L.U.: The comparative role of friction in local out-of-plane mechanisms of masonry buildings. Pushover analysis and experimental investigation. Eng. Struct. **126**, 158–173 (2016). https://doi.org/10.1016/j.engstruct.2016.07.036
11. Shi, Y., D'Ayala, D., Prateek, J.: Analysis of out-of-plane damage behaviour of unreinforced masonry walls. In: 14th International Brick and Block masonry Conference, pp. 02–17. The University of Newcastle, Australia (2008)
12. Restrepo Vélez, L.F., Magenes, G., Griffith, M.C.: Dry stone masonry walls in bending—part I: static tests. Int. J. Arch. Herit. **8**(1), 1–28 (2014). https://doi.org/10.1080/15583058.2012.663059
13. Barsotti, R., Bennati, S., Ochsendorf, J.A., Tirabasso, C.: Scale models for the experimental analysis of the collapse mechanisms of masonry bay windows under horizontal actions. COMPDYN **2017**, 15–17 (2017)
14. Deck, O., Singh, A.: Analytical model for the prediction of building deflections induced by ground movements. Int. J. Numer. Anal. Meth. Geomech. **36**(1), 62–84 (2012). https://doi.org/10.1002/nag.993
15. D'Altri, A.M., De Miranda, S., Castellazzi, G., Sarhosis, V., Hudson, J., Theodossopoulos, D.: Historic barrel vaults undergoing differential settlements. Int. J. Arch. Herit. **14**(8), 1196–1209 (2020). https://doi.org/10.1080/15583058.2019.1596332
16. Ritter, S., Giardina, G., DeJong, M.J., Mair, R.J.: Centrifuge modelling of building response to tunnel excavation. Int. J. Phys. Model. Geotech. **18**(3), 146–161 (2018). https://doi.org/10.1680/jphmg.16.00053
17. Laefer, D.F., Hong, L.T., Erkal, A., Long, J.H., Cording, E.J.: Manufacturing, assembly, and testing of scaled, historic masonry for one-gravity, pseudo-static, soil-structure experiments. Constr. Build. Mater. **25**(12), 4362–4373 (2011). https://doi.org/10.1016/j.conbuildmat.2011.03.066
18. Dalgic, K.D., et al.: Large scale experimental settlement tests to evaluate structural models for tunnelling-induced damage analysis. In: Barla, M., Di Donna, A., Sterpi, D. (eds.) Challenges and innovations in geomechanics. IACMAG 2021. Lecture Notes in Civil Engineering, vol. 126. Springer, Cham. https://www.doi.org/10.1007/978-3-030-64518-2_20
19. Dalgic, D.K., et al.: Design and construction of a test setup to investigate ground settlement response of large-scale masonry building models. Presented at the 3rd Conference on Testing and Experimentation in Civil Engineering, TEST&E 2022 Smart Technologies, FCT NOVA, Campus de Caparica (2022)
20. Giardina, G., Marini, A., Hendriks, M.A., Rots, J.G., Rizzardini, F., Giuriani, E.: Experimental analysis of a masonry façade subject to tunnelling-induced settlement. Eng. Struct. **45**, 421–434 (2012). https://doi.org/10.1016/j.engstruct.2012.06.042
21. Giardina, G., Marini, A., Riva, P., Giuriani, E.: Analysis of a scaled stone masonry facade subjected to differential settlements. Int. J. Arch. Herit. **14**(10), 1502–1516 (2020). https://doi.org/10.1080/15583058.2019.1617911
22. Bui, T.T., Limam, A., Sarhosis, V., Hjiaj, M.: Discrete element modelling of the in-plane and out-of-plane behaviour of dry-joint masonry wall constructions. Eng. Struct. **136**, 277–294 (2017). https://doi.org/10.1016/j.engstruct.2017.01.020
23. Gagliardo, R., Portioli, F.P.A., Cascini, L., Landolfo, R., Lourenço, P.B.: A rigid block model with no-tension elastic contacts for displacement-based assessment of historic masonry structures subjected to settlements. Eng. Struct. **229**, 111609 (2021). https://doi.org/10.1016/j.engstruct.2020.111609

24. Portioli, F., Cascini, L.: Assessment of masonry structures subjected to foundation settlements using rigid block limit analysis. Eng. Struct. **113**, 347–361 (2016). https://doi.org/10.1016/j.engstruct.2016.02.002
25. Colombo, C., Fernandes, L., Savalle, N., Lourenço, P.B.: Tilting tests for masonry structures: design and preliminary numerical modeling. Presented at the 14th Canadian Masonry Simposium, pp. 1–11 (2021)
26. XELLA Company: Silka blocks (2022). https://www.xella.com/en_US/

A Discussion on the Determination of Permeability and Absorption in Concrete

Michela Monaco, Roberto Serpieri, Mariateresa Guadagnuolo, and Giorgio Frunzio

Abstract Periodic and non-routine inspections on buildings, infrastructures, and sites of historical or architectural interest frequently involve a necessary deepening of the knowledge of natural or artificial stone materials. The quality and functional performance, the state of conservation, and possible pathologies of stone materials of structures and building envelopes, as a norm, have to be evaluated by performing tests and samplings with a minimal degree of invasiveness. This last requirement, aiming at the limit of nondestructive testing, stems from the necessity to find a balance among preservation of structural, historical, and artistic integrity of the inspected stone materials, an acceptable level of gained knowledge on the built element, and sufficient reliability of the deployed diagnostic activities. While the requirement of least invasiveness is common to many inspective and diagnostic practices belonging to different technical sciences, such as structural engineering, architecture, and restoration, as well known, however, the conditions of minimum knowledge gain and minimum acceptable reliability can be seldom granted by methods of testing that are completely nondestructive. The last century of investigations has shown the pivotal role of permeability for durability assessment of building stones and concrete, with the possibility of reducing invasiveness by using smaller stone samples in uniaxial water-permeation tests. This contribution presents a review on past and present experimental methods for determining permeability in concrete,

M. Monaco
Dipartimento di Ingegneria, Università degli Studi del Sannio, Benevento, Italy
e-mail: monaco@unisannio.it

R. Serpieri (✉) · M. Guadagnuolo · G. Frunzio
Dipartimento di Architettura e Disegno Industriale, Università Della Campania "Luigi Vanvitelli", Aversa, Caserta, Italy
e-mail: roberto.serpieri@unicampania.it

M. Guadagnuolo
e-mail: mariateresa.guadagnuolo@unicampania.it

G. Frunzio
e-mail: giorgio.frunzio@unicampania.it

C. Chastre et al. (eds.), *Testing and Experimentation in Civil Engineering*,
RILEM Bookseries 41, https://doi.org/10.1007/978-3-031-29191-3_16

some of which are also applicable to other porous building materials, with a discussion on optimality criteria for testing and sampling which is carried out in the light of an historical perspective and of a view towards the Life Cycle Assessment of interventions on the built heritage.

Keywords Concrete permeability standards · Life cycle assessment · Minimal invasiveness · Reinforced concrete cover

1 Introduction

The 2030 Agenda for sustainable development sets a series of objectives to achieve a better future. The world of constructions is strongly involved in this complex process. The problem of finding best practices for the assessment and maintenance of building heritage is more consciously framed today within the methodologies of Life Cycle Assessment (LCA), in the light of an increased awareness that social, infrastructural and environmental issues and policies cannot be faced by singles compartments but need a global evaluation [1]. Reinforced Concrete (RC) structures are great part of the built heritage in suburban districts, where the lack of maintenance due to the economic conditions of the citizens combined with the low quality of constructions do not allow to easily fulfill the Goal 11 "*Make cities and human settlements inclusive, safe, resilient and sustainable*" [2].

Pursuing sustainable housing in sustainable cities means that refurbishment interventions should be based on accurate studies on degradation causes and correct choice of intervention techniques, especially in the case of RC structures realized in the past decades and now showing evident degradation marks. In RC structures permeability can be a primary reason for concrete deterioration, reinforcing steel corrosion and other damage mechanisms [3]. Freeze–thaw damage due to the water absorbed, variation in the elastic properties and in the concrete alkalinity, intrusion of salt-laden air and water are only some of the problems faced by an exposed concrete during its life showing that the determination of permeability is necessary for concrete durability assessment and in particular for the evaluation of inspecting procedure time intervals, since the concrete cover is often the vulnerable ring in the performance, serviceability and durability chain [4]. Demands associated with periodic maintenance interventions on RC structures are in fact estimated in Life Cycle Impact Assessment (LCIA) by evaluating the harm to environment in terms of primary Gross Energy Requirement (GER) and of CO_2 equivalent emissions (GWP—Global Warming Potential). LCIA performs these estimations accounting for the entire energy chain all through the life cycle of the building from the phase of resources extraction to their final use.

The maintenance and refurbishment time intervals, which constitute an input necessary for LCA, are also strongly related to the building components material properties, whose knowledge in existing structures is generally based on inspection techniques [5] since often the material characteristics at the time of construction are not known and the material properties are the reference framework for structural health monitoring. The relevance of information provided by on site survey should in fact be related to the feasibility of the test, its invasiveness and disturbance to the building and its complexity of execution [6]. Larger test campaigns involving destructive or semi-destructive tests are in general performed when advanced structural problems are ongoing. The simple replacement of the concrete cover is on the other hand a common refurbishment intervention that can easily provide field samples to be tested.

Research significance. Proceeding in the light of an historical perspective and of a view towards the Life Cycle Assessment of interventions on the built heritage, this contribution presents the main results of a review of past and present experimental methods for determining permeability in concrete [7], some of which are also applicable to other porous building materials, with a discussion on optimality criteria for testing and sampling.

The permeability standards actually in force are based on a conventional permeability test over thicker specimens, which appear to be more suited for new RC constructions (EN 12,390-8) [8–11]. Conversely, a literature review of the experimental studies of the first half of the past century provides information about permeability tests on thin specimens [12] which can be carved out from the concrete cover. These tests on thinner specimens appear more suitable for existing structures and more compatible with the "*primum non nocere*" principle applied to a building.

This contribution discusses the feasibility of open-flow permeability tests on concrete cover, and their inclusion in a complete framework inclusive of LCA. The geometrical similarity of concrete cover fragments and the tile-shaped specimens commonly tested in the first half of last century is examined as a possible base for a renewed practice for testing existing structures and for improving the current regulations for permeability determination.

Document organization. Paragraph 2 discusses the role of maintenance interventions on RC buildings in LCA assessment. Paragraph 3 reviews past and present experimental methods to evaluate permeability enucleating main features of interest for the present study. In paragraph 4 a process for extraordinary maintenance of concrete cover in a RC structure is proposed and is presented together with a discussion on the possibility, based on experimental tests available in literature, of inferring correlations among permeability and mechanical properties of concrete, useful for assessing concrete durability and structural performance based on different parameters.

2 Existing Structures: LCA and Experimental Tests

In a LCA perspective, ordinary and extraordinary maintenance interventions on existing buildings should be subjected, like all the actions on environment, to a cradle-to-grave or cradle-to-cradle analysis technique in order to assess the environmental impacts associated with all the stages of an intervention's life. The smaller the time interval between two interventions, the higher the environmental impact. The following subsections give a brief description of LCA for RC structures and an evaluation of the environmental incidence of a concrete cover replacement/refurbishment intervention.

2.1 LCA for Interventions on Concrete Structures

The LCA of RC buildings is strongly influenced by the service life of its structural elements. LCA methodology regards building components as systems subjected during their life cycles to input and output flows of matter and energy and determines the resulting environmental impact in terms of GER and CO_2 equivalent emissions GWP. Although most of the energy spent during the life cycle of RC structures is ordinarily consumed during their use for anthropic activities, a significant share, whose quantification depends on the duration of the designed service life, is consumed during the other phases of material production, transportation, construction, end-of-life, included periodic maintenance and extraordinary structural maintenance.

Attention should be paid to these last two phases, since the wider the refurbishment intervals, the lower the percentage of energy spent in the production, transportation, construction, and end-of-life phases of the materials employed for replacement and the end of life of the replaced concrete. It has been estimated that if more ambitious standards were applied to new buildings or to the refurbishment of existing ones by extending their useful life, up to 30–45 million tons of CO_2 per year could be saved [13].

In particular, excluding steel reinforcements, the percentage of GWP of concrete (in kg eq. CO_2/m^3) over the total GWP of a cubic meter of building materials is, on average, two orders of magnitude higher compared to the corresponding percentages of other building materials [14]. Since interventions of concrete cover replacements are actually the most diffused extraordinary maintenance interventions (EMI), a deeper look into the concrete cover durability properties appears to be a key issue to extend the service life of RC. Interventions are usually planned when concrete cover spalling is already at intermediate or advanced stages of progression to prevent further significant loss of the resistant section of the structural element (Fig. 1).

2.2 Intervention Intervals and Sustainability

An evaluation of the environmental impact scenarios associated with reiterated concrete cover maintenance with constant periodicity during a hypothetical service life of 100 years is carried out for a typical social housing four-storey pilotis-type RC building located in a suburban area of the south of Italy. Building data and degradation scenario are taken as resulting from actual inspection of a real building constructed between 1970 and 1980 located in the province of Caserta. Excluding the stairwell,

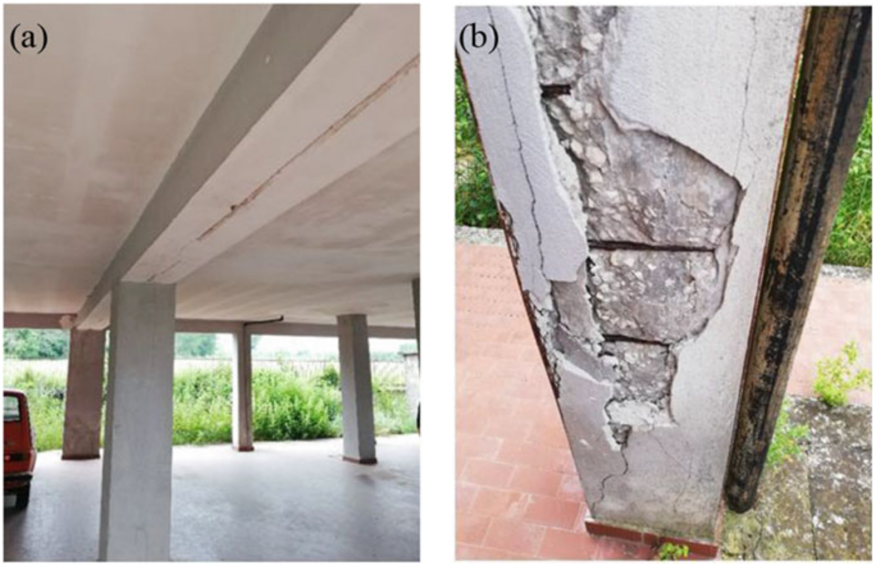

Fig. 1 Ground floor of a typical RC building with pilotis (**a**) and conditions of a ground floor column 50 years after construction in nonaggressive environment (**b**)

the building structure, which is regular in height, essentially consists of a regular frame of equally interspaced columns and horizontal beams. Columns organization in the building plan is a 3×7 regular array, with 16 out of 21 columns in perimetral position. On the open ground floor, where inspection allowed to observe concrete cover delamination on several columns as shown in Fig. 1, 52 over 84 column faces are computed to be directly exposed to weathering while on the other three storeys the computed fraction of exposed column faces is 20/84. An analogous computation of exposed beam faces gives at any slab a fraction of 16/128.

Based on the design sections of the frame elements, shown in Fig. 2, computation of the percentage of concrete section area to be replaced in a hypothetical 4 cm concrete cover replacement at the open ground story leads to figures of 25% for the (a.1) column, 30% for the (a.2) column, 23% for the (b.1) downstand beam, 20% for the (b.2) flat beam. On account of these figures and of the information that the volume of columns is approximately 25% of the total volume of columns and beams and that perimetral beams are of down-stand type, a rough computation of the volume of concrete cover to be replaced in a hypothetical intervention on all exposed surfaces leads to a value ranging between 4 to 5% of the original concrete volume.

Taking for the Percentage of Replaced Concrete (PRC) in an intervention the upper rounded value stemming from the calculation above, PRC = 5, and contemplating the possibility that more than one replacement intervention can be required in the course of the service life of SL = 100 years conventionally attributed to the building [15], if the years between one intervention and a successive one are indicated by T, the overall PRC during the service life turns out to be:

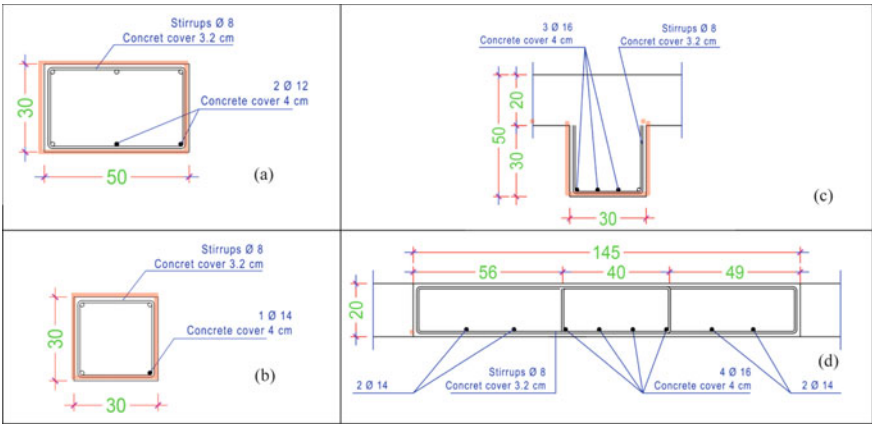

Fig. 2 Design sections of frame elements: **a** type 1 column; **b** type 2 column; **c** downstand beam; **d** flat beam

$$\text{Overall } PRC = \frac{SL}{T} \cdot PRC \cdot 100 = \frac{100}{T} \cdot \frac{5}{100} \cdot 100$$

Figure 3 plots the overall PRC as function of T considering for the reintervention time a range from a minimum of 10 years to a maximum of 100 years and shows that, if a not so unrealistic figure of one intervention every 20 years is taken, a figure of 25% increment of global warming potential associated with extraordinary maintenance is computed.

Assuming simplistically the GWP related to anthropic activities associated with building usage to be a variable uniform in time along the course of 100 years—what seems a reasonable assumption which allows to rule out delicate demographic projections—optimality in terms of GWP is trivially achieved when T is maximized, a conclusion which is also supported by more detailed studies [16].

3 Past and Present Experimental Methods for Permeability Determination

3.1 Literature Review

In the first half of XX century, along with the growth of RC construction, the development of experimental methods for determining the physical–chemical properties of reinforced concrete underwent a parallel growth. Table 1 synoptically reports the main features of the experimental methods and setups (testing methods, sample size, sealing method and duration) for the determination of concrete permeability.

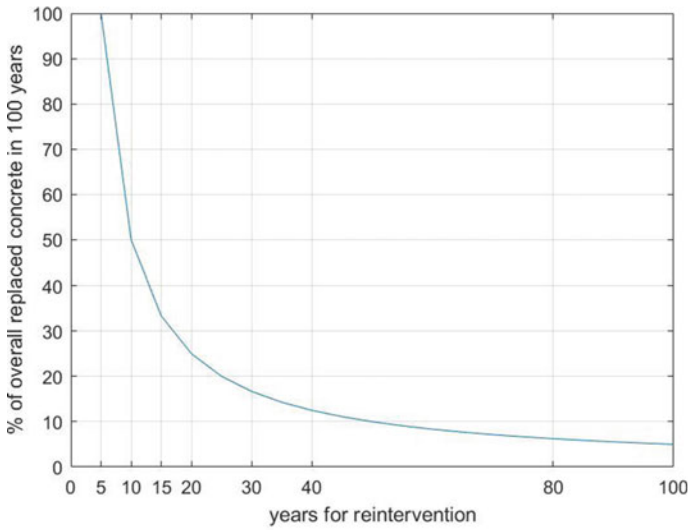

Fig. 3 Percentage of overall concrete to be replaced in 100 years as function of hypothesized periods for reintervention

The main interesting aspects of the tests performed in the first decades of last century are the accurate descriptions of the testing methodology and setups, the repeatability and the simple relations among the physical and mechanical parameters. In a study articulated in six parts, Madgwick in 1932 [12] contributed a comprehensive investigation into fundamental physical properties of porous building materials covering the experimental determination of porosity, absolute porosity, saturation coefficient, permeability and absorptivity of several natural and artificial building materials including stones, bricks and plasters. Fundamental contributions by Madgwick are the proof of concept and the ordinary application of simple methodologies, based both on water and air permeation, on building material specimens cut or molded in a thin tile-like shape whose thickness can be brought even down below 1.3 cm. The shape of the testing specimen is that of a small tile through which a steady, or non-steady, flux of fluid is imposed. For space reasons we limit here just to a brief mention of other fundamental contributions which cannot find room in Table 1.

One of the earliest published studies on concrete permeability is a bulletin by Withey and Wiepking [17] summarizing several basic findings obtained at the University of Wisconsin on broken stone concrete among which the evidence that water-tightness markedly improves until cement/aggregate ratio reaches values in the range $0.14 \div 0.17$ and cement/voids volume ratio reaches $0.45 \div 0.55$. Muskat [18] advised the use of gas flow experiments for measuring intrinsic permeability in consideration of several practical advantages.

Klinkenberg [19] investigated the gas-slippage effect by comparing determinations of intrinsic permeability obtained with gas and liquids, finding, at atmospheric pressure for the tested media and fluids, a maximum discrepancy contained within a

Table 1 Historical review on permeability testing methods (K_2 indicates intrinsic permeability)

Author(s), year	Testing physical principle and/or method	Specimen thickness L_h and shape ratio $\frac{L_h}{L_p}$	Pressure [MPa] and duration	Main findings of research	Sealing method
Glanville (BBRS) [23]	Steady-state permeation of water	$L_h = 5.8cm$ $\frac{L_h}{L_p} \leq 0.5$	0.7 MPa, duration $\leq 1day$ in most test	Permeability caused by both air- and excess-water-voids; systematic investigation of a wide range of proportions *water:cement:sand:gravel*; time elapsed after casting is the main factor influencing permeability	Slurry of neat cement
McMyllan and Lyse [24]	Steady-state permeation of water; use of standard pipe fittings	$L_h = 2.54cm$ till pressures of 0.14 MPa; apparatus allows for specimens of any desired thickness	$0.14 \leq p \leq 1$ MPa	Admixtures of celite, pumicite and soapstone increase permeability while admixtures of cement and hydrated lime decrease it; testing under continuous open flow allows observation of solvent action of water	Mixture of 50% rosin and 50% paraffin

(continued)

Table 1 (continued)

Author(s), year	Testing physical principle and/or method	Specimen thickness L_h and shape ratio $\frac{L_h}{L_p}$	Pressure [MPa] and duration	Main findings of research	Sealing method
Norton and Pletta [25]	Permeation of water; featuring air reservoirs; apparatus much more complex and less easily duplicatable than McMyllan and Lyse (1929); report of inclusion of a coil bedded in Portland cement "*used to heat the casting*"	Specimens 15.24 × 30.48 cm, much larger than those reported by McMyllan and Lyse (1929);	Up to 0.69 MPa	Claimed that "*there is no relationship between permeability and absorption*"	Asphalt and gypsum plaster
Madgwick [12]	Absolute porosity (manometric principle); permeability to air (chronometric) with fixed air bulb of known volume; absorptivity and permeability to water (by reading of rate on capillary tube in front of a millimeter scale)	$L_h \geq 1.3$ cm Recommended $\frac{L_h}{L_p} \leq \frac{1}{6}$	Air permeability: $p_{min} = 0.0005$ $p_{max} = 0.014$ duration < 2300 s; duration of 7 h for $K_2 > 10^{-13} m^2$	Seminal work for different methodologies; proof of concept for absolute porosity measurement by manometric methods; proof of concept for repeatability and accuracy of different methods with air and water, both steady-state and transitory	Faraday wax (rosin + beeswax + venetian red)

(continued)

Table 1 (continued)

Author(s), year	Testing physical principle and/or method	Specimen thickness L_h and shape ratio $\frac{L_h}{L_p}$	Pressure [MPa] and duration	Main findings of research	Sealing method
Dunagan, Ernst [26]		$\frac{L_h}{L_p} = 0.25$		Study of 6 admixtures (diatomaceous silica, bentonite, water repelling cement, hydrated lime and early strength cement) found all to adversely affect watertightness	Greased gasket of natural rubber sheets
Ruettg et al. [20, 21]	1935: water permeation; presence of pressurized oxygen tanks in the apparatus; 1936: use of salt water and standard percolation test	In 1935: $L_h = 45.72cm$ for large broken stone aggregates and $\frac{L_h}{L_p} = 1.0$; in 1936: $L_h = 5.08cm$ and $\frac{L_h}{L_p} = 0.33$	$0.91 \leq p \leq 3.05$ MPa; duration: 200 to 500 h on average		
Powers et al. [27]	Steady-state water permeation on neat cement pastes, actuated by mercury standpipes	$L_h = 1.07cm$; $\frac{L_h}{L_p} = 0.4$	Few days on average, or even some weeks for most impervious pastes	Minimum permeability obtained for highly controlled cement paste at $\frac{w}{c} = 0.38$, $K_2 = 3 \cdot 10^{-22} m^2$	Grease coating and gasket

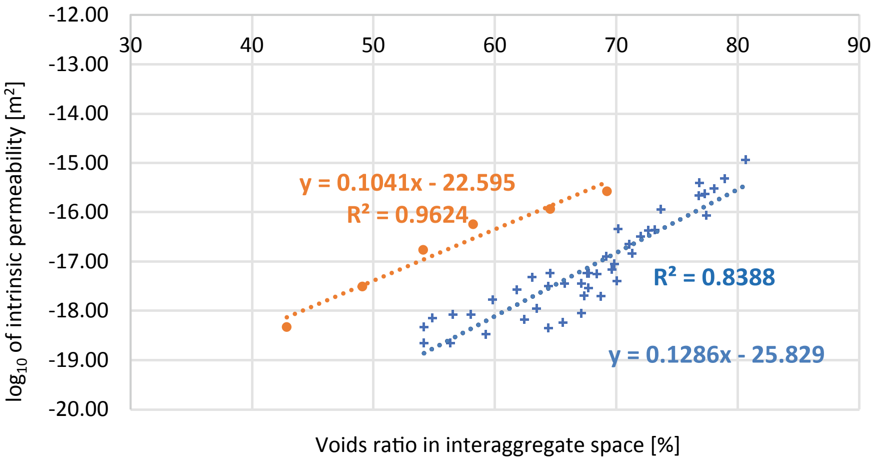

Fig. 4 Intrinsic permeability versus the porosity within the cement paste, tests by Glanville [23] (blue crosses) and by Ruettgers et al. [21] (orange bullets)

150% figure. In a comprehensive study on cement pastes using characterizations of the specific surface by adsorption isotherms and values obtained from experimental data published by Ruettgers et al. in 1935 and in 1936 [20, 21], Powers and Brownyard [22] obtained purely theoretical predictions of permeability, achieving, for a $\frac{w}{c}$ ratio equal to 0.5, reasonable predictivity of the orders of magnitude of permeability of pastes.

Glanville [23] accurately described tests performed after 28 days water curing on a large set of different concrete mixes. Figure 4 presents in a semi-logarithmic plane the intrinsic permeability versus the voids ratio obtained by Glanville on concrete, and the results on neat cement pastes by Ruettgers et al. [20, 21] and Fig. 5 shows the corresponding experimental relation between voids and strength. Data on cement pastes show a shift toward lower values of porosity.

3.2 Current Test Standards for Concrete Watertightness

Similarly to Table 1, standards currently in force are presented in Table 2 highlighting the main testing features (testing methods, sample size, preconditioning and duration) which are deemed to be relevant to the hypothesis investigated in the present study: the feasibility of tests on tile-like specimens extracted from the concrete cover.

In the history of standards for concrete permeability testing two main trends can be discerned: experiments evaluating the intrinsic permeability by enforcing unidirectional Stationary Flow conditions (SF), and those aiming at a merely conventional evaluation of the Depth of Penetration (DP) in a massive specimen subject to a predetermined hydraulic head. In the European National standards, mainly based on the

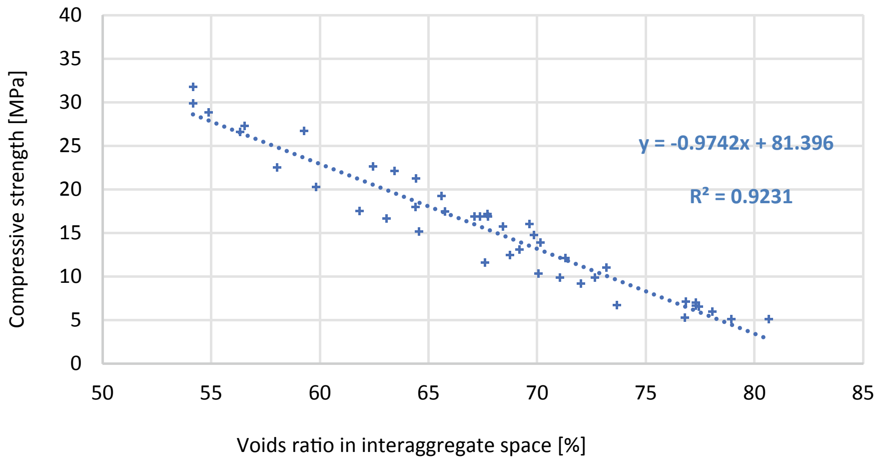

Fig. 5 Concrete strength versus porosity within the cement paste [23]

EN 12,390-8, the significant push towards a conventional testing method is evident. This circumstance may be in part due to the possible simpler execution of DP tests. Unfortunately, the application of these methods to existing structures is problematic due to the strong invasiveness of samples extraction. As it is shown in the previous paragraph, the SF method, regardless of the specific methodology performed, gives results that can be directly correlated with other mechanical properties of the material (i.e., strength) and allows evaluation of permeability in a separate form from capillary head and absorptivity.

4 Discussion

Watertightness has been judged by the Texas highway department to be "*probably the single most important parameter influencing the corrosion of reinforcement in concrete*" [31]. Intrinsic permeability is a parameter more basilar and objective than absorption since the former, differently from the latter, can be regarded as a purely geometrical property of a porous solid medium depending only on the porosity and the specific surface and, as such, less affected by hygrothermal and environmental factors [32, 33] and consequently more easily relatable to durability, as well as to strength and other mechanical properties. Figure 6a shows the semilogarithmic plot of permeability-strength data by Glanville [23] for concretes after 28 days curing, fitted by a linear law. This graph is compared with the plot of Fig. 6b on the right examining the correlation between absorption and strength obtained from data reported by Parrott [34] and Moradian [35, 36]. Glanville's data relative to lower concrete strength, under 10 MPa, have been excluded from the left plot.

Table 2 Current standard permeability methods

Standard	Testing method	Samples	Preconditioning	Apparatus and test duration
CRD C163 [28]	Laboratory, only for w/c ratio 0.4–0.7. Unidirectional flux. Declared steady-state flow	Drilled samples, height 3 times the nominal maximum aggregate size, or 1/2 the diameter of the specimen	Vacuum saturation in deionized water for a minimum of 72 h	Complex apparatus, triaxial cell, use of compressed nitrogen gas source for confining
ASTM C1585 [29]	Absorption, laboratory test, gravimetric measures, complex apparatus	Drilled or molded sample 100 ± 6 mm diameter disc, a length of 50 ± 3 mm	Drying at 50 ± 2 °C and humidity 80% ± 0.5	At least 8 days
ASTM C642 [30]	Absorption, laboratory test, gravimetric measures	Large samples, volume >350 cm^3 (or approximately 800 g)	Oven dried and then completely immersed	
UNI EN 12,390–8 [9]	Constant pressure, 500 kPa, depth penetration measure after splitting	Laboratory-cast cubic, cylindrical or prismatic specimens. Surface to be tested >150 mm, other dimension >100 mm	Not declared	Apparatus ISO/DIS 7032. Duration 72 ± 2 h
DIN 12,390-8 [10]	Laboratory, unidirectional flux, non steady-state, depth penetration measure after splitting	Laboratory-cast cubic, cylindrical or prismatic specimens. Surface to be tested >150 mm, other dimension >100 mm	Not declared	Apparatus ISO/DIS 7032. Duration 72 ± 2 h
BS EN 12,390-8 [8]	No precision data available. Unidirectional flux, non steady-state, depth penetration measure after splitting	Laboratory-cast cubic, cylindrical or prismatic specimens. Surface to be tested >150 mm, other dimensions >100 mm	Not declared	Apparatus ISO/DIS 7032. Duration 72 ± 2 h
RILEM TC 230-PSC [4]	Permeability: increasing pressure (0.15–0,30 MPa), calculation of permeability coefficient. Absorption: gravimetric measures	Circular disks, diameter 150 mm and height 50 mm	Oven dried, 50 °C, test at 20 ± 2 °C	Minimum 14, maximum 27 days, Cembureau permeameter

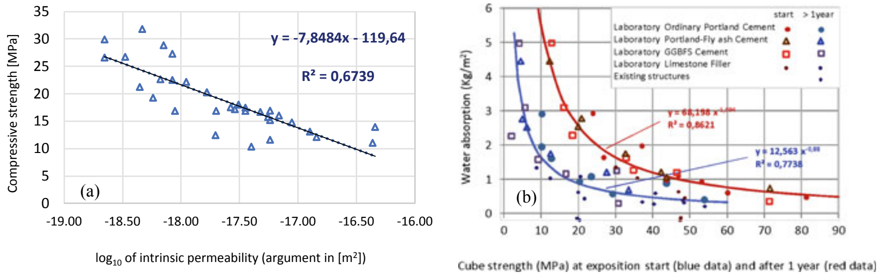

Fig. 6 **a** Least-square linear fitting of concrete strength versus intrinsic permeability ratio (data from [23]); **b** water absorption versus cubic strength in concrete (data from [34–36])

As documented in Table 2, at least along the last three decades of the first half of the last century, specimens cast (or cut) in tile-like form having thickness in the range from approximately 1–5 cm have been ordinarily employed in unidirectional SF permeability measurements, and the ensuing results have been considered reliable enough to support the design and construction of hydraulic infrastructures as important as the Colorado Hoover dam. It is worth noting that, although the testing methods of this period specific for concrete were mainly intended for new-cast materials, and the perspective of assessing the quality of the existing concrete-made built environment was far, such a thickness range suits the opportunity (very desirable at present times) of extracting tile-like specimens from the concrete cover in an existing RC structure to conveniently minimize the first term of the triad of diagnostical decision factors *invasiveness/reliability/insight* symbolized in Fig. 7 (left).

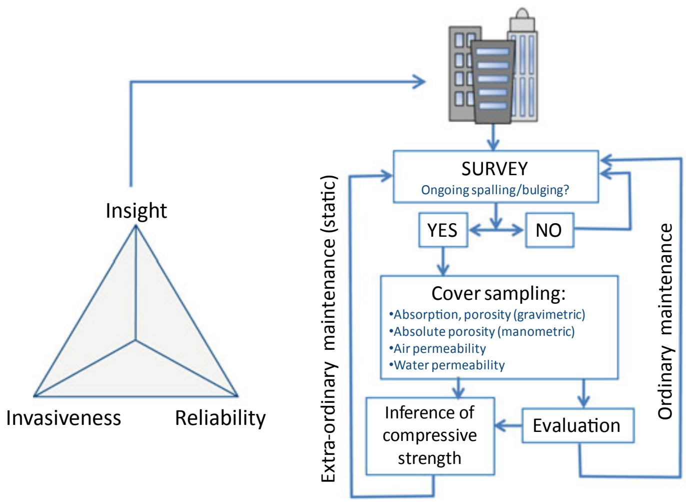

Fig. 7 Preliminary diagnostic decision factors correlated to the proposed flowchart of integrated actions for the diagnosis on an existing RC structure

The withdrawal of large concrete samples for permeability testing, and in general for determination of material properties, appears not advisable owing to its invasiveness. The size of the samples prescribed by current standards appears to be indicated for cast-in-place specimens in new RC constructions only. The review of the experimental methods for permeability determination has been purposedly limited herein to the first half of last century, due to the strong change in the experimental approach occurred in the decades after 1950 during which the bursting increase of RC heritage (even of low quality) has pushed towards laboratory and in-situ methods which probably, at least in the intentions of the regulators, were designed to be more expeditious (see, e.g., Figg [37]). It is the opinion of the authors that an advancement towards a more comprehensive knowledge of the material properties of existing RC constructions can be achieved by exploiting permeability testing strategies implemented in the first half of the past century and which appear also currently implementable for more agile testing of smaller specimens which can be easily obtained, by carving in tile-like shape, from parts of concrete cover. Such testing procedures appear advisable to improve current approaches for permeability testing both by virtue of their reduced invasiveness and of their superior documented reliability and repeatability.

Measurement of permeability, absorption and porosity from cover sampling provides a first valuable basis of diagnostic information of reduced invasiveness cost, up to the limit of near-zero-invasiveness in case of presence of spalled concrete cover regions for which concrete cover disposal and substitution is scheduled. These measures can give to professionals in charge of the structural diagnosis a comprehensive set of information about the physical–mechanical properties of concrete. A testing procedure can be thus designed which envisages measurement of permeability, as well as of absolute porosity and absorptivity, from samples carved from concrete cover by employing the repeatable low-controlled-error methodologies described in detail by Madgwick [12] on thin tile-like specimens. Testing apparatuses similar to those devised by this author or by other authors such as McMyllan and Lyse [24] can be employed for this purpose. From such basis of permeability data, projections can be drawn of the time required for water, oxygen and carbon dioxyde to penetrate up to a sufficient depth (and in sufficient stoichiometric quantity) to determine a degree of corrosion progression significant for possible further concrete spalling and for possible structurally significant reduction of rebar section.

Such a near-zero-invasiveness watertightness database on concrete cover—which at the discretion of the responsible engineer or architect can be optionally integrated and consolidated at a more advance stage of the diagnostic investigation by strength and permeability data from a more invasive campaign—provides in any case a first fundamental pool of information from which strength and other mechanical parameters to be employed in structural assessment can be inferred on a statistical basis from correlations such as those in Fig. 6.

The inferences from permeability of concrete strength and of the time required by oxidizing agents to penetrate across predetermined safety thresholds provide fundamental information for the technical appraisal of the service-life of the structure on the basis of which environmental LCA-based criteria and value-for-money decisions can be implemented to identify (based also on a permeability-based appraisal of replacing materials) optimal OMI and/or EMI interventions and to schedule intervention periodicities.

Figure 7 shows a proposed flowchart for integrating actions of surveying, sampling, LCA evaluation and decision-making on an existing RC construction for which a refurbishment intervention is planned or under appraisal. In this flowchart the 1926 data from BBRS is regarded as a standard reference and the determination of the physical properties obtainable by application of Madgwick's standard to concrete cover specimens is pivotal both for the choice of the structural assessment strategy and for the choice of the refurbishment intervention.

5 Conclusions

The study summarized in this contribution shows, on a historical documental basis, that, while most recent active standards currently consist of measurements of water intake, the preferred practices in the first half of the past century were based on steady-state open-flow methods. Compared to the former, the advantages, emerged from the whole study (Monaco et al. [7]) and herein summarized, of open-flow testing methods are: (1) the possibility of appreciating the solvent action of water in a given mixture and detect the possible presence of significant additions of soluble components; (2) documented higher reliability and repeatability; (3) shorter test durations; (4) lower invasiveness. Lower invasiveness is granted, in particular, by the possibility of employing tile-like specimens, which can be sampled from the outer concrete cover of RC members so as to preserve integrity of the stirrups-confined core, and/or even from spalled regions or from regions undergoing incipient delamination.

Despite being almost one century old, the methodologies described by Madgwick, based on air and water flow, stand out for their relative simplicity without detriment to repeatability and accuracy. The full set of properties investigated by Madgwick (porosity, absolute porosity, permeability, capillary head) defines a group of fundamental diagnostic parameters employable to obtain projections of the time required by water, oxygen and carbon dioxide to penetrate inside the concrete and possibly reach rebars. Permeability data for concrete mixtures reported by Glanville appear consistent with measurements for cement pastes obtained by Powers and coworkers. Since these data are supported by exhaustive information on concrete mixes as well as by compressive strength data, the actual requirements of Life Cycle Impact Assessment for refurbishment of existing buildings could consider these concretes as a standard class to set for comparison with existing concretes having, in general, low-quality mixes affected by uncertainties in mix proportions, use of admixtures (such as gypsum) and manufacturing.

Recommendations for future research proceeding along the direction traced in this study include a theoretical and experimental Life Cycle Impact Assessment of a concrete building element, object of appraisal for ordinary maintenance planning and possible extraordinary maintenance, aiming at careful bounding of experimental and theoretical uncertainties. Such research would benefit from a supplementary investigation of general correlations of practical relevance in air and water permeability testing, specifically suited for thinner tile-like samples, and from a second supplementary investigation examining the specific role of the amount of space available for capillary permeation through the cement paste.

References

1. Neri P., et al.: Verso la valutazione ambientale degli edifici. Life Cycle Assessment a supporto della progettazione eco-sostenibile, Alinea Editrice, Firenze, Italy, (in Italian) (2008)
2. Pradhan, P., Costa, L., Rybski, D., Lucht, W., Kropp, J.P.: A systematic study of sustainable development goal (SDG) interactions. Earth's Future **5**(11), 1169–1179 (2017)
3. Moore, D.G., Klodt, D.T., Hensen, R.D.: Protection of steel in prestressed concrete bridges. National Cooperative Highway Research Program (NCHRP), Report 90 (1970)
4. Beushausen, H., Luco, L.F.: Performance-based specifications and control of concrete durability. RILEM State-of-the-art report TC 230-PSC, 66–72 (2016)
5. Bossio, A., Faella, G., Frunzio, G., Guadagnuolo, M., Serpieri, R.: Diagnostic reliability in the assessment of degradation in precast concrete elements. Infrastructures **6**(11), 164 (2021)
6. Guadagnuolo, M., Donadio, A., Tafuro, A., Faella, G.: Experimental behavior of concrete columns confined by transverse reinforcement with different details. Open Constr. Build. Technol. J. **14**(1) (2020)
7. Monaco, M., Guadagnuolo, M., Frunzio, G., Serpieri, R.: A critical review of one hundred years of permeability tests for the Life Cycle Assessment of concrete structures. (Under review on Construction and Building Materials) (2022)
8. BS EN 12390-8: Testing hardened concrete: depth of penetration of water under pressure (2009)
9. UNI EN 12390-8: Prove sul calcestruzzo indurito - Parte 8: Profondità di penetrazione dell'acqua sotto pressione, Ente Italiano di Normazione (in Italian) (2019)
10. DIN 12390-8: Prüfung von Festbeton - Teil 8: Wassereindringtiefe unter Druck (in German) (2019)
11. EN 12390-8: Testing hardened concrete - Part 8: depth of penetration of water under pressure, CEN- European Committee for Standardization (2019)
12. Madgwick, E.: An investigation into some of the properties of porous building materials. Published in six parts in The London, Edinburgh, and Dublin Philosophical Magazine and Journal of Science: Parts I and II 12:81, 1155–1168; Parts III and IV 13:85, 632–650; Part V 14:89, 180–191; Parts VI and VII 14:91, 486–496 (1932)
13. Palacios Muñoz, B.: A methodology to estimate buildings lifespan and its impact on ICA-the case of buildings with reinforced concrete structure., Ph.D. thesis, University of Zaragoza (2020)
14. Abouhamad, M., Abu-Hamd, M.: Life cycle assessment framework for embodied environmental impacts of building construction systems. Sustainability **13**, 461 (2021)
15. Marsh, R.: Building lifespan: effect on the environmental impact of building components in a Danish perspective. Architect. Eng. Des. Manag. **13**, 80–100 (2017)
16. Palacios-Muñoz, B., Peuportier, B., Gracia-Villa, L., López-Mesa, B.: Sustainability assessment of refurbishment vs. new constructions by means of LCA and durability-based estimations of buildings lifespans: a new approach. Build. Environ. **160**, 106203 (2019)
17. Withey, M.O., Wiepking, C.A.: The permeability of broken stone concrete, University of Wisconsin bulletin, Engineering, Ser. 9, 1245. See also: The Engineer, weekly journal, June 27, 1924, Office for Publication and Advertisements, London, pp. 720–721 (1923)

18. Muskat, M.: The Flow of Homogeneous Fluids Through Porous Media. McGraw-Hill Book Company, Inc. (1937)
19. Klinkenberg, L.J. The permeability of porous media to liquids and gases. In: 'Drilling and Production Practice', New York, American Petroleum Institute, pp. 200–213 (1941)
20. Ruettgers, A., Vidal, W.N., Wing S.P: An investigation of the permeability of mass concrete with particular reference to Boulder dam. In: American Concrete Institute Proceedings, vol. 31, p. 382 (1935)
21. Ruettgers, A., Vidal, W.N., Wing, S.P.: Authors' closure in the discussion of paper: "an investigation of the permeability of mass concrete with particular reference to Boulder dam." Am. Concr. Inst. Proc. **32**, 378 (1936)
22. Powers, T.C., Brownyard, T.L.: Studies on the physical properties of hardened cement pastes. Part 7. Permeability and absorptivity. J. Am. Concr. Inst. **43**, 865–880 (1947)
23. Glanville, W.H.: The permeability of Portland cement concrete. In: Building Research Station, Department of Science and Industrial Research, London, Great Britain, Technical paper no. 3 (Also published in serialized format on Building: the magazine for the architect, builder, property owner and merchant between October 1926-July 1927, Sydney: Building Publishing Co.) (1926, 1931)
24. McMyllan, F.R., Lyse, I.: Some permeability studies of concrete. In: Journal of the American Concrete Institute Proceedings 101–124 (1929)
25. Norton, P.T., Pletta, D.H.: The permeability of gravel concrete. J. Proc. **27**(5), 1093–1132 (1931)
26. Dunagan, W.M., Ernst, G.C.: A study of the permeability of a few integrally water—proofed poncretes. ASTM Proc. **34**(1), 383–392 (1934)
27. Powers, T.C., Copeland, L.E., Hayes, J.C., Mann, H.M.: Permeability of Portland cement paste. J. Am. Concr. Inst. **26**(3), 285–298 (1954)
28. CRD-C163-92: Test Method for Water Permeability osssssf Concrete Using Triaxial Cell, U.S. Army Corps of Engineer (1992)
29. ASTM C1585: Standard Test Method for Measurement of Rate of Absorption of Water by Hydraulic-Cement Concretes, American Society for Testing and Materials (2013)
30. ASTM C642: Standard Test Method for Density, Absorption, and Voids in Hardened Concrete, American Society for Testing and Materials (2021)
31. Houston, J.T., Atimtay, E., Ferguson, P.M.: Corrosion of reinforcing steel embedded in structural concrete. Research Report No. 112-1F. Research Project Number 3-5-68-112. Texas Highway Department (1972)
32. Kozeny, J.: Über kapillare leitung des Wassers im Boden (Aufstieg, Versickerung und Anwendung auf die Bewässerung). Sitzungsberichte der Kaiserlichen Akademie der Wissenschaften in Wien – Mathematisch-NaturwissenSchaftliche Classe, 136 (Abt. IIa) 271–306 (1927)
33. Carman, P.C: Permeability of saturated sands, soils, and clays. J. Agric. Sci. **29**, 262–273 (1939)
34. Parrott, L.J.: Water absorption in cover concrete. Mater. Struct. **25**(5), 284–292 (1992)
35. Moradian, M., Shekarchi, M., Aabdollah, M., Alidadi, R.: Assessment of long-term performance of a 50-year-old jetty in the south of Iran. J. Perform. Constr. Facil. **26**(5), 633–643 (2012)
36. Moradian, M., Chini, M., Shekarchi, M.: Durability performance of a structure made with high-performance concrete and prefabricated elements in a marine environment. J. Perform. Constr. Facil. **29**(6), 04014174, 1–12 (2015)
37. Figg, J.W.: Methods of measuring the air and water permeability of concrete. Mag. Concr. Res. **25**(85), 213–219 (1973)

Physical Methods and Scanning Electron Microscopy for Evaluation of Bioclogging in Geotextiles

Maria Vitoria Morais, Leonardo Marchiori, António Albuquerque, and Victor Cavaleiro

Abstract Wastewater induced biological clogging (or bioclogging) is a common mechanism in geotextiles used in several applications in environmental sanitation and environmental geotechnics works, such as earth-based wastewater treatment plants, earth ponds for mining residues and sanitary landfills. Permeability tests or weighing experiments are currently used for detecting physical clogging but are unable to detect the evolution of clogging caused by microbiological activity (bioclogging). The association of tracer tests, complemented with scanning electron microscopy (SEM) and weighting experiments would be an advance for the understanding and evaluation of bioclogging. Understanding how the biological parameters behave in a restricted way, without interference from physical and chemical parameters, could help in the definition of measures to avoid the problem and increase geotextiles lifespan. Preliminary experiments carried out in Petri dishes with non-woven geotextile and domestic wastewater showed a quick adhesion and growth of biofilm in this material, allowing the development of a laboratory setup for bioclogging tests in porous materials.

Keywords Non-woven geotextiles · Bioclogging · Biofilm · Permeability · SEM · Weighing

1 Introduction

Geotextiles have been extensively used as protection and filter materials in earth-based wastewater treatment plants (e.g. stabilization ponds and constructed wetlands), infiltration systems, dams and ponds for storing mining residues and sanitary landfills. The occurrence of clogging in geotextiles is very common, leading to

M. V. Morais (✉) · L. Marchiori · A. Albuquerque
Civil Engineering and Architecture Department, University of Beira Interior, FibEnTech and GeoBioTec, Covilhã, Portugal
e-mail: vitoria.morais@ubi.pt

V. Cavaleiro
Civil Engineering and Architecture Department, University of Beira Interior, GeoBioTec, Covilhã, Portugal

C. Chastre et al. (eds.), *Testing and Experimentation in Civil Engineering*, RILEM Bookseries 41, https://doi.org/10.1007/978-3-031-29191-3_17

economic losses, negative environmental impacts, and extraction of natural resources for replacing degraded structures and materials.

This phenomenon develops on a microscopic scale, involving the processes of blinding, blocking and internal clogging of the mesh, and has been evaluated using permeability tests and SEM [1–4]. Some methods may be developed together such as weighing method and tracer experiments [5]. Tracer tests, using non-conservative tracers, appear to be more accurate in detecting poor flow distribution and the development of stagnant areas, dead volumes, hydraulic short circuits, internal recirculation, and longitudinal dispersion. Biofilm adhesion and growth in solid surfaces occurs at micro scale when in contact with wastewater biomass. Biological and chemical clogging are connected processes and more complex than physical clogging, as they are developed by the microorganism's activity, essentially bacterial, and are sensitive to temperature variation, organic substrates, inhibitory compounds, oxygen, and nutrients necessary for their maintenance and growth. Therefore, scanning electron microscopy (SEM) techniques may be associated to physical methods to better understand biofilm formation and compounds transport [1, 6].

Preliminary experiments of biofilm colonization in a non-woven geotextile were carried out in Petri dishes, with the use of a synthetic medium, to identify the predominant mechanism of obstruction, through SEM analysis at the end of 15 days, simulating applications of geotextiles as filter material.

2 Methods for Bioclogging Evaluation

2.1 Permeability and Permittivity Tests

To evaluate the clogging rate in geotextiles, the most frequent test is the permeability and permittivity test. According to ASTM D 4491, permeability can be defined as the flow rate of a liquid under a differential pressure through a material, while permittivity is the volumetric flow rate of water per unit of cross-sectional area per unit of load under laminar flow conditions, in the normal direction through a geotextile [9]. Once microorganisms develop in the geotextile mesh, the biofilm fills the geotextile voids and changes its permeability.

ASTM D1987, which test bioclogging of geotextiles or soil-geotextiles filters, is primarily oriented to landfill leachate but can be performed with any liquid sourced from a given location or synthesized from a predetermined mixture of biological microorganisms [7], this test consists on a flow column passing through a specimen, in a cylindrical configuration, internal diameter of 100 mm and height of 200 mm, consisting of a containment ring for placement of the geotextile cell, through of the flow between the upper and lower tubes to allow uniform flow. Some authors use a layer of soil, of variable size, adjustable to achieve the desired compaction in the empty spaces, before and/or after the geotextile layer [10–16]. The proportions of soil/cylinder height range from 2.0/4.0 to 2.5/4.0, the size of the cylinder used for the tests also varies among the studies already carried out [10, 12]. However, there is a warning against the use of this soil/geotextile combination regarding the difficulty of distinguishing which material is clogging, although it is the scheme that best represents the existing filtration systems.

The specimens used for the tests must be sealed with covers that have inlet and outlet piping connections to allow flow from an upper reservoir, in cases of tests with constant head test, or standpipe in test cases with falling head test.

Thus, it is possible to calculate the flow per unit area of the system through the aver-age flow that is measured during the test, where this value is divided by the cross-sectional area of the geotextile for the flow per unit of flow. Reference [7] guides the calculation of permittivity for a constant load using Darcy's formula (Eq. (1)):

$$\frac{k}{e} = \psi = \frac{q}{A(\Delta h)} \tag{1}$$

where q = flow rate (m^3/s); A = cross sectional area (m^2); k = coefficient of permeability (m/s); e = geotextile thickness (m), Δh = change in total head (m); and ψ = permittivity (s^{-1}).

For [7], it can normally take up to 40 days for biological activity to start, grow and reach an equilibrium condition. Although the standard provides the necessary guidelines for the detection of biological clogging, but there is no way to differentiate the parallel occurrence of physical and biochemical clogging. For differentiation it is necessary to verify through scanning electron microscopy [17].

The first permeability tests of geotextile filters in landfills were carried out by [8], in contact with leachate, and showed results of physical clogging with the deposition of larger particles causing the filling of the geotextile and, later, the formation of biofilms was evidenced, generating a clogging due to biological activity.

For [4], regardless of the geotextiles used, the clogging process can be divided into three stages. Being the first stage around 1 day, when a reduction in permeability is al-ready noticed, second stage between 1 to 60 days, permeability can drop steadily, where it is likely that microorganism deaths due to lack of nutrients will occur, and the third stage, after 60 days, when a significant decrease in permeability is noticed.

Silva [18] found a permeability reduction from 1.0×10^{-3} (cm/s) to 1.0×10^{-8} (cm/s) for the time of 35 days. While [15] measured a reduction from 4.0×10^{-3} (m/s) to 3.5×10^{-5} (m/s), [19] measured 8.0×10^{-1} (cm/s) to 6.0×10^{-3} (cm/s) for the same time interval. Geotextile filters in landfill leachate collection systems, when clogged, can suffer a drop in hydraulic conductivity of 2–5 orders of magnitude [20].

2.2 Scanning Electron Microscopy

The use of SEM is a qualitative method that helps in the differentiation of physical, chemical, biological clogging. It is necessary to correlate the SEM images with the permeability results, as the microscopic analysis always depends on the chosen sample and there may be places with greater or lesser density of biofilm, which tends to be a disadvantage in the evaluation of the results [4]. To differentiate physical from biochemical fouling, energy dispersive X-ray spectroscopy (EDS) analyzes can also be used coupled with SEM.

In addition, performing the SEM in the cross section of the geotextile helps in differentiating the clogging mechanisms, whether blocking, blinding or internal clogging. However, despite being a 2D image visualization method, it is possible to work the image angle and, during the execution of the method, it is possible to observe the entire mesh through the microscope and identify the main obturation processes present there.

Some research [3, 18] used SEM for non-woven geotextiles in cross-sections and claimed that it was not possible to perform this type of analysis on geotextiles since preparation phase do not maintain geotextile's structure intact, unable to prepare the specimen. In both studies, it was observed that the internal pores of the geotextile remained open after the permeability test, resulting in the idea of a blinding process.

2.3 Weighing Experiments

The weighing method was used by [12, 21] to measure clogging through the masses, used by Eq. (2). The test consists of weighing the geotextile samples before and after their contact with the liquid in question to be studied.

$$R = \frac{m_1 - m_0}{m_0} \tag{2}$$

where R = clogging rate; m_1 = weight of the clogged geotextile (g); m_0 = weight of the virgin geotextile (g). When R is greater than 0, the mass of the geotextile is greater than its virgin mass, which means that clogging substances are trapped in the geotextile. The geotextile samples must be of the same size so that there is a comparison to be made.

2.4 Tracer Experiments

Tracing tests is one of the methods which evaluate deviations from the ideal flow of a system. Once the flow is considered quasi-permanent, this test can identify the fluid distribution and define a density function of the residence times of the volume elements that is commonly referred to as the residence time distribution curve (RTD) [22–24].

One of the best methods to determine and analyze the flow paths of built-up filters is the evaluation of the variation of RTD moments (mean residence time and variance) through a tracer test, as normally used in reactor processes. Two ideal reactors are commonly considered: the plug-flow reactor and the steady-state continuous-flow reactor [25]. The detection of clogged zones, or dead volume zones, and hydraulic short-circuiting can be detected through the tracer recovery rate (i.e., the ratio between the total mass of tracer detected in the effluent (M_S) and the mass initially introduced (M_0)) [26]. These results help to evaluate the interferences present in the flow of the system. For geotextile filters, it is possible to measure the percentage of interference that biofilms may cause.

Tracer tests involve the injection of a chemical (e.g. a salt such as sodium chloride (NaCl) or a dye such Blue Dextran, both non-conservative tracers), which is not reactive or does not interfere with biological processes inside a geotextile filter. A spot injection (i.e. a quickly injection of a defined volume) or a continuous injection (i.e. an injection of a defined volume in a time t) is normally used at the inlet, being evaluated the system's response at the outlet through water sample collection for plotting the exit concentration–time curves. The variation of the salt or dye concentration in water at the inlet and outlet is measured using a conductivity meter (for salts) or a colorimeter (for dyes). The tests are executed for cleaning conditions (no biofilm) and for different times of biofilm development. As biofilm growth and biologging develops exit curves will be delayed and mean residence time, variance and tracer mass recovery will give answers on the extension of dead-volumes in the system (i.e. the extension of biologging). Despite not being a commonly used test to assess the degree of clogging of geotextiles, tracing tests can identify the mechanisms that cause flow resistance, since the tracer molecules follow different paths through the column vs time. Low values of mass recovery (M_S/M_0) may indicate the occurrence of retention mechanisms in the porous medium.

3 Preliminary Tests on Biofilm Growing in a Non-woven Geotextiles

Preliminary biofilm tests were performed in Petri dishes to assess the potential for biofilm growth on a non-woven geotextile without the presence of compound flow.

Ten samples of non-woven geotextile with a weight of 30 g/m^2 and 90 mm in diameter were cut and placed in Petri dishes. Approximately 1 mL of biomass was added to each of the plates, previously acclimatized in a semi-continuous reactor, from lyophilized sludge from the Boidobra ETAR (Covilhã, Portugal), which contained 6,680 mg/L SSV, 8,420 mg/L SST, 311, 2 mg/L COD, 135.3 mg/L C, 11.2 mg/L N-NH_4, C/N of 12 and pH of 7.4. The biomass was placed above the geotextile, inside an aqueous medium with initial concentrations of 450 mg COD/L, 25 mg NH_4-N/L and 19 mg PO_4-P/L. The Petri dishes were kept closed for a period of 15 days in a refrigerator with a temperature of 20°. At the end of the immersion period, the

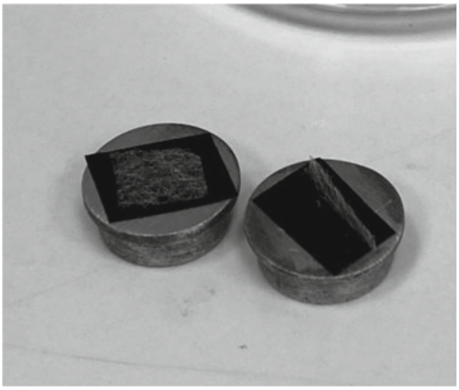

Fig. 1 Geotextile samples cut to metallize in gold

samples that obtained a better development of the biofilm on the geotextile were selected to perform the SEM analysis. Small sections of the geotextile were cut, then covered in a glutaraldehyde solution, where they were left to rest for 12 h. Following the procedure used by [3], the samples were dehydrated in alcohols with concentrations of 50, 60, 70, 80, 90 and 100% of alcohol in mixtures of alcohol: distilled water.

After dehydration, the samples were dried in a controlled environment of 25 ℃ and SEM analyzes were performed. The procedure performed by [3] suggests the use of an oven at 35° for drying, however it was chosen not to do so because the structure of the chosen geotextile was too thin and could damage it. For the SEM procedure, the samples were glued on a carbon-based adhesive tape to bronze pieces (Fig. 1). The Scanning Electron Microscope (SEM) (Hitachi, model S-2700; RONTEC, USA) was used to perform the images.

4 Analysis and Discussion

The SEM images show the formation and stabilization of the biofilm with the immersion of the geotextile for a period of 15 days (Figs. 2 and 3). It is assumed that the material found in the biofilm has its composition organisms of biological origin, since the material introduced was a lyophilized biomass. However, EDS tests are necessary to complement the chemical composition of the biofilm formed.

Figure 4 presents a SEM image of the geotextile in cross section. Although some authors demonstrate some difficulty in performing cross-sectional images, it was not necessary to discard any sample. A scalpel was used to make the cut. It is possible to distinguish the type of clogging, which can be internal clogging, blinding, or blocking. Looking at Figs. 2 and 4 it is possible to admit that the biofilm fills the entire cross-section of the geotextile, causing internal clogging. This type of behavior differs from those found [3] which found blinding, may be due to the weight of the geotextile, since the material tested was much thinner than the used in this study.

Fig. 2 SEM images on geotextile samples (×200)

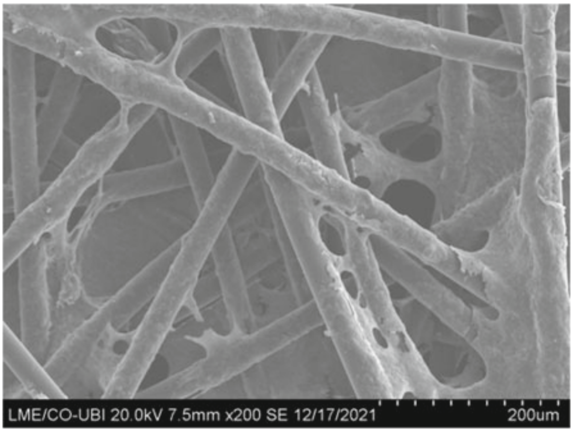

Fig. 3 SEM images on geotextile samples (×500)

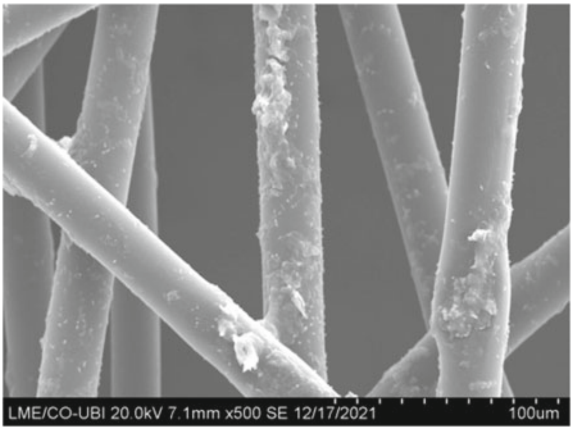

Fig. 4 SEM images on geotextile samples cross section (×85)

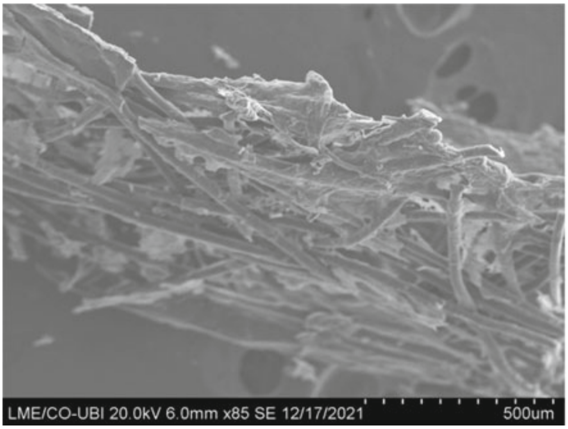

After the results of these tests, a new laboratory setup was developed for allowing permeability tests in association with weighting and tracing, complemented with SEM, in geotextile samples, or other similar porous materials, fed with any type of wastewater, and that is now being used for continuing this research.

5 Conclusions

Despite the effectiveness of the tests above for monitoring the variation of permeability in filter systems and the considerable number of studies on biological clogging, most studies focus only on the concept of permeability, seeking to understand little about biofilms, their formation, composition, and activity. Currently, research showing images generated by SEM is limited to illustrative agents of the evolution of permeability, which sometimes generate ambiguity as to the active clogging mechanism (blinding, blocking and internal clogging of the mesh).

The association of SEM and weighing methods and tracers developed in parallel would increase the knowledge of the development of biofouling, which could be an important step to understand the process of colony formation of these microorganisms and later, develop an interruption methodology for the problem and define measures to prolong geotextiles lifespan. To follow up on this preliminary investigation, an experimental setup was developed that is currently underway, which will allow the development of permeability, weighing tests and traces coupled with SEM analysis.

References

1. Mendonca, M., Ehrlich, M.: Column test studies of ochre biofilm formation in geotextile filters. J. Geotech. Geoenviron. Eng. **132**(10), 1284–1292 (2006). https://doi.org/10.1061/(ASCE)1090-0241(2006)132:10(1284)
2. Sani, A., Scholz, M., Babatunde, A., Wang, Y.: Impact of water quality parameters on the clogging of vertical-flow constructed wetlands treating urban wastewater. Water Air Soil Pollution **224**, 1488 (2013). https://doi.org/10.1007/s11270-013-1488-2
3. Silva, J., Lodi, P.: Evaluation of superficial and internal clogging of geotextiles. Int. J. Civ. Eng. **18**, 1125–1137 (2020). https://doi.org/10.1007/s40999-020-00524-5
4. Palmeira, E., Remigio, A., Ramos, M.: Bernardes, R: a study on biological clogging of nonwoven geotextiles under leachate flow. Geotext. Geomembr. **26**, 205–219 (2008). https://doi.org/10.1016/j.geotexmem.2007.10.006
5. Miszkowska, A., Lenart, S., Koda, E.: Changes of permeability of nonwoven geotextiles due to clogging and cyclic water flow in laboratory conditions. Water **9**(9), 660, 1–15 (2017). https://doi.org/10.3390/w9090660
6. Martinez-Carvajal, G., Oxarango, L., Adrien, J., Molle, P., Forquet, N.: Assessment of X-ray computed tomography to characterize filtering media from vertical flow treatment wetlands at the pore scale. Sci. Total. Environ. **658**, 178–188 (2019). https://doi.org/10.1016/j.scitotenv.2018.12.119
7. ASTM D1987-18: Standard test method for biological clogging of geotextile or soil/geotextile filters

8. Koerner, G.R., Koerner, R.M.: Biological activity and potential remediation involving geotextile landfill leachate filters. In: Geosynthetic Testing for Waste Containment Applications, ASTM STP 1081, American Society for Testing Materials, pp. 313–334 (1992)
9. ASTM D4491-99a: Water Permeability of Geotextiles by Permittivity
10. Abbasi, B. et al: Modeling of permeability reduction in bioclogged porous sediments. J. Geotech. Geoenviron. Eng. **144**(4) 04018016.1–8 (2018). https://doi.org/10.1061/(ASCE)GT.1943-5606.0001869
11. Koerner, R.M., Koerner, G.R.: Landfill leachate clogging of geotextile (and soil) filters. In: Geosynthetic Research Institute, Philadelphia, pp. 1–164 (1991)
12. Guo, C., et al.: Influence of clogging substances on pore characteristics and permeability of geotextile envelopes of subsurface drainage pipes in arid areas. Geotext. Geomembr. **48**(5), 735–746 (2020)
13. Palmeira, E.M.: Fatores Condicionantes do Comportamento de Filtros Geotêxteis. 4o Simpósito Brasileiro de Geossintéticos, Porto Alegre (2003)
14. Yaman, C., Martin, J.P., Korkut, E.: Effects of wastewater filtration on geotextile permeability. Geosynth. Int. **13**(3), 87–97 (2006). https://doi.org/10.1680/gein.2006.13.3.87
15. Palmeira, E.M., Remígio, A.F.N., Ramos, M.L.G., Bernardes, R.S.: A study on biological clogging of nonwoven geotextiles under leachate flow. Geotext. Geomembr. **26**(3), 205–219 (2008). https://doi.org/10.1016/j.geotexmem.2007.10.006
16. Vieira, J.L., Abramento, M., Campos, M.V.W.: Experimental study of clogging in drainage systems (2010)
17. Yaman, C., Martin, J.P., Korkut, E.: Geotextile Biofilters for Wastewater Treatment. North American Geosynthetics Society, Las Vegas (2005)
18. Silva, J.L.V.: Colmatação biológica de geotêxteis. Universidade de São Paulo, master dissertation, São Paulo (2013)
19. Remígio, A.F.N.: Estudo da Colmatação Biológica de Sistemas Filtro-Drenantes Sintéticos de Obras de Disposição de Resíduos Domésticos Urbanos Sob Condições Anaeróbia. Universidade de Brasília, doctoral thesis, Brasilia (2006)
20. Rowe, R.K: Geosynthetics and the minimization of contaminant migration through barrier systems beneath solid waste. In: Sixth International Conference on Geosynthetics (1998)
21. Liu, W., Luo, W., Jia, Z., Bu, F., Pan, Y., Tang, S., Yuan, H., Li, S.: Experimental study on geotextile envelope for subsurface drainage in Yellow River Delta. Nongye Gongcheng Xuebao/Trans. Chin. Soc. Agric. Eng. **29**(18), 109–116 (2013). https://doi.org/10.3969/j.issn.1002-6819.2013.18.014
22. Albuquerque, A., Bandeiras, R.: Analysis of hydrodynamic characteristics of a horizontal subsurface flow constructed wetland. Water Pollut. Nat. Porous Media Differ. Scales **22**, 329–338 (2007)
23. Bandeiras, R.M.: Avaliação da influência da vegetação na variação das características hidrodinâmicas em leitos de escoamento subsuperficial e horizontal. Universidade da Beira Interior, masters dissertation, Covilhã (2009)
24. Albuquerque, A.: Spatial variation of longitudinal dispersion in LECA-based vegetated beds. Defect Diffus. Forum **326–328**, 279–284 (2012). https://doi.org/10.4028/www.scientific.net/DDF.326-328.279
25. Chazarenc, F., Merlin, G., Gonthier, Y.: Hydrodynamics of horizontal subsurface flow constructed wetlands. Ecol. Eng. **21**(2–3), 165–173 (2003). https://doi.org/10.1016/j.ecoleng.2003.12.001
26. Silva, F.C.M.: Avaliação da capacidade reativa de solos residuais destinados à infiltração de águas residuais tratadas. Universidade da Beira Interior, doctoral thesis, Covilhã (2015)

A Comparative Experimental Campaign to Estimate the Normal Interface Stiffness of Dry-Joint Masonry Structures

Carla Colombo, Georgios Vlachakis, Nathanaël Savalle, Anastasios I. Giouvanidis, Luciano Fernandes, Christiam C. Angel, Federica Vadalà, and Paulo B. Lourenço

Abstract Dry-joint masonry structures are particularly vulnerable to earthquakes and their dynamic response strongly depends on the interaction between units. Therefore, the precise characterisation of their behaviour is of paramount importance. This study performs an experimental campaign to estimate the normal interface stiffness of dry-joint masonry specimens. Owing to the lack of standardised experimental procedures, two experimental methods are herein presented, namely deformation-based and vibration-based. Despite their fundamental differences, the results reveal very good agreement between the methods, which, in turn, capture well the marked non-linear dependency between the normal stress and the normal interface stiffness. Importantly, the outcomes of the present study also serve as a validation framework

C. Colombo (✉) · G. Vlachakis · A. I. Giouvanidis · L. Fernandes · C. C. Angel · F. Vadalà · P. B. Lourenço
Department of Civil Engineering, Institute for Sustainability and Innovation in Structural Engineering (ISISE), ARISE, University of Minho Campus de Azurém, 4800-058 Guimarães, Portugal
e-mail: carla.colombo95@gmail.com

G. Vlachakis
e-mail: giorgovlachaki@gmail.com

A. I. Giouvanidis
e-mail: agiouvanidis@civil.uminho.pt

L. Fernandes
e-mail: luciano@civil.uminho.pt

C. C. Angel
e-mail: cc.angel222@gmail.com

F. Vadalà
e-mail: federicavadala03@gmail.com

P. B. Lourenço
e-mail: pbl@civil.uminho.pt

N. Savalle
Université Clermont Auvergne, Clermont Auvergne INP, CNRS, Institut Pascal, 63000 Clermont-Ferrand, France
e-mail: nathanael.savalle@uca.fr

C. Chastre et al. (eds.), *Testing and Experimentation in Civil Engineering*,
RILEM Bookseries 41, https://doi.org/10.1007/978-3-031-29191-3_18

between the two methods, providing confidence for their independent or concurrent use.

Keywords Normal interface stiffness · Dry-joint · Masonry structures · Deformation-based tests · Vibration-based tests

1 Introduction

Dry-joint masonry structures are particularly vulnerable to seismic actions [1], while their safeguard is an important societal demand [2]. Nevertheless, a reliable description of their dynamic behaviour still faces challenges [3]. To this end, numerical models are commonly employed, which require from the user the choice of the units' mechanical properties and the description of their interaction. Overall, the mechanical properties of units have a limited effect on the global behaviour of dry-joint masonry assemblies, in contrast with their interaction which plays a decisive role [4–6]. As a matter of fact, dislocations and failures of such structures occur at the dry-joint interfaces.

One of the main parameters that governs the interaction of dry-joints is the interface stiffness. Despite its strongly non-linear nature [7, 8], researchers commonly assume constant values on an empirical basis [9–11], as dedicated experimental studies are scarce. In fact, there are no standardised experimental procedures available, while the scientific literature is dispersed in different fields of engineering [12]. In more detail, the experimental techniques found in the literature to characterise the interface stiffness may be categorised as: (i) deformation-based [13–16], (ii) vibration-based [10, 15, 17, 18], and (iii) wave-based [19–22]. The deformation-based method measures directly the interface deformation of the joint upon loading. The vibration-based method relies on the identification of the dynamic properties of a system and consequently the estimation of the interface stiffness. Furthermore, the wave-based method quantifies the reflection of waves travelling through the joint and correlates it with the interface stiffness. Finally, it is worth highlighting that there are only a few studies that compared the different techniques without, however, notable outcomes in terms of agreement [14, 15, 23].

This work presents an experimental campaign for the characterisation of the normal interface stiffness of dry-joint limestone specimens. A wide range of the normal stress at the interface is investigated in order to explore and quantify the non-linear response of the normal interface stiffness. Moreover, given the lack of standardised experimental methods and comparative studies, the deformation-based and vibration-based methodologies are herein adopted and compared thoroughly.

2 Experimental Campaign

2.1 Material and Specimens

The material adopted for the tests consists of limestone specimens of density $\rho = 2237.7$ kg/m^3. The experimental campaign involves the adoption of two different specimen geometries in accordance with the type of tests performed. In this regard, Fig. 1a and b show two representative cylinders employed for the deformation-based tests and five representative parallelepiped blocks used for the vibration-based tests, respectively. Moreover, Table 1 provides an overview of the geometrical specifications and the number of tests performed with respect to each method. Note that the dimensions of the specimens are in the order of several centimetres (5–15 cm) and thus of comparable scale with real masonry units (commonly spanning around 5–50 cm). Nevertheless, extrapolating the present results to masonry with larger units should be done with caution since size effects could be influential.

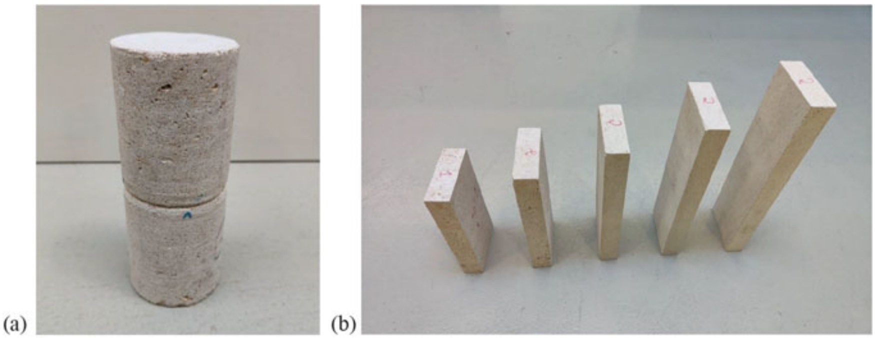

Fig. 1 Limestone specimens: **a** half-cylinders employed for the deformation-based tests and **b** parallelepiped blocks of different heights adopted for the vibration-based tests

Table 1 Geometrical characteristics of all specimens employed and total number of tests

Type of test	Radius R [mm]	Height H [mm]	Width B [mm]	Length L [mm]	Number of tests
Elastic modulus and compressive strength	69.6 (CoV = 0.0%, N = 5)	178.5 (CoV = 1.1%, N = 5)			5 and 5
Deformation-based	64.7 (CoV = 1.2%, N = 7)	85.5 (CoV = 1.8%, N = 7)			10 and 10
Vibration-based		200–750 (N = 60)	49.9 (CoV = 1.7%, N = 60)	150.8 (CoV = 0.5%, N = 60)	210

The evaluation of the mechanical properties of the limestone units involves the determination of their compressive strength *fc* by means of uniaxial compression tests [24] on cylindrical specimens (Table 1). An average compressive strength *fc* equal to 47.6 MPa (CoV = 7.9%, N = 5) is found. In addition, the elastic modulus *E* is evaluated [24]. Uniaxial compression tests up to one third of *fc* are performed, and a mean value of 32.7 GPa is measured (CoV = 4.7%, N = 5) (Table 1).

2.2 Deformation-Based Tests

The deformation-based experimental method is often employed to characterise the interface stiffness of dry-joints [13–16]. This approach consists of imposing normal forces at the joint and measuring the corresponding relative displacement in the direction of loading. The normal interface stiffness k_n is evaluated through the joint closure $u_{j,n}$ that occurs when normal stress σ_n is applied (Fig. 2a):

$$k_n = \frac{d\sigma_n}{du_{j,n}} \tag{1}$$

Similarly to Young's modulus evaluations [24], the experimental setup consists of an actuator loading the specimen in the normal direction, while it records the force through the actuator's load cell and the displacement through external Linear Variable Differential Transformers (LVDTs) (Fig. 2b). This time, the setup involves the introduction of a dry-joint by stacking two cylindrical specimens, whose dimensions are reported in Table 1. The displacement record of the LVDTs, u_{LVDT}, includes two kinds of compliance: one attributed to the deformability of the bodies and another one stemming from the interface. Therefore, the joint closure $u_{j,n}$ can be obtained

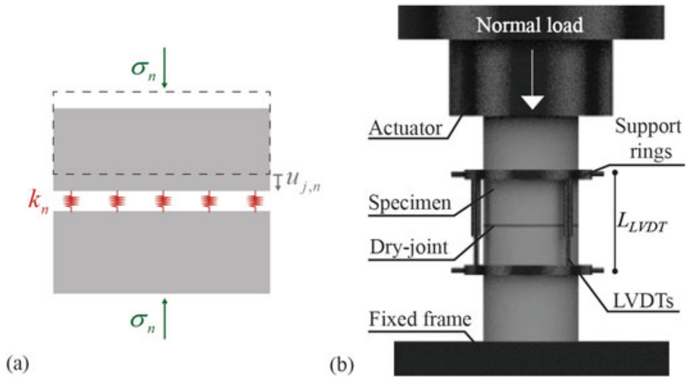

Fig. 2 **a** Mechanical scheme describing the normal behaviour of the interface upon compression, and **b** joint-closure experimental setup

as follows:

$$u_{j,n} = u_{LVDT} - \frac{\sigma_n \cdot L_{LVDT}}{E} \tag{2}$$

where L_{LVDT} represents the specimen's height monitored by the LVDTs (Fig. 2b), while E is the elastic modulus of the material.

Two control procedures are adopted to investigate accurately the joint response for low and high stress levels. For high stress levels, force-controlled (FC) tests are employed. They consist of five loading–unloading cycles, which initiate in a contact state between the specimen and the actuator and proceed with progressive loading/unloading cycles up to one third of fc. Nevertheless, since FC tests necessarily retain contact between the specimens, they are unable to estimate low stress levels with accuracy. In this regard, displacement-controlled (DC) protocols are employed. Similarly, five loading–unloading cycles compose the DC tests, yet each cycle is independently performed, with the actuator detached from the specimen both at the initiation and the end of the test. Overall, ten FC and ten DC tests are conducted, each one of them composed of five loading–unloading cycles.

2.3 Vibration-Based Tests

The vibration-based experimental method constitutes an alternative approach for characterising the interface stiffness of dry-joints [10, 15, 17, 18]. Herein, the dry-joint under investigation is obtained from two specimens in contact (Fig. 3a): (i) a stocky bottom specimen glued to the ground, and (ii) a slender top specimen free-standing on the former. Four piezoelectric accelerometers measure the system dynamics. More specifically, one accelerometer is located in the bottom specimen to monitor the substructure dynamics (not related to the dry-joint under investigation), two accelerometers are placed anti-diametrically on the top of the free-standing specimen in the y-y direction, while a fourth accelerometer records in the x-x direction (Fig. 3a). The acquisition duration is 30 min with a sampling rate of 2000 Hz.

Two different experimental setups are adopted in this work. The first focuses on the influence of the normal stress variation on the normal interface stiffness. More specifically, five specimens of the same dimensions B = 49.3 mm (CoV = 0.3%, N = 5), L = 151.0 mm (CoV = 0.6%, N = 5), H = 398.6 mm (CoV = 0.1%, N = 5) are loaded with progressive addition of steel plates (maximum of nine), each one of mass equal to 10.91 kg (Fig. 3a). Such configuration allows the study of normal stress at the interface up to 0.14 MPa. Finally, the connection between the plates and the top block is ensured by two glued L-profiles (Fig. 3a). The second experimental setup aims to investigate the effect of the surface variability on the normal interface stiffness. For this purpose, 60 specimens of equal plan dimensions and variable height (Table 1) are tested. The variation of the specimens allows investigating the influence

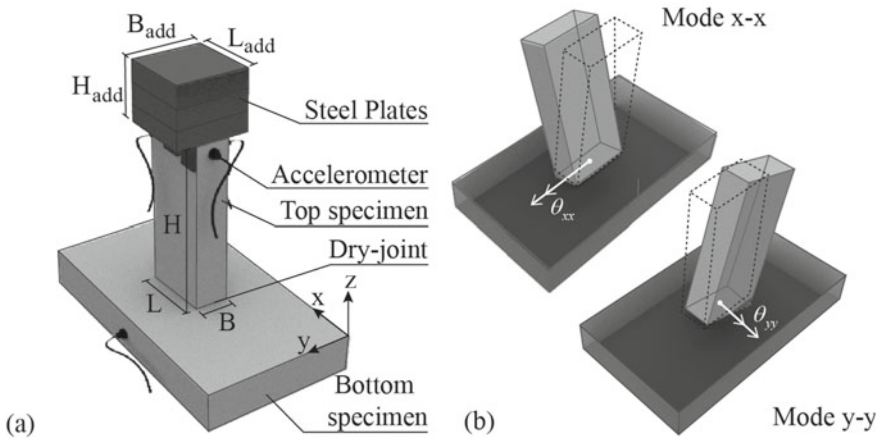

Fig. 3 Vibration-based test: **a** experimental setup, and **b** rotational mode shapes over the x-x and y-y axes

of surface variability on the results, while the variation of their height permits the examination of a very low stress window between 0.004 MPa to 0.016 MPa.

The normal interface stiffness is estimated by studying the system dynamics adopting the Enhanced Frequency Domain Decomposition (EFDD) method [25], which provides experimental evidence of the system's frequency of vibration f_{exp}. Assuming fixity of the bottom specimen and rigidity of the free-standing specimen, two rotational modes correlated to k_n are identified, being over the x-x and y-y axes, respectively (Fig. 3b). The generalised mass M_{gen} and generalised stiffness K_{gen} of each mode can be estimated as the moment of inertia of the top specimen over the interface and the second moment of area of the interface, respectively. More specifically, for the mode over the x-x axis they read:

$$M_{gen} = m\left(\frac{1}{12}B^2 + \frac{1}{3}H^2\right) + \left\{m_{add}\left(\frac{1}{12}\left(B_{add}^2 + H_{add}^2\right) + \left(H + \frac{H_{add}}{2}\right)^2\right)\right\} \tag{3}$$

$$K_{gen} = \frac{1}{12}k_n B^3 L \tag{4}$$

and respectively for the mode over the y-y axis:

$$M_{gen} = m\left(\frac{1}{12}L^2 + \frac{1}{3}H^2\right) + \left\{m_{add}\left(\frac{1}{12}\left(L_{add}^2 + H_{add}^2\right) + \left(H + \frac{H_{add}}{2}\right)^2\right)\right\} \tag{5}$$

$$K_{gen} = \frac{1}{12}k_n B L^3 \tag{6}$$

where m is the mass of the specimen, m_{add} is the additional mass of the steel plates, and B_{add}, L_{add} and H_{add} are the geometrical dimension of the additional mass (Fig. 3a). Hence, the normal interface stiffness k_n is computed by introducing Eqs. (3)–(6) into Eq. (7):

$$K_{gen,i} = M_{gen,i} \cdot \left(2 \cdot \pi \cdot f_{exp,i}\right)^2 \tag{7}$$

3 Normal Interface Stiffness

3.1 Deformation-Based Results

Figure 4a plots the normal interface stiffness k_n against the normal stress σ_n of one representative FC joint closure test for high stress levels under loading and unloading cycles. The joint shows a marked non-linear response with a stiffer behaviour as the normal stress σ_n increases. This is attributed to the increase of the actual area in contact at the micro-scale of the asperities [8, 26]. Furthermore, the joint appears to follow different load paths upon primitive loading, i.e. under normal stresses not previously attained, (e.g. A to B$^-$ (in red) or D to E (in yellow)), and non-primitive unloading (e.g. B$^+$ to C (in blue)) or reloading (e.g. C to D (in green)). In more detail, the primitive loading path (e.g. A to B$^-$ (in red) or D to E (in yellow)) presents lower values in comparison with the non-primitive loading paths (e.g. B$^+$ to C (in blue), or C to D (in green)). Moreover, the transition from primitive loading to unloading (e.g. B$^-$ to B$^+$) presents a discontinuity in the interface stiffness, while the transition from non-primitive to primitive loading (e.g. C to D (in green)) occurs in a smooth manner.

Figure 4b collects the results of the normal interface stiffness k_n from all the joint closure tests against the normal stress σ_n. This includes the tests for both the FC tests for higher stress levels and the DC tests for lower stress levels, while a further distinction is adopted for the primitive or non-primitive loading state. Figure 4b indicates a good continuity among the two test typologies (FC and DC), with the primitive loading determining a lower bound for the interface stiffness. Overall, the normal interface stiffness shows a gradual increase with the normal stress. Note that the marked scatter of the non-primitive stiffness data stems from the cyclic reverse of the tests (alike B$^-$ to B$^+$ of Fig. 4a).

3.2 Vibration-Based Results

Figure 5a plots the modal frequencies identified after the vibration-based tests against the normal stress σ_n applied at the dry-joint. Herein, a distinction is made among the groups of tests that included the variation of slenderness and the addition of steel plates. As expected, for each normal stress level, the frequency of mode x-x

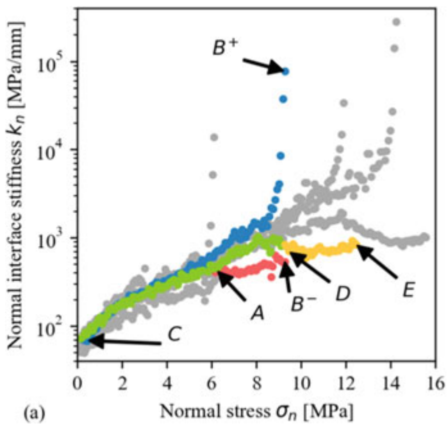

Fig. 4 Normal interface stiffness of **a** one representative FC joint closure test under loading–unloading cycles for high stress levels, and **b** experimental data after 20 joint closure tests, both for FC tests for higher stress levels and the DC tests for lower stress levels

precedes the one of y-y, while both decrease with the increase of the specimens' mass (which also causes an increase of the normal stress σ_n). Following the methodology described in Sect. 2.3 (i.e. Eqs. (3)–(7)), Fig. 5b transforms the experimental frequencies of Fig. 5a to values of normal interface stiffness k_n. Figure 5b shows that the two identified modes (i.e. over the x-x and y-y axes) provide equivalent estimations of the normal interface stiffness, with the mode x-x having a slightly bigger scatter. Similarly with the deformation-based outcomes (Fig. 4), the interface stiffness increases with the normal stress, even for the low range of normal stress variation presented herein.

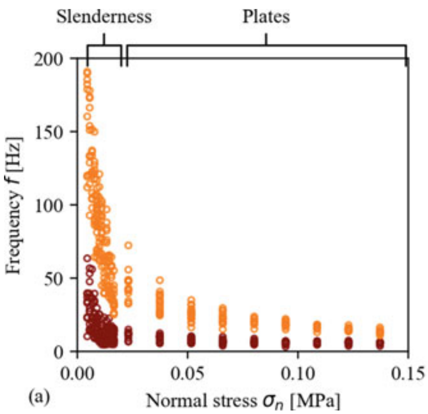

Fig. 5 **a** Identified modal frequencies after 210 vibration-based tests, and **b** the corresponding normal interface stiffness

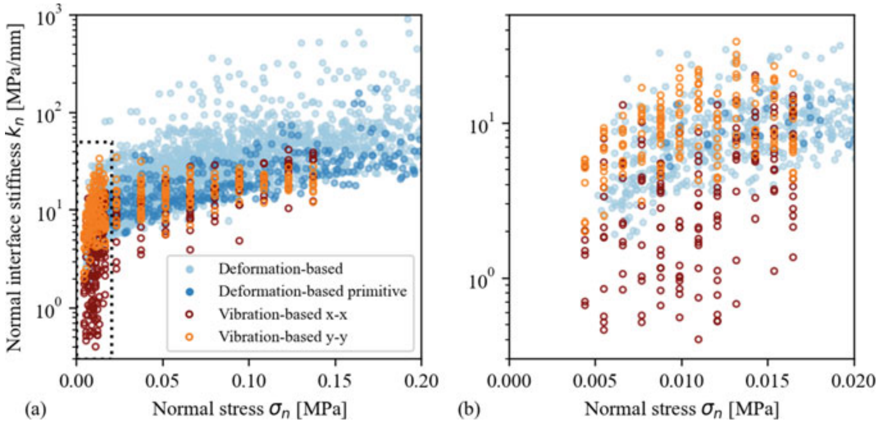

Fig. 6 **a** Comparison of deformation-based and vibration-based methods in estimating the normal interface stiffness, and **b** closer look of **a**

3.3 Comparison of Deformation- and Vibration-Based Results

Considering the fundamentally different nature of the two experimental methods adopted, i.e. the deformation-based and vibration-based, it is of paramount importance to cross-validate their estimations. Therefore, Fig. 6 presents the normal interface stiffness k_n acquired by both methods, against the acting normal stress σ_n at the dry-joint. In general, Fig. 6 indicates a very good agreement between the two methods, both in terms of measured values and dependency on the normal stress. In more detail, the vibration-based results appear to match better with the primitive loading data of the deformation-based approach, while the mode y-y of the vibration-based approach seems to provide a closer estimation in comparison with the deformation-based outcomes. To the best of the author's knowledge, such a good agreement has not been attained in literature before. Furthermore, the comparison of Fig. 6 demonstrates that the two methods could be used alternatively by researchers to estimate the normal interface stiffness, depending on their available resources (e.g. equipment, specimens, time, etc.) or expected outcomes.

4 Conclusions

This study provides a detailed experimental quantification of the normal interface stiffness of dry-joint limestone specimens. Given the lack of standardised experimental procedures, two conceptually different approaches are benchmarked and consequently compared, i.e. the deformation-based and vibration-based methods.

The deformation-based method estimates the interface stiffness by measuring the stress-deformation joint closure response. The tests show a marked non-linear response, with an increase of the normal interface stiffness together with the normal stress. Moreover, the interface stiffness shows a strong dependency on the loading path, being smaller upon primitive loading with respect to non-primitive loading or unloading.

The vibration-based method estimates the normal interface stiffness by measuring the dynamic characteristics of a system with a dry-joint. Two vibrational modes are identified herein and in turn employed to compute the normal interface stiffness. Both modes provide similar interface stiffness estimations and thus may be used in conjunction.

Finally, despite their fundamental differences, the two adopted methods show notable agreement in estimating the normal interface stiffness. This match, on one hand cross-validates the two methods and on the other hand provides confidence in their alternative use.

Future research on the topic could aim for the characterisation of the tangential interface stiffness, or extend the comparison with wave-based techniques. Eventually, the outcomes of the present campaign could be utilised to construct experimentally informed constitutive laws.

References

1. Vlachakis, G., Vlachaki, E., Lourenço, P.B.: Learning from failure: damage and failure of masonry structures, after the 2017 Lesvos earthquake (Greece). Eng. Fail. Anal. **117**, 104803 (2020). https://doi.org/10.1016/j.engfailanal.2020.104803
2. Roca, P., Lourenço, P.B., Gaetani, A.: Historic Construction and Conservation (2019). https://doi.org/10.1201/9780429052767
3. De Felice, G., De Santis, S., Lourenço, P.B., Mendes, N.: Methods and challenges for the seismic assessment of historic masonry structures. Int. J. Archit. Herit. **11**(1), 143–160 (2017). https://doi.org/10.1080/15583058.2016.1238976
4. ElGawady, M.A., Ma, Q., Butterworth, J.W., Ingham, J.M.: Effects of interface material on the performance of free rocking blocks. Earthq. Eng. Struct. Dyn. **40**(4), 375–392 (2011). https://doi.org/10.1002/eqe.1025
5. Mehrotra, A., DeJong, M.J.: A methodology to account for interface flexibility and crushing effects in multi-block masonry collapse mechanisms. Meccanica **55**(6), 1237–1261 (2020). https://doi.org/10.1007/s11012-020-01161-x
6. Vlachakis, G., Giouvanidis, A.I., Mehrotra, A., Lourenço, P.B.: Numerical block-based simulation of rocking structures using a novel universal viscous damping model. J. Eng. Mech. **147**(11), 04021089 (2021). https://doi.org/10.1061/(asce)em.1943-7889.0001985
7. Biwa, S., Hiraiwa, S., Matsumoto, E.: Stiffness evaluation of contacting surfaces by bulk and interface waves. Ultrasonics **47**(1–4), 123–129 (2007). https://doi.org/10.1016/j.ultras.2007.08.005
8. Kim, J.Y., Baltazar, A., Rokhlin, S.I.: Ultrasonic assessment of rough surface contact between solids from elastoplastic loading-unloading hysteresis cycle. J. Mech. Phys. Solids **52**(8), 1911–1934 (2004). https://doi.org/10.1016/j.jmps.2004.01.006
9. Pulatsu, B., Bretas, E.M., Lourenço, P.B.: Discrete element modeling of masonry structures: Validation and application. Earthq. Struct. **11**(4), 563–582 (2016). https://doi.org/10.12989/eas.2016.11.4.563

10. Kim, J., Lorenzoni, F., Salvalaggio, M., Valluzzi, M.R.: Seismic vulnerability assessment of free-standing massive masonry columns by the 3D discrete element method. Eng. Struct. **246**, 113004 (2021). https://doi.org/10.1016/j.engstruct.2021.113004
11. Al Shawa, O., de Felice, G., Mauro, A., Sorrentino, L.: Out-of-plane seismic behaviour of rocking masonry walls. Earthq. Eng. Struct. Dyn. **41**, 949–968 (2012). https://doi.org/10.1002/eqe
12. Vakis, A.I., et al.: Modeling and simulation in tribology across scales: an overview. Tribol. Int. **125**(February), 169–199 (2018). https://doi.org/10.1016/j.triboint.2018.02.005
13. Bandis, S.C., Lumsden, A.C., Barton, N.R.: Fundamentals of rock joint deformation. Int. J. Rock Mech. Min. Sci. **20**(6), 249–268 (1983). https://doi.org/10.1016/0148-9062(83)90595-8
14. Fantetti, A., Mariani, S., Pesaresi, L., Nowell, D., Cegla, F., Schwingshackl, C.: Ultrasonic monitoring of friction contacts during shear vibration cycles. Mech. Syst. Signal Process. **161**, 107966 (2021). https://doi.org/10.1016/j.ymssp.2021.107966
15. Gimpl, V., Fantetti, A., Klaassen, S.W.B., Schwingshackl, C.W., Rixen, D.J.: Contact stiffness of jointed interfaces: a comparison of dynamic substructuring techniques with frictional hysteresis measurements. Mech. Syst. Signal Process. **171**, 108896 (2022). https://doi.org/10.1016/j.ymssp.2022.108896
16. Kulatilake, P.H.S.W., Shreedharan, S., Sherizadeh, T., Shu, B., Xing, Y., He, P.: Laboratory estimation of rock joint stiffness and frictional parameters. Geotech. Geol. Eng. **34**(6), 1723–1735 (2016). https://doi.org/10.1007/s10706-016-9984-y
17. Shi, X., Polycarpou, A.A.: Measurement and modeling of normal contact stiffness and contact damping at the meso scale. J. Vib. Acoust. Trans. ASME **127**(1), 52–60 (2005). https://doi.org/10.1115/1.1857920
18. Zhao, G., Xiong, Z., Jin, X., Hou, L., Gao, W.: Prediction of contact stiffness in bolted interface with natural frequency experiment and FE analysis. Tribol. Int. **127**(June), 157–164 (2018). https://doi.org/10.1016/j.triboint.2018.05.044
19. Baltazar, A., Rokhlin, S.I., Pecorari, C.: On the relationship between ultrasonic and micromechanical properties of contacting rough surfaces. J. Mech. Phys. Solids **50**(7), 1397–1416 (2002). https://doi.org/10.1016/S0022-5096(01)00119-3
20. Drinkwater, B.W., Dwyer-Joyce, R.S., Cawley, P.: A study of the interaction between ultrasound and a partially contacting solid-solid interface. Proc. R. Soc. A Math. Phys. Eng. Sci. **452**, 2613–2628 (1955, 1996). https://doi.org/10.1098/rspa.1996.0139
21. Dwyer-Joyce, R.S., Drinkwater, B.W., Quinn, A.M.: The use of ultrasound in the investigation of rough surface interfaces. J. Tribol. **123**(1), 8–16 (2001). https://doi.org/10.1115/1.1330740
22. Nagy, P.B.: Ultrasonic classification of imperfect interfaces. J. Nondestruct. Eval. **11**(3–4), 127–139 (1992). https://doi.org/10.1007/BF00566404
23. Mulvihill, D.M., Brunskill, H., Kartal, M.E., Dwyer-Joyce, R.S., Nowell, D.: A comparison of contact stiffness measurements obtained by the digital image correlation and ultrasound techniques. Exp. Mech. **53**(7), 1245–1263 (2013). https://doi.org/10.1007/s11340-013-9718-5
24. ASTM D7012-14E1: Standard test methods for compressive strength and elastic moduli of intact rock core specimens under varying states of stress and temperatures. Am. Soc. Test. Mater. (2017). https://doi.org/10.1520/D7012-14E01
25. Magalhães, F., Cunha, Á., Caetano, E., Brincker, R.: Damping estimation using free decays and ambient vibration tests. Mech. Syst. Signal Process. **24**(5), 1274–1290 (2010). https://doi.org/10.1016/j.ymssp.2009.02.011
26. Greenwood, J.A., Williamson, J.B.P.: Contact of nominally flat surfaces. Proc. R. Soc. London. Ser. A. Math. Phys. Sci. **295**(1442), 300–319 (1966). https://doi.org/10.1098/rspa.1966.0242

Thermal Properties of Polymer Floor Coating with Alternative Granite Powder Filler

Kamil Krzywiński, Łukasz Sadowski, Katarzyna Fedoruk, and Adam Sieradzki

Abstract The study presents the results of the thermal analysis of epoxy resin coating and waste granite powder as an alternative filler to quartz sand. For thermal analysis, differential scanning calorimetry and dilatometry method was used. The results show that adding granite powder to epoxy resin does not change glass transition temperature. It only reduces the specific heat capacity of the composite.

Keywords Epoxy resin · Industrial floor · Granite powder · Wastes

1 Introduction

The top layer of floor construction depends on the purpose. In housing construction, investors prefer to use wooden panels or ceramic tiles. In the storage hall, users need durable cementitious slabs. However, floors in high-quality industry buildings are often finished with epoxy resin (ER) coating. The epoxy resin protects lower layers (mostly concrete slabs) against chemicals, fuels, and oil aggression. The polymer layer allows for obtaining chemical aggression resistance. It is easy to clean up and can create a free-joint floor. The epoxy resin has higher mechanical properties than the concrete substrate [1, 2]. Therefore, it enhances the durability of floor construction.

Usually, epoxy resin coating has from 1 to 3 mm in height. To obtain a thick epoxy resin coating, it is necessary to use a filler, for example, quartz sand. It also reduces production costs. However, this material is not renewable. Also, in many countries, the natural sources of sand are dwindling. Thus, the quartz sand should be replaced with any type of waste [3] with similar properties. In Poland, this kind

K. Krzywiński (✉) · Ł. Sadowski
Department of Materials Engineering and Construction Processes, Wroclaw University of Science and Technology, Wroclaw, Poland
e-mail: kamil.krzywinski@pwr.edu.pl

K. Fedoruk · A. Sieradzki
Department of Experimental Physics, Wroclaw University of Science and Technology, Wroclaw, Poland

C. Chastre et al. (eds.), *Testing and Experimentation in Civil Engineering*,
RILEM Bookseries 41, https://doi.org/10.1007/978-3-031-29191-3_19

of waste can be granite powder (GP) [4] obtained during the mechanical treatment of granite blocks or slabs and raw material extraction. It has similar properties to quartz sand. Therefore, the authors used waste granite powder as a potential filler in an epoxy resin coating.

The glass transition temperature T_g of epoxy resin can be affected by filler type [5, 6], curing temperature [7, 8], or hardener type [9, 10]. Accordingly, in this study, the authors presented studies related to the thermal properties of epoxy resin to consider its effect on glass transition temperature, which is crucial for mechanical properties. A decrease of T_g of epoxy resin is undesirable. It is because epoxy resin loses its mechanical properties [9], changing its state from glassy to rubbery.

2 Materials and Methods

2.1 Epoxy Resin and Granite Powder

The commercially available epoxy resin Sto BB OS (2020) was used in this study. The epoxy resin was prepared using components A and B with a weight ratio of 100:25. The components were mechanically mixed for 3 min using a drilling machine to obtain a uniform consistency. After 7 days of curing, specimens obtained designed strength.

The waste granite powder sourced from Strzegom city, Poland, was used as a potential filler for epoxy resin coating. The material was stored in an oven for 1 day at 90 °C before it was used in epoxy resin. The maximum sieve size of the filler is 0.14 mm. Figure 1 presents the size distribution of granite powder.

Three specimens with different content of granite powder were prepared for analysis. One reference sample without GP was also prepared to verify influence of filler on thermal properties of the composite. Table 1 presents the weight ratio of all prepared specimens.

2.2 Thermal Analysis

The thermal properties of epoxy resin were studied using differential scanning calorimetry. The measurements were carried out with the METTLER-TOLEDO calorimeter using the FRS5 + sensor. Small particles of epoxy resin with a size of 1–3 mm and a weight of ~20 mg were locked in an aluminum pan. The measurements were carried out in a temperature range from −100 °C to 130 °C (with a temperature ramp of 10 °C/min).

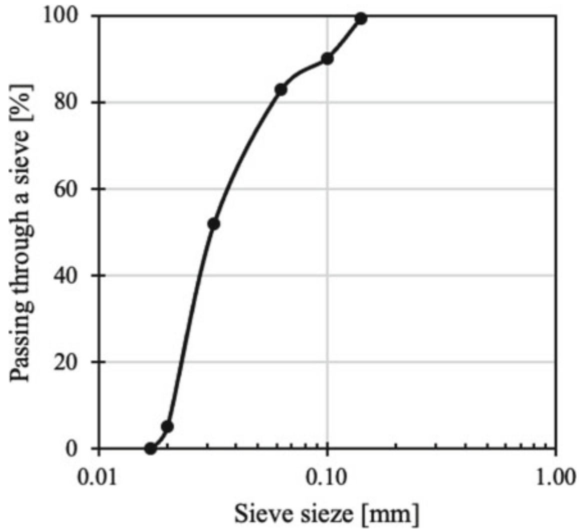

Fig. 1 Particle size distribution of granite powder

Table 1 Description of the specimens with weight ratio

Specimen	Weight ratio		
	Epoxy resin	Hardener	Granite powder (GP)
ER_REF	100	25	0
ER_2.5%GP	100	25	2.5
ER_10%GP	100	25	10
ER_15%GP	100	25	15
ER_30%GP	100	25	30

3 Results and Discussion

The differential scanning calorimetry results show that specific heat capacity c grows with increasing temperature (Fig. 2). The non-linear growth of c is typical for polymer materials [10]. A lower value of c for granite powder decreases the specific heat capacity of the composite. The difference between c curves in the temperature range from −20 °C to 80 °C is not constant. In lower temperatures (below 30°C), the Δc is more constant than those above 30 °C.

The obtained results made it possible to calculate the average c for three stages (glassy state, glass transition, and rubbery state). Equations of average c for each epoxy are presented in Table 2. For each specimen, glass transition T_g was also estimated. It is visible that granite powder does not affect T_g. All glass transition temperature results are in the range of 34.5 °C with an average difference of 0.86% compared to the reference sample. The glass transition temperature is close to the curing temperature, which significantly affects obtained results. Similar behavior was observed by Carbas et al. [7]. It can be stated that specimens with granite powder

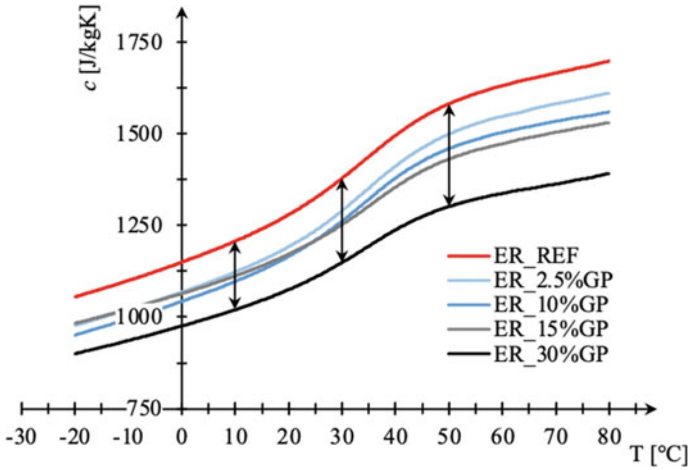

Fig. 2 Specific heat capacity of epoxy resin modified with granite powder

exhibit similar thermal behavior to reference epoxy resin. The glass transition zone is very similar for each specimen. The only significant change is a decrease of the specific heat capacity *c,* which in 34 °C is 1426, 1339, 1309, and 1185 J/kgK for specimen with the addition of 0, 2.5, 10, 15, and 30% or granite powder, respectively.

Table 2 presents trend line equations presented in Fig. 3. Compared to reference, ER specimens with GP have a lower slope. It can also be noticed in Fig. 4. The lower slope of the trend line means that specific heat capacity growth is reduced for specimens with a higher volume of granite powder. It explains the difference between Δc in −20 °C and 80 °C for ER_REF and ER_30%GP, which is 156 and 306 J/kgK. Trend lines slop decreases for the glassy and rubbery state. The slope for the reference sample is lower in glass transition temperature compared to specimens with 2.5 and 10% of GP.

Table 2 The trend line equations for three temperature stages

Specimen	Glassy state	Glass transition	Rubbery state
ER_REF	y = 5.49x + 1155	y = 11.8x + 1024	y = 3.44x + 1424
ER_2.5%GP	y = 5.26x + 1073	y = 12.3x + 920	y = 3.29x + 1349
ER_10%GP	y = 5.25x + 1047	y = 11.9x + 904	y = 2.93x + 1328
ER_15%GP	y = 4.63x + 1068	y = 10.4x + 939	y = 2.99x + 1293
ER_30%GP	y = 4.29x + 979	y = 9.0x + 877	y = 2.68x + 1175

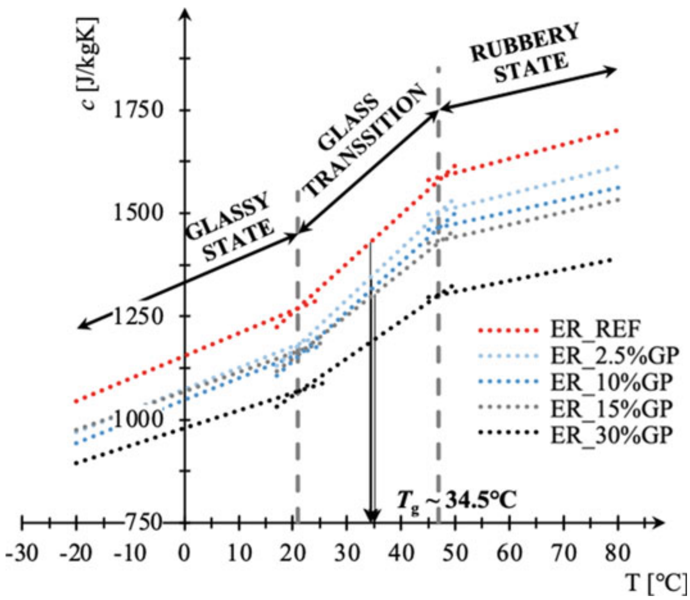

Fig. 3 Trend lines of specific heat capacity for three different stages

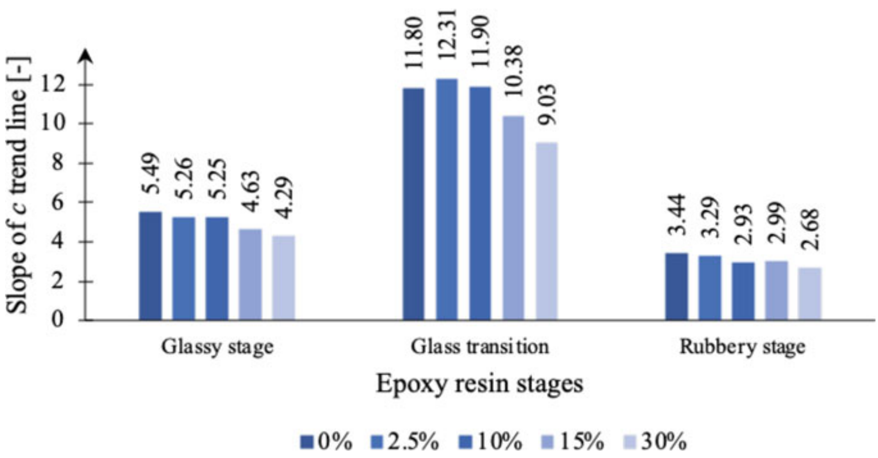

Fig. 4 The slope of the *c* trend lines is taken from Table 2

4 Conclusions

Based on the obtained results, it can be stated that the addition of granite powder to epoxy resin matrix does not decrease glass transition temperature T_g. It means that the mechanical properties of polymer composite cannot be affected by the change of thermal properties of composite because glass transition temperature is stable for each epoxy resin with a different volume of granite powder. Adding GP decreases specific heat capacity, which can also affect thermal conductivity. Moreover, composites with a higher volume of GP tend to decrease the slope of c growth. This trend can be related to changes in thermal conductivity at different temperatures.

Future works should focus on analyzing the mechanical properties of epoxy resin composite with different volumes of granite powder. Tests should be carried out in temperatures related to a glassy state, glass transition, and rubbery state.

Acknowledgements The authors received funding from the project supported by the National Centre for Research and Development, Poland [grant no. LIDER/35/0130/L-11/19/NCBR/2020 “The use of granite powder waste for the production of selected construction products”].

References

1. Krzywiński, K., Sadowski, Ł, Stefaniuk, D., Obrosov, A., Weiß, S.: Engineering and manufacturing technology of green epoxy resin coatings modified with recycled fine aggregates. Int. J. Precis. Eng. Manuf.-Green Technol. **9**(1), 253–271 (2022)
2. El Awad, S.: The Inference of the Mechanical Properties of Materials at Micro and Meso-Scale via the Micro-Bending Technique (Doctoral dissertation, University of Houston, 2020)
3. Chowaniec, A., Sadowski, Ł, Żak, A.: The chemical and microstructural analysis of the adhesive properties of epoxy resin coatings modified using waste glass powder. Appl. Surf. Sci. **504**, 144373 (2020)
4. Chajec, A.: Granite powder vs. fly ash for the sustainable production of air-cured cementitious mortars. Materials **14**(5), 1208 (2021)
5. Krzywiński, K., Sieradzki, A., Sadowski, Ł, Królicka, A., Chastre, C.: Thermal wear of epoxy composite modified with rutile titanium dioxide. Compos. Struct. **282**, 115127 (2022)
6. Chowaniec, A.: Using waste limestone powder as filler in a toxic epoxy resin coating and its influence on adhesive properties. Chem. Eng. Trans. **88**, 1063–1068 (2021)
7. Carbas, R.J.C., Marques, E.A.S., Da Silva, L.F.M., Lopes, A.M.: Effect of cure temperature on the glass transition temperature and mechanical properties of epoxy adhesives. J. Adhes. **90**(1), 104–119 (2014)
8. Jin, N.J., Yeon, J., Seung, I., Yeon, K.S.: Effects of curing temperature and hardener type on the mechanical properties of bisphenol F-type epoxy resin concrete. Constr. Build. Mater. **156**, 933–943 (2017)
9. Gupta, V.B., Drzal, L.T., Lee, C.C., Rich, M.J.: The temperature-dependence of some mechanical properties of a cured epoxy resin system. Polym. Eng. Sci. **25**(13), 812–823 (1985)
10. Teixeira, P., Akhavan-Safar, A., Carbas, R.J., da Silva, L.F.: Influence of the cure state on mechanical properties of an epoxy-based adhesive: experimental characterization and numerical simulation. Polym. Adv. Technol. **33**(4), 1163–1170 (2022)

Absorption Tests of Binary and Ternary Mortar Mixtures and Their Relationship with Compressive Strength

Nemesio Daza, Yoleimy Ávila, Andrés Guzmán, and Joaquín Abellán-Garcia

Abstract As the environmental and circular economy issues have become one of the most important worldwide matters, the researchers have focused on reducing the carbon footprint of all kinds of cementitious materials. One of the most effective ways to reduce CO_2 emissions is the partial substitution of cement with mineral admixtures in concrete and mortars without jeopardizing their mechanical and durability properties. The positive impact on the environment is especially relevant when those mineral admixtures come from industrial byproducts. However, international standards do not offer sufficient guidelines to characterize mortar mixtures that incorporate byproducts as mineral admixtures. Nonetheless, some of those waste mineral admixtures allow for improving properties, such as capillary absorption and mechanical performance in mixtures. The method proposed in this research allows establishing the absorption capacity of the mortar through an experimental setup based on the porosity of the specimens. This research found a relationship between absorption and compressive strength, validating the inverse relationship between both properties and preparing the path for new standardizations for the mineral admixtures used.

Keywords Mortars · Waste mineral admixtures · Capillary absorption · Compressive strength · Sustainability

N. Daza (✉)
Gemas, Universidad Simón Bolívar, Barranquilla, Colombia
e-mail: nemesiod@uninorte.edu.co

Y. Ávila
CERIS-Civil Engineering Research and Innovation for Sustainability, Instituto Superior Técnico, Universidade de Lisboa, Lisboa, Portugal

Y. Ávila · A. Guzmán · J. Abellán-Garcia
Department of Civil and Environmental Engineering, Universidad del Norte, Barranquilla, Colombia

C. Chastre et al. (eds.), *Testing and Experimentation in Civil Engineering*,
RILEM Bookseries 41, https://doi.org/10.1007/978-3-031-29191-3_20

1 Introduction

At present, the scope of application of international standards is limited to traditional materials (i.e. cement, sand), which indirectly excludes new materials that have become relevant in the construction sector. For instance, ASTM C1403 [1], present the method for the water absorption rate by capillarity of mortar mixtures, which is determined with 50 mm side cubic specimens. The standard provides a methodology applicable to mixtures made from cement (OPC: Ordinary Portland Cement), sand, and water, with a slump flow of 110 ± 5 mm. However, it is not stated if this standard works in the same way in mortar mixes made with low w/c ratios (i.e., 0.485) and incorporating waste minerals admixtures. This limitation can also be observed in EN-1015–18:2003 [2] test method. The study of capillarity in binary and ternary mortar mixtures (sand, water, cement, and mineral admixtures) should be subjected to standard to provide an appropriate characterization of these mixtures compared to traditional mortar mixtures. This requirement is mainly because the addition of mineral admixtures could significantly affect the mechanical and durability properties of the cementitious material [3, 4]. These results, considering existing guidelines, should be consistent with the theory that mentions an inversely proportional relationship between capillarity and compressive strength of mortar mixtures. Furthermore, some of the waste mineral admixtures utilized in the last decades could have a nonconventional chemical composition, such as the fluid catalytic cracking catalyst residue, that lead to reactions in the mortar that affect the material's behavior [5].

Therefore, adapting current standards and standards allows the development of new study techniques updated to new robust technologies [6], whose primary focus is to reduce the carbon footprint of mortars, thus promoting sustainable development [7]. The absorption of water by capillarity test in mortar mixtures allows inferring the durability of the material [8]. In aggressive environments (i.e., sulfate attack, carbonation), a high absorption capacity is directly proportional to the number of interconnected pores, which would facilitate the internal migration of agents that weaken the structure [9]. However, the mortar mixtures made from the incorporation of treated industrial byproducts could lead to a cementitious material whose mechanical behavior also evolves differently over time depending on its curing ages.

Mineral admixtures with pozzolanic features, such as silica fume, rice husk ash, fly ash, or sludge ash, when incorporated into the mortar mixtures, allow to obtain an increase in the ultimate strength [3, 4, 8]. Moreover, their incorporation in most cases improves durability properties because they allow a greater formation of C–S–H within the cementitious matrix, fulfilling the internal voids and leading to a less porous material with fewer entrances for harmful agents [9]. In contrast to the above, other mineral admixtures could negatively affect some of mortars' mechanical or/and durability properties. For instance, the addition of phosphogypsum (PG), a byproduct generated from the phosphorus fertilizer industry, has been analyzed as a mineral admixture for mortar and pastes. Bhadauria and Thakare [10] reported that incorporating 5% of PG improves up to 4.32% of the compressive strength at 28 d of curing, while at three days of curing, there was an increase of 35.50%. However, the same authors also mention that the replacement of OPC by 10% of PG decreases the compressive strength of the mortar by 25.42% and 18.38% at 3 and 28 d, respectively. Hence, their study proved that a waste mineral admixture could provide the mortar with different mechanical behaviors at different dosages and curing ages.

This research studied the relationship between water absorption by capillarity and compressive strength in binary and ternary mortars made with nitrophosphogypsum (NPG) and water treatment plant sludge ash (CS, from *calcined sludge*, at 600 °C for 2 h) as mineral admixtures, with a w/c ratio of 0.485.

2 Materials and Methods

2.1 Materials

In the present study, an ordinary Portland cement (OPC) provided by the company ARGOS was employed. As mineral admixtures, two industrial byproducts were used as partial replacement of cement (10% weight to weight): CS obtained by calcination of water treatment plant sludge (WTPS) and NPG. The NPG samples were collected at the production site of a fertilizer generating industry located in Barranquilla, Colombia. The WTPS were supplied by the drinking-water-treatment plant of the local city utility company, which takes the water from the Magdalena River. The WTPS were received wet and were exposed to the sun for 36 h. For its part, the NPG was received dry. Both byproducts were individually calcined at 600 °C for 2 h, in a Nabertherm oven with a heating rate of the oven around 10 °C/min (600 °C/h) by using a cooling rate of −5 °C. /min (−300 °C/h) and forced draft (see Fig. 1a and b). Then, the calcined products were crushed in a Retsch model PM200 crushing mortar and passed through the No. 200 sieve. Once the materials were treated, the NPG and the CS obtained a yield of 72.26% and 9.71%, respectively.

The density of the waste mineral admixtures was determined from the parameters established in ASTM C188 [11], obtaining values of 2.83 and 2.82 g/cm^3 for NPG and CS, respectively. Figure 2 shows the scanning electron microscopy (SEM) for the mineral admixtures considered, performed on the JEOL JSM-5600 model SEM equipment. NPG presented a crystalline morphology with an elongated appearance, with the presence of impurities adhered to the surface of the material. On the other hand, it was observed that the CS presented an inhomogeneous morphology in some areas with needle-like shapes and flat and porous surfaces. The most representative chemical oxides present for NPG are: 52.74% SO_3, 39.80% CaO and 2.48% SiO_2. Additionally, for CS are: 61.59% SiO_2, 21.36% Al_2O_3 and 10.83% Fe_2O_3.

On the other hand, the fine aggregate used comes from the quarries of Santo Tomás, Atlántico. This sand has a fineness modulus of 1.98 according to standard ASTM C-136 [12], a specific gravity of 2.61, water absorption of 0.78%, and humidity of 3.86% according to the ASTM C128 [13]. This sand was purchased from a commercial establishment. Finally, the freshwater used complies with the guidelines established in the ASTM C1602 [14].

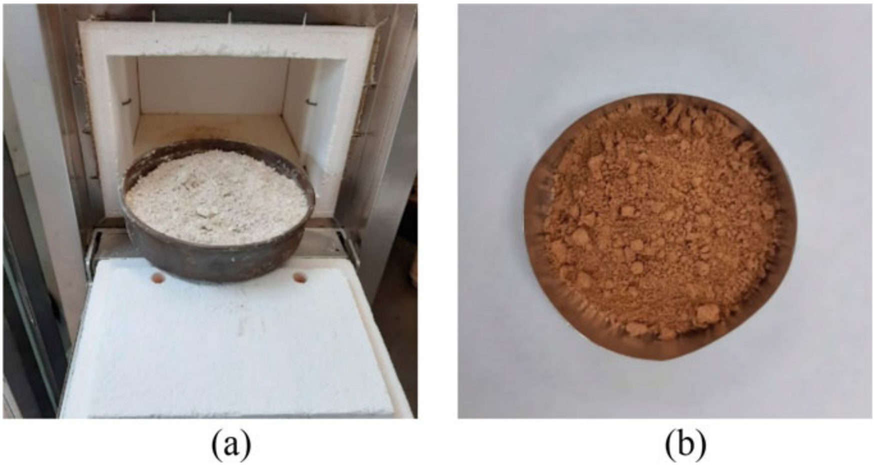

Fig. 1 Treated NPG (**a**) and treated WTPS (**b**)

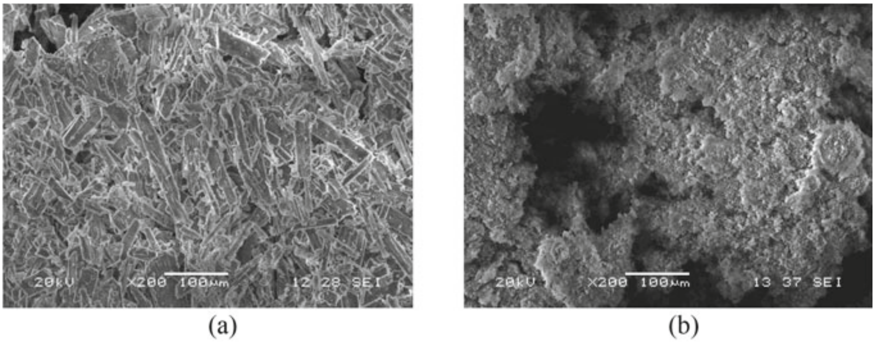

Fig. 2 SEM images: **a** NPG, **b** CS

2.2 Mix Design, Mixing Procedure, and Testing Methods

Mortar specimens with 50 mm × 50 mm × 50 mm dimensions were manufactured for the testing procedures. The mixing, molding, and curing procedures were conducted following the standards ASTM C305 [15], ASTM C109 [16], and ASTM C511 [17], respectively. The proportion in weight used to prepare the mortar mix design was 1:3, one part of binder for every three parts of sand. For its part, the water to binder ratio was maintained at a value of 0.485. Table 1 shows the proportions of the materials used for each of the types of mortar. Five types of mixtures were produced with different percentages of NPG and CS as cement replacement: 10% NPG with 0% CS (MN10S0), 10% CS with 0% NPG (MN0S10), 5% NPG with 5% CS (MN5S5), 0% NPG with 15% CS (MN0S15), and 5% NPG with 10% CS (MN5S10). A control test was elaborated only with OPC (M0) to establish comparisons.

Table 1 Mix proportions in kg/m^3 of mortars

Mix	Sand	OPC	NPG	CS	Water
M0	1833.28	666.65	0.00	0.00	325.84
MN10S0	1833.28	599.98	66.66	0.00	325.84
MN0S10	1833.28	599.98	0.00	66.66	325.84
MN5S5	1833.28	599.98	33.33	33.33	325.84
MN0S15	1833.28	566.65	0.00	100.00	325.84
MN5S10	1833.28	566.65	33.33	66.66	325.84

For each of the considered dosage mixtures, six specimens were executed. Three specimens were used for the absorption test and the leftover three for the compressive strength tests. Both tests were conducted at 28 d. The compressive strength of the mortar mixtures was determined after 28 days of curing as established in the standard ASTM C109 [16].

For the absorption test, the procedure continues as follows. After the specified time, the absorption specimens were dried in the oven at a temperature of 100 °C (Fig. 3a)) until weighing at two-hour intervals showed an increase in mass loss of less than 0.2%. Fulfilling the above, they were removed from the oven and cooled at room conditions for 2 h (24 ± 8 °C and relative humidity of less than 80%). After that, the specimens were placed on 3 mm diameter separators into a container, ensuring a distance between the lower face of the specimens and the surface of 3 mm and immersion of 3.0 ± 0.5 mm (Fig. 3b)). Once the assembly was done, the container was sealed to prevent water evaporation (Fig. 3c)). Specimens were weighed after 0.25 h ± 0.5 min, 1 h ± 2 min, four h ± 10 min, and 24 ± 15 min. Before each weighing, surface water was removed. Then, the measured weight was recorded. After each weighing, specimens were put back into the water setup assembly until the minimum immersion height of 6 mm was obtained according to the previous specifications.

(a) (b) (c)

Fig. 3 Oven drying of specimens (**a**), test setup (**b**), covering to avoid water evaporation (**c**)

The measurement of capillarity absorption (A_T) of 50 mm cubic mortar specimens was estimated according to Eq. (1). W_T y W_0 are the final and initial masses of the specimen for each instant in time *T; L_1* y L_2 correspond to the submerged superficial lengths of the sample. Equation (2) corresponds to the calculation of the relative percentage of absorption $\%A_T$, where A_s represents the capillary water absorption of the mortar at 24 h. Also, the compressive strength measurement in MPa (σ) was measured with a compression testing machine, as established in ASTM C109 [16].

$$A_T = (W_T - W_0)/(L_1 \times L_2) \tag{1}$$

$$\%A_T = (A_T - A_s) \times 100\% \tag{2}$$

Finally, a trend line was drawn between the capillary absorption capacity and the compressive strength of the mortar specimens.

3 Results and Discussion

3.1 Effect of Supplementary Cementitious Materials on the Capillary Absorption

The results of the capillary absorption (A_T) test and standard deviation (Sd) for each instant T are presented in Tables 2 and 3. After 24 h of testing, the capillary absorption coefficients for all mixtures ranged between 0.890–1.018 g/cm^2.

The results obtained from the compressive strength are presented in Table 4. It is observed that the control test obtained the highest compressive strength capacity among the other mixes.

As shown in Fig. 4, the water absorption coefficient is not directly proportional to the percentage of OPC replacement. However, the graph shows similar trends for all mortar dosages with the measurement times. The MN10S0 mixture obtained

Table 2 Capillary absorption (A_T) in g/cm^2

Mix	Time (h)					
	0	0.25	0.5	1	4	24
M0	0.000	0.201	0.280	0.371	0.640	0.912
MN10S0	0.000	0.182	0.310	0.448	0.812	1.018
MN0S10	0.000	0.166	0.252	0.348	0.619	0.892
MN5S5	0.000	0.302	0.381	0.486	0.789	0.943
MN0S15	0.000	0.249	0.319	0.418	0.710	0.900
MN5S10	0.000	0.303	0.371	0.463	0.754	0.905

Table 3 Standard deviation of A_T in g/cm^2

Mix	Time (h)					
	0	0.25	0.5	1	4	24
M0	0.000	0.006	0.009	0.014	0.024	0.002
MN10S0	0.000	0.010	0.013	0.018	0.026	0.007
MN5S5	0.000	0.009	0.010	0.016	0.012	0.007
MN5S10	0.000	0.063	0.035	0.024	0.023	0.013
MN0S10	0.000	0.005	0.010	0.008	0.005	0.007
MN0S15	0.000	0.010	0.012	0.015	0.007	0.007

Table 4 Compressive strength (average and standard deviation) at 28d

Max	CStr (MPa)		
M0	34.01	±	1.69
MN10S0	17.67	±	0.76
MN5S5	28.86	±	1.63
MN5S10	32.68	±	0.30
MN0S10	31.32	±	0.16
MN0S15	28.21	±	2.28

a water absorption coefficient 11.61% higher than the control mixture, contrasting with the result obtained by MN5S5 (only 3.40% higher than M0). The latter shows that although both typologies were made with a 10% replacement of OPC (weight to weight ratio), when the replacement is made entirely by NPG, the absorption capacity of the mortar mixtures increases. The mixtures made with CS as mineral admixture showed a slight decrease in the absorption coefficient. This is mainly due to the pozzolanic reaction given between portlandite - and free SiO_2 in the CS [18], leading to a greater formation of C–S–H, which is the main hydration product associated with the ultimate strength of the mortar; furthermore, this reaction densifies the network of pores in the cementitious matrix. As a consequence, a smaller pore diameter reduces the mixture's final absorption [3, 19]. As shown in Table 2, the incorporation of CS in dosages higher than 10% produces a change in the trend, increasing the AT value as the CS percentage rises [20]. This can be associated with the necessity of portlandite crystals (CH) to trigger the pozzolanic reaction. As the amount of cement reduces, so does the CH, and beyond that inflection point of partial substitution, further cement replacement does not produce more C-S–H gel but the contrary [21, 22].

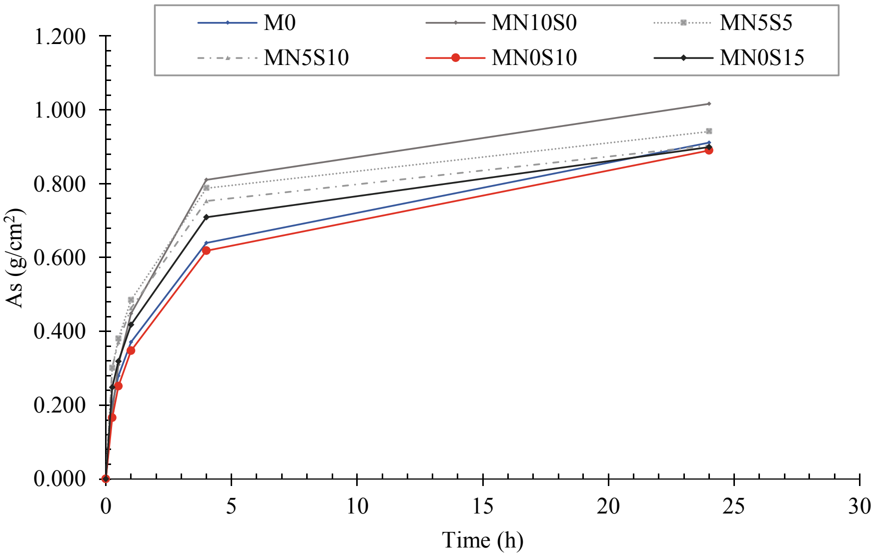

Fig. 4 Absorption curve by dosage

3.2 Relationship Between Absorption and Compressive Strength

Figure 5 shows the relationship between the capillary absorption of water and the compressive strength for all mixtures made at 28 d of curing. The results obtained confirm an inversely proportional relationship between water absorption and the compressive strength of the mortar mixtures after 28 days of curing [23].

Due to the pozzolanic properties of CS, the free calcium hydroxides -CH- and free SiO_2 give rise to the formation of C–S–H, which is the main hydration product associated with the final strength of the mortar [18]. In the same way, it densifies the network of pores in the cementing matrix. However, because NPG interacts faster than OPC with water, the formation of gypsum takes place, which has a crystalline and fragile structure, conducting to the formation of ettringite (C–A–$\overline{S}$–H), therefore leading to a decrease in the compressive strength of the mortar [9]. The implementation of mortars with high absorption properties negatively affects the processes derived from corrosion because it can store sulfates and chlorides in its pore network, deteriorating the mortar and avoiding its function as a protective layer of structural concrete [9], even giving way to other pathologies such as the formation of secondary ettringite.

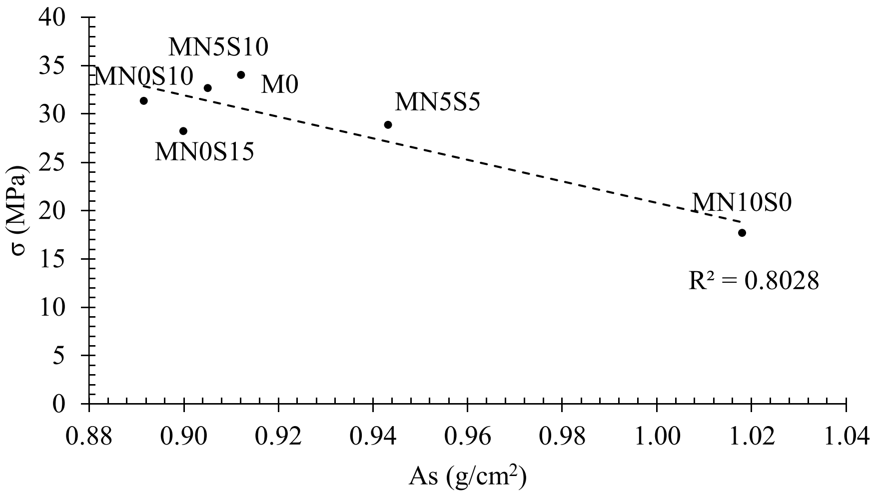

Fig. 5 Compressive strength versus absorption (28 d)

4 Conclusions

The present investigation evaluated the applicability of the current standards to measure the properties of compressive strength and absorption of mortar mixtures when incorporating mineral admixtures obtained from industry byproducts. This work focused its efforts on analyzing the variability of results according to the type of mixture used. From the analysis, the following conclusions can be drawn:

- A relationship between compressive strength and absorption, measured according to current standards, is maintained in the binary and ternary mixtures proposed in this research.
- According to the OPC replacement ratio, binary and ternary mortar mixes made with CS and NPG did not show a linear behavior. The latter can be ascribed to the different chemical, physical and mechanical characteristics of the waste mineral admixtures added to the mortar, thereby leading to different chemical reactions inside the cementitious material.

The following recommendations and future work are given:

- The estimation of the coefficient of capillary absorption based on the current standards allows a general view of the compressive strength results for mortar mixtures. However, it is recommended that the ages and measurement times be adjusted according to the characteristics of the waste mineral admixtures when used.
- Analogously to the case of the compressive strength test, the recording of the capillary absorption coefficient at different curing ages should also be considered. The latter is based on the fact that each waste mineral admixture, depending on

its chemical composition, generates a different reaction kinetics than that of the OPC in conjunction with the other materials that compound the mortar mix.

- Future research that attempts to standardize methods of characterizing and evaluating the performance of waste mineral admixtures when used in mortar and concrete mixtures is encouraged. Green construction is growing rapidly, and current methods will not be appropriate in the near future for establishing comparisons between supplementary cementitious materials or “green” mineral admixtures.

References

1. ASTM International: ASTM C1403- 15: Standard Test Method for Rate of Water Absorption of Masonry Mortars. West Conshohocken, PA: ASTM International, 2015. https://compass.astm.org/EDIT/html_annot.cgi?C1403+15
2. Asociación Española de Normalización y Certificación: UNE-EN 1015-18:2003: Methods of test for mortar for masonry - Part 18: Determination of water absorption coefficient due to capillary action of hardened mortar. AENOR, 2003
3. Lothenbach, B., Scrivener, K., Hooton, R.D.: Supplementary cementitious materials. Cem. Concr. Res. **41**(12), 1244–1256 (2011). https://doi.org/10.1016/j.cemconres.2010.12.001
4. de Godoy, L.G.G., Rohden, A.B., Garcez, M.R., Da Dalt, S., Bonan Gomes, L.: Production of supplementary cementitious material as a sustainable management strategy for water treatment sludge waste. Case Stud. Constr. Mater. **12**, e00329 (2020). https://doi.org/10.1016/j.cscm.2020.e00329
5. Torres Castellanos, N., Fernández Gómez, J.A., Nuñez Lopez, A.M.: Effect of FC3R on the properties of ultra-high-performance concrete with recycled glass. DYNA **86**(211), 84–93 (2019). https://doi.org/10.15446/dyna.v86n211.79596
6. Kawalkar, R., Dubey, H.K., Lokhande, S.P.: A review for advancements in standardization for additive manufacturing. Mater. Today Proc. **50**, 1983–1990 (2022). https://doi.org/10.1016/j.matpr.2021.09.333
7. Vishwakarma, V., Uthaman, S.: Environmental impact of sustainable green concrete. In: Liew, M.S., Nguyen-Tri, P., Nguyen, T.A., Kakooei, S. (Eds.) Smart Nanoconcretes and Cement-Based Materials, Elsevier, pp. 241–255 (2020). https://doi.org/10.1016/B978-0-12-817854-6.00009-X
8. Gao, Y., Cui, X., Lu, N., Hou, S., He, Z., Liang, C.: Effect of recycled powders on the mechanical properties and durability of fully recycled fiber-reinforced mortar. J. Build. Eng. **45**, 103574 (2022). https://doi.org/10.1016/j.jobe.2021.103574
9. Alaghebandian, N., Mirvalad, S., Javid, A.A.S.: Durability of self-consolidating concrete and mortar mixtures containing ternary and quaternary cement blends exposed to simulated marine environment. Constr. Build. Mater. **259**, 119767 (2020). https://doi.org/10.1016/j.conbuildmat.2020.119767
10. Bhadauria, S., Thakare, R.B.: Utilisation of phosphogypsum in cement mortar and concrete. In: 31st Conference on our world in Concrete & Structures, Singapore, 2006, p. 9. http://cipremier.com/100031016
11. ASTM International: ASTM C188-17: Standard Test Method for Density of Hydraulic Cement. ASTM International, West Conshohocken, PA (2017). https://doi.org/10.1520/C0188-17
12. ASTM International: ASTM C136/C136M-19: Standard Test Method for Sieve Analysis of Fine and Coarse Aggregates. West Conshohocken, PA: ASTM International. https://www.astm.org/Standards/C136

13. ASTM International: ASTM C128-15: Standard Test Method for Relative Density (Specific Gravity) and Absorption of Fine Aggregate. ASTM International, West Conshohocken, PA (2015). https://doi.org/10.1520/C0128-15
14. ASTM International: ASTM C1602-C1602M-18: Standard Specification for Mixing Water Used in the Production of Hydraulic Cement ConcreteStandard Specification for Mixing Water Used in the Production of Hydraulic Cement Concrete. ASTM International, West Conshohocken, PA (2018). https://doi.org/10.1520/C0511-21
15. ASTM International. ASTM C305-20: Standard Practice for Mechanical Mixing of Hydraulic Cement Pastes and Mortars of Plastic Consistency. ASTM International, West Conshohocken, PA (2020). https://doi.org/10.1520/C0305-20
16. ASTM International: ASTM C109/C109M - 21: Standard Test Method for Compressive Strength of Hydraulic Cement Mortars (Using 2-in. or [50-mm] Cube Specimens). ASTM International, West Conshohocken, PA (2021). https://doi.org/10.1520/C0109_C0109M-21
17. ASTM International: ASTM C511–21: Standard Specification for Mixing Rooms, Moist Cabinets, Moist Rooms, and Water Storage Tanks Used in the Testing of Hydraulic Cements and Concretes. ASTM International, West Conshohocken, PA (2021). https://doi.org/10.1520/C0511-21
18. de Medeiros-Junior, R.A., Munhoz, G. da S., de Medeiros, M.H.F.: Correlations between water absorption, electrical resistivity and compressive strength of concrete with different contents of pozzolan. Rev. ALCONPAT **9**(2) (2019). https://doi.org/10.21041/ra.v9i2.335
19. Adewuyi, A., Baithshupile, O., Franklin, S.O., Udasi, G.K., Kanyeto, O.J.: Assessment of potentials of treated wastewater sludge ash as a partial replacement of cement. J. Multidiscip. Eng. Sci. Stud. **2**(12), 5 (2016). http://www.jmess.org/wp-content/uploads/2016/12/JMESSP13420253.pdf
20. Liu, Y., et al.: Effect of alum sludge ash on the high-temperature resistance of mortar. Resour. Conserv. Recycl. **176**, 105958 (2022). https://doi.org/10.1016/j.resconrec.2021.105958
21. Krejcirikova, B., Ottosen, L.M., Kirkelund, G.M., Rode, C., Peuhkuri, R.: Characterization of sewage sludge ash and its effect on moisture physics of mortar. J. Build. Eng. **21**, 396–403 (2019). https://doi.org/10.1016/j.jobe.2018.10.021
22. de Lima, F., Ingunza, D., del Pilar, M.: Effects of Sewage Sludge Ashes Addition in Portland Cement Concretes, pp. 189–191 (2015). https://doi.org/10.2991/cmes-15.2015.55
23. da Silva Calderón, B., García, A., Pineda, P., García, R.: Valorization of phosphogypsum in cement-based materials: limits and potential in eco-efficient construction. J. Build. Eng. 102506 (2021). https://doi.org/10.1016/j.jobe.2021.102506

Precision of Test Methods for Hot Mix Asphalt

José Neves, Cláudia Silva, and Ana Duarte

Abstract The paper presents the Portuguese experience in the precision evaluation of test methods for hot mix asphalt (AC 14 surf and AC 20 base). The repeatability and reproducibility values were determined based on Proficiency Test Schemes involving several laboratories. The tests were performed from 2007 until 2021. The paper analyses the soluble binder content, maximum density (Method A), bulk density (Procedure B), and Marshall properties (stability and flow). The results were compared with the European standards' precision data. The analysis confirmed a wide variation of the precision data. Precision was not always constant, but, in some cases, it did seem to be influenced by the characteristics of the bituminous mixture, contrary to the variation presented in the test standards. In general, a lower reproducibility was observed.

Keywords Hot mix asphalt · Precision · Proficiency test schemes · Repeatability · Reproducibility · Test methods

1 Introduction

Precision is a general term related to the dispersion of results between independent tests performed on the same or similar samples under predetermined conditions, in general, the repeatability and reproducibility conditions. The repeatability expresses the precision of the test results obtained in the same laboratory, with the same operator, and under other identical conditions. Reproducibility refers to the precision of results obtained from the same test method but carried out by different laboratories and operators under various test conditions (e.g., different equipment).

J. Neves (✉)
CERIS, Department of Civil Engineering, Architecture and Georesources, Instituto Superior Técnico, Universidade de Lisboa, Lisbon, Portugal
e-mail: jose.manuel.neves@tecnico.ulisboa.pt

C. Silva · A. Duarte
RELACRE, Lisboa, Portugal

C. Chastre et al. (eds.), *Testing and Experimentation in Civil Engineering*, RILEM Bookseries 41, https://doi.org/10.1007/978-3-031-29191-3_21

Usually, the standard tests present the precision data related to the corresponding results. This information could be helpful in certain experimental activities, e.g., test methods validation and measurement uncertainty determination. However, it is always important to update information related to precision data from new experiments that more realistically can express the specificities of a sector, region, or country. Proficiency Testing Schemes (PTS) are interlaboratory comparisons that consist of the organization, execution and evaluation of tests carried out on the same or similar samples by several laboratories (at least two), according to a pre-established protocol. PTS provide information to the participants enabling the performance and quality assessment of their laboratory routines. The precision evaluation of the test methods is another objective of the PTS.

RELACRE is the Association of Accredited Laboratories of Portugal that, since 1990, represents the testing community of several sectors, including the construction sector [1]. RELACRE is a member of the European Federation of National Associations of Measurement, Testing and Analytical Laboratories (EUROLAB). Within the activities of the Technical Committee of Construction Materials [1], RELACRE organizes PTS of the test's methods for bitumen binders and bituminous mixtures annually, among other construction materials (e.g., concrete, aggregates, and soils). PTS have allowed studying the repeatability and reproducibility of several laboratory methods on various types of materials and conditions [2, 3]. One of the major challenges of this type of PTS is the lack of reference materials. The number of participants usually requires many samples, sometimes prepared in complex conditions to guarantee homogeny properties.

The main contributions of the paper are:

(1) Information on the precision of the various tests carried out under the PTS.
(2) Comparison of the results with precision data of the correspondent European standards.

The paper describes the RELACRE experience on the precision evaluation of tests for hot mix asphalt: asphalt concrete (AC 14 surf and AC 20 base). Precision was evaluated regarding repeatability and reproducibility conditions based on PTS performed from 2007 until 2021.

2 Methodology

2.1 Materials

Tests were carried out on Asphalt Concrete—AC 14 surf and AC 20 base—following EN 13108-1 [4]. The bituminous mixtures were produced in accordance with the technical requirements of the Portuguese Road administration CETO ("Infraestruturas de Portugal") [5]. Figure 1 presents the grain size distributions of the bituminous mixtures (upper and lower limits of the required range).

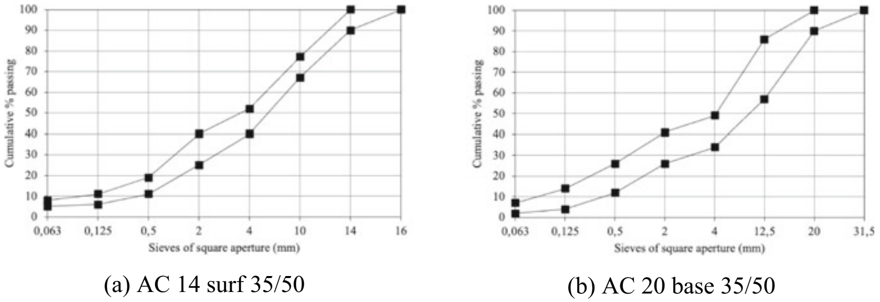

Fig. 1 Limits of the grain size distribution of the aggregates of the bituminous mixtures

Table 1 presents the petrographic origin of the aggregate—limestone, basalt, and granite—and the grade of the bitumen— 35/50 and 50/70 (penetration expressed in 10^{-1} mm)—for all the PTS (2007–2021). Tables 2 and 3 contain the bitumen specifications and aggregates, respectively, in accordance with CETO [5].

Table 1 Bituminous mixtures

Year	HMA	Aggregate (petrographic origin)	Bitumen (penetration grade 0.1 m)
2007	AC20 base	Limestone	50/70
2008	AC20 base	Limestone	50/70
2009	AC20 base	Limestone	50/70
2010	AC20 base	Limestone	35/50
2011	AC20 base	Basalt	50/70
2012	AC20 base	Limestone	35/50
2013	AC20 base	Limestone	35/50
2014	AC20 base	Limestone	35/50
2015	AC14 surf	Granite	35/50
2016	AC14 surf	Granite	35/50
2017	AC14 surf	Granite	35/50
2018	AC14 surf	Granite	35/50
2019	AC14 surf	Granite	35/50
2020	AC14 surf	Granite	35/50
2021	AC14 surf	Granite	35/50

Table 2 Specifications of the bitumen [5]

Property		Standard	Unit	Values	
				35/50	50/70
Penetration		EN 1426	0.1 mm	35–50	50–70
Softening point		EN1427	ºC	50–58	46–54
Durability RTFOT (EN 12,607-1)	Penetration	EN 1426	0.1 mm	$\geq$ 53	$\geq$ 50
	Softening point	EN 1427	ºC	$\leq$ 11	$\leq$ 11
	Variation in mass	EN 12,607-1	%	$\leq$ 0.5	$\leq$ 0.5
	Penetration Index	EN 12,591	–	$\geq$ 1.5 $\leq$ 0.7	$\geq$ 1.5 $\leq$ 0.7
	Fraass breaking point	EN 12,593	ºC	$\leq$ -5	$\leq$ -8
Fire point		EN ISO 2592	ºC	$\geq$ 240	$\geq$ 230
Kinematic viscosity (135 ºC)		EN 12,595	nm^2/s	$\geq$ 370	$\geq$ 295
Paraffin wax content		EN 12,606-2	% (m/m)	$\leq$ 4.5	$\leq$ 4.5
Solubility		EN 12,592	%	$\geq$ 99.0	$\geq$ 99.0

Table 3 Specifications of the aggregates [5]

Property	Standard	Unit	Values	
			AC 20 base	AC 14 surf
Assessment of fines—Methylene blue value	EN 933–9	g/kg	$\leq$10	$\leq$10
Particle shape—Flakiness index	EN 933–3	%	$\leq$30	$\leq$20
Resistance to fragmentation—Los Angeles coefficient	EN 1097–2	–	$\leq$40	$\leq$30
Resistance to wear—micro-Deval coefficient	EN 1097–1	–	$\leq$25	$\leq$15
Water absorption	EN 1097–6	%	$\leq$2	$\leq$1

2.2 *Experimental Procedure*

RELACRE has organized the PTS according to ISO/IEC 17043 [6], which provides the requirements for developing and managing PTS.

Most of the laboratory participants were accredited entities according to EN ISO/IEC 17025 [7]. A code number was attributed to identify each laboratory and to ensure confidentiality. The laboratory pivot was responsible for the asphalt mixture production and the samples preparation according to the EN 12697-28 [8] of Hot Mix Asphalt (HMA). Figure 2 shows the bituminous mixtures used to prepare the specimens and evaluate the soluble binder content and the maximum density. In these tests, three determinations were performed by each laboratory. In Fig. 3 it can be observed the specimens compacted in accordance with EN 12697-30 [9] and applying 50 blows to each side. Three specimens were distributed to each participant

Fig. 2 Bituminous mixtures production

Fig. 3 Specimens preparation

of PTS to determine Marshall properties (Stability and Flow) and bulk density. In each laboratory, the same operator tested three samples in repeatability conditions (three replicates).

3 Results and Discussion

In general, the statistical analysis of results was based on ISO 5725 [10, 11]. Cochran's and Grubbs's tests were used to detect and remove outlier data. Statistical analysis of parameters was based on ISO 5725-1 [10], ISO 5725-2 [11], and ISO 13528 [12].

The following parameters were determined:

- Average (y) and standard deviation (s) of the averages.
- Variances of the repeatability (s_r^2) and of the reproducibility (s_R^2).
- Coefficients of variation of the repeatability (CV_r) and of the reproducibility (CV_R).
- Repeatability (r) and reproducibility (R) limits.

The evaluation of the precision was established for the following tests methods and test parameters of the CEN series of EN 12697 standards for bituminous mixtures:

- EN 12697-1—Soluble binder content by the centrifuge extractor method, including the determination of the residual mineral matter in the binder extract by incineration (Method B.1.5) [13].
- EN 12697-5—Determination of the maximum density (Procedure A—Volumetric procedure) [14].
- EN 12697-6—Determination of bulk density of bituminous specimens (Procedure B: Bulk density—Saturated surface dry (SSD)) [15].
- EN 12697-34—Marshall test [16]: Stability (F) and flow (S).

An example of statistical parameters is presented in Table 4 related to the PTS performed in 2021 [17]. This table contains the precision values of repeatability and reproducibility for each parameter of laboratory tests. The limits of repeatability and reproducibility depend on the correspondent standard deviations (equal to the square root of the variations) according to the relationships of the Eqs.(1) and (2).

$$r = 2.83 s_r \tag{1}$$

$$R = 2.83 S_R \tag{2}$$

European standards provide precision data obtained from experiments on materials from different geographical regions within the European Union. Table 5 contains the summary of the repeatability and reproducibility limits presented in the standard and obtained for the most similar conditions obtained in PTS. In the cases of EN 12697-1 and EN 12697-6, precision limits are expressed in function of the oversize of the aggregate on an 11,2 mm test sieve. This parameter (A), expressed in percentage, was estimated for the bituminous mixtures according to the grain size distribution presented in Fig. 1. The values were interpolated and are A = 21.1 (AC 14 surf) and A = 33.1 (AC 20 base).

In general, the precision data of European standards is constant, only depending on the material type in some parameters. In this paper, the precision limits of PTS were analyzed for each type of bituminous mixture to obtain relationships in the function of the correspondent parameter value (average value of the participant laboratories). In next analysis it was tried to establish a linear tendency of the variation of the results. The objective was only to confirm precision data's constant or not constant variation.

Figure 4 shows the repeatability (Fig. 4a) and reproducibility (Fig. 4b) of the determination of soluble binder content by the centrifuge extractor method. The dispersion of results in both cases is high. The quality of the results was worse than the precision presented in Table 5 [13] for the case of reproducibility. Neves et al. [18] presents a more detailed study on the precision concerning the binder content determination by centrifuge extractor.

Table 4 Precision values of PTS performed in 2021 [17]

Parameter	Precision values							
	y	s	s_r^2	s_R^2	$CV_r(\%)$	CV_R (%)	r	R
EN 12697-1								
Soluble binder content (%)	4.9	0.13	6.42×10^{-3}	22.1×10^{-3}	1.64	3.03	0.23	0.42
EN 12697-5								
Maximum density (Mg/m^3) Procedure A	2.469	0.0213	1.27×10^{-4}	5.40×10^{-4}	0.46	0.94	0.032	0.066
EN 12697-6								
Bulk density (Mg/m^3) Procedure B	2.355	0.0115	9.44×10^{-5}	19.4×10^{-5}	0.41	0.59	0.028	0.039
EN 12697-34								
Stability (kN)	11.0	1.65	0.527	3.07	6.60	15.9	2.1	5.0
Flow (mm)	3.2	0.31	0.0241	0.110	4.85	10.4	0.4	0.9

Table 5 Precision data of the European standards [13–16]

Standard	Parameter	Repeatability r	Reproducibility R
EN 12697-1 (Experiment 2)	Soluble binder content (%)	0.39 (AC 14) 0.46 (AC 20)	0.53 (AC 14) 0.60 (AC 20)
EN 12697-5 (Procedure A)	Maximum density (Mg/m^3)	0.011	0.022
EN 12697-6 (Procedure B)	Bulk density (Mg/m^3)	0.023 (AC 14) 0.027 (AC 20)	0.035 (AC 14) 0.042 (AC 20)
EN 12697-34 (Asphalt Concrete)	Stability (kN)	1.7	2.2
	Flow (mm)	0.7	0.8

Figure 5 presents the repeatability (Fig. 5a) and reproducibility (Fig. 5b) of the maximum density obtained by Procedure A, the volumetric test method using the pycnometer. Both repeatability and reproducibility showed higher results than expected for the test standard EN 12697–5 [14]. In the case of the reproducibility limit, it was observed a tendency to increase in function of the maximum density.

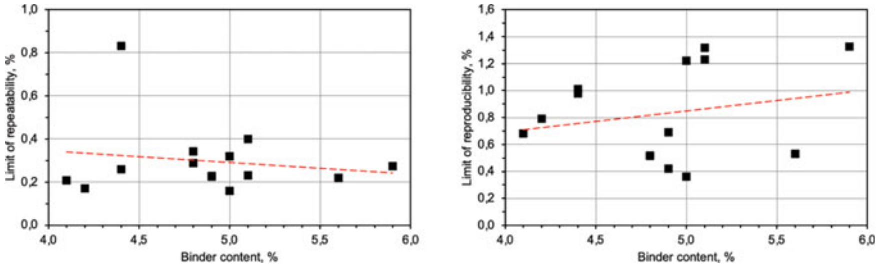

(a) Repeatability (b) Reproducibility

Fig. 4 Precision of soluble binder content

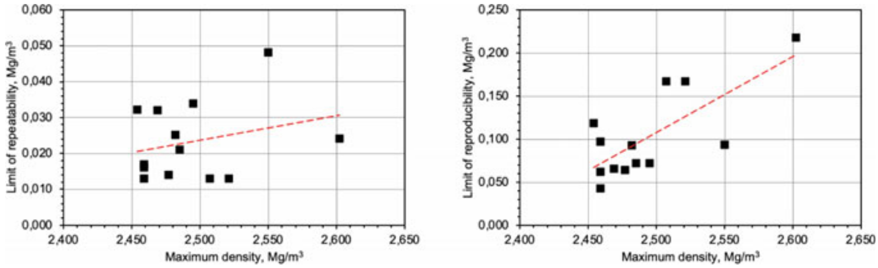

(a) Repeatability (b) Reproducibility

Fig. 5 Precision of maximum density

In Fig. 6 it is observed the repeatability (Fig. 6a) and reproducibility (Fig. 6b) of the bulk density, determined according to the Procedure B of the EN 12,697-6 [15] (Saturated surface dry method). In this case, precision data reveals better performance than the reported values in the test standard (see Table 5). In the case of reproducibility, it seems to exist a decreased tendency of the limit R depending on the bulk density.

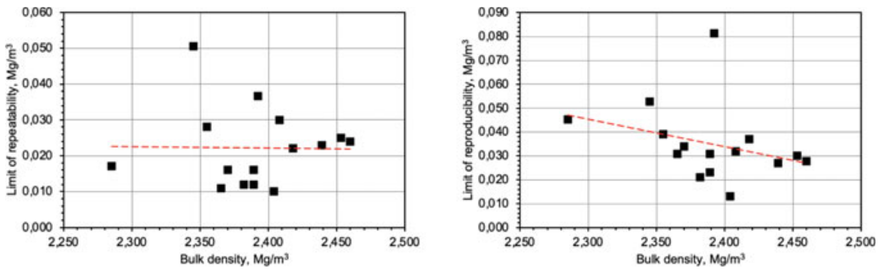

(a) Repeatability (b) Reproducibility

Fig. 6 Precision of bulk density

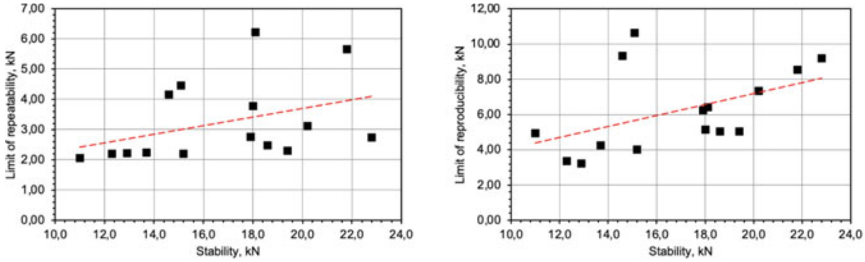

Repeatability Reproducibility

(a) Stability

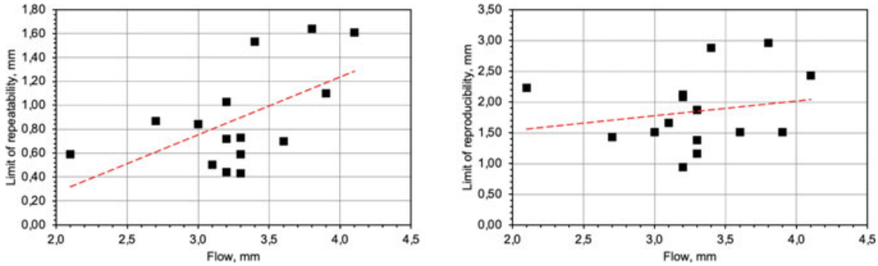

Repeatability Reproducibility

(b) Flow

Fig. 7 Precision of Marshall properties

Figure 7 illustrates de variation of the precision data for Marshal properties: stability (Fig. 7a) and flow (Fig. 7b). It was observed a high dispersion of the results and limits of repeatability (r) and reproducibility (R) are higher than values presented in EN 12697-34 [16] (see Table 5).

Portuguese experience revealed a significant difference from the precision data presented in the European test standards. In general, the repeatability and reproducibility limits were higher, which means that the precision data of test standards could be too conservative. Some trends were observed that deserve to be studied in more detail. In some cases, it could be possible to demonstrate that precision is not constant but depends on the parameter value of the type of bituminous mixture.

4 Conclusion

The paper described the Portuguese experience on the precision evaluation of test methods for hot mix asphalt (AC 14 surf and AC 20 base). The repeatability and reproducibility values were determined based on the results obtained on Proficiency

Test Schemes (PTS) that have involved several test methods and laboratory entities. The paper analyzed the precision values obtained between 2007 and 2021 and compared them with the correspondent precision data presented in the European standards. It was concluded that some differences were observed.

The precision values can be helpful to stimulate the analyses of methods and equipment performance and, consequently, the improvement of future PTS.

Acknowledgements This work is part of the research activity carried out at Civil Engineering Research and Innovation for Sustainability (CERIS) and has been funded by Fundação para a Ciência e a Tecnologia (FCT) in the framework of project UIDB/04625/2020.

References

1. RELACRE Homepage. Accessed 12 April 2021. https://www.relacre.pt
2. Neves, J., Duarte, A.M., Almeida, C., Silva, C., Candeias, R.: Analysis of Portuguese experience on proficiency tests schemes in concrete and aggregates. In: 2nd International Proficiency Testing Conference, Romania (2009)
3. Neves, J., Duarte, A.M., Silva, C., Candeias, R.: Contribution of PTS to the laboratory and in situ studies related to soils compaction tests. In: 4th International Proficiency Testing Conference, Romania (2013)
4. CEN: EN 13108-1. Bituminous mixtures – Material specifications – Part 1: Asphalt Concrete. European Committee for Standardization, Belgium (2016)
5. IP: CETO – Caderno de Encargos Tipo Obra. Materials (Specifications). Portuguese Road Administration (In Portuguese) (2014)
6. ISO/IEC: ISO/IEC 17043. Conformity assessment – General requirements for proficiency testing (2010)
7. CEN: EN ISO/IEC 17025. General requirements for the competence of testing and calibration laboratories. European Committee for Standardization, Belgium (2018)
8. CEN: EN 12697-28. Bituminous mixtures – Test methods – Part 28: Preparation of samples for determining binder content, water content and grading. European Committee for Standardization, Belgium (2020)
9. CEN: EN 12697-30. Bituminous mixtures – Test methods – Part 30: Specimen preparation by impact compactor. European Committee for Standardization, Belgium (2018)
10. ISO: ISO 5725-1. Accuracy (trueness and precision) of measurement methods and results. Part 1: general principles and definitions. International Organization for Standardization, Switzerland (1994)
11. ISO: ISO 5725-2. Accuracy (trueness and precision) of measurement methods and results. Part 2: Basic method for the determination of repeatability and reproducibility of a standard measurement method. International Organization for Standardization, Switzerland (1994)
12. ISO: ISO 13528. Statistical methods for use in proficiency testing by interlaboratory comparisons. International Organization for Standardization, Switzerland (2005).
13. CEN: EN 12697-1. Bituminous mixtures – Test methods – Part 1: Soluble binder content. European Committee for Standardization, Belgium (2020)
14. CEN: EN 12697-5. Bituminous mixtures – Test methods – Part 5: Determination of the maximum density. European Committee for Standardization, Belgium (2018)
15. CEN: EN 12697-6. Bituminous mixtures – Test methods – Part 6: Determination of bulk density of bituminous specimens. European Committee for Standardization, Belgium (2020)
16. CEN: EN 12697-34. Bituminous mixtures – Test methods – Part 34: Marshall test. European Committee for Standardization, Belgium (2020)

17. RELACRE: Materiais de construção – Misturas Betuminosas 2021. Relatório Final. Referência EAP/MC/202, Edição 1, Associação de Laboratórios Acreditados de Portugal, Lisboa (In Portuguese) (2021)
18. Neves, J.: Comparison of binder content determination by centrifuge extractor and ignition test methods for HMA. In: International Airfield & Highway Pavements Conference, US (2019)

Assessment of Mechanical and Physical Behaviour of Sandstones Through Quasi Non-destructive Tests

Marco Ludovico-Marques and Carlos Chastre

Abstract An experimental programme was carried out in order to assess physical properties, such as porosity and mechanical behaviour, through compression and drilling strength of sandstones, classified as lithic arkose. These stones are similar to those found on St. Leonard's church at Atouguia da Baleia village in the Western region of Portugal. This monument's façades were selected because of the extent and depth of the most important degradation pattern exhibited, the alveolization. The Drilling Resistance Measurement Test is an important way to survey the extent of stone weathering on historical building stones due to the correlation of porosity and compressive strength with the drilling strength parameter. It is also a less intrusive and quasi-non-destructive portable test. The drilling time is even lower than other tests duration for lower porosity materials. Absolute differences between experimental and predicted values of porosity obtained on these sandstones through correlations with drilling strength are in general lower than 13%. Considering the best correlation, these absolute differences are up to 6%.

Keywords Drilling strength · Compressive strength · Porosity · Sandstones

1 Introduction

Sandstones of historical buildings in Atouguia da Baleia monuments were studied, aiming at the mineralogical characterization and the evaluation of their experimental physical and mechanical behaviour to assess stone weathering. St. Leonard's Church façades were selected (Fig. 1) because of their degradation patterns, being the most important the alveolization (ICOMOS-ISCS) [1], which was caused by the prolonged

M. Ludovico-Marques (✉)
ESTBarreiro and INCITE, Polytechnic Institute of Setúbal, 2839-001 Lavradio, Portugal
e-mail: marco.marques@estbarreiro.ips.pt

C. Chastre
CERIS and Department of Civil Engineering, NOVA School of Science and Technology, Universidade NOVA de Lisboa, Lisbon, Portugal
e-mail: chastre@fct.unl.pt

C. Chastre et al. (eds.), *Testing and Experimentation in Civil Engineering*,
RILEM Bookseries 41, https://doi.org/10.1007/978-3-031-29191-3_22

salt effect and its closeness to the sea, since it was built in the Middle Ages. Its construction started presumably in the twelfth century. The petrographic study and the physical characterization of the stone used made it possible to obtain the intrinsic signature of the same, in order to identify similar stones and allow the extraction of them from walls in the church vicinity [2–4], once the coeval-quarry was not found. A major increment of physical parameters, such as porosity values, up to 40–50% [5] can be obtained during weathering of sandstone blocks. Physical and mechanical weathering prevails over chemical weathering during buildings' lifetime, set aside sulphation of surfaces and acid rains effect on carbonate natural stone cements.

Ultrasonic pulse velocity (UPV) and the Schmidt hammer (rebound hammer) are two examples of simple and not expensive NDT that can be used to assess porosity and allow the estimate of the elastic parameters and prediction of the extent of stone weathering [6, 7] on building blocks.

The compressive strength of sandstones is dependent on porosity; however, several days are required for testing supported on Archimedes principle or at least several hours if mercury intrusion porosimetry is considered to determine the open porosity. The previous extraction of stone samples with adequate fitted dimensions that respect the monument integrity is needed and these test procedures are destructive.

An alternative is to use a true non-destructive test (NDT) such as the RILEM test of water absorption under low pressure [8], a much quicker test, requiring only from several minutes to one hour for open porosity values higher than 15%. The drilling strength obtained by the Drilling Resistance Measurement Test (DRMT) [2–4] is a less intrusive and quasi-non-destructive test that can be used to assess not only the

Fig. 1 Portal of St. Leonard's South façade showing alveolization patterns

compressive strength of stones, but also the porosity of blocks and other structural elements in order to determine the extent of stone weathering. The drilling time could be higher than the Karsten tube test duration for higher porosity materials; however its portability is a major advantage when service life surveys based on extent of weathering are required.

2 Experimental Programme

The petrographic study carried out on representative samples revealed four typologies of sandstones similar to those found on St. Leonard's church and surrounding ancient buildings, classified as lithic arkose, according to Folk [9], with carbonate cement. The observations of thin sections of these representative samples carried out under a polarizing microscope (Fig. 2), allowed to obtain their mineral composition through modal analysis. Varieties A and B are composed of around 30–32% quartz and 34–40% carbonates, and varieties C and M of about 20–25% carbonates and 40–51% quartz. All varieties have about 4–6% of mica minerals and around 3–7% of matrix, clays minerals included. Kaolin clay was identified through Scanning Electronic Microscopy (SEM). The average size of grains of quartz and feldspar in the sandstone varieties A and B ranges from 0.1 to 0.13 mm (fine grained), 0.15–0.18 mm to 0.24 mm in varieties C and M (medium to fine-grained).

Microporosity settled as the percentage of pores radii lower than 7.5 μm [10], of 80–85% in variety B, more than 90% in variety C and about 75% in variety M, was obtained by mercury intrusion porosimetry. 5 cm-long cubic specimens were sawed from stone blocks of varieties B, C and M in order to carry out open porosity, compression and drilling strength tests, because only these three typologies were found in the monument.

2.1 Open Porosity and Densities

Recommendations of RILEM [8] and EN1936 [11] were followed to determine porosity (n). The specimens were saturated under vacuum and then Archimedes principle was used to obtain pore volumes accessible to water through hydrostatic weighing, allowing to calculate porosity. Bulk and real densities were also determined through the relation of values of the dry mass of the samples and their total volumes, encompassing porosity values in the former property and not considering them in the latter parameter.

The average values of porosity of sandstones range from 4.1% of variety A and 6.9% of variety B to 12.7% of variety C and 18.5% of variety M. The average values of bulk density vary from 2594 kg/m^3 (typology A) and 2510 kg/m^3 (typology B) to 2343 kg/m^3 (typology C) and 2179 m^3 (typology M). The average values of real density range from 2705 kg/m^3 (variety A) to 2697 kg/m^3 (variety B) and

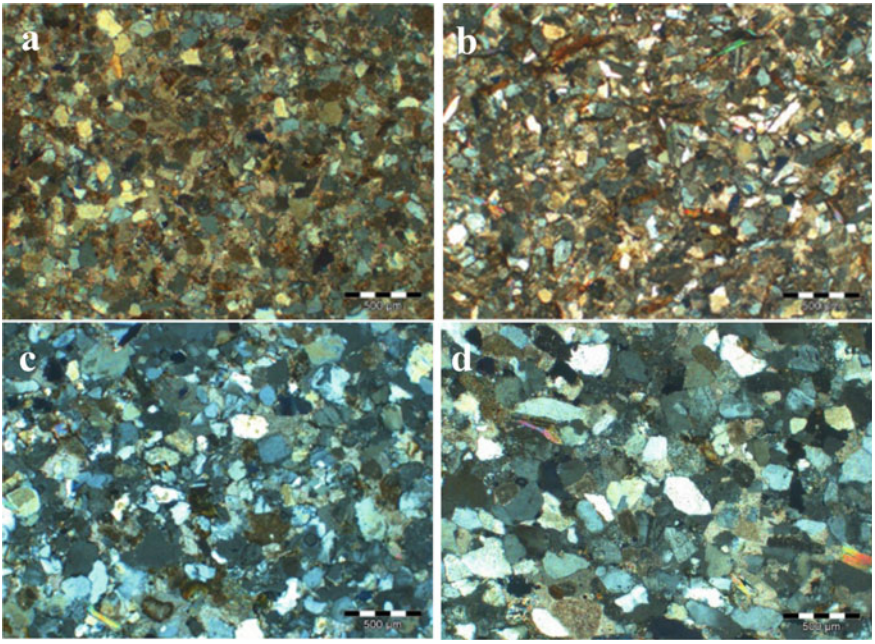

Fig. 2 Thin-section observations under polarizing microscope (crossed nicols) of the four sandstone varieties (magnification: ×40). **a** A, **b** B, **c** C, **d** M

2684 kg/m^3 (variety C) and 2671 kg/m^3 (variety M). Porosity values obtained by mercury intrusion porosimetry vary between 6.6% of typology B, 12.8% of typology C and 16.3% of typology M. Slight differences were obtained between values of open porosity assessed by water and by mercury intrusion, due to the variation of wettability between water and mercury values and to the different ranges of injection pressures used.

2.2 Compressive Strength

A Seidner servo-controlled press, model 3000D, with load capacity up to 3000 kN and a piston stroke of 50 mm was used to carry out monotonic uniaxial compression tests with an axial displacement control rate of 10 μm/s in order to achieve the compressive strength (σ_c) [3].

2.3 Drilling Strength

The Drilling Resistance Measurement Test (DRMT) was used to determine the drilling strength (σ_d) of three sandstone varieties. A stepper-controlled movement of a drilling head on a slide towards the stone specimens on a holder was performed by a portable micro drilling device with a load cell [2]. Figure 3 shows the micro drilling device with laboratory configuration. The drilling head is handled on a telescopic support rod when the tests are carried out in situ. Maximum drill hole depths up to 25 mm were carried out on sandstone specimens, through Diaber tungsten drill bits 5 mm in diameter and a triangular tip. A speed rotation of 600 rpm and an advancing rate of 10 mm/min was the drilling parameters followed because allowed to obtain an adequate range of drilling strength values. Drilling strength profiles were corrected of tip wear due to abrasion on the same stone type with the same drill bit, according to Singer et al. [12]. Abrasion increases linearly with drilling length and the correction factor of tip wear allows to calculate the corrected drilling strength values through a regression analysis.

3 Results

Experimental results of drill strength obtained on cubic samples of typologies B, C and M downwards the drilling profiles are shown on Fig. 4. Table 1 shows the values of the former parameter and the corresponding values of porosity recorded on these samples.

Figure 5 exhibits the experimental data of compressive strength and porosity obtained on thirty-nine cubic specimens belonging to the four varieties of sandstones studied, being the drilling strength values reported on varieties B, C and M.

It is possible to obtain the Eq. (1) from the correlation between compressive strength and porosity values reported on Fig. 5:

$$\sigma_c = 178.7e^{-0.096n} \tag{1}$$

Equation (2) is a correlation between porosity and drilling strength data given in Table 1.

$$\mathrm{n} = 19.8 - 12.82\sigma_d \tag{2}$$

Equation (2) is indicated in Fig. 5a and the coefficient of determination R^2 = 0.995.

Equation (3) is the correlation between compressive strength and drilling strength values, through Eqs. (1) and (2) (Fig. 5a).

$$\sigma_c = 178.7e^{1.2\sigma_d - 1.9} \tag{3}$$

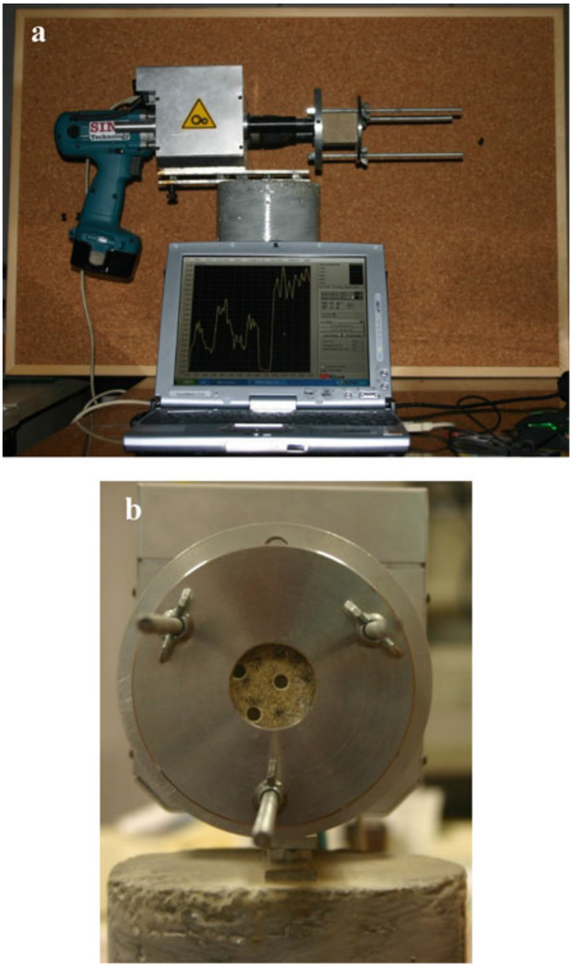

Fig. 3 Laboratory configuration of DRMTS portable apparatus. **a** Test equipment, **b** image of specimen holder showing drills on surface of a sample of variety M

Equation (4) is another correlation found for porosity, settled as a function of drilling strength data shown in Table 1. It is reported in Fig. 5b and the coefficient of determination R^2 is also 0.995.

$$n = 18.8 - 12.5\sigma_d \tag{4}$$

Equation (5) allows to determine the compressive strength from drilling strength data, through Eqs. (1) and (4).

$$\sigma_c = 178.7e^{1.2\sigma_d - 1.8} \tag{5}$$

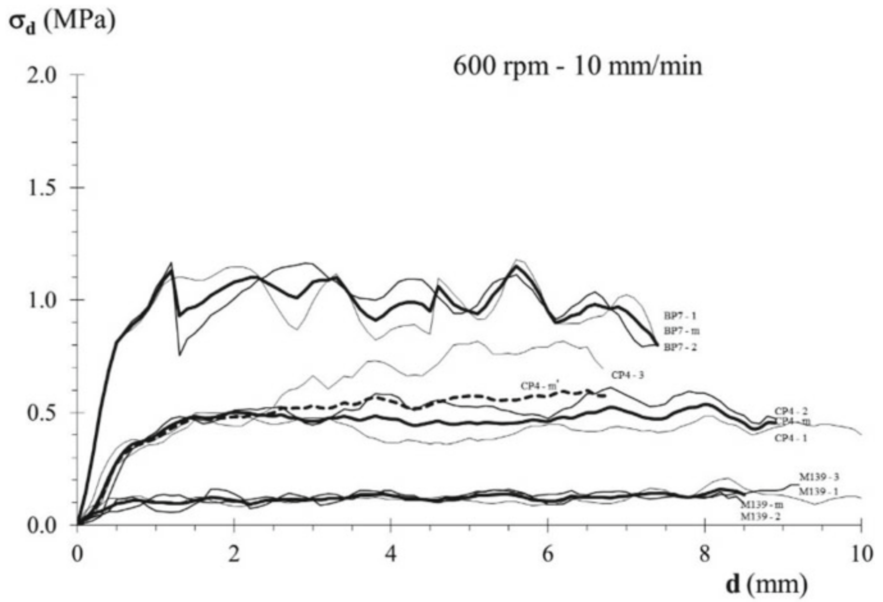

Fig. 4 Drilling strength profiles obtained on sandstone specimens of varieties B, C and M

Table 1 Drilling strength parameters obtained by DRTMS on specimens of the three sandstones varieties, carried out at 600 rpm–10 mm/min, related to porosity values

Specimens—drills	n (%)	σ_d (MPa)
BP7—1	7.0	1.0
BP7—2	7.0	1.0
CP4—1	13.9	0.5
CP4—2	13.9	0.4
M139—1	18.6	0.1
M139—2	18.6	0.1
M139—3	18.6	0.1

The Eq. (6) is another correlation with a good agreement between experimental and predicted values of porosity obtained from drilling strength values (Fig. 5c).

$$n = 21.225e^{-1.082\sigma_d} \tag{6}$$

Compressive strength and drilling strength of sandstone specimens are strongly correlated with their porosity values [2] and also the values of this latter parameter and the values of drilling strength, as shown.

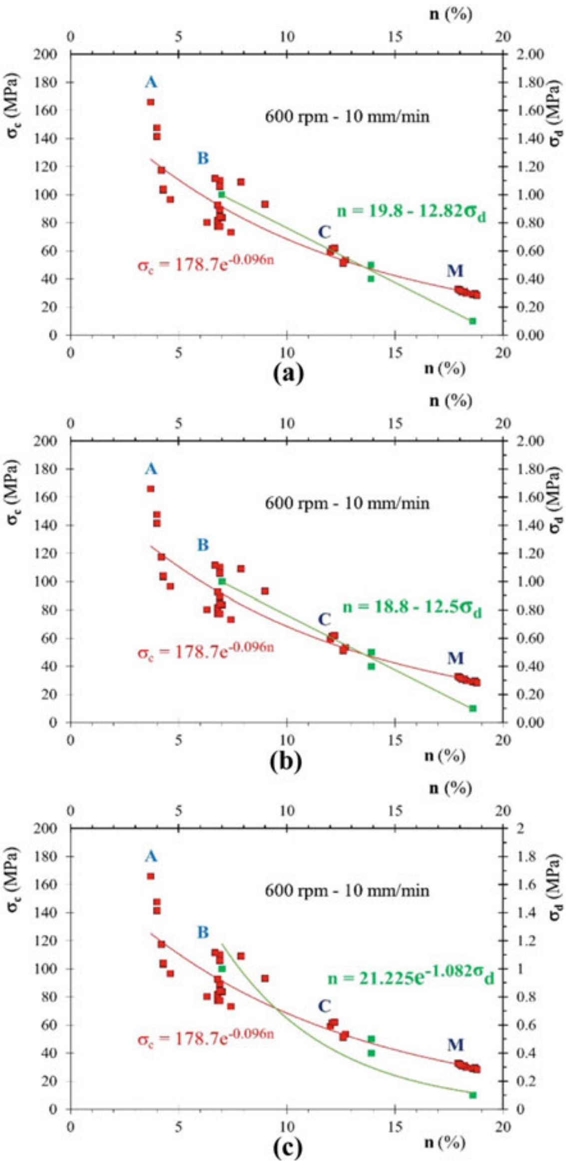

Fig. 5 Experimental data reported of σ_c (red dots) and σ_d (green dots) related to n. **a** and **b** Correlations of σ_c with n and n as a function of σ_d. **c** Correlation of n with σ_d

Table 2 Absolute differences between predicted porosity values and experimental results

Samples/drills	σ_d (MPa)	n (%)	Predicted n by Eq. (2)	Predicted and exp. absolute difference n (%)	Predicted n by Eq. (4)	Predicted and exp. absolute difference n (%)	Predicted n by Eq. (6)	Predicted and exp. absolute difference n (%)
BP7—1	1	7	7	0.3	6.3	11.1	7.2	2.7
BP7—2	1	7	7	0.3	6.3	11.1	7.2	2.7
CP4—1	0.5	13.9	13.4	3.8	12.6	10.8	12.4	12.5
CP4—2	0.4	13.9	14.7	5.3	13.8	0.7	13.8	1
M139—1	0.1	18.6	18.5	0.4	17.6	6	19	2.4
M139—2	0.1	18.6	18.5	0.4	17.6	6	19	2.4
M139—3	0.1	18.6	18.5	0.4	17.6	6	19	2.4

Table 2 shows the values of porosity predicted by Eqs. (2), (4), and (6) through the values of drilling strength. Absolute differences between predicted porosity values and experimental results of porosity values are also reported. These values of absolute differences are generally lower than 13% and up to 6% regarding predicted porosity values calculated from Eq. (2).

Absolute differences obtained through Eq. (2) are the lowest values in comparison with those determined respectively by the Eqs. (6) and (4). Average values of absolute differences between predictions of porosity obtained from Eqs. (2), (6), and (4) and the corresponding experimental results are the following: 1.6, 3.7, and 7.4%.

In just one sample the predicted value of porosity supported on Eq. (2) gives the highest absolute difference.

4 Conclusions

The experimental programme described allowed to evaluate porosity through compression and drilling strength of sandstones (lithic arkoses), similar to the stones on the façades of St. Leonard’s church at Atouguia da Baleia village.

Porosity values obtained by Eqs. (2), (4), and (6) have good agreement with experimental data of the sandstones tested. Absolute differences between the predicted and experimental values of porosity given by correlations with drilling strength are in general lower than 13%, being up to 6% when the best correlation of Eq. (2) is considered.

The Drilling Resistance Measurement Test can survey the extent of stone degradation on stones of monuments based on the correlation of porosity and compressive strength with the drilling strength parameter.

References

1. International Council on Monuments and Sites/International Scientific Committee for Stone (ICOMOS-ISCS): Illustrated glossary on stone deterioration patterns (2008)
2. Ludovico-Marques, M.: Contribution to the knowledge of the effect of crystallization of salts in the weathering of sandstones: application to the built heritage of Atouguia da Baleia. Ph.D. thesis in Portuguese, Universidade NOVA de Lisboa, Lisbon (2008)
3. Ludovico-Marques, M., Chastre, C.: Consolidation works on sandstone monuments: a new approach. In: Handbook of Materials Failure Analysis with Case Studies from the Construction Industries, pp. 235–254. Elsevier (2018)
4. Chastre, C., Ludovico-Marques, M.: Nondestructive testing methodology to assess the conservation of historic stone buildings and monuments. In: Handbook of Materials Failure Analysis: With Case Studies from the Construction Industries, pp. 255–294. Elsevier (2018)
5. Palchik, V.: Influence of the porosity and elastic modulus on uniaxial compressive strength in soft brittle porous sandstones. Rock Mech. Rock Eng. **32**(4), 303–309 (1999)
6. Vasconcelos, G., Lourenço, P.B., Alves, C.A., Pamplona, J.: Ultrasonic evaluation of the physical and mechanical properties of granites. Ultrasonics **48**(5), 453–466 (2008)
7. Yasar, E., Erdogan, Y.: Estimation of rock physicomechanical properties using hardness methods. Eng. Geol. **71**, 281–288 (2004)
8. RILEM: Recommended tests to measure the deterioration of stone and to assess the effectiveness of treatment methods. Mater. Struct. **13**(75), 175–253 (1980)
9. Folk, R.: Petrology of Sedimentary Rocks. Hemphill Publishing, Austin (1974)
10. Pellerin, F.: La porosimetrie au mercure appliquee a l' etude geotechnique des sols et des roches. Bull. Liaison Lab. Ponts Chaussés **106**, 105–116 (1980)
11. EN 1936: Natural stone test method-determination of real density and apparent density, and of total and open porosity. European Standard (1999)
12. Singer, B., Hornschild, J., Snethlage, R.: Strength profiles and correction functions for abrasive stones. In: Proceedings of the Workshop DRILLMORE—Drilling Methodologies for Monuments Restoration, Munich. Firenze, Centro Stampa Toscana Nuova (2000)

Inspection, Monitoring, and Automatic Damage Identification

Design and Construction of a Test Setup to Investigate Ground Settlement Response of Large-Scale Masonry Building Models

Korhan Deniz Dalgic, Cennet Yesilyurt, Burcu Gulen, Yiyan Liu, Sinan Acikgoz, Muhammed Marasli, and Alper Ilki

Abstract Underground construction activities such as tunnelling and deep excavations in urban areas may impact a significant number of surface structures and cause damage. Tunnelling-induced damage can often be repaired, but at great expense, due to significant repair costs and associated project delays. Within this context, damage caused by excavation-induced ground movements on heritage masonry buildings requires further attention, due to the cultural value and vulnerability of these assets. There is a need for experimental studies to better understand the structural response of these buildings to excavation-induced ground movements. In this study, a test setup was designed and constructed to examine the response of an experimental building model, replicating historic masonry structures, against differential settlement effects. The settlement apparatus relies on controlled jacking of large steel beams to apply differential displacements to the building. A specific tunneling scenario was considered for the design of the settlement apparatus. The constructed test setup is validated by evaluating the displacement profiles of the steel beam for different tests, with or without building. Differences between the differential settlements experienced by the steel beam and the building highlights how building weight and progressive damage may increase compliance to ground movements.

Keywords Ground settlement · Tunnelling · Test setup · Masonry buildings · Damage

K. D. Dalgic (✉) · C. Yesilyurt
Department of Civil Engineering, Izmir Institute of Technology, 35430 Urla, Izmir, Turkey
e-mail: korhandenizdalgic@iyte.edu.tr

B. Gulen · Y. Liu · S. Acikgoz
Department of Engineering Science, University of Oxford, Oxford OX1 3PJ, UK

M. Marasli
Fibrobeton, Merkez Mahallesi, Taskopru Koyu, 161-1, 81100 Ihsaniye, Duzce, Turkey

A. Ilki
Faculty of Civil Engineering, Istanbul Technical University, 34469 Maslak, Istanbul, Turkey

C. Chastre et al. (eds.), *Testing and Experimentation in Civil Engineering*,
RILEM Bookseries 41, https://doi.org/10.1007/978-3-031-29191-3_23

1 Introduction

Underground construction activities such as tunnelling and deep excavations usually result in changes in the stress state of soil. This leads to vertical and horizontal ground movements on the surface. The vertical component of resultant ground movement is called settlement. Masonry structures are quite sensitive to differential effects of settlements (non-uniform variation of vertical ground movements) due to their low tensile strength.

Numerous researchers have studied the interaction between buildings and excavation-induced ground movements through analytical [1], semi-analytical [2] and numerical methods [3]. In contrast, experimental studies in this area are scarce.

Laefer et al. [4] constructed 1/10 scaled low-rise reinforced concrete (RC) frame structures in a testbed filled with dry sand and tested them by subjecting to the simulated ground settlements caused by an adjacent model excavation. Giardina et al. [5] produced one 1/10 scaled masonry wall specimen [1.5(l) $\times$ 0.05(w) $\times$ 1.2(h)] m and then subjected it to an artificial hogging-type settlement profile which imitated the settlement effects caused by a tunnelling activity in the vicinity of the represented masonry building. The wall specimen was built on a steel I beam connected to a fixed and rigid steel frame. The settlement profile was created by applying vertical displacements at one end of the steel I beam. Ritter et al. [6] conducted a series of geotechnical centrifuge tests to investigate the settlement response of the masonry specimens. They investigated the impact of tunnelling activities in the sand. Scaled masonry building models were produced by 3D printing, adopting an adjusted material density to account for scaled stress states of small, printed walls. The lack of large-scale building models with realistic building features (e.g. floor structures) are noteworthy.

In addition to these experimental studies, there are several well-documented case studies [7]. However, field investigations feature significant uncertainties concerning building and soil characteristics and present limited data on structural response. Due to these limitations, field investigations often do not allow systematic evaluation of building damage response to settlements. Therefore, there is a need for further experimental work on large-scale settlement response of building models, with detailed instrumentations to better understand the structural settlement response.

The current study explains the design methodology and construction of a settlement test setup. The appropriateness of the setup is validated with site measurements. The experimental settlement response of one large scale (1/2) masonry building model is briefly discussed to highlight the repeatability of the applied settlement profile and demonstrate the different structural responses of the building with different weight.

2 Masonry Building Model and Design of a Settlement Test Setup

2.1 Building Model

Masonry building model, representative of Akaretler Row Houses (the prototype buildings) in Istanbul, Turkey, were constructed. The properties of prototype buildings were previously characterized [8]. The Akaretler Row Houses were built around 1875 in the south part of Istanbul and are considered one of the best examples of the civil architecture of their period because of their neoclassical facades, ornaments, and location. Although the original load-bearing masonry walls were partly conserved, some parts of the existing floors were demolished. It is also reported that some vaulted floors were replaced with RC slabs during the previous restorations. Solid clay bricks were used in the construction of the walls. The bond pattern was cross-bond (English bond), and mortar joints were 10–35 mm thick in horizontal and 10–20 mm thick in vertical directions. The walls were constructed over strip foundations made of stone units. A general view of Akaretler Row Houses, its load-bearing walls and RC slabs are presented in Fig. 1.

Before constructing building model, the size, geometry and position of repeating architectural features on load bearing walls (i.e. walls' length&height, windows' length&height, the positions of openings and the size of lintels) were determined. The experimental model captured these characteristics at half-scale, but neglected some decorative aspects (like balconies). The model (3O-RF) is shown in Fig. 2.

The building model consists of two masonry walls connected via RC floors at two elevations: mid-height and top level of the walls (Fig. 2). The building model features a cast in-situ RC slab floor structure; this was inspired by the retrofitted slab floors of the Akaretler row houses. The RC slab cross-section size was chosen with reference to Akaretler Row Houses and reinforcement was chosen to ensure elastic response. The relatively large scale of the experiments allowed investigating the influence of this type of floor structure, which was not investigated in previous research.

Fig. 1 Akaretler row houses, load-bearing masonry walls and RC floors [8]

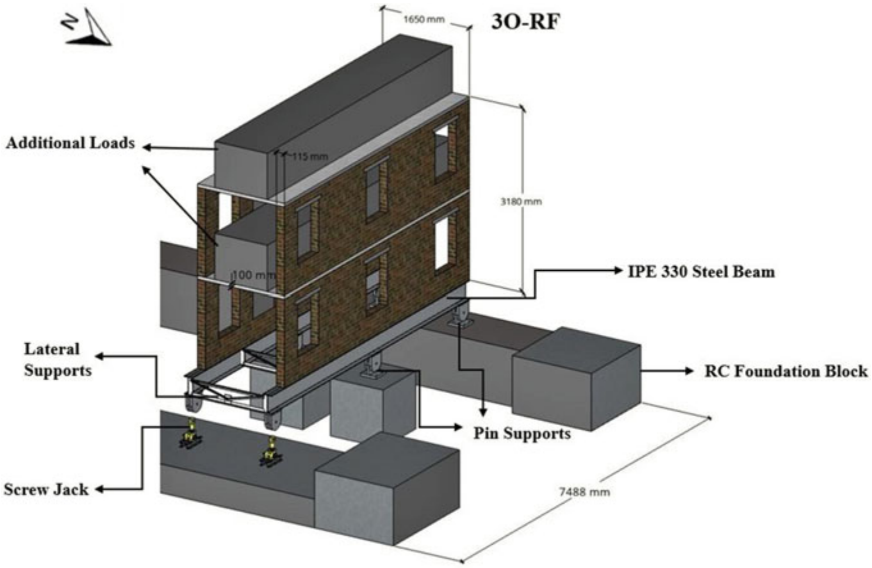

Fig. 2 Half-scaled building model with additional weight loads (7.8 tonnes for each floor)

The influence of vertical loads (comprised partly of the building self-weight) on the settlement response of buildings has previously been examined through numerical studies [9]. Special attention was paid to the application of vertical loads during the settlement tests. Vertical load analysis performed for the prototype building considering a specific tributary area for floor and other loads (i.e. roof loads) revealed that base stress under the ground storey walls is expected to be around 0.2 MPa. To achieve comparable stresses at base of the walls of the scaled building model, additional weight loads were used (Fig. 2). For this purpose, RC blocks having 1 m length, 1 m width and 0.6 m height were placed slowly and symmetrically on both mid- and top floors. Note that top storey walls and top floor were constructed after the placement of mid-floor additional loads. For the model building, 7.8 tonnes of additional load was placed per floor. Later, the amount of additional loads was increased to explore structural response to settlements.

The presence of two identical parallel walls for the building model enabled a critical evaluation of the repeatability of structural response.

2.2 Settlement Scenario

Buildings may be located at different positions in a settlement trough (Fig. 3). The convex section of the settlement profile is called the “hogging zone”. This zone is

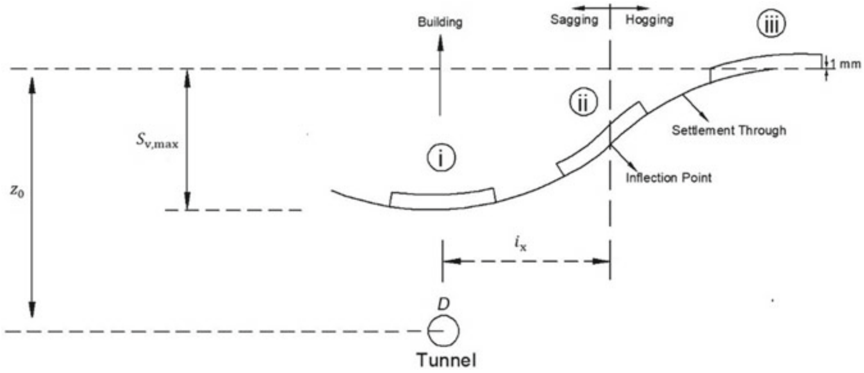

Fig. 3 A typical settlement trough due to tunnelling and different possible positions of surface buildings

Table 1 Parameters that represent the tunnel excavation scenario

Max settlement, $S_{v,max}$ (m)	0.090
Tip settlement, v_{tip} (m)	0.050
Volume loss, V_l (%)	1.1
Tunnel diameter, D (m)	12.2
Distance of the inflection point from the tunnel centre, i_x (m)	5.50
Trough width parameter, K	0.25
Tunnel axis depth, z_o (m)	22

considered to impose higher damage risk to masonry buildings. The current settlement test setup was designed to replicate a part of the hogging zone of a tunnelling project scenario in sand. Table 1 presents the parameters regarding the adopted scenario. According to this, the tunnel is 12.2 m in diameter (D) and 22 m deep from the surface (z_0). The volume loss (V_1) associated with this scenario is 1.1%. Building is located 5.5 m away from the tunnel centre in the hogging zone. This distance also corresponds to distance of the inflection point from the tunnel centre (i_x). The soil parameter (K) is chosen as 0.25 for sand soil. The max settlement ($S_{v,max}$) above the tunnel centre is 90 mm. The max settlement under the building is 50 mm.

2.3 Design of Settlement Test Apparatus

Building model was constructed directly on steel IPE 330 beams (Fig. 2). These beams were used not only as supports but also to generate settlements. Settlements were created by deforming steel beams by utilizing the screw jacks connected at the

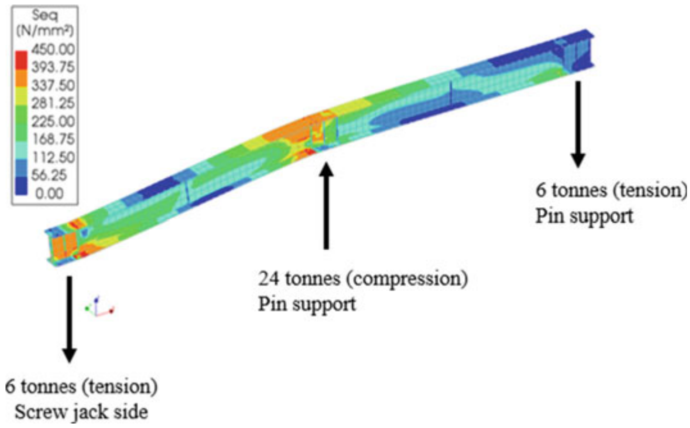

Fig. 4 Stress distribution and vertical support reactions of IPE 330 steel beams at 60 mm tip displacement

free ends of the beams. The cross-section properties of IPE beams were determined considering total vertical loads (from building self-weight and additional loads) and the settlement effects. Figure 4 shows the support reactions and Von Mises stress distributions under the action of both vertical loads and settlement effects at the max tip displacement (max vertical displacement applied by screw jack) of 60 mm. As can be seen in this figure, the steel beam reaches almost yielding (350 MPa) at mid-length top flange sections at this level. Majority of the tests required the prototype building to experience up to 50 mm settlement, corresponding to 25 mm of displacement at the beam free end. However, in some tests, the 60 mm design limit was exceeded to explore damage for greater differential settlements, up to 90 mm. Since the beam had significant plastic reserve capacity, additional displacements and local yielding did not cause issues.

Steel beams were connected to heavy RC foundation blocks through moment-free pin connections at two locations (Fig. 2). Since all the construction and tests were carried out in an open space (no strong floor), heavy RC foundation blocks were needed to provide a rigid supporting system for IPE steel beams. For the building model (3O-RF in Fig. 2), the volume and, accordingly, the weight of the RC foundation blocks were increased by adding top sections. In this way, any possible lifting of RC blocks due to tension forces transferred from the back and front pin supports during the settlement tests was prevented.

The design of pin connections was made as per AISC 360 section D5.2 [10] by considering the calculated support reactions. According to this, the minimum of tensile rupture of pins, shear rupture of hinge plates and bearing strength of the hinge plates considered as the governing failure mode in the design. Herein, the bearing strength of the hinge plates controls the design. The design of base plates was made as per another AISC design guide [11]. The base plates were anchored to the heavy RC foundation blocks using four M24 chemical anchors.

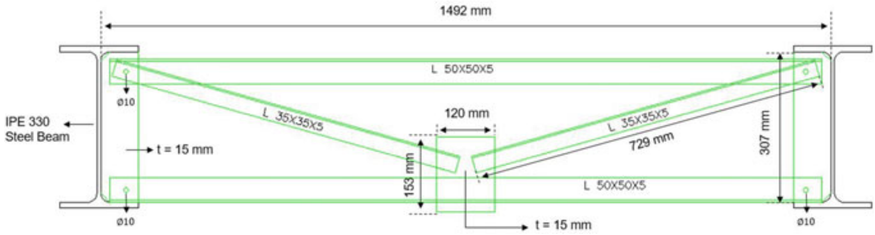

Fig. 5 Details of lateral bracing

Since IPE steel beams had to be loaded up to (and sometimes beyond) elastic limits, preventing any potential lateral buckling and torsion of the parallel IPE 330 beams was critical. To this end, the span lengths of parallel IPE beams between the pin connections were reduced by adding lateral braces made up 50 × 50 × 5 and 35 × 35 × 5 mm equal steel angles (Fig. 5). In addition, stiffener plates with 15 mm thickness were welded between the top and bottom flanges of IPE beams at pin support regions and free ends to support webs and prevent flanges' bending.

2.4 Site Validations for Settlement Test Setup Before the Construction of the Building Model

Prior to building construction, it was desirable to test the settlement apparatus to observe whether IPE steel beams could replicate desired hogging type settlement profile when deformed. Therefore, the beams were tested in-situ before constructing masonry building model. Figure 6 shows bare steel beams, screw jacks, pin supports, RC foundation blocks and instruments to measure the beam deflections due to applied settlements. The parallel beams were bent in the desired hogging form by rewinding threaded rods connected to the screw jacks, up to the elastic limit of 60 mm displacement at the beam free end. To validate the appropriateness of achieved in-situ hogging settlement profile, the vertical displacements of steel beams were measured using six Linear Variable Displacement Transducers (LVDTs) and recorded by a computer (Fig. 6). Figure 7 compares the experimental settlement data obtained with LVDTs, the deformed shape according to finite element analyses and Gaussian empirical function (with parameters defined in Table 1). As can be seen, in-situ settlements of IPE steel beams without masonry superstructure model are in line with both numerical and empirical target functions for the settlement profile. On the other hand, vertical displacements obtained during 3O-RF building Test 1 (building is present on the steel beams and 7.8 tonnes additional load is applied per floor) are very close to theoretical and empirical displacements derived for the case without superstructure.

During the construction of masonry building model, the parallel steel beams were supported by temporary supports located close to the free end of parallel beams.

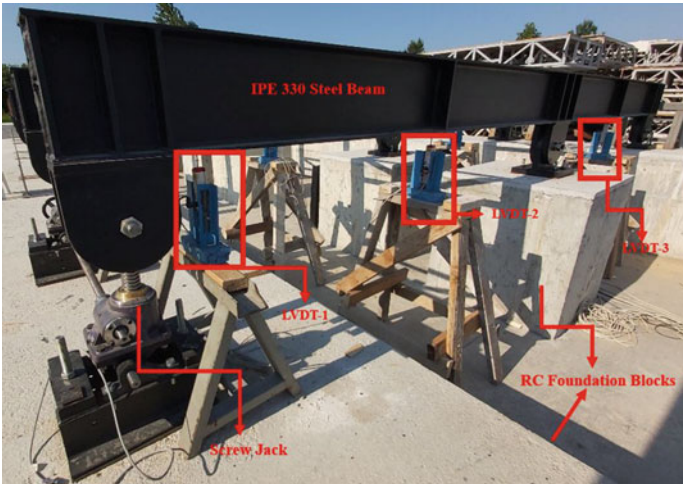

Fig. 6 Settlement test setup validations

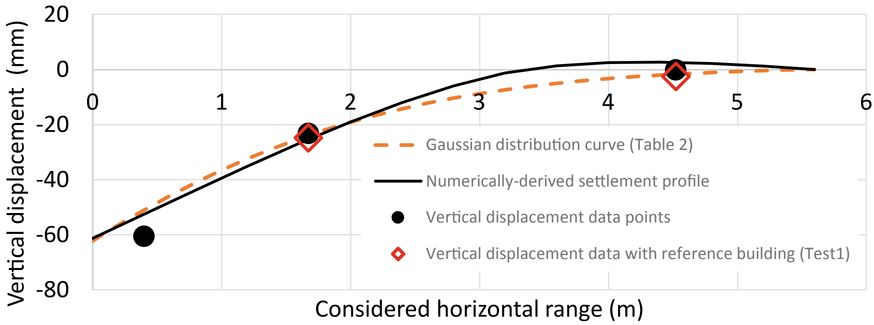

Fig. 7 Comparison between the in-situ bare test setup vertical displacements (without building model) and theoretical deformed shapes for bare test setup

3 Experimental Testing of the Masonry Building

Temporary supports were removed just after the installation of screw jacks before each settlement test. Due to vertical loads, the deflections of IPE steel beams remained small (less than 1 mm in the vertical direction at mid-span) following the construction of the masonry building model and the displacement of additional loads.

Figure 8 shows the schematic drawings of the front wall of the building model (3O-RF) after being tested under the effect of varying levels of vertical loads and similar differential settlements. While Fig. 8a corresponds to the aforementioned reference case for the vertical loading scheme (7.8 tonnes per floor), Fig. 8b, c show the instances in which vertical load levels were increased or the application

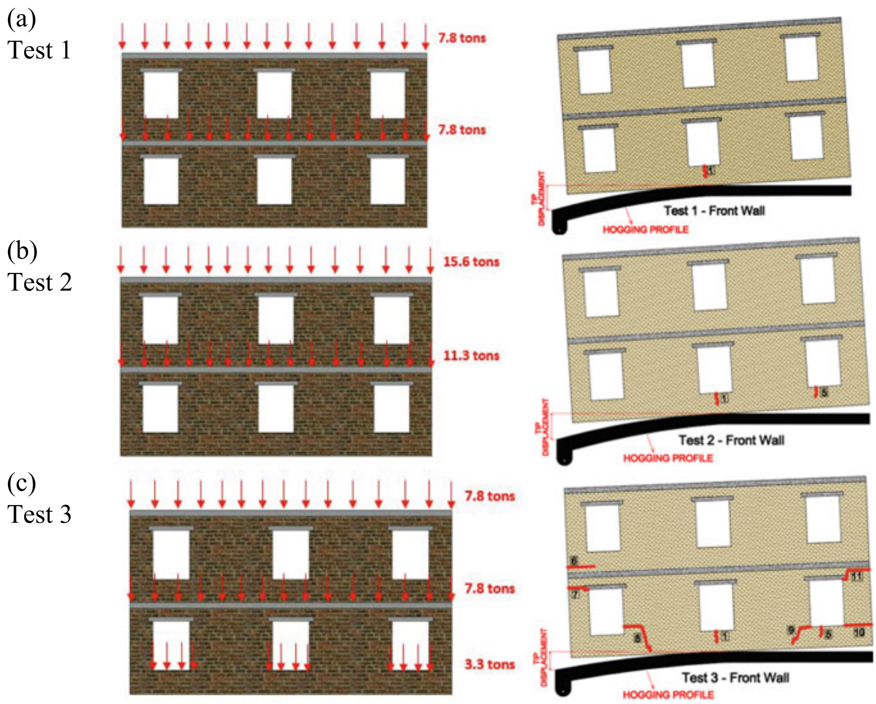

Fig. 8 Settlement tests for the reference building model (3O-RF)

of the additional loads changed (i.e., a part of additional loads was loaded from the ground storey window sills). The overall response and the distribution of wall damage were similar to the previously published numerical predictions [12]. The monitored displacements and the overall symmetry in damage patterns on parallel walls (front and back walls) confirmed that the walls experienced similar damage when subjected to the same settlement profiles.

Gap formation between masonry walls and supporting IPE steel beams was a clear indication of the low level of conformity. The largest gaps between the steel beam and the building were observed during Test 1. The introduction of additional vertical loads on Test 2 reduced the gap openings, but did not increase the differential settlements experienced by the building. During these tests, the building model experienced slight damage. Test 3 explored a different weight arrangement, while subjecting the building to the same settlement profile. The formation of damage during the early stages of the test allowed the building to follow the steel beam and experience the same differential settlements as the beam. These series of tests demonstrate how the settlement apparatus was used to explore the influence of a key aspect (building vertical load) on settlement induced damage.

4 Conclusions

The design of a settlement apparatus to apply realistic hogging settlement profiles to realistic half-scale masonry building is discussed in this paper. The apparatus features two parallel steel beams supported on two hinges in their own planes and connected laterally. They simulate excavation induced differential settlements when jacked at their free end. Test results (without and with building on the steel beams) show that the settlement apparatus effectively captures the expected settlement profiles, with good repeatability. In the paper, a small subset of results are presented, where a building model is tested under varying vertical loads while being subjected to a specific settlement profile, to observe how building loads influence settlement-induced damage. The settlement apparatus might also allow the investigation of other key aspects, such as the influence of window openings and different floor systems on settlement induced damage; these aspects will be the subject of future studies.

References

1. Burland, J., Wroth, C.: Settlement of buildings and associated damage. In: Proceedings of Conference on Settlement of Structures, Cambridge (1974)
2. Potts, D.M., Addenbrooke, T.I.: A structure's influence on tunnelling induced ground movements. Proc. Inst. Civ. Eng. - Geotech. Eng. **125**, 109–125 (1997)
3. Augarde, C.E., Burd, H.J., Houlsby, G.T.: A three dimensional finite element model of tunnelling. In: Pande, V., Pietruszczak (eds.) Numerical Models in Geomechanics. Balkema, Rotterdam (1995)
4. Laefer, D.F., Ceribasi, S., Long, J.H., Cording, E.J.: Predicting RC frame response to excavation-induced settlement. J. Geotech. Geoenviron. Eng. **135**(11), 1605–1619 (2009)
5. Giardina, G., Marini, A., Hendriks, M.A.N., Rots, J.G., Rizzardini, F., Giuriani, E.: Experimental analysis of a masonry façade subject to tunnelling-induced settlement. Eng. Struct. **45**, 421–434 (2012)
6. Ritter, S., Giardina, G., Dejong, M.J., Mair, R.J.: Influence of building characteristics on tunnelling-induced ground movements. Geotechnique **67**(10), 926–937 (2017)
7. Burland, J., Standing, J., Jardine, F.: Building Response to Tunneling: Case Studies from Construction of the Jubilee Line Extension. CIRIA Special Publication Series: Thomas Telford, London (2001)
8. Ispir, M., Demir, C., Ilki, A., Kumbasar, N.: Material characterization of the historical unreinforced masonry Akaretler Row Houses in Istanbul. J. Mater. Civ. Eng. **22**(7), 702–713 (2010)
9. Bloodworth, A.G., Houlsby, G.T.: Three dimensional analysis of building settlement caused by shaft construction. In: Proceedings of an International Symposium on Geotechnical Aspects of Underground Construction in Soft Ground, Tokyo (1999)
10. AISC Homepage: https://www.aisc.org/Specification-for-Structural-Steel-Buildings-ANSIAISC-360-16-1 (07 July 2016)
11. AISC Homepage: https://www.aisc.org/Design-Guide-1-Base-Plate-and-Anchor-Rod-Design-Second-Edition (May 2006)
12. Dalgic, K.D., Gulen, D.B., Acikgoz, S., Burd, H., Hendriks, M.A.N., Giardina, G., Ilki, A.: Large scale experimental settlement tests to evaluate structural models for tunnelling-induced damage analysis. Lect. Notes Civ. Eng. **126**, 164–171 (2021)

Metrological Characterization and Traceability of the Strain Column Measurement Standard

Luís Martins, Ricardo Mendes, Alexandre Pinheiro, and Álvaro Ribeiro

Abstract This paper describes the development of experimental methods for the metrological characterization and traceability of an in house produced strain column measurement standard, for use in hardened concrete compression machine testing. The performed characterization included the determination of dimensional (diameter, height) and geometrical quantities (flatness, shape, parallelism, perpendicularity, circularity and cylindricity) using a three-dimensional coordinate measuring machine, and the evaluation of the strain measurement accuracy and uniformity. Traceability to the International System of Units (SI) was achieved by calibration using a laser interferometer. The obtained estimates and measurement uncertainties supported its conformity assessment, considering the applicable EN 12390-4 normative tolerances and adopted decision rule (hypothesis test, without guard bands, assuming a type I error of 1% and a Gaussian probability density function). This work allowed concluding that the produced strain column complies with all the normative technical requirements and can be used in the metrological testing of hardened concrete compression machines.

Keywords Strain column · Testing machine · Hardened concrete

1 Introduction

The experimental activity performed by LNEC—the Portuguese National Laboratory for Civil Engineering in the Civil Engineering context, contributes significantly to the safety and quality improvement of civil construction. The performed activities include the experimental study of construction materials such as concrete, which is the focus of this paper.

This type of material is used in numerous and relevant infrastructures and public constructions, namely, in buildings, dams, geotechnical, hydraulic and transport structures. In particular, the physical and chemical experimental testing of concrete

L. Martins (✉) · R. Mendes · A. Pinheiro · Á. Ribeiro
LNEC—National Laboratory for Civil Engineering, Lisbon, Portugal
e-mail: lfmartins@lnec.pt

C. Chastre et al. (eds.), *Testing and Experimentation in Civil Engineering*,
RILEM Bookseries 41, https://doi.org/10.1007/978-3-031-29191-3_24

contributes for knowledge improvement about the behavior and performance of this type of material, during its life cycle. Within the several available tests which contribute for this assessment, special attention is given in this paper to the experimental determination of hardened concrete compression resistance, with a normative framework given by standard EN 12390-3 [1]. This framework has a high impact in the quality of the compression resistance results since it defines the technical requirements related to the main material resources which intervene in the mentioned test, namely, molds, specimens, and compressive testing machines.

In the specific case of hardened concrete compression machines, with a normative framework given by standard EN 12390-4 [2], a set of requirements is defined regarding the compression force (measurement, control, and transmission) and their construction, namely, the main components: plates, spacers, and accessories. In the geometrical perspective, standard EN 12390-4 [2] mentions the periodic metrological testing of the compression machine for verification of the upper plate (self-alignment and movement restriction) and of the remaining components alignment.

This test implies the use of a normalized [2] standard measurement—a strain column—which corresponds to a metallic cylinder (composed by a steel, chromium, and nickel alloy) instrumented with thermally compensated electrical strain gauges in four points, forming two diametrical opposing pairs in the central region of its lateral surface, as shown in Fig. 1.

Each point corresponds to a complete Wheatstone bridge, composed by four strain gauges, two of them related the measurement of the axial strain and the remaining two to the measurement of the circumferential strain. The maximum permissible compression load that can be applied to the strain column corresponds to 2000 kN.

This paper describes the performed studies aiming the dimensional and geometric metrological characterization of a strain column produced by LNEC, and the establishment of its measurement traceability to the International System of Units (SI),

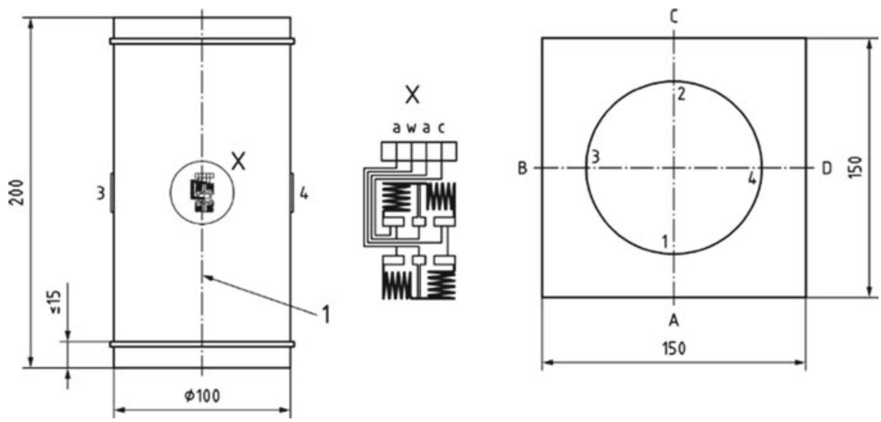

Fig. 1 Location of the strain gauges in the column [2]

through the definition of a dedicated calibration method, noticing that no information about this is provided in standard EN 12390-4 [2]. These studies contributed for the accurate knowledge of the instrumental measurement uncertainty and reproducibility of the produced measurement standard and, consequently, for confidence and comparability enhancement of the experimental results obtained in hardened concrete compression machines.

The experimental application context of the strain column in the metrological testing of hardened concrete compression machines is briefly described in Sect. 2 of this paper while, in Sect. 3, the developed experimental methods are described in detail, including the normalized strain uniformity test mentioned in Annex A.3 of [2]. The obtained experimental results (measurement estimates and uncertainties) are presented in Sect. 4, including the corresponding conformity assessment [3–5] related to the strain column requirements compliance, considering the applicable normative tolerances and decision rule. The conclusions of this work are mentioned in Sect. 5 of the paper.

2 Metrological Testing of Compression Machines

As mentioned in the Introduction, the strain column is used in metrological testing of hardened concrete compression machines for the verification of: (i) the self-alignment of the upper plate; (ii) the alignment of components; and (iii) the upper plate movement restriction.

The same test method is used for the first two mentioned verifications [2], which consists in the inclination of the upper plate in specific directions, followed by the application of a compressive load to a certain force step where readings are simultaneously obtained from each of the four strain column measurement chains. The self-alignment of the machine's upper plate is expressed through the difference between the maximum and minimum strain ratios in each measurement point. The machine components alignment is given by the average value of the strain ratio in each measurement point.

With respect to the verification of the upper plate movement restriction, the normalized test method [2] consists of the displacement of the strain column relative to the plate axis, previously to the load application and for a known and specific set of positions in the lower plate, without any adjustment in the upper plate. The movement restriction is evaluated in two directions in all the testing steps, based on the variation of the strain ratio per displacement unit.

Standard EN 12390-4 [2] provides the maximum permissible values for each of the mentioned verifications, required for the conformity assessment of the tested compression machine.

3 Experimental Methods

3.1 Dimensional and Geometrical Characterization

This section describes the experimental method applied in the dimensional and geometrical characterization of the strain column during its mechanical production stage. In the conformity assessment context, a set of normative requirements is defined in [2] for the strain column which includes its diameter, height, flatness, shape and parallelism of the upper and lower surfaces, perpendicularity of the upper and lower surfaces relative to the vertical axis, circularity and cylindricity. Table 1 summarizes the mentioned measurement quantities and corresponding tolerance intervals and descriptions.

Considering the quantities and normative tolerances mentioned in Table 1, the three-dimensional coordinate measurement contact method was selected for the dimensional and geometrical characterization of the strain column [6]. This method consists in the determination of three-dimensional spatial coordinates of points located in surfaces of the interest object, in this case, the upper, lower, and lateral surfaces of the strain column. The collected coordinates are then used as input information in computational algorithms for the virtual construction of geometrical

Table 1 Dimensional and geometrical requirements of the strain column

Quantity	Tolerance interval	Description
Diameter	100 mm ± 1 mm	Dimensional requirement
Height	200 mm ± 1 mm	Dimensional requirement
Flatness	0.0 mm – 0.03 mm	Each of the upper and lower surfaces of the column must be comprise between two parallel planes with a maximum relative distance of 0.03 mm relative to each other
Shape	Not applicable	Each of the upper and lower surfaces of the column cannot be convex, i.e., they must be plain or concave
Parallelism	0.00 mm – 0.06 mm	Each of the upper and lower surfaces of the column must be comprised between two parallel lines relative to the opposite surface with a maximum distance of 0.06 mm between them
Perpendicularity	0.00 mm – 0.03 mm	The column's axis must be comprised between parallel lines, perpendicular to one of the surfaces (top or down), with a maximum relative distance of 0.03 mm
Circularity	0.00 mm – 0.02 mm	The circular cross-section of the column in any plane perpendicular to its axis must be comprise between two concentric circles with a maximum relative distance of 0.02 mm
Cylindricity	0.00 mm – 0.04 mm	The lateral surface of the column must be comprised between two coaxial cylinders with a maximum relative distance of 0.04 mm

elements (such as lines, circumferences, and planes) which support the calculation of the dimensional and geometrical output quantities.

This measurement method is experimentally implemented using a three-dimensional coordinate measurement machine (CMM) as a reference equipment. In this study, an SI traceable DEA Gamma 2203 CMM was used, being characterized by an instrumental measurement accuracy of 0.005 mm, and a resolution equal to 0.001 mm in a measurement interval of 1.5 m × 1 m × 1 m. This CMC is located at the LNEC's Applied Metrology Laboratory, in a controlled environment laboratorial room (air temperature between 20 °C ± 1 °C and relative humidity lower than 65%), which allows minimizing the uncertainty component related the thermal and hygroscopic expansion/contraction linear effects. To assure the correct environmental conditioning, the strain column was placed in the laboratorial room 12 h before its measurement, while the CMM was activated one hour before.

Preliminary operations included the strain column cleaning with a soft cloth and isopropyl alcohol, and the CMM parameterization using a standard sphere for the position and radius determination regarding the applied contact stylus.

3.2 Calibration

This section describes the developed method for the calibration of the strain column, aiming the SI traceability of this measurement standard and the determination of its instrumental measurement uncertainty. The obtained value is required for the metrological confirmation of the strain column, being the normative target instrumental measurement uncertainty equal to 0.1% or $5 \cdot 10^{-6}$ (whichever is greater) [2]. Due to this accuracy level requirement, the proposed calibration method is based in laser interferometry [7].

This technique is based in the interference optical phenomenon of two laser beams with the same wavelength. The emitted laser beam passes through an optical splitter which allows, simultaneously, the beam propagation to a mobile retroreflector and the return of the original emitted beam. The interference of the two laser beams—original and reflected—allows generating a set of fringes in a photoelectronic detector. Any change of the retroreflector position in the optical circuit is reflected in a variation of the interference fringes counting in the detector. Additional rigorous knowledge about the laser wavelength and the refraction index of the propagation medium (indirectly obtained from air temperature, relative humidity, and atmospheric pressure), allows the determination of the retroreflector displacement.

The experimental implementation of this calibration method was performed using LNEC's laser interferometer (brand Renishaw, model XL-80), which was used as the reference standard, with a known instrumental relative measurement uncertainty of $5 \cdot 10^{-6}$. In addition, a compressive uniaxial testing machine was used to install the strain column and a force transducer, as shown in Fig. 2.

The laser interferometry optical circuit was defined in the testing machine, being composed by: (i) a laser unit (with source and photodetector) fixed in the lower

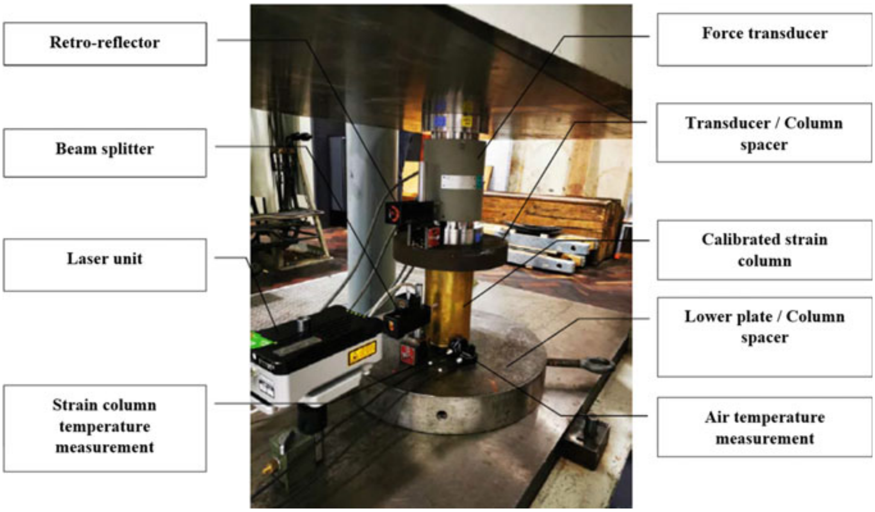

Fig. 2 Experimental apparatus for the strain column calibration

plate; (ii) a beam splitter horizontally and vertically aligned with the laser unit and the machine loading axis, respectively, and place on top of a rigid spacer (used for load transmission between the strain column and the lower plate of the machine); (iii) a retroreflector vertically aligned with the beam splitter and the machine loading axis, fixed to a rigid spacer placed between a force transducer and the strain column. An environmental measurement station related to the laser interferometer was placed nearby the described optical circuit, namely, the air temperature sensor and the material temperature sensor (fixed to the strain column to compensate for the thermal expansion/contraction linear effect).

This apparatus allowed applying known compressive force steps to the strain column and to record its dimensional variation between load steps and the corresponding reference strain, which was compared with the electrical readings of the four measurement chains on the strain column.

3.3 Uniformity

The characterization of the strain uniformity was performed by a standard test method (see Annex A.3 of [2]), consisting in the successive application of compression force steps to the strain column in four testing positions—0°, 90°, 180°, and 270°—relative to its axis, keeping the upper surface parallel and centered relative to the upper load plate of a testing machine (class 1 or better). This test can be performed for load levels equal to 200 kN, 800 kN, and 2000 kN (or the maximum capacity of the machine, if lower than 2000 kN), and other intermediate optional levels (400 kN and 1600 kN, for example).

The strain readings, related to each of the four gauges in the column, were recorded for the several testing positions and applied load steps and used for the following calculations: (i) the average strain reading; (ii) the strain ratio; (iii) the average strain ratio.

3.4 Conformity Assessment

In this work, the performed conformity assessment of the tested strain column applied, as the decision rule, a hypothesis test (without guard bands) assuming a type I error of 1% and a Gaussian probability density function, Φ, using Eqs. (1) and (2)

$$P_C = \Phi\left(\frac{y - T_L}{u(y)}\right) \quad (1)$$

$$P_C = \Phi\left(\frac{T_U - y}{u(y)}\right) \quad (2)$$

where P_C is the conformity probability, T_L and T_U are, respectively, the normative tolerance lower and upper limits, y is the measurement estimate and $u(y)$ is the standard measurement uncertainty [4].

4 Results

4.1 Dimensional and Geometrical Characterization

Table 2 presents the probabilistic formulation of the uncertainty components identified for the dimensional and geometrical measurement of the strain column, considering the applied experimental method and reference equipment.

Due to the linearity of dimensional or geometrical measurement model, the combined measurement uncertainty was obtained by the application of the Uncertainty Propagation Law [8], being expressed by Eq. (3)

$$u(L) = \sqrt{u^2(L)_{s,i} + u^2(L)_{s,d} + u^2(L)_{s,r} + u^2(L)_{s,0} + u^2(L)_{s,res} + u^2(L)_{i,rep} + u^2(L)_{i,tem}} \quad (3)$$

Measurement estimates of the strain column diameter are shown in Table 3, which were computationally obtained from five virtual circumferences, approximately with

Table 2 Uncertainty budget for dimensional and geometrical measurements

Uncertainty component	Source of uncertainty	Probability distribution	Standard uncertainty	Degrees of freedom
$u(L)_{s,i}$	Instrumental accuracy	Gaussian	0.0025 mm	50
$u(L)_{s,d}$	Instrumental drift	Triangular	0.0015 mm/$\sqrt{6}$	50
$u(L)_{s,r}$	Instrumental repeatability	Gaussian	0.003 mm	50
$u(L)_{s,0}$	Measurement zero	Uniform	0.0005 mm/$\sqrt{3}$	50
$u(L)_{s,res}$	Resolution	Uniform	0.0005 mm/$\sqrt{3}$	50
$u(L)_{i,rep}$	Test repeatability	Gaussian	s	$n-1$
$u(L)_{i,tem}$	Thermal effects	Uniform	1 °C·11.5·10^{-6} °C^{-1}·L mm/$\sqrt{3}$	50

the same relative distance between them and uniformly distributed along the strain column axis.

With respect to the strain column height, its measurement was supported in two virtual planes, representing the upper and lower surfaces, and in the determination of the maximum and minimum distances between them. The obtained results are shown in Table 4, being the presented height estimate the average value of the measured distances.

Table 3 Strain column diameter results

Diameter @ 1/6 of the height (mm)	Diameter @ 1/3 of the height (mm)	Diameter @ 1/2 of the height (mm)	Diameter @ 2/3 of the height (mm)	Diameter @ 5/6 of the height (mm)
100.016	100.013	100.012	100.011	100.009
Average value (mm)	95% expanded uncertainty (mm)		Tolerance interval (mm)	Conformity probability (%)
100.012	0.0085		[99; 101]	100

Table 4 Strain column height results

Height values	Test #1 Measured value (mm)	Test #2 Measured value (mm)	Test #3 Measured value (mm)
Maximum	199.932	199.932	199.934
Minimum	199.904	199.905	199.906
Average value (mm)	95% expanded uncertainty (mm)	Tolerance interval (mm)	Conformity probability (%)
199.919	0.017	[199; 201]	100

The spatial coordinates of points collected in the upper and lower surfaces also allowed determining the parallelism between them and their individual flatness and geometrical shape. Considering the upper surface has a reference surface, the perpendicularity quantification was supported in the virtual construction of a plane representative of that surface, while the axis was obtained from five circumferences equally distributed along the strain column. The results are shown in Table 5.

The computational construction of the virtual circumferences allowed quantifying, simultaneously, the circularity and the cylindricity of the strain column, being the obtained results shown in Tables 6 and 7, respectively.

Table 5 Geometrical results of the upper and lower surfaces

Test identification	Parallelism estimate (mm)	Flatness estimate (mm)		Perpendicularity estimate (mm)
		Upper surface	Lower surface	
# 1	0.027	0.020	0.014	0.020
# 2	0.027	0.021	0.014	0.022
# 3	0.028	0.021	0.015	0.021
Average value (mm)	0.027	0.021	0.014	0.021
95% expanded uncertainty (mm)	0.0081	0.0081	0.0081	0.0081
Tolerance interval (mm)	[0.00; 0.06]	[0.00; 0.03]	[0.00; 0.03]	[0.00; 0.03]
Conformity probability (%)	100	99	100	99

Table 6 Circularity results

Circularity @ 1/6 of the height (mm)	Circularity @ 1/3 of the height (mm)	Circularity @ 1/2 of the height (mm)	Circularity @ 2/3 of the height (mm)	Circularity @ 5/6 of the height (mm)
0.004	0.004	0.006	0.005	0.005
Average value (mm)	95% expanded uncertainty (mm)		Tolerance interval (mm)	Conformity probability (%)
0.005	0.0081		[0.00; 0.02]	100

Table 7 Cylindricity results

Test #1 (mm)	Test #2 (mm)	Average value (mm)	95% expanded uncertainty (mm)	Tolerance interval (mm)	Conformity probability (%)
0.014	0.010	0.012	0.0095	[0.00; 0.04]	100

4.2 Calibration

Table 8 presents the probabilistic formulation of the uncertainty components identified for the strain measurement in the performed calibration, considering the applied experimental method and reference equipment.

Being the strain measurement model expressed by Eq. (4)

$$\varepsilon = \frac{\Delta L}{L_0}, \tag{4}$$

and defined by the ratio between the strain column height variation, ΔL, due to the compression load, and its initial height value, L_0, the application of the Uncertainty Propagation Law [8] provides the following expression, Eq. (5), for the corresponding combined measurement uncertainty

$$u(\varepsilon) = \sqrt{c_{\Delta L}^2 \cdot u^2(\Delta L) + c_{L_0}^2 \cdot u^2(L_0)} \tag{5}$$

where $c_{\Delta L} = 1/L_0$ and $c_{L0} = -\Delta L/{L_0}^2$.

Table 8 Uncertainty budget for the strain measurement in the calibration

Uncertainty component	Source of uncertainty	Probability distribution	Standard uncertainty	Degrees of freedom
$u(L_0)$	Initial height of the strain column*	Gaussian	0.0084 mm	63
$u(\Delta L)$	Measured height variation	Gaussian	0.00010 mm	150
$u(\Delta L)_{s,i}$	Instrumental accuracy	Gaussian	$2.5{\cdot}10^{-6}{\cdot}\Delta L$ mm	50
$u(\Delta L)_{s,d}$	Instrumental drift	Triangular	$1.0{\cdot}10^{-6}{\cdot}\Delta L$ mm/$\sqrt{6}$	50
$u(\Delta L)_{s,0}$	Measurement zero	Uniform	$5.0{\cdot}10^{-5}$ mm/$\sqrt{3}$	50
$u(\Delta L)_{s,res}$	Measurement resolution	Uniform	$5.0{\cdot}10^{-5}$ mm/$\sqrt{3}$	50
$u(\Delta L)_{i,e}$	Short-term stability	Uniform	$5.0{\cdot}10^{-5}$ mm/$\sqrt{3}$	50
$u(\Delta L)_{i,tem}$	Thermal effects	Uniform	0.1 °C·11,5·10^{-6} °C$^{-1}{\cdot}\Delta L$ mm/$\sqrt{3}$	50

*Obtained from the dimensional characterization (see Table 4)
ΔL—height variation estimate (a maximum value of 0.5085 mm was observed for a compression force close to 2000 kN)

Table 9 Strain column calibration results

Load level (kN)	Estimate (10^{-6})	95% expanded uncertainty (10^{-6})	95% expanded uncertainty (%)
200	411.17	0.51	0.12
400	661.89	0.51	0.077
600	901.74	0.51	0.056
800	1140.71	0.52	0.046
1600	2077.22	0.54	0.026
2000	2532.53	0.56	0.022

Table 9 shows the obtained estimates and (absolute and relative) expanded uncertainties (in a 95% level of confidence) for the strain measurements performed at different compression load levels.

These results can be compared with the target instrumental uncertainty ($5 \cdot 10^{-6}$ or 0.1%) defined in the normative framework of the strain column [2], showing that the tested strain column complies with normative accuracy requirement, i.e., its instrumental uncertainty is always lower or equal to the target instrumental uncertainty (even for the relative instrumental uncertainty related to the 200 kN step, considering the rounding of the relative target instrumental uncertainty).

4.3 *Uniformity*

The average strain estimate, $\overline{\varepsilon}$, is determined from the four strain readings related to the corresponding measurement points in the strain column, for each load level. In this work, the standard measurement uncertainty, $u(\overline{\varepsilon})$, of the average strain was assumed as the combination (using the Uncertainty Propagation Law) between the target standard uncertainty, $u(\varepsilon_n)$, of the individual strain measurements (equal to $2.5 \cdot 10^{-6}$), and the average experimental standard deviation related to the strain measurement sample.

In addition, being the strain ratio, R_n, defined by Eq. (6)

$$R_n = \frac{\varepsilon_n - \overline{\varepsilon}}{\overline{\varepsilon}} = \frac{\varepsilon_n}{\overline{\varepsilon}} - 1 \tag{6}$$

the application of the Uncertainty Propagation Law [8] allows expressing the corresponding combined measurement uncertainty as Eq. (7)

$$u(R_n) = \sqrt{c_{\varepsilon_n}^2 \cdot u^2(\varepsilon_n) + c_{\overline{\varepsilon}}^2 \cdot u^2(\overline{\varepsilon})} \tag{7}$$

where $c_{\varepsilon_n} = \frac{1}{\overline{\varepsilon}}$ and $c_{\overline{\varepsilon}} = -\frac{\varepsilon_n}{\overline{\varepsilon}^2}$.

Table 10 Results of uniformity strain test

Load level (kN)	Estimates and expanded uncertainties of the average strain ratio			
	0°	90°	180°	240°
200	0.008 89 ± 0.000 65	−0.000 73 ± 0.000 49	−0.009 53 ± 0.000 43	0.001 37 ± 0.000 58
400	0.002 88 ± 0.000 14	−0.001 48 ± 0.000 13	−0.002 69 ± 0.000 12	0.001 29 ± 0.000 14
600	0.001 57 ± 0.000 06	−0.001 12 ± 0.000 06	−0.001 33 ± 0.000 06	0.000 87 ± 0.000 06
800	0.003 34 ± 0.000 46	−0.006 49 ± 0.000 34	−0.005 25 ± 0.000 33	0.008 39 ± 0.000 50
1600	0.000 70 ± 0.000 11	−0.003 14 ± 0.000 09	−0.002 10 ± 0.000 10	0.004 55 ± 0.000 14
2000	−0.004 63 ± 0.000 07	0.004 24 ± 0.000 49	−0.002 18 ± 0.000 08	−0.007 43 ± 0.000 07

The measurement uncertainty of the average strain ratio, $u(\overline{R_n})$, was quantified by the maximum uncertainty value considering the sample of experimental strain ratio values observed in the four measurement points in the strain column. Table 10 shows the estimates and 95% expanded measurement uncertainties of the average strain ratio obtained for the applied load levels in the uniformity test.

Considering the normative tolerance intervals defined for the uniformity test (±0.02 for a load close to 200 kN, and ±0.01 for a load higher than 200 kN) [2], the conformity probability obtained for all positions and load levels was equal to 100%.

5 Conclusions

The metrological study of the strain column produced by LNEC allows concluding that this measurement standard complies with the normative requirements—dimensional, geometrical, accuracy and uniformity—related to its use in the metrological testing of hardened concrete compression machines. This conclusion is supported in the performed conformity assessment based in the adoption of a decision rule (hypothesis test, assuming a type I error equal to 1%), which considers both the normative tolerances related to each requirement [2] and the obtained experimental results (estimates and measurement uncertainties).

Future work in this field will be focused on the determination of the strain column instrumental drift, based in regular calibration results, and the evaluation of its impact in the instrumental measurement uncertainty of the studied reference standard.

References

1. EN 12390-3: Testing hardened concrete—part 3: compressive strength of test specimens. CEN—European Committee for Standardization, Brussels (2019)
2. EN 12390-4: Testing hardened concrete—part 4: compressive strength—specification for testing machines. CEN—European Committee for Standardization, Brussels (2019)
3. JCGM 106: Evaluation of measurement data—the role of measurement uncertainty in conformity assessment. BIPM—Bureau International des Poids et Mesures, Sèvres (2012)
4. EUROLAB TR1: Decision rules applied to conformity assessment. Technical Report No. 1/2017, EUROLAB—European Federation of National Associations of Measurement, Testing and Analytical Laboratories, Brussels (2017)
5. ILAC G8:09: Guidelines on decision rules and statements of conformity. ILAC—International Laboratory Accreditation Cooperation, Silverwater (2019)
6. Ribeiro, A., Martins, L.: Caracterização dimensional e geométrica de corpo cilíndrico para calibração de máquinas de ensaio à compressão de betão endurecido. Report 78/2013—CIC/NQM, LNEC—National Laboratory for Civil Engineering, Lisbon (2013)
7. Lipinski, G.: Mesures dimensionnelles par interférométrie laser. Techniques de l'Ingénieur—traité Mesures et Contrôle (1995)
8. JCGM 100: GUM 1995 with minor corrections—evaluation of measurement data—guide to the expression of uncertainty in measurement. BIPM—Bureau International des Poids et Mesures, Sèvres (2008)

Experimental Design for Building Retrofit Studies: The Assessment of the Thermal Behaviour of a Solar Passive Retrofit Solution

Sara Brito-Coimbra, Daniel Aelenei, Maria Glória Gomes, and António Moret Rodrigues

Abstract Most of Portuguese residential building stock is obsolete in terms of thermal comfort and, as a result, they have poor energy performance. One of the main reasons for the poor performance are structural thermal bridges on façades, which are areas where thermal energy is significantly lost during the heating season. To solve this problem, a novel approach of the Trombe wall system, named Solar Bridge Retrofit Solution (SBRS), was proposed. This paper presents the experimental measuring procedure designed to assess the thermal behaviour of the SBRS, during the heating and cooling season. Several experimental results are also presented and analysed.

Keywords Experimental design · Thermal behaviour · Trombe wall · SBRS

1 Introduction

Most of the Portuguese residential buildings are obsolete in terms of thermal comfort and energy efficiency and need to be retrofitted towards today's standards of thermal and energy performances. These buildings are characterized by high heating energy demands, which is particularly concerning for a country with "mild climate" conditions [1, 2]. These statements come in contrast to the great solar availability in Portugal, which, according to Brito-Coimbra et al. [3], is not widely leveraged to research and develop new solar passive systems or approaches. To fill this gap, Aelenei et al. [4] designed an innovative approach based on the use of the classical Trombe wall system applied to structural thermal bridge areas of the façade.

S. Brito-Coimbra (✉) · D. Aelenei
NOVA School of Science and Technology, NOVA University of Lisbon, Lisbon, Portugal
e-mail: sara.brito.coimbra@gmail.com

D. Aelenei
Center of Technology and Systems, UNINOVA, Caparica, Portugal

M. G. Gomes · A. M. Rodrigues
CERIS, DECivil, Instituto Superior Técnico, Universidade de Lisboa, Lisbon, Portugal

C. Chastre et al. (eds.), *Testing and Experimentation in Civil Engineering*,
RILEM Bookseries 41, https://doi.org/10.1007/978-3-031-29191-3_25

The proposal of new innovative approaches is crucial to the development of building design. However, the feasibility of new proposals must be assessed. This can be done by means of properly designed experimental studies that ensure adequate and reliable data for the assessment.

This communication addresses the experimental design study to assess the thermal behaviour of the retrofit system proposed by Aelenei et al. [4].

2 The Retrofit Solution

According to 2011 Portuguese Census [5], nearly 33% of residential buildings were built between 1971 and 1990. Typically, the façade design of these buildings consists of a reinforced concrete structure filled with non-bearing masonry walls and does not include a thermal insulation layer, as shown in Fig. 1.

Portuguese residential buildings are mostly thermally retrofitted with External Thermal Insulation Composite Systems (ETICS) (see Fig. 2a). However, to leverage the solar availability in Portugal, Aelenei et al. [4] proposed an innovative solution that only targets structural thermal bridge areas of the façade, while allowing to implement ETICS in the remainder opaque areas. The complementary solution consists of a Trombe wall system which, instead of targeting large areas of the South façade, it is only applied in the frame structure (concrete columns, beams, slabs, etc.) area of the façade, where the structural thermal bridges are located. As Fig. 2b shows, for the masonry wall above, the proposed retrofit solution applies only to the concrete column area. This retrofit approach is mainly designed to be applied to residential buildings built during 1970–1990 [1].

This novel approach has the same working principle of the classical Trombe wall. During daytime hours, the transmitted part of the solar radiation goes into the air space, between the external transparent skin and the external wall, creating a greenhouse effect. However, by targeting the structural thermal bridges (concrete columns and beams), the solar radiation absorbed activates a large amount of thermal mass, which can store the thermal energy for long periods of time, in addition of transferring part of the energy to the indoor environment. In this way, this system

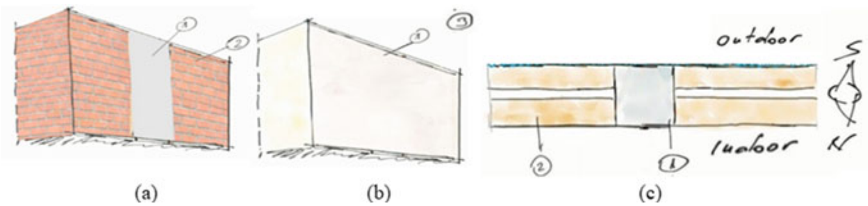

Fig. 1 Conceptual drawing of a non-retrofitted façade of a 1971–1990 Portuguese residential building: **a** prior to the painting **b** following the painting and its **c** horizontal cross section: 1—concrete column; 2—masonry wall; 3—wall finish

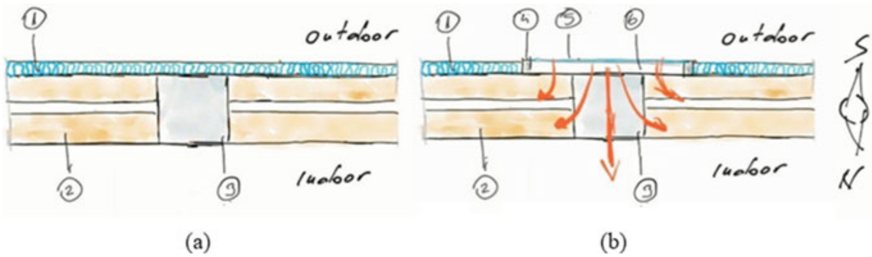

Fig. 2 Conceptual drawing of the horizontal cross section of a façade retrofitted with **a** ETICS; **b** ETICS and SBRS: 1—ETICS; 2—masonry wall; 3—concrete column; 4—frame of the glazing; 5—external transparent skin layer (glazing); 6—air cavity of the SBRS; adapted from [4]

will not only lower the heat losses but also allows for solar heat gains, which, in the case of the traditional approach that uses ETICS, is not possible.

By combining a solar passive technology (Trombe wall system) with retrofit of thermal bridge areas, this innovative solution was named Solar Bridge Retrofit System (SBRS) [4].

To assess the thermal behaviour of the SBRS during the heating season, and its behaviour during the cooling season, multiple monitoring campaigns were devised during the year 2020 and 2021. The experimental design consisted of monitoring and recording various parameters (i.e., temperatures, heat fluxes, solar radiation), during both winter and summer time. In addition, a thermographic survey was carried out during wintertime. Furthermore, the experimental study was also designed to allow studying the influence of ventilation of the air space during summertime (see Fig. 3b). For more details of the SBRS please refer to [1].

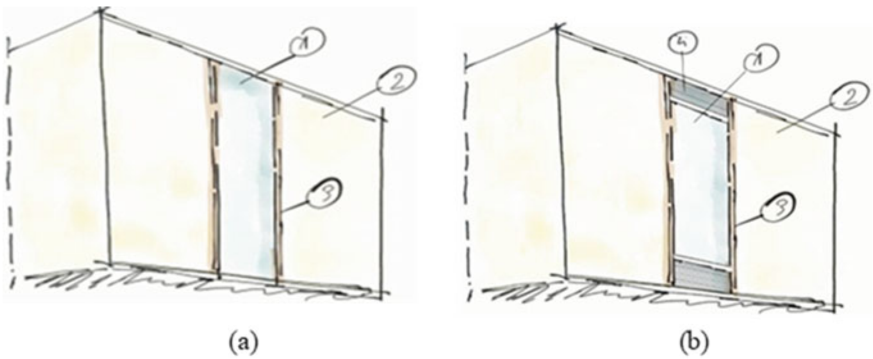

Fig. 3 Conceptual drawing of a façade with SBRS—**a** without and **b** with vents at the external transparent skin layer. 1—external transparent skin layer (glazing); 2—masonry wall retrofitted with ETICS; 3—frame of the glazing; 4—vents

3 The Design of the Experimental Setup

The experimental study consisted of the design, construction, instrumenting and monitoring of a test cell built on the rooftop of the Department of Civil Engineering at NOVA FCT, in Caparica, Portugal (see Fig. 4). Due to roof structural limitations, only one test cell was built for testing. For this reason, only one configuration could be tested at a certain time over multiple monitoring campaigns. The test cell measures $1.1 \times 3.0 \times 1.20$ m in width, depth and height, respectively. The constructive design of the South facing wall resembles the façade design of 1971–1990s residential buildings: cavity wall centred by a concrete column (see Fig. 5a, b). The calculated thermal transmittance of the cavity wall and the concrete column is 1.1 and 2.9 W/m^2 K, respectively. The SBRS consists of a double-glazing mounted on a plastic frame (PVC), distanced 5 cm from the outer surface.

Fig. 4 Photo of the test cell built to study the thermal behaviour of the SBRS

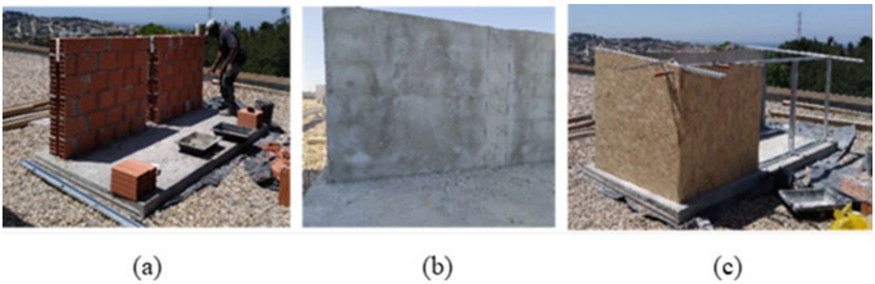

Fig. 5 Construction of the test cell: **a** cavity wall being constructed; **b** the wall after plastering; **c** the wall after thermal insulation

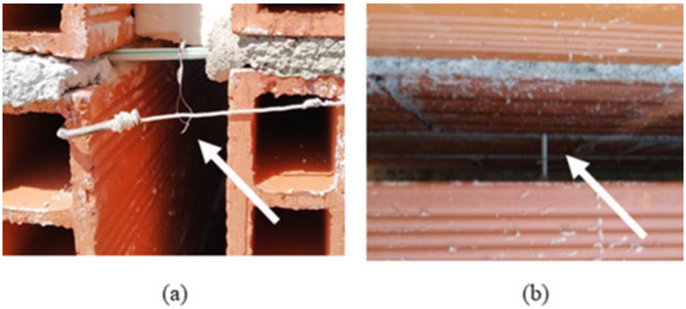

Fig. 6 Temperature sensors (thermocouples type T) being installed within the cavity of the masonry wall: **a** front view of the sensor in the air space of the cavity wall; **b** top view

The remaining test cell envelope elements (walls and roof) consists of a lightweight structure made of (from the inside to the outside) an OSB (Oriented Strand Board) layer (1.8 cm), and EPS insulation layer (4 cm) (see Fig. 5c). The calculated U-value of this lightweight solution is 0.71 W/m^2 K.

The design of the test cell and location of different sensors to acquire data regarding the thermal behaviour of the proposed system were planned in the beginning of the experimental design. Figure 6 shows the temperature sensors (thermocouples) being placed inside the cavity wall during the construction of the test cell.

Table 1 shows the list of equipment employed during the monitoring campaigns and the corresponding accuracy. The map with the location of the equipment across the test cell and the SBRS is illustrated in Fig. 7.

Thermohygrometers were used to measure the temperature and relative humidity of the outdoor environment and indoor environment inside the test cell. To measure surface temperatures of the wall and external transparent skin, the temperature of the air cavity of the masonry wall and the temperature of the air space of the SBRS, thermocouple type-T were used. Furthermore, for measuring the heat flux at inner and outer surface of the wall, heat flux sensors were used. Also, to measure wind velocity and direction and the horizontal global solar radiation, a wind sensor and pyranometer were placed in the vicinity of the test cell, respectively (see Fig. 8).

To avoid miss readings error due to the direct solar radiation exposition, the thermocouples used to measure the temperatures at the outer surface of the South wall and on the external transparent skin were screened [6].

Because in this study there were required nearly 30 sensors (depending on the monitoring campaign), two dataloggers were used, namely a Delta-T DL2e datalogger and a Delta-T GP2 datalogger for continuous data acquisition. Both dataloggers were placed inside the test cell to record data every 10 min.

To analyse the temperature distribution (qualitative analysis) at the inner surface of the wall where the SBRS was applied, a thermographic survey was carried out using an infrared thermographic camera FLIR™ C3. The thermograms were obtained with the camera placed at a distance of 2.0 m from the inner surface of the South facing wall and 30-min intervals, from 6 pm to 12 am.

Table 1 List of equipment used during the monitoring campaign

Equipment	Symbol (units)	Measurement	Accuracy
Thermocouple type T	T1 up to T19 (°C)	Inner/outer surface temperature of the wall/glazing Temperature of the air cavity of the masonry wall Temperature of the air cavity of the SBRS	±0.5 °C
	Tout (°C)	Outdoor air temperature	
Thermohygrometer (Probe)	Tint (°C) RHint (%)	Indoor air temperature Indoor relative humidity	±0.1 °C ±2%
Thermohygrometer (TinyTag®)	Tout (°C) Tint (°C) RHout (%) RHint (%)	Outdoor air temperature Indoor air temperature Outdoor relative humidity Indoor relative humidity	±0.1 °C ±3.0%
Heat flux sensor	F1 up to F3 (W/m^2)	Heat flux at the inner/outer surface of the wall	±3%
Pyranometer	P1 (W/m^2)	Horizontal solar radiation	<7 W/m^2
Wind sensor	WV (m/s) WD (°)	Wind velocity Wind direction	±1.1% ±4°

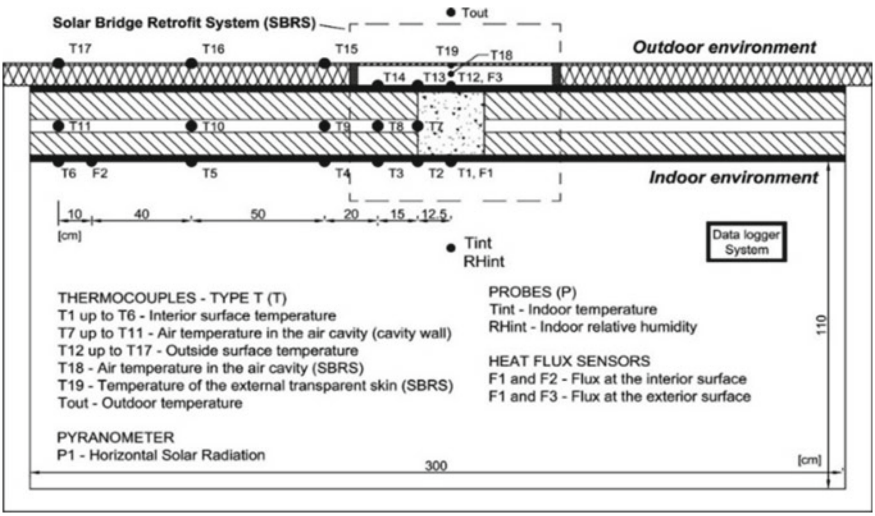

Fig. 7 The map with the location of the sensors across the test cell and SBRS (horizontal cross-section of the test cell)

Fig. 8 Sensors: **a** pyranometer, **b** wind sensor (location in the experimental setup); **c** wind sensor

4 Results

The results shown and discussed in this section refer to data obtained during sunny days of the monitoring campaigns devised during March 2020 (winter monitoring campaign) and September 2021 (summer monitoring campaign). The 15th of March represents a typical day of the heating season. The 8th and 18th of September are two typical days of the cooling season. However, throughout the day on the 8th of September, the vents at the external transparent skin layer were opened and, as a result, the air space of the SBRS was vented, whereas on 18th of September the vents were closed.

4.1 Results from the Heating Season

Table 2 summarizes the main features of the measured temperatures of the outdoor environment (Tout), indoor environment (Tint), SBRS air space (T18), inner surface of the concrete column (T1), masonry wall within SBRS (T3) and masonry wall covered with ETICS (T6), at 135 cm from the thermal bridge between the concrete column and masonry wall. The table also presents the main features of the horizontal global solar radiation (P1).

As can be seen from Table 2, the minimum, maximum and average temperature of the inner surface of the concrete column and masonry wall within SBRS were higher than the surface temperature of the masonry wall covered with ETICS. Among the

Table 2 Summary of the results in terms of temperatures (Tout, Tint, T18, T1, T3 and T6) and horizontal global solar radiation (P1)

	P1 (W/m^2)	Tout (°C)	Tint (°C)	T18 (°C)	T1 (°C)	T3 (°C)	T6 (°C)	T18—Tout (°C)	T1—Tint (°C)
Min	–	10.6	14.0	13.2	14.4	14.2	13.9	–	–
Max	836	24.4	18.4	34.0	18.3	18.1	17.9	9.6	−0.1
Avg	216	16.2	15.9	21.5	16.2	15.8	15.6	5.3	0.3

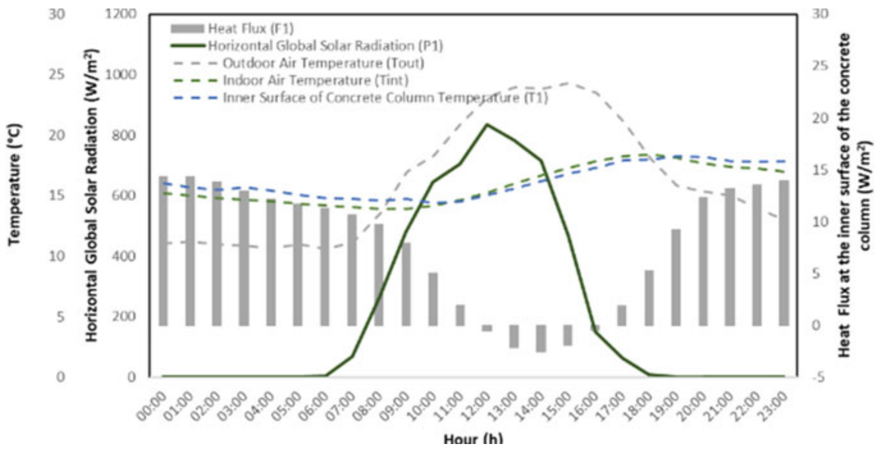

Fig. 9 Temperatures, heat flux and solar radiation during 15th March 2020—closed vents

three surfaces, the inner surface of the concrete column experienced the highest temperatures values. These results are pointing out the fact that the frame structure does allow for solar heat gains during the heating season when the façade is retrofitted with SBRS. Besides, in average, the temperature of the inner surface of the concrete column (T1) was higher than the indoor air temperature (Tint), which means that the heat flux was mainly in the direction pointing from the concrete column to indoors (heat gains). The heat flux density of the inner surface of the concrete column measured with the F1 sensor during a 24 h period (15th March 2020) is illustrated in Fig. 9.

Positive value means heat flux occurs from the column to the indoors (heat gains), whereas negative value means heat flux occurs from indoors to the column (heat losses). The figure also shows the outdoor air (Tout), indoor air (T1) and inner surface of concrete column (T1) temperatures, together with the horizontal global solar radiation (P1).

As is seen from Fig. 9, except for the period between 12:00 and 16:00 when the flux is negative, the SBRS exhibits heat gains, which is what is desired during the heating season. Besides, this heat flux direction occurs mainly during the night-time hours, which is the period when residential buildings are typically occupied. Therefore, the proposed retrofit solution, the SBRS, helps enhancing the indoor thermal comfort during the heating season.

4.2 Results from the Cooling Season

Two SBRS configurations were tested during the cooling season. One with the vents opened and another with the vents closed. Table 3 summarizes the main features of the

Table 3 Summary of the results in terms of temperatures (Tout, Tint, T18 and T1) and horizontal global solar radiation (P1)

8th September (vents opened)	P1 (W/m^2)	Tout (°C)	Tint (°C)	T18 (°C)	T1 (°C)	T18—Tout (°C)	T1—Tint (°C)
Min	–	19.0	26.8	20.7	24.9	–	–
Max	993.9	25.3	28.5	32.7	26.6	7.5	−2.0
Avg	542.5	20.8	27.5	23.8	25.7	3.1	−1.8
18th September (vents closed)	*P1* (W/m^2)	*Tout* (°C)	*Tint* (°C)	*T18* (°C)	*T1* (°C)	*T18—Tout* (°C)	*T1—Tint* (°C)
Min	–	15.9	24.7	21.9	24.5	–	–
Max	940.5	25.8	27.0	43.8	27.3	18.0	0.3
Avg	515.8	19.7	25.8	29.4	25.8	9.7	0.0

measured outdoor environment (Tout), indoor environment (Tint), SBRS air space (T18), inner surface of the concrete column (T1) temperatures on 8th of September 2021 (open vents) and on 18th of September 2021 (closed vents). The table also shows the main features of the horizontal global solar radiation (P1).

As is seen from Table 3, the temperature difference between air cavity (T18) and outdoor (Tout) in the case with open vents and in the case with closed vents was, on average, 3.1 °C and 9.7 °C, respectively. These results support expectations that the natural ventilation of the cavity may prevent the unwanted heat gains during the cooling season. Therefore, the ventilation of the air space significantly impacts the thermal behaviour of the proposed retrofit solution.

The heat flux density of the inner surface of the concrete column measured with F1 sensor during a 24 h period of 8th and 18th of September of 2021 is illustrated in Figs. 10 and 11, respectively. Positive value means heat flux occurs from the column to the indoors (heat gains), whereas negative value means heat flux occurs from indoors to the column (heat losses). Both figures also show the outdoor air (Tout), indoor air (T1) and inner surface of concrete column (T1) temperatures, along with the horizontal global solar radiation (P1).

As can be observed from Fig. 10, when the SBRS vents are opened, the heat flux is negative, meaning that it occurs from indoors to the concrete column (heat losses), which is what is desired during the cooling season. However, when the SBRS has the vents closed (Fig. 11), the heat flux occurs mostly from the concrete column to the indoors (heat gains), which is not wanted during the cooling season.

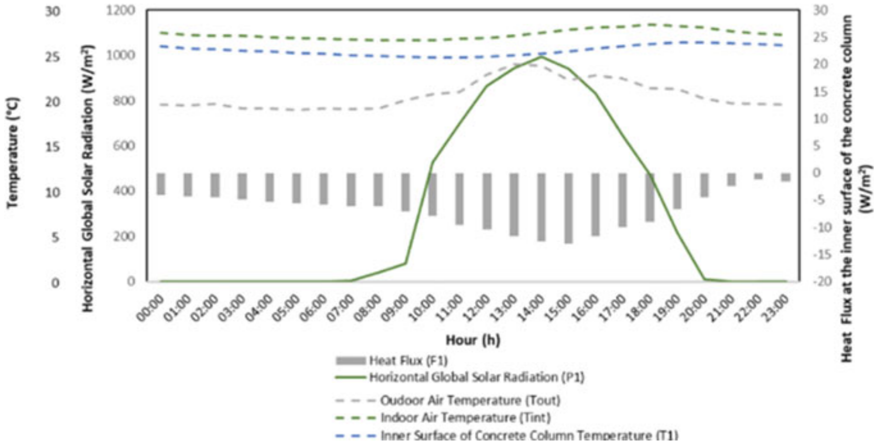

Fig. 10 Temperatures, heat flux and solar radiation during 8th September 2021—opened vents

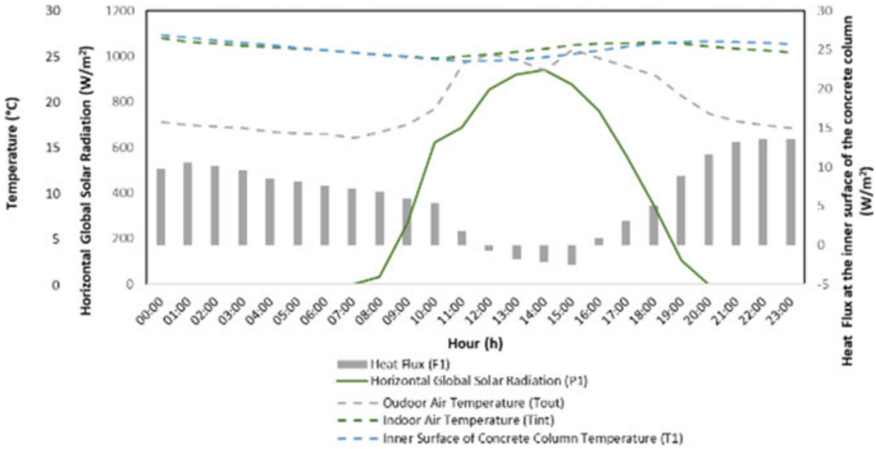

Fig. 11 Temperatures, heat flux and solar radiation during 18th September 2021—closed vents

5 Conclusion

As a result of a rigorous experimental design, it was possible to investigate the thermal behaviour of the proposed retrofit solution, the Solar Bridge Retrofit System, during the cooling and the heating season. The experimental design showed that SBRS:

– is relatively easy to be applied to façades (good integration).
– fulfils both energetic and constructive functions.
– helps enhance winter thermal performance and can be adapted to summertime.

The data presented in this study, collected during experimental campaigns, is an asset to validate a numerical model. All in all, it can be stated that the results obtained from an experimental study are crucial for the overall proposal of new constructive solutions.

Acknowledgements This study was supported by the Portuguese Foundation of Science and Technology (FCT), doctoral grant PD/BD/135171/2017 under the Eco Construction and Rehabilitation (EcoCoRe) doctoral program. The authors also gratefully acknowledge the support of Vítor Silva and Jorge Silvério from FCT NOVA for their contribution in the construction of the experimental test cell and in the installation of the SBRS. And, the authors are gratefully acknowledging the contribution of João Gomes from CAIXIAVE for supplying the double-glazing and the PVC frame.

References

1. Abreu, M.I., Oliveira, R.: O contexto atual da reabilitação energética do parque edificado em portugal. In: Congresso Construção 2012, pp. 1–12. https://bibliotecadigital.ipb.pt/handle/10198/10310 (2012). Accessed 12 Dec 2017
2. Magalhães, S.M.C., Leal, V.M.S.: Characterization of thermal performance and nominal heating gap of the residential building stock using the EPBD-derived databases: the case of Portugal mainland. Energy Build. **70**, 167–179 (2014). https://doi.org/10.1016/j.enbuild.2013.11.054
3. Brito-Coimbra, S., Aelenei, D., Gloria Gomes, M., Moret Rodrigues, A.: Building façade retrofit with solar passive technologies: a literature review. Energies **14**(6), 1774 (2021). https://doi.org/10.3390/en14061774
4. Aelenei, D., Brito-Coimbra, S., Glória Gomes, M., Moret Rodrigues, A.: Solar bridge retrofit system: an innovative solution to renovate structural thermal bridge areas. Energy Build. **236**, 110784 (2021). https://doi.org/10.1016/j.enbuild.2021.110784
5. INE: Censos 2011 Resultados Definitivos (2012). ISBN 978-989-25-0148-2
6. Stazi, F., Mastrucci, A., di Perna, C.: Trombe wall management in summer conditions: an experimental study. Sol. Energy **86**(9), 2839–2851 (2012). https://doi.org/10.1016/j.solener.2012.06.025

Condition Assessment of a Metallic Runway Beam Based on Dynamic and Static Testing

Diogo Ribeiro, Cristina Alves Ribeiro, Jorge Leite, Cássio Bragança, Manuel Silva, Nuno Pinto, Pedro Conceição, and António Gaspar

Abstract This work describes the experimental evaluation of the structural condition of a metallic runway beam located in a heavy industry facility. The study involved carrying out an ambient vibration test, aiming the identification of the modal parameters of the beam, in addition to a static test under the action of a transportation vehicle carrying heavy raw material. The static test was mainly focused on the measurement of deformations and displacements on critical sections of the beam. The results of both tests will be useful for the experimental calibration of the numerical model of the beam developed by the designers, which will provide support for the structural rehabilitation and strengthening of the runway beam.

Keywords Structural condition assessment · Runway beam · Ambient vibration test · Static tests · Transportation vehicle

D. Ribeiro (✉) · J. Leite
CONSTRUCT-LESE, Polytechnic of Porto—School of Engineering, Porto, Portugal
e-mail: drr@isep.ipp.pt

C. A. Ribeiro
Senqual, Vila Nova de Gaia, Portugal

C. Bragança
Department of Structural and Geotechnical Engineering, Polytechnic School at the University of São Paulo, São Paulo, Brazil

M. Silva
Polytechnic of Porto—School of Engineering, Porto, Portugal

N. Pinto
CONSTRUCT-LESE, University of Porto—Faculty of Engineering, Porto, Portugal

P. Conceição · A. Gaspar
IDOM Engenharia—Serviços de Engenharia e Consultoria, Lda., Lisbon, Portugal

C. Chastre et al. (eds.), *Testing and Experimentation in Civil Engineering*, RILEM Bookseries 41, https://doi.org/10.1007/978-3-031-29191-3_26

1 Introduction

The increasing environmental concerns and the restricted budget of many infrastructure managers has been led to an increasingly reuse of existing metallic structures. In most cases, this reuse involves some type of structural rehabilitation/strengthening to prepare the structure for more severe loading and environmental conditions. To guarantee the success of these strengthening operations, recent studies [1–3] stand out the need to have a deep knowledge about the current structural integrity conditions for the optimal design of strengthening solutions and, afterwards, evaluate their effectiveness.

Mirza et al. [4] studied the effectiveness of retrofit techniques in increasing the fatigue life of railway bridge beams. To guide the retrofit actions, numerical and experimental studies were carried out on a beam from an old bridge, with 120 years of use, and a new one. Based on these studies, cracks were introduced in the numerical model in critical locations, and, in the areas affected by the stress concentration of the crack, structural strengthening actions were proposed. These actions proved to be quite effective in smoothing the stress field in the critical region as well as extending the fatigue life of the beam. Another important finding of the study was the lower strength capacity of the old beam when compared to the numerical predictions. This was attributed to the existence of damage, which was increasingly accumulated during its use, and was not properly defined in the numerical simulation.

Due to these uncertainties regarding the integrity of an existing structure as well as the imprecisions in modeling some complex structural behaviors, most of authors [1, 5–7] use numerical models calibrated with experimental data to plan, execute and evaluate the performance of strengthening structural interventions.

Based on calibrated numerical models, Ghorbanzadeh et al. [5] conducted a parametric study to find optimal geometries for structural details intended to strengthen beam-column joints in metallic structures. Based on these studies the authors proposed an optimized solution to reinforce existing pinned steel connections. Results indicated a significant increase in the tensile resistance and rotation capacity of the joint, increasing its robustness to prevent progressive collapse of a building under extreme loading scenarios, as well as accomplishing the design standards requirements.

Rodrigues et al. [1] proposed a strain monitoring system based 80 fiber optic sensors to monitor all stages of the structural rehabilitation of a historic railway bridge. The monitoring system, with the support of a calibrated numerical model, proved to be crucial for understanding the structural behavior of the bridge and planning the stages of replacement of the damaged elements. Once the rehabilitation works were completed, the monitoring system allowed the evaluation of the effectiveness of the strengthening strategies, as well as the calibration of an updated numerical model of the bridge, to serve as a basis for further interventions during life cycle.

Given the importance of properly characterizing the structural behavior for rehabilitation interventions, this work presents the stages of an experimental condition assessment of a metallic runway beam. The runway beam is part of an overhead crane designed to transport very high loadings inside a large-scale industrial facility. The structural behavior of the beam was evaluated based on two types of tests. First, an ambient vibration test was performed to estimate the natural frequencies, damping coefficients and modes of vibration resorting to dedicated modal identification techniques. Second, the deformations and displacements were monitored at several points of the beam during the bridge crane operation transporting heavy loads. The data and conclusions derived from these tests will better guide the designers in the elaboration of optimal solutions for the structural strengthening.

2 The Metallic Runway Beam

The runway beam under study (RWB7) is connected to an identical neighboring beam (RWB9). Both beams are simply supported on metallic pillars and have a span length of 15.0 m (Fig. 1a). The connection between RWB7 and RWB9 is performed by bracings disposed in the form of a plane truss on the horizontal plane, which is connected to the top flanges of the main beams. A transport vehicle, which is part of an overhead crane, runs on the RWB7 beam moving heavy raw material through an industrial facility.

The cross section of the beams (Fig. 1b) is a welded I profile with a height of 1820 mm and a width of 450 mm. The thickness of the web plates and the flanges is equal to 20 mm and 30 mm, respectively. On the outer face of both flanges there are reinforcement plates. These reinforcement plates are 550 mm wide, 30 mm thick and welded to the flanges at their ends. The runway beam includes an A100 type rail attached to the upper face of the reinforcement plate by proper fixing devices. In Fig. 1b the typical cross-sections of the runway beam and rail are presented, as well as the rail fixing devices.

3 Ambient Vibration Test

The ambient vibration test of the runway beam aimed to estimate the natural frequencies, damping coefficients and mode shapes in the vertical and transversal directions.

3.1 Experimental Setup

Figure 2 depicts the measurement positions used during the ambient vibration test. A testing technique based on fixed reference points (marked in red in Fig. 2) and mobile points (marked in yellow in Fig. 2) was adopted. The response was evaluated

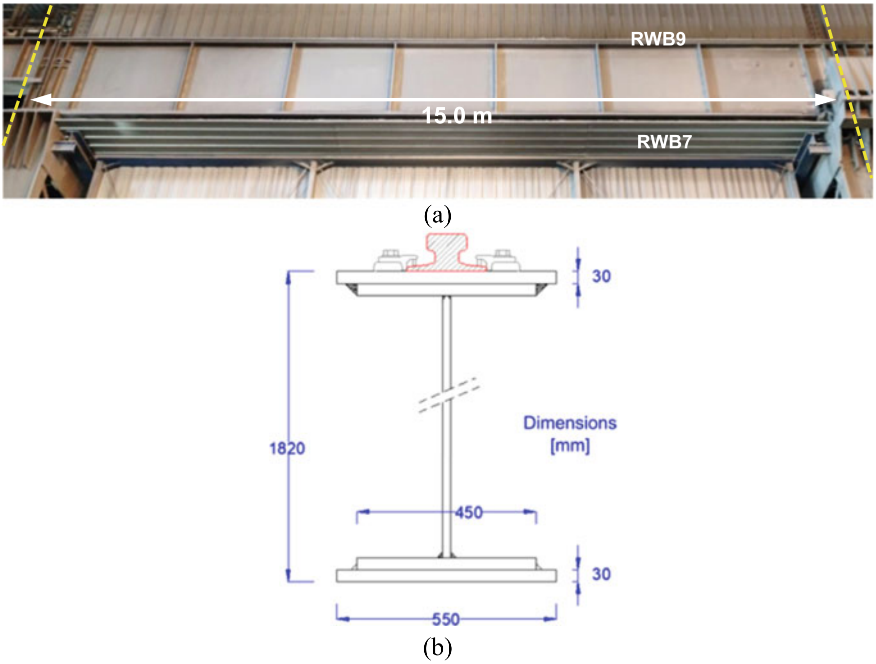

Fig. 1 Runway beams: **a** overview and **b** cross section of RWB7 beam

in terms of accelerations in a total of 20 measurement points. Points 1–8 and points 13–20 were located on the lower flange of beams RWB7 and RWB9, respectively, and points 9–12 were located on the upper flange of beam RWB7. The points were disposed in a regular mesh to facilitate the visualization of the mode shapes.

In total 10 high-sensitivity piezoelectric accelerometers PCB model 393B12, with a measurement range of ±0.5 g, a sensitivity equal to 10 V/g and a frequency range of 0.15–1000 Hz, were used during the tests. The accelerometers were fixed to the runway beam trough welded angles as presented on the details of Fig. 2. Since only 10 accelerometers were available, the test was conducted in four different experimental setups keeping the reference accelerometers in the same position.

The data acquisition was performed by means of a NI cDAQ-9178 system using three modules NI 9234 for IEPE-type accelerometers with a resolution of 24 bits. The time series were acquired over periods of 8 min with a sampling frequency of 2048 Hz, posteriorly decimated to a frequency of 256 Hz.

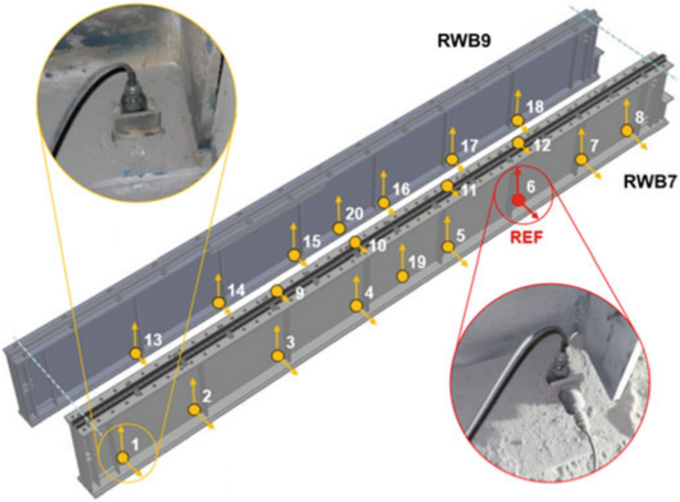

Fig. 2 Ambient vibration test: fixed (red) and mobile (yellow) accelerometers positions

3.2 Modal Identification

The identification of modal parameters was performed by applying the Enhanced Frequency Domain Decomposition method (EFDD). The average and normalized singular values of the spectra matrix of all experimental setups, obtained by applying the EFDD method, are presented in Fig. 3. The identification of the most relevant natural frequencies was performed by evaluating the abscissa in correspondence with the peaks of the curve of the first singular value. In the Fig. 3 the peaks corresponding to the 7 identified vibration modes of the runway beam, whose natural frequencies are ranged between 4.29 and 61.98 Hz, are highlighted by red circles.

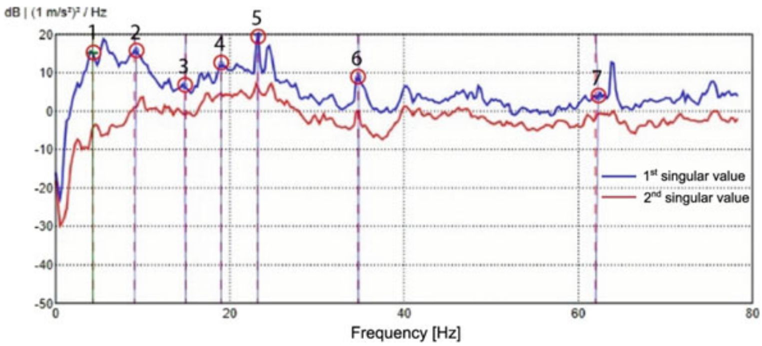

Fig. 3 EFDD method—average and normalized singular values of the spectral density matrices and identified operational modes

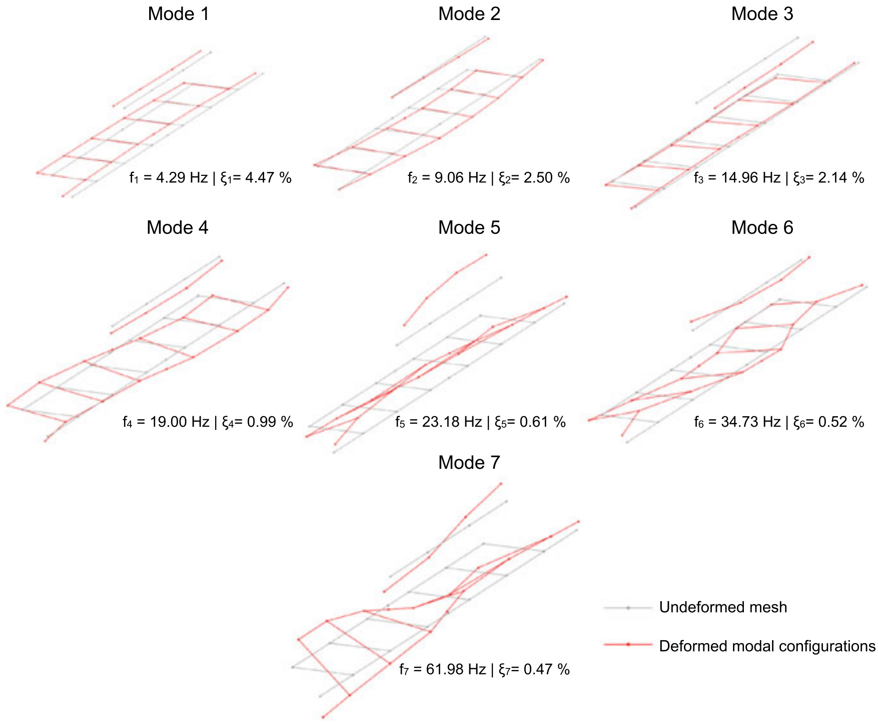

Fig. 4 Modal configurations for 1st to 7th modes (undeformed/deformed shapes) and indication of derived experimental modal parameters

The modal configurations, natural frequencies and damping coefficients associated with each of the 7 identified modes are presented in Fig. 4 based on a perspective view.

The analysis of modal configurations allows to identify modes associated with bending/torsion movements of beams and support columns with very good definition. Mode 1 is possibly associated with the bending movement of the support pillars in the transverse direction, which can be indirectly confirmed by the rigid body translation movement of the beam. Mode 2 is associated with the transverse bending movement of the lower flanges of both beams, with negligible vertical movements and practically no transverse movements at the supports. It is interesting to notice the absence of movements of the upper flange of RWB7 beam. In mode 3 transverse and differential bending movements occur between the upper and lower flanges of the beams with no significant vertical movements. Mode 4 is associated with the second transverse bending movement of the lower flanges of both beams. Once again, the upper flange of RWB7 has a negligible movement in the transverse direction. Mode 5 refers to the out-of-phase first vertical bending mode of each of the beams. This out-of-phase bending causes a global torsion effect, since when one beam goes up the other goes down and vice versa. In this mode the beam also presents some transversal displacements that cannot be neglected. Mode 6 is related to the 3rd transverse bending movement of the lower flanges of both beams. The movements of the upper flange in the transverse direction appear to be synchronous with the movements of the lower chords. In this case the beam also shows some vertical displacements that cannot be neglected. Finally, mode 7 refers to the second vertical bending movement of each of the beams. The modal configuration is anti-symmetrical and formed by two semi-waves. Like in mode 5, the movements of both beams are out-of-phase, resulting in a non-uniform global torsion effect. Regarding the modal damping coefficients, all values remained between 0.47 and 4.47%, and a reduction of the damping values occur with the increase of the natural frequency.

4 Static Tests Under Operational Live Loads

In this section, the details and results of the static tests conducted under the action of a heavy loading from the transport vehicle are presented. These tests aim a better understanding of the structural behavior of the runway beam under the loading schemes to which is normally subjected. During the tests were performed the measurement of deformations, displacements, and temperatures in various sections of the RWB7 beam.

4.1 Experimental Setup

This subsection describes the instrumentation installed on the runway beam for measuring the displacements and deformations during the operation of the transportation vehicle carrying heavy raw material at high temperatures. The instrumentation was divided into two groups: (i) transducers for measuring deformations and temperatures, and (ii) transducers for measuring displacements.

Strain and Temperature Measurements. The strain measurement system involved the installation of 14 electrical resistance strain gauges in critical locations of the beam. This system also included two thermos-resistors for measuring the temperatures on the beam surface. Figure 5 presents the positioning scheme adopted for the 14 strain gauges (E1 to E14) and the two temperature sensors (TR1 and TR2). All the strain gauges were weldable encapsulated sensors, model LS31HT-6/350VE from HBM, with pre-installed wires, self-compensated for the effect of temperature and with a nominal resistance equal to 350 $\Omega \pm 0.4\%$. This strain gauge model was selected due to its high resistance to aggressive environments with high temperatures, being compatible with the industrial conditions in which the test was conducted. The connection of the strain gauges to the acquisition system was carried out in a three-wire 1/4 Wheatstone bridge circuit. The thermos-resistors are RS-Pro weldable sensors, model Pt 100, and are connected to the data acquisition by 2 wires.

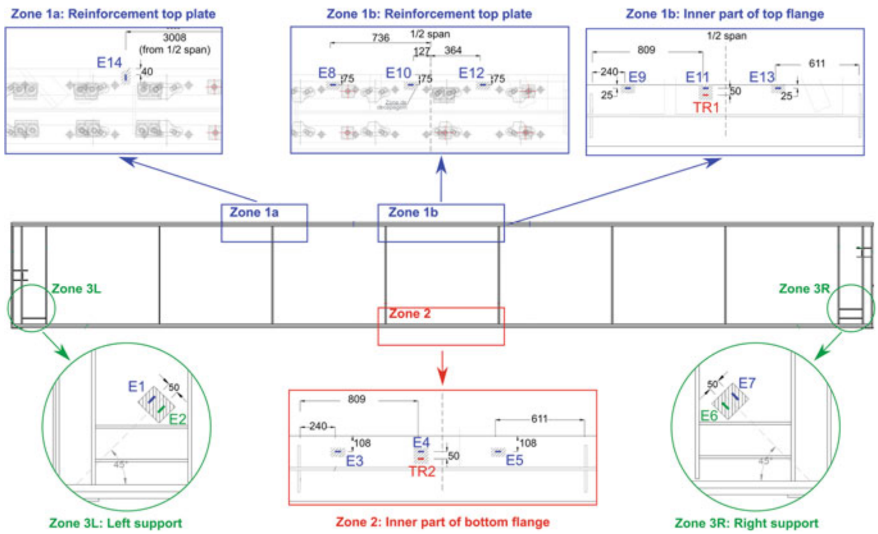

Fig. 5 Location zones of strain gauges (E1 to E14) and thermos-resistors on (TR1 and TR2) the runway beam. Dimensions in (mm)

Displacement Measurement. The displacement measurement system involved measuring the vertical displacements of the runway beam, as well as measuring the relative vertical displacement between the upper flange reinforcement plate and its top flange. This last measurement intended to track a possible gap between these two components. The measurement of the vertical displacements of the beam was performed using a precision topographic system based on a Leica TCRM 1203 total station and topographic reflective targets (prisms type) fixed to the beam in 7 individual positions depicted in Fig. 6 (T1 to T7). The measurement technique is based on optical principles and ensures measurement errors on the vertical displacements less than ±1 mm. The relative displacement measurement involved the installation of a spring-type LVDT, model DCTH 1000A from RDP. The LVDT was fixed to the beam's web by means of a welded plate and clamps, and the extremity of the external shaft was in direct contact with the under face of the reinforcing top plate (Fig. 6). Therefore, a punctual drilling of the upper flange of the beam was carried out, as detailed in Fig. 6.

Data Acquisition System. The data acquisition of the static tests under operational loads was performed by means of a NI cDAQ-9188 system and using NI 9236 modules for signal conditioning of strain gauges, NI 9217 modules for conditioning the thermo-resistance signal and NI 9239 modules for conditioning the LVDT signal.

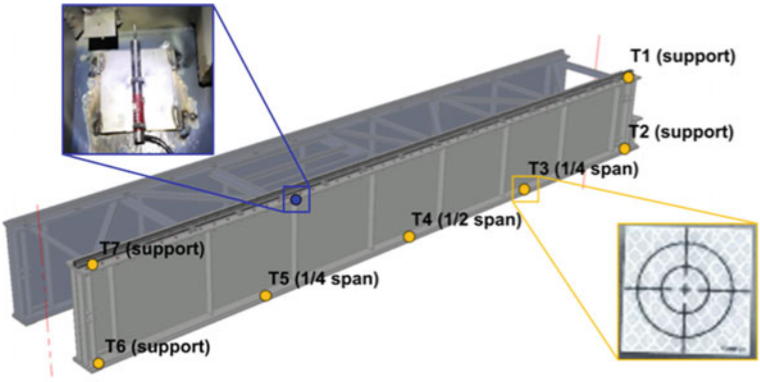

Fig. 6 Displacement measurement setup: Indication of the positioning of topographic targets (T1 to T7) and LVDT

4.2 *Loading Strategy*

The loading strategy consisted of positioning the heavy load transport vehicle in two different positions. The first position (Fig. 7a) is the one that resulted in the highest shear force value (V_{max}). The second position (Fig. 7b) induces the highest bending moment value (M_{max}). Both positions were estimated with the support of a numerical model. A schematic representation of the crane over the beam in the positions of V_{max} and M_{max} is presented in Fig. 7.

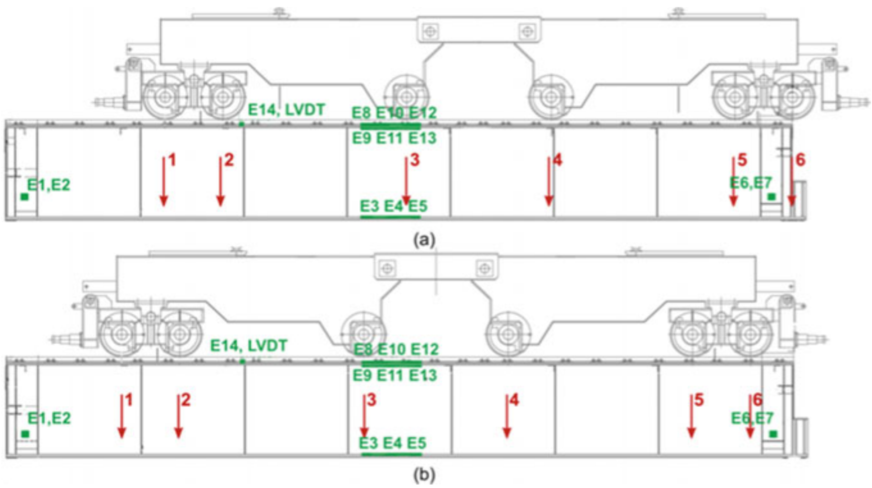

Fig. 7 Positions of the bridge crane wheels, of extensometers E1 to E14 and of the LVDT on the runway beam for the maximum values of: **a** shear force (V_{max}), and **b** bending moment (M_{max})

The exact position of the bridge crane wheels is aligned or very close to some sensors' positions. For example, in the positioning of the bridge crane for V_{max}, it is visible that wheel 3 is on the alignment of the strain gauges E12/E13/E5, while in the positioning for M_{max}, the same wheel is on the alignment of the strain gauges E8/E9/E3. In case of V_{max} positioning, there is also a proximity of the wheel 2 to the strain gauge E14 and to the LVDT.

4.3 Results and Analysis

Figure 8 presents the stress records (derived from the deformations), the relative displacements between the reinforcing top plate and the upper flange of the beam and the temperature for the V_{max} and M_{max} positions. In the time histories the V_{max} position was reached approximately at 16:11, while the M_{max} position was reached approximately at 16:14.

Based on the results it is possible to observe that the stress values in the strain gauge pairs E9/E3, E11/E4 and E13/E5 are quite similar, however, with compressive stresses on the upper flange and tension stresses on the lower flange. This was expectable since the sensors are installed at approximately the same distance from the geometric center of the I profile.

On the other hand, the stress values recorded on the upper face of the reinforcing top plate (E8, E10 and E12) do not follow the assumption of a linear variation of stresses in the section. The stresses recorded at these locations seem to be closely dependent on the position of the wheels, i.e., on the fact that the wheels positions are (or not) close to the section where the sensor is installed. This finding seems to indicate a relevant local behavior of the reinforcement plate due to a poor transmission of stresses with the upper flange.

The stress values recorded on the strain gauge E14, positioned in the direction transverse to the beam axis, seem to corroborate the fact that there is an important local behavior of the reinforcing plate, since they are highly dependent on the position of the load. As examples, it should be refereed the V_{max} position, where the second wheel (see Fig. 7) is positioned in the vicinity of the strain gauge E14, and the M_{max} position, where there are no wheels close to the strain gauge E14. In the case of V_{max} position, there was a very significant increase in the stresses in the transverse direction, while in the M_{max} position these values are practically null.

Furthermore, the values of the relative displacement between the reinforcement top plate and the upper flange reveal that these plates are not effectively connected. This can be seen by the result regarding the position of V_{max}, for which the 2nd wheel is close to the LVDT section, and there is a visible variation in the relative displacement when the vehicle leaves this position. Once again, this finding confirms the local behavior of the reinforcement plate: it tends to contact with the upper flange in the case of a nearby wheel; or tends to recover and remain a gap with the removal of the wheel. Regarding the temperature levels, it remained almost constant near 45 °C.

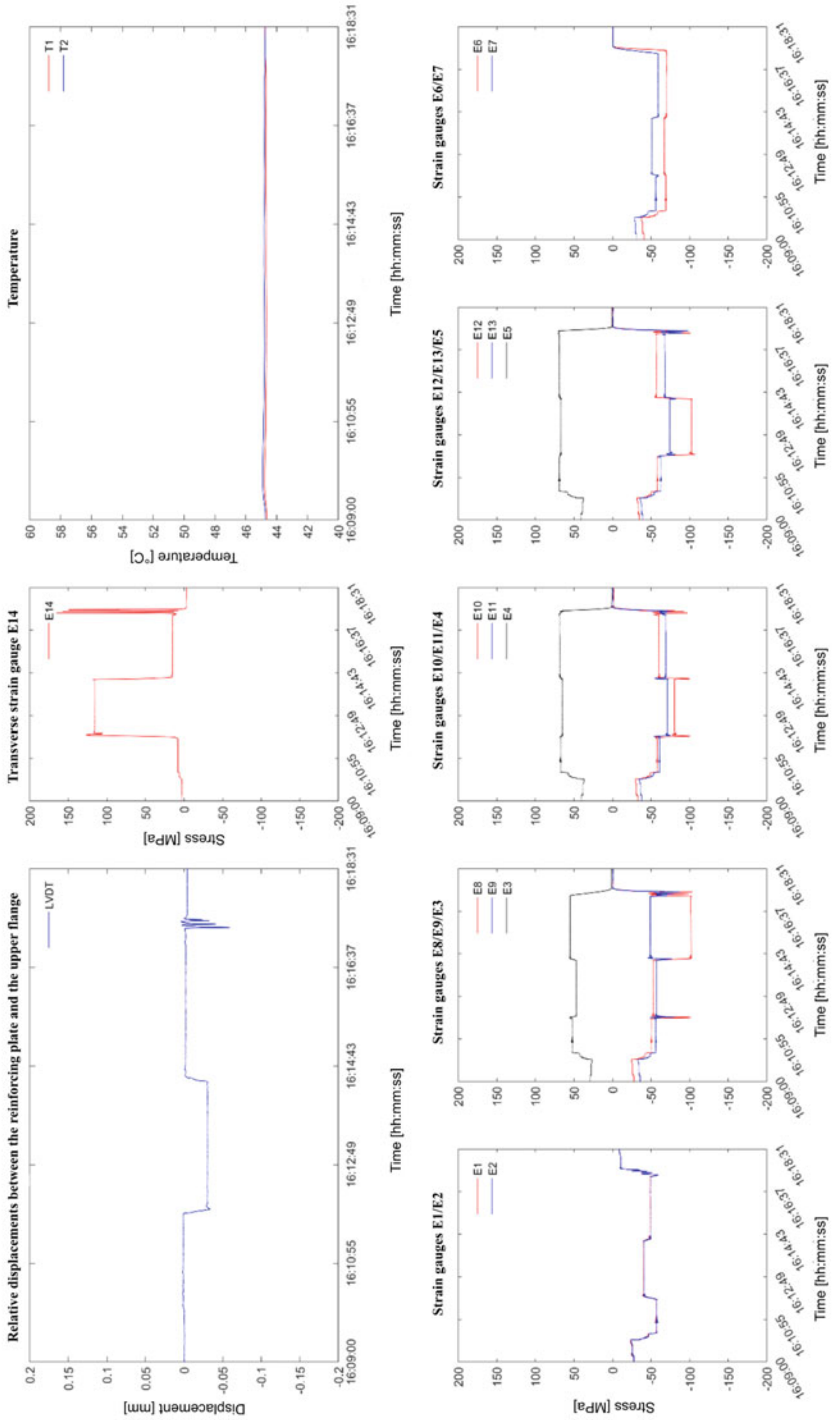
Relative displacements between the reinforcing plate and the upper flange
LVDT
Displacement [mm]
Time [hh:mm:ss]
Transverse strain gauge E14
E14
Stress [MPa]
Time [hh:mm:ss]
Temperature
T1
T2
Temperature [°C]
Time [hh:mm:ss]
Strain gauges E1/E2
E1
E2
Stress [MPa]
Time [hh:mm:ss]
Strain gauges E8/E9/E3
E8
E9
E3
Time [hh:mm:ss]
Strain gauges E10/E11/E4
E10
E11
E4
Time [hh:mm:ss]
Strain gauges E12/E13/E5
E12
E13
E5
Time [hh:mm:ss]
Strain gauges E6/E7
E6
E7
Time [hh:mm:ss]

◀**Fig. 8** Measurement results on the static test under operational loads for V_{max} and M_{max} positions: strain gauges, LVDT and temperature sensors

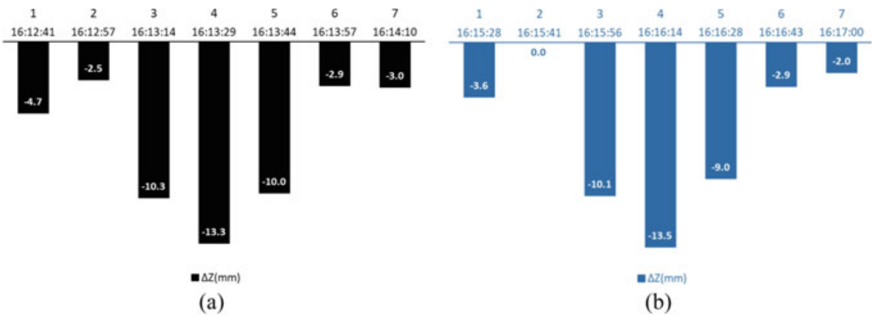

Fig. 9 Measurement of vertical displacements based on a topographical survey for targets T1 to T7: **a** V_{max} position, and **b** M_{max} position

The values of the absolute vertical displacements derived from the topographic survey for the V_{max} and M_{max} positions are presented in Fig. 9a, b respectively. The maximum displacement values were obtained in the ½ span section and are equal to 13.3 mm/13.5 mm for V_{max} and M_{max} positions, respectively. The results also evidence a consistent deformed configuration of the beam, which is virtually visible by sequentially analyzing the displacements between positions of targets T2 to T6. Non-zero vertical displacements were also recorded in both supports (targets T1/T2 and T6/T7) and with values of the same magnitude in most situations.

5 Conclusions

In this work, the results of the experimental condition assessment of a metallic runway beam were presented. The study included two phases, an ambient vibration test and a static test under operational live loads.

The ambient vibration test was intended to characterize the natural frequencies, damping coefficients and modal configurations of the RWB7 beam in the transverse and vertical directions. The application of the EFDD method to the experimental records allowed the identification of 7 global vibration modes with frequencies ranged between 4.29 and 61.98 Hz and referring to bending/torsion modes with very good definition.

The static test under operational live loads involved the measurement of strains, temperatures, and displacements in different parts of the RWB7 beam, as well as the relative displacement between the reinforcement top plate and the upper flange. Additionally, the absolute vertical displacements of the runway beam were measured with the support of a precision topographic survey. The results led to conclude that the reinforcement top plate was not properly connected to the beam upper flange. This finding was proven due to the non-linear distribution of the stresses along the beam cross section and particularly at the level of the reinforcement top plate. Additionally, it was possible to observe an important local structural behavior strongly dependent on the position of the loads, as stated by the transverse stresses in the reinforcement top plate and in the relative displacements measured between the reinforcement top plate and the upper flange.

In future developments, the calibration of a numerical model of the runway beam will be performed based on the results of the ambient vibration test, as well as the results of the static tests under operational live loads. The model calibration strategy will involve an iterative methodology based on genetic algorithms [8, 9]. The updated models will give an important contribute for the designers in achieving optimized strengthening solutions, and consequently, an extension of the beam life cycle.

Acknowledgements This work has been financially supported by Base Funding—UIDB/04708/2020 and Programmatic Funding—UIDP/04708/2020 of the CONSTRUCT—Instituto de I&D em Estruturas e Construções—funded by national funds through the FCT/MCTES (PIDDAC). Cássio Bragança would like to acknowledge the financial support under grant #2022/13045-1, São Paulo Research Foundation (FAPESP)

References

1. Rodrigues, C., Cavadas, F., Félix, C., Figueiras, J.: FBG based strain monitoring in the rehabilitation of a centenary metallic bridge. Eng. Struct. **44**, 281–290 (2012). https://doi.org/10.1016/j.engstruct.2012.05.040
2. Xie, Q., Zhang, J.: Experimental study on failure modes and retrofitting method of latticed transmission tower. Eng. Struct. **226**, 111365 (2021). https://doi.org/10.1016/j.engstruct.2020.111365
3. Chen, X., Ding, M., Zhang, X., et al.: Experimental investigation on seismic retrofit of gravity railway bridge pier with CFRP and steel materials. Constr. Build. Mater. **182**, 371–384 (2018). https://doi.org/10.1016/j.conbuildmat.2018.06.102
4. Mirza, O., Shill, S.K., Mashiri, F., Schroot, D.: Behaviour of retrofitted steel structures using cost effective retrofitting techniques. J. Constr. Steel Res. **131**, 38–50 (2017). https://doi.org/10.1016/j.jcsr.2016.12.026
5. Ghorbanzadeh, B., Bregoli, G., Vasdravellis, G., Karavasilis, T.L.: Pilot experimental and numerical studies on a novel retrofit scheme for steel joints against progressive collapse. Eng. Struct. **200**, 109667 (2019). https://doi.org/10.1016/j.engstruct.2019.109667
6. Sangiorgio, V., Nettis, A., Uva, G., et al.: Analytical fault tree and diagnostic aids for the preservation of historical steel truss bridges. Eng. Fail. Anal. **133**, 105996 (2022). https://doi.org/10.1016/j.engfailanal.2021.105996
7. Clementi, F., Pierdicca, A., Formisano, A., et al.: Numerical model upgrading of a historical masonry building damaged during the 2016 Italian earthquakes: the case study of the Podestà palace in Montelupone (Italy). J. Civ. Struct. Health Monit. **7**, 703–717 (2017). https://doi.org/10.1007/s13349-017-0253-4
8. Alves, V.N., de Oliveira, M.M., Ribeiro, D., et al.: Model-based damage identification of railway bridges using genetic algorithms. Eng. Fail. Anal. **118**, 104845 (2020). https://doi.org/10.1016/j.engfailanal.2020.104845
9. Costa, C., Ribeiro, D., Jorge, P., et al.: Calibration of the numerical model of a short-span masonry railway bridge based on experimental modal parameters. Procedia Eng. **114**, 846–853 (2015). https://doi.org/10.1016/j.proeng.2015.08.038

Modelling and Validation of Models

Numerical Simulation of RC Beams Strengthened by Post-tensioning

Márcia Duarte, Carla Marchão, and Rita Gião

Abstract In the present paper, a numerical simulation performed in the structural analysis framework OpenSeesPy (Python interpreter for OpenSees) of post-tensioned strengthening solutions for RC beams in frame systems, proposed by Gião and Muhaj, is presented. Two reference specimens (VR2 and CB1) and three strengthened specimens were evaluated—one specimen strengthened with non-adherent exterior post-tensioning strands (VPE) and the other two specimens strengthened with interior post-tensioning strands with anchorages by bonding (CB2 and CB3). The two strengthened solutions under analysis aimed to improve the hysteretic behaviour of the beams and, if the techniques are applied to frames, avoid the development of unidirectional plastic hinges. The models were loaded simultaneously with cyclic horizontal displacements and significant gravity loads. The numeric results are analysed and validated by comparison with the experimental ones. The strengthened solutions displayed greater energy dissipation and minor residual deformations than the reference specimens, showing to be adequate seismic strengthening techniques.

Keywords Experimental tests · Numeric simulation · Model calibration and validation · OpenSees

M. Duarte (✉) · C. Marchão
Civil Engineering Department, FCT NOVA, Caparica, Portugal
e-mail: m.duarte@campus.fct.unl.pt

C. Marchão
e-mail: c.marchao@fct.unl.pt

R. Gião
Civil Engineering Department, ISEL IPL, Lisboa, Portugal
e-mail: ana.giao@isel.pt

C. Marchão · R. Gião
CERIS, Lisbon, Portugal

C. Chastre et al. (eds.), *Testing and Experimentation in Civil Engineering*,
RILEM Bookseries 41, https://doi.org/10.1007/978-3-031-29191-3_27

1 Introduction

The seismic design is essential to promote an adequate structural response, allowing structures to dissipate the energy transmitted by the earthquakes, through plastic deformations without significant loss of their resistance—Ductile behaviour. In fact, seismic design without taking advantage, directly or indirectly, of the non-linear behaviour would result in a substantial increase of resistance and, consequently, in a significant increase of the building cost. In this sense, Eurocode 8 [1] introduces a design philosophy—Capacity Design—which recommends that reinforced concrete structures located in seismic regions must assume ductile failure mechanisms, with energy dissipation and present a residual resistance avoiding global or local structure collapse. Taking advantage of the high redundancy degree of frame systems, the non-collapse fundamental requirement leads to the formation of plastic hinges in strategic locations, previously defined and designed for this purpose. It is intended to avoid, for example, the concentration of hinges in columns of a single floor—Fig. 1a—Soft-storey—which corresponds to an unwanted fragile failure mechanism. Thus, the columns in frames systems are designed, considering an increase in resistance, inducing the formation of plastic hinges in the beams—Strong column—weak beam principle—which corresponds to the desirable mechanism associated with the formation of plastic hinges at the beams ends and at the column base—Fig. 1b. This type of mechanism exhibits a reversible behaviour associated with the formation of reversible hinges.

However, if the span is relatively large and/or the gravity load is significant, a second hinge may form in the span. In these cases, when subjected to a seismic load, the beam-bearing capacity is attained for hogging moments (near the column) and for sagging moments (in the span). This behaviour corresponds to the formation of two hinges in each direction. However, when the frame system sway occurs in the reverse direction, there is no full inversion of the hinge plastic behaviour, leading to

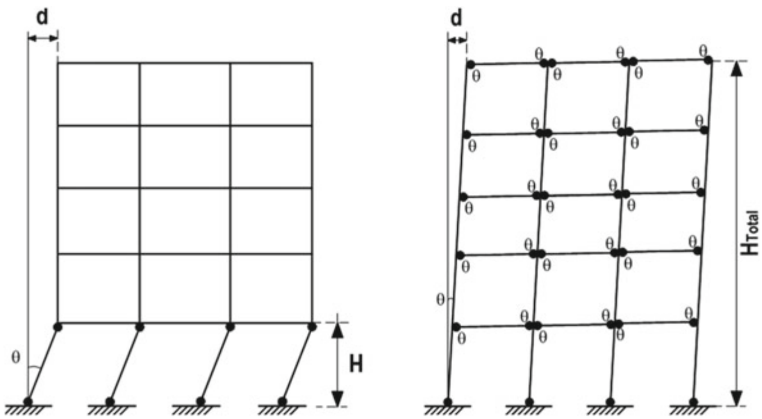

Fig. 1 Frame system failure mechanisms (adapted from Gião [7])

a residual deformation in the beam, and consequently to a progressive accumulation of deformation-unidirectional hinges [2–6]. Thus, the failure mechanism associated with the formation of this type of hinge does not present a reversible response and is characterized by a progressive accumulation of deformation.

NZS 3101-2 [9] considers the existence of unidirectional plastic hinges in the failure mechanisms of frame systems and recommends that these types of plastic hinges should be avoided in ductile frames through additional reinforcement in the beams span.

The fact that the improvement of the global structure response can be attained through the strengthening of the beams in beam-column connections, justifies the research for new RC beam-column connection solutions with high seismic performance. Several techniques might be used to strengthen RC beams, such as: reinforced concrete jacketing; steel plates; fiber reinforced polymer sheets or plates; etc. Following a Damage Avoidance Design approach, Gião [7] and Muhaj [8] proposed strengthening solutions with external post-tensioning in order to limit damage and attain high seismic performance of structural systems, eventually reducing repair cost and building downtime after a seismic event. The present paper aims to assess the ability to simulate numerically the behaviour of the strengthening solutions proposed by Gião [7] and Muhaj [8] when subject simultaneously to cyclic horizontal loading and significant gravity loading. Both strengthening techniques consist of applying post-tensioning to the beams, to reduce deformation and increase strength capacity and energy dissipation.

2 Description of the Experimental Specimens

2.1 Reference and Strengthened Specimens

As mentioned above, in frame systems, assuming the strong column—weak beam seismic principle, the non-linear behaviour is concentrated in the beam critical zones. Gião [7] and Muhaj [8] presented two experimental research works focused on the improvement of the beam's behaviour, to enhance the global structure response. The tested specimens consisted of cantilevers with a length of 1.5 m, that corresponded to a simplification of a reinforced concrete frame with a 4.5 m span, considering that the point of the null moment was located at a third of the span of the beam. It should be noted that a T cross section was considered for the beam, to reflect the contribution of the slab.

The column was modelled using a rigid block, whose geometry was conditioned by the test setup and the subsequent need to fix the specimen to the strong floor.

In order to improve the plastic hinges' behaviour, in both experimental campaigns were presented strengthening solutions by post-tensioning, to increase energy dissipation capacity and reduce residual deformations. The geometry and reinforcement of the specimens tested by Gião [7] are shown in Fig. 2.

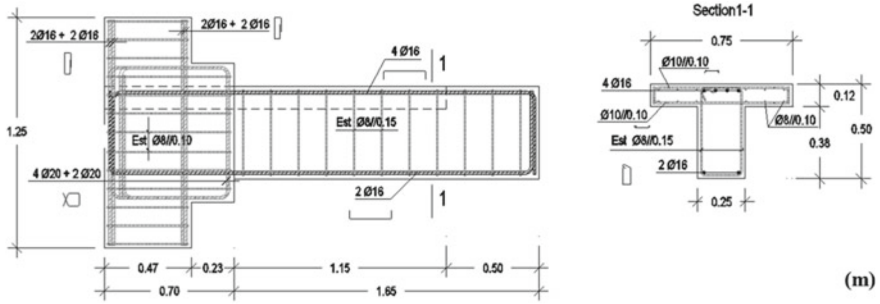

Fig. 2 Beam specimen—overall geometry and reinforcement details (adapted from Gião [7])

Beam VR2 is the reference specimen. Beam VPE was strengthened by the application of two exterior post-tensioning strands, with mechanical anchorages at both ends, with the layout shown in Fig. 3.

The geometry and reinforcement of the specimens tested by Muhaj [8] are shown in Fig. 4.

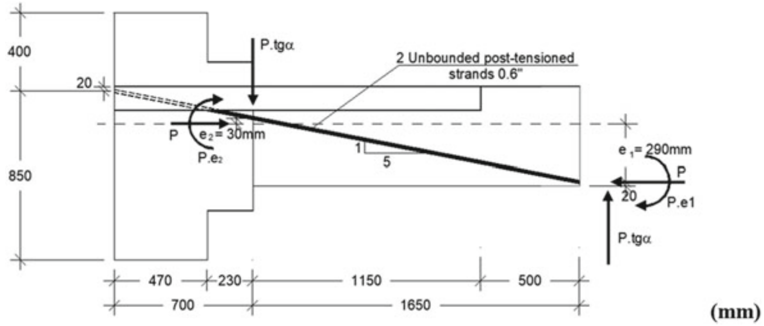

Fig. 3 Specimen VPE—detailing of the strengthening solution [7]—front elevation

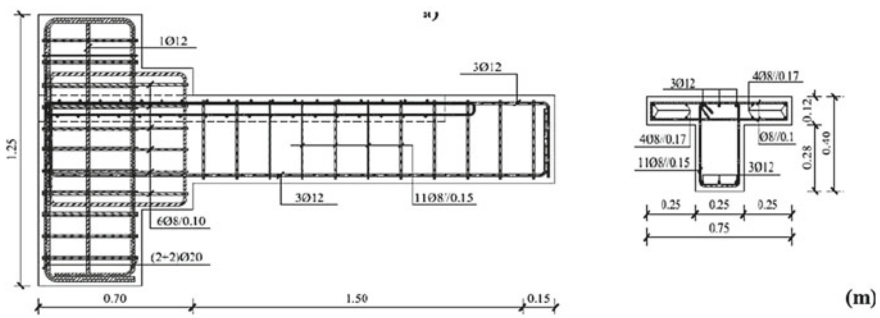

Fig. 4 Beam specimen—overall geometry and reinforcement details (adapted from Muhaj [8])

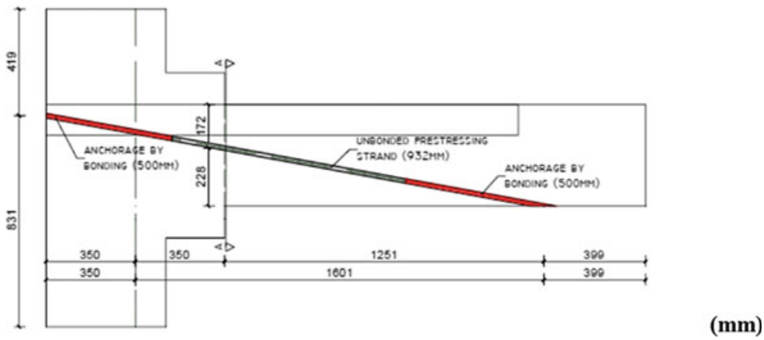

Fig. 5 Specimen CB2—detailing of the strengthening solution [8]—front elevation

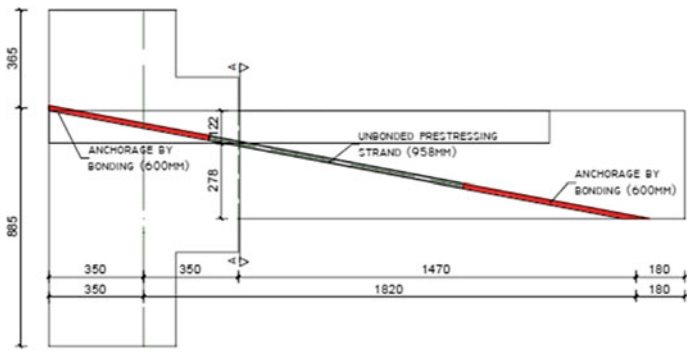

Fig. 6 Specimen CB3—detailing of the strengthening solution [8]—front elevation

Beam CB1 is the reference specimen. Beams CB2 and CB3 were strengthened through the application of two interior post-tensioning strands, with anchorages by bonding at both ends in a predefined length (achieved through the injection of adhesive material). The post-tensioning layouts used in specimens CB2 and CB3 are presented in Figs. 5 and 6, respectively.

2.2 Materials Characterization

The mechanical properties of the materials used in the analysed specimens are summarised in Tables 1 and 2.

Table 1 Concrete mechanical properties

Specimen	fcm (MPa)	fctm (MPa)	E (GPa)
VR2	44.8	3.78	34.5
VPE	41.7	3.61	33.8
CB1	25.2	2.26	28.3
CB2	37.9	2.80	33.2
CB3	39.2	3.05	33.2

Table 2 Reinforcing steel mechanical properties

Specimen	φ (mm)	fy (MPa)	εy (%)	ft (MPa)	εu (%)
VR2 and VPE	8	475.2	0.24	621.7	10.3
	10	454.1	0.23	576.8	15.34
	16	472.7	0.24	601.4	15.42
CB1	8	555.3	0.28	650.0	10.8
	12	541.5	0.27	630.4	15.4
CB2 and CB3	8	547.4	0.27	640.5	10.5
	12	515.6	0.26	618.9	12.3

2.3 Test Setup and Procedure

The experimental campaigns were conducted at the Laboratory of Heavy Structures of NOVA School of Science and Technology. The specimens were fixed vertically to the strong floor and horizontally to the reaction wall (by post-tensioning bars), as shown in Fig. 7. The horizontal load was applied using an actuator with ±500 kN load capacity and 500 mm (±250 mm) displacement range.

The load test procedure [10] is illustrated in Fig. 8. The first step corresponds to the imposition of a pre-established gravity load, followed by the subsequent steps (where FC means force-controlled, DC means displacement-controlled): (i) (DC) Imposition of pre-established displacement (+Δ); (ii) (FC) Unloading until the value of the gravity load is re-established; (iii) (DC) Imposition of a pre-established displacement-controlled unloading (−Δ); (iv) (FC) Loading until the value of the gravity load is re-established.

Each amplitude displacement is repeated for three cycles, starting from the reference amplitude: $\Delta = \pm 1.0 \cdot d0, \pm 2.0 \cdot d0, \pm 3.0 \cdot d0, \pm 4.0 \cdot d0, \pm 5.0 \cdot d0, \pm 6.0 \cdot d0, \ldots$, up to failure. Evaluation of the cycle's amplitude was based on first yield displacement, which was estimated experimentally before starting the cyclic test of both beams. First yield displacement was estimated by monitoring the strain in the longitudinal reinforcement while imposing horizontal displacement on the specimen.

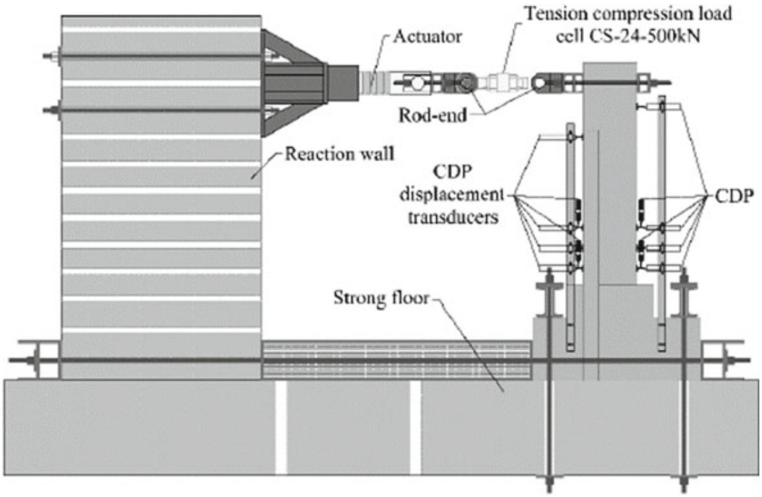

Fig. 7 Test setup [8]

Fig. 8 Loading history—typical load cycle [10]

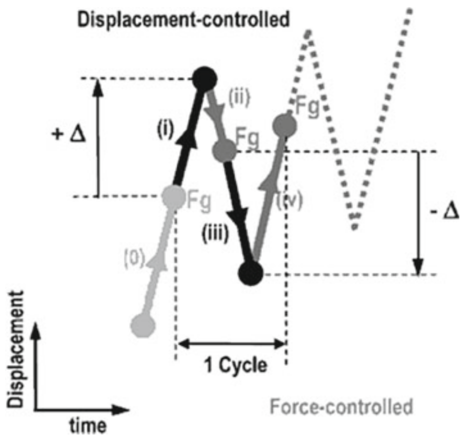

2.4 Experimental Results

The load-displacement relations obtained by Gião [7] for beams VR2 and VPE are shown in Fig. 9. The significant points of these diagrams are presented in Tables 3 and 4.

The load-displacement relations obtained by Muhaj [8] for beams CB1, CB2 and CB3 are shown in Fig. 10. The significant points of these diagrams are presented in Table 3.

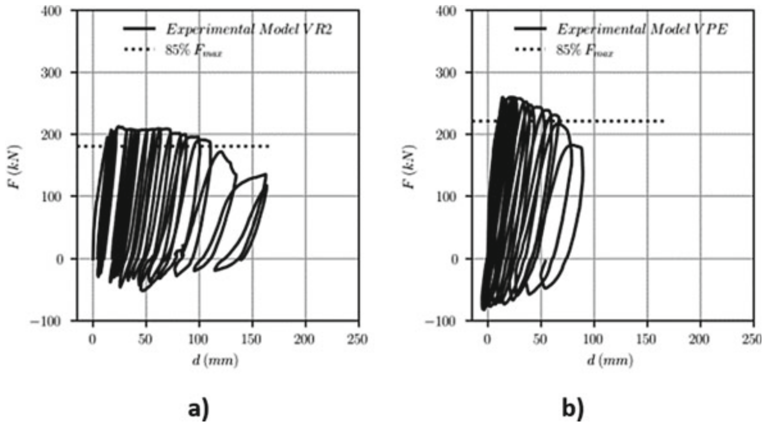

Fig. 9 Experimental results obtained by Gião [7]: **a** VR2 and **b** VPE

Table 3 Notable points for specimens VR2 and VPE experimental hysteretic response [7]

	VR2		VPE	
	Force (kN)	Displ. (mm)	Force (kN)	Displ. (mm)
Yielding (+)	202.0	12.6	250.0	9.7
Yielding (−)	−63.4	−4.5	−78.9	−2.5
Maximum force (+)	212.5	24.0	260.1	22.8
Maximum force (−)	−51.7	46.5	−82.2	−3.62

Table 4 Notable points for specimens CB1, CB2 and CB3 experimental hysteretic response [7]

	CB1		CB2		CB3	
	Force (kN)	Displ. (mm)	Force (kN)	Displ. (mm)	Force (kN)	Displ. (mm)
Yielding (+)	98.5	12.5	127.6	13.0	136.0	16.8
Yielding (−)	−14.6	−1.2	−47.9	−3.8	−54.6	−5.4
Max. Force (+)	100.3	75.9	126.9	51.3	139.7	44.8
Max. Force (−)	−33.4	39.7	−51.6	0.1	−54.6	−5.4

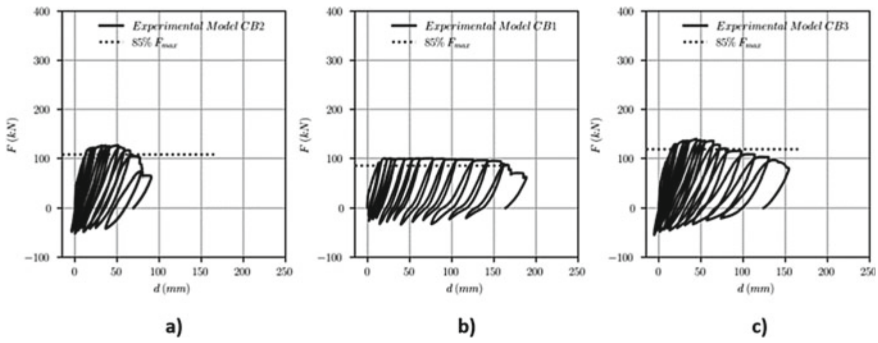

Fig. 10 Experimental results obtained by Muhaj [8]: **a** CB1, **b** CB2 and **c** CB3

3 Numerical Simulation of the Strengthened Specimens

3.1 Elements

The behaviour of the experimental specimens was simulated in OpenSeesPy using distributed plasticity elements with force formulations (nonlinearBeamColumn) [11]. The numerical models were built using 3 nonlinearBeamColumn elements. The first two, next to the restraint, were discretized considering 3 integration points, while in the third, due to its extension, only 2 points were considered (Fig. 11). It should be noted that the elements extension was determined considering the post-tensioned strands layout and the location of the rigid elements represented in Fig. 11.

Next to the restraint, a fictitious element of zero length (zero-length section element) was considered in order to simulate the effect of a possible reinforcement slipping.

It should be noted that both the above-mentioned elements neglect the shear deformation effect. This behaviour was considered indirectly through a new element

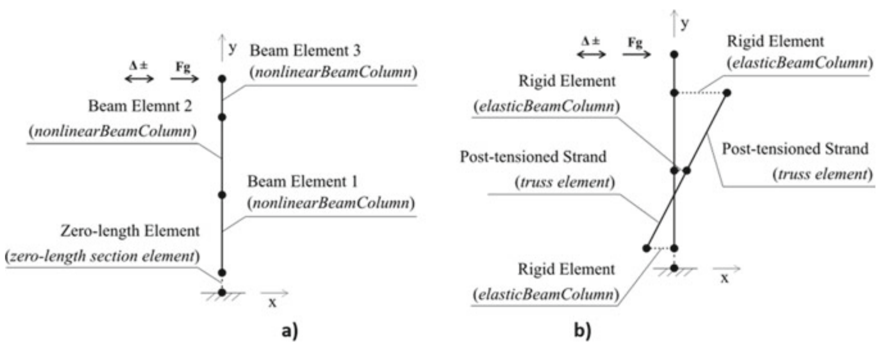

Fig. 11 Elements used in the numerical models: **a** general design and **b** post-tensioned strands

with a linear elastic response, whose slope of the elastic curve corresponded to the shear stiffness of the sections. This element was then added, in parallel to the nonlinearBeamColumn and zero-length section element, in order to simulate the shear deformation.

For the strengthened beams, the post-tensioned strands were modelled using elements with axial stiffness only (truss) and OpenSeesPy material "Steel02" [11], in the case of non-adherent sections, or "Bond SP01" [11], for adherent ones. The strands were then associated with the beam through elasticBeamColumn elements with a modified moment of inertia so that they could be considered rigid elements.

3.2 Section Discretization

The numerical models admitted that the beams had a T-section along their entire length to simulate the presence of the slab. Regarding their geometry, the dimensions of the experimental specimens were respected (Fig. 12).

Each of the sections was discretized into fibers (Fig. 13), to which the behaviour of a UniaxialMaterial was assigned.

This discretization reflected the delimitation of the concrete confined by the stirrups. Two confined cores were thus considered, one in the web and the other in the flange of the beams. The characteristics of each of these cores were determined by taking into account the spacing of the stirrups and the length of the elements,

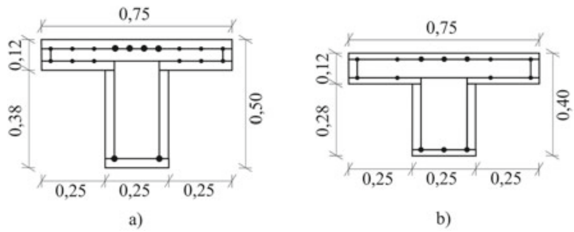

Fig. 12 Beam cross-section geometry: **a** Gião [7] and **b** Muhaj [8]

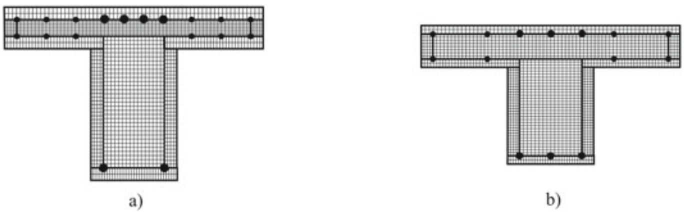

Fig. 13 Beam cross-section fibers: **a** Gião [7] and **b** Muhaj [8]

as proposed by Yang and Jeremic [12] and Coleman and Spacone [13]. Additionally, fibers were considered for reinforcing steel and, when relevant, post-tensioned strands.

For the beams VR2 and CB1, four different sections were considered, the first corresponding to the zero-length element and the remaining to each of the nonlinearBeamColumn elements. As mentioned, the parameters regarding the confined concrete in the nonlinearBeamColumn elements were obtained as proposed by Yang and Jeremic [12] and Coleman and Spacone [13].

As for the strengthened beams, since the prestress applied to VPE was non-adhesive, the model was defined using cross sections identical to VR2 (with the due adaptations to the material properties), adding in parallel an element with only axial stiffness (truss element) associated with OpenSeesPy material “Steel02”.

In beams CB2 and CB3, a fiber was added to the cross-section of the zero-length element for the simulation of the post-tensioned strands' behaviour, while the nonlinearBeamColumn elements maintained the same section of beam CB1 (with the necessary changes to the material properties). The post-tensioned strands were modelled as shown in Fig. 11, assigning them the properties “Bond SP01” OpenSeesPy material to the adhesive section and “Steel02” to the non-adhesive section.

3.3 Numeric Results

The experimental hysteretic response of the two reference specimens (VR2 and CB1) and the three strengthened specimens (VPE, CB2 and CB3) are presented and compared with the numerical results in Figs. 14 and 15, through force-displacement diagrams. The failure criterion adopted in the numerical simulation corresponds to the instant when the materials of the fiber section exceed ultimate stresses/strains. As observed, the numeric simulation can reproduce the hysteretic response of the experimental models. Discrepancies between experimental and numerical results are more pronounced in terms of displacements than in terms of forces. In fact, the numerical models presented a reasonable accuracy in terms of forces.

Tables 5 and 6 present the numerical results for the notable points of the hysteretic response.

For specimens VR2 and VPE, it can be observed that the strengthened solution reduced residual deformation and enhanced load capacity. A strength increases of 24% was observed in both directions.

For specimens CB1, CB2 and CB3, the strengthened solutions also exhibit a deformation decrease and load capacity increase. In specimen CB2, a strength increase of approx. 30%, in relation to the reference specimen CB1, was observed in both directions. In the case of specimen CB3, the strength increase in the hogging direction was 40–50%.

In terms of displacement, the reduction was similar in both strengthened solutions. In the hogging direction, the observed displacement decrease was considerable and there was an inversion of the sign of the displacements in the sagging

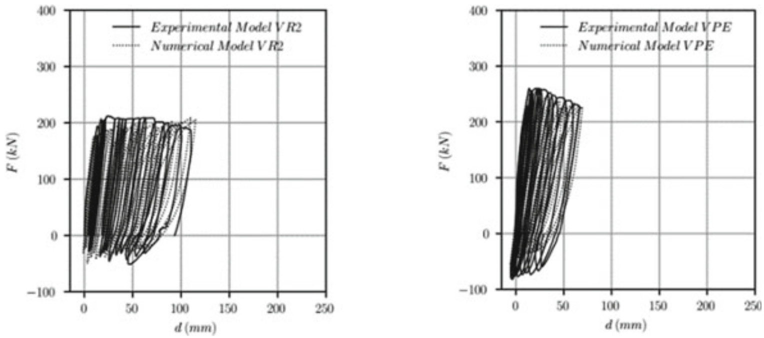

Fig. 14 Comparation between numeric simulation and the experimental response of Gião's specimens VR2 and VPE [7]

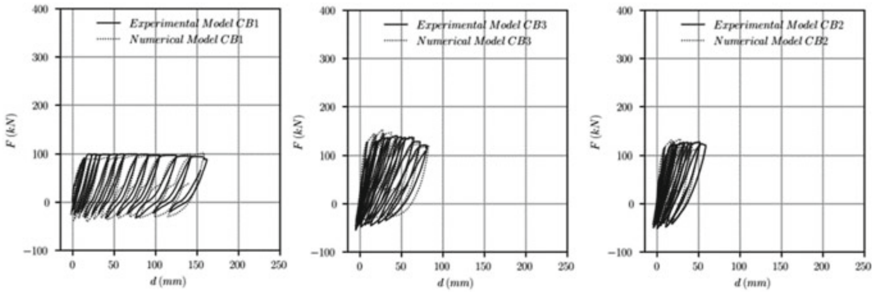

Fig. 15 Comparation between numeric simulation and the experimental response of Muhaj's specimens CB1, CB2 and CB3 [8]

Table 5 Notable points of the numerical hysteretic response for VR2 and VPE models [1]

	VR2		VPE		VPE/VR2 ratio	
	Force (kN)	Displacement (mm)	Force (kN)	Displacement (mm)		
Yielding (+)	194.52	9.47	240.95	8.60	1.24	0.91
Yielding (−)	−32.11	2.80	−42.68	−5.11	1.33	–
Maximum force (+)	208.42	109.99	257.66	24.16	1.24	0.22
Maximum force (−)	−49.12	2.39	−57.71	−6.15	1.17	–

direction, corroborating the suggestion of a more recentred behaviour, with reduced deformation and damage for the strengthened solutions.

Table 6 Notable points of the numerical hysteretic response for CB1, CB2 and CB3 specimens [8]

	CB1		CB2		CB3		CB2/CB1 ratio		CB3/CB1 ratio	
	Force (kN)	Disp. (mm)	Force (kN)	Disp. (mm)	Force (kN)	Disp. (mm)				
Yielding (+)	96.77	10.87	125.5	7.07	137.79	6.97	1.30	0.65	1.42	0.64
Yielding (−)	−32.84	−2.76	−41.18	−5.49	−30.46	−4.31	1.25	–	0.93	–
Max. force (+)	101.58	158.71	132.62	28.2	152.6	27.35	1.31	0.18	1.50	0.17
Max. force (−)	−39.41	16.33	−51.15	−5.08	−44.93	−5.73	1.30	–	1.14	–

4 Conclusions

The main objective of the present study was to numerically evaluate the performance of strengthening solutions, proposed by Gião [7] and Muhaj [8], for RC frame beams subjected simultaneously to cyclic horizontal and significant gravity loads. Two reference specimens (VR2 and CB1) and three strengthened specimens were simulated—one strengthened with non-adherent exterior post-tensioned strands (VPE) and two strengthened with interior post-tensioning strands with anchorages by bonding (CB2 and CB3).

The simulation and numerical analysis were developed with the framework OpenSeesPy (a recent Python interpreter for OpenSees [11]), using elements of distributed plasticity with force-based formulations (nonlinearBeamColumn). The sections were discretized into fibers, to which the non-linear behaviour of the materials was attributed.

According to the obtained results, presented in this paper, can be concluded that the numerical results reproduce adequately the beams' experimental behaviour, validating the numerical model's ability to simulate reasonably the hysteretic response. The strengthened solutions show a reduction of deformation and enhanced load capacity and exhibit a more recentred and adequate hysteretic behaviour.

References

1. Eurocode 8: EN1998-1: Design of structures for earthquake resistance—Part 1: General rules, seismic actions and rules for buildings. CEN, Brussels, Belgium (2004)
2. Park, R., Paulay, T.: Reinforced Concrete Structures. John Wiley & Sons, New York (1975)
3. Fenwich, R., Dely, R., Davidson, B.: Ductility demand for uni-directional and reversing plastic hinges in ductile moment resisting frames. Bull. N.Z. Soc. Earthq. Eng. **32**(1) (1999)
4. Fenwich, R., Meggett, L.: Seismic behaviour of a reinforced concrete portal frame sustaining gravity loads. Bull. New Zealand Natl. Soc. Earthq. Eng. **22**(1) (1989)
5. Walker, A., Dhakal, R.P.: Assessment of material strain limits for defining different forms of plastic hinge region in concrete structures. Bull. N.Z. Soc. Earthq. Eng. **42**(2), 86–95 (2009)
6. Gião, R., Lúcio, V.J.G., Chastre, C.: Gravity load effects on the behaviour of reinforced concrete beam critical zones subjected to cyclic loads. Eng. Struct. **181**, 503–518 (2017). https://doi.org/10.1016/j.engstruct.2018.12.045.(2019)
7. Gião, A.R.: Ligação Viga-Pilar de Alto Desempenho Sísmico. Ph.D. Thesis. FCT UNL (2012)
8. Muhaj, H.: Seismic strengthening of reinforced concrete beams by post-tensioning with anchorages by bonding. Ph.D. Thesis. FCT UNL (2020)
9. NZS 3101-2: Concrete Structures Standard—Commentary. Standards New Zealand, Wellington, New Zealand (2006)
10. Gião, A.R., Lúcio, V., Chastre, C. (2014). Assessing the behaviour of RC beams subject to significant gravity loads under cyclic loads. Eng. Struct. **59**, 512–521 (2014)
11. Mazzoni, S.: OpenSees—Command Language Manual (2006)
12. Yang, H., Jeremic, B.: Calibration of Uniaxial Concrete Material Model for Reinforce Concrete Beam/Column. University of California, Davis (2020)
13. Coleman, J., Spacone, E.: Localization issues in force-based frame elements. J. Struct. Eng. ASCE **127** (2001). https://doi.org/10.1061/(ASCE)0733-9445(2001)127:11(1257)

Accident Prediction Model Applied to Motorway A29 in Portugal

Sara Ferreira, António Couto, António Lobo, Suellen Souza, César De Santos-Berbel, and João Neves

Abstract Road accidents are still one of the biggest public health problems in the world, and research must be stepped up to tackle the issue. The present study describes the development of a statistical model for predicting accidents occurring on motorway segments over the period 2015–19. The case study comprises 218 tangents and curves, separately for either direction, of motorway A29 in Portugal, which is operated by Ascendi under a concession awarded by the Portuguese state. Exposure, geometric design variables, and annual trend were incorporated to the model, considering a negative binomial probability distribution, and a flexible function form allowing non-constant elasticity values was utilized. In addition to the exposure variables, the geometric design risk factors found to be significant were the horizontal curvature, and the presence of deceleration lane. A significant decreasing in accident annual trend was also observed. The fitted model was validated using cumulative residual plots. The results obtained allowed the prediction of accident frequency as well as the identification of the design risk factors.

Keywords Accident prediction model · Geometric design · Motorways · Risk factors · Road safety

S. Ferreira (✉) · A. Couto · A. Lobo
CITTA—Centro de Investigação do Território Transportes e Ambiente, Faculdade de Engenharia da Universidade do Porto, Porto, Portugal
e-mail: sara@fe.up.pt

S. Souza
Faculdade de Engenharia da Universidade do Porto, Porto, Portugal

C. De Santos-Berbel
Departamento de Estructuras y Física de Edificación, Universidad Politécnica de Madrid, Madrid, Spain

J. Neves
Ascendi IGI—Inovação e Gestão de Infra-Estruturas S.A., Porto, Portugal

C. Chastre et al. (eds.), *Testing and Experimentation in Civil Engineering*, RILEM Bookseries 41, https://doi.org/10.1007/978-3-031-29191-3_28

1 Introduction

Road accidents are still one of the biggest public health problems in the world. In Portugal, data from the National Road Safety Authority (ANSR) indicate that in the year 2019 there were 626 deaths nationwide, resulting in an economic and social cost of 1.6% of the National gross domestic product [1]. According to data from the Portuguese Association of Concessionary Companies of Motorways or Bridges with Tolls (APCAP), in 2019 there were 2,358 accidents with victims on motorways under concession to companies belonging to this association, which is 1% less than the figure for 2018 [2]. The Strategic Plan for Road Safety 2021–2030—Vision Zero 2030, currently being drawn up by ANSR, sets the primary goal of achieving the mark of zero deaths and serious injuries on Portuguese roads and highways by the year 2030. In this context, the objective of this study is the development of a model that predicts the frequency of accidents on motorways, which will allow the identification of the main geometric design factors that contribute to the occurrence of accidents. The construction of prediction models will also act as a decision support tool for the selection and implementation of strategic measures and road safety management.

This paper presents the application of the model to the case of the A29 motorway in Portugal, which is operated by Ascendi under a concession awarded by the Portuguese state. For this first exploratory analysis, it was necessary to create a database suitable for the selected segmentation approach and based on Ascendi existing data. Thus, from the total accident data (with and without victims) from 2015 to 2019, a generalized linear model with negative binomial (NB) distribution was adjusted.

2 Background

Although road accidents are random and non-predictable events (it is impossible to determine where, when, and how an accident will occur), the number of accidents may be subject to causal or intervention analysis. The characteristics of the road infrastructure, vehicles and driver behavior can affect the probability of an accident occurring. As such, the long-term accident frequency (expected number of accidents per unit of time) results from a causal process. This expected number of accidents is not constant, i.e. it varies in time and space, and is an integer and non-negative number. The variation attributed to various causal factors is defined as the systematic component and can, at the outset, be influenced and controlled. For the purposes of road safety policy strategy, it is this systematic component that is of interest to study [3].

In this context, the statistical analysis of accident frequency has been based on generalized linear models (GLM), traditionally assuming Poisson distribution to represent the random component. With this in mind it is possible to apply numerous proven efficient inference methods [4]. Indicating a single factor that generated a given accident is a complex and often inaccurate task, since several aspects make up a combination of risks that resulted in this event. The main conditions, failures or actions that cause the traffic accident are called contributing risk factors, which indicate the circumstances that gave rise to the accident, thus giving indications on how it could be avoided [5].

Accident frequencies fluctuate over time at a given observation point. Such fluctuations make it difficult to determine whether changes in the observed accident frequency occur because of changes in site conditions or natural fluctuations [6]. When a period with a comparatively high accident frequency is observed, it is statistically likely that the next period will be followed by a comparatively lower frequency. Similarly, a period of low accident frequency will probably be followed by a period of high accident frequency. This tendency is known as regression to the mean (RTM). The bias of RTM effect is accounted for when treatment effectiveness, i.e. the reduction in accident frequency or severity, and site selection is based on a long-term average accident frequency. However, variations in site conditions over time make it difficult to attribute changes in expected average accident frequency to specific conditions. These also limit the number of years that can be included in a study. If longer time periods are studied, to improve the accident frequency estimate and take account of natural variability and RTM, it becomes likely that changes in site conditions have occurred during the study period. One way around this limitation is to estimate the expected average accident frequency for the specific conditions for each year in a study period by developing accident prediction models, which can incorporate certain characteristics of the network.

2.1 Statistical Modeling

NB is a probability distribution largely used for accident prediction models based on crash count data [7]. The NB model is an extension of the Poisson model to overcome possible overdispersion in the data. The NB probability distribution assumes that the Poisson parameter follows a Gamma probability distribution. The model results in a closed-form, mathematical equation to handle the relationship between the mean and variance structures. The NB model is derived by rewriting the Poisson parameter for each observation i as:

$$\lambda_i = \mathrm{E}(y_\mathrm{i}) = \mathrm{EXP}(\beta_i \cdot X_i + \varepsilon_i) \tag{1}$$

where X_i is a vector of explanatory variables, β_i is a vector of unknown regression coefficients, and $\mathrm{EXP}(\varepsilon_i)$ is a gamma-distributed error term with mean 1 and variance α^2. Adding the latter term allows the variance to differ from the mean as:

$$\mathrm{VAR}[y_\mathrm{i}] = \mathrm{E}[y_\mathrm{i}]\,[1 + \alpha \cdot \mathrm{E}[y_\mathrm{i}]] = \mathrm{E}[y_\mathrm{i}] + \alpha \cdot \mathrm{E}[y_\mathrm{i}]^2 \tag{2}$$

Poisson regression is a limited model of the NB regression model as α approaches zero, which means that the selection between these two models depends on the value of α. The α parameter is usually known as the overdispersion parameter. Accident data are indeed usually overdispersed. The degree of overdispersion in a NB model, is estimated along with the coefficients of the regression equation [8].

An ordinary log-linear function is used to represent the relationship between explanatory variables and the dependent variable (accident frequency). However, this function assumes constant elasticity for the estimation parameters, which is a limitation in the analysis of the effects of explanatory variables on accident risk [7].

Interaction effects between explanatory variables have been studied in the road safety research, normally assessed by logistic regression. Ferreira and Couto [9] examined the possibility of using a flexible function form allowing non-constant elasticity values, exploring the use of the translog function usually used in the field of economics to let the elasticity vary with the values of other explanatory variables.

To select the proper relationship between the dependent variable and explanatory variables, a method proposed by Hauer and Bamfo was applied [10]. Basically, the Integrate-Differentiate method consists of drawing an Empirical Integral Function for each explanatory variable and then comparing the shape with the pre-established graphs of well-known functions (power, gamma, exponential or polynomial functions). The function with the most similar shape is selected to represent the relationship between the dependent variable and the explanatory variable being investigated.

2.2 Design Risk Factors

Exposure factors in highway safety comprise segment length, traffic flow and composition, which are fundamental to undertake meaningful and statistically sound analyses [6]. Furthermore, accurate highway geometric design parameters are essential contributing factors for establishing the relationship between accident frequency and explanatory factors [11–13]. Literature suggests that the geometric design parameter that most affects road safety is the horizontal curvature or curvature change rate (CCR) [6, 14–16]. In addition to horizontal curvature features, cross-sectional design features have been found to affect the safety of multilane highway facilities, mainly lane width and shoulder width [17–19]. Safety performance functions have been developed to quantify the risk associated to highway exits and entrances [20]. Previous research has found that highway accidents are more frequent on deceleration lanes and exit ramps than on acceleration lanes and entrance ramps [21–23].

3 Data Description

The concession *Costa da Prata* has a length of approximately 105 km, and comprises four motorway sections, namely, A44, A29 and, partially, A25 and A17. From a preliminary analysis, it was found that A29 motorway stands out from the others, with an average accident occurrence of over 50% of all crashes of the concession for

Fig. 1 Location of the section studied of A29 motorway (edited from Openstreetmap)

the period under study. The A29 is a 53 km long suburban motorway that connects A25 motorway, in the north-east of Aveiro, to the A20 motorway located in south of the Porto metropolitan area and Freixo's Douro bridge (Fig. 1). In the 5 years under analysis (2015–2019), a total of 599 accidents occurred.

For the development of the model, the annual average daily traffic (AADT) per direction, for each of the five years, and the length of the segment were contemplated as variables of exposure to accidents. Concerning the segmentation, the tangents and curves were considered including the counterpart spirals within the latter ones, and separately for each direction. The segmentation thus defined makes it possible to consider the horizontal alignment features at an optimal level of aggregation to analyze each segment with accuracy [24]. For each of the segments, the geometric and operational elements describing them were calculated, according to the variables presented in Table 1. The accident location precision was equal to or less than 10 m as provided by the concessionaire database, which made it possible to assign them accurately to the corresponding segment.

Geometric variables include cross sectional features such as right shoulder width, roadway width, and number of lanes. Horizontal curvature is contemplated in the binary variable "Curve" (0 if tangent, 1 if curve) and in CCR, measured as the ratio of deflection angle to length (gon/km). Proportion of acceleration or deceleration lane refer to the share of length of such lanes overlapped with the segment (there could be more than one), and it is therefore a unitless variable. It must be noted that, if more than one deceleration lane is overlapped with the segment the value of this

Table 1 Statistical description of variables

Variable	Average	Standard deviation	Min. value	Max. value
Number of accidents	0.55	1.0	0.0	10.0
Length (m)	482,9	353.4	15.0	2112.0
AADT (vehicles/day)	13,971.7	6945.9	5022.0	24,024.0
Percentage of heavy vehicles	13.6	6	4.8	25.2
Right shoulder width (m)	2.90	0.63	1.50	3.75
Roadway width (m)	3.63	0.12	3.50	3.75
Number of lanes	2.2	0.5	2	4
Proportion of acceleration lane	0.20	0.39	0.0	2.0
Proportion of deceleration lane	0.20	0.37	0.0	1.74
Curve	0.61	0.49	0	1
CCR (gon/km)	37.9	35.7	0.0	109.9
Year	3	1.58	1	5

variable may exceed 1. According to previous studies, a variable reflecting the crash annual trend was also included in the model [25]. The total number of segments is 218, which corresponds to 1,090 observations for the period studied.

Several authors pointed out potential that covariates showing variability in space such as weather effects, driver population, and land use are rarely measured or accounted for in highway safety models [26]. Given that the segments belong to a single connected motorway and the total distance covered is relatively short, it can be assumed that these variables do not greatly affect the model performance, and therefore the potential effect of spatial autocorrelation is little.

Figure 2 illustrates the evolution of average traffic volumes and accidents per year over the studied period. A decreasing trend in the number of crashes is observed. Considering the accidents occurring each year on a segment as independent observations instead of grouping them for the whole period under study allows a time trend to be included in the model, which might help increase the variation explained by the model.

4 Methodology

For the fit of the accident prediction model, the integrate-differentiate method by Hauer and Bamfo [10] was applied to the explanatory variables used in this study. It consists of seeking the functional form relating the expected accident frequency to each independent variable. For each independent variable, the values are sorted and the difference between the nearest higher and nearest lower variable value divided by two determines a range which is multiplied by the counterpart accident count. An empirical integral function is obtained by adding up these values similarly to

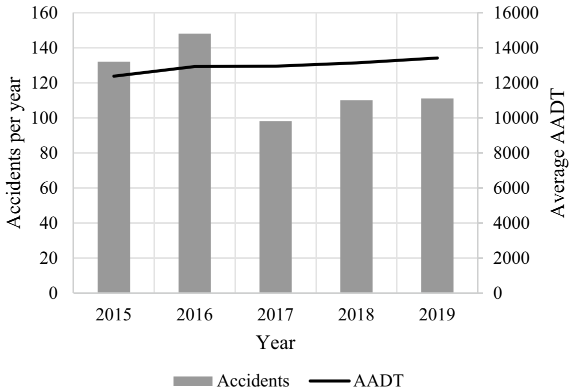

Fig. 2 Evolution of average traffic volumes and accidents per year

the integration midpoint rule. Representing the plot of cumulative area versus the variable under consideration one can estimate the functional form behind the empirical integral function (Fig. 3). This procedure revealed that the relationships between accident frequency and both AADT and segment length could be described by the exponential function. In the case of the rest of variables, the exponential function was also found to be the most suitable to describe the aforementioned relationship, except the annual trend, which was included as power function. However, its mathematical modelling can be done interchangeably as an exponential function.

The estimation of the regression parameters was performed on NLOGIT 5 software, using the maximum likelihood method.

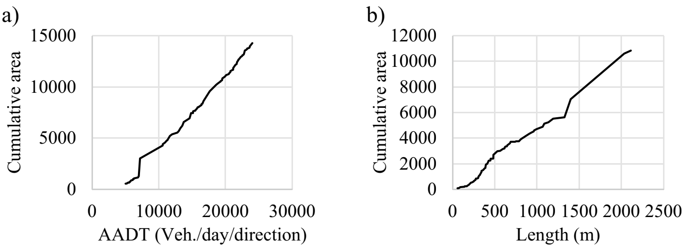

Fig. 3 Empirical integral functions for model variables **a** AADT; **b** Segment length

5 Results and Discussion

5.1 Fitted Model

The results obtained through the application of the model with BN distribution are shown in Table 2. The variables that did not show statistical significance (confidence level below 90%) were excluded. The estimate of the variable length was obtained for the values in km, and the estimate of AADT was obtained for the counterpart values in vehicles per day and direction.

The estimated value of the overdispersion parameter suggests the existence of overdispersion of crash occurrence, confirming that the negative binomial distribution is more appropriate than the Poisson distribution. The model equation is:

$$\begin{aligned}\lambda_i = & EXP(-2,3032 + 0,8101 \cdot L + 0,0714 \cdot AADT \\ & + 0,4505 \cdot PDL - 0,464 \cdot Curve + 0,013 \cdot CCR) \cdot 0,9417^{Y}ear\end{aligned} \quad (3)$$

A Durbin-Watson test was performed to check whether there is a correlation in the disturbances obtained from the model estimation [27]. The D-W statistic was 1.952 and its associated p-value was 0.1371 which indicates that the null hypothesis could not be rejected at the 90% confidence interval, concluding that there is no significant autocorrelation in the residuals. Therefore, the authors' assumption about spatial and temporal autocorrelation was verified.

In order to analyze the relevance of each variable in the model, it is now important to interpret whether the estimated values for the coefficients indicate the relationship between the accidents and the explanatory variables in accordance with what is referred to in the literature and what is expected. The sign of the estimates indicates that the exposure variables, AADT and segment length, have a positive effect on the occurrence of accidents, showing that an increase of the AADT and length leads to an increase in the estimated number of accidents.

Table 2 NB model results

Variable	Estimate	Standard deviation	p-value
Constant	−2.3032	0.2622	0.0000
Length	0.8101	0.1845	0.0000
AADT	0.0714	0.0102	0.0000
Proportion of deceleration lane	0.4505	0.1032	0.0000
Curve	−0.4640	0.2129	0.0293
CCR	0.0130	0.0026	0.0000
Year	−0.06010	0.0340	0.0769
Overdispersion parameter	0.4825	0.1109	0.0000

Table 3 Goodness of fit measures

Variable	Value
Log likelihood function	−1013.26
Restricted log likelihood	−1035.96
SD	1028.74
Pearson's Chi-square	1043.91

The variables that represent the geometric characteristics of the segments showing statistical significance are the proportion of the length of deceleration lanes and the type of segment, i.e., tangent or curve (binary variable). In this case, it turns out that the higher the proportion of deceleration lane length overlapped with the segment, the higher the estimated number of accidents. Contrary to expectations, it turns out that tangents are associated with an increase in the estimated number of accidents when compared with curved segments. The pseudo-elasticity of this variable can be computed from the estimate [28], resulting in an increase of 59% in the crash count when the segment is a tangent. In the case of the latter, as expected, the greater the CCR, the higher the estimated number of accidents.

Finally, the estimate of the variable *year*, which measures the annual trend, suggests that the number of crashes decreases 5.8% per year.

Goodness of fit measures of NB model are shown in Table 3. In addition to log likelihood function and restricted log likelihood, two commonly used measures are the scaled deviance (SD) and the Pearson's χ^2 statistic. Both values are close to the number of the degrees of freedom (1083), indicating a good model fit [29].

5.2 *Model Validation*

Goodness of fit measures are limited to describing how the accident prediction model fits overall. To further assess the quality of the fitted models in terms of absence of bias, cumulative residual (CURE) plots have been used [30]. This validation method was applied to the distribution of cumulative residuals for quantitative explanatory variables. It consists of verifying graphically that the cumulative residuals for the data sorted by the values of each variable fall within certain limits and are balanced around the null value. The upper and lower limits for each observation i, would be given by $2\widehat{\sigma}'_i$ where $\widehat{\sigma}'_i$ has the following expression:

$$\widehat{\sigma}'_i = \pm\widehat{\sigma}_i \cdot \sqrt{1 - \frac{\widehat{\sigma}^2_i}{\widehat{\sigma}^2_n}} \tag{4}$$

where $\widehat{\sigma}'_i$ is the limit of the residuals accumulated for the variable of analysis; $\widehat{\sigma}_i$ is the square root of the variance $\widehat{\sigma}^2_i$; $\widehat{\sigma}^2_i$ is the variance of the accumulated residuals up to the *i-th* segment; and $\widehat{\sigma}^2_n$ is the variance of the total accumulated residuals in the segment sample.

CURE plots of five model variables are displayed in Fig. 4. The length CURE plot shows a balanced line round the abscissa axis, although it exceeds the $\pm 2\widehat{\sigma}'_i$ limits slightly for the segments with shorter length. The AADT CURE plot reveals a slightly less balanced trace which lies within the boundaries in all ranges except for the segments with less traffic volume. Regarding the CCR CURE plot, it fits adequately into the residuals range, delimited by the dashed line, and is balanced around the abscissa axis. Noting that the variable proportion of deceleration lane accounts for the ratio of length of deceleration lane to overlapped length with the segment, the CURE plot of this variable can be conceived. In this case, although the line remains within the boundaries, a slight bias is observed given that the values below 1 lay on negative CURE whereas the values greater than 1 yield positive CURE. Finally, year CURE virtually do not exceed the boundaries while showing somewhat balanced layout.

6 Conclusions

The present study describes the development and validation of a statistical model for predicting accidents occurring on motorway segments in Portugal based on data from the period 2015–19. This study allowed an analysis of the existing database and the best approach to data treatment and segmentation to be considered.

In line with the results of previous studies, variables measuring geometric design risk factors, namely CCR, curve and the presence of a deceleration lane, as well as annual trend were significant and showed good performance in the model validation. Concerning the variables quantifying risk exposure, although their level of significance is unquestionable, the cumulative residuals slightly exceeded the $\pm 2\widehat{\sigma}'$ interval for certain limited ranges. These results suggest that a model with better fit might be obtained if the sample is stratified.

There are some interesting topics to focus on and explore as future work developments. It is recommended that the study be expanded to the entire concession *Costa da Prata*, as well as to the other motorways in the Ascendi network. With the expansion of the database, it will be possible to identify risk factors, as well as to compare these same factors on the different motorways operated by the concessionaire. The expansion of the model sample will allow the development of accident modification functions. It is also expected that, in the future, this type of model will be considered for accident prediction, constituting a decision support tool to improve road safety. Furthermore, the development of a random parameter model is suggested to take the segment sample heterogeneity into account.

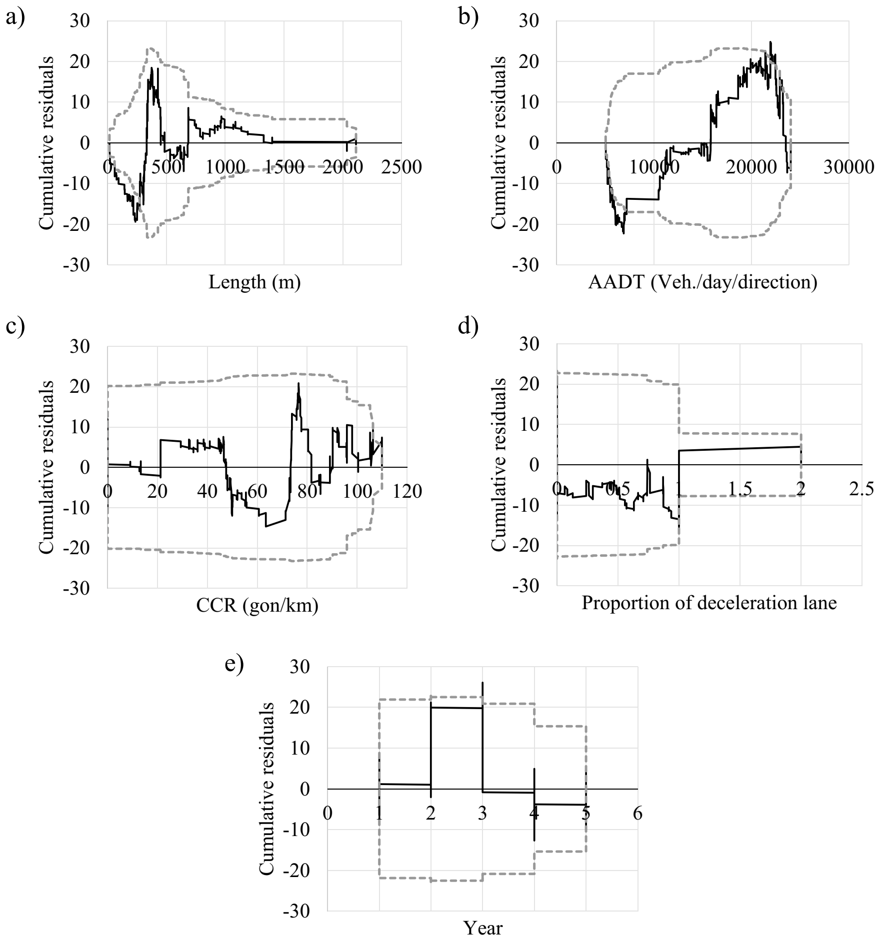

Fig. 4 Cumulative residuals for the model variables **a** segment length; **b** AADT; **c** CCR; **d** proportion of deceleration lane; **e** year

Acknowledgements The authors gratefully acknowledge the financial support of Universidad Politécnica de Madrid (PROGRAMA PROPIO DE I+D+I 2021, short-term research stay September–December 2021). The authors would also like to thank the support of ASCENDI IGI—Inovação e Gestão de Infraestruturas, S.A. for providing the data used in this study.

References

1. Autoridade Nacional de Segurança Rodoviária (ANSR): Relatório anual de segurança rodoviária. ANSR, Lisbon (2019)
2. Associação Portuguesa das Sociedades Concessionárias de Autoestradas ou Pontes com Portagens (APCAP): Anuário estatístico de segurança rodoviária. APCAP, Lisbon (2019)
3. Ferreira, S.: A segurança rodoviária no processo de planeamento de redes de transporte em meio urbano. Doctoral thesis. Faculdade de Engenharia da Universidade do Porto, Porto (2010)
4. Fridstrøm, L.: Disaggregate Accident Frequency and Risk Modelling, a Rough Guide. Institute of Transport Economics. Oslo, Norway (2015)
5. Chagas, D.: Estudo sobre fatores contribuintes de acidentes de trânsito urbano. Master thesis. Escola de Engenharia. Universidade Federal do Rio Grande do Sul (2011)
6. American Association of State Highway and Transportation Officials (AASHTO): Highway safety manual. AASHTO, Washington, DC (2010)
7. Lord, D., Mannering, F.L.: The statistical analysis of crash-frequency data: a review and assessment of methodological alternatives. Transp. Res. Part A Policy Pract. **44**(5), 291–305 (2010)
8. Ambros, J., Jurewicz, C., Turner, S., Kieć, M.: An international review of challenges and opportunities in development and use of crash prediction models. Eur. Transp. Res. Rev. 10(2) (2018)
9. Couto, A., Ferreira, S.: A note on modeling road accident frequency: a flexible elasticity model. Accid. Anal. Prev. **43**(6), 2104–2111 (2011)
10. Hauer, E., Bamfo, J.: Two tools for finding what function links the dependent variable to the explanatory variables. In: Proceedings of the International Co-operation in Theories and Concepts in Traffic Safety 1997 Conference, pp. 1–18 (1997)
11. Sameen, M.I., Pradhan, B.: Assessment of the effects of expressway geometric design features on the frequency of accident crash rates using high-resolution laser scanning data and GIS. Geomat. Nat. Haz. Risk **8**(2), 733–747 (2017)
12. De Santos-Berbel, C.: A methodology for sight distance analysis on highways, alignment coordination, and their relation to traffic safety. Doctoral thesis. Universidad Politécnica de Madrid, Madrid (2017)
13. Khedher, M.B.B., Yun, D.: Generalized linear models to identify the impact of road geometric design features on crash frequency in rural roads. KSCE J. Civ. Eng. **26**(3), 1388–1395 (2022)
14. Montella, A., Colantuoni, L., Lamberti, R.: Crash prediction models for rural motorways. Transp. Res. Rec. **2083**, 180–189 (2008)
15. Haynes, R., Lake, I.R., Kingham, S., Sabel, C.E., Pearce, J., Barnett, R.: The influence of road curvature on fatal crashes in New Zealand. Accid. Anal. Prev. **40**(3), 843–850 (2008)
16. Cafiso, S., Montella, A., D'Agostino, C., Mauriello, F., Galante, F.: Crash modification functions for pavement surface condition and geometric design indicators. Accid. Anal. Prevent. **149**, 105887 (2021)
17. McLean, J.: Review of accidents and rural cross section elements including roadsides. Research Report ARR 297. Australian Road Research Board, Vermont South (1996)
18. Prinsloo, B., Goudanas, C.: Development of a crash prediction model for rural Roads in NSW. In: Proceedings of the 21st Australian Road Research Board and 11th Road Engineering Association of Asia and Australasia Conference (2003)
19. Turner, S., Bone, I., Jackett, M.: New Zealand accident prediction models and their applications. In: Proceedings of the 21st Australian Road Research Board and 11th Road Engineering Association of Asia and Australasia Conference (2003)
20. Zhao, J., Guo, Y., Liu, P.: Safety impacts of geometric design on freeway segments with closely spaced entrance and exit ramps. Accid. Anal. Prev. **163**(June), 106461 (2021)
21. Bauer, K.M., Harwood, D.W.: Statistical models of accidents on interchange ramps and speed-change lanes. Report No. FHWA-RD-97-106. Federal Highway Administration, Kansas City (1997)

22. Lord, D., Bonneson, J.A.: Calibration of predictive models for estimating safety of ramp design configurations. Transp. Res. Rec. **1908**, 88–95 (2005)
23. Twomey, J.M., Heckman, M.L., Hayward, J.C., Zuk, R.J.: Accidents and safety associated with interchanges. Transp. Res. Rec. **1385**, 100–105 (1993)
24. Da Costa, J.O., Jacques, M.A.P., Pereira, P.A.A., Freitas, E.F., Soares, F.E.C.: Portuguese two-lane highways: Modelling crash frequencies for different temporal and spatial aggregation of crash data. Transport **33**(1), 92–103 (2018)
25. Lord, D., Persaud, B.N.: Accident prediction models with and without trend: application of the generalized estimating equations procedure. Transp. Res. Rec. **1717**, 102–108 (2000)
26. Agüero-Valverde, J., Jovanis, P.: Analysis of road crash frequency with spatial models. Transp. Res. Rec. **2061**, 55–63 (2008)
27. Abdulhafedh, A.: How to detect and remove temporal autocorrelation in vehicular crash data. J. Transp. Technol. **07**(02), 133–147 (2017)
28. Washington, S.P., Karlaftis, M.G., Mannering, F.L.: Statistical and Econometric Methods for Transportation Data Analysis, 2nd edn. Chapman and Hall/CRC, Boca Raton (2010)
29. McCullagh, P., Nelder, J.A.: Generalized Linear Models. Chapman and Hall, New York (1998)
30. Hauer, E.: The Art of Regression Modeling in Road Safety. Springer, London (2015)

Numerical Modeling of Reinforced Concrete T-Beams

Helisa Muhaj, Carla Marchão, Válter Lúcio, and Rita Gião

Abstract ATENA Engineering 3D software was used to build various numerical models of a RC specimen that was tested in the Laboratory of Heavy Structures of NOVA School of Science and Technology. Specimen CB0 was the reference one of a broader experimental campaign. The sensitivity analysis was carried out after the experimental campaign, aiming to understand better the influence of different factors, such as the FE type and size, and the fracture energy. The obtained results were compared with the experimental results of beam CB0. The behaviour of the numerical model built with 40 mm quadrilateral FE was found to be the most appropriate one.

Keywords Sensitivity analysis · RC beams · Numerical modelling · Triangular/quadrilateral finite elements

1 Introduction

Beam CB0 was the reference specimen of an experimental campaign that aimed to study different seismic strengthening solutions [1]. The specimen was tested following a loading procedure that combines the gravity load with the cyclic displacements, simulating a seismic situation (as proposed by Gião et al. [2]. Since the experimental campaigns are more complex than the numerical studies (i. e. take longer, are more expensive, need numerous devices for monitoring, have limited results, etc.), the need for numerical analysis arose.

H. Muhaj (✉) · C. Marchão · V. Lúcio
Civil Engineering Department, NOVA School of Science and Technology, Caparica, Portugal
e-mail: h.muhaj@campus.fct.unl.pt

H. Muhaj
PPE—Planeamento e Projectos De Engenharia, Lda, Lisbon, Portugal

C. Marchão · V. Lúcio · R. Gião
CERIS, Lisbon, Portugal

R. Gião
Civil Engineering Department, Lisbon Superior Engineering Institute, Lisbon, Portugal

C. Chastre et al. (eds.), *Testing and Experimentation in Civil Engineering*, RILEM Bookseries 41, https://doi.org/10.1007/978-3-031-29191-3_29

The finite element software ATENA Engineering 3D [3, 4] was used to simulate the behaviour of beam specimen CB0 under static incremental loading. Previous studies have shown that the application of this loading protocol [5] does not influence the failure mode of the tested beams.

Two types of finite elements (FE) were considered for the study of the behaviour of beam CB0, namely triangular (3-noded/tetra) and quadrilateral (4-noded/brick) FEs. The FE's size ranged from 50 to 80 mm for triangular FE and from 40 to 80 mm for quadrilateral FE. Moreover, two different formulations were used for defining the fracture energy. All the results are compared between them as well as with the experimental results. The computational time, the cracking pattern and more importantly, the overall performance of the numerical models was considered for defining parameters that better replicate the experimental test.

The conclusions of the sensitivity analysis presented in this paper were then used to model different strengthened beams that were part of the experimental campaign (these results are outside the scope of the current paper). The numerical models could predict the behaviour of these beams and various parameters could be monitored before performing the experimental tests. The concrete principal strains, stress evolution along the conventional mild steel reinforcement as well as along the prestressing steel strands (bonded/unbonded lengths), cracking pattern, etc., could be investigated before the actual tests.

2 The Experimental Campaign

2.1 Specimen CB0

The performance of full-scale RC T-beam, referred herein as specimen CB0 (and as VR2 in the original document), was studied experimentally by Gião et al. [2]. The length of the beam represented 1/3 of the beam's clear span. The specimen represented the length between the beam-column joint and the contraflexure point of the beam under a combination of cyclic loading with gravity load.

Specimen CB0 reinforcement details and cross section are presented in Fig. 1a, b.

The experimental campaigns were conducted at the Laboratory of Heavy Structures of NOVA School of Science and Technology. As shown in Fig. 2, the specimens were fixed vertically to the strong floor and horizontally to the reaction wall. The horizontal load was applied using an actuator with ±500 kN load capacity and 500 mm (±250 mm) displacement range.

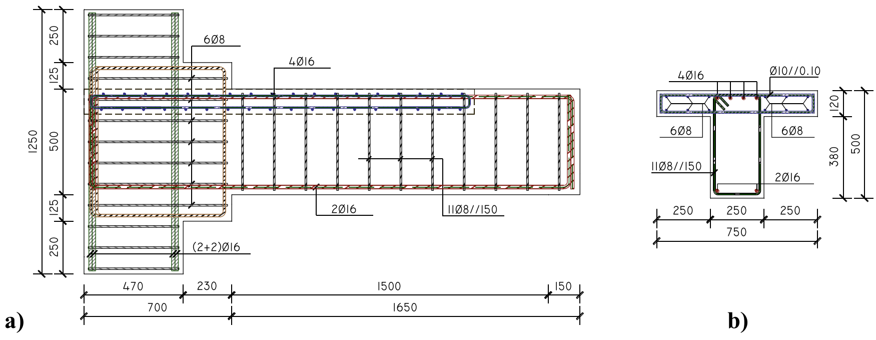

Fig. 1 Beam CB0: **a** Geometry and reinforcement details and **b** cross-section [2]

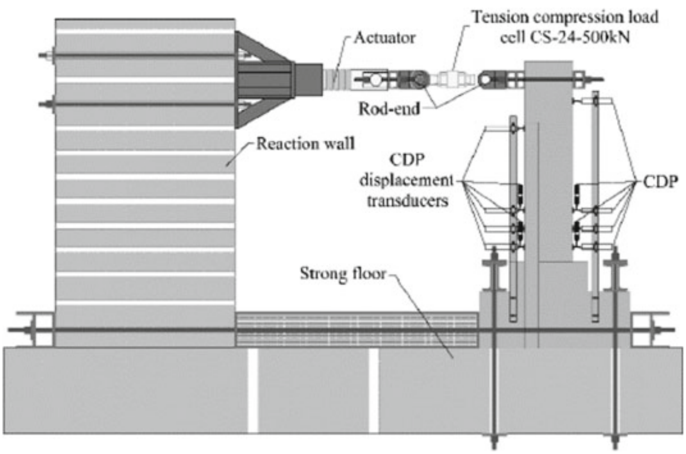

Fig. 2 Test setup [5]

2.2 The Experimental Results

Load-displacement diagram of specimen CB0 is shown in Fig. 3. The load capacity of specimen CB0 was 212.5 kN, while the ultimate displacement was 111.6 mm. The adopted failure criterion in the experimental test was the decrease of load capacity below 85% of its maximum value. Excessive residual deformations were observed at failure.

This specimen had concrete failure, as it can be noticed in Fig. 4. Concrete crushing and buckling of the longitudinal bars were observed in the compressed region of the beam (Fig. 4c). Moderate concrete spalling was observed in the tensioned region of the beam (see Fig. 4b).

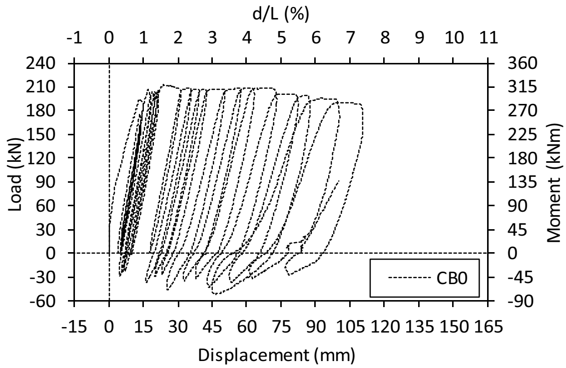

Fig. 3 Load-displacement diagram of specimen CB0 [2]

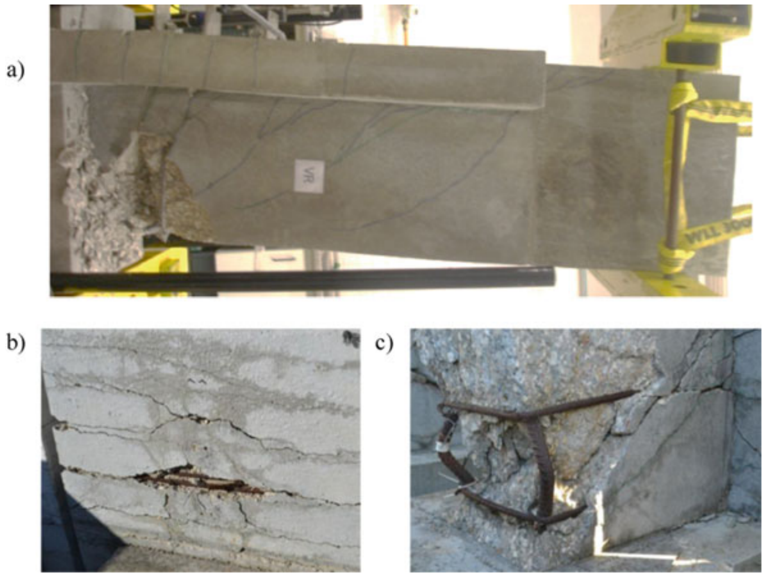

Fig. 4 Beam CB0: **a** side view of cracking pattern at failure, **b** cracking pattern in the tensioned region of the beam; **c** rupture of the bottom longitudinal bars by buckling [2]

3 Sensitivity Analysis

3.1 Numerical Models of Beam CB0

ATENA 3D is an engineering program based on the finite element method, which is suitable for modelling reinforced concrete structures. In all the ATENA models that are presented in this publication, concrete was modelled through 'S-beta Material',

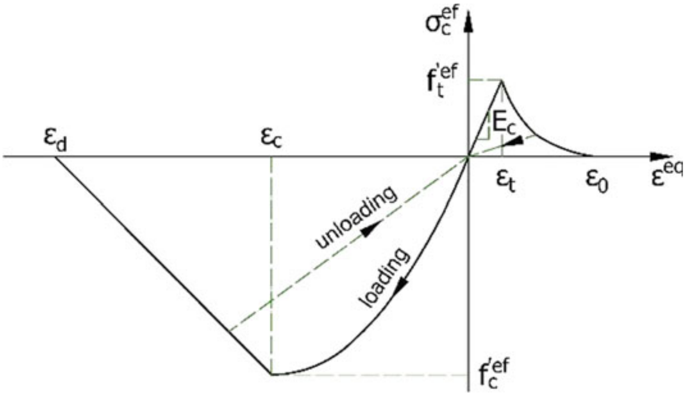

Fig. 5 ATENA Engineering 3D S-Beta model [6], concrete uniaxial stress-strain law [11]

presented in Fig. 5 [6]. This concrete model includes nonlinear concrete behaviour in compression and nonlinear fracture mechanics of concrete in tension. The hardening/softening plasticity model is based on Menetrey and Willam [7] failure surface. The compressive strength of concrete after cracking is reduced based on Modified Compression Field Theory (MCFT) of Vecchio and Collins [8] and Bentz et al. [9]. Concrete tensile behaviour is based on Rankine failure criterion. Tension crack propagation is modelled based on exponential Hordijk crack opening law [10].

The experimental values of the concrete compressive strength were considered in the numerical models. The value of the elasticity modulus was reduced by 10% due to the use of limestone aggregates [12] and the tensile strengths had also a reduction of 10% to consider shrinkage, as proposed in ATENA documentation [3, 4]. The critical compressive displacement and plastic strain at compressive strength were calculated following Eqs. (1) and (2), respectively, according to ATENA documents [13]:

$$w_d = -5 \times 10^{-4} (\text{in } m) \tag{1}$$

and

$$\varepsilon_{cp} = f_c / E \tag{2}$$

where:

f_c is concrete compressive strength
E is concrete modulus of elasticity

Fracture energy G_F is calculated by Eq. (3) in accordance with fib Model Code [14]:

$$G_F = 73 \times \mathrm{f}_{\mathrm{cm}}^{0.18} \tag{3}$$

where $f_{cm} = f_{ck} + 8$ MPa represents the mean compressive strength of concrete in MPa, and and G_F units are N/m.

The crack opening displacement, *w*, is obtained from strains according to Crack Band Theory [15] and modified by the orientation factor proposed in Cervenka et al. [16]. The shear factor coefficient is 20, which represents the default ATENA value based on experimental results of Walraven and Reinhardt [17]. The crack model coefficient value ranges between 0 and 1, representing respectively rotational [8, 18] and fixed crack model [19]. The rotated crack model coefficient, equal to 0.5, was chosen for all models, i.e., crack lines are fixed as soon as they are opened so far that the softening law drops to 0.5 times the initial tensile strength [4].

The FE models in ATENA were built in full scale and their geometry, reinforcement details and support conditions replicated the experimental specimen (CB0). The models were built using macro-elements which have distinct material characteristics (steel/concrete/etc.) and can be refined into finite elements with defined sizes and types. The types of solid finite elements available in ATENA Engineering 3D are tetrahedron and brick elements, shown in Fig. 6a, b. [6]. These elements are also referred in ATENA documentation as tetra and brick elements, respectively. Numerical models of beam CB0 with both tetrahedron and brick FE with different sizes were built and compared in the sensitivity analysis.

The reinforcement bars in all numerical models were modelled as one-dimensional bars, characterized by multilinear stress-strain curves obtained from the experimental results. Buckling of reinforcement was considered by following the instructions of ATENA documentations [4]. The interface between steel reinforcement bars and concrete [6] was modelled with a bond-slip relationship according to fib Model Code [14].

ATENA Standard Newton-Raphson algorithm with 40 iterations per step was used as solution method in all the numerical models that are presented in this publication. The geometry and reinforcement details of beam CB0 numerical model are shown in Fig. 7a, b. Bond between reinforcement bars and concrete in this analysis (according to fib Model Code [14]) was considered. Stress-slip diagrams of reinforcement bar

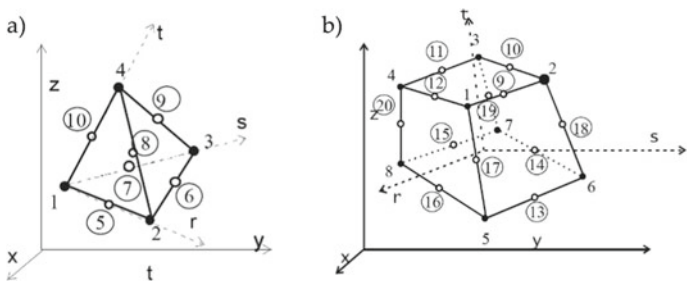

Fig. 6 Geometry of 3D solid elements in ATENA Engineering 3D: **a** tetrahedron and **b** brick (quadrilateral) [6]

main diameters of beam CB0 are shown in Fig. 8. Both types of FEs available in ATENA Engineering 3D were considered for studying beam CB0 behaviour, namely tetrahedron and brick FEs. The finite element's size ranged from 40 to 80 mm. The load was applied as an incremental point load on a steel plate, positioned 1500 mm from beam support (i. e. the column block), similarly with the experimental tests (see Fig. 7a).

Concrete experimental characteristics and all the other characteristics that were required to simulate the concrete model of beam CB0, are given in Table 1.

E is the modulus of elasticity
ν is the Poisson's ratio
f_{cm} is the mean compressive strength
f_{ctm} is the tensile strength
w_d is the critical compressive displacement, (default value)
ε_{cp} is the plastic strain at compressive strength

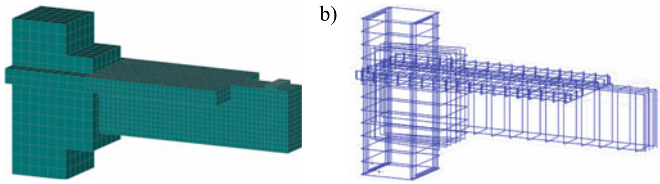

Fig. 7 Numerical model of beam CB0: **a** overall geometry; **b** reinforcement geometry

Fig. 8 Bond stress-slip diagrams for all bar reinforcements in beam CB0

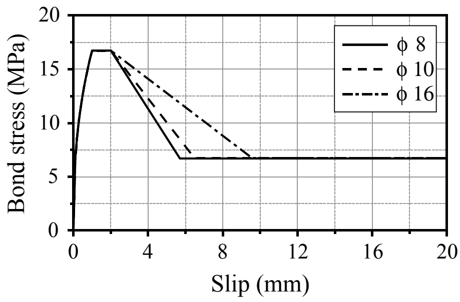

Table 1 ATENA 3D Sbeta Material parameters for beam CB0

Beam Model	E (GPa)	ν (-)	f_{cm} (MPa)	f_{ctm} (MPa)	w_d (m)	ε_{cp} (-)	$r_{c,lim}$ (-)
CB0	31.05	0.2	44.81	3.03	-5E-04	1.44E-03	0.8

Beam Model	G_F (Vos [20]) (N/m)	G_F (MC 2010 [14]) (N/m)	e (-)	β (-)
CB0	94.6	144.7	0.52	0

$r_{c,lim}$ is the reduction of compressive strength due to cracks (default value)
G_F is the fracture energy
S_F is the shear factor (default value)
e is the failure surface eccentricity and defines the roundness of the failure surface (default)
β is the multiplier for the plastic flow direction (for $\beta = 0$ the material volume is preserved)

3.2 Influence of Size and Type of Finite Elements

The cracking pattern and concrete principal strains in models built with tetrahedron FEs are presented in Fig. 9. The mesh size considered in the models was 50 mm, 60 mm, 70 mm and 80 mm and the obtained results are shown in Fig. 9a–c and d respectively. The sizes of the FEs were chosen within recommended limits [3], whereas models with mesh size smaller than 50 mm could not be built due to limitations on the maximum number of FE that can be analyzed by the program.

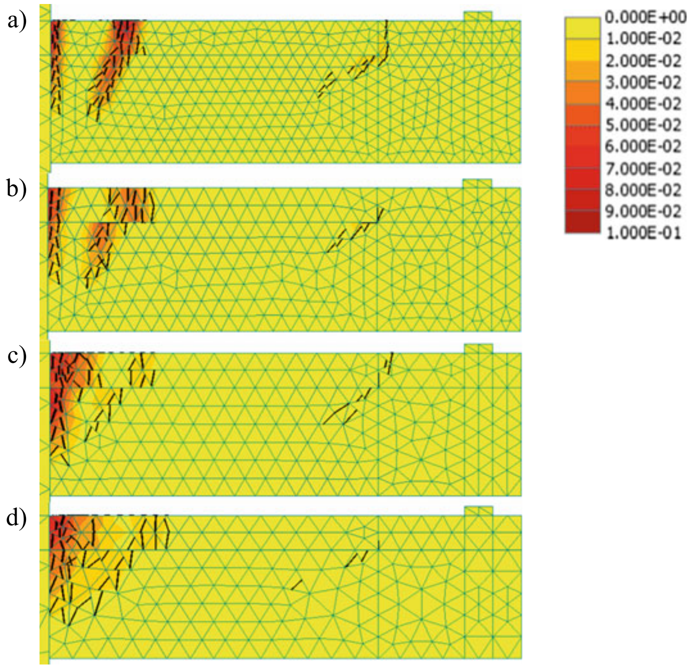

Fig. 9 CB0—principal concrete strain and crack pattern of models built with tetrahedron FE (i. e. 3-noded or tetra FE) with mesh size: **a** 50 mm, **b** 60 mm, **c** 70 mm, **d** 80 mm (the minimum crack width shown is 5×10^{-4} m)

The numeric models with different mesh sizes presented acceptable results in terms of orientation and cracking distribution—Fig. 8—indicating that the FE models provide a suitable simulation. However, the model with 50 mm FE size shows a more precise and exact cracking pattern.

In numerical models with larger mesh size (in the present case, 80 mm), it is difficult to capture local cracking. For instance, in the region of beam discontinuity where the T-section turns into a rectangular section (see Fig. 7), almost no damage is observed (see Fig. 9d). In the numerical model with mesh size 50 mm, shown in Fig. 9a, the color of the iso-area of concrete strain indicates a higher level of strains and the cracking in this region is more noticeable. A similar development of cracking pattern was observed during test of beam CB0, shown in Fig. 4. For same mesh size, the model had convergence problems, thus the ultimate displacements had distinct values. Therefore, the results given in Fig. 9 are shown for the same level of applied displacement on beams (i. e. 40 mm).

The principal strain iso-areas and cracking patterns of numerical models with brick FE (i. e. 4 noded or brick FE) with sizes 40 mm, 50 mm, 60 mm, 70 mm and 80 mm are shown in Fig. 10. The cracking pattern of models shown in Fig. 10 gets sharper as the FE size decreases. Moreover, the sections that suffer the highest concrete strains can be detected easier.

The cracking pattern observed in models with quadrilateral FE differs from the previous models built by triangular elements with relatively large FE size (70 mm and 80 mm). However, the models with different types of FE turn more similar as the size of the FE decreases.

The load—displacement curves obtained from the analysis of models with tetrahedron and brick elements with the same mesh size are plotted in Fig. 11a–d for all the FE sizes that were described early (40–80 mm). In general, models with tetrahedron FE were characterized by a slightly higher initial stiffness and load capacity when compared to the models built with brick elements. In the present study, the models with brick FE had, in general, inferior ultimate displacement when compared with models built with tetrahedron FE (except for mesh size 40 mm). Moreover, the models with brick elements needed less computing time when compared with models with tetrahedron elements, since the total number of FE in these models was much lower than in models with tetrahedron elements.

Between the described models, whose results are summarized in Fig. 11, the behavior of numerical model with brick FE with 40 mm size was very similar with the experimental behavior of beam CB0.

3.3 Influence of Fracture Energy

All the numerical models that were presented earlier used the fib Model Code [14] expression to calculate the fracture energy, G_F, given by Eq. (4):

$$G_F = 73 \times \mathrm{f}_{\mathrm{cm}}^{0.18} \times z \tag{4}$$

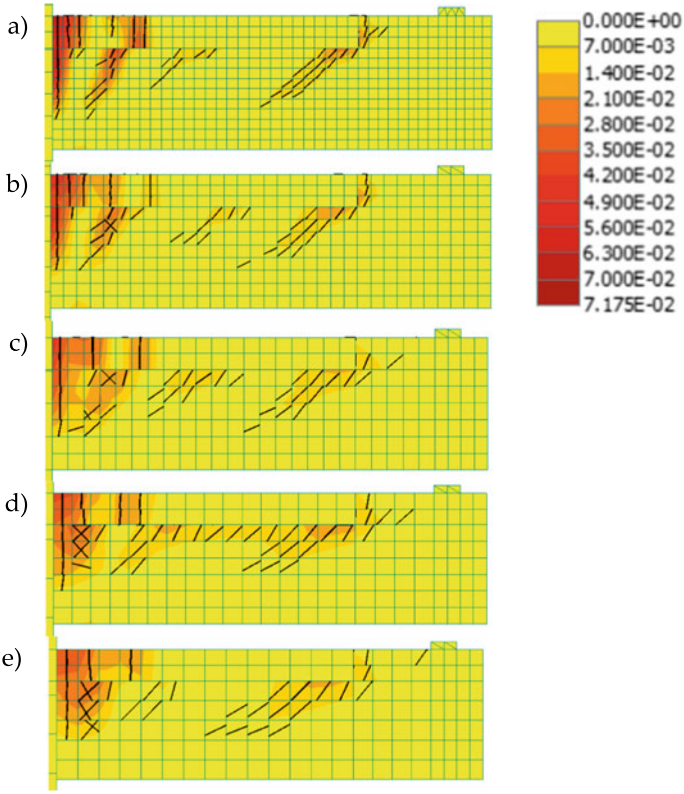

Fig. 10 CB0—principal concrete strain and crack pattern for models built by brick FE with different mesh sizes: **a** 40 mm, **b** 50 mm, **c** 60 mm, **d** 70 mm, **e** 80 mm (the minimum crack width displayed is 5×10^{-4} m)

However, in literature, different authors have proposed other expressions to estimate the fracture energy. For comparison, apart from the models presented earlier (in which the fracture energy was calculated according to fib Model Code [14]), another model for beam CB0 was built following the Vos [20] expression for fracture energy:

$$G_F = 2.5 \times 10^{-5} \times f_{ctm} \quad (5)$$

where f_{ctm} represents the mean tensile concrete strength in MPa.

The obtained results are given in Fig. 12. The initial stiffness of the numerical model built following Vos [20] formulation was slightly lower than that of the model built following fib Model Code [14] formulation. The peak load of both models was almost identical, as well as the post-peak behaviour up to a beam rotation of around 4.0% (see Fig. 12). However, the model with fracture energy based on Vos [20] expression had a significant drop of load after 4.0% beam rotation, whereas the other model followed the experimental hysteretic curve up to beam failure.

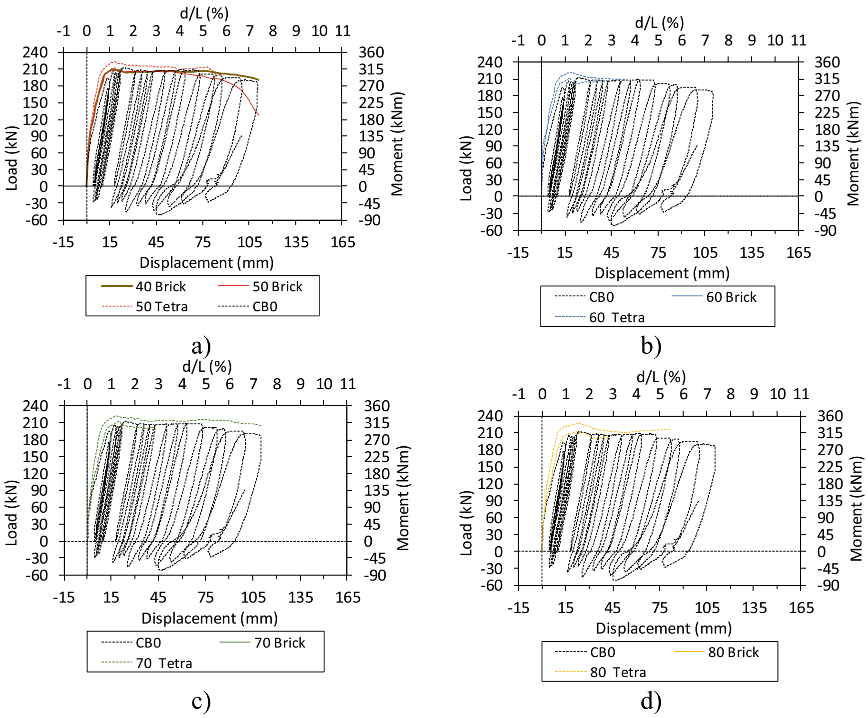

Fig. 11 CB0—load-displacement diagrams for similar mesh sizes and different FE: **a** 40 mm brick, 50 mm brick and tetrahedron, **b** 60 mm brick and tetrahedron, **c** 60 mm brick and tetrahedron and **d** 80 mm brick and tetrahedron

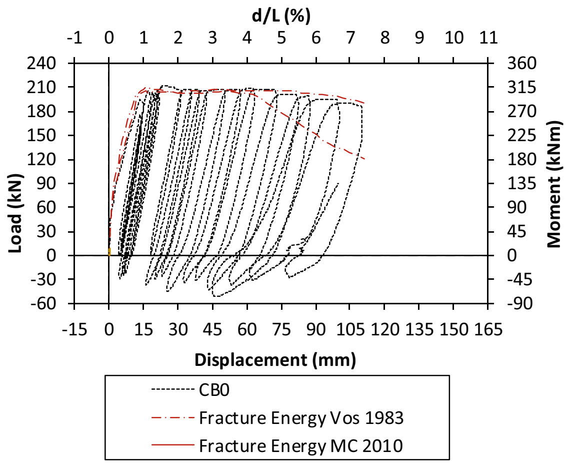

Fig. 12 CB0—load-displacement diagrams for two different values of the fracture energy, based on Vos [20] and fib model code [14] formulations

The numerical model built considering fib Model Code [14] fracture energy resembled better the experimental results.

4 Conclusions

Based on the performed sensitivity analysis, it can be concluded that the numerical models built with brick FE of 40 mm size had a similar performance with the beam tested experimentally.

A very reasonable agreement was observed between the experimental and numerical overall performance.

The initial stiffness, the maximum load, as well as the ultimate displacements of the numerical model were very similar to the results observed experimentally. Moreover, the cracking patterns were also comparable.

Regarding the computational time, the numerical model with brick FEs required much less time than the model with tetrahedron FEs.

References

1. Gião, R., Lúcio, V.J.G., Chastre, C.: Characterisation of unidirectional fibre reinforced grout as a strengthening material for RC structures. Constr. Build. Mater. **137**, 272–287 (2017). https://doi.org/10.1016/j.conbuildmat.2017.01.131
2. Gião, R., Lúcio, V., Chastre, C.: Assessing the behaviour of RC beams subject to significant gravity loads under cyclic loads. Eng. Struct. **59**, 512–521 (2014). https://doi.org/10.1016/j.engstruct.2013.11.012
3. Červenka, V., Červenka, J.: ATENA program documentation part 2-2, User's Manual for ATENA 3D (2015)
4. Pryl, D., Červenka, J.: ATENA program documentation, Part 11–Troubleshooting Manual (2016)
5. Muhaj, H., Marchão, C., Lúcio, V., Gião, R.: Experimental evaluation of cyclic loading test procedure including gravity load on RC beams. Struct. Concr. **20**, 1292–1306 (2019). https://doi.org/10.1002/suco.201800255
6. Červenka, V., Jedele, L., Červenka, J.: ATENA program documentation—Part 1. Theory (2018)
7. Menetrey, P., Willam, K.J.: Triaxial failure criterion for concrete and its generalization. ACI Struct. J. **92**, 311–318 (1995)
8. Vecchio, F.J., Collins, M.P.: Modified compression-field theory for reinforced concrete elements subjected to shear. J. Am. Concr. Inst. **83**, 219–231 (1986). https://doi.org/10.14359/10416
9. Bentz, E.C., Vecchio, F.J., Collins, M.P.: Simplified modified compression field theory for calculating shear strength of reinforced concrete elements. ACI Struct. J. **103**, 614–624 (2006). https://doi.org/10.14359/16438
10. Hordijk, D.A.: Local approach to fatigue of concrete. Technische Universiteit Delft (1991)
11. Chen, W.-F.: Plasticity in reinforced concrete. J. Ross Publ. (2007; 1982)
12. EN 1992-1-1: Eurocode 2: Design of concrete structures—Part 1-1: General rules and rules for buildings. CEN European Comittee for Standartization, Brussels, Belgium (2004)
13. Červenka, J., Jendele, L.: ATENA program documentation, Part 6, Input File Format (2016)

14. fib Model Code. Model Code 2010—Final Draft, vol 1, Bulletin 65. Federation Internationale Du Beton, Lausanne, Switzerland (2012)
15. Bažant, Z.P., Oh, B.H.: Crack band theory for fracture of concrete. Mater. Struct. **16**, 155–177 (1983)
16. Červenka, V., Pukl, R., Ozbolt, J., Eligehausen, R.: Mesh sensitivity effects in smeared finite element analysis of concrete structures. Fram **2**, 1387–1396 (1995)
17. Walraven, J.C., Reinhardt, H.W.: Theory and experiments on the mechanical behaviour of cracks in plain and reinforced concrete subjected to shear loading (1981)
18. Crisfleld, M.A., Wills, J.: Analysis of R/C panels using different concrete models. J. Eng. Mech. **115**, 578–597 (1989). https://doi.org/10.1061/(ASCE)0733-9399(1989)115:3(578)
19. Červenka, V., Červenka, J., Pukl, R.: ATENA—a tool for engineering analysis of fracture in concrete. Sadhana Acad. Proc. Eng. Sci. **27**, 485–492 (2002). https://doi.org/10.1007/BF02706996
20. Vos, E.: Influence of loading rate and radial pressure on bond in reinforced concrete (1983)

New Sensors and Technologies

Estimation of River Flow Discharges Using Image Processing

Rodrigo Santos and João Nuno Fernandes

Abstract In the scope of water resources management, the regular measurement of river flow discharge is an essential tool to control and monitor natural variances and the prevention of damages in case of extreme events. The proposed method is based on Large-scale Image Velocimetry (LSPIV) i.e. on the analysis of a sequence of images and the measurement of the 2D velocity field at the surface of a watercourse. The present study consisted on the evaluation of this technique for the measurement of flow discharge based on experimental cases. The size and shape of the tracers and the relation between the depth-averaged and surface velocities were investigated by means of laboratory and in situ experiments. In addition, two LSPIV freeware software were tested and the quality of their results were analysed and compared to traditional measurements. The accuracy of the measurements seems to reach acceptable thresholds and the results were promising. Nevertheless, for a wider use of this technique, further research should be taken to solve specific issues.

Keywords Water resources management · River discharge · Measurements · LSPIV · Tracers.

1 Introduction

Effective management of water resources should be based on reliable information, among which frequent monitoring of river flow discharge is essential. Among others, this information is required to control and ensure the consumption needs of volumes of water in urban and rural areas, the production of hydropower and the management of extreme events such as droughts or floods.

R. Santos
Universidade Nova de Lisboa, Lisbon, Portugal

J. N. Fernandes (✉)
Departamento de Hidráulica e Ambiente, Laboratório Nacional de Engenharia Civil, Lisbon, Portugal
e-mail: jnfernandes@lnec.pt

C. Chastre et al. (eds.), *Testing and Experimentation in Civil Engineering*,
RILEM Bookseries 41, https://doi.org/10.1007/978-3-031-29191-3_30

River discharge monitoring is also important for the implementation of bilateral agreements in relation to international rivers to balance the use of water resources in order to benefit different countries avoiding diplomatic issues and protect surface water, groundwater and ecosystems.

Furthermore, compliance with current legislation requires reliable and flexible mechanisms for constant monitoring of flows in rivers.

Taking into account the importance of the evaluation of river discharges, flow measurement technologies have undergone into several changes to make them faster and more effective. The optimization of surface runoff recording systems must be carried out through rigorous planning and prior knowledge of the general characteristics of fluvial regimes. In this way, for relevant streams, it is essential to carry out measurements at strategic points and in relevant cross sections along the river and understand the contribution of the various sub-basins and possible retention in reservoirs or lakes.

Following the classification of Boiten [1], flow measurement methods can be divided into (i) Section-velocity method,(ii) Structural method and (iii) Flow curve method.

The section-velocity method is an isolated measurement that consists on the integration of the average section velocity by the cross-sectional area of the watercourse. The structural method is a continuous measurement that uses the installation of fixed hydraulic structures to compute the flow discharge by using a known rating curve (i.e. relationship between the flow and the hydraulic head). Finally, the flow curve method is a continuous measurement based on the evaluation of the flow by measuring the hydrometric level. In this case, the relationship between these two quantities must be regularly calibrated. A continuous record of levels in this section is then used to compute the flow discharge. Once the flow curve expression has been calibrated, monitoring the flow over time becomes simpler. Due to the constant alteration of river sections, caused by sediment transport and consequent phenomena of sedimentation or erosion, frequent calibration of the rating curve should be performed.

Large Scale Particle Imaging Velocity (LSPIV) uses sequential images of the flow surface with a known frequency and computes the 2d velocity. So far, it has been used in several research projects (see, for instance, [2]).

The present work aims at evaluating the possibility of LSPIV to determine the flow discharge in river reaches with known geometry. Issues such as the type and size of tracers to be used or the accuracy of this technique will be investigated by means of laboratorial and in situ experiments.

2 Methods

The section-velocity method is based on the continuity equation and on the definition of flow (Q) i.e. the integration, over the area, A, of the velocity, V, perpendicular to that area, $Q = \int V \mathrm{d}A$.

From an operational point of view, the measuring cross section must be selected according to the alignment of the flow with the downstream direction (typically a straight reach).

The main features to measure flow discharges using LSPIV are: (i) the cross section area; (ii) the particle image velocity technique (e.g. its accuracy) and (iii) the relation between depth-averaged and surface velocities.

The cross section area can be obtained by regular surveys of the bathymetry. The frequency depends mainly on the nature of the bed material. Downstream alluvial reaches are characterized by temporal changes whereas mountain reaches feature a more stable and fixed bed due to their rocky nature. Depending on the river width and flow discharge, area may be obtained by traditional (e.g. scaled ruler) or ultrasound methods. The issues related to this component will not be covered in this work, i.e. cross sectional area is considered to be known a priori.

After the video recording of the river surface, the first step of particle image velocimetry (PIV) technique must be the improvement of the image quality. It is convenient to filter the images to increase the contrast and enhance the identification of the tracers. The evaluation of the displacement of the tracers between two images is made through cross-correlation. This statistical method tries to identify the pattern of each particle in successive interrogation areas (IA), one per time step (see [3] for further details). Tracers will then be searched in a Search Area (SA), included in IA.

Statistical analysis of cross correlation is then performed to determine the displacement of the tracers. In a pair of consecutive images, the pixel with a higher similarity index is assumed to have the higher probability of displacement. This process will be applied to all IAs.

Using the same concept, LSPIV differs from PIV as it is applied to wider areas and it uses different lighting and image capture methods. Generally, PIV uses high-speed cameras, while LSPIV uses common cameras and doesn't need laser light source to illuminate the particles. Therefore, LSPIV has advantages over PIV, as it can be used in more situations, resulting in a more practical method. On the other hand, PIV has a higher definition and acquisition frequency, especially useful for turbulence studies.

First LSPIV tests were performed in Japan in the mid-1990s [4–7] introduced the concept of LSPIV as one PIV extension for large discharge areas in-situ conditions. The author identified reflections caused by the sun and the existence of standing waves as the main limitation of this method.

After the measurement of surface velocity, the next feature to look into for the measurement of flow discharge in river using LSPIV is the relation between the depth-averaged (V_a) and the surface (V_s) velocities. Taking into account the vertical logarithm profile of the velocity, several authors tried to characterize the coefficient, C, between these two velocities, i.e., $C = V_a / V_s$. Bed roughness, Reynolds number and hydraulic radius were identified as the main factors for the change of C (see, for instance, [8]).

Hauet et al. [9] proposed a simple relationship for C depending on the hydraulic radius, R_h. For shallow waters ($R_h < 1$ m), C is approximately 0.8 and it increases linearly reaching 0.9 for R_h equal to 5 m. Furthermore, Hauet et al. [9] observed the increase of C with the decrease of the bed roughness.

Le Coz et al. [10] identified the main source of errors for LSPIV measurements, namely, the existence of suspended material interfering with the performance of the equipment, wind that introduces significant disturbance in the flow and movements of the camera. The uncertainties of the LSPIV measurements were studied by Kim [11] and Muste et al. [12] that estimated an average error of approximately of 10%.

To ensure the quality of the LSPIV measurement, according to USGS [13], minimum requirements for the camera are a resolution of 640 × 480 pixels and a frequency of 15 frames per second. The video recording must have a duration of at least 1 min, in order to have the possibility to choose the best period of the recording. A minimum of four fixed reference points should be included so that distances can be easily known.

3 Experimental Procedure

The estimation of the river discharge in rivers with image processing techniques may involve several uncertainties and difficulties. The general procedure is presented in Fig. 1.

In this work, 2 software were tested to obtain the surface velocities from the surface recordings, PIVlab [3] and Fudaa [14].

Experimental measurements in laboratorial and in-situ facilities will allow the evaluation of the tracers and the LSPIV method in the estimation of the flow discharge. The comparison between real and estimated flow discharges is used to evaluate the accuracy of the method.

The experiments were conducted in 2 different channels where the discharge was known and the measurement with traditional methods was possible. Figure 2 shows the cross sections of these channels, namely, (i) compound channel with a central

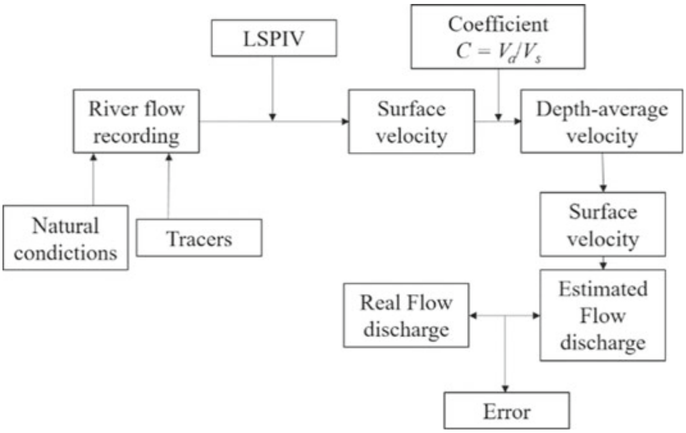

Fig. 1 Procedure to estimate river flow discharge using LSPIV

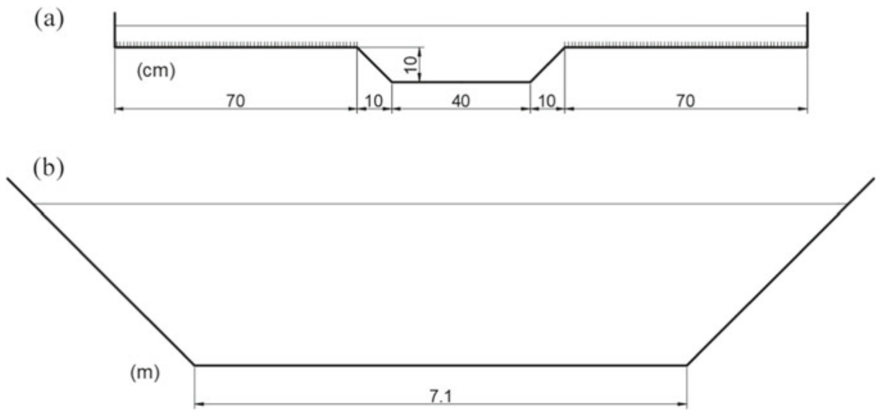

Fig. 2 Main characteristics of **a** compound channel; and **b** trapezoidal channel

main channel and two lateral floodplains; and (ii) trapezoidal channel with lateral banks with slope 1:1.

The experiments were divided into the following parts:

A. **Trapezoidal section of the compound channel (using central single channel)**

A1 using PIVlab, one flow and two tracers
A2 four flows and two software

B. **Compound channel**

B1 using PIVlab, one flow and three tracers
B2 two software and three flows

C. **Trapezoidal channel**

Two software, one flow and three tracers.

For parts A and B, a GoPro 3 camera with a resolution equal to 1280 × 960 pixels and an acquisition frequency equal to 47.95 Hz was used.

For part C, a drone (Hubsan ZINO PRO) was used. It is equipped with a 4 k definition (3840 × 2160 pixels) and acquisition frequency of 30 Hz.

Regarding the tracers, 6 different types were used, namely, polystyrene spheres with 3 mm of diameter, and squared papers of 1, 2, 2.5, 4 and 8 cm.

ADV vectrino (Nortek) was used to evaluate the velocity in parts A and B whereas an Acoustic Doppler Current Profiler (ADCP, Aquadopp Profiler 1 MHz from Nortek) was used in part C.

4 Results

4.1 Part A

For the trapezoidal cross section, an interrogation area of 0.6 m wide and 0.5 m long was chosen. Recordings of 1.5 min were considered in this case.

In component A1 (Simple trapezoidal section, flow $Q = 20$ l/s, 2 tracers and 1 software—PIVlab), the aim was to compare the results obtained with two different tracers, namely, polystyrene spheres or squared papers. Measurements were performed only in one half of the channel due to the symmetry of the channel.

Main results are presented in Fig. 3.

Tracers made of polystyrene spheres had much smoother and more regular surface velocity curve than 2.5 cm side papers. Even during the experiments, it was much easier to seed the flow with the spheres as these tracers provided a better dispersed and uniform pattern.

Using the coefficient C provided by Hauet et al. [9] to calculate the average velocities with the polystyrene spheres for concrete channels with hydraulic radius lower than 1 m, flow discharge for the entire channel was 17.2 l/s corresponding to a total error of 13.9%.

In component A2, four flow discharges (5, 10, 15 and 20 l/s) and two software were analysed. All tests were performed with polystyrene spheres as tracers. Results are presented in Fig. 4.

The general pattern of velocities is rather similar to the velocities obtained with ADV. PIVlab results present a parabolic surface velocity profile in which the velocity increases in the inclined margin and remains constant in the remaining section. With Fudaa the formats of surface velocity graphs are not so regular and similar to each other. Surface velocities obtained with Fudaa are slightly higher than those obtained with PIVlab and ADV.

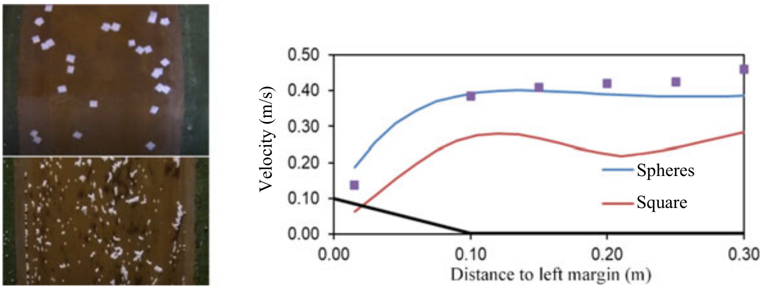

Fig. 3 Photograph of the channel with squared paper (top left) and polystyrene spheres (lower left) as tracers and results of the velocities (purple squares stand for the results with ADV)

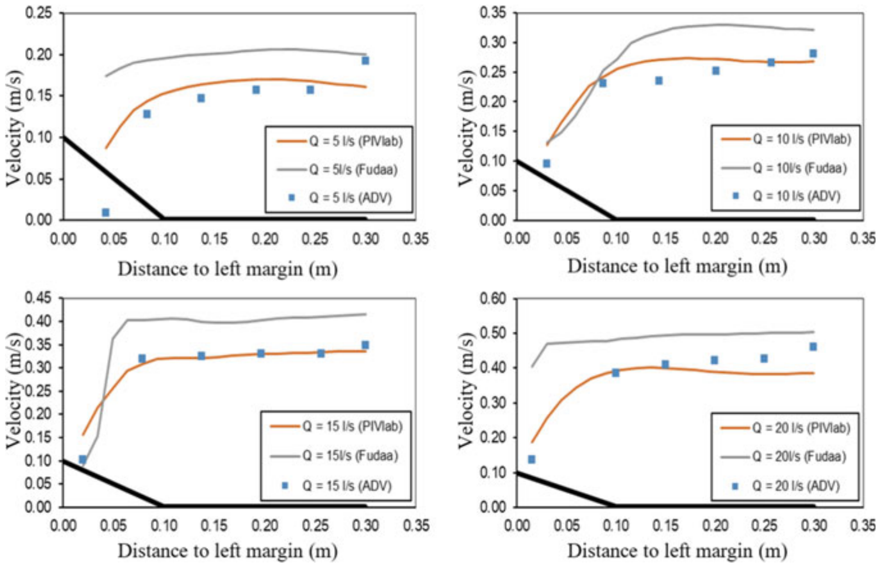

Fig. 4 Velocity comparison for two software and several flow discharges

Assuming a coefficient *C* to calculate the average velocities equal to 0.9, the average error on the calculation of flow discharge was about 16% using Fudaa and 4% using PIVlab.

Regarding the results in this component it was observed that to obtain the same flow discharge a coefficient *C* equal to 0.93 to 1.0 with PIVlab and from 0.75 to 0.82 with Fudaa was needed.

4.2 Part B

In order to obtain the average velocities through the ADV, measurements were taken at 20 different points of the cross section.

In the first part, B1, three tracers were tested (polystyrene spheres and two types of squared papers with 4 cm and 8 cm) and only PIV lab was used to evaluate the surface velocities.

The velocity distributions for LSPIV tests and using ADV are presented in Fig. 5.

Comparing the surface velocity obtained with these tracers with the depth-averaged velocities from ADV, it can be confirmed that the results with polystyrene spheres as a tracer seem more coherent.

The surface velocities obtained with the three tracers shows a small decline in the center of the section where the velocity should reach its maximum. This decline can be explained by the insufficient density of tracers in the central section.

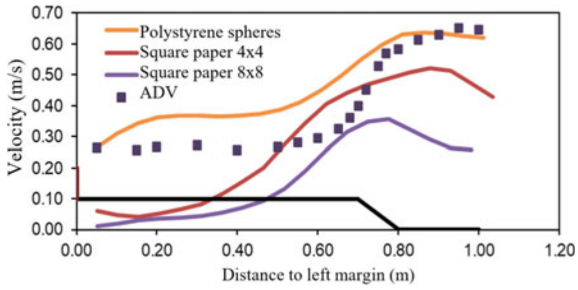

Fig. 5 Velocity comparison for three tracers

Using typical values for coefficient C (as presented for part A), the average errors in the prediction of the total discharge were 4% for spheres, 28% for squared papers 4 cm and 57% for squared papers 8 cm. It is clear that these two last tracers were unable to effectively characterize the surface velocity of water as they provide much lower surface velocities. Therefore, polystyrene was used in the remaining laboratory tests.

For part B2, three flow rates and two software were tested. The objective was to study the behavior of the coefficient C and to understand which software produces better results. Total discharge of 38.80 l/s, 46.60 l/s and 58.90 l/s were used.

Figure 6 presents the results for this part B2.

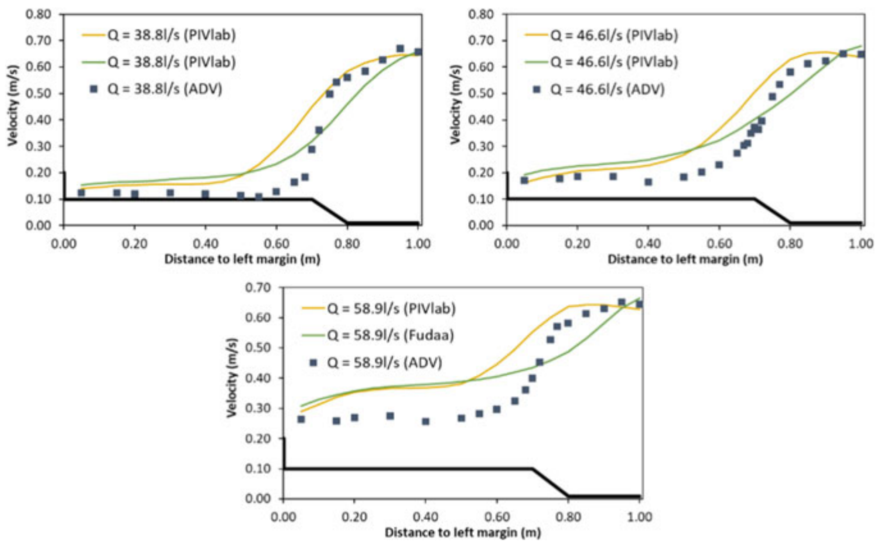

Fig. 6 Comparison of the surface velocities obtained with the LSPIV and the average velocities of the ADV in the compound cross section

The results for the velocities obtained using Fudaa and PIVlab are rather similar. Comparing the velocity values in the different sections, it can be seen that in the floodplain (covered with synthetic grass) the surface velocities increase with the flow and are higher than the depth-averaged velocities. In the main channel (made of polished concrete) the surface velocities are slightly higher than the average velocities and converge more or less to the same value in the center of the section. This suggests that the use of a single coefficient for the whole channel may be incorrect. Near the interface, the results may be affected by the flow structures typically observed in compound channels, namely the large-scale horizontal cells and the secondary flow.

In test B2, a possible variation of the coefficient C, applied to the surface velocities was tested in order to obtain the corrected depth-average velocities and the flow discharge in each subsection (main channel and floodplains).

Using the results of PIVlab, the better agreement of the velocities in each subsection were obtained using an average coefficient C equal to 0.97 in the main channel and equal to 0.66 in the floodplains. In part A2, a coefficient equal to 0.99 was obtained for a single trapezoidal section.

In all cases, it is important to highlight the difficulty in ensuring a good distribution of tracers on the water surface.

4.3 Part C

Similarly to the laboratory tests, the velocity section method was used to find the flow rate. Velocity was measured initially with an ADCP and then using LSPIV method.

It should be noted that the ADCP provides a velocity profile in depth, starting to measure about 10 cm below the level of the device and acquiring values every 10 cm. With this device it is possible to have a rough idea of the bathymetry, as the results near the bottom are incoherent.

As it was not possible to recover the tracers, only paper was used because they are easily biodegradable and therefore less harmful to the environment. Analyzing the laboratory tests, it was possible to conclude that better results were obtained with small tracers. In this case, squared tracers with 1, 2 and 4 cm were used.

The results obtained for this component are presented in Fig. 7.

The results obtained with PIVlab are rather regular and relatively superior to the depth-averaged velocities obtained with ADCP. The surface velocity plot is very similar to those obtained in the laboratory, where the surface velocity increases at the beginning of the section and then tends to remain constant towards the center of the section. The surface velocities obtained with the tracers of 1 and 2 cm of side are very similar and somehow superior to the velocities obtained with the tracer of 4 cm. For this software, the size of the tracers is not critical.

Regarding the results of Fudaa (Fig. 7b), there is much more influence of the tracers. The 1 and 2 cm side tracers present surface velocities relatively higher than the average velocities of the ADCP and very similar to the velocities obtained with the PIVlab.

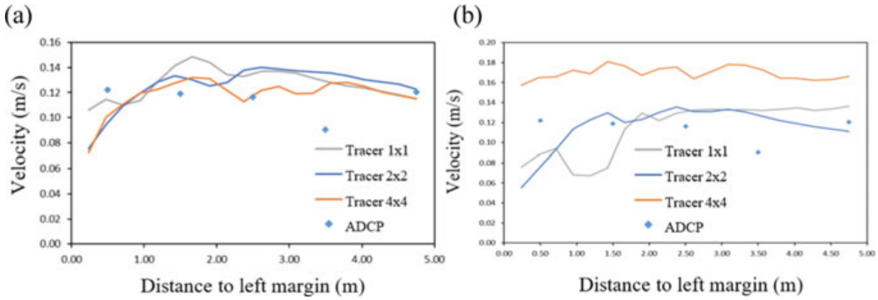

Fig. 7 Depth-averaged velocities with ADCP and surface velocities with LSPIV with several tracers **a** using PIVlab and **b** using Fudaa

Using the section-velocity method with the bathymetry and the velocities obtained with ADCP, the resulting flow discharge is 1.12 m^3/s.

From the theoretical framework and the results obtained in the laboratory, the coefficient C is expected to be between 0.9 and 1. As the concrete was not so smooth as in the laboratory and there was some vegetation in the bottom of the channel, it is expected an increase of the difference between the depth-average and surface velocities and a coefficient C of 0.9 was chosen.

With the exception of the measurement with 4 cm tracer with Fudaa, the error obtained for the flow discharge is rather small. The measurement with PIVlab resulted in an average error of 2.7%, which is quite satisfactory.

For the results of PIVlab, the average value of the coefficient C to obtain the theoretical flow discharge is 0.875.

5 Conclusions and Further Research

The use of the LSPIV method for the measurements of flow discharges in rivers was analysed in this paper. Knowing the bathymetry of the section, this method allows a simple and quick assessment of flow rates, presenting several positive points when compared to the traditional devices.

The performance of two software—PIVlab and Fudaa—was evaluated. Despite the similar results, it was clear that the velocities were better estimated using PIVlab. This software also proved to be easier and faster to apply. Some other differences are related to the options related to the pre-treatment in PIVlab with the possibility to enhance the images in order to emphasize tracer appearance.

It was observed that a good density and an uniform pattern of tracers are essential to obtain good results with LSPIV. This was one of the main differences between laboratory and field tests. In the laboratory, the tracers were placed on the surface of the water from one of the sides. From this positioning it was quite difficult to guarantee a good density and uniformity of tracers in the measurement cross section.

In the field test, the tracers were thrown from a bridge, at about 5 m above the water level, which allowed a better density and coverage.

In almost all cases, the coefficient applied to surface velocities to obtain the depth-average velocities increased with the increase in the hydraulic radius.

For reaches with low roughness, such as polished concrete, the coefficient must be between 0.95 and 1. With higher roughness, such as gravel, pebbles or vegetation, the coefficient must be between 0.85 and 0.95.

LSPIV confirmed to be a good alternative for the measurement of velocities in rivers and, therefore, a good possibility for estimating the flow. In the cases analysed in this work, the LSPIV presented an average error of 5% in the calculation of the flow.

Acknowledgements This work was supported by FEDER and Fundação para a Ciência e Tecnologia in the scope of the Project MixFluv—Mixing layers in fluvial systems (PTDC/ECI-EGC/31771/2017).

References

1. Boiten, W.: Hydrometry (IHE Delft lecture note series). In: AA Balkema **256** (2003). https://doi.org/10.1201/9780203971093
2. Muste, M., Fujita, I., Hauet, A.: Large-scale particle image velocimetry for measurements in riverine environments. Water Resour. Res. **44**, 2008 (2008)
3. Thielicke, W., Stamhuis, E.J.: PIVlab—towards user-friendly, affordable and accurate digital particle image velocimetry in MATLAB. J. Open Res. Softw. (2014). https://doi.org/10.5334/jors.bl
4. Fujita, I., Komura, S.: Application of video image analysis for measurements of river-surface flows. Proc. Hydraul. Eng. (1994). https://doi.org/10.2208/prohe.38.733
5. Aya, S., Fujita, I., Yagyu, M.: Field-observation of flood in a river by video image analysis. Proc. Hydraul. Eng. (1995). https://doi.org/10.2208/prohe.39.447
6. Fujita, I., Aya, S., Deguchi, T.: Surface velocity measurement of river flow using video images of an oblique angle. In: Proceedings, Congress of the International Association of Hydraulic Research, IAHR (1997)
7. Fujita, I., Muste, M., Kruger, A.: Large-scale particle image velocimetry for flow analysis in hydraulic engineering applications. J. Hydraul. Res. (1998). https://doi.org/10.1080/00221689809498626
8. Polatel, C.: Indexing by free surface velocity: a prospect for remote discharge estimation. In: 31st IAHR Congress 2005: Water Engineering for the Future, Choices and Challenges (2005)
9. Hauet, A., Morlot, T., Daubagnan, L.: Velocity profile and depth-averaged to surface velocity in natural streams: a review over a large sample of rivers. E3S Web Conf. **40** (2018). https://doi.org/10.1051/e3scof/20184006015
10. Le Coz, J., Camenen, B., Peyrard, X., Dramais, G.: Uncertainty in open-channel discharges measured with the velocity-area method. Flow Meas. Instr. (2012). https://doi.org/10.1016/j.flowmeasinst.2012.05.001
11. Kim, Y.: Uncertainty analysis for non-intrusive measurement of river discharge using image velocimetry. Ph.D. Thesis, The University of Iowa (2006)
12. Muste, M., Xiong, Z., Schöne, J., Li, Z.: Validation and extension of image velocimetry capabilities for flow diagnostics in hydraulic modeling. J. Hydraul. Eng. (2004). https://doi.org/10.1061/(ASCE)0733-9429(2004)130:3(175)

13. United States Geological Survey: Guidelines for the collection of video for large scale particle velocimetry (LSPIV)—OSW surface velocity workgroup—myUSGS Confluence (2018). https://my.usgs.gov/confluence/pages/viewpage.action?pageId=546865360
14. Jodeau, A.M., Hauet, A., Coz, J.L.: Fudaa-LSPIV Version 1.6.4 User Manual (2018). https://forge.irstea.fr/attachments/download/2791/Fudaa-LSPIVUserManual.pdf

Damage Evolution in Physical Scale Model Tests of a Stretch of the Breakwater of Peniche Harbour

Rute Lemos, Conceição Fortes, João Alfredo Santos, and Ana Mendonça

Abstract During physical scale model tests of rubble mound breakwaters, the assessment of the eroded volume of the armour layer subjected to incident sea waves can be determined from consecutive surveys of the surface of the armour layer after each test run. This enables one to assess the damage level of the structure by comparing erosion profiles and by the eroded volume between consecutive surveys of the tested section. The present study aimed to evaluate the damage evolution of a section of the Peniche harbour west breakwater, whose armour layer is made of tetrapods, A dimensionless damage parameter was computed, based on the eroded volume at the end of each test. The test program consisted of three test series (A, B and C) with different durations and wave conditions sequences, considering the low-water level (water depth of 0.20 m at the toe of the structure) and high-water level (0.24 m) and sea states with peak periods Tp = 1.70 s and Tp = 1.98 s and significant wave heights, H_{m0}, ranging between 0.12 m and 0.19 m. The model was built and operated according to Froude's similarity law, with a geometrical scale of 1:50. The eroded volume assessment was done by means of armour layer surveys based on the Time of Flight (ToF) methodology, using a Kinect sensor position. The surveys produced 3D surface models, at the beginning and the end of the test series, when the whole extension of the armour layer was dry and visible, and after each intermediate test, when part of the armour layer was submerged. A comparative analysis was made, based upon the damage level obtained with the three different test series (with different durations and wave conditions sequences).

Keywords Breakwater · Damage evolution · Position sensor · 3D surface model

R. Lemos (✉) · C. Fortes · A. Mendonça
LNEC—Laboratório Nacional de Engenharia Civil, Lisbon, Portugal
e-mail: rlemos@lnec.pt

J. A. Santos
ISEL—Instituto Superior de Engenharia de Lisboa, Instituto Politécnico de Lisboa, Lisbon, Portugal

CENTEC—Centre for Marine Technology and Ocean Engineering, Instituto Superior Técnico, Lisbon, Portugal

C. Chastre et al. (eds.), *Testing and Experimentation in Civil Engineering*,
RILEM Bookseries 41, https://doi.org/10.1007/978-3-031-29191-3_31

1 Introduction

To optimize the hydraulic design of rubble-mound breakwaters, physical scale model tests are often necessary and overtopping and hydraulic stability tests are the most common ones.

The assessment of the damage evolution (in stability tests) during scale model tests of rubble-mound breakwaters is traditionally made by comparing the erosion profiles, which are representative of the tested section, and by determining the eroded volume of the tested section between consecutive surveys. Armour layer damage is then characterized by parameters based either on the number of displaced armour units, as is the Nod parameter [1], or on dimensionless parameters based on the eroded area of a profile of the armour layer, such as S (Broderick and Ahrens 1982) or the eroded depth, E [2, 3].

Recently, several techniques have been developed for surveying the outer envelope of the armour layer of rubble-mound breakwaters in scale model tests. A review of these techniques can be found in Campos et al. [4]. Such techniques include photogrammetry, LIDAR and Time of Flight systems, which enable very accurate 3D surface models of the armour layer of the breakwater model to be obtained. In this context, [5] and [6] used a procedure for reconstructing submerged scenes from stereo-photos where the refraction at the air-water interface is corrected, thus allowing the surveys of the armour layer surface to be made without the need to empty the flume or tank where the tests take place. More recently, Musumeci [7], Sande et al. [8] and Lemos et al. [6] used a methodology using a position sensor which enabled to gather 3D scans of armour layers composed by cubipods and Antifer cubes.

This paper describes three scale model test series (A, B and C) whose objective was to evaluate damage evolution of a stretch of the Peniche harbour west breakwater whose armour layer is made of tetrapods.

For test series A (a long-duration test series), each wave condition was run until damage stabilization occurs, beginning with the lowest water level in an increasing intensity sequence. Test series B and C were intended to simulate damage from a sequence of individual storms with a well-defined duration. Test Series B was carried out with increasing water levels whereas test series C was carried out with decreasing water levels.

After this introductory section, the experimental facilities and the tests carried out are presented in Sect. 2. Section 3 presents the procedures for surveying the armour layer, whereas in Sect. 4, the results obtained are presented and discussed. The paper ends with the conclusions chapter.

2 Physical Model and Test Conditions

The experiments were performed at the Ports and Maritime Structures Unit (NPE) of the Hydraulics and Environment Department of the Portuguese Laboratory for

Civil Engineering (LNEC), in the COI1 wave flume, which is approximately 50 m long, with an operating width of 0.8 m and an operating water depth of 0.8 m. The flume is equipped with a piston-type wave-maker that combines both irregular wave generation and dynamic absorption of reflected waves identified with two wave gauges located in front of the wave paddle (Fig. 1).

The model was built and operated according to Froude's similarity law, with a geometrical scale of 1:50. The armour layer was made of 160 kN tetrapods laid on a slope of approximately 2:3. The prototype cross-section is presented in Fig. 2.

The bottom of the wave flume has a 26 m long smooth slope (1.6%), followed by a 4.3% slope that represented the sea bottom in front of the breakwater section (Fig. 3).

Ten resistive-type wave gauges were deployed along the wave flume. The wave gauges AW1 and AW2 measured the wave conditions near the wavemaker, while probes S1 to S5 characterized the wave propagation along the flume.

The wave parameters used to describe the test conditions are those obtained close to the wave generator.

Figure 4 illustrates an overview of the cross-section built in the flume.

Fig. 1 Overview of the irregular wave flume COI1

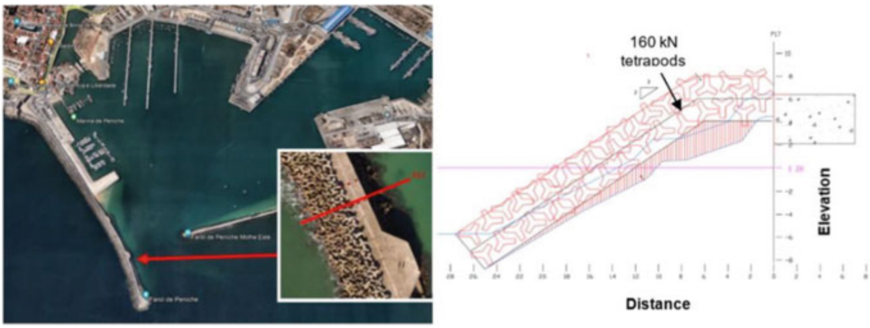

Fig. 2 Section location and characteristics

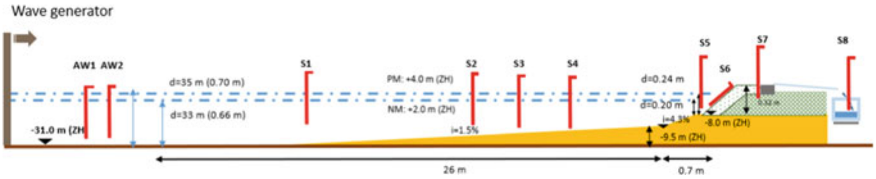

Fig. 3 Bottom and layout of the resistive wave gauges along the flume

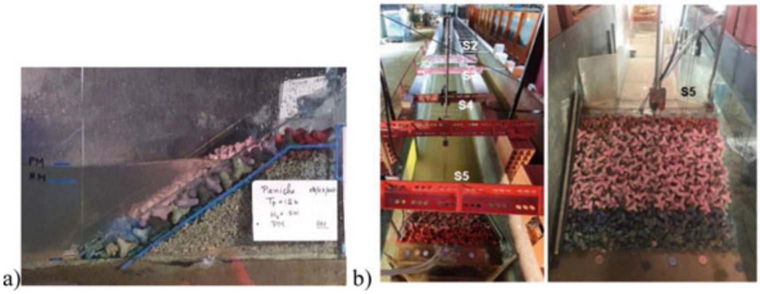

Fig. 4 Cross section of Peniche breakwater and resistive wave probes along the flume

The tests were carried out considering two sea water levels: the low-water level (LWL), with a water depth of 0.20 m at the toe of the structure and a depth of 0.66 m at the deepest part of the flume and the high-water level (HWL), with a water depth of 0.24 m at the toe of the structure and a depth of 0.70 m at the deepest part of the flume.

The wave conditions considered were peak periods of 1.70 s and 1.98 s (12 s and 14 s at prototype, respectively) and significant wave heights, of 0.12 m, 0.14 m and 0.16 m. (6.0 m, 7.0 m and 8.0 m at prototype, respectively). Table 1 summarizes the considered test conditions.

The longest test series, series A, aims to confirm the stabilization of damage of the armour layer when subjected to a sea state with constant characteristics. Thus, a given test condition, characterized by a significant wave height (H_{m0}) and peak period, (T_p) with a duration of 1000 waves, is repeated until the number of armour units displaced from their original position does not change at the end of two consecutive tests.

Then, the test series continues, using the next test condition, with increasing energy. The test sequence started with the mean water level, and then it changed to the high-water level.

Test series B and C have limited test durations. Test B was conducted with increasing water levels and peak periods and test C with decreasing water levels and peak periods.

Each test series was carried out without reconstruction of the model.

Table 1 Water levels and wave conditions for test series A, B and C

Series	Test	T_p (s)	Hm0 (m)	Depth at the toe (m)	Test duration (s)	Number of test runs	Test runs
A	1	1.70	0.12	0.13	1680	Until damage stabilization	T59–T61
	2	1.70	0.14	0.13	1680		T62–T65
	3	1.70	0.16	0.13	1680		T66–T69
	4	1.98	0.14	0.17	1980		T70–T73
	5	1.98	0.16	0.17	1980		T74–T77
	6	1.98	0.18	0.17	1980		T78–T81
B	1	1.70	0.12	0.13	1680	1	T82
	2	1.70	0.14	0.13	1680	4	T83–T86
	3	1.70	0.16	0.13	1680	4	T87–T90
	5	1.98	0.18	0.17	1980	4	T91–T94
	6	1.98	0.16	0.17	1980	4	T95–T98
C	4	1.98	0.14	0.17	1980	2	T99 and T100
	5	1.98	0.16	0.17	1980	4	T101–T104
	6	1.98	0.18	0.17	1980	4	T105–T108
	2	1.70	0.14	0.13	1680	4	T109–T112
	3	1.70	0.16	0.13	1680	4	T113–T116

3 Materials and Methods

The definition of damage in rubble mound breakwaters depends on aspects such as the typology, design, armour unit type, or the functional requirements of the structure. Damage is usually defined by the degree of reshaping of the armour layer and therefore associated to the failure mode and can be quantified by the eroded volume or number of units removed [9].

Damage characterization can be achieved by using an adequate damage descriptor, as the commonly used displacement counting method, where damage, D, can be related to any definition of movements including rocking. The relative number of moving units can also be related to the total number of units inside a vertical strip of width D_n (the nominal diameter) stretching from the bottom to the top of the armour layer. For this strip displacement definition [1] used the term Nod for units displaced out of the armour layer and Nor for rocking units. The disadvantage of Nod and Nor is the dependence of the slope (strip) length [10].

Table 2 Thresholds of S for different damage levels, for non-overtopped two-layers conventional breakwaters, according to [12] and the Rock Manual (2007) (adapted from Campos et al. [4, 9])

	Dimensionless eroded parameter (S)						
	Threshold 1		Threshold 2–3			Threshold 4	
Cot α	Damage initiation	Start of damage	Iribarren's damage	Initiation of destruction	Intermediate damage	Destruction	Failure
1.5	1.5	2	2.5	6.5	3–5	12	8
2	2	2	3	8	4–6	14	8
3	2.5	2	3.5	9.5	6–9	16	12
4	3	3	4	11	8–12	18	17

The damage descriptor used in the present work was the dimensionless damage parameter $S = \frac{A_e}{D_n^2} S = \frac{A_e}{D_n^2} S = \frac{A_e}{D_n^2}$, defined by Broderick [11] where A_e is the eroded area of the profile and D_n is the nominal diameter of the block. S can be interpreted as the number of squares with side length D_{n50} which fit into the eroded area.

The improvements and availability of accurate 3D survey techniques based on scanning instruments as LIDAR and photogrammetry techniques, as well as the development of artificial vision algorithms make it possible to combine different damage descriptors.

This was the case of the present study. As the damage parameter S is less suitable in the case of complex types of armour units like tetrapods, due to the difficulty in defining a surface profile, to minimize this uncertainty it was decided to compute the mean eroded area by using the total eroded volume of the entire armour layer.

By dividing the eroded volume (Ev) at the end of a test run by the section usable width (X, in this case 0.72 m), one obtained the section mean eroded area ($A_e = \frac{E_v}{X} A_e = \frac{E_v}{X}$) and subsequently, the dimensionless damage parameter $S = \frac{A_e}{D_n^2}$.

Table 2 summarizes the thresholds of S, for different damage levels, according to [12] and the Rock Manual (2007).

The equipment used for damage evolution assessment was the Microsoft Kinect© position sensor that was placed above the breakwater, to get a 3D model of the armour layer.

The acquisition of depth values by the Kinect© is determined by the Time of Flight (ToF) method, where the distance between the points of a surface and the sensor is measured by the time of flight of the light signal reflected by the surface. In other words, ToF imaging refers to the process of measuring the depth of a scene by quantifying the changes that an emitted light signal encounters when it bounces back from objects in a scene.

The Kinect sensor was positioned 1.5 m from the crest of the structure in a fixed structure above the flume (Fig. 5a) and its survey parameters were: Voxel (volume pixel) for meter: 256; Voxel volume resolution for the three coordinated axis x, y and z: 512 voxel. That means that the volume of each scanned scene is 2 m x 2 m x 2 m. The acquisition distance range was between 0.5 m and 8 m.

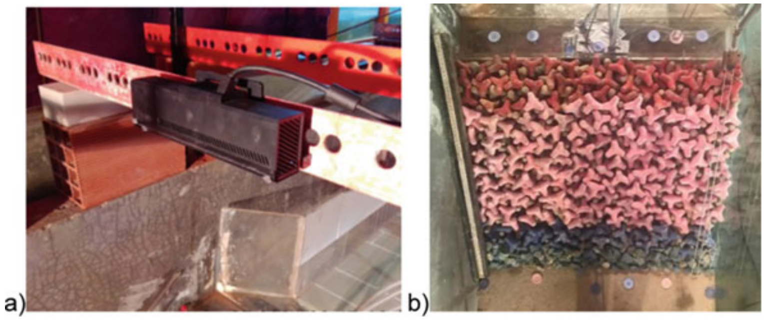

Fig. 5 **a** Position sensor Kinect. **b** Ground control points

Note that the voxel is a 3D unit of the image, just as for digital photographs, a pixel is a 2D unit of the image. It is a volume element that represents a specific grid value in 3D space.

Surveys were carried out without water in the flume, at the beginning and at the end of each test series, and with water at the end of each intermediate test.

To reference the point clouds resulting from the surveys, 12 ground control points (GCP) were used, Fig. 5b. They were materialized with coloured buttons placed at the bottom of the channel, in front of the toe of the armour layer and on the superstructure. The coordinates of these control points were obtained with a total station before the start of the test series.

The post-processing of surveys conducted with water in the flume, comprised a previous alignment of the point clouds with a cloud obtained without water in the flume, to correct the submerged part of the survey, as the infrared light from the sensor has little capacity to cross water depths greater than 0.05 m. This fine alignment was performed using the Iterative Closest Point, ICP algorithm [13] available in the open-source software CloudCompare [14].

The eroded volume computation relied on the gridding process of the cloud(s), by choosing a grid step. This step defines the size of the elementary cells used in the volume computation. To compute the volume, *CloudCompare* sums the contribution of each cell. This contribution is the volume of the elementary parallelepiped corresponding to the elementary cell area, multiplied by the distance difference between clouds ($dV = grid\ step * grid\ step * distance$).

In the present work, after several experiences with grid steps ranging from 1 to 10 mm, the best combination of point density and depth estimation was obtained with a step of 2 mm. Steps smaller than 2 mm conducted to an overestimated depth, while grid steps higher than 2 mm led to an important loss of point density.

4 Results and Discussion

From the damage characterization resulting from the survey of the armour layer of the entire breakwater usable section, it was possible to compute the overall eroded volume. Thus, an averaged eroded area was computed by dividing the eroded volume by the section width (0.72 m). Note that, as the eroded area is an average value, eroded areas in different individual profiles can differ from this value, depending on the heterogeneity of the damage location. Figure 6 shows the point cloud resulting from surveys carried out with the Kinect© sensor at the beginning and at the end of series A (before Test 59 and after Test 81, respectively), as well as the map of distances between both point clouds.

The results presented in Table 3 show the damage values (S) measured at the end of each test run, with a duration of 1000 waves, corresponding to a given wave condition tests 1 to 6, for test series A. According to Table 2, the damage level is clearly at "start of damage" with small variations with the water level and with the peak period, increasing with the significant wave height (Fig. 7).

For test series B (Fig. 8 and Table 4) the damage evolution trend was quite different from the long-duration test A. Damage increases with the water level and with the peak period. At the end of the LWL tests, the damage level denotes a start of damage but at the beginning of tests with HWL the damage level rose to "Intermediate Damage" (Fig. 9).

For test series C (Fig. 10 and Table 5) there is a "start of damage" level, showing no evolution during the test series. Damage stabilization occurred at the end of the tests with HWL, with almost no variation during tests conducted with LWL and Tp = 1.70 s (Fig. 11).

For test series C there is a "start of damage" level, showing no evolution during the test series. Damage stabilization occurred at the end of test with HWL, with almost no variation during tests conducted with LWL and Tp = 1.70 s (Fig. 10).

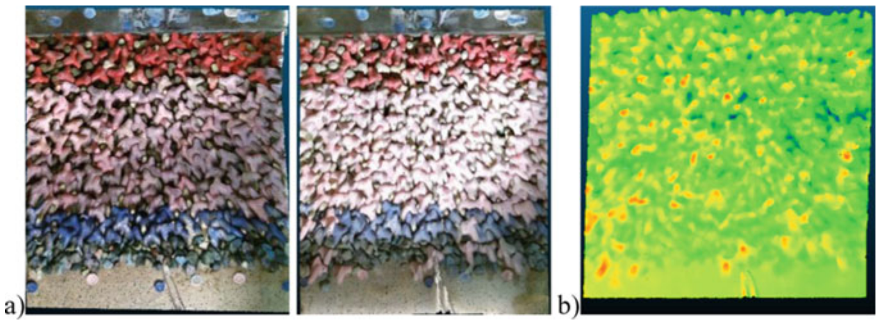

Fig. 6 Survey conducted at the beginning and at the end of test series A. **a** Clouds of points of initial and final surveys. **b** Distance map (blue: erosion; red: deposition)

Table 3 Dimensionless damage parameter obtained during test Series A

Test	Test run	Number of waves	S (Ae/Dn^2)
1	59	1000	1.40
	60	2000	1.40
	61	3000	1.50
2	62	4000	1.30
	63	5000	1.40
	64	6000	1.60
	65	7000	1.30
3	66	8000	1.30
	67	9000	1.40
	68	10,000	1.30
	69	11,000	1.30
4	70	12,000	1.40
	71	13,000	1.40
	72	14,000	1.40
	73	15,000	1.70
5	74	16,000	1.40
	75	17,000	1.40
	76	18,000	1.50
	77	19,000	1.50
6	78	20,000	1.40
	79	21,000	1.60
	80	22,000	1.90
	81	23,000	1.90

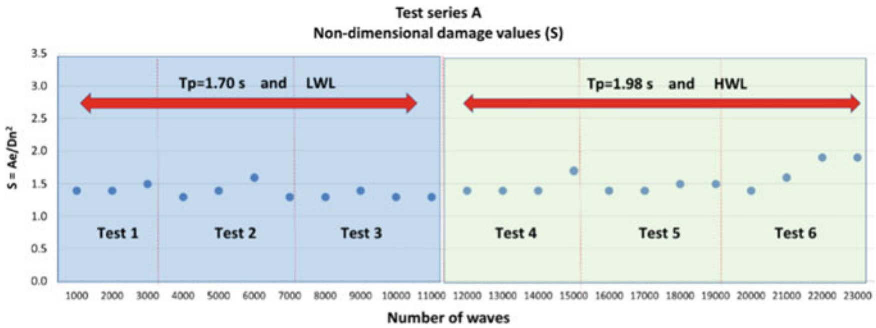

Fig. 7 Damage evolution during test series A

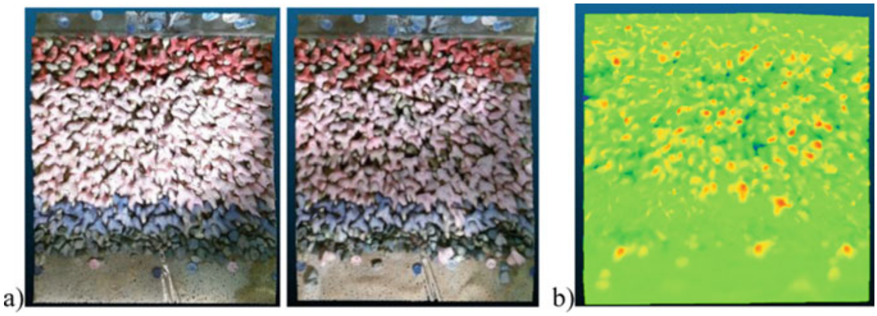

Fig. 8 Survey conducted at the beginning and at the end of test series B. **a** Clouds of points of initial and final surveys. **b** Distance map (blue: erosion; red: deposition)

Table 4 Dimensionless damage parameter obtained during test series B

Test	Test run	Number of waves	S (Ae/Dn^2)
1	82	1000	1.60
2	83	2000	1.20
	84	3000	1.40
	85	4000	1.40
	86	5000	1.20
3	87	6000	1.20
	88	7000	1.50
	89	8000	1.80
	90	9000	1.70
5	91	10,000	2.30
	92	11,000	2.90
	93	12,000	3.00
	94	13,000	2.80
6	95	14,000	3.00
	96	15,000	2.80
	97	16,000	2.90
	98	17,000	2.20

5 Conclusions

This paper described the three scale model test series (A, B and C) with different test sequences and durations, whose objective was to evaluate damage evolution of a stretch of the Peniche harbour west breakwater.

Damage measurement was made using the Kinect© position sensor, which proved to be quite effective in obtaining three-dimensional surface models of the armour

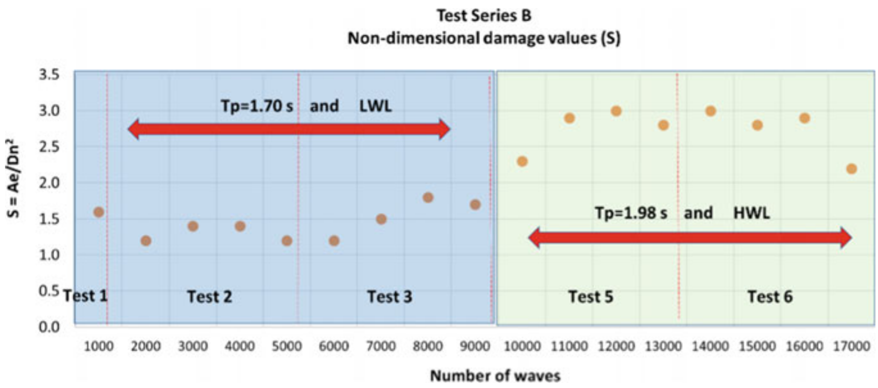

Fig. 9 Damage evolution during test series B

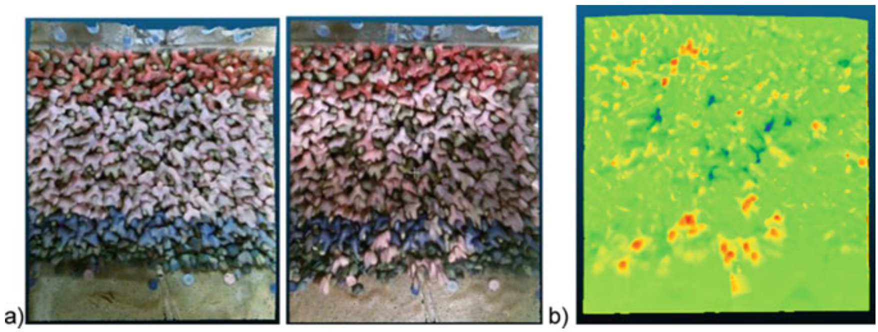

Fig. 10 Survey conducted at the beginning and at the end of test series C. **a** Clouds of points of initial and final surveys. **b** Distance map (blue: erosion; red: deposition)

layers (tetrapods) of the breakwater model. It was possible to obtain damage measurements, such as volume and eroded area. The comparison between initial and final clouds of points resulting from the model survey, enabled to compute the eroded volumes.

The damage descriptor *S* computation was based upon the eroded volume and evolved with different trends for the three-test series.

For the longest test series, series A, which aims to confirm the stabilization of damage of the armour layer when subjected to a sea state with constant characteristics, the damage level is a "start of damage" with small variations with the water level and with the peak period, increasing with the significant wave height.

Regarding test series B conducted with increasing water levels ant peak periods, damage increases with the water level and with the peak period.

Results obtained with test series C, with decreasing water levels and peak periods, showed no evolution during the test series. Damage stabilization occurred at the end of test with HWL (start of damage), with almost no variation during tests conducted with LWL and Tp = 1.70 s.

Table 5 Dimensionless damage parameter obtained during test series C

Test	Test run	Number of waves	S (Ae/Dn^2)
4	99	0	2.00
	100	1000	2.00
5	101	2000	2.00
	102	3000	2.10
	103	4000	2.00
	104	5000	1.90
6	105	6000	2.10
	106	7000	2.00
	107	8000	2.10
	108	9000	2.00
2	109	10,000	1.90
	110	11,000	1.90
	111	12,000	1.90
	112	13,000	1.90
3	113	14,000	1.90
	114	15,000	1.90
	115	16,000	2.00
	116	17,000	1.90

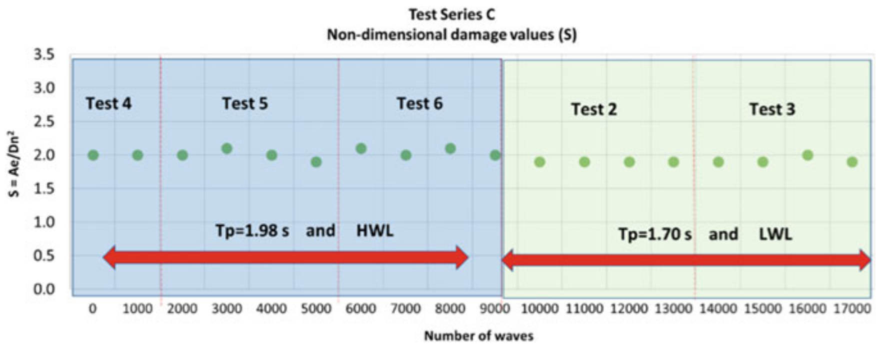

Fig. 11 Damage evolution during test series C

Test series B and C, with the same wave conditions, but with different sequences, conducted to a different damage evolution. Despite both tests conducted to a mild damage, series B proved to be the most unfavourable test sequence.

Future work will comprise tests with localized damage, with more extensive damage levels, to test a dimensionless damage parameter based upon localized eroded volume, as well as on the dimensionless eroded depth.

Acknowledgements This work was carried out within the scope of the projects: PTDC/ECI-EGC/31090/2017 BSafe4Sea and PTDC/EAM-OCE/31207/2017 To-Sealert, both funded by the Portuguese Research Foundation (FCT).

References

1. van der Meer, J.W.: Rock slopes and gravel beaches under wave attack. Ph.D. Thesis, Delft Hydraulics communication no. 396, Delft Hydraulics Laboratory, Delft, The Netherlands (1988)
2. Hofland, B., Disco, M.A.R.K., Van Gent, M.R.A.: Damage characterization of rubble mound roundheads. In: Proceedings of CoastLab2014, Varna, Bulgaria (2014)
3. Hofland, B., et al.: Measuring damage in physical model tests of rubble mounds. In: Coasts, Marine Structures and Breakwaters 2017: Realising the Potential, pp. 929–940. ICE Publishing (2018)
4. Campos, A., Castillo, C., Molina-Sanchez, R.: Damage in rubble mound breakwaters. Part II: review of the definition, parametrization and measurement of damage. J. Mar. Sci. Eng. **8**(5), 306 (2020)
5. Ferreira, R., Costeira, J.P., Santos J.A.: Stereo reconstruction of a submerged scene. In: Marques, J.S., Pérez de la Blanca, N., Pina, P. (Eds.) Pattern Recognition and Image Analysis. IbPRIA 2005. Lecture Notes in Computer Science, vol. 3522. Springer, Berlin, Heidelberg (2005)
6. Lemos, R., Santos, J.A., Fortes, C.J.: Rubble mound breakwater damage assessment through stereo photogrammetry in physical scale laboratory tests. Ribagua **4**(2), 84–98 (2017)
7. Musumeci, R.E., et al.: 3-D monitoring of rubble mound breakwater damages. Measurement **117**, 347–364 (2018)
8. Sande, J., et al.: Application of scanning techniques for damage analysis in rubble mound breakwaters. In: Proceedings of 7th International Conference on the Application of Physical Modelling in Coastal and Port Engineering and Science (Coastlab18), Santander (2018)
9. Campos, A., Castillo, C., Molina-Sanchez, R.: Damage in rubble mound breakwaters. Part I: historical review of damage models. J. Mar. Sci. Eng. **8**(5), 317 (2020)
10. Construction Industry Research and Information Association. The Rock Manual. The Use of Rock in Hydraulic Engineering, 2nd edn. CIRIA, London, UK (2007)
11. Broderick, L.: Riprap stability, a progress report. In: Coastal Structures, pp. 320–330. ASCE, Reston, VA, USA (1983)
12. Vidal, C., Losada, M.A., Medina, R., Losada, I.: Análisis de La Estabilidad de Diques Rompeolas. Diques Rompeolas **1**, 17–34 (1994)
13. Chen, Y., Medioni, G.: Object modelling by registration of multiple range images. Image Vis. Comput. **10**(3), 145–155 (1992)
14. Girardeau-Montaut, D.: Détection de changement sur des données géométriques tridimensionnelles. Diss. Télécom ParisTech (2006)

SfM Photogrammetry as a Tool to Monitor Slope Erosion and Evaluate Bio-Stabilization Treatment

Román Fernández Rodríguez and Rafaela Cardoso

Abstract Soil erosion in slopes mainly occurs due to runoff water. Biocementation may be an alternative to traditional stabilisation methods to prevent this phenomenon. In this research, enzyme induced calcium carbonate precipitation (EICP) was tested to analyse its efficiency in preventing soil erosion. To do so, two small slopes made of uniform-graded size sand were built in the laboratory and subjected to a water thread with constant flow to simulate runoff water. The first was the control test, untreated, while the second was treated by spraying with enzymes and feeding solution. The formation of ravines was monitored during and after the runoff test by using structure from Motion (SfM) photogrammetry. Image acquisition was performed with a mobile phone and a point cloud was generated to analyse the slopes surfaces and quantifying the amount of erosion on each slope. Finally, the percentage of carbonate precipitated in the enzymatically-treated slope was calculated after the end of the test.

Keywords SfM photogrammetry · Slope erosion · Laboratory test · EICP · Bio-cementation

1 Introduction

The study on the mechanisms of soil erosion is fundamental to design efficient remediation solutions. When triggered by heavy rainfall episodes, soil erosion mainly occurs due to runoff water. This type of erosion can lead to significant economic and environmental impact at the design and maintenance of earth structures such as roads and earth dams [1]. This phenomenon is aggravated in semi-arid areas, especially in non-cohesive soils [2]. Considering a climate change scenario, in which extreme

R. Fernández Rodríguez (✉) · R. Cardoso
CERIS/Instituto Superior Técnico, University of Lisbon, Lisbon, Portugal
e-mail: roman.fernandez@tecnico.ulisboa.pt

R. Cardoso
e-mail: rafaela.cardoso@tecnico.ulisboa.pt

C. Chastre et al. (eds.), *Testing and Experimentation in Civil Engineering*,
RILEM Bookseries 41, https://doi.org/10.1007/978-3-031-29191-3_32

precipitations would become more frequent, it is worth to explore new solutions to improve the resistance of soil to erosion by runoff.

The biocementation treatment can be suitable to prevent slope erosion by runoff water and its potential for this purpose is investigated in this paper. Biocementation is a relatively new technique. It consists in using biological agents (bacteria or enzymes) to produce calcium carbonate (biocement), which acts binding the grains and improving soil strength and stiffness. This is an eco-friendly soil treatment technique alternative to the use of Portland cement. [3]. Examples of the use of this technique for several purposes can be found in the literature such as improving the load bearing capacity of foundation soils [4], improving the properties of compacted earth in building applications [5] or minimising coal dust pollution in open-pit coal mines [6].

When enzymes are used to achieve the precipitation of biocement the technique is called enzymatic induced calcium carbonate precipitation (EICP). In these cases, urease enzymes (generally obtained from plants) are used. The role of the enzymes is to catalyse the hydrolysis of the urea ($CO(NH_2)_2$) present in the feeding solution supplied during the soil treatment Eq. (1). Subsequently, a precipitate of calcium carbonate ($CaCO_3$) is produced in the presence of calcium ions, also supplied in the feeding solution Eq. (2).

$$CO(NH_2)_2 + 2H_2O \rightarrow 2NH_4 + CO_3^{2-} \quad (1)$$

$$C_a^{2+} + CO_3^{2-} \rightarrow C_aCO_3 \quad (2)$$

The efficiency of EICP to prevent ravine formation in slopes is investigated in this paper, by comparing the evolution of breach formation in a treated and untreated small scale sand slopes under the action of a continuous water thread. In this way, the aim was to be able to compare the results of the erosion test when carried out on a soil in its natural state and after having been enzymatically treated.

Structure from motion (SfM) photogrammetry was adopted, using cell phone photographs taken during the erosion test, to define topographical models to monitor the evolution of the erosion channels. The accuracy of the models thus obtained was checked in previous tests using a terrestrial laser scanner (TLS) [7].

The experimental setup of the slopes and the evolution of the breach are described, as well as the conditions under which accurate results can be found when using SfM photogrammetry.

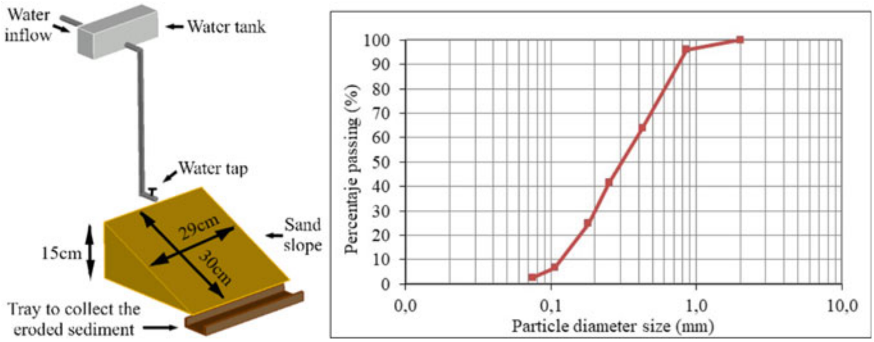

Fig. 1 Experimental setup and grading size distribution curve of the sand used

2 Materials and Methods

2.1 Materials and Experimental Setup

Two small slopes (15 cm high, 30 cm long and 29 cm wide, 27° inclination) were built in the laboratory with commercial river sand, uniform graded size with average diameter $D_{50} = 0.3$ mm (classifies as poorly graded sand SP according to the Unified Soil Classification System). The grading size distribution curve is in Fig. 1. The minerals present are only quartz and feldspars. This sand, in dry state, was carefully placed to ensure homogeneous void ratio (e) of 0.78. For this void ratio, permeability measured in a constant water head test is 2×10^{-4} m/s The first slope was the control test, untreated, while the second was treated by spraying with enzymes and feeding solution. Details are provided in the following section.

Three days after the end of their treatment, a water thread with constant flow was applied on each slope to simulate runoff water. A water tank was used to guarantee a constant flow rate of 0.12 L/min, controlled by using a tap. The outlet pipe had a diameter of 5 mm and was positioned 1 cm above the top of the slope. All components can be seen in Fig. 1.

2.2 Slopes Treatment

One of the slopes was treated by biocementation to promote the precipitation of calcium carbonate in the soil pores and analysing effectiveness of this layer in preventing water erosion. The treatment consisted in spraying first 100 ml solution of distilled water and powder urease enzyme with a concentration of 3 g/L, followed by spraying 200 ml of feeding solution. This solution was prepared using 0.5 M equimolar solutions of urea and calcium chloride (source of calcium) and 1:10 diluted growth medium [8]. This process was repeated for 5 consecutive days. The second slope was the control case, untreated and used as a reference. It was sprayed with 300 ml of water every day for 5 days, just to ensure that both slopes had the same water content before the beginning of the erosion test.

2.3 Determination of Calcium Carbonate Content

The calcium carbonate content is the relationship between the mass of calcium carbonate and the total mass of the soil. The mass of calcium carbonate is the mass loss of the soil caused by being washed with hydrochloric acid (HCl 0.5 M), all measurements were done in previously oven dried soil samples at 104 ºC for 24 h [9].

3 Experimental Results

Figure 2 shows the surface condition of the slopes after 9 min of testing. As can be seen, on the untreated slope an erosive channel developed along its entire length while on the slope treated by bio-cementation there was any erosion due to runoff water for the same test time as the reference slope.

The percentage of carbonate precipitated in the treated slope was calculated using acid dissolution (HCl 0.5 M), obtaining a value of 1.8%. This confirms that biocementation has occurred, explaining the resistance to runoff erosion observed.

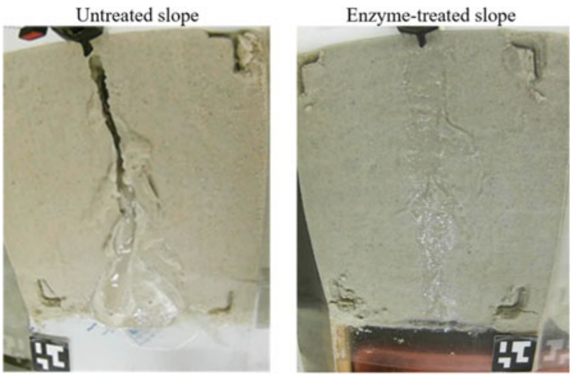

Fig. 2 State of the slopes after 9 min of testing (top view)

4 SfM Breach Monitoring

Each slope was photographed before, during and after the tests using a Huawei mobile phone with a 13 MPx camera. These images were later treated on a Structure from Motion (SfM) photogrammetry-based application, named Eyescloud3D (https://www.eyescloud3d.com) to obtain high-density point clouds. This technique is based on the acquisition of overlapping images and the use of algorithms to perform the images matching process, determining the points of union between them [10]. To obtain accurate results when using this technique some basic rules must be considered when taking the photographs, specifically: avoid casting shadows on the object, maintain the same distance between camera and object in all photos and guarantee a high percentage of overlap between the pictures.

The point clouds so obtained were later imported into Cloud Compare software (www.cloudcompare.org) to analyse the geometry and evolution of the erosion channel produced during the runoff test in each slope. Figure 3 summarises the image acquisition process using the untreated slope as example.

Figure 4 presents the evolution of the topography in a vertical cross section 2 cm distant from the tap for both slopes. Although the erosive channel reaches its maximum depth right under the tap, it was decided to select this little further area downstream to draw the topographic profiles and analyse the evolution of the erosion process because it is when the breach is wider and minimises the shadow effect. As reported in [7], when the erosion channels are deep and narrow shadows can reduce the accuracy of SfM reconstructions. With the exception of these drawbacks, in that same paper it is specified that the average error when comparing SfM and TLS reconstuctions is 0.5 mm (with an uncertainty of ±0.7 mm).

The formation of the breach and its evolution over time is perfectly visible in the untreated slope, while in the enzyme-treated slope there is almost no changes in its surface. This confirms both the efficiency of the EICP treatment against breach

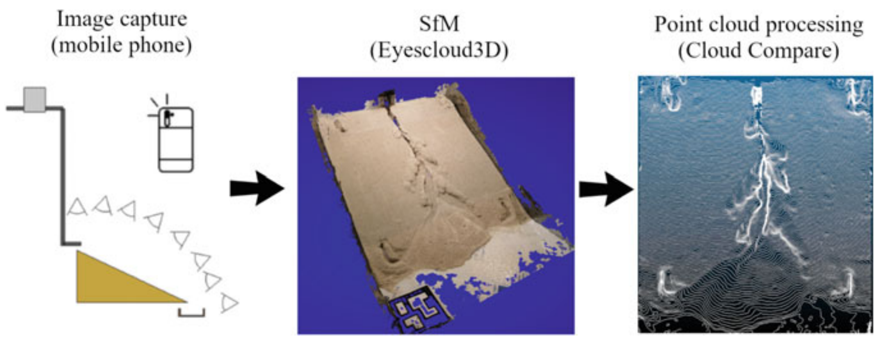

Fig. 3 Image processing

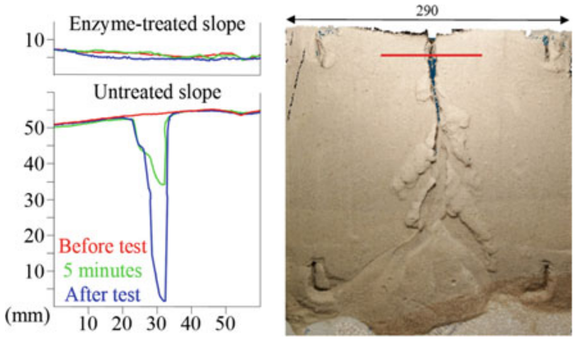

Fig. 4 Transverse profiles of the erosion channel (left) and profiles position (right). Units in mm

formation and the capability of SfM photogrammetry to monitor and compare the evolution of these erosional processes over time.

5 Conclusions

A significant improvement was obtained with the biocementation treatment even with relatively low amounts of precipitated carbonate. This proves that EICP treatment can be a good alternative to other traditional soil stabilisation methods.

Low-cost SfM photogrammetry performed with a mobile phone has a great potential to be used in the monitoring of soil treatments effectiveness to prevent erosion, although further work is needed to determine its applicability to a real scale case.

Acknowledgements The authors would like to thank the Foundation for Science and Technology (FCT, I.P.) of Portugal for funding project BIOSOIL (Ref PTDC/ECI-EGC/32590/2017).

References

1. Powledge, G.R., Ralston, D.C., Miller, P., Chen, Y.H., Clopper, P.E., Temple, D.: Mechanics of overflow erosion on embankments. ii: Hydraulic and design considerations. J. Hydraul. Eng. **115**(8), 1056–1075 (1989). https://doi.org/10.1061/(ASCE)0733-9429(1989)115:8(1056)
2. Chehlafi, A., Kchikach, A., Derradji, A., Mequedade, N.: Highway cutting slopes with high rainfall erosion in Morocco: evaluation of soil losses and erosion control using concrete arches. Eng. Geol. **260**, 105200 (2019). https://doi.org/10.1016/j.enggeo.2019.105200
3. Almajed, A., Tirkolaei, H.K., Kavazanjian, E., Hamdan, N.: Enzyme induced biocementated sand with high strength at low carbonate content. Sci. Rep. **9**, 1–8 (2019). https://doi.org/10.1038/s41598-018-38361-1
4. Van Paassen, L., Ghose, R., van der Linden, T., van der Star, W., Van Loosdrecht, M.: Quantifying biomediated ground improvement by ureolysis: large-scale biogrout experiment. J. Geotech. Geoenviron. Eng. **136**, 1721–1728 (2010)

5. Cuccurullo, A., Gallipoli, D., Bruno, A.W., Augarde, C., Hughes, P., La Borderie, C.: Earth stabilisation via carbonate precipitation by plant-derived urease for building applications. Geomech. Energy Environ. **30**, 100230 (2022). https://doi.org/10.1016/j.gete.2020.100230
6. Wu, M., Hu, X., Zhang, Q., Zhao, Y., Sun, J., Cheng, W., Fan, Y., Zhu, S., Lu, W., Song, C.: Preparation and performance evaluation of environment-friendly biological dust suppressant. J. Clean. Prod. **273**, 123162 (2020). https://doi.org/10.1016/j.jclepro.2020.123162
7. Fernández Rodríguez, R., Ponte, M., Bento, R., Cardoso, R.: Potential of mobile application based on structure from motion (SfM) photogrammetry to monitor slope fast erosion by runoff water. Catena **216**(Part A), 106359 (2022). https://doi.org/10.1016/j.catena.2022.106359
8. Centeno, D.F., Borges, I., Duarte, S.O.D., Monteiro, G.A., Cardoso, R.: Comparison of experimental techniques for biocementation of sands considering homogeneous volume distribution of precipitated calcium carbonate. In: 4th European Conference on Unsaturated Soils (E-UNSAT 2020), vol. 195, E3S Web Conf. (2020). https://doi.org/10.1051/e3sconf/202019505004
9. Choi, S.G., Park, S.S., Wu, S., Chu, J.: Methods for calcium carbonate content measurement of biocemented soils. J. Mater. Civ. Eng. **29**, 06017015 (2017). https://doi.org/10.1061/(asce)mt.1943-5533.0002064
10. Carrivick, J., Smith, M., Quincey, D.: Current applications of structure from motion in the geosciences. In: Structure from Motion in the Geosciences, pp 124–158. John Wiley & Sons Ltd (2016). https://doi.org/10.1002/9781118895818

An Open-Source 2D Digital Image Correlation Software: Case Study on the Hyperelastic Behaviour of Silicone-Based Material

João C. A D. Filho, Luiz C. S. Nunes, and José Xavier

Abstract Digital Image Correlation (DIC) is an optical-numerical method used to compute displacement and strain fields of target surfaces. This method has been widely implemented in the study of structures and to perform inspections, at several observation scales. Several software have been already proposed to carry out DIC measurements. In this study, a new integrated open-source DIC software is presented, so-called iCorrVision-2D. This DIC software includes a build-in grabber and post-processing modules that are not usually available on other open-source or commercial DIC software. The accuracy of this software is verified using an experimental dataset of silicone-based specimens subjected to uniaxial tensile test. The isotropic hyperelastic behaviour of the silicone-based specimens was investigated using the Neo-Hookean, Mooney-Rivlin, Lopez-Pamies, Ogden and Yeoh models. Results indicate that this software can be efficiently used to reconstruct the displacement and strain maps, yielding consistent mechanical properties for the hyperelastic material. This case study is important to illustrate the reliability of DIC on measuring deformations that have been used to extract relevant mechanical properties. This software can then be used consistently for other engineering applications.

Keywords Digital Image Correlation · Open-source · Python · Isotropic hyperelastic models · Silicone

J. C. A. D. Filho (✉) · L. C. S. Nunes
Laboratory of Opto-Mechanics (LOM), Department of Mechanical Engineering (PGMEC-TEM), Universidade Federal Fluminense (UFF), Rua Passo da Pátria, 156, Bloco E, Sala 210, Niterói, ZIP Code 24210-240, Rio de Janeiro, Brazil
e-mail: joaocadf@id.uff.br

J. Xavier
UNIDEMI, Department of Mechanical and Industrial Engineering, NOVA School of Science and Technology, NOVA University of Lisbon, Caparica, Portugal

C. Chastre et al. (eds.), *Testing and Experimentation in Civil Engineering*, RILEM Bookseries 41, https://doi.org/10.1007/978-3-031-29191-3_33

1 Introduction

The Digital Image Correlation (DIC) is a non-contact optical method that can be used to compute the full-field deformations of a specimen subjected to any loading condition [1]. Recently, the use of DIC is gathering great interest across several scientific areas, including civil engineering. For instance, this optical method was implemented on the study of fiber reinforced concrete beams [2] and used to characterize bifurcated cracks on bridges [3]. One of the advantages of DIC over classical counterparts is the capability of measuring displacements and strains without direct contact. Moreover, it can be used in non-destructive tests, in-situ monitoring [4] and in fracture mechanics [5, 6]. Therefore, several inspections of structures can be carried out using DIC.

Currently, a great number of DIC commercial and open-source software were developed [7]. Among the commercial solutions, we can highlight MatchID [8], VIC-2D [9] (Correlated Solutions) and ARAMIS (GOM) [10]. Open-source or open access codes have also been proposed in the past years to overcome license cost and propose specific-based algorithms and capabilities. However, most of them require a licensed platform to be executed. For instance, NCorr [11, 12] is a well-known open-source DIC software written in Matlab. On the other hand, although there are some solutions that were developed in Python, for example py2DIC [7], there are no open-source projects with integrated grabber and post-processing modules. Inevitably, users are restricted to use proprietary software for image acquisition and for visualization. It is clear that there is a gap within open-source DIC solutions regarding the development of an integrated system. Moreover, some commercial and open-source software can be black boxes with respect to DIC settings. Some important parameters, such as sub-pixel interpolation factor, are not available for direct modifications using the graphical user interface (GUI).

The main purpose of this work is to present a new complete open-source DIC software written in Python computational language, so-called iCorrVision [13, 14], in particular its DIC-2D version (iCorrVision-2D). For validation purposes, an experimental uniaxial tensile test was performed using specimens made of silicone rubber-like material. The mechanical behaviour of the silicone is investigated by means of the DIC measurements. The algorithm is tested for the reconstruction of homogeneous full-field displacements and strains of the specimens subjected to an uniaxial loading condition. The objective is to investigate the accuracy of the method on extracting the non-linear hyperelastic mechanical response of the material.

2 DIC Overview

There are already a great number of open- and closed-source DIC solutions available in the literature and market. Over the past decades, the DIC systems (hardware and software) were gradually improved to functional solutions. Among the commercial software, the closed-source algorithms developed by Correlated Solutions [9], GOM [10], MatchID [8], LaVision [15], EikoSim [16], Dantec Dynamics [17], CorreliSTC [18] and Imetrum [19] can be highlighted. On the other hand, to overcome license limitations and the closed access to the base algorithm, some academic-based open-source codes have been recently formulated, such as Digital Image Correlation Engine (DICe) [20], NCorr [11, 12], py2DIC [7], YaDICs [21], μDIC [22, 23], RealPi2dDIC [24], ADIC2D [25], ADIC3D [26], UFreckles [27] and GPUCorrel [28]. Figure 1 gives an overview of the number of publications in Scopus database and the year of the first published work of each DIC software. The predefined searching keywords were set using digital image correlation (DIC) and the given name of each DIC software. As can be seen, the GOM Correlate software [10] is the most cited commercial software within all considered DIC solutions, followed by VIC [9] and MatchID [8]. Among the open-source software, NCorr has received great attention from the scientific community since its first publication [11, 12]. Moreover, Fig. 2 depicts the percentage of publications of each open-source or free access DIC software. As it can be concluded, NCorr and DICe were the most used software among all available solutions. Both software have an intuitive graphical user interface (GUI) that can be used for visualization.

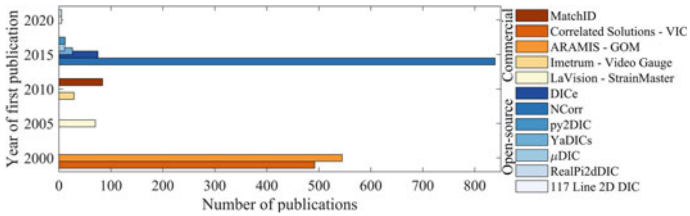

Fig. 1 Amount of publications in Scopus for different DIC software

Fig. 2 Percentage of publications in Scopus for different open-source or free access DIC software

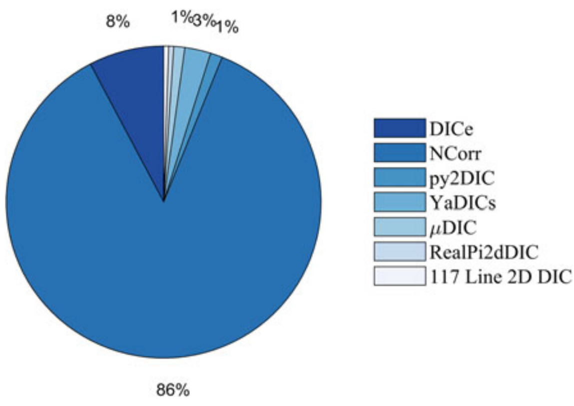

3 iCorrVision-2D

Figure 3 illustrates the user graphical interface of the iCorrVision-2D correlation module that was written in Python computation language. It should be mentioned that the use of Python is justified by the large open-source scientific computing, image processing and visualization libraries, such as Numpy, Matplotlib, OpenCV and SciPy. This free, dynamic and object-oriented language is often used in literature to develop several open-source projects [7]. The iCorrVision-2D software includes the image acquisition (iCorrVision-2D Gabber) and post-processing (iCorrVision-2D Post-processing) modules that can be used to capture the images of specimens being tested and for visualization, respectively. As can be seen, the user can control a great number of correlation parameters, such as the reference subset size (RSS), search subset size (SSS), subset step (ST), interpolation strategy, filtering options, correlation function and correlation criterion. It should be remembered that some of these DIC settings are not available for modifications regarding both commercial and open-source projects. Therefore, it is easy to customize the correlation according to the test using the GUI without the necessity of modifying the base algorithm. However, care must be taken when selecting these parameters. Usually, a parametric analysis is recommended before carrying out the correlation.

DIC is a powerful subset-based optical method that can be used to extract full-field measurements. This optical method does not require fiscal contact with the samples and can be used in both destructive and non-destructive tests. For in-plane measurements, a high-resolution camera coupled with macro zoom lens is required to capture instantaneous image sets of the specimens at the beginning and during the test. In order to perform the template matching between the captured images, the plane surface of the specimens must be coated with a random speckle pattern. The image correlation is performed using DIC algorithms by means of correlation functions. For further information, see reference [1].

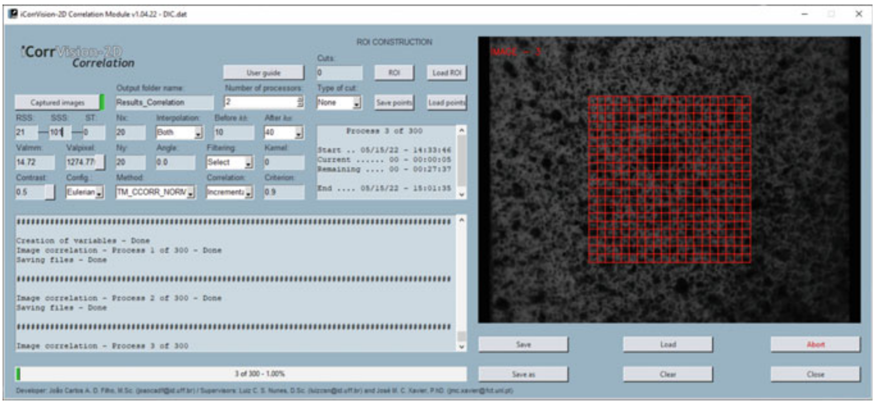

Fig. 3 iCorrVision-2D correlation module

4 Materials and Methods

4.1 Specimen and Experimental Set-Up

Four tensile specimens were manufactured from a RTV-2 silicone rubber (polydimethylsiloxane—model 4-150 RTV from Moldflex®, São Paulo—Brazil). The mixture of the liquid rubber-like material with catalyst was performed using a mass ratio of 100:3, following the manufacturer recommendations. A flat sheet of silicone with 200 × 150 × 3 mm^3 of dimension was fabricated and the material was cropped using a sharp blade into test pieces with 150 × 15 × 3 mm^3 of dimension. It should be highlighted that the dimensions were in accordance with the Saint–Venant principle to ensure a uniform stress field at the middle portion of specimens. Figure 4a schematically illustrates the silicone-based tensile specimens.

The uniaxial tensile tests were conducted at room temperature of 25 ºC under quasi-static loading condition, with a cross-head velocity of 8 mm/min. Figure 4c shows the experimental set-up used in this work where a 50 kgf (≈500 N) load cell was used to measure the applied load. The mechanical test was coupled with an optical system consisting of a high-resolution Basler Ace camera (A1300 − 200 um) camera mounted on a 1/2” 13–130 mm MLH-10X Close-up Manual Zoom lens. The optical axis of the camera-lens system was carefully aligned to be perpendicular to the specimen surface. Therefore, the sensor was positioned parallel to the flat ROI, defining a direct conversion factor between the image plane (in pixels) and object plane (in millimeters). Moreover, in order to mitigate the effect of lens distortion, the region of interest (ROI) was focused at the center of the field of view (FOV). To guarantee the matching between images, the surface of the specimens was coated with a random speckle pattern produced by an overspray of black paint, as illustrated in Fig. 4b. Light sources were used to enhance the quality of the captured images. Table 1 shows the DIC setting used to configure the iCorrVision-2D software.

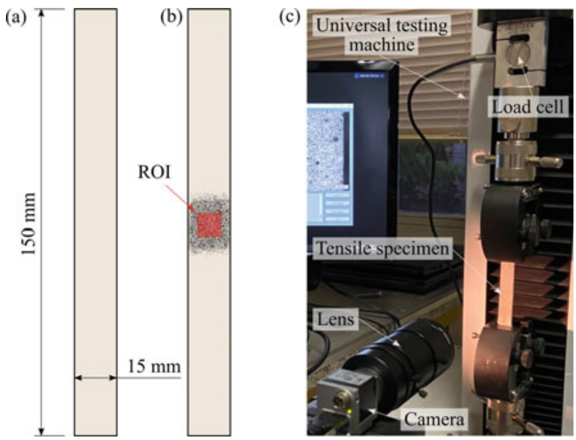

Fig. 4 **a** Schematic representation of the tensile specimen, **b** depicted region of interest (ROI) with 6 × 6 mm^2 and **b** adopted experimental arrangement

Table 1 iCorrVision-2D DIC settings for tensile tests

Correlation parameters	Value
Reference subset size (RSS)	21
Target subset size (SSS)	101
Mean calibration factor (pixels/mm)	1274.77/14.72
Steps	20/20
Image interpolation and sub-pixel level (bicubic spline)	10×/40×
Correlation criterion	0.9
Correlation criterion and configuration	Incremental/Eulerian
Correlation function	TM_CCORR_NORMED

4.2 *Isotropic Hyperelastic Models*

The strain energy function (W) of a hyperelastic material can be written as function of the deformation gradient tensor $\mathbf{F}$ [29], given by

$$\mathbf{F} = \frac{\partial \mathbf{x}}{\partial \mathbf{X}} = \frac{\partial \mathbf{u}}{\partial \mathbf{X}} + \mathbf{I} \text{ with } \mathbf{u} = \mathbf{x} - \mathbf{X}, \tag{1}$$

where $\mathbf{x}$ and $\mathbf{X}$ are the current (deformed) and reference (undeformed) configurations, respectively, $\mathbf{u}$ is the displacement vector that can be extracted from DIC measurements and $\mathbf{I}$ is the identity matrix. For isotropic materials, W is dependent on the first three strain tensor invariants [29]

$$I_1 = \lambda_1^2 + \lambda_2^2 + \lambda_3^2,\ I_2 = \lambda_1^2\lambda_2^2 + \lambda_2^2\lambda_3^2 + \lambda_3^2\lambda_1^2 \text{ and } I_3 = \lambda_1^2\lambda_2^2\lambda_3^2, \tag{2}$$

where λ_i are the principal stretches with $i = 1, 2, 3$.

Table 2 shows the main isotropic hyperelastic strain energy functions available in literature, such as the Neo-Hookean [30], Mooney-Rivlin [30], Lopez-Pamies [31], Ogden [30] and Yeoh [32] models. It is known that the rubber-like material used in this work exhibits a hyperelastic behaviour. The parameters C_i (with $i = 10, 20,$ 30 and 01), μ_i (with $i = r$ and p) and α_i (with $i = r$ and p) can be represented by non-negative material constants that can be estimated using inverse optimization algorithms, such as Levenberg–Marquardt. From W and $\mathbf{F}$, the Cauchy stress tensor (true stress) can be encountered as follows [29]

$$\boldsymbol{\sigma} = (\det \mathbf{F})^{-1}\mathbf{F}\left(\frac{\partial W}{\partial \mathbf{F}}\right)^T. \tag{3}$$

From Eqs. (1), (2) and (3) and the strain energy functions given in Table 2, the true stress tensor can be found in terms of the principal stretches.

Table 2 Hyperelastic constitutive models for isotropic materials

Material model	Strain energy function (W)	
Neo-Hookean [30]	$W_{NH} = C_{10}(I_1 - 3)$	(4)
Mooney-Rivlin [30]	$W_{MR} = C_{10}(I_1 - 3) + C_{01}(I_2 - 3)$	(5)
Lopez-Pamies [31]	$W_{LP} = \sum_{r=1}^{M} \frac{3^{1-\alpha_r}}{2\alpha_r}\mu_r\left(I_1^{\alpha_r} - 3^{\alpha_r}\right)$	(6)
Ogden [30]	$W_O = \sum_{p=1}^{n} \frac{\mu_p}{\alpha_p}\left(\lambda_1^{\alpha_p} + \lambda_2^{\alpha_p} + \lambda_3^{\alpha_p} - 3\right)$	(7)
Yeoh [32]	$W_Y = \sum_{n=1}^{3} C_{n0}(I_1 - 3)^n$	(8)

5 Results and Discussion

The experimental dataset was extracted from the uniaxial tensile test performed in this work (see Sect. 4.1). The potentialities of iCorrVision-2D software in reconstructing the full-field displacements and the mechanical behaviour of a rubber-like material can be investigated using this proposed case study. The captured images of the tensile tests were used as input of the iCorrVision-2D software with the DIC settings summarized in Table 1. For illustrative purposes, Fig. 5a, b show the computed full-field u_1- and u_2-displacements (x_1- and x_2-directions), respectively, extracted in the last image, prior to the complete failure. The iCorrVision-2D Post-processing module was used to generate figures for visualization. As can be seen, the reconstructed displacements are homogenous, as expected, and since the uniaxial tensile test was performed in x_1-direction, the u_1-displacement is higher than u_2-displacement.

Figure 6a illustrates the mean measured force and the standard deviations as function of the cross-head displacement of the universal testing machine. A good

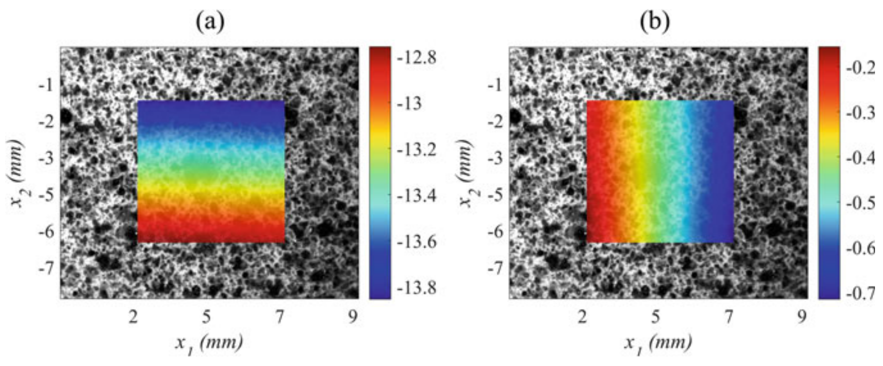

Fig. 5 **a** u_1- and **b** u_2-displacements (x_1- and x_2-directions) extracted from DIC measurements using iCorrVision-2D

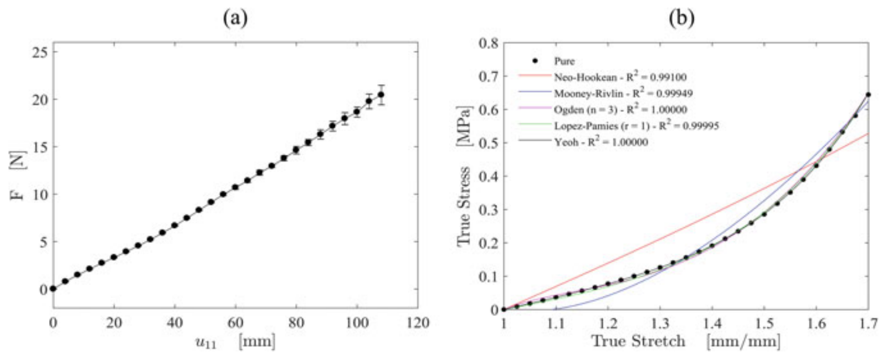

Fig. 6 **a** Applied force (N) as a function of the cross-head displacement of the universal testing machine and **b** true stress as function of true stretch obtained by DIC

repeatability of results can be observed. In fact, a small dispersion of results is expected for homogeneous isotropic materials, such as the rubber used in this work. The true stress oriented in x_1-direction can be encountered by means of the measured force as follows

$$\sigma_{11} = \lambda_1 \frac{F}{A_o} \text{ with } \lambda_1 = \frac{l_f}{l_o}, \tag{9}$$

where A_o is the initial cross-sectional area, defined by the initial width times the initial thickness of the tensile test pieces, l_f is the deformed length and l_o is the initial length in x_1-direction that were obtained by means of DIC measurements.

From the computed stress and stretch, the material parameters can be estimated by means of the Levenberg–Marquardt algorithm using the isotropic hyperelastic constitutive equations (see Sect. 4.2). Figure 6b shows the mean Cauchy stress as function of the true stretch of the tensile silicone-based specimens and the reconstruction of the hyperelastic mechanical response using the models shown in Table 2. The R^2 statistical factor was used to evaluate the degree of reconstruction of the constitutive curves. Such factor can be determined by

$$R^2 = 1 - \frac{SS_{res}}{SS_{tot}} \text{ with } SS_{res} = \sum_i (y_i - f_i)^2,$$
$$SS_{tot} = \sum_i (y_i - \overline{y})^2 \text{ and } \overline{y} = \frac{1}{n}\sum_{i=1}^{n} y_i, \tag{10}$$

where n is the size of the dataset, y_i is the measured values and f_i is the predicted values.

As can be seen from Fig. 6b, it is clear that the Neo-Hookean and Mooney models cannot describe the mechanical response of the rubber-like material used in this work. On the other hand, the Ogden, Lopez-Pamies and Yeoh models can be employed

Table 3 Adjusted coefficients of the Yeoh model

C_{10} [MPa]	C_{20} [MPa]	C_{30} [MPa]
0.0599	0.0129	0.0155

and the statistical factor R^2 of the reconstructions using Ogden and Yeoh models was exactly 1, which means that an exact match was found. From Fig. 6b, it can be observed that the Yeoh model is able to describe with satisfactory accuracy the mechanical response of the silicone material. Table 3 shows the adjusted coefficients for the Yeoh model.

6 Conclusions

In this work, a new open-source DIC software, so-called iCorrVision-2D, is presented. The accuracy of the algorithm was verified for a case study consisting in the reconstruction and identification of the mechanical behaviour of an isotropic hyperelastic material. Uniaxial tensile tests were performed using silicone-based specimens. Five different models commonly used in literature were employed to describe the mechanical behaviour of the silicone. Results indicated that the Yeoh model is the most appropriate model to be employed for such material, giving a coefficient of determination R^2 equal to 1. Additionally, the iCorrVision-2D software demonstrated to be a robust DIC solution to extract deformations with satisfactory accuracy and spatial resolution from the measured full-field displacements. The proposed iCorrVision-2D software plays an important role in open-source DIC solutions due to the capability of maintaining the entire DIC chain from image acquisition to the post-processing of results under the same integrated system. Therefore, third party software are not required for iCorrVision-2D users. Besides, the proposed software was implemented in Python computational language to remove its dependence on licensed platforms (e.g., Matlab). It should be emphasized that iCorrVision-2D stands out over other open- and closed-source DIC software due to its great number of functionalities and DIC parameters that can be accessed and modified by the end user. The proposed iCorrVision-2D software, along with documentation and manual, can be found on the GitHub repository as follows: https://github.com/jcadf/iCorrVision_2D. This software can be used and tested in several engineering applications. Moreover, new modules and functionalities can be developed in future releases to increase the range of applicability of the given software.

Acknowledgements The authors would like to acknowledge Fundação para a Ciência e Tecnologia (FCT-MCTES) throughout the project PTDC/EMD-EMD/1230/2021 (AneurysmTool) and UIDB/00667/2020 (UNIDEMI), and the support provided by the Brazilian Government funding agencies FAPERJ and CNPq. Moreover, this work was financed in part by the Coordenação de Aperfeiçoamento de Pessoal de Nível Superior (CAPES)—Finance Code 001.

References

1. Pan, B., Qian, K., Xie, H., Asundi, A.: Two-dimensional Digital Image Correlation for in-plane displacement and strain measurement: a review. Meas. Sci. Technol. **20**(6), 062001 (2009)
2. Funari, M.F., Verre, S.: The effectiveness of the DIC as a measurement system in SRG shear strengthened reinforced concrete beams. Crystals **11**(3), 265 (2021)
3. Al-Salih, H., Juno, M., Collins, W., Bennett, C., Li, J.: Application of a Digital Image Correlation bridge inspection methodology on geometrically complex bifurcated distortion-induced fatigue cracking. Fatigue Fract. Eng. Mater. Struct. **44**(11), 3186–3201 (2021)
4. Cunha, F., Santos, T., Xavier, J.: In situ monitoring of additive manufacturing using Digital Image Correlation: a review. Materials **14**(6), 1511 (2021)
5. Filho, J., Xavier, J., Nunes, L.: An alternative Digital Image Correlation-based experimental approach to estimate fracture parameters in fibrous soft materials. Materials **15**(7), 2413 (2022)
6. Nunes, L.C.S., Reis, J.M.L.: Experimental investigation of mixed-mode-I/II fracture in polymer mortars using Digital Image Correlation method. Lat. Am. J. Solids Struct. **11**, 330–343 (2014)
7. Belloni, V., Ravanelli, R., Nascetti, A., Di Rita, M., Mattei, D., Crespi, M.: py2DIC: a new free and open source software for displacement and strain measurements in the field of experimental mechanics. Sensors. **19**(18), 3832 (2019)
8. MatchID Homepage. https://www.matchid.eu/. Accessed 16 May 2022
9. Correlated solutions-VIC-2D and VIC-3D Homepage. https://www.correlatedsolutions.com/. Accessed 16 May 2022
10. Aramis-GOM Correlate Homepage. https://www.gom.com/. Accessed 16 May 2022
11. Blaber, J., Adair, B., Antoniou, A.: Ncorr: open-source 2d Digital Image Correlation matlab software. Exp. Mech. **55**(6), 1105–1122 (2015)
12. Ncorr Homepage. https://www.ncorr.com/. Accessed 16 May 2022
13. Filho, J.C.A.D., Nunes, L.C.S., Xavier, J.: iCorrVision-2D: an integrated python-based open-source Digital Image Correlation software for in-plane measurements (Part 1). SoftwareX **19**, 101131 (2022)
14. Filho, J.C.A.D., Nunes, L.C.S., Xavier, J.: iCorrVision-3D: An Integrated Python-based Open-source Digital Image Correlation Software for In-plane and Out-of-plane Measurements (Part 2). SoftwareX **19**, 101132 (2022)
15. Lavision–StrainMaster Homepage. https://www.lavision.de/en/products/strainmaster/index.php. Accessed 16 May 2022
16. EikoSim Homepage. https://eikosim.com/en/use-cases/digital-image-correlation-lattice-structures/. Accessed 16 May 2022
17. Dantec Dynamics Homepage. https://www.dantecdynamics.com/. Accessed 16 May 2022
18. CorreliSTC Homepage. https://www.correli-stc.com/. Accessed 16 May 2022
19. Imetrum Homepage. https://www.imetrum.com/products/digital-image-correlation/. Accessed 16 May 2022
20. Turner, D., Crozier, P., Reu, P.: Digital image correlation engine (DICe). Sandia National Laboratory. Albuquerque, NM, USA (2015)
21. Yet another Digital Image Correlation software (YaDICs) Homepage. http://yadics.univ-lille1.fr/. Accessed 16 May 2022
22. Olufsen, S.N., Andersen, M.E., Fagerholt, E.: μDIC: an open-source toolkit for digital image correlation. SoftwareX **11**, 100391 (2020)
23. Solav, D., Moerman, K.M., Jaeger, A.M., Genovese, K., Herr, H.M.: MultiDIC: an open-source toolbox for multi-view 3D digital image correlation. IEEE Access **6**, 30520–30535 (2018)
24. Das, P.P., Elenchezhian, M.R.P., Vadlamudi, V., Reifsnider, K., Raihan, R.: RealPi2dDIC: a low-cost and open-source approach to in situ 2D digital image correlation (DIC) applications. SoftwareX **13**, 100645 (2021)
25. Atkinson, D., Becker, T.: A 117 line 2D digital image correlation code written in MATLAB. Remote Sens. **12**(18) (2020)
26. Atkinson, D., Becker, T.: Stereo digital image correlation in matlab. Appl. Sci. **11**(11) (2021)

27. Julien, R.: Ufreckles v 2.0. Zenodo (2018)
28. Couty, V., Witz, J.F., Lecomte-Grosbras, P., Berthe, J., Deletombe, E., Brieu, M.: GPUCorrel: a GPU accelerated Digital Image Correlation software written in Python. SoftwareX. **16**, 100815 (2021)
29. Spencer, A.: Theory of invariants. Continu. Phys. **1**, 239–353 (1971)
30. Kim, B., Lee, S.B., Lee, J.: A comparison among Neo-Hookean model, Mooney-Rivlin model, and Ogden model for chloroprene rubber. Int. J. Precis. Eng. Manuf. **13**, 759–764 (2012)
31. Lopez-Pamies, O.: A new I1-based hyperelastic model for rubber elastic materials. Comput. Rendus Mec. **338**, 3–11 (2010)
32. Yeoh, O.H.: Some forms of the strain energy function for rubber. Rubber Chem. Technol. **66**, 754–771 (1993)

Point Fixed Tempered Laminated Glass Panels Subjected to Wind Load: Data Acquisition Through Electrical Strain Gauges/Displacement Transducers Versus Digital Image Correlation

Afonso Mesquita, Eliana Inca, Cláudio Martins, and Sandra Jordão

Abstract In the context of the tempered laminated glass panels submitted to the wind's action effect, such panels are commonly used in the construction of buildings' facades, taking into account their notable resistance to mechanical actions while maintaining the characteristic of luminosity requested by the architectural options. This work approaches the characterisation of the structural behaviour of laminated glass panels punctually supported by bolts fixed on glass surface with structural adhesive. Each panel, fixed by means of 4 stainless steel articulated connectors, includes an EVASAFE® or PVB interlayer between the two foils of the laminated structural glass, being subjected to air pressure applied through the laboratory's pressurised air system and controlled by means of a valve. The pressure value is obtained using a mechanically calibrated sensor connected to a specific software through a compatible datalogger. The data collected by the strain gauges/displacement transducers are compared with those provided by digital image correlation (DIC) equipment. The maximum stress is also calculated at the central point on each panel. The technology of instrumentation and data acquisition using digital image correlation presents advantages in terms of efficiency and reduction of error in experimental tests as long as the optical reliability is ensured, making it advantageous in the case of structural glass compared to the traditional methods for data acquisition. Four measurement points are displayed for the desired comparison. A good result between both technologies were obtained for displacements and strains on the critical points in that panels.

Keywords Structural tempered laminated glass panels · Wind load · Strain gauge/displacement transducer · Digital image correlation

A. Mesquita (✉) · E. Inca · C. Martins · S. Jordão
ISISE, Civil Engineering Department, FCT, University of Coimbra, Coimbra, Portugal
e-mail: acbdm@uc.pt

C. Chastre et al. (eds.), *Testing and Experimentation in Civil Engineering*,
RILEM Bookseries 41, https://doi.org/10.1007/978-3-031-29191-3_34

1 Introduction and Research Considerations

The experimental campaign that is underway within the scope of the GF Seismic Project [1], in course at the Civil Engineering Department of the University of Coimbra, encompassed the study of tempered laminated glass panels with EVASAFE®, PVB and SENTRYGLAS® interlayer films, including different types of fixing bolts.

The correspondent first phase has addressed the problem of the structural behaviour of each panel, individually analysed, when subjected to a distributed load perpendicularly applied to the plane of the glass, such as that corresponds to the wind action [1, 2]. The inherent second phase encompasses the testing of a sector of a full-scale facade with 9 panels and the study of the respective structural behaviour under the effect of the seismic action, imposed by a reference building, previously analysed according to the guidelines of the EC8.

Taking advantage of the enormous potential that the new digital image correlation (DIC) systems present nowadays, a comparison was made in the strains and displacements data recorded between that type of system and the more traditional data acquisition system. As in any applied research activity with laboratory tests, there is the need to obtain reliable records of the physical quantities to be measured. Effectively, the dataloggers equipments (that has been in use for decades, with successive upgraded versions) allows the recording of data based on electrical resistance extensometry (for strains) and linear variable differential transducers (for displacements). As a matter of fact, the DIC corresponds to a non-contact technology that is independent of the material under analyse or the length-scale in cause, and that can be used in a wide variety of applications to investigate and characterise the deformation of solids, the glass panels in this particular case.

In the first phase of the mentioned project, the threaded shanks of the respective stainless steel connectors were bolted to plates included in the layout system built for the idealised tests initial phase of the project, as reproduced in Fig. 1. To carry out each test, that layout requires the placement of the glass panel on the 4 supports, materialised by the articulated head bolts, which are supported on the plates of the corresponding beams (HEA) that are connected to the transversal beams (HEA) bolted to the support columns (HEB) of the whole frame.

The stainless steel connectors bonded to the surface of the outer face of the glass panel, related to the analysed tests in the present work, correspond to one of the three options produced by the Fitechnic® system [3], marketed by Pentagonal Lda company [4], in what concerns to the possibilities of point fixed laminated glass panels (PFLGP). The tempered laminated glass panels were fabricated with lateral dimensions of 1490 mm $\times$ 1490 mm and a nominal thickness equal to 10 mm + 1,52 mm + 6 mm, corresponding to the external foil, interlayer and internal foil, respectively. Geometrically, a width of 10 mm and a depth of approximately 17 mm (almost that thickness) characterise the mentioned joints on the panel's perimeter.

Thus, for each tested panel and according to Fig. 1, the experimental correspondent procedure has involved the following steps:

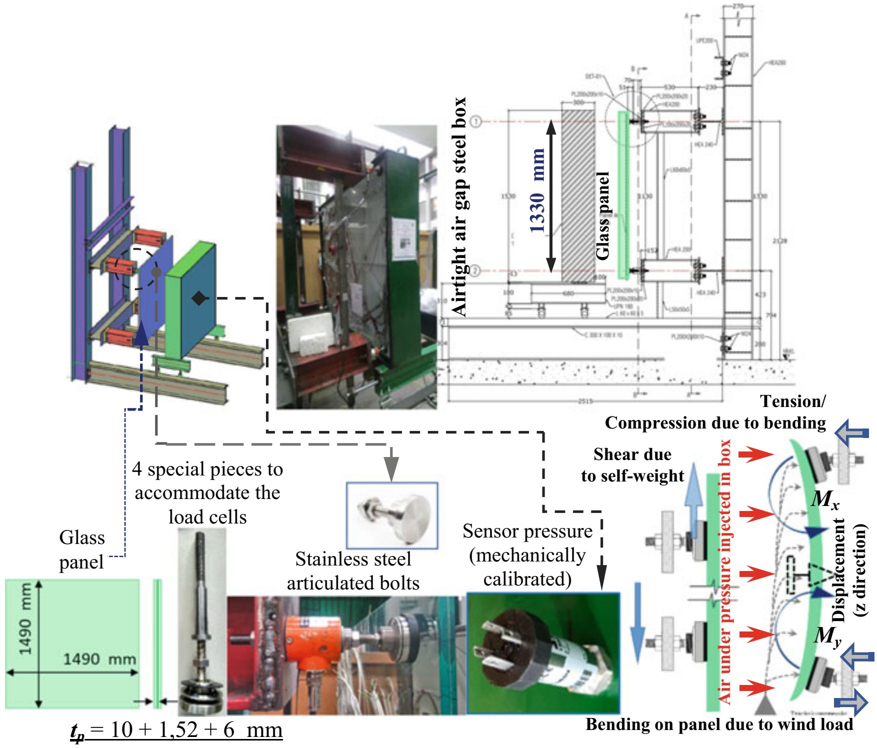

Fig. 1 Layout of part B of the 1st phase of GF Seismic Project: reaction frame, steel box and glass panel test element; internal forces of bi-axial bending due to orthogonal load (air pressure)

i. the application of the structural adhesive (Sika® [5]) on the heads of the four stainless steel bolts, which axis is located at 80 mm from each corner of panel, according to the fabricators' recommendations (Fitechnic® [3] for stainless steel bolts—AISI 316 and Vidromax [6] for the glass panels);
ii. the instrumentation positioning on the inner face of the panel with 29 electrical strain gauges, which results points are not discuss in the presented analysis;
iii. the closure of the steel box and the application of a silicone sealant (Sika® [7]) around the entire perimeter of the correspondent joints between that box and the glass panel, in order to provide an airtight air gap;
iv. the instrumentation positioning on the outer face of the test piece, regarding to the thickest foil of the panel, equally instrumented with electrical strain gauges (28 in the previous tests of the first laboratorial campaign, but reduced to 15 in the last three tests considered in this work, T26/27/28, following [8, 9]), as presented in Fig. 2. This reduction was due to the DIC optical restrictions concerning the brightness and the quality of the image capture in the usable area of the panel for the records.

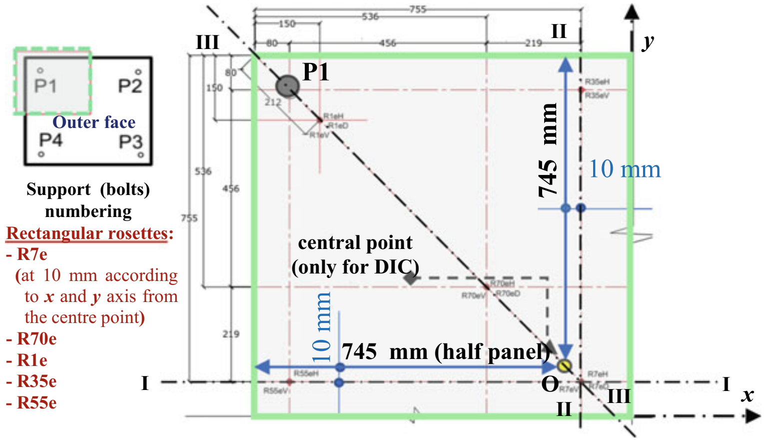

Fig. 2 Instrumentation of glass panels (outer face)—identification of the centre point (O)

It must be said that the referred outer face of the general glass panel positioned in the air steel box would correspond to the internal face of the panel if it were framed in the context of a real building, once the bolts are always positioned towards the inside of the panes.

In the cases under analysis on the selected area for comparison with results between TML/HBM datalogger and DIC, the electrical strain gauge includes rectangular rosettes, being arranged along the axes I-I, II-II and III-III (Fig. 2), where the 2 diagonals are aligned with the centres of each of the diametrically opposed bolt pairs.

The rosette nº 7, identified in Fig. 2, was positioned at the point of intersection of the I-I and II-II axes, which are 10 mm away from the true geometric centre of the panel, as concretised on the internal face of the panel. Although the point for recording the strains is not correspondent with the geometrical centre, it was the best approximation for practical implementation for the correspondent comparison with the DIC records.

In order to record the orthogonal displacements of the critical points of glass panels during the phase of the load (air pressure) increase, were selected transducers (LVDTs—TML®, Fig. 3). For this purpose, the points for the positioning of the various measurement sensors were previously identified using simple numerical models, selecting those that showed the highest values of the referred kinematic parameters. Regarding the outer face of the panel, a plastic strap connected to a wire transducer was used near its centre point for measuring the correspondent orthogonal displacement (LVDT 1—point A), whose identification follows the scheme presented in Fig. 3, exploring the free space near the rosette nº 7e. This same figure also includes the identification and arrangement of the guidelines for the experimental records and graphical interpretation within the panel's geometry.

A total of 4 wire transducers were positioned in order to be able to record, on the basis of that type of sensor, the value of the orthogonal displacement at selected points

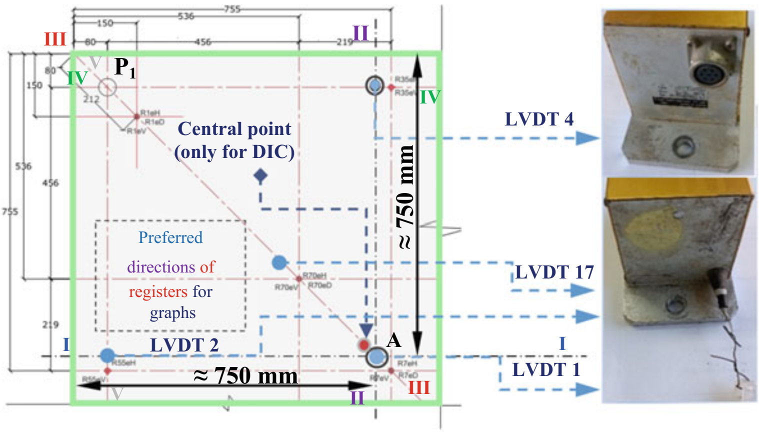

Fig. 3 Instrumentation of the glass panels outer face with displacement transducers (wire LVDTs): Selected area for comparison with results between TML®/HBM® and DIC system

on the outer face of the panels. However, a practical difficulty for the comparison at the same point between two different data collection systems resides in the fact that it is not optically feasible to measure through the DIC system the displacement or the strain in a given point if it has some other object fixed therein belonging to another displacement or strain value collection system. By analogy with the previous tests, 3 LVDTs were also placed at the rear face of the air steel box, in order to evaluate its movement, although restricted by 4 threaded rods to the HEA beams of the resistant frame of the layout illustrated in Fig. 1. In Fig. 3 is shown the arrangement of the wire transducers on the outer face of the panels and their recording lines, with 3 possibilities (vertical, horizontal and diagonal directions).

The comparison of the results obtained between the initially mentioned technology (extensometry and LVDTs—datalogger TML®), assumed to be traditional, with the digital image correlation—DIC, following [10–12], is complemented by a numerical analysis based on Abaqus® software. Thus, the results of displacements outside of the original panel's plane, as well as the correspondent strains in the 4 points considering the horizontal, vertical and diagonal midlines (according to the marked area in the first quadrant of the outer face of the tested panels), were extracted in accordance with [13].

2 Digital Image Correlation Considerations

The use of the DIC equipment for the acquisition of data laboratory requires knowledge of the hardware and software associated with the selected optical and computational system, as well as a set of concepts inherent to the fundamentals of its operation.

Although not being the specific purpose of this work to detail the intrinsic aspects of the systems used in digital image correlation, a brief synthesis of the main concepts and considerations are presented in order to interpret the basic parameters that compromise the image acquisition by the system used in the analysed tests. As references, the concept, methods and displacement/strain field calculation are well detailed in [10] and, specially, in [11]. According to several authors [10–12, 14], the technology underlying the digital image correlation (DIC) allows successful performing the mechanical characterisation in terms of surface deformations of a structural element (or structure), either in two or three dimensions, without the need for physical contact with it, being assumed, nowadays, as a powerful and very useful technology. The methodology established by DIC is based on the analysis of several points on the surface of a specimen, through the successive capture of images. A correlation algorithm is used, in which the correspondence is made between two consecutive images, referring to moments before and after the deformation of the object to be evaluated. In general, the initial image is divided into several sections, called subsets, and those are searched for in the next image. Each subset corresponds to a set of pixels, and the objective of the algorithm is to determine its new position, trying to identify which are the intensity values of those pixels in terms of cartesian coordinates (x, y, z). The algorithm determines the movement that a certain block has made when moving from one configuration to another, in the context of a previously selected area (search zone of the algorithm), designating this area as the region of interest, obtaining, thus, the desired displacements and, through them, determining the correspondent strains.

In order to ensure that there is not more than one correspondence for a certain block, the surface of the specimen under analysis is previously prepared with the application of white or grey matte paint (therefore, with no brightness) over which a rain of black paint is applied through a random pattern (speckle). To ensure that this matching is done in a more accurate way, a stochastic pattern applied uniformly over the surface of the specimen under study is recommended. The experimental procedure for implementing this technique is essentially subdivided into three fundamental steps, contemplating the preparation of the specimen, the data acquisition and the data analysis. The images are obtained through a high performance digital camera for focusing and photography. The illumination of the test piece during the image acquisition is of utmost importance, considering the intention to obtain the best possible accuracy regarding the visualisation of the desired target. The described technology is able to perform in plane (DIC-2D) and out-of-plane (DIC-3D) deformation measurements. For 3D measurements, more than one camera is required, ensuring the necessary setup and calibration. The implementation of the digital image correlation methodology for the 3D case leads to the possibility of obtaining the out-of-plane displacement of the structure, thus allowing a wider set of information about the behaviour of the structure under analysis.

As a synthesis of the work performed by Yuan et al. [10], was studied the scheme of the setup used in its test in order to collect measurements, by means of DIC technology, for the characterisation of the bending deformation of a specimen referring to a monolithic glass panel, with 1,0 m side, subjected to a wind load. The points tested were considered by those authors with measurement through digital indicators (respectively located in the upper right and lower left quarter of the external surface of the glass panel, according to the symmetry). In that study, D_i represented the displacement measured at 8 points outside the plane of the glass selected for the purpose through digital transducers (with 0,01 mm precision). E_j represented the strain at 8 points marked for characterisation of the surface deformation by means of rosettes. Thus, the differences concerning the referred example and the present specimens are well identified in terms of the used layout as well as the inherent panels geometric characteristics. Nevertheless, the methodology adopted is similar in what concerns the DIC equipment dispositions and the stereo system for 3D applicability, which means the binocular stereovision for the imaging system, as specifically detailed in Fig. 4 for the performed tests, according the recommendations proposed in [11]. The deformed shape of the panel FE model [13] is indicated in the Fig. 4 also. The painted panel as well as the reduced area for measurements when the influence of the layout supporting beams and the lateral boards of the panel are discounted by optical difficulties is included too. A starting point and the general correlation zone is considered for panels. The sequence of photos and images inserted in Fig. 4 describes the general setup adopted for tests T26/27/28 using the DIC equipment—Dantec [15] and the generalised scheme considered for its implementation procedures. Specifically, are illustrated the global layout used to test the painted glass panel, the illumination (left, right and superior projectors), both cameras to capture the optical images, the baseline distance between them, as well as the focal distance, important for the optical images of the panel's movement. The area of the panel, including the points where are positioned the strain gauges and the terminal points of the wire transducer displacement, is also visible in the monitor of the DIC equipment.

Figure 4 indicates the graduated scale table for the DIC calibration also. The calibration target corresponds to a reference square that consists of a defined shape grid pattern manufactured to a surface, being used to calibrate the projection of a DIC experiment together with the Dantec Dynamics' DIC software (Istra4D). Each target has its own identification and properties, including background and foreground colour, format and layout, serial number, nominal grid square size, thickness and standard deviations of the square grid intersections. In the analysed cases, the referred DIC equipment [15] is certified and is calibrated in Istra4D according to the target's physical properties. The mentioned calibration process involves the measurement of the x, y and z intersection coordinates. The relevant parameters for DIC equipment were selected according to general information given by Infaimon company (programme and mentioned equipment) [15] as well as by the calibration attempts proposed by the ISISE Laboratory Manager. In addition, the correspondent values initially considered for the 3D DIC equipment parameters, which were introduced in the Istra4D software (3D camera calibrating settings) are summarized in Fig. 5.

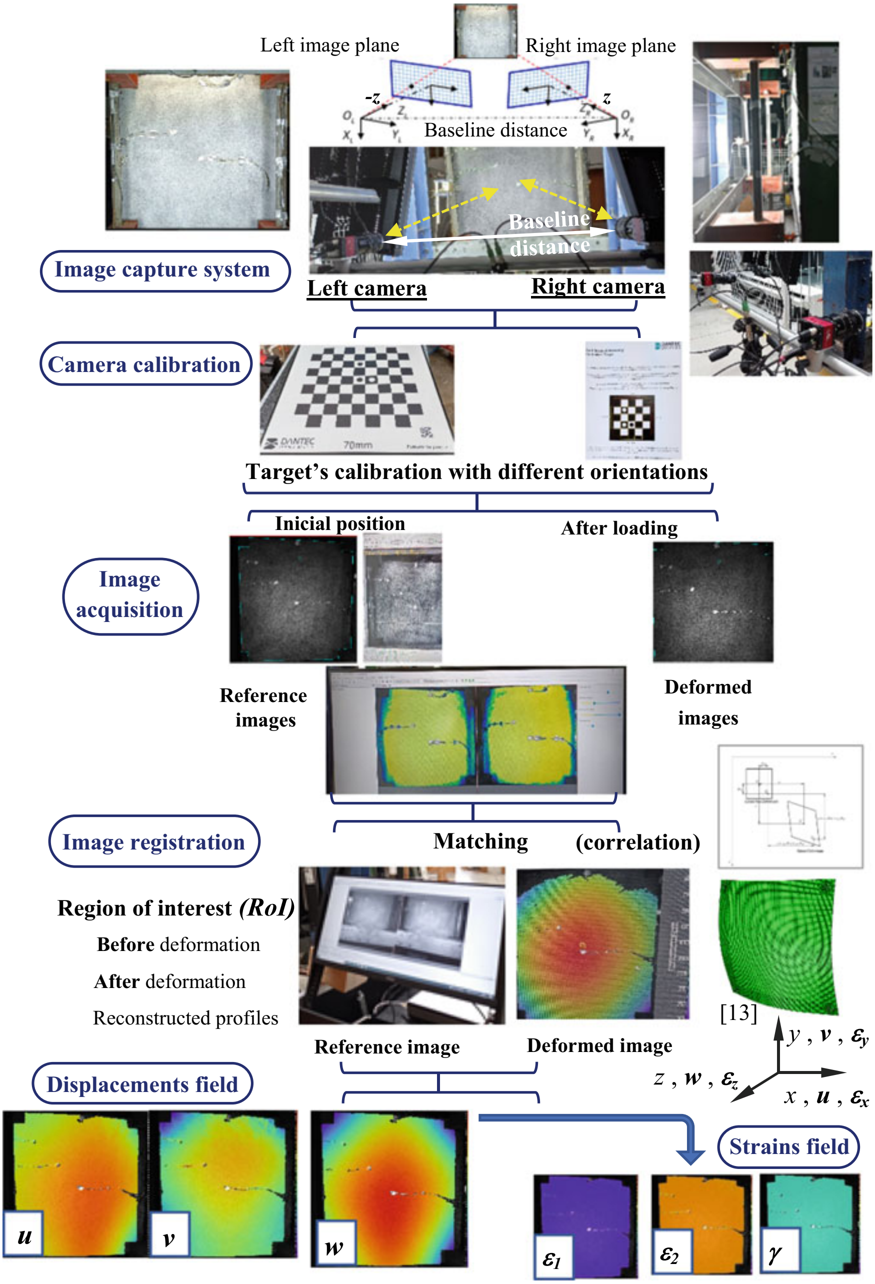

Fig. 4 Experimental setup for tests T26/27/28 using digital image correlation equipment at Structural Mechanics Laboratory—ISISE, Civil Engineering Department, University of Coimbra: Implementation procedures of 3D (Stereo)—DIC technology, adapted from [11]

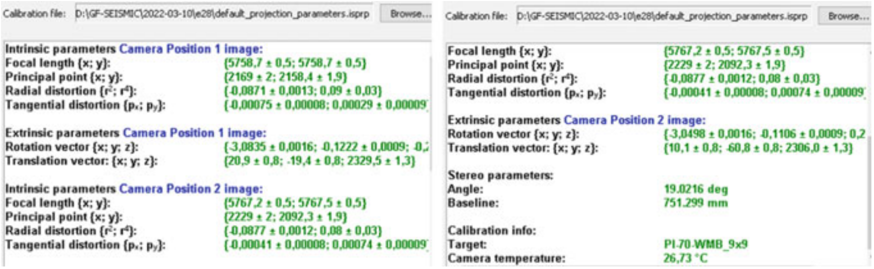

Fig. 5 DIC relevant parameters: data referent to cameras 1 and 2—Dantec/Istra4D [15]

3 Results

3.1 Introduction

The list of control points for each test is presented in order to export the DIC results. With reference to Figs. 2 and 3, five points were considered: (i) Centre point corresponding to LVDT 1 and rosette R7; (ii) Left point-centre line corresponding to LVDT 2 and rosette R55; (iii) Upper point-centre point corresponding to LVDT 4 and rosette R35; (iv) Point on diagonal line corresponding to LVDT 17 and rosette R70. For each point in the previous tests an "area" is defined, which referring to the closest polygon near the desired strain gauge, selecting in the software the following options for the desired physical parameters:

(a) Displacement according to z (out of plane)—Displacement (z direction);
(b) Engineering strain, (principal directions 1/2)—Eng. Principal Strain 1 & 2;
(c) Lagrangian strain, (principal directions 1/2)—Lagrang. Principal Strain 1 and 2.

3.2 Test 26 (Glass Panel with EVASAFE Interlayer Film)

Figure 6 presents the superposition of the load–displacement diagrams concerning the LVDTs 1, 4 and 17, according to the previous numbering. The continuous lines are considered for DIC results, while the dashed lines refer to the datalogger TML® results. As referred on Fig. 3, the panel's centre point (745 mm; 745 mm) was used on DIC equipment (Dantec®) to obtain the correspondent orthogonal displacements' values (under z direction). Several zones exhibit a graphical coincidence between the datalogger's and DIC recorded values.

Figure 7 presents the superposition of the load-strain diagrams concerning the principal values ε_1 and ε_2 in the rosettes 7, 35 and 70. The continuous lines are adopted for DIC results while the dashed lines are representative of the datalogger TML® results. A more consistent graphical coherence is visible in the case of ε_2 for

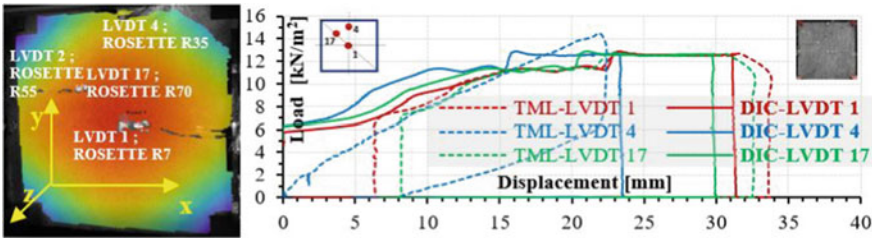

Fig. 6 Test E26: comparison TML/DIC for displacements (LVDT 1/4/17); DIC—area results

rosettes nº7/35/70, while such coherence for the first principal strain is not observed for the first two cases.

For the same test (T26), Fig. 8 presents for rosette nº 7 the comparison between TML® and DIC results for Lagrangian and Engineering principal strains, ε_1 and ε_2, taking into account an introduced correction once observed a timing delay and an optical error, treated with a smooth function (procedure repeated for several diagrams). The graphical evolution of the Lagrangian and Engineering principal strains (continuous lines for DIC results) are coincident for both cases represented in the mentioned figure.

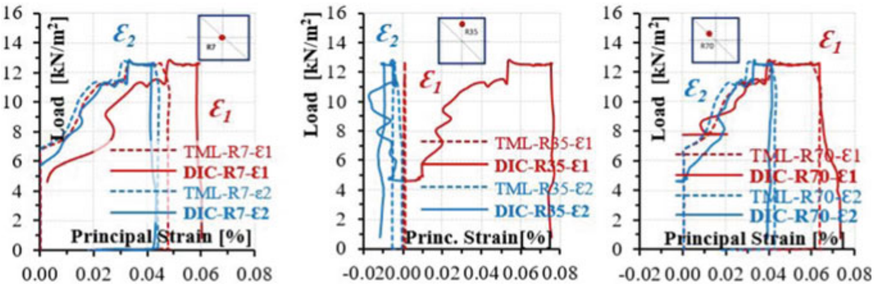

Fig. 7 Test E26: comparison TML/DIC for princ. strains ε_1 and ε_2: rosettes 7/35/70

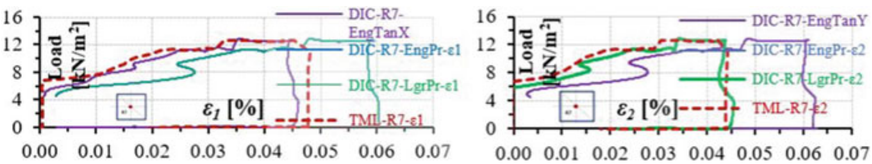

Fig. 8 Comparison TML/DIC for lagrangian and engineering principal strains

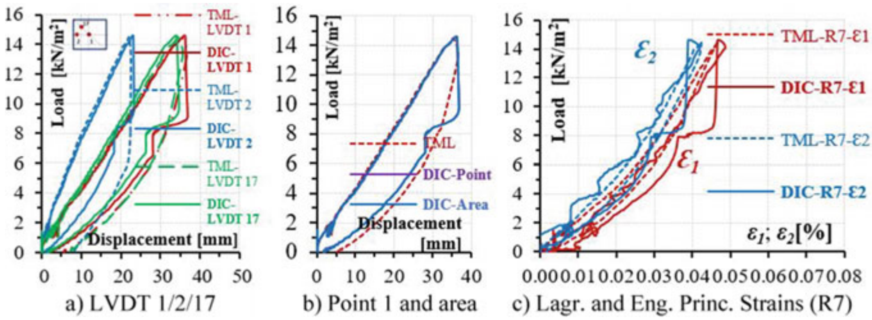

Fig. 9 Test E27: TML/DIC results for displacements and principal strains

3.3 *Test 27 (Glass Panel with PVB Interlayer Film)*

Figure 9 presents the superposition of the load–displacement diagrams concerning the LVDTs 1, 2 and 17. A well agreement is observed between TML and DIC results for displacement in such positions during the loading phase (Fig. 9a and b). If considered the comparison for the results related to a point and a surrounding area, marked in the DIC, for the maximum displacements (z axis), it can be observed that the presented graphical superposition is quite close for them and include some coincident zones (Fig. 9b). Thus, extracting results in the considered point or circle, around that point (O), has basically the same effect. The principal strains (Fig. 9c) are very close.

3.4 *Test 28 (Glass Panel with PVB Interlayer Film)*

In what concerns test T28, the load–displacement diagrams are similar concerning the tests T26 and T27 (Fig. 10). For principal strain ε_2 the graphical evolution between HBM® and DIC results is relatively close but for strain ε_1 such comparison it is much more distant (as observed in the second and third diagrams of Fig. 10).

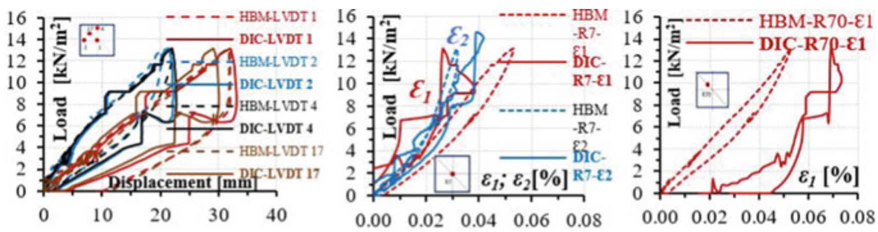

Fig. 10 Test E28: HBM/DIC results for displacements and principal strains (R7; R70)

3.5 Comparison Ratios

For the 3 considered tests are presented in Table 1 the values of displacement, principal strain and principal stress obtained for the centre/relevant points (A or B, and O, Fig. 3) correspondent to the TML® (or HBM®) datalogger and Dantec® DIC results, respectively. The determination of the experimental principal stresses (σ_1 and σ_2), at the referenced points, is based on the utilization of the expressions of the theory of elasticity, as presented in [8, 9], according the mentioned simplification on the panel´s interlayer film and considering the Young's modulus and Poisson's ratio of the glass material. The considered strains in the values selected for Table 1 correspond to the Lagrangian principal strain, instead of the Engineering principal strain, both provided by the DIC software. The measurements recorded by dataloggers, connected to devices as the strain gauges and transducers, revealed lower values for principal strains in tests T26 and T27 but higher for test T28 (ε_1). Regarding the displacements along the z-axis, the values recorded on dataloggers were higher for tests 26 and 27 but little lower for T28.

In general, the determined ratios between the TML or HBM results and DIC results, whether for displacements, strains or stresses, are relatively close to 1. However, the DIC results for principal strain ε_1 for test 28 and shear strain γ for test 27 constitutes exceptions. The farthest cases (for regular cases) concern the principal strain ε_2 in test 26 and the principal stresses in test 28, with a gap of 15, 62 and 23%, respectively. All the other cases show much smaller percentage differences, which demonstrated that the introduced DIC technology not only was capable of achieving full-field bending deformation measurements for the glass panel but also could obtain comparable measurement results in comparison with the conventional dataloggers technologies.

4 Conclusions

The deformations of the tested glass panels were measured according two different equipment and technologies, being compared with each other. It should be mentioned the fact that, any possible light errors make it difficult to capture images by the DIC and consequently the accuracy of the evaluation of displacements and the determination of the strains. However, it can be observed that the general values obtained through the DIC equipment are quite similar to the ones registered by the TML®/HBM® equipment. The mean value for the displacement ratio (including the three tests) is equal to 1,03 while the same mean for the principal strain ε_1 is equal to 1,3. For principal strain ε_2 the correspondent mean value is equal to 0,92. Concerning the principal stresses ratio, a global result of 1,18 and 0,95 were obtained respectively for σ_1 and σ_2, which are, naturally, dependent of principal strains. Thus, based on those observations and independently of the exact localization of the centre point of each panel and measurement reference, it can be concluded that the ratio between

Table 1 Comparison results for tests T26/27/28: TML (or HBM)/DIC ratios

Physical parameter	T26			T27			T28			Average
	TML	DIC	$\frac{X_{TML}}{X_{DIC}}$	TML	DIC	$\frac{X_{TML}}{X_{DIC}}$	HBM	DIC	$\frac{X_{HBM}}{X_{DIC}}$	
	Point A/B	Point O		Point A/B	Point O		Point A/B	Point O		
Displacement (z)	24,3	23,9	1,02	35,6	33,4	1,07	31,87	31,98	1,00	1,03
Princi. strain ε_1	0,0345	0,0367	0,94	0,0467	0,0497	0,94	0,0531	0,0264	2,01	1,30
Princi. strain ε_2	0,0324	0,0281	1,15	0,0423	0,0438	0,97	0,0316	0,0501	0,63	0,92
Shear strain γ	0,0019	0,0018	1,06	0,0032	0,0010	3,20	0,0062	0,0060	1,03	1,76
Princi. stress σ_1	30,25	31,20	0,97	40,70	43,13	0,94	43,74	27,04	1,62	1,18
Princi. stress σ_2	29,03	26,22	1,11	38,16	39,72	0,96	31,31	40,75	0,77	0,95
Max. load, w	16,90		<u>1,04</u>	14,59		<u>1,35</u>	13,14		<u>1,18</u>	<u>**1,19**</u>

Lagrangian principal strains (1, 2 and shear strain). TML®; HBM®; Dantec (Istra4D) ®
Displacements [mm]; Strains [%]; Stresses [MPa]; Load [kN/m^2]; <u>x average value</u>

datalogger's results over the DIC is relatively near of the unity for the most part of the presented results that characterise the behaviour of the panels. It is therefore concluded that the DIC equipment provides reliable results with regard to the records of traditional dataloggers, with advantages contactless equipment, fewer material and time consumed for practical preparations.

Acknowledgements The authors express their gratitude to the Portuguese Foundation for Science and Technology (FCT) for the granted support within the research project GF SEISMIC POCI-01-0145-FEDER-032539.

References

1. Jordão, S., Inca, E., Mesquita, A.: GF SEISMIC Project Annual Report: Structural Glass Façades Subjected to Seismic Loading. Submitted to the Portuguese Foundation for Science and Technology–POCI-01-0145-FEDER-032539. ISISE/DEC-FCTUC (2020). (in Portuguese)
2. EN 1991-1-4: 2005+A1. Eurocode 1: Actions on structures-Part 1–4: General actions-Wind actions. CEN-European Committee for Standardization, Brussels (2010)
3. Fitechnic®, Glass Fixing System: Point Fixing Catalog (2019). https://fitechnic.com/point-fixing/
4. Pentagonal–Project Catalog (2017). https://pentagonal.com/projectos/
5. Product data sheet: Sikasil SG-500–Silicone structural adhesive. Sika® (2016)
6. Tempered laminated glass panels: produced by Vidromax, SA–Portugal, according to EN 1279-5+A2 (2013), EN 14449 (2008) and EN 12150-2 (2010)
7. Product data sheet: Sikasil WS-605 S–High performance sealant. Sika® (2009)
8. Mesquita, A., Inca, E., Jordão, S.: Experimental and analytical analysis of point fixed tempered laminated glass panels. Composites meet sustainability. In: Proceedings of the 20th European Conference on Composite Materials, ECCM2022, 26–30 June, Lausanne, Switzerland (2022). (Submitted)
9. Mesquita, A., Jordão, S., Inca, E.: Experimental and analytical evaluation of point fixed tempered laminated glass panels. In: Proceedings of XIII Congress of Metallic and Mixed Construction (CMM). Coimbra, Portugal, pp. 277–286 (2021). (in Portuguese)
10. Yuan, Y., Zhou, Y., Liu, W., Chen, J.: Flexural deformation characterization of glass panel in curtain walls based on digital image correlation technique. Constr. Build. Mater. **260**, 119819 (2020). https://doi.org/10.1016/j.conbuildmat.2020.119819
11. Pan, B.: Digital image correlation for surface deformation measurement: historical developments, recent advances and future goals. Measurement Science and Technology. Institute of Solid Mechanics. Beihang University, Beijing, China (2018). https://doi.org/10.1088/1361-6501/aac55b
12. A good practices guide for digital image correlation. In: Jones, E.M.C., Iadicola, M.A. (eds.) Standardisation, Good Practices, and Uncertainty Quantification Committee. International Digital Image Correlation Society (iDICs) (2018)
13. Inca, E., Jordão, S., Bedon, C., Mesquita, A., Rebelo, C.: Numerical analysis of laminated glass panels with articulated bolted point fixings. In: Proceedings of XIII Congress of Metallic and Mixed Construction. CMM. Coimbra, Portugal, pp. 545–554 (2021). (in Portuguese)
14. Homepage. https://www.sciencedirect.com/topics/engineering/digital-image-correlation
15. Dantec Dynamics, v:4.4.7.577. Istra4D DIC Software Package. Licence information and sale by Infaimon (2018–2021)

Image Analysis Techniques to Characterize Scaled Embankment Failures

Solange Mendes, Sílvia Amaral, Teresa Alvarez, Rui Aleixo, António Muralha, Teresa Viseu, and Rui M. L. Ferreira

Abstract The present work consists in the application of image analysis techniques to characterize the failure by overtopping of a scaled embankment dam that was experimentally tested in a medium-scale facility located at the National Laboratory of Civil Engineering. These techniques were used to describe the failure of the small-scale dam by defining the 3D profile of the dam body in several time instants. This was performed with depth images and with the characterization of the surface velocities of the flow near the breach based on the application of Particle Tracking Velocimetry (PTV) algorithm. The characterization of the 3D reconstruction of the failed dam and surface velocity maps in the breach vicinity were based on the post processing analysis of high-definition (HD) digital images and depth images, strategically acquired around the dam. This work assesses the usefulness of image analysis techniques for the applications herein presented.

Keywords Image analysis techniques · Depth sensors · 3D reconstruction · Particle image velocimetry · Surface velocity maps

1 Introduction

The continuous advance in image quality of the current cameras and also the constant improving of the recording frequency followed by the development of image processing algorithms have allowed to expand the knowledge in several applications.

Measurement techniques based on image acquisition and post-processing, hereafter referred to as image acquisition techniques, are being increasingly used in different fields of engineering. They allow data to be obtained in space and time,

S. Mendes (✉) · T. Alvarez · R. Aleixo · R. M. L. Ferreira
CERIS, Instituto Superior Técnico, Av. Rovisco Pais, 1, 1049-001 Lisboa, Portugal
e-mail: svmendes@lnec.pt

S. Amaral · A. Muralha · T. Viseu
Laboratório Nacional de Engenharia Civil, Av. do Brasil, 101, 1700-066 Lisboa, Portugal

C. Chastre et al. (eds.), *Testing and Experimentation in Civil Engineering*, RILEM Bookseries 41, https://doi.org/10.1007/978-3-031-29191-3_35

making possible to characterize a wide range of variables, even with a rapidly varying nature and in a non-intrusive manner.

Other authors have also used image acquisition techniques, in order to directly acquire information from the images captured, such as, Misra et al. [1] who described a method for the estimation of the instantaneous air–water interface of a hydraulic jump through an image processing method, namely, textured segmentation from particle image velocimetry (PIV) images.

In the specific case of embankment failure tests, the image acquisition techniques have been used in several studies over time, to determine breach erosion evolution, near-breach velocities, and dam morphology. For instance, Dupont et al. [2] evaluated the time evolution of the dam profile erosion from the images captured with a video camera by means of an original image processing algorithm.

In Bento et al. [3] the evolution of breach cross section results from the trace of a laser sheet with the free surface and the submerged embankment body was determined by digital image post-processing, specifically, by image analysis over a simple thresholding algorithm, likewise used by Soares-Frazão et al. [4].

Near-breach flow velocities were analyzed by using three video cameras to obtain 3-dimensional velocity measurements as referred in Orendorff et al. [5].

Regarding dam morphology, Amaral et al. [6] performed a complete characterization of the breach digital model terrain evolution by using a Kinect Sensor. As explained in the above studies, the approaching flow velocity and the breach geometry are variables that can suffer rapid variations. Some image acquisition techniques were used in this study for the 3D reconstruction of the failed dam body in several time instants and in the characterization of the flow surface velocities near the breach.

The image acquisition techniques here presented are based in the data analysis of a zoned embankment dam failure test performed in an experimental facility located at the National Laboratory for Civil Engineering, specifically developed to perform these types of tests.

Note that this failure test uses a reduced scale but does not reproduce any real dam, being an approach to allow the study of the failure process of embankment dams by overtopping.

This process involves both hydraulic and geotechnical phenomenology, so that obtaining similarity conditions regarding the mechanical behavior of the failure evolution and its characteristics cannot be defined just by similar hydraulic considerations. On the one hand, the forces that dominate the hydraulic processes are the gravity and the inertia, of which a Froude similarity could be used, but on the other hand, erodibility in this type of test also depends on soil strength properties that do not obey this similarity.

The problem of scaling factors in this type of testing, in particular, how the embankments erodibility should be scaled was studied in detail by the team and is explored in Amaral et al. [7].

In this work Sect. 2 presents the details of the dam breach experiment performed under the scope of this study, namely the experimental facility where it was conducted, the geotechnical characterization of the soils composing the embankment, the instrumentation and monitoring methods used in data acquisition and which variables were monitored. Section 3 concerns the application of image analysis techniques to the data acquired in the failure test, namely, the lateral erosion of the breach, the water levels variation in the downstream settling basin, the surface velocity maps near the breach and the 3D characterization. Section 4 presents the final conclusions and some remarks which were designed based on the image analysis applications used in this study.

2 Dam Breach Experiment

2.1 Experimental Facility

The experimental test was conducted in an experimental facility, corresponding to a medium-scale channel with 1.2 m wide and 0.45 m high. This channel is equipped with an elevated reservoir that allows the supply of flow up to about 30 l/s. The main channel allows the creation of a 1.3 m^3 reservoir, in which a Ø200 bottom sewer is implemented, for rapid emptying purposes, in case it is necessary to interrupt the experiment. Downstream the main channel, there is a settling basin with 3.7 m long, 2.0 m width and 0.6 m depth where the sediments removed from the dam body are deposited, preventing their inflow into the recirculation circuit. In the downstream channel, perpendicular to the latter, the effluent flow exits through a calibrated v-notch weir (Fig. 1).

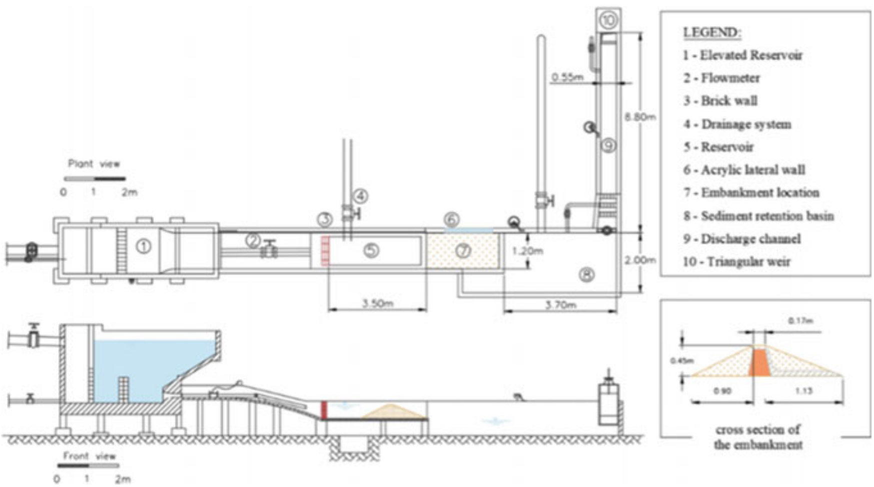

Fig. 1 Plant and front view of the experimental facility

2.2 Experimental Procedure

The experimental protocol for the failure by overtopping of the scaled embankment dam in the facility previously described, after the geotechnical process of construction the embankment on site, is summarized in the following steps:

(1) water fill of the elevated reservoir to its maximum filling capacity (Fig. 1 no. 1);
(2) water fill of the reservoir (Fig. 1 no. 5) to a level of about 0.20 m below the crest of the dam;
(3) fill the downstream sediment settling basin (Fig. 1 no. 8);
(4) assembly of all the equipment's and lighting system in the respective positions and obtain calibration images for the post-processing purposes;
(5) finish filling the reservoir up to the level of the breach;
(6) turn on all the image acquisition equipment's and light support;
(7) Initiate the experiment by opening the control water inflow;
(8) manual deployment of the seeding particles into the flow on the reservoir during the test.

The experiment was interrupted to characterize the morphology of the breach. For this purpose, the inflow was stopped and simultaneously the bottom outlet was opened in the reservoir, interrupting the continuous failure process, until such time as the constructed experimental embankment is eroded by the overtopping phenomenon.

2.3 Geotechnical Characterization of the Soils

The soils adopted in the body of zoned embankment test were carefully selected considering the geotechnical characteristics required for the dam core and the side slopes. Note that in this type of study, the erosion phenomena are very dependent on the geotechnical conditions of the soil, not only in respect to the grain size distribution curves, but also in what concerns the implemented material conditions, i.e., the water content and compaction degree.

In this experiment, a zoned embankment dam with 0.45 m heigh, 1.2 m wide and with a crest 0.17 m was constructed with a fine silty-sand in the upstream and downstream slopes and clay soil in the central core, according to the unified soil classification system (USCS) [ASTM D2487 [8]]. The drains and filters were also designed to ensure the transition between the slopes and the core (Fig. 2).

The soils selected for each part of the dam were submitted to geotechnical tests for the determination of their intrinsic characteristics. These included the particles density test, Casagrande test for the evaluation of liquidity limit, determination of plasticity limit, grain size distribution analysis by sieving and sedimentation and Standard Proctor compaction test (Fig. 3 and Table 1). The degree of compaction and water content adopted in the experimental embankment dam were those based on the optimal values from the standard Proctor test (Table 1) which were monitored during

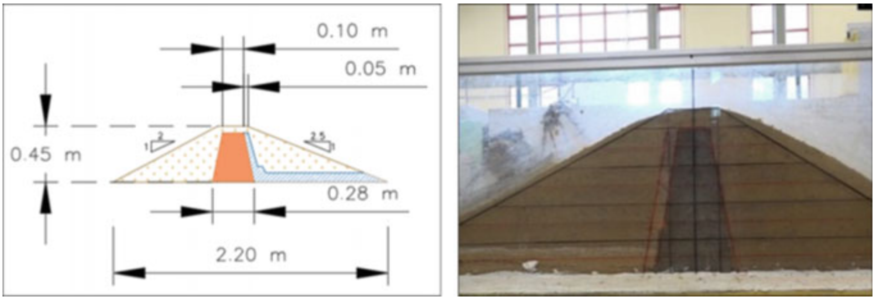

Fig. 2 Zoned dam cross section

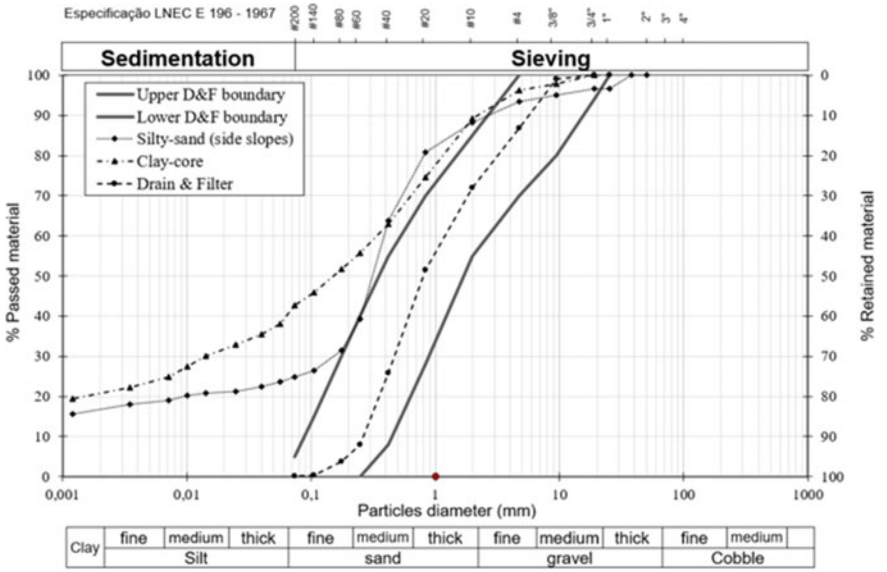

Fig. 3 Grain size distribution curves of the materials used in the side slopes, core and drain and filters of the experimental zoned embankment dam

construction through the collection of samples from each lift with the consequent geotechnical analysis.

2.4 *Monitored Variables and Equipment's*

The layout of the experimental facility and the equipment's used are shown in Fig. 4. In such manner, based on image analysis techniques, the extraction of the temporal variations of the following variables was possible:

Table 1 Main geotechnical characteristics of the experimental embankment dam

Materiais	$\gamma_d^{máx}$	w	RC	Δw	$w_L/w_P/PI$	k (m/s)	G
Areia siltosa	19.94	9.8	95	−0.6	17.5/–/–	1.2×10^{-7}	2.67
Argila	17.20	17.6	98	−1.1	41.1/22.3/18.8	–	2.68

$\gamma_d^{máx}$—maximum dry unit weights (KN/m^3); w—water content (%); RC—relative compaction (%); Δw—deviation from optimal water content (%); w_L—liquid limit (Atterberg limits) (%); w_P—plastic limit (Atterberg limits); PI—Plasticity Index (%); k—soil permeability (m/s); G—particles density (–)

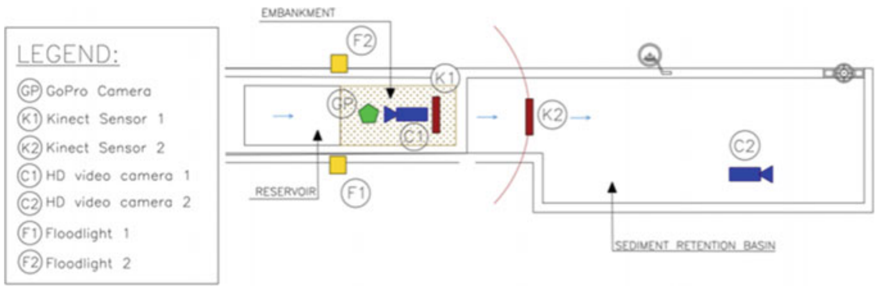

Fig. 4 Layout of the image acquisition equipment used in the experimental set-up

1. temporal evolution of the lateral erosion of the breach;
2. water levels inside the downstream settling basin;
3. surface velocity maps in the breach proximity;
4. 3D reconstruction of the dam morphology.

The monitoring layout required for the characterization of the previous variables encompassed 2 HD video cameras (Fig. 4–C1, C2), 2 motion sensors (Kinect sensor—holding 2 internal cameras, 1 Red Green Blue camera and 1 depth camera, Fig. 4–K1, K2), a video camera with an acquisition rate suitable for PTV applications (1 GoPro acquiring at a rate of 30fps, Fig. 4–GP) combined with 2 high-power floodlights placed in each side channel wall upstream the dam (Fig. 4–F).

Variable 1 was extracted from the images of the HD video camera 1 C1 placed above the experimental embankment, monitoring the breach lateral erosion from a top point of view. Variable 2 was determined by processing the footage of HD video camera 2 placed about 1 m above the settling basin monitoring a graduated scale.

Variable 3 was based on the data acquired with a GoPro camera installed on the top of the dam body immediately before the entrance of the flow in the delimited breach that allowed high-speed acquisition of images, and is, therefore, suitable to calculate surface velocity maps through PTV applications. To ensure good contrast between the tracer particles and the flow, the image quality was increased by two floodlights paired with soft boxes placed on each side of the channel.

Variable 4 was measured by using two motion-sensing devices (Kinect sensors) that were combined to obtain 3D reconstructions of the dam morphology before, during and after the failure. One was placed on the top of the dam, aligned with its centreline and the other was moved around the dam to obtain a complete scan of the 3D volume to reconstruct. To obtain a reliable characterization through these motion-sensing devices the dam body survey at the target instants was conducted dry, i.e., without the presence of flow under the breaching dam, thus avoiding errors caused by the presence of water. That is, at each failure instant measured, the water level in the upstream reservoir was lowered and water flow throughout the dam was stopped. To ensure a common referential in all 3D reconstructions, four targets with known coordinates were fixed to the channel walls.

3 Results of the Application of Image Analysis Techniques to the Acquired Data

3.1 Temporal Evolution of the Lateral Erosion of the Breach

The breach lateral erosion (variable 1) was obtained from the footage recorded from the HD video camera 1 (Canon) installed on the top of the dam (Fig. 4C1). This equipment was placed on the top of the dam body, perpendicular to the crest, 2.5 m above monitoring the breach lateral evolution during the failure process.

A post-processing procedure, subtraction Matlab algorithm, was applied to pairs of consecutive images, allowing the characterization of the breach width across time (lateral erosion of the breach).

This procedure consisted in calculating the pixel intensity in a given region of interest, the respective length of the dam crest, and evaluating the pixel difference between consecutive images that allowed the determination of the breach width increasing in three distinct sections: upstream, crest and downstream, as shown by Fig. 5.

Figure 6 shows the breach width variation across the failure evolution of the zoned embankment dam, where instant A stands out when there is total erosion of the initial breach of the embankment and instant B with the total falling of the downstream side of the experiment.

3.2 Water Levels Inside the Downstream Settling Basin

The water level variation inside the downstream settling basin (variable 2) was determined by processing the footage HD video camera C2 (Fig. 4) that was placed at 0.70 m from the facility side wall of the basin to visualize a graduated scale there installed from which the water level can be inferred, Fig. 7a).

This variable was evaluated with the application of a detection algorithm in Matlab, which consisted in the identification of the interface between the level and

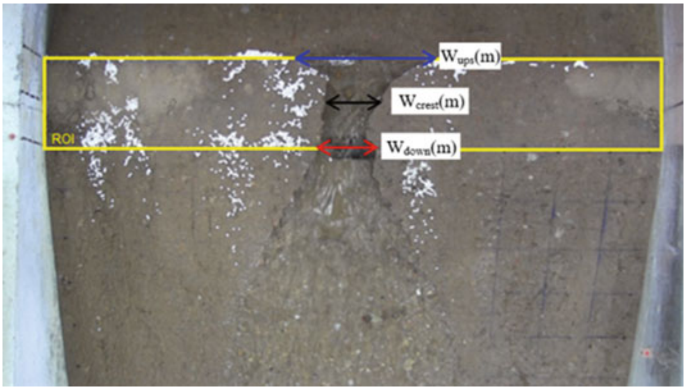

Fig. 5 Original image acquired with the top camera (C1) and corresponding sections for measuring the lateral evolution of the breach: upstream, at the crest and downstream

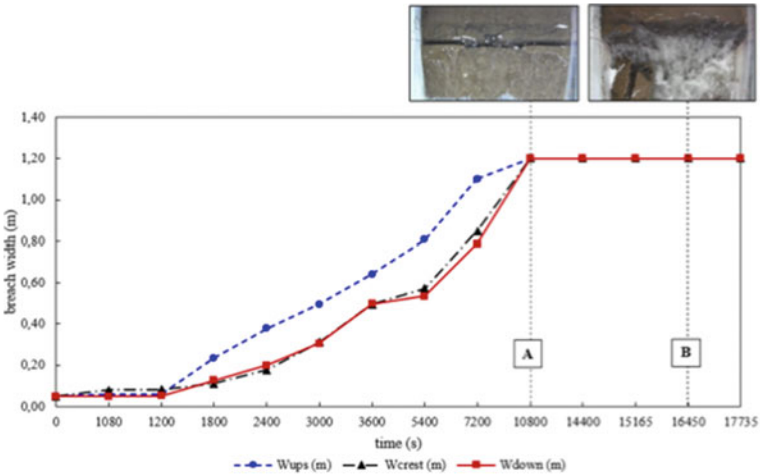

Fig. 6 Variation of the breach width during the experiment (lateral evolution of the breach). Instant A (t = 10 800 s): total disappearance of the initial breach; Instant B (t = 16 450 s): complete collapse of the downstream side

the water, based on the variation of the pixel intensity, in the images recorded by the camera. This methodology is applied between the area of the figure corresponding to the submerged zone and the area of the figure corresponding to the emerged zone.

Figure 7b) illustrates a part of the variation of the water level from the beginning of the test (t = 00:00:00 s) to the instant of the first stop, where the downstream level is no longer supplied by the breach effluent flow.

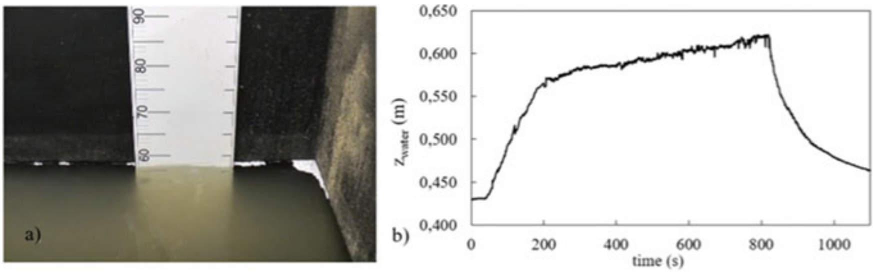

Fig. 7 Measurement of downstream levels: **a** image captured by the HD camera C2–reference graduated-scale; **b** temporal variation of water levels within the sedimentation basin

3.3 Surface Velocity Maps in the Breach Proximity

The surface velocity field in the breach approach area, variable 3, was determined by applying a Particle Tracking Velocimetry (PTV) algorithm written in Matlab [9, 11] using the images captured by the GoPro camera. One calibration board to cover all the dam body width (1.2 m) with 5 × 5 cm cells. This board was used for calibration of the images acquired with the referred equipment. Two calibration images were taken with the calibration board placed at the lowest and higher-level coordinates of the water, once during the failure process the water level in the reservoir will differ. This is of major importance to accurately convert pixels in spatial coordinates.

Particle Tracking Velocimetry is a Lagrangian technique that relies on the identification of individual tracers in each frame of a footage and respective matching of particles between frames. In the present case, the matching procedure is based on the Voronoï tessellation of space allowing to better deal with the presence of velocity gradients in the flow [11]. Around each detected particle, the Voronoï polygons are drawn. By uniting the centers of the adjacent Voronoï polygons, one defines the so called Voronoï star. The Voronoï stars will be used to match the particles and to determine the displacement of the particles [11]. In this method each successfully identified and tracked particle will hold a velocity vector, v, and the velocity of the i-particle between frames j and j + 1 is given by:

$$\mathbf{v}_{\mathrm{i}} = \frac{r_{i,j+1} - r_{i,j}}{dt} \tag{1}$$

where $r_{i,j+1}$ is the position vector of particle i in frame $j + 1$ and $r_{i,j}$ is the position vector of particle j in frame j. and dt is the time interval between consecutive frames.

The operation sequence is here described with the visual aid of Fig. 8. Figure 8a depicts a raw flow image where the tracers are visible; in Fig. 8b the image is corrected for the distortion and the identified particles in frame j are visible in Fig. 8c; a zoom and Voronoï tessellation of space is shown in Fig. 8d; and, finally, Fig. 8 depicts the obtained velocity field.

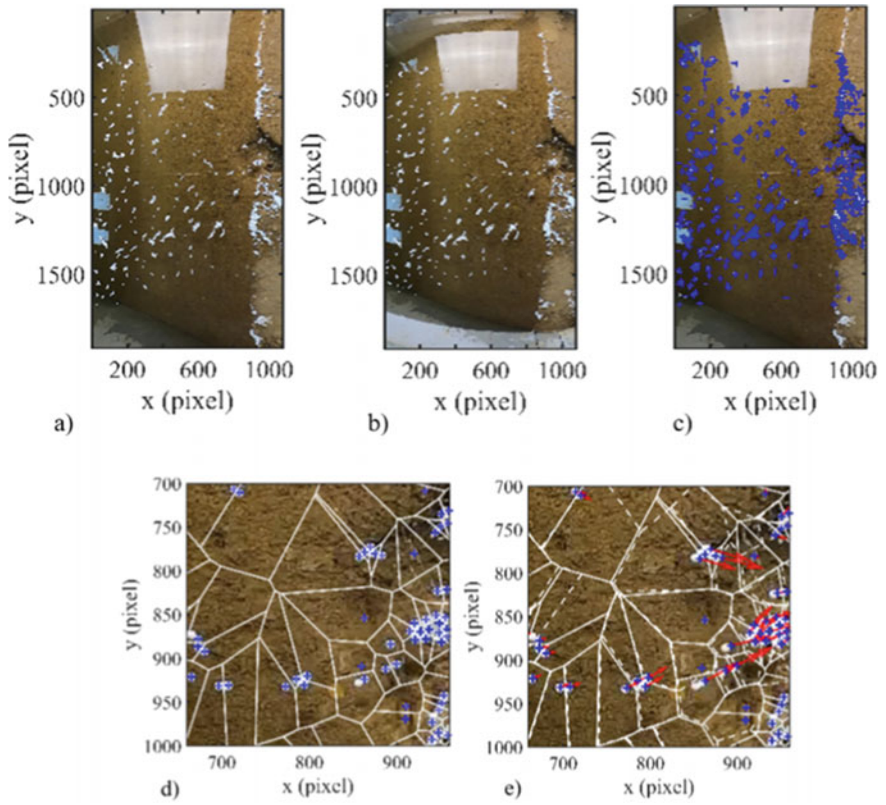

Fig. 8 **a** Raw image acquired by the GoPro camera; **b** rectified image; **c** detected particles. **d** zoom and Voronoï diagram; **e** computed velocity field and Voronoï diagram at time t (solid lines), and t + dt (dashed) lines

PTV holds a velocity vector at the location of each detected and successfully tracked particle. This means that the velocity field data points are randomly dispersed, that is, data is presented in a non-structured grid. Therefore, it is not trivial to analyse the spatial velocity distribution nor compare it with other instants, since the vectors will not be at the same locations. A binning procedure is used to determine a structured grid. This procedure consists in dividing the field-of-view in $m \times n$ intervals [9]. At each time instant the average velocity inside each bin is calculated. It is possible to consider a time average in each bin where the time averages are calculated bin by bin. This allows also to define statistical variables of the flow [10]. The binning is illustrated in Fig. 9 and Fig. 10a and b depicts the binned velocity field at two instants of the dam-breach process.

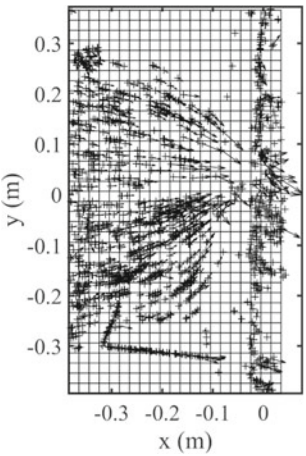

Fig. 9 Example of application of the binning method. The field of view is divided into bins and in each bin, the average velocity is computed can be computed with the vectors present at each bin

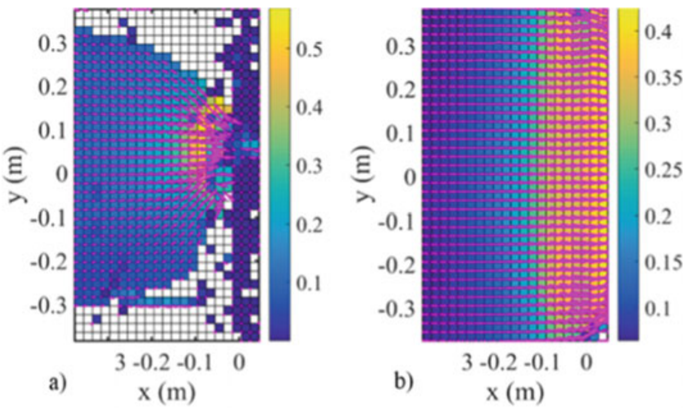

Fig. 10 Surface velocity fields **a** Binned mean velocity field during 203 s at t = 1320 s; **b** Binned mean velocity field during 159 s at t = 15,480 s

3.4 3D Reconstruction of the Dam Morphology

The 3D reconstruction of the dam morphology during the breaching process (variable 4) was carried out with the aid of two motion-sensing devices, as presented in Sect. 2.3, Fig. 4. These sensors are composed of two internal cameras, an RGB and an infrared that allow both the acquisition of coloured and depth images.

In this way, the 3D reconstruction of the failed dam was obtained from a set of acquisitions taken from the top and several other positions around the dam, assuring the georeferenced points were gathered (Fig. 11). It should be noted that to correctly

Fig. 11 Layout adopted for the Kinect Sensor during testing and location of targets of known coordinates for the characterization of the 3D dam morphology during the failure

characterize the evolution of the breach and avoid the problems caused by the presence of water, namely the variation of the refraction index, it was necessary to interrupt the breaching process, by cutting the flow and emptying the upstream reservoir almost instantaneously.

The process of georeferencing and cleaning the depth images acquired was carried out using the Cloud Compare software which included the following steps: (i) identification of the target points that were located in different places of the facility, in the point clouds; (ii) association of the real coordinates with the identified points, consequently georeferencing the point clouds to the same coordinate system; (iii) elimination of the points located out the area of "interest" (the points that clearly did not correspond to the dam); (iv) merging the several clouds composing the full scan into a single point cloud—final cloud; and (v) application of a noise filter to remove the outlier points, i.e., the points that clearly result from errors of measurement.

After processing and cleaning all the acquired points, the final point cloud obtained for each analyzed instant was later imported into ParaView software: the dam in failure at the corresponding time instants was reconstructed and the contour lines were obtained. The experimental test used as an example had a total duration of 07:42:19 s and was interrupted six times to perform this 3D characterization of the dam morphology during the failure. The 1st and 2nd stops can be classified as the breaching process initiation; the 3rd and 4th stops represent the process of mass detachment episodes and the 5th stop shows the configuration of the embankment nearly at the final moments of the experiment. Figure 12 demonstrates the 3D reconstruction of the dam morphology corresponding to the 1st, 3rd and 5th stops that resulted from the application of ParaView software.

These 3D reconstructions of dam in several time instants of the failure make it possible to obtain longitudinal or cross-sectional profiles of the dam in failure at any location of interest, Figs. 13 and 14.

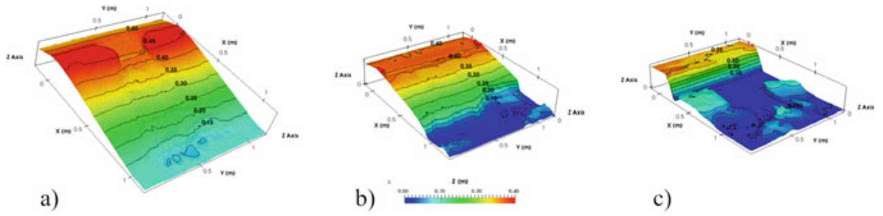

Fig. 12 3D reconstruction of the breach morphology evolution: **a** 1st stop: t_1 = 00:38:23 s; **b** 3rd stop: t_3 = 04:10:48 s; **c** 5th stop: t_5 = 07:13:28 s

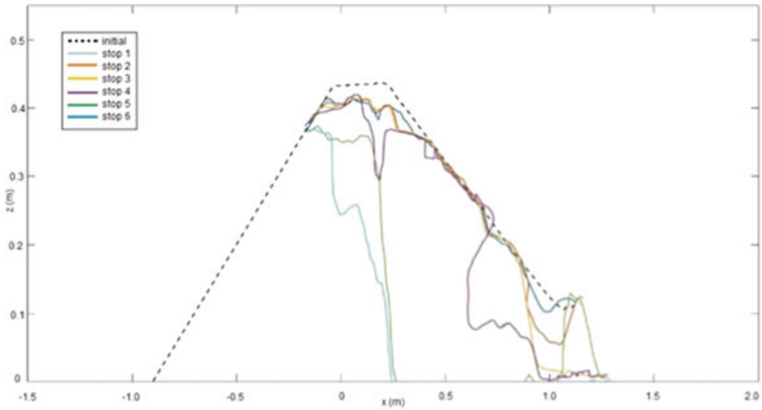

Fig. 13 Evolution of the longitudinal profile of the failed dam in its centreline

4 Conclusions

With the proposed methodology, it was possible to describe the failure process of a scaled zoned embankment dam in non-intrusive approach. From the post-processing of the acquired images, it was possible to: (i) determine the lateral evolution of the breach erosion with a subtraction algorithm analysis; (ii) the water level inside the downstream channel with a detection algorithm; (iii) the velocity field by means of a PTV approach and the (iv) 3D reconstruction of the dam morphology by means of the use of a Kinect sensor combined with two different software's that allow point clouds treatment and multi-platform data analysis, respectively CloudCompare and ParaView.

Concerning the evolution of the lateral erosion of the breach during the experiment, from the analysis of this variable it was possible to fully understand the evolutionary state of erosion for this zoned embankment test. Although the test in question lasted approximately 7 h it was noted that only up to third hour existed lateral erosion of the breach, after this instant a total disappearance of the initial breach took place, and thus the evolutionary process of the failure by overtopping was given only in the

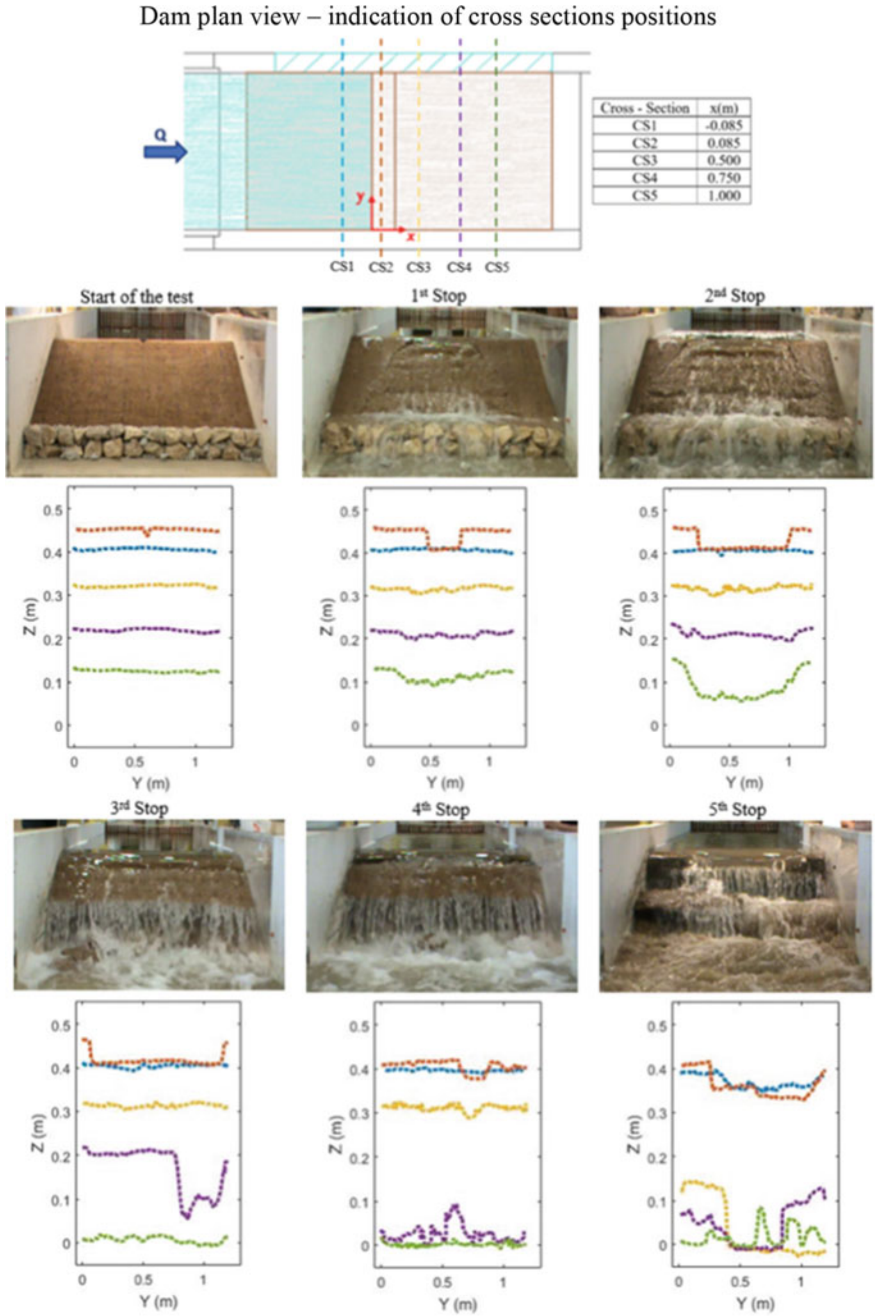

Fig. 14 Evolution of the dam morphology in each stop of the experiment in the cross-sections indicated above

downstream side of the embankment. So, it can be said that for the evaluation of this variable the analysis from the images captured by C1 proved to be very functional.

Regarding the analysis of the water level variation in the downstream sedimentation basin, the algorithm created for the analysis of this variable was possible. However, being this a destructive test, the mixing of water with the earthfill masses that fall during the process, together with the tracer particles used to characterize variable 3, made difficult the application of this methodology, but not ineffective. Thus, we conclude that for this specific case the use of image analysis was more challenging to achieve for the measurement of downstream flow levels.

The surface velocity field in the breach approach area was achieved through the application of the commonly used in this type of experiments, PTV technique. Some difficulties were encountered due to the environmental conditions where the experiment was made.

The presence of the ceiling windows in the pavilion of the laboratory created difficulties in the image processing once the degree of light changed during the day and the experiment took several hours to finish. For this reason, two floodlights with soft boxes were used, to aid the light conditions but the reflection of the soft boxes was visible in the flow images from the GoPro camera, making the PTV algorithm identify the edge of the soft box reflection in the water as a particle, which included extra time in removing these false positives. This procedure proved to be suitable for obtaining accurate results and proved to be computationally efficient, despite the difficulties encountered during the experiment and the extra time spent assessing this variable, which was not initially foreseen.

Lastly, the Kinect Sensor equipment has proven to be highly efficient for acquisition of point clouds for 3D surface reconstruction purposes. Therefore, the methodology adopted in the 3D reconstruction of dam morphology revealed to describe accurately the dam breach evolution in the analyzed time instants.

In general, this work has demonstrated the potential of using methodologies based on digital image analysis for the non-intrusive characterization of hydraulic variables in the experimental context.

References

1. Misra, S.K., Thomas, M., Kambhamettu, C., Kirby, J.T., Veron, F., Brocchini, M.: Estimation of complex air–water interfaces from particle image velocimetry images. Exp. Fluids **40**, 764–775 (2006). https://doi.org/10.1007/s00348-006-0113-1
2. Dupont, E., Dewals, B., Archambeau, P., Erpicum, S., & Pirotton, M.: Experimental and numerical study of the breaching of an embankment dam. In: 32nd IAHR Biennial Congress-Harmonizing the Demands from Art and Nature (2007)
3. Bento, A.M., Amaral, S., Viseu, T., Cardoso, R., Ferreira, R.M.: Direct estimate of the breach hydrograph of an overtopped earth dam. J. Hydraul. Eng. **143**(6), 06017004 (2017)
4. Soares-Frazão, S., Le Grelle, N., Spinewine, B., Zech, Y.: Dam-break induced morphological changes in a channel with uniform sediments: measurements by a laser-sheet imaging technique. J. Hydraul. Res.**45**, 87–95 (2007)

5. Orendorff, B., Rennie, C.D., Nistor, I.: Using PTV through an embankment breach channel. J. Hydro-Environ. Res. **5**(4), 277–287 (2011). https://doi.org/10.1016/j.jher.2010.12.003
6. Amaral, S.: Experimental Characterization of the Failure by Overtopping of Embankment Dams. Ph.D. thesis, Instituto Superior Técnico, Universidade de Lisboa (2017)
7. Amaral, S., Caldeira, L., Viseu, T., Ferreira, R.M.L.: Designing experiments to study Dam Breach Hydraulic Phenomena. J. Eng. (2020). https://doi.org/10.1061/(ASCE)HY.1943-7900.0001678
8. ASTM: Standard practice for classification of soils for engineering purposes (unified soil classification system). ASTM D2487. West Conshohocken, PA: ASTM (2011)
9. Aleixo, R., Soares-Frazão, S. Zech, Y.: Velocity-field measurements in a dam-break flow using a PTV Voronoï imaging technique. Exp. Fluids **50**(6), 1633–1649 (2010)
10. Aleixo, R., Soares-Frazão, S. Zech, Y.: Statistical analysis methods for transient flows–the dam-break case (2018). https://doi.org/10.1080/00221686.2018.1516700
11. Capart, H., Young, D., Zech, Y.: Voronoï imaging methods for the measurement of granular flows. Exp. Fluids **32**, 121–135 (2002)

Monitoring the Madeira Airport Protection Breakwater Using Visual and Unmanned Aerial Vehicle Observations

Rui Capitão, Maria Graça Neves, Pedro Sousa, António Cachaço, Francisco Barros, Paulo Tavares, Pedro Moreira, Conceição Fortes, Décio Rodrigues, and Elsa Franco

Abstract An aerial monitoring system was developed for the maritime structures that protect the foundation columns of the Madeira Island Airport runway infrastructure, in the scope of the research project MEGE, to complement the already existing monitoring program of visual observations. For the aerial monitoring of the berm breakwater, with about 770 m in length, a fast data acquisition system was envisaged. Imaging techniques acquired through a high-resolution camera coupled to an unmanned aerial vehicle (UAV) were used, which allowed for a very fast and efficient automated procedure, compatible with the difficult accessibility to the structure on the seaside. Point clouds corresponding to the breakwater geometry were obtained from the set of aerial images from the camera on board of the UAV, using photogrammetric techniques. In this paper, the two complementary parts of the monitoring of this structure are described and some results are presented.

Keywords Visual monitoring · UAV monitoring · Berm breakwater

1 Introduction

In order to protect the foundation and the base of the columns that support the runway extension of the Madeira airport from the sea wave action, a berm breakwater was built, Fig. 1, along with the "Posto de Socorros a Náufragos" breakwater, being both structures under the jurisdiction of ANA—Aeroportos de Portugal, S.A. The berm breakwater has a development of about 770 m in length and is aligned from SW

R. Capitão (✉) · M. G. Neves · C. Fortes
LNEC, Laboratório Nacional de Engenharia Civil, Lisboa, Portugal
e-mail: rcapitao@lnec.pt

P. Sousa · A. Cachaço · F. Barros · P. Tavares · P. Moreira
INEGI, Instituto de Ciência e Inovação em Engenharia Mecânica e Engenharia Industrial, Porto, Portugal

D. Rodrigues · E. Franco
ANA Madeira Aeroportos, Santa Cruz, Madeira, Portugal

C. Chastre et al. (eds.), *Testing and Experimentation in Civil Engineering*,
RILEM Bookseries 41, https://doi.org/10.1007/978-3-031-29191-3_36

Fig. 1 General view of the berm breakwater and the foundation columns of the airport runway extension, April 2021

to NE, parallel to the rows of columns, with a slope base level largely above the bathymetric of 13.6 m (ZH).

The berm breakwater is a structure with dynamic behaviour, consisting of rocky blocks, with weights between 5 and 40 kN and a profile of 4(H):3(V). As this structure has a deformable slope, a safety line was defined in its design located at a distance (30 m) from the axis of the alignment of the seaside row of the outer columns, a line that must not be exceeded. In this case, intervention is required so as not to compromise the stability of the structure.

Since it is a dynamic structure, it is quite important to know the evolution of this breakwater along its lifecycle, to identify the preliminary stages of damages and the need (or not) of repairing works in due time. This will avoid the progression of damages that could put the foundation in danger and the base of the columns that support the runway of the airport, as well it will avoid extra costs. In this framework and following the LNEC's OSOM+ program of visual observations [1], visual inspections were made in October 2009, June 2012 and December 2013, and a qualitative photo comparison of the different inspections has been performed. Although these visual campaigns give a general view of the evolution of the breakwater and identify the main damage problems, it does not characterize the whole breakwater in a more quantitative and detailed way (profiles, damage volumes, etc.).

In this context, a research project, MEGE— "Structural Monitoring of Large Structures" was proposed with the aim of developing, implementing and operating a system to monitor the structural evolution of Madeira International Airport. The system has two components: the support structure of the runway extension and the berm breakwater that protects the former structure. This paper focuses on the analysis of the berm breakwater.

For the berm breakwater the implemented process will add up to do the existing program of visual observations, and can be divided into two main phases, one corresponding to image acquisition and another to post-processing. The first operation corresponds to use the UAV and capturing the images. The second supports photogrammetric image processing for acquiring 3D point clouds. These point clouds are processed to detect possible changes in the breakwater shape that may have occurred in the time interval between the two flights.

Ideally, monitoring campaigns should be performed at least once a year and after any relevant storm, comparing the campaign results (photos, point clouds, DEM models) obtained in the different instances and identifying possible changes in the geometric configuration of the breakwater. In this way, it is possible to identify movements within the structure occurred between the two instances. With this detailed and accurate information, it is then possible to verify the condition of the structure and analyse in detail areas with stability problems, where blocks were either displaced from its resting positions or even broken. In addition, different surveys can be compared to examine the evolution of structural integrity and identify areas that require intervention to maintain structural function and stability throughout the expected lifespan.

Here the work developed for OSOM+ program and MEGE project for the berm breakwater is presented.

2 The Berm Breakwater

The purpose of the berm breakwater is to protect the foundation and the base of the columns supporting the airport runway extension infrastructure in Santa Cruz (Madeira Island Airport) against sea wave action.

Berm breakwaters are dynamic structures, consisting of rock-fill blocks that are significantly lighter than the weight of the protective armour elements of conventional breakwaters, and also being the thickness of the protective layer much greater than that of those conventional breakwaters. In this type of structure, the profile is expected to deform under the action of waves, resulting in an S-shaped equilibrium configuration, in which the less inclined section of the profile, with higher resistive capacity, is in the active zone of the breakwater [2]. Since this structure has a deformable slope, a safety line was defined in the project, from the axis of the alignment of the front row of the outer columns of the runway structure. According to the project design [3], this distance should not be less than 30 m. The berm breakwater profile was designed for a 50-year return period design wave, with a significant wave height, Hs, of 5.5 m and consists of an all quarry run rockfill core with a 4(H):3(V) slope, protected by a selected rockfill armour with weights between 5 and 40 kN and a thickness of 9 m. The design crest of the profile was 4.1 m (ML), ML being the mean level, corresponding to +1.4 m (CD), Fig. 2.

3 Visual Observation Monitoring

Since 1986, LNEC has been systematically observing maritime structures based on structure monitoring campaigns (a program now-called OSOM+) to monitor

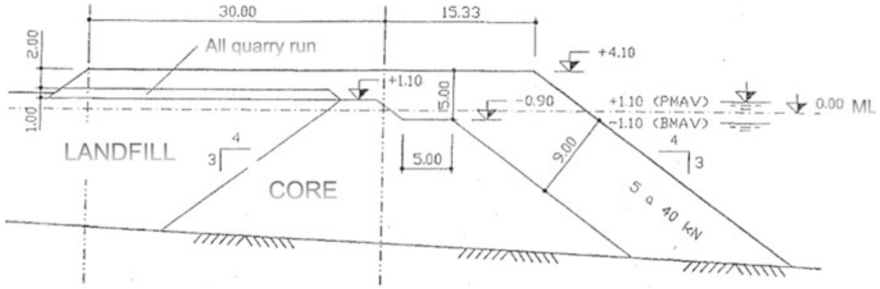

Fig. 2 Cross-sectional profile of the berm breakwater (referred to the ML)

and predict the behaviour of offshore structures along the Portuguese coast and recommend timely maintenance interventions on these structures as needed.

Regarding the evolution of this berm breakwater after its construction, the information available at LNEC refers to visual inspections taken by LNEC technicians in October 2009, June 2012 and December 2013, and to information about surveys carried out in 2018, reported in [3]. Between the year of the first visual inspection (2009) and the year of the second (2012), this breakwater has undergone many of the expected changes in this type of structure (dynamic behaviour structure). The June 2012 campaign witnessed the worsening of the degradation locations identified in 2009, and the emergence of others. At that time, it turned out that the eastern half of the protection was much more affected than the western half [4]. The intense leakage of riprap blocks at the eastern end of the breakwater structure, in the NE zone, was the most worrisome situation at the time. It was thought to be caused by a presumed concentration of wave energy, possibly amplified by the effects risen by the proximity of a large rocky outcrop and by the near permanent maritime structures. However, the erosion line, even in the most eroded sections, was still beyond the safety line of the structure.

Visual observations in 2014 confirmed that two sections of the structure were severely damaged: one is approximately located between the middle of the structure and the eastern edge of the structure, and the other is at the transition from the breakwater to the related infrastructure "Água de Pena" bathing area [4]. In these sections, the distance between the crest of the breakwater and the axis of the columns was less than 30 m, which is to say that, at some points, the safety line had already been exceeded by a few meters.

In Fig. 3 one can observe the evolution of the berm breakwater profile at three instances in time: (a) in December 2013; (b) in October 2019 and (c) in April 2021. Note, however, that tide level conditions are different (lower) in the last observation.

In August 2018 topographic and 3D Multibeam surveys were carried out, the results of which were presented in [3], together with the results of surveys conducted in February 2014 and June 1999. That report states that in two sections the crest setback exceeds the design safety line: from column 14 to 22 (central zone), with about 160 m and between columns 29 and 33, in the NE zone, with about 30 m (see

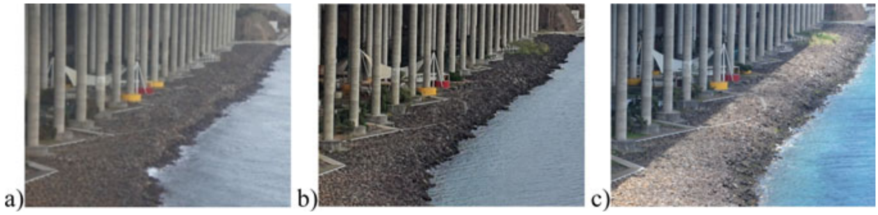

Fig. 3 Berm breakwater in: **a** Dec. 2013; **b** Oct 2019; **c** Apr. 2021

Fig. 4 for identification of referred columns). The crest setbacks registered in the whole structure were generally less than 2 m, reaching a maximum of 3.5 m in the central zone.

In October 2019, the slope continued to show signs of degradation along the breakwater, with the eastern half of the protection being significantly more affected than the western half. It was noted that the safety margin was exceeded in front of some columns (14–22, 30 and 32).

In April 2021 a visual observation was performed by LNEC for this breakwater, including the characterization of its current condition.

Also, during the 2021 campaign, at certain points considered more relevant (see those in Fig. 5), measurements of the distance between the axis of the columns and the slope crest were taken. The measurements are displayed in Fig. 6, which shows the distances measured at each column and the 30 m line, considered in the project as the minimum safety value. The accuracy of the measurement is about ±0.4 m. Measurement errors include uncertainty in defining points defined as vertices, uncertainty in orientation perpendicular to the column, and uncertainty due to the flexibility of the tape measure.

Fig. 4 Reference points on the berm breakwater

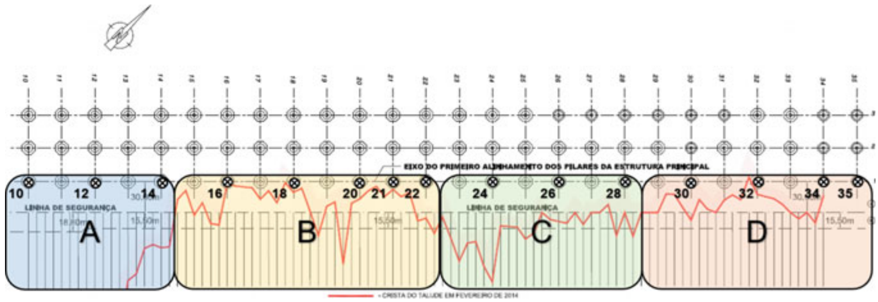

Fig. 5 Identification of sections (A to D) and reference points (10, 12, 14, 16, 18, 20, 21, 22, 24, 26, 28, 30, 32, 34 and 35)—adapted from [3]

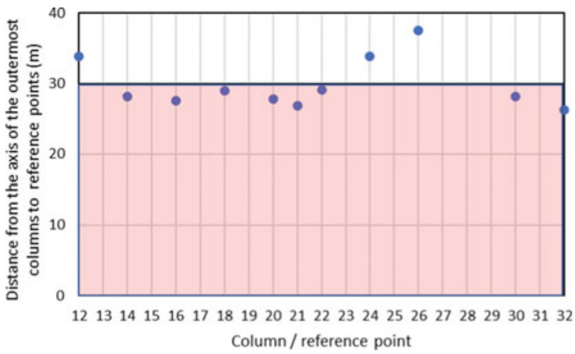

Fig. 6 Distances (in m) from the axis of the outermost column to homonymous reference points

In general, and referring to both Fig. 6 and a wide number of available photographs taken during the 2021 campaign, it can be seen that:

- The slope shows a considerable number of rockfill elements moved in the area in sections A to D revealing some locations of degradation. In particular, in front of columns 16 and 21, the slope deterioration is readily apparent;
- There is a lack of blocks in the area to the east of section A and sections B and C;
- The safety margin has clearly been exceeded in front of columns 14, 16, 18, 20, 21, 22, 30 and 32, with an approximate value varying between 3.7 m (column 32) and 0.9 m (column 22), below the safety line;
- In front of column 18, rockfill blocks from the slope are still there, but there was no evolution compared to 2019.
- In front of column 35, on the existing retaining wall, the same anomalies referred to in October 2019 were also observed, namely distances between blocks on the order of 7 cm, an area with the corner of a degraded block and a distance between blocks on the order of 7 cm and three deteriorated slabs. These distances did not change in the observation performed in April 2021.

Table 1 Levels assigned to the current condition of the berm breakwater in 2021

Section	Level
A	1
B	3
C	2
D	3

According to the campaign of April 2021, the following classifications were assigned to the current condition of the berm breakwater in the year 2021, see Table 1. In this Table, level 1 means that the element/section is in good condition, although showing occasional signs of slight degradation; level 2 indicates that the element/section is slightly degraded; and level 3 suggests that the element/section is degraded.

From the results presented, one should highlight the need to intervene on the structure, especially in sections B and D, to ensure compliance with the distance from the crest to the design safety line.

Presently, in June 2022, repair work is underway on this maritime structure to restore the originally intended project to ensure compliance with the distance from the crest to the design safety line. This work will likely be completed by November 2022, after which new inspections will be carried out both visual and aerial observations using the existing UAV System, described below.

4 The Unmanned Aerial Vehicle (UAV) System

4.1 Image Acquisition

During the 2021 campaign, at the same time visual inspection was conducted, an aerial observation was also carried out. For this, a UAV system was used, complemented with the appropriate control software. As the main body, a "DJI Matrice 600 Pro" drone was selected with a payload consisting of a "DJI Ronin MX" gimbal and a "Phase One iXM-50" high-resolution camera. This camera offers a resolution of 50 MP (Megapixel) at a maximum acquisition rate of 2 fps (frames per second) and was specially manufactured for aerial photography applications (see Fig. 7).

For control, it was necessary to use several applications, namely:

(i) UgCS ground station software (SPH Engineering, Latvia), with which the flight mission plans were planned and executed;
(ii) DJI Go flight controller application (DJI, China), which was used to configure the UAV flight parameters; and
(iii) iX Capture image acquisition application (Phase One, Denmark), used to control the camera.

Fig. 7 UAV system in flight to acquire aerial images

The images were acquired via programmed routes allowing the repeatability of acquisitions in both position and perspective. The route shown in Fig. 8 is the path travelled by the drone followed in one of its missions. Two acquisitions were made with the same route, just varying the camera angle as to obtain more perspectives and thus minimize blind spots in the point cloud.

Flights over the berm breakwater follow a planned path first in the north-east direction, until near the end of the structure, where it is necessary to do a small detour towards the ocean before continuing until the end. Then, the path is repeated in the opposite direction, and with a different camera orientation. Figure 9 shows images of two complementary flights with the same route but different perspectives.

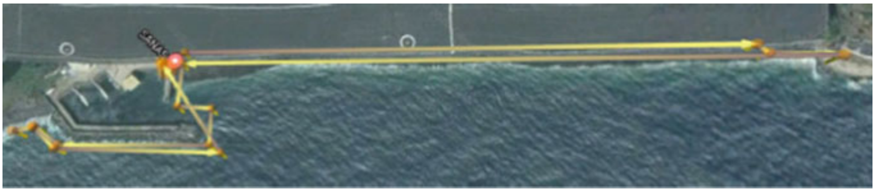

Fig. 8 UAV flight mission

Fig. 9 Images of the first flight over the berm breakwater and the drone's direction of travel

4.2 Photogrammetric Image Processing

After the flight, the acquired images were processed using the Pix4DMapper software (Pix4D SA, Switzerland) and the resulting point clouds were processed using the CloudCompare tool (GPL software, cloudcompare.org).

Due to the camera solution used, it was necessary to start the image acquisition before take-off. After each image acquisition, data from the camera's XQD memory card was transferred to the computer and images in transit were deleted. After that, the images, initially recorded by the camera in proprietary format IIQ (Intelligent Image Quality file format), were converted to TIF (Tag Image file Format). The EXIF (EXchangeable Image file Format) information from these images was also transferred, in order to secure the GNSS (Global Navigation Satellite System) information needed to use as input for processing with the Pix4DMapper photogrammetry software. Figure 10 shows the point cloud of the berm breakwater, for which a GSD (ground sampling distance) of 3.9 mm was obtained with an average reprojection error of 0.076 px (pixel) in the calibration.

To minimize point cloud matching errors, it was also necessary to manually define the correct GPS accuracy values to the ones guaranteed by the UAV. This procedure allows the software to position the camera on each image in a precision volume two hundred times smaller than the volume referring to the precision selected by default. This increase in accuracy of location is translated into faster processing and better correlation, thus minimizing error occurrence.

Image processing with Pix4DMapper is to be performed at two moments in time, before and after any event that causes changes in the geometric configuration of the berm breakwater. A software tool was developed to read and process the PLY format exported by Pix4D to get a regular profile along the breakwater length. Previously it was planned to carry out this operation with CloudCompare, but added development time was compensated by the increased automation and control, as well as the high computational demand of the CloudCompare's graphical interface in a cloud with such a high number of points.

Fig. 10 Resulting point clouds of the berm breakwater, April 2021

Processing starts by rotating the entire point cloud at a predefined fixed angle, corresponding to the orientation of the breakwater with respect to the North direction, resulting in the axis system shown in Fig. 11.

A spacing between profiles and the thickness of the profiles is then defined. For each profile, points within a range of Y coordinates are selected according to the location and thickness of the profile. Inside of this selection, bins were defined, evenly spaced in the X direction, and each one is matched by the mean altitude (Z coordinate) of its points, thus defining the profile.

Another program was also developed that, after rotating this point cloud, allows exporting sections as new point clouds between two Y values. This facilitates further processing in CloudCompare due to the decrease in the total number of points to view and process at once. As an example, 1250 images were acquired in two distinct flights, which generated a cloud of approximately 370 million points. The cloud in its full extent is represented in Fig. 10 and an approximate view can be seen in Fig. 12.

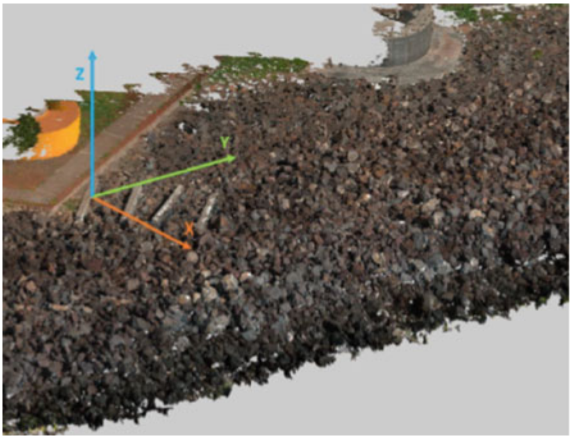

Fig. 11 Coordinate system used in the processing of clouds of points


Fig. 12 Detail of the berm breakwater point cloud

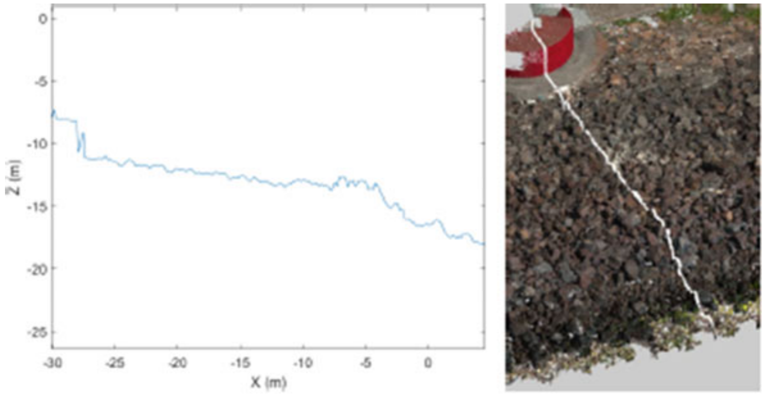

Fig. 13 Example of a berm breakwater profile and their approximate location (in white) in the point cloud

Due to the large dimensions of the breakwater and its horizontal parallel orientation, the drone's camera's field of view actually covers only the breakwater. Therefore, the point cloud contains few unwanted points, and as such, it is not necessary to delete cloud sections to continue processing.

Based on the acquired information it is also possible to extract profiles along the breakwater. Figure 13 shows example profiles, as well as their representation in the point cloud, using a 0.2 m thick profiles and 0.1 m thick bins. By visually inspecting the obtained point clouds and profiles, it can be concluded that these are a good representation of the local geometry of the structure.

5 Conclusions

This work presents two different, but complementary parts of the monitoring system developed for the berm breakwater that protects the foundation columns of the airport infrastructure in Santa Cruz (Madeira Island Airport). This is a special maritime structure with about 770 m in length, that, due to its dynamic profile functioning, needs to be regularly inspected to verify its structural stability.

Based on the OSOM+ program of visual observations, the first methodology was applied to verify its current condition and evolution and, if possible, to predict its future behaviour and enable recommendation of timely maintenance interventions. This made it possible to observe that many expected changes in this type of structure (with dynamic behaviour) have occurred at this breakwater.

Under the MEGE project, a UAV system comprising an unmanned aerial vehicle carrying a camera, was also used for 3D model and profile acquisitions. Aerial images were acquired through pre-programmed routes, which allowed an increased repeatability of acquisition regarding both positioning and perspective. After the flights, acquired images were processed using Pix4DMapper and the resulting point clouds were processed. A custom software tool was prepared to read the point cloud and generate regular profiles along the breakwater length, with a predefined spacing between profiles and with the same reference axis. This system enabled a fast and efficient automated procedure to obtain 3D profiles of the whole breakwater.

Results of the two different (but complementary) methodologies allows one to more soundly verify the evolution of this breakwater and establish a tentative repairing schedule in advance.

In fact, repair work is currently underway on this marine structure to restore the original project. This work will likely to be finished by November 2022, after which a new inspection will be performed both by carrying out visual observation and aerial observation, using the existing UAV.

References

1. Capitão, R., Lemos, R., Henriques, M.J., Fortes, C.J.E.M., Neves, M.G., Silva, L.G., Reis, M.T.: Systematic observation of maritime works. The new OSOM+. In: Proceedings of the 5th Hydrographic Engineering Days, Lisbon, pp. 466–469 (2018)
2. van der Meer, J., Sigurdarson, S.: Design and Construction of Berm Breakwaters. Advanced Series on Ocean Engineering, vol. 40. World Scientific Publishing Co. Pte. Ltd., London (2017)
3. Consulmar: Estruturas marítimas do Aeroporto da Madeira. Relatório da Condição. Rel. No O.1728.00 (in Portuguese) (2018)
4. Silva, L.G., Fortes, C.J.E.M.: Estruturas marítimas do Aeroporto da Madeira. Parecer sobre o seu estado atual. LNEC Technical Report 26/2014–DHA/NPE (in Portuguese) (2014)

Management and Monitoring of Civil Works Using Geographic Information Technology

Pedro Varela, Filipe Morais, José Sousa, Sara Sanches, Adriana Neves, Eliana Carreira, and Alexandra Ferreira

Abstract As part of the operation and maintenance of road infrastructure, was developed a methodology based on mobile applications with ESRI technology to support the management and monitoring of civil works, capable of obtaining multimedia records on site and geographical visualization of work carried out in the field of road infrastructure maintenance. The typology of works presented in the article is of vegetation maintenance of slopes and the preparation phase of the respective works consists both in the collection of slopes with visual inspections, as well as in the risk analysis of slopes with high density of invasive species and trees near the road. With the creation of maps and registration applications adapted for each project (vegetation maintenance service), it is intended to provide the Contractors with real-time geographical orientation, and consequently, a greater operational performance. The intelligent registration and storage of information collected on site, the management platform, integration and validation of data and the production of reports aim to support decision-making in the context of the management of these projects. The methodology presented aims to carry out the progressive digital transition of the procedures previously used, optimizing with the use of geographic technology the efficiency of the management of the civil works.

P. Varela (✉) · F. Morais · J. Sousa · S. Sanches · A. Neves · E. Carreira · A. Ferreira
ASCENDI IGI, Edifício Litografia Lusitana Praça Mouzinho de Albuquerque, Porto, Portugal
e-mail: pvarela@ascendi.pt

F. Morais
e-mail: fmorais@ascendi.pt

J. Sousa
e-mail: jrsousa@ascendi.pt

S. Sanches
e-mail: ssanches@ascendi.pt

A. Neves
e-mail: aneves@ascendi.pt

E. Carreira
e-mail: ecarreira@ascendi.pt

A. Ferreira
e-mail: aferreira@ascendi.pt

C. Chastre et al. (eds.), *Testing and Experimentation in Civil Engineering*,
RILEM Bookseries 41, https://doi.org/10.1007/978-3-031-29191-3_37

Keywords Management and monitoring of civil works and services · Digital transition · Geographical visualization of civil works · Evidence recording · Intelligent data management

1 Introduction

Road transport networks assume a social and economic responsibility, of great impact, in the development of any country and the operation and maintenance of road transport must ensure an adequate level of service, in order to provide safety for road users. In the context of the management of road infrastructure, the main guidelines are the level of service and the safety of road users, based on preventive action in the maintenance and conservation of them [1]. Aiming to ensure the above assumptions, it was developed a project based on the development of a solution capable of collecting georeferenced multimedia data on site and automatically storing its information in a specific database for each project. The solution allows, in real time, to locate and directly access the collected multimedia data, from a map built for each road maintenance work. Currently the solution [2] applies to vegetation maintenance works on geotechnical structures (Slopes). With this project, it is intended to contribute to the management and monitoring of civil works, using geographic information technology, since it aggregates the following tools: (i) density maps of invasive species and maps of risk trees near the road to optimize and prioritize interventions (e.g., vegetation maintenance work); (ii) real-time geographical visualization of the work to be carried out, thus providing substantial efficiency for both the asset manager and the contractor; (iii) intelligent collection and storage of information recorded on site; (iv) data management, integration and validation platform that supports decision-making in the context of project management; (v) production of global and detailed reports by concession, motorway or contract work. Figure 1 shows the various phases that constitute the methodology of management and monitoring of civil works.

This document is divided into 3 main chapters. It begins with an introduction, in which the scope of the work is contextualized, with a presentation of the main goals proposed and the respective tools and methodologies to achieve them. The second chapter describes the several steps of the methodology used. The last chapter presents the main conclusions and the future work.

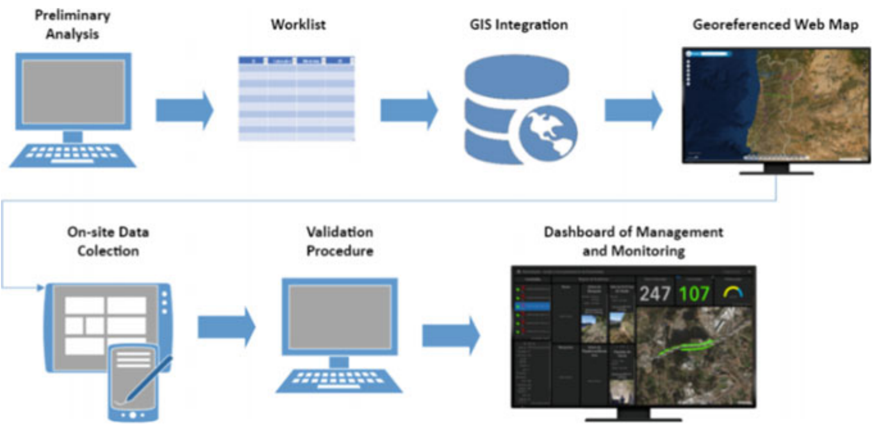

Fig. 1 Methodology workflow

2 Methodology

2.1 *Preliminary Analysis of Works*

The motorway network operated by Ascendi is located between the north and center of the Portugal and in the Greater Lisbon area (Fig. 2), connecting the coast to the interior of Portugal. This geographical dispersion promotes a wide variety of geological, meteorological, topographic and hydrogeological characteristics in the soils [3], and consequently a substantial diversity of flora and fauna. This diversity of the flora implies greater attention and criteria in the definition of vegetation maintenance works, since it is pretend to achieve greater control over invasive species.

In order to achieve the proposed goal, invasive species density and species dispersal maps (Fig. 3) are used, from which a risk analysis is obtained. This analysis intends to locate the area of greatest density of invasive species.

This analysis is complemented by checking the map of trees near the road (Fig. 4). The areas with trees that are most close to the road are integrated into the lists of vegetation maintenance work aimed at the safety of users.

Visual inspection (observation) of slopes is a key activity of the Inspection Plan of these structures [1] since it allows to collect registration information, identify pathologies/occurrences, classifying them by states, in order to identify and monitor the evolution of pathologies and plan maintenance and/or conservation actions [4].

Aiming to properly perform these visual inspections, the vegetation maintenance work list is also composed of the slopes that will be inspected throughout the year (Figs. 5 and 6). The integration of the analyses mentioned provides the production of lists of optimized vegetation maintenance work and allows the prioritization of the areas for each year.

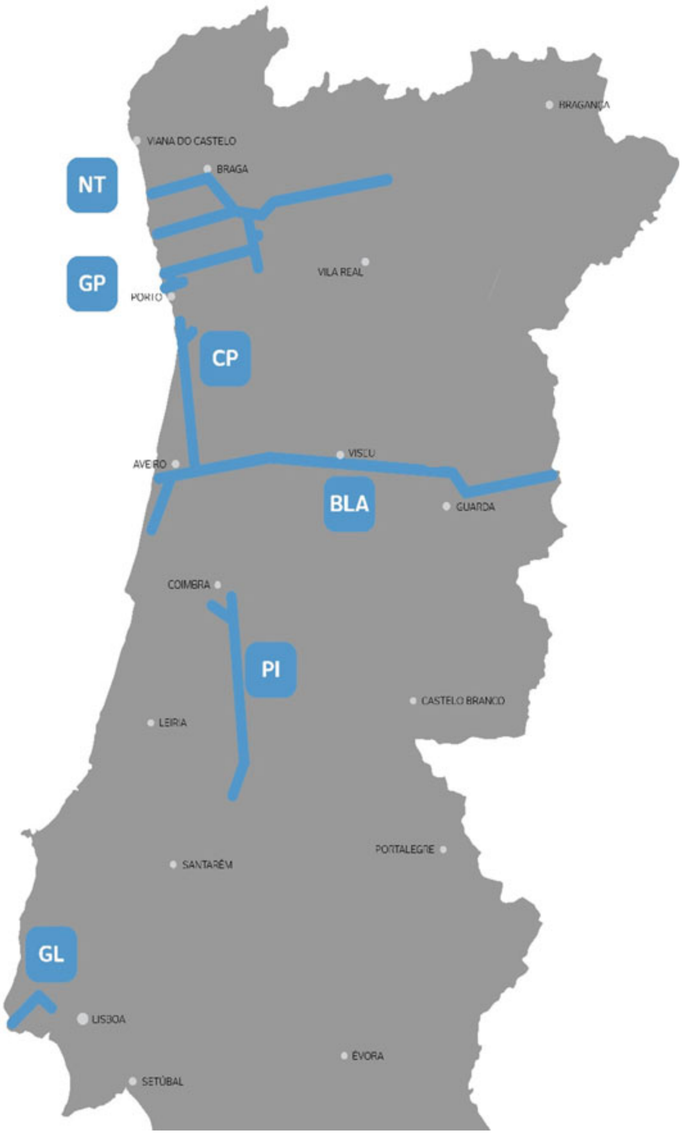

Fig. 2 Map of Ascendi's motorway network

2.2 GIS Information Integration Process

After the definition of the list of vegetation maintenance work to be carried out on the slopes, the processing and integration of the respective information in GIS [5] is

Fig. 3 Invasive species density and species dispersal maps

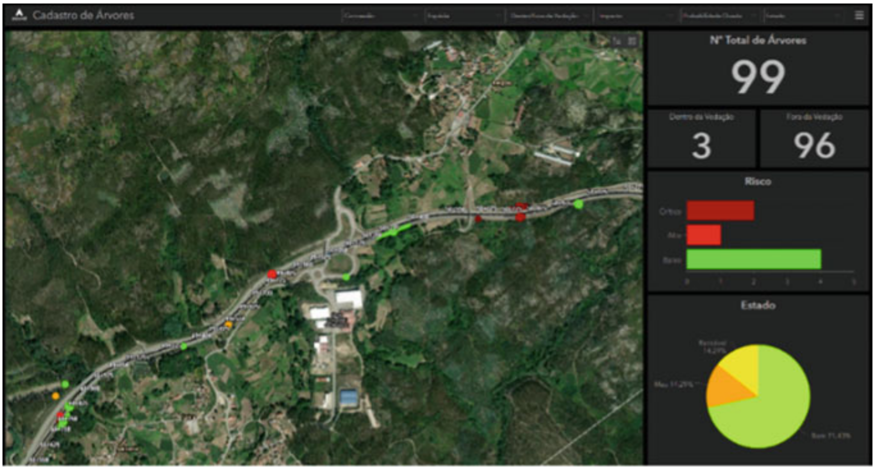

Fig. 4 Risk map of trees near the road

Fig. 5 Visual inspections campaigns

Localização (Autoestrada / Sublanço)	Contagem de TALUDES com Necessidade de Desmatação Integral	Quantidade de Elementos de Drenagem Superficial por sublanço	Nº de Taludes de Aterro	Nº de Taludes de Escavação
A11	412	3808		
Apúlia - EN205	27	132	16	11
Barcelos - Braga Oeste	57	666	31	26
Braga Oeste - Braga (Ferreiros)	21	227	17	4
Calvos - Vizela	40	452	20	20
Celeirós - Guimarães Oeste	80	580	47	33
EN15 - EN211	19	156	12	7
EN205 - Barcelos	39	445	26	13
EN211 - Castelões (A4)	5	38	5	0
Felgueiras - Lousada	38	399	24	14
Guimarães Oeste - Selho	11	42	10	1
Ligação à EN14 - Circular	11	73	8	3
Lousada - EN15	39	313	25	14
Vizela - Felgueiras	25	285	13	12

Fig. 6 Analysis of the slopes with vegetation maintenance and visual inspections to be carried out

followed up, in order to obtain a georeferenced viewer integrated with the information contained in the list of works (Fig. 7).

The process consists of the following phases [6]: (i) crossing the list of identified works with the central database through matriculation which is unique for each slope, (ii) publication of a web layer with the resulting data that combine the registered lopes and their components with an indication that those will be the target of intervention, (iii) creation of a web map with the road network, the published web layer and the surface drainage for tablet/mobile application, (iv) inclusion of the asset components in the catalogue of the collection application on the website.

2.3 Applications for on Site Data Collection

The monitoring and management of civil works is a key activity on road maintenance. In this context, a mobile solution was developed that combines the following applications: (i) ArcGIS Field Maps; (ii) ArcGIS Survey123.

The first consists of a georeferenced map with the locations of the works to be carried out (see 1st image in Fig. 8) [7]. From this map the user selects the asset (Ex. Slope) for which he will collect data (evidence of work, such as road maintenance work). Data collection starts from the link described as “Register” that grants direct access to the second application—the registration form, in which evidence is collected according to the scheme represented in Fig. 8.

2.4 Evidence Validation Process

After the onsite collection of multimedia data, the evidence validation process follows. This consists on the asset manager validation of the work performed (Fig. 9),

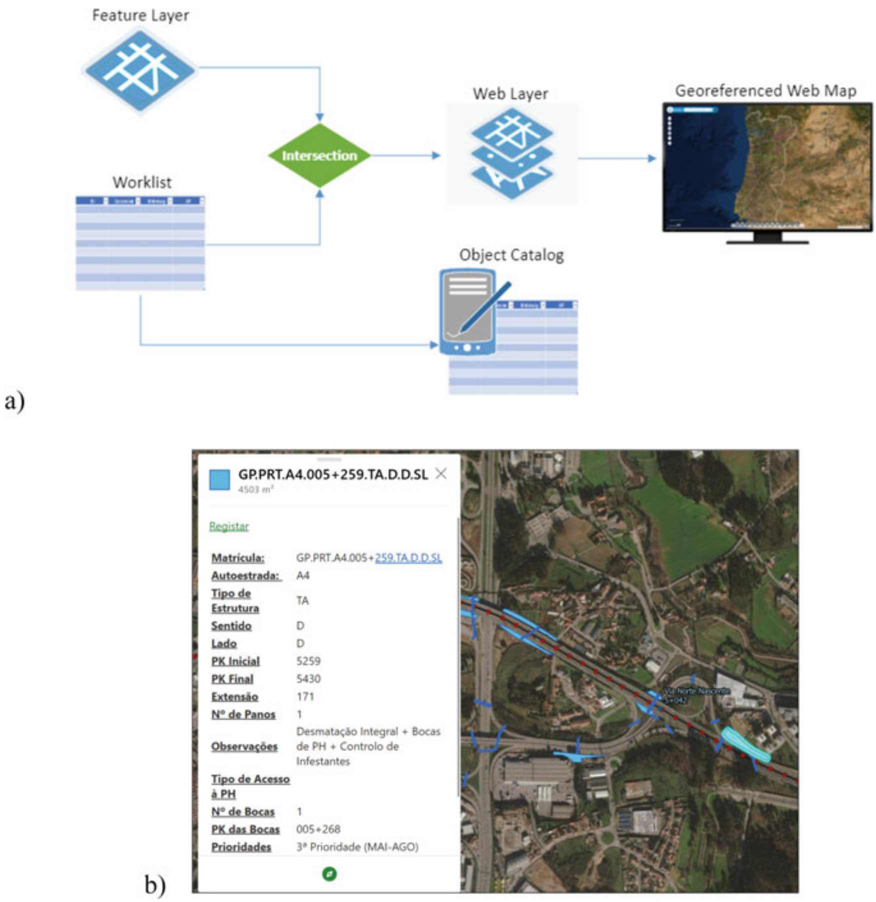

Fig. 7 Integration process—**a** Integration Flow, **b** Georeferenced viewer with integrated information

which is based on the verification of the conformity of all the contracted requirements in the lists of works [7]. The validation routine of the work aims to ensure the regularity of monitoring the vegetation maintenance work, as well as update with reliable data, the platform of management and monitoring of the work (Fig. 10).

2.5 *Management and Control of Road Works*

The management and control platform of multimedia evidence collected on site, and updated in real time, consists of interactive management dashboards, combining the location of the assets with the respective information obtained, allowing the

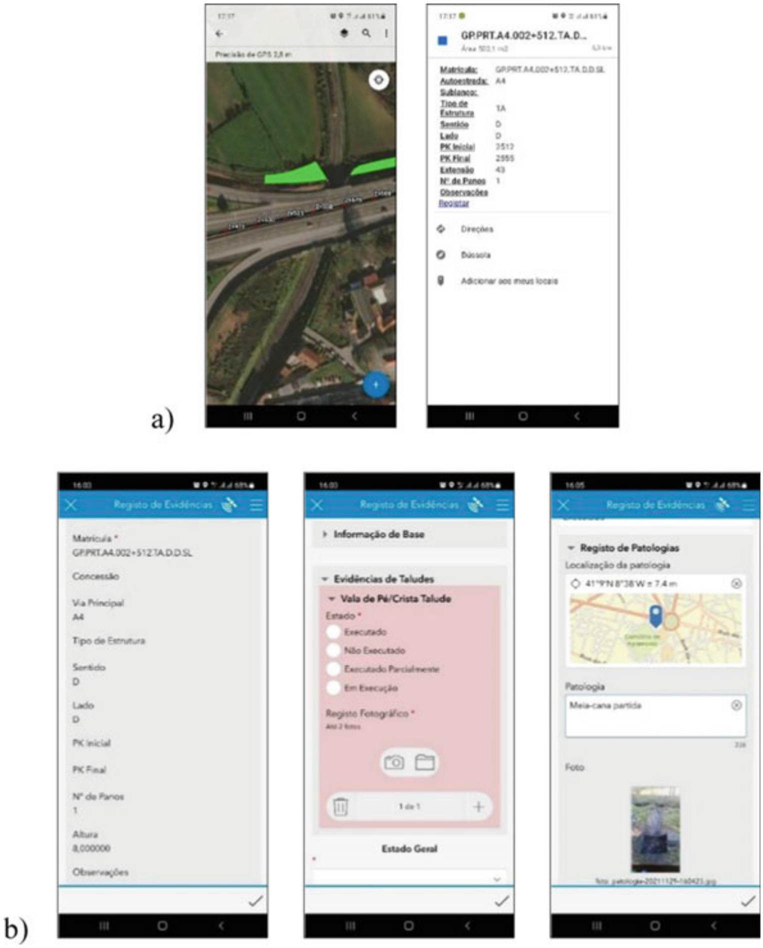

Fig. 8 Application use scheme—a Georeferenced Map and b Evidence registration form

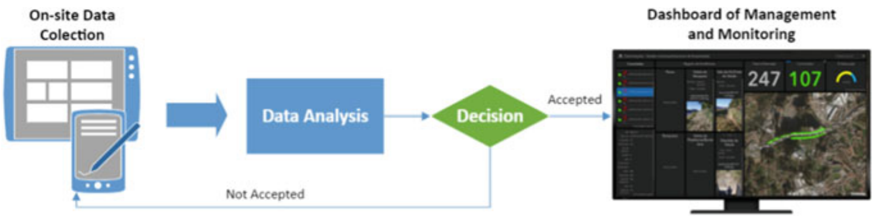

Fig. 9 Evidence validation workflow

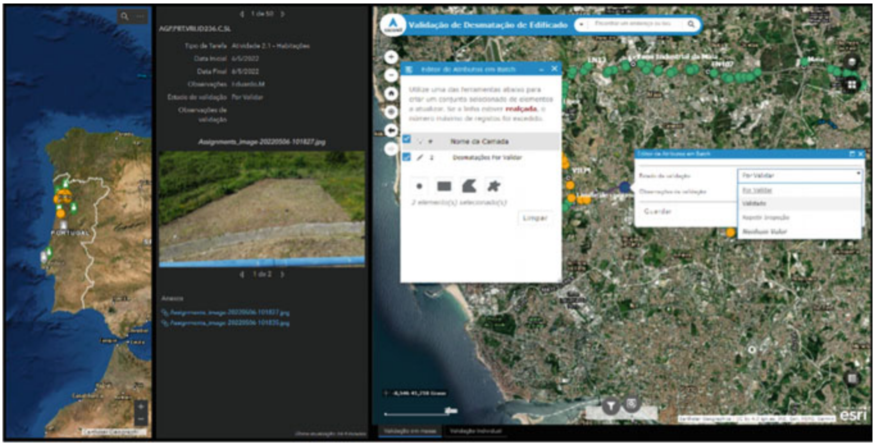

Fig. 10 Process of validation of work evidences

manager of the project:—to ascertain the quality,—compliance of the work carried out, and—to support the decision-making as shown in Fig. 11.

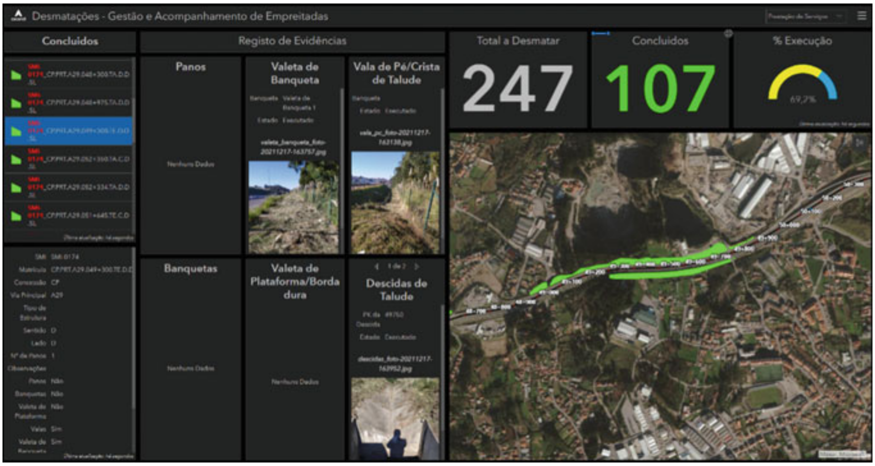

Fig. 11 Interactive dashboard for management and control of civil works

3 Conclusions

The use of geographic information technology has made it possible to optimize the management and monitoring of road infrastructures, providing greater efficiency in the analysis of the information collected, which is:—uniform,—standardized,—innovative, and—useful to confirm and highlight the work performed. In addition to the tools presented, this solution allows the obtaining of comprehensive and detailed reports of ongoing works and is an assistant in the management and control of the work. This solution is currently operational and is used in several vegetation maintenance works. It aims to use digital transition tools to achieve gains in terms of:—temporal efficiency,—quality control, and decision-making in the management of projects.

With experience and the evolution of the volume of data collected, we conclude that this tool will tend to be increasingly effective, given that the detail of the asset manager's analysis will increase, as will the quality of the multimedia evidence. As a future goal, the intention is to expand this methodology to all types of highway maintenance and conservation work. In addition to the features and gains mentioned above, this tool contributes to a more sustainable management of the projects, as it reduces the consumption of paper, being the consultation of the georeferenced maps, the registration of the work and validation carried out in a centralized platform. Digital transformation presupposes a change of mentality in the business culture, and with the latest technology of geographic information system, it is provided tools for contractors and employees to ensure the success of this great transformation that aim to improve performance and obtain greater process efficiency.

References

1. Ascendi: Plano de Controlo e Qualidade–Concessões e Subconcessões (2013)
2. Field Operations | Field Apps to Optimize Efficiency. https://www.esri.com/en-us/arcgis/products/field-operations/overview. Accessed Nov. 29, 2021
3. Ferreira, A., Varela, P.: Geotechnical Infrastructure Observation and Auscultation Manual (2022)
4. Ferreira, A., Neves, A., Sanches, S.: Sustims-Muros & Taludes. 9° Congr. Rodoviário Port. (2018). http://66.39.134.64/docs/A54S222-9CRP_Artigo_147.pdf. Accessed Nov. 27, 2019
5. Hellawell, E.E., Lamont-Black, J., Kemp, A.C., Hughes, S.J.: GIS as a tool in geotechnical engineering. Proc. Inst. Civ. Eng. Geotech. Eng. **149**(2), 85–93 (2001). https://doi.org/10.1680/geng.2001.149.2.85
6. Reddy, G.P.O.: Spatial data management, analysis, and modeling in GIS: principles and applications. In: Reddy, G.P.O., Singh, S.K. (eds.) BT-Geospatial Technologies in Land Resources Mapping, Monitoring and Management, pp. 127–142. Springer International Publishing, Cham (2018)
7. Arora, N., Ogra, A.: Mobile GIS for construction quality managers and surveyors (2012)

Development of a Cohesive Model for CFRP-To-Steel Bonded Joints for Low and High Temperatures

Hugo Biscaia, Miguel Machado, Marta Carvalho, Telmo Santos, and Yongming Yang

Abstract This work analyses the impact of low and high temperatures on the bond between Carbon Fiber Reinforced Polymers (CFRP) and steel substrates. The aim of the experimental tests is to study the local and global bond behaviors of CFRP-to-steel joints under different temperature conditions. The results suggest that high temperatures are more severe for the joints than negative ones. Based on the experiments and on the data collected from the literature, a unified and updated cohesive model with temperature dependency is proposed.

Keywords CFRP · Steel structures · Bond · Temperature · Cohesive modeling

1 Introduction

The use of Carbon Fiber Reinforced Polymers (CFRP) to repair and strengthen existing structures has spread all over the world. However, the influence of temperature variations on the bond between the CFRP and the steel substrates is a key aspect of the success of the externally bonded reinforcement technique. Despite the influence of low temperatures on the bond performance of CFRP-to-steel joints is still barely known, high temperatures are known to severely affect these joints [1]. Therefore, researchers, e.g. [2], have been testing several CFRP-to-steel bonded joints under different temperature conditions to improve the current understanding of the bond performance of these joints in the presence of a positive temperature variation. Two main parameters are known to affect these bonded joints. One is the difference between the thermal expansion coefficient between the CFRP composite and the steel substrate that increases the interfacial slips of the joint. The other one is the glass transition temperature (T_g) of the adhesive used to bond the CFRP composite to the

H. Biscaia (✉) · M. Machado · M. Carvalho · T. Santos
NOVA School of Science and Technology, Caparica 2829-516, Portugal
e-mail: hb@fct.unl.pt

Y. Yang
School of Mechanics and Safety Engineering, Zhengzhou University, Zhengzhou, China

C. Chastre et al. (eds.), *Testing and Experimentation in Civil Engineering*,
RILEM Bookseries 41, https://doi.org/10.1007/978-3-031-29191-3_38

steel substrate. In this case, when the temperature reaches T_g, the adhesive, usually an epoxy resin, loses its initial vitreous state and shifts to a rubbery state. This means that the initial properties of the adhesive are severely degraded, which compromises the bond between materials. Such degradation can be explained through the local bond behavior of the CFRP-to-steel joint which allows us to obtain design-oriented equations to predict the full debonding process [3] or to study other situations using a numerical strategy where the finite difference [1], finite element [4, 5] or discrete element method [6] can be used. Therefore, the present work aims to increase the available experimental data on the bond performance of CFRP-to-steel joints under temperature variations as well as to propose a unified and updated cohesive model that can be implemented into a numerical procedure and thereby estimate the impact of low and high temperatures on these joints.

2 Experimental Program

2.1 Characterization of the Materials

Two different CFRP composites were used. One was fabricated at the Harbin Institute of Technology in China and another one was supplied by a local Sika supplier. The first one, herein denoted has a HIT-CFRP composite that has a width and thickness of 25 mm and 1.46 mm, respectively, whereas the Sika-CFRP composite has a corresponding width and thickness of 20 mm and 1.26 mm. The determination of the mechanical properties of the CFRP followed ASTM D 3039/D 3039-00 [7]. Based on 10 HIT-CFRP flat coupons, the calculated mean tensile strength (f_{fm}) and strain (ε_{fm}) were 1824 MPa (Coefficient of Variation—CoV = 4.1%) and 1.00% (CoV = 5.1%), respectively. The calculated mean elastic modulus was $E_{fm} = 180.5$ GPa (CoV = 2.5%). In the case of the Sika-CFRP composites, the 5 flat coupons led to the following mean results: $f_{fm} = 1836$ MPa (CoV = 2.8%), $\varepsilon_{fm} = 1.13\%$ (CoV = 9.6%) and $E_{fm} = 163.3$ GPa (CoV = 4.2%).

The adhesive used to bond the CFRP composites to the steel substrate was a two-component thixotropic epoxy resin (SIKADUR-30) and it was supplied by a local supplier. The mechanical properties of the adhesive were based on 4 flat coupons (with a dog bone configuration) that allowed us to determine a mean tensile strength (f_{rm}), a mean rupture strain (ε_{rm}) and a mean elastic modulus (E_{rm}) of, respectively, 21.8 MPa (CoV = 7.6%), 0.33% (CoV = 12.5%) and 8.4 GPa (CoV = 3.0%). Moreover, according to the supplier, the vitreous transition temperature of the resin is 67 °C.

The steel was not experimentally determined and the values given by the supplier were assumed. Therefore, the tensile strength of the steel is $f_s = 540$ MPa whilst its yielding strength is 400 MPa. The elastic modulus of the steel was considered to be $E_s = 210$ GPa.

2.2 Geometry and Manufacturing of the Specimens

All the CFRP-to-steel bonded joints had a double lap configuration and all were tested under a steady-state temperature condition, i.e. after imposing the temperature variation to the specimens an external load was applied to them until failure. The specimens consisted of two steel bars with 50 × 5 mm (width × thickness) with two different lengths of 150 mm and 260 mm each (see Fig. 1) with a gap between them of 10 mm.

Before the bonding operations, the manufacturing of these joints consisted of preparing the materials. To that end, the surfaces of the steel bars were first pretreated with a sander and then cleaned with acetone to remove any existing dust or grease from the steel surfaces. The surfaces of the CFRP strips were also cleaned with acetone. Then, the two components (A and B) of the adhesive were mixed according to the recommendations of the supplier, i.e. both parts were mixed with a ratio of 3:1 by weight until a homogeneous mixture was obtained. The bonded area on the steel bars was limited by masking tape and the adhesive was put on this area. The thickness of the adhesive along the bonded length was kept constant by using a small acrylic bar with 1 mm of thickness on the steel bars parallel to the CFRP strips. Then, the CFRP laminate was placed on the adhesive and, finally, a weight was put on top of the CFRP strip. After, 48 h this operation was repeated for the other side of the specimens. The specimens were left for curing at room temperature conditions for one week, i.e. approximately 20 °C.

After this period, and to induce the debonding in one side of the specimens, a mechanical anchorage was installed to the shorter steel plate. The other side of the specimen was kept free of any additional anchorages and its free bonded length varied between 150 mm and 200 mm. The motive to change this bonded length lies in the effective bond length of the CFRP-to-steel joint that tends to grow with high temperatures. The effective bond length is, per definition, the length beyond which the bond strength of the joint cannot increase anymore [2, 3]. So, to avoid the bond strength of the specimens could not be affected by this parameter, the specimens subjected to high-temperature levels had the longest bonded length whereas the specimens with a bond length of 150 mm were mainly used to study the influence of negative temperature variations on CFRP-to-steel joints. It is noteworthy to mention that the dimensions of the specimens (see example in Fig. 1) were all limited by the

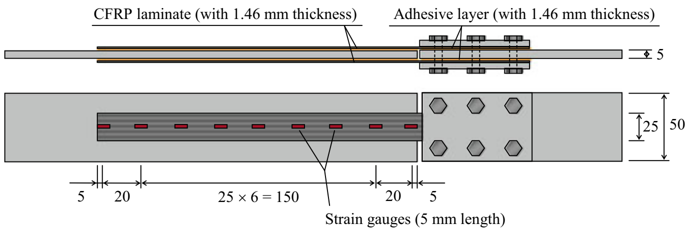

Fig. 1 Scheme of one type of specimen subjected to high temperatures. Dimensions in mm

dimensions of the testing machines available in the laboratory and by the dimensions of the heating chamber.

2.3 Test Setup and Test Procedure

Although two test procedures were followed in this work, one for positive temperature variations and another one for negative temperature variations, the test setup adopted in all the specimens are the same, i.e. all the specimens were subjected to a pull–pull loading (see Fig. 2). In the case of the negative temperature variations, the specimens were tested in an MTS tensile machine with 100 kN of capacity (see Fig. 2a) whereas a Zwick machine with a maximum capacity of 50 kN (see Fig. 2d) was used for the testing of the specimens subjected to positive temperature variations. The interval considered for the negative temperature variations ranged between −216 °C and 0 °C whilst the interval considered for the positive temperature variations stayed between 0 °C and 75 °C. It should be noted that due to the lack of a chamber where such negative temperatures could be created, a container with a cylinder shape was printed in a 3D printer inside which the specimens were placed (see Fig. 2b and c). The negative temperatures were then created by throwing into the container a liquid at the idealized temperature. Therefore, to obtain a temperature approximately of −20 °C, an anti-freezing liquid was kept in a freezer at around −28 °C whilst temperatures of −80 °C and −196 °C were achieved through the use of dry ice and liquid nitrogen, respectively. Such cryogenic temperature level intends to simulate the temperature in outer space and thereby, allow us to analyze the possibility of using CFRP-to-metallic joints in space applications. Nevertheless, the results obtained from these two last temperature conditions are herein considered preliminary results. To control the temperature of the specimens during the tests, a regular thermography camera was used also as well as a regular thermometer that measured the liquid inside the container (see Fig. 2b) during the test.

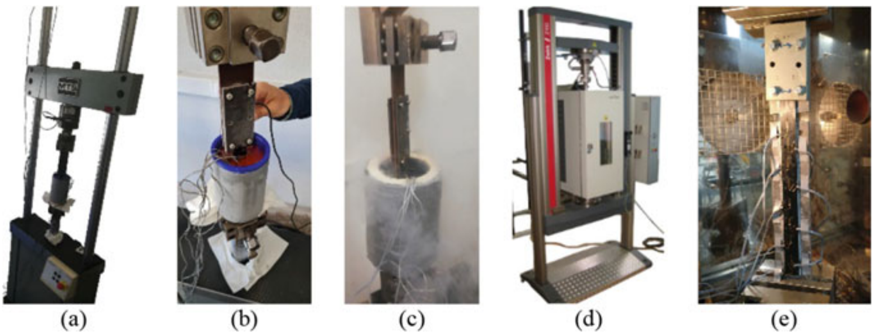

Fig. 2 Test setup of the specimens subjected to negative and positive temperature variations

The CFRP strains were measured by using strain gauges from a TML supplier (CFLA-6-350-11-6FB3LT-F and BFLA-5-5-3L) that were bonded onto the CFRP strips (see Fig. 1). Although for opposite reasons, the procedures adopted in all the specimens were similar and included 3 different phases. Since negative and positive temperatures will cause the tension or the compression of the specimens, respectively, the first phase considered the specimens attached only to the inferior grip of the tensile machine. Therefore, no mechanical loads were considered in this first phase and the CFRP strains measured during this phase are due to the temperature variations caused by the liquid (negative temperatures) or by the heating chamber (positive temperatures). After the strains in the CFRP seemed to register a stable value, the upper grip was attached to the specimens which correspond to the second phase of the testing procedure. The third phase is the initiation of the loads transmitted to the specimens in which, and since two different tensile machines were used, a regular displacement of 0.01 mm/s was considered for the specimens under negative temperatures and a regular load of 80 N/s was considered for the specimens under positive temperatures. Since both load increments are quite small, no influence on the experimental results was expected to occur.

3 Experimental Program

In total, 34 specimens were manufactured and tested until now. The complete list of the specimens tested in this work is shown in Table 1. It should be noted that despite all specimens having been manufactured at the same time, a gap of approximately 3 years between the tests with positive and negative temperatures required the consideration of new reference tests. Therefore, in Table 1, it can be seen three types of specimens with no temperature variation, i.e. $\Delta T = 0$ °C. The adopted designation (ID) of the specimens had the following designation "CS/X/Y/n" which logic is explained next. The "CS" denotes Carbon and Steel and "X" indicated the CFRP supplier, "Sika" or "HIT". For "Y", it is identified as the temperature of the test, and "n" is a sequential ID number to distinguish the repeated tests carried out in the experimental program. However, in those cases where the tests were not repeated, such as under temperatures of −80 °C and 50 °C, their designation was shortened to only "CS/X/Y". So, as an example, the designation CS/HIT/T-20/02 means this CFRP-to-steel bonded joint was manufactured with the CFRP laminate provided by HIT and it was a second test where a temperature of −20 °C was considered.

Table 1 ID of the specimens

ID of the specimens	Bonded length, L_b (mm)	No. of tests	Temperature, T (°C)	Temperature variation, ΔT (°C)
CS/Sika/T20/01|05	150	5	20	0
CS/Sika/T-20/01|05	150	4	−20	−40
CS/Sika/T-80	150	1	−80	−100
CS/Sika/T-196/01|02	150	2	−196	−216
CS/HIT/T20/01|04	150	4	20	0
CS/HIT/T-20/01|04	150	4	−20	−40
CS/HIT/T20/01|03	150	3	20	0
CS/HIT/T35/01|02	200	5	35	15
CS/HIT/T50	200	1	50	30
CS/HIT/T65/01|02	200	2	65	45
CS/HIT/T80/01|02	200	2	80	60
CS/HIT/T95/01|02	200	2	95	75

4 Results and Discussions

4.1 *Bond Capacity*

To analyze the bond capacity of the CFRP-to-steel joints, the maximum loads obtained in each specimen as well as the average value obtained in each analyzed case are indicated in Fig. 3. The results are grouped in three different figures (from Fig. 3a to c) to facilitate their analysis. So, regarding the negative temperatures, the tests suggest that the bond capacities of the CFRP-to-steel joints tend to decrease with the decrease in the temperature. For instance, when the temperature drops to −20 °C, the maximum load transmitted to the CFRP decreased by approximately 22% in the specimens whether they were built with Sika or HIT CFRP laminates. Since only the CS/Sika specimens were tested under −80 °C and −196 °C, the decreases of the maximum loads in these specimens were approximately 64% and 88% from the reference average value (tested at $T = 20$ °C). Such reductions may indicate that the adhesive used may not be adequate for so low temperatures. In fact, the supplier recommends its use for applications where temperatures may vary between 8 °C and 35 °C.

In the other case with positive temperatures, the same effect can be observed, i.e. the maximum loads transmitted to the CFRP-to-steel specimens tend to decrease with the increase of the temperature. In this case, when the temperature was increased from 20 °C to 35 °C, the load capacity of the joints was almost not affected which confirms the recommendation made by the supplier. As the temperature was increased, and the temperature of T_g was reached, the loads transmitted to the joints tended to decrease rapidly. Even at $T = 65$ °C, the bond capacity loss of the joints was 31%, and for the

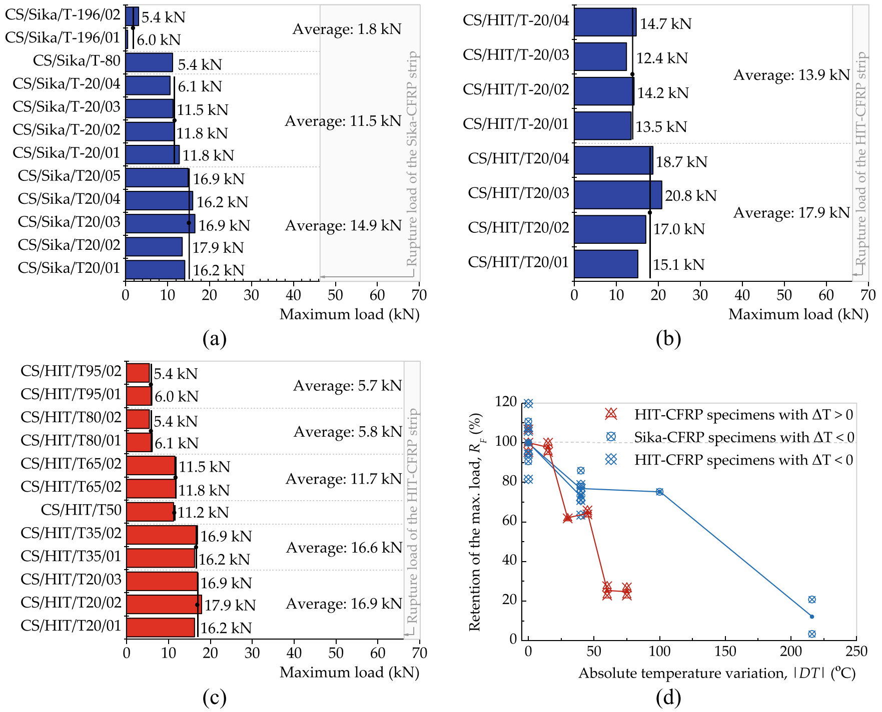

Fig. 3 Maximum loads in all specimens (**a**)–(**c**) and their degradation with the temperature variation—in absolute value (**d**)

other two higher temperature levels the loads transmitted to the joints were reduced by approximately 66%.

To analyze the degradation of the CFRP-to-steel joints due to the temperature influence, the following retention parameter was defined:

$$R_F = 100 \times F_{\max,Ti} / F_{\max,T0} \tag{1}$$

where $F_{\max,Ti}$ and $F_{\max,T0}$ are, respectively, the maximum loads transmitted to the CFRP strip at the test temperature T_i and at the reference temperature T_0, i.e. at room temperature of 20 °C. So, considering the HIT-CFRP specimens subjected to the temperature variations of ($\Delta T = -40$ °C and 45 °C) it can be noticed from Fig. 3d that the influence of positive temperature variations is more severe for the CFRP-to-steel bonded joints than the negative variations. For instance, the calculated average retentions of the specimens CS/HIT/T65/01 and CS/HIT/T65/02 correspond to a decrease of the maximum load of approximately 35% whereas specimens CS/HIT/T-20/01 to CS/HIT/T-20/04 had an average decrease of approximately 27%. Even considering specimen CS/HIT/T50 (with $\Delta T = 30$ °C) the load decrease is higher (38%) than that calculated for the specimens CS/HIT/T-20/01 to CS/HIT/T-20/04.

With the aim of estimating the bond capacity of the CFRP-to-steel bonded joints more accurately, the present results were inserted into a list of other results that can be found in the literature. Compared with a previous work carried out by the authors [2] where a total of 166 results were considered, the current model was now updated with a total of 351 results meanwhile available in the literature. Furthermore, the number of tests with negative temperature variations has also increased from only 4 tests (ranging from −40 °C to −20 °C) to 31 tests ranging now a broader interval of negative temperatures (between −196 °C and −16 °C). Another important improvement to the original model in [2] is the assumption that, under negative temperature variations, the bond capacity of the CFRP-to-steel joints can be affected and therefore, should be considered. It should be noticed also that due to the so limited number of existing tests with negative temperatures, more tests are needed under these negative temperatures allowing us to predict the maximum loads of CFRP-to-steel joints with higher accuracy. For all these reasons, the proposed model is designated as a preliminary analytical model whereas the original one is hereafter denoted as an "old" analytical model. In Fig. 4a the analytical model is compared with the "old" one and, at the same time, the experimental data is shown. So, based on all the available data, the preliminary model now proposed is:

$$F_{\max}(T)/F_{\max,0} = \{f_3 - (1 - f_3)/\left[1 + \exp\left(-f_4\left(T/T_g + f_5\right)\right)\right]\} \times \{1 - 1/\left[1 + \exp\left(-f_1\left(T/T_g - f_2\right)\right)\right]\} \quad (2)$$

where $f_1, f_2, f_3, f_4,$ and f_5 are dimensionless parameters that can be obtained by a fitting procedure where the sum of the quadratic errors between Eq. (2) and the experimental data is minimized. In this case, the values of these parameters were found to be $f_1 = 3.476$, $f_2 = 1.403$, $f_3 = 0.022$, $f_4 = 1.878$ and $f_5 = 1.783$. The first term in parenthesis in Eq. (2) intends to estimate the maximum loads of the CFRP-to-steel joints subjected to negative temperature while the aim of the other term in parenthesis is to predict the maximum loads when the temperature

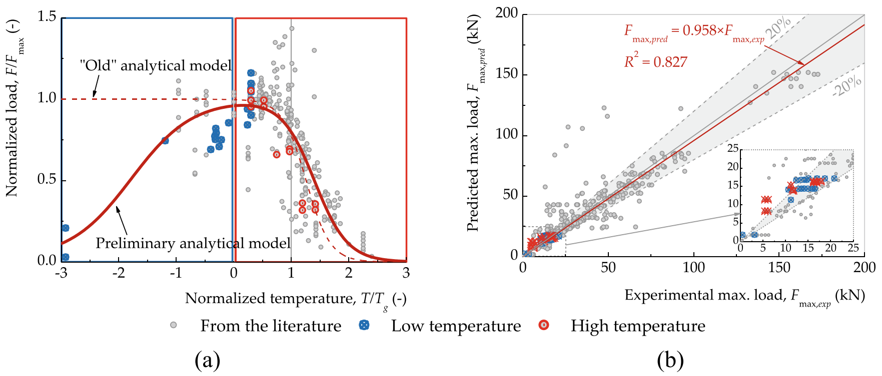

Fig. 4 Proposed semi-empirical analytic model (**a**) and its accuracy (**b**)

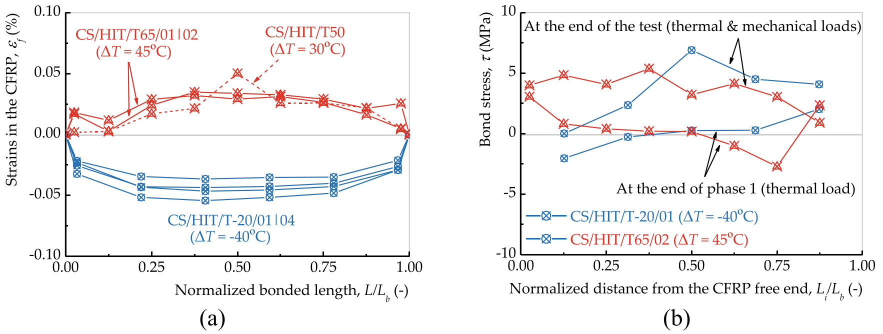

Fig. 5 CFRP strains throughout the bonded length due to temperature variations (**a**) and bond stresses within the interface throughout the bonded length (**b**)

variations are positive. This explains why the values obtained for f_1 and f_2 had a slight variation from their original values ($f_1 = 4.804$ and $f_2 = 1.258$) [2]. The accuracy of Eq. (2) is shown in Fig. 4b. The results show that the predicted maximum load ($F_{\max,pred}$) is slightly underestimated by 4% with an R^2 of 0.827 which reveals a good approximation to the experimental data of the preliminary analytical model. Moreover, only the results obtained from some Sika and HIT specimens fell outside the interval of -20% to 20% of deviation.

4.2 CFRP Strains Caused by Temperature Variations

The strains developed in the CFRP during the temperature variations, i.e. at the end of the first phase of the test procedure are shown in Fig. 5a. Despite the opposite signal, the absolute strains in the CFRP are quite similar in these cases. In terms of absolute values, the results show that the highest strains are concentrated at the center of the CFRP-to-steel joints. Since both CFRP ends are free, the strains tend to zero at these two points of the bonded length as expected. Nevertheless, the CFRP strains developed in all the specimens are too far away from their rupture value which means that temperature per se cannot lead the CFRP to a cohesive rupture in the composite. Therefore, due to the high stiffness of the steel bar, it would be expected that the adhesive and/or the interfaces adhesive-CFRP or steel-adhesive are the regions where the degradation of the joints may be localized.

4.3 Interfacial Bond Stresses

The determination of the interfacial bond stresses can be made from the equilibrium of a finite length dx of the CFRP bonded to the substrate, e.g. [8]:

$$\tau\left(x_{i+1/2}\right) = (1+\beta)\cdot E_f t_f(\varepsilon_{i+1}-\varepsilon_i)/(x_{i+1}-x_i) \tag{3}$$

where β is the ratio between the axial stiffnesses of the CFRP and the steel; E_f and t_f are, respectively, the elastic modulus and the thickness of the CFRP; the difference $(\varepsilon_{i+1} - \varepsilon_i)$ corresponds to the strain difference between two consecutive strain measurements and $(x_{i+1} - x_i)$ corresponds to the distance between those two strain measurements.

As an example, Fig. 5b shows the bond stress distributions throughout the bonded length of specimens CS/HIT/T-20/01 and CS/HIT/T65/02 at the end of phase 1 of the test (i.e. due to the thermal loading only) and at the end of the test (i.e. at failure). Due to the thermal loading only, the bond stresses developed in the specimens have opposite signals. However, as the loads are applied to the specimens, the bond stresses tend to increase at the CFRP-loaded end, and when the maximum bond stress ($\tau_{\max}$) is reached it tends to decrease afterwards. As the debonding process continues, the localization of $\tau_{\max}$ tends also to move towards the CFRP-free end.

5 Unified and Updated Cohesive Model

5.1 Local Bond Behavior

Depending on the type of materials of the bonded joint, the shape of the local bond behavior may show different patterns. In the case of CFRP-to-steel joints, it is usually accepted that the local bond behavior can be represented by a bilinear relationship that relates the bond stresses developed within the interface with the slips. This bond–slip relationship is characterized by a first elastic stage followed by a softening and linear stage. In the transition between stages, the interface reaches its maximum bond stress (τ_m) with a slip s_m. The complete separation of materials is reflected in the bond–slip relationship at the end of the softening stage when no bond stresses develop within the interface. At this point, the slip is denoted s_f. The area under this bilinear bond–slip relationship is denoted as the fracture energy (G_F) which, under a pull–pull test, corresponds to a pure fracture mode II. However, due to the temperature influence, these parameters will change (see Fig. 6a). So, the "old" analytical model [2] considers all of these by assuming that the elastic stiffness (K_E), the softening stiffness (K_S), and the fracture energy all vary with temperature variations.

Based on the experimental results herein reported plus the ones recently available in the literature, the "old" analytical model [2] is now unified and updated in order to consider the influence of negative temperature variations. Therefore, the elastic and the softening stiffnesses, and the fracture energy of the CFRP-to-steel joint can be estimated according to:

$$\begin{aligned} K_E(T)/K_{E,0} = &\left\{k_{e3} - (1-k_{e3})/\left[1+\exp\left(-k_{e4}\cdot\left(T/T_g + k_{e5}\right)\right)\right]\right\} \\ &\times\left\{1 - 1/\left[1+\exp\left(-k_{e1}\cdot\left(T/T_g - k_{e2}\right)\right)\right]\right\} \end{aligned} \tag{4}$$

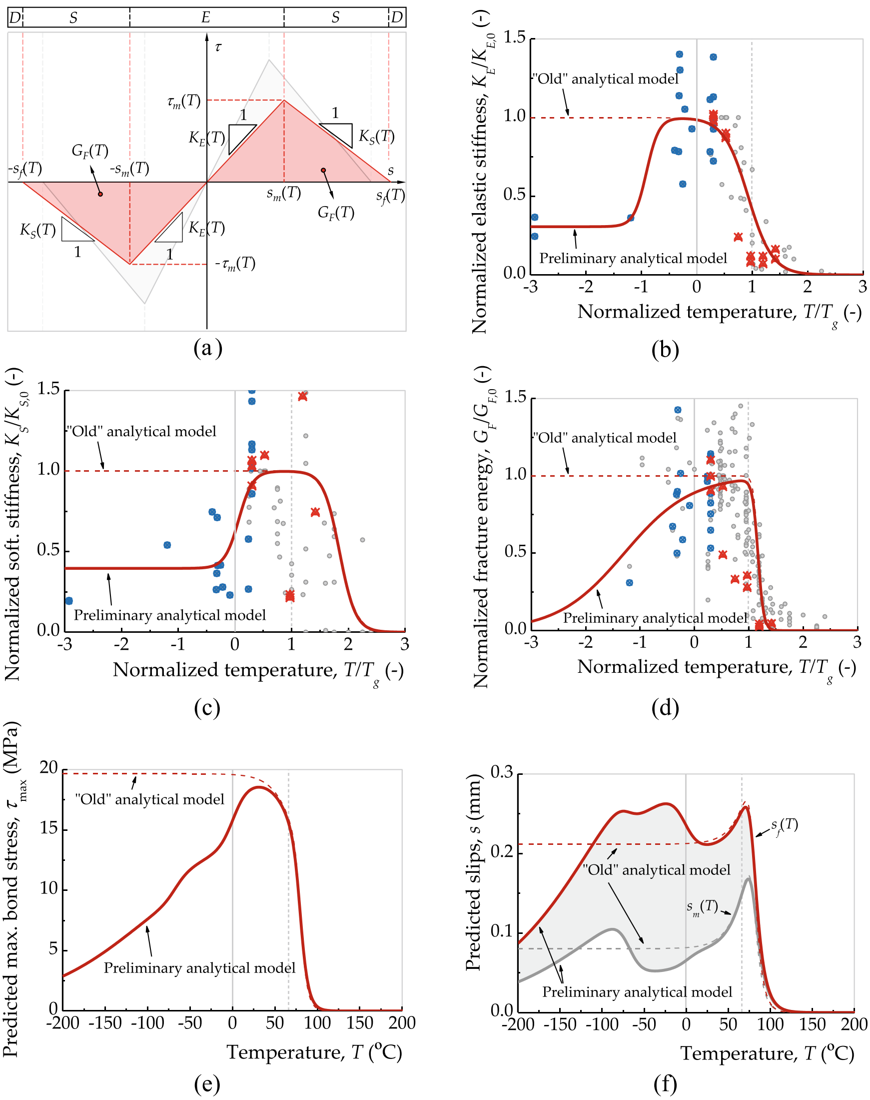

Fig. 6 Temperature-dependent cohesive model

$$K_S(T)/K_{S,0} = \left\{k_{s3} - (1 - k_{s3})/\left[1 + \exp\left(-k_{s4} \cdot \left(T/T_g + k_{s5}\right)\right)\right]\right\} \times \left\{1 - 1/\left[1 + \exp\left(-k_{s1} \cdot \left(T/T_g - k_{s2}\right)\right)\right]\right\} \quad (5)$$

$$G_F(T)/G_{F,0} = \left\{g_3 - (1 - g_3)/\left[1 + \exp\left(-g_4 \cdot \left(T/T_g + g_5\right)\right)\right]\right\} \times \left\{1 - 1/\left[1 + \exp\left(-g_1 \cdot \left(T/T_g - g_2\right)\right)\right]\right\} \quad (6)$$

where k_{e1} to k_{e5}, k_{s1} to $k_{s5,}$ and g_1 to g_5 are all dimensionless parameters that were obtained by fitting Eqs. (4)–(6) with the experimental data through a minimization process where the condition to minimize the sum of the quadratic errors between results was used; $K_{E,0}$ and $K_{S,0}$ are the elastic and softening stiffnesses of the joint determined with $\Delta T = 0$, i.e. with no influence of the temperature; and $G_{F,0}$ is the pure mode II fracture energy calculated when $\Delta T = 0$. Fig. 6a–dshow the development of Eqs. (4)–(6) along with the experimental data available in the literature and makes also a comparison with the "old" analytical model [2]. The values of these dimensionless parameters were found to be $k_{e1} = 4.560$ (previously 4.953), $k_{e2} = 0.924$ (previously 1.000), $k_{e3} = 0.306$, $k_{e4} = 8.746$, $k_{e5} = 0.910$, $k_{s1} = 7.079$ (previously 6.401), $k_{s2} = 1.843$ (previously 1.000), $k_{s3} = 0.396$, $k_{s4} = 8.000$, $k_{s5} = 0.331$, $g_1 = 19.092$ (previously 10.176), $g_2 = 1.169$ (previously 1.107), $g_3 = 0$, $g_4 = 1.625$, $g_5 = 1.291$.

Based on the properties of the bilinear bond–slip relationship, the variations of $\tau_{\max}$, s_m and s_f, can be determined, respectively, through the following expressions:

$$\tau_{\max}(T) = \{2G_F(T) \cdot K_E(T) \cdot K_S(T)/[K_E(T) + K_S(T)]\}^{0.5} \tag{7}$$

$$s_{\mathrm{m}}(T) = \{2G_F(T) \cdot K_S(T)/[K_E(T) \cdot (K_E(T) + K_S(T))]\}^{0.5} \tag{8}$$

$$s_f(T) = \{2G_F(T) \cdot [K_E(T) + K_S(T)]/[K_E(T) \cdot K_S(T)]\}^{0.5} \tag{9}$$

Fig 6e and f show the influence of temperature on $\tau_{\max}$, s_m, and s_f for a CFRP-to-steel joint with $K_{E,0} = 244.1$ MPa/mm (i.e. $\tau_{\max,0} = 19.65$ MPa), $K_{S,0} = 149.6$ MPa/mm (i.e. $s_{m,0} = 0.081$ mm), and $G_{F,0} = 2.081$ N/mm (i.e. $s_{f,0} = 0.212$ mm) [9]. Furthermore, a comparison between the current proposed model with the "old" one is also shown in Fig. 6e and f. Unlike the "old" model, the results herein obtained suggest that negative temperature variations degrade also the local bond behavior of CFRP-to-steel joints. Nevertheless, negative temperature variations seemed to have a smoother impact than positive temperature variations. For instance, with a temperature of $T = 100$ °C the maximum bond stress decays to 0.36 MPa whilst for $T = -100$ °C the maximum bond stress is still 7.61 MPa, which represents a decrease of approximately 61%. Similar observations can be drawn for the slips (see Fig. 6f). However, in some negative temperature levels, the slips predicted by the current model are even higher than those predicted by the "old" model where negative temperatures had no impact on these parameters. This occurs when $s_m \in\,]-129$ °C; -67 °C[and $s_f \in\,]-111$ °C; 16 °C[.

5.2 Numerical Example

To show how the proposed model can be useful for the prediction of the bond behavior of CFRP-to-steel joints, the debonding process of specimens CS/HIT/T-20/01|04 and

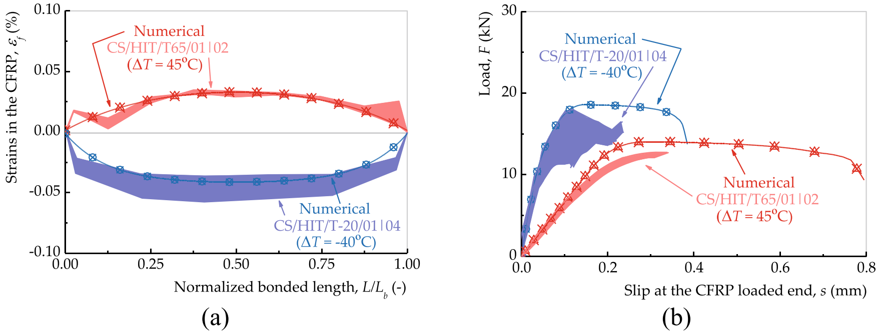

Fig. 7 Distribution of the CFRP strains (**a**) and load–slip curves (**b**)

CS/HIT/T65/01|02 were simulated each with LS-DYNA R12 through a tridimensional model. Despite the thermal expansion coefficients of the CFRP and steel have not been experimentally measured, it was assumed the following typical values for CFRP and steel $\alpha_f = 0.3 \times 10^{-6}$/°C and $\alpha_s = 12 \times 10^{-6}$/°C, respectively [9]. The CFRP strains developed throughout the bonded length and the load–slip relationship obtained from both cases are shown in Fig. 7a and b, respectively.

The results that the CFRP strains before the applications of the loads are very well predicted. Nevertheless, when subjected to negative temperature variations, the CFRP strains are slightly higher than those obtained from the numerical model. The load-slip curves shown in Fig. 7b show that positive temperatures lower than T_g are still more damaging than negative ones. Moreover, the results obtained from the simulations of negative temperature variations were closer to the experimental data than the results obtained from the positive temperature variations. This may be explained by the scarce results available in the literature on the negative side of the temperature which leads the model to closely predict the experimental results obtained in this study. On the other hand, with a larger number of tests carried out with CFRP-to-steel joints with positive temperatures, the numerical simulations, in this case, overestimate the debonded load of the joints by approximately 20%. In this case, the numerical simulations showed also a higher plateau at maximum load than that experimentally obtained.

6 Conclusions and Future Work

The results allowed us to conclude that the load capacity of the specimens is mainly affected by higher temperatures. The proposed model reflects this behavior, which is quite accentuated when the temperature reached the T_g of the adhesive. Based on a wide database, these degradations were incorporated into a unified and updated cohesive model that when implemented into a numerical procedure, the debonding process of the simulated specimen could be well simulated. Due to the lack of results on the influence of negative temperature variations on CFRP-to-steel joints, a gap was identified which needs to be mitigated in the future with more tests to confirm and/or adjust the current proposed analytical model.

Acknowledgements The authors gratefully acknowledge the support of the Foundation for Science and Technology (FCT — MCTES) for its financial support via the project UIDB/00667/2020 (UNIDEMI) and exploratory project JOIN4SPACE (EXPL/EME-APL/0994/2021).

References

1. Biscaia, H.C., Chastre, C., Viegas, A., Franco, N.: Numerical modelling of the effects of elevated service temperatures on the debonding process of FRP-to-concrete bonded joints. Compos. B Eng. **70**, 64–79 (2015)
2. Biscaia, H., Ribeiro, P.: A temperature-dependent bond-slip model for CFRP-to-steel joints. Compos. Struct. **217**, 186–205 (2019)
3. Biscaia, H., Chastre, C., Silva, M.A.G.: Analytical model with uncoupled adhesion laws for the bond failure prediction of curved FRP-concrete joints subjected to temperature. Theoret. Appl. Fract. Mech. **89**, 63–78 (2017)
4. Biscaia, H.: The influence of temperature variations on adhesively bonded structures: a non-linear theoretical perspective. Int. J. Non-Linear Mech. **113**, 67–85 (2019)
5. Biscaia, H.: Closed-form solutions for modelling the response of adhesively bonded joints under thermal loading through exponential softening laws. Mech. Mater. **148**, 103527 (2020)
6. Biscaia, H., Micaelo, R., Chastre, C.: Cyclic performance of adhesively bonded joints using the Distinct Element Method: damage and parametric analysis. Compos. B Eng. **178**, 107468 (2019)
7. ASTM D. 3039/D 3039-00. Standard test method for tensile properties of polymer matrix composite materials, p. 10 (2000)
8. Biscaia, H.C., Canejo, J., Zhang, S., Almeida, R.: Using digital image correlation to evaluate the bond between carbon fibre-reinforced polymers and timber. Struct. Health Monit. **21**(2), 534–557 (2022)
9. Biscaia, H., Carvalho, M., Martins, A.P., Micaelo, R.: Interfacial failure of circular or tubular hybrid bonded joints: A theoretical description. Eng. Fail. Anal. **132**, 105936 (2022)

Automatic Classification of Facades Using Image Colour Differences

Marta Torres-González, Jónatas Valença, Ana Silva, and Maria P. Mendes

Abstract Non-invasive vision-based approaches provide the precision and reliability required for building facade inspection. A method based on automatic image classification to detect and map the materials and anomalies in building facades is presented and compared with a traditional visual inspection and classification.

Keywords Image processing · Façade coating · Colour analysis · Anomalies · Automatic mapping

1 Introduction

The development in digital imaging and computer systems are enabling innovative computer vision solutions to support the inspection and evaluation of buildings facades' conservation state. These cost-effective and non-invasive approaches rely on digital cameras, computers and algorithms, and are being preferred to those traditional methods. Solutions based on analysis of multi-spectral images, including visible (VIS) and near infrared (NIR) regions of the electromagnetic spectrum, were presented to map materials and anomalies [1]. Latest improvements include the use of hyperspectral image analysis based on image clustering [2], and HSV (Hue, Saturation and Value) colour system to detect biological colonization and colour characterization and variation on surfaces [3, 4]. However, not rarely, the methods mentioned are difficult to apply by non-computer vision specialists.

M. Torres-González (✉) · J. Valença · A. Silva · M. P. Mendes
CERIS, IST-ID; Ulisboa, Lisboa, Portugal
e-mail: mtorres18@us.es

J. Valença
e-mail: jonatas.valenca@tecnico.ulisboa.pt

A. Silva
e-mail: ana.ferreira.silva@tecnico.ulisboa.pt

M. P. Mendes
e-mail: mpaulamendes@tecnico.ulisboa.pt

C. Chastre et al. (eds.), *Testing and Experimentation in Civil Engineering*,
RILEM Bookseries 41, https://doi.org/10.1007/978-3-031-29191-3_39

The widespread of commercial robotic platforms for data acquisition, such as unmanned aerial vehicle (UAV), opens new possibilities to the construction sector [4, 5]. However, the automation of data acquisition and processing are still under research and in development to be a user-friendly tool for facade inspection. Further, the availability of powerful machine and deep learning tools promotes its application in building inspection [6, 7]. The disadvantages of the aforementioned methods are generally related to the difficulties of the algorithms in dealing with surfaces that present multiple and combined materials and anomalies, such as the presence of biological colonization, moisture stains, delamination, efflorescence, among other anomalies commonly found on building facades.

Furthermore, the automatic classification is also influenced by the light conditions during the inspection. The external elements such as air conditioning equipment, facilities or trees results in a more complex classification of the images and requires a more detailed work. In addition, the innovative deep learning applications, which work as "black boxes", often require large and comprehensive training datasets to be generalized and extend the limits of validation beyond the training set.

Thus, the development of methods in computer vision that are simple to implement and understandable by non-experts represents an important contribution to this field.

This paper presents a method based on image classification to detect and map pathology in building facades, namely: (i) location of critical areas, with a high probability of containing damages; (ii) identification of materials and anomalies; (iii) detailed and comprehensive maps of results. In order to assess their effectiveness, the proposed method was applied to the facades of three identical buildings in Bairro de Alvalade, in Lisbon, each one with a different degradation condition. The results were compared with a traditional visual classification for validation purposes. The analysis enables to evaluate the ability of the method to identify materials and anomalies with similar photometric characteristics, and its capacity for location and mapping with high efficiency. The outputs of the method allow a reliable evaluation and reduce the inspection time, decreasing the possibility of human error and enabling process automation.

2 Method

The proposed method takes advantages of classifying images at the pixel level based on the HSV and CIELab (Commission internationale de l'éclairage) colour systems, the latter to detailed evaluation of Colour Differences (hereinafter, ΔE). Classification is performed on the visible light spectrum and based on colour differences against a user-selected colour reference. Besides the anomalies usually identified, the method can also take into account aesthetic parameters due to slight colour variation. The main steps of the method proposed are the following:

(i) Image acquisition $\rightarrow$ automatic and structured image acquisition of facades with a camera Nikon D810 and a focal length of 50 mm (7369 $\times$ 4912 pixels) mounted in a *GigaPan* robotic head. The set-up allows to capture a set of images of a selected scene in a pre-define order, to build gigapixel panoramas of the facades;

(ii) Build ortho-mosaics → post-processing the set of images to create the high-quality panoramas in the *Image Composite Editor* software, and build high resolution ortho-mosaics of the facades in *Adobe Photoshop*;

(iii) Traditional visual inspection → definition and labelling of materials and pathology by using a drawing software, *i.e. Autodesk Autocad v.2021*. This consists of the identification and mapping of all the stains present in the facades. This step works as a reference to assess the level of accuracy of virtual image processing;

(iv) Color evaluation → The images are processed in the three HSV channels and the ΔE is computed [8]. To establish whether the changes in colour are appreciable by the human eye, the ΔE is calculated according to Standard EN 15,886:2010 [8]. If it is greater than five ($\Delta E > 5$), the colour variation is perceptible by the human eye, being admissible values less than ten ($\Delta E < 10$).

3 Case Study

The proposed method was applied to the facades of three identical buildings built in 1948 in Bairro de Alvalade, at Lisbon, Portugal. This neighbourhood was developed in the 1940s as part of the urban expansion policies of the city of Lisbon and promotion of new housing areas, led by the Engineer Duarte Pacheco and established in the Lisbon Urbanization Master Plan (PDUL). This plan foresaw the construction of 12.000 dwellings for a population of 45.000 inhabitants in an area of about 230 hectares. To significantly increase the number of social housing, the previous model of single-family housing is replaced by collective housing, with a maximum of four floors to avoid the placement of elevators, according to a left/right typology [9].

A large-scale construction program of *Economic Income Houses* started between 1947 and 1956. The case studies belong to Cell I and were built in 1948. They are in João Lúcio St. (the front façades of No.4, No.7, and No.9), a one-way street with a parking line for vehicles and abundant vegetation that grows in the front gardens of each private property. In this regard, it is important to note that the city's climate – average annual minimum temperatures of 13.6 °C, maximum mean temperature 21.8 °C, minimum relative humidity of 47.6%, maximum relative humidity of 85.4% and a rainfall rate of 66.6 mm according to the records from 1998 to 2018 by the meteorological station situated in Lat: 38º46'N; Lon:09º08W; Alt.:104 m, from *Instituto Português do Mar e da Atmosfera* (IPMA). The orientation of the street – east/west – favors the growth of trees, shrubs, and all kinds of biological organisms, as the high degree of soil moisture and the indirect sunlight in the front gardens shows this fact. The facades of properties No. 7 and No. 9 do not receive the direct incidence of solar radiation at any time because they have north orientation (Fig. 1).

Fig. 1 General overview of Alvalade neighbourhood at Lisbon, Portugal, and location (red circle) of the three identical buildings (#4, #7 and #9)

These case studies' facades present a main central entrance to six dwellings, a central core of vertical communication, fourteen windows and four balconies with locksmith, a large cornice of ceramic tiles, wiring for electrical installations and external air conditioning equipment fixed to the façade (Fig. 2). The main materials used in the cladding of the facades are red brick glazed, a plinth half a meter high made of cement mortar, and current renderings with yellow pigments. The construction of these buildings was based on modular coordination principles. As stated in the *Regulamento Geral de Construção Urbana* [10], all the dwellings had reinforced concrete slabs on the floors of the kitchens and bathrooms, while the rest were built with wooden beams and Portuguese floors. Also noteworthy is the introduction of reinforced concrete beams on all floors on the facades.

The three facades were built more than 50 years ago, and a progressive state of degradation has been evident from worst to best – from façade No.4 to façade No.9 –, as it can be shown in Fig. 2. Façade No. 4 presents the worst state of conservation, since it is the only one without maintenance intervention. Despite its current appearance, this façade is the one that has been better "in situ" preservation conditions due to the direct sunlight, as it is in South orientation. On the contrary, façade No.9 (North orientation) was recently renovated, presenting fewer anomalies, and it is considered the reference to be used for the comparison. The anomalies considered in this work were the stains – superficial dirty, runoff, raising damps,

Fig. 2 Three facades analysed in João Lúcio street at Bairro de Alvalade, Lisbon: (**a**) building No.4; (**b**) building No.7; and (**c**) building No.9

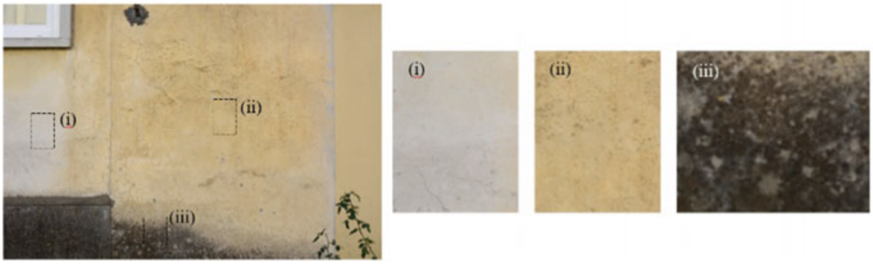

Fig. 3 State of degradation of the cladding: (**i**) salts, (**ii**) presence of superficial dirt, and (**iii**) biological colonization (Images of the No.7 front façade)

thermophoresis, biological growth, corrosion stains and graffiti – mainly originated due to the moisture and the relative humidity conditions in this area of the city. As it can be shown in Fig. 3, the cladding does not present the original colour in all façades, and lighter and darker areas can be found.

4 Results and Discussion

4.1 Anomalies Mapping by Visual Inspection

The panorama obtained for the three case studies allows to elaborate a planimetric survey as defined in Sect. 2. All the stains present in the facades were drawn in a traditional time-consuming manual approach, distinguishing between dark and light stains (Table 1).

4.2 Anomalies Mapping by Image Classification

A previous general analysis was performed in the H, S and V channels for colour thresholder evaluation. A Matlab App [10] facilitates the expedite selection of the main yellow colour of the façade in the H (hue) channel (Fig. 4). This allows not only to obtain an automatic general mask that eliminate external elements (e.g., trees, cars, windows or air conditioning machines), but also to obtain an indicative percentage of the façade in healthy state of conservation (Table 2). In this method, the yellow colour linked to a good state of conservation is related to the human perception, because the H channels values are just slight affected by shadows and brightness, which in the HSV colour system are manifested in the other channels.

This is an approach to obtain rapid and general results. However, these results could be improved by working directly with the post-processing image that includes a mask for eliminating unnecessary pixels' information, together with a study of the

Table 1 Planimetric survey and mapping of the stains (visual inspection)

	Façade No. 4	Façade No.7	Façade No.9
Original image (250ppp)			
	108.79m^2 - Cladding area	98.84m^2 - Cladding area	108.00m^2 - Cladding area
Building elevation			
	South orientation	North orientation	North orientation
Planimetric survey	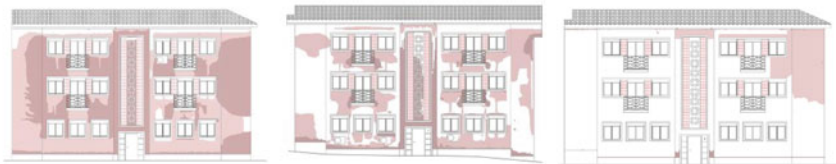		
	100.49m^2 – 53.07% - Dark stains 42.75m^2 – 39.29% - Light stains 100.49m^2 – 92.37% - Total stains	17.27m^2 – 17.47% - Dark stains 34.69m^2 – 35.10% - Light stains 51.96m^2 – 52.57% - Total stains	1.472m^2 – 1.36% - Dark stains 16.707m^2 – 15.47% - Light stains 18.179m^2 – 16.83% - Total stains

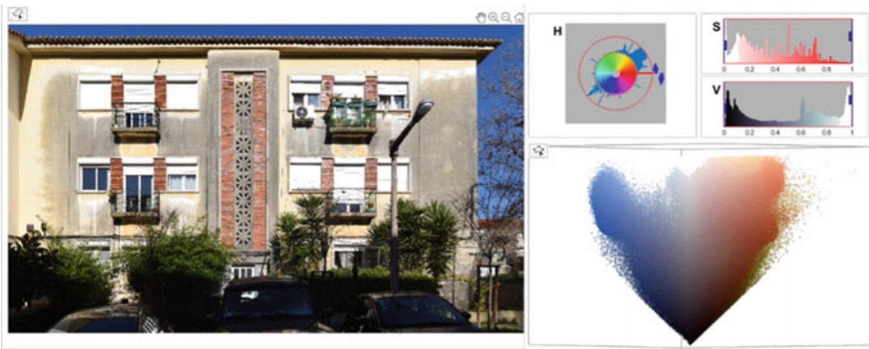

Fig. 4 Visualization of the colour thresholder (example of façade No.4)

colour difference (ΔE). Table 3 presents the results based in the analysis of ΔE and taking as reference the yellow colour (indicated in Table 3 with a red rectangle), considering that colour as good state of conservation of the façade. Then, the maps for ΔE < 10, ΔE < 15, ΔE < 20 and ΔE < 30 allow to map stains areas.

Table 2 HSV analysis of the 3 façades

	Façade No.4	Façade No.7	Façade No.9
Original mosaic			
Automatic mask		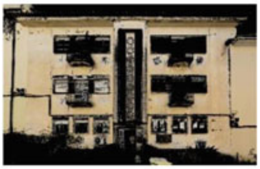	
Cluster adjusted	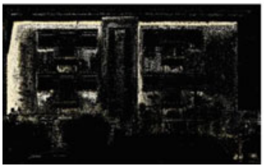 59.5%	 65.2%	 70.9%

4.3 *Comparison of Manual Drawing and Image Classification*

Different facts were revealed when comparing manual drawing carried out in Sect. 4.1 with the image processing analysis of the images in Sect. 4.2. Figure 5 presents the comparison between the areas mapped with stains from both methods. The results showed that regardless of the method applied, facade No. 4 clearly presented the worst apparent state of conservation, since almost the entire surface is stained.

Stains in Facade No.4 are well differentiated of the cladding reference yellow colour, and the maps obtained for $\Delta E < 20$ are close to the measurement manually obtained (Fig. 5). On the opposite side, results of Facade No. 9 indicate the best state of conservation and demonstrate that the classification with $\Delta E < 10$ (considered the maximum value perceptible by human eye) is closely to the values obtained manually. The results also demonstrate that image processing based on ΔE have the necessary precision to reproduce a careful visual inspection, due to the similar results for $\Delta E > 10$. Thus, the use of expedite image processing methods works properly with the case studies evaluated: (i) for high level stains, results similar to traditional manual mapping are achieved for $\Delta E < 20$ or $\Delta E < 30$, corresponding to differences clearly perceptible to human eye [i.e., Façade No.4]; (ii) for low level of stains, the results that better match the traditional method are achieved for $\Delta E < 10$, where the colour differences start to be hard to be perceived by the human eye [i.e., Façade No.9]. In any case, as long as the colour difference is greater than 10 ($\Delta E > 10$), it will be

Table 3 Analysis of ΔE in the 3 case studies

	Façade No.4	Façade No.7	Façade No.9
Original image			
Image with mask	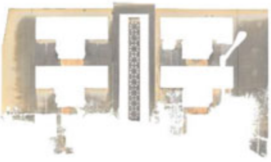 (30,453,611 px)	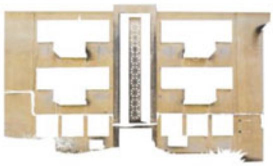 (27,571,516 px)	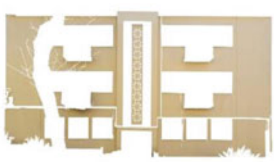 (24,690,532 px)
ΔE<10	 0.78 %	 28.88%	 17.17%
ΔE<15	 52.30%	 84.52%	 95.26%
ΔE<20	 91.36%	 89.21%	 98.27%
ΔE<30	 96.53%	 94.80%	 99.13%

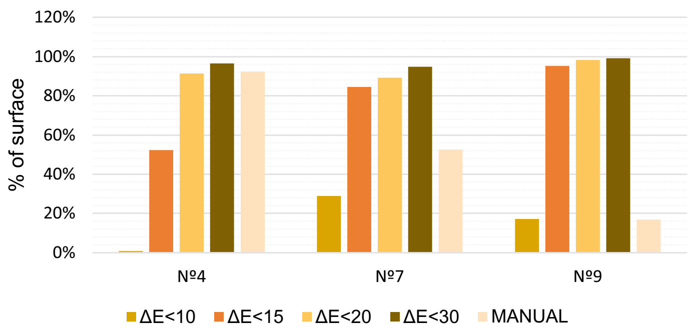

Fig. 5 Comparison between results obtained by two classification methods (manual and automatic)

indicating that the building façade has a high probability of requiring maintenance intervention.

5 Conclusions

The method presented enables the analysis of facades' state of conservation, revealing it as a valuable tool to support facade inspection and diagnosis throughout colour differences. The final maps of the building facades allow the location of critical areas from the areas with stains, with a higher probability of containing anomalies.

The results show that the method based on colour differences (ΔE) to a reference colour defined by the user allows mimicking a traditional visual inspection. Further, the automation reduces the inspection time, bias evaluation, and improves the accuracy, reducing human intervention. A visual inspection may be less accurate on Facade No.9 when compared with Facades No.4 and No.7, since ΔE can identify slight colour differences that cannot be observed with the naked eye.

Photographs of each case study present a different yellow colour in the cladding depending on lighting/shadows. The HSV enables the chromatic characterization of colours. However, the advantage of use a reference colour to measure relative differences is that it is not necessary to obtain the real colour of the cladding.

A drawback of the method presented is its performance for façade panoramas with 'noise' elements, such as urban furniture, vegetation, vehicles, that hide parts of the façade from the panorama. This means that the total area analysed by both methods does not coincide. However, the error is often not relevant at this specific scale of work and can be mitigate with image surveys from different points of view.

Future works will analyse the effectiveness of the proposed method not only in the detection and quantification of stains in other cladding materials, but also in the detection of other anomalies (*e.g.* cracks and detachments).

Acknowledgements The authors gratefully acknowledge the CERIS Transversal seed project Feeling the City (CERIS BASE 2020-2023/UIDB/04625/2020) and the financing granted by the VI PPIT-US. J. Valença and A. Silva also acknowledges the financial support of the Portuguese Science and Technology Foundation (FCT) through the project CEECIND/04463/2017 and CEECIND/01337/2017, respectively.

References

1. Valença, J., Gonçalves, L.M.S., Júlio, E.: Damage assessment on concrete surfaces using multi-spectral image analysis. Constr. Build. Mater. **40**, 971–981 (2013). https://doi.org/10.1016/j.conbuildmat.2012.11.061
2. Santos, B.O., Valença, J., Júlio, E.: Automatic mapping of cracking patterns on concrete surfaces with biological stains using hyper-spectral images processing. Struct. Control Heal. Monit. **26**, 1–15 (2019). https://doi.org/10.1002/stc.2320
3. Oliveira Santos, B., Valença, J., Júlio, E.: Classification of biological colonization on concrete surfaces using false colour HSV images, including near-infrared information. **10680**, 13–22 (2018). https://doi.org/10.1117/12.2307728.
4. Miranda, J., Valença, J., Júlio, E.: Colored concrete restoration method: for chromatic design and application of restoration mortars on smooth surfaces of colored concrete. Struct. Concr. **20**, 1391–1401 (2019). https://doi.org/10.1002/suco.201900006
5. Chen, K., Reichard, G., Akanmu, A., Xu, X.: Geo-registering UAV-captured close-range images to GIS-based spatial model for building façade inspections. Autom. Constr. **122** (2021). https://doi.org/10.1016/j.autcon.2020.103503
6. Guo, J., Wang, Q., Li, Y., Liu, P.: Façade defects classification from imbalanced dataset using meta learning-based convolutional neural network. Comput. Civ. Infrastruct. Eng. **35**, 1403–1418 (2020). https://doi.org/10.1111/mice.12578
7. Lee, K., Hong, G., Sael, L., Lee, S., Kim, H.Y.: Multidefectnet: multi-class defect detection of building façade based on deep convolutional neural network. Sustain. **12**, 1–14 (2020). https://doi.org/10.3390/su12229785
8. AENOR, Conservation of cultural property. Test methods. Colour measurement of surfaces. EN-15886:2010, Spain (2011)
9. Ferrito, T.F.C.: Avaliação sísmica de um edifício "de placa" do Bairro de Alvalade Análise Linear e Não Linear, University of Lisbon, (2014)
10. Moler, C.: Matlab R2021b, (2021). https://www.mathworks.com/products/matlab.html

Wireless Sensors for Measuring Main Kinematic Parameters in Dynamic Tests Involving Intense Impacts

Seyedsajjad Hosseini, João Guerreiro, João Gomes Ferreira, Luís Guerreiro, and Rita Moura

Abstract This study presents the development of two types of wireless sensor systems, one based on high-speed cameras and the other on high-capacity MEMS accelerometers. These sensors are intended for application in two experimental tests related to the ongoing SHELTER project aiming at developing a seismic shelter to protect human lives. In the **first test**, a half-scaled masonry building accommodating a half-scaled shelter on its top will be led to collapse over a shaking table for assessing the SHELTER impact accelerations during the building collapse. The **second test type** consists of free-fall of the SHELTER structure, supplied with a safety chair and a crash test dummy, to evaluate the shock accelerations on the human body. These damaging tests would not allow using the wired sensors often used in dynamic tests. Consequently, four wireless accelerometer sets containing two ±200 g accelerometers in the horizontal axes and one ±500 g accelerometer for the vertical direction were considered. In the building collapse test, these accelerometers will be installed in the half-scale shelter (four corners). In the free-fall tests, the accelerometers will be located in the shelter (three corners) and on the safety chair to hand out the large instant acceleration. Complementary measurements will be performed based on high-speed cameras and a large set of "optical + infrared" targets. These targets will be bonded to the under-studied model components in both tests. All sensors and targets were prepared and assembled in LNEC, where the shaking table test will be performed, and the sensor calibrations were carried out.

Keywords Wireless system · Impact acceleration · Impact velocity · MEMS accelerometer · Digital image correlation (DIC)

S. Hosseini · J. Guerreiro · J. G. Ferreira (✉) · L. Guerreiro
CERIS, IST, Universidade de Lisboa, 1049-001 Lisboa, Portugal
e-mail: joao.gomes.ferreira@tecnico.ulisboa.pt

S. Hosseini
e-mail: seyedsajjad.hosseini@tecnico.ulisboa.pt

R. Moura
Teixeira Duarte, Engenharia e Construções, 2740-265 Porto Salvo, Oeiras, Portugal

C. Chastre et al. (eds.), *Testing and Experimentation in Civil Engineering*,
RILEM Bookseries 41, https://doi.org/10.1007/978-3-031-29191-3_40

1 Introduction

In many seismic regions with the collapse risk of vulnerable masonry buildings, in case of moderate to large earthquake occurrence, apart from vast destruction, the number of casualties and deaths may lead to catastrophe and huge losses. The project SHELTER—Structural Hyper-resisting Element for Life-Threatening Earthquake Risk [1] has been attempting to minimize fatal risk in vulnerable buildings by developing a high-strength steel structure containing different safety equipment. This safe zone in an apartment should be located in accessible places, such as the corridor, without hampering its day-to-day function. To have a desirable and robust structure, the design part of the steel structure was accomplished under several assumed severe load cases [2] and complemented with the experimental campaign that will be explained briefly herein. As an initial step, the static tests (diagonal and vertical tests) on two different proposed prototypes simulating the worst-case scenarios of the load cases were performed to assess the global and local behavior of the prototype [3].

A fundamental requirement of an earthquake shelter is to have a robust structure, for being protective against the airborne objects, falls of the rubbles, and the weight of heavy debris. Another possible event is if the floor hosting the unit is situated on the higher altitudes, and the building collapse results in the shelter falling from the upper floors and hitting the lower ones with exceedingly high acceleration. Consequently, to save people's lives inside the shelter and deal with this issue, a safety chair with a shock absorber system has been proposed for the survival of the shelter occupants by reducing the force on the sensitive parts of their bodies.

For the analysis and the design process of this equipment (safety chair and shock absorber system), a complex representation of the human body was performed numerically. In these analyses, the impact velocity was considered according to the fall acceleration equal to 0.5 g obtained from footage analysis of some building collapses [4].

Besides the numerical analyses, two different tests have been defined to understand better this phenomenon: the impact of acceleration and velocity during the building collapse and the influence of the safety chair on the shock reduction over the human body.

Through the first test, a half-scaled masonry building that represents a building vulnerable to earthquakes was built to be tested over a shaking table in Laboratório Nacional de Engenharia Civil (LNEC). A steel protection structure and a safety net will be installed around the model to prevent damage to the laboratory site. Correspondingly, an assembled half-scaled shelter unit will be placed on the upper floor of this masonry building. Due to the essence of this test which is engaged with high acceleration and the devastated model during the collapse, using a typically wired accelerometer is inconceivable. The high-capacity accelerometer sets and high-speed cameras are employed in the test to measure the impact accelerations and velocities. In order to assess the performance of the safety chair, the second experiment was considered to be performed at the operational center of Teixeira Duarte, in Montijo. The test is ascertained using the assembled safety chair with a shock absorber system installed between two frames of a full-scaled shelter unit, and the shelter would be connected to an overhead crane. In this test, to evaluate the influence of this equipment for diminishing the impact force on the human body, simulating the fall of the shelter unit when the building is being devastated during a severe earthquake, an anthropomorphic test device (ATD) renowned as a "crash test dummy" will be used. The types of sensors in this test will be mainly common to the shaking table test.

2 Description of the Tests

2.1 *Shaking Table Test—Collapse of a Half-Scaled Masonry Building with a Half-Scaled* Shelter *on Its Top*

The shaking table experiment is defined to perform a test on two parallel masonry walls connected with four timber slabs representing the place where the *shelter* unit is going to be installed. The design and construction of this building were meant to simulate one of the worst vulnerabilities of masonry buildings to the seismic actions, the pancake-type collapse, and to investigate the subsequent forces on the *shelter* structure and covered people inside during the fall path. These four wooden slabs and two seven-meter parallel walls built with a feeble stone masonry material over a concrete foundation (Fig. 1a) are constructed as a 1:2 scaled building on the shaking table with a half-scaled *shelter* (Fig. 1b) on the last floor. According to the numerical model of this test, as mentioned before, the building pancake collapse occurrence is expected, and the *shelter* will be impacted severely on the lower floors. As the test will be vastly destructive, the model is surrounded by large steel protection filled with wooden planks and enclosed with a safety net to the seismic lab ceiling (Fig. 1c).

Since the model in this test is of a large-scale type, its repetition is not feasible. So, to achieve the main objectives of the experiment, all developed sensors must be tested under different harsh conditions and must be calibrated with an accurate

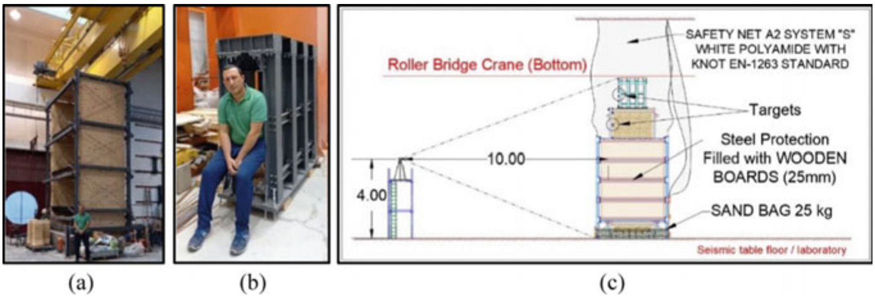

Fig. 1 Half-scaled masonry building (**a**); half-scaled *shelter* structure (**b**); the side view of the model, steel protection, and safety nets with the positions of the targets and cameras 10 m away from the model (**c**)

device to ensure reliability. One of the instrumentation types in this test is high-capacity accelerometers. These electronic devices will be fixed on the four corners of the half-scaled shelter to its base plate for measuring intense impact accelerations instantly during the collapse. Another measurement system comprises four high-speed cameras with a capturing rate of between 300 and 1000 frames per second (fps) intended to follow the targets on the model for studying movements of different parts and evaluating the accelerations (averaged) during the collapse. In this test, all sensors and high-speed cameras will be triggered by the shaking table command. After finishing the tests, the measured acceleration on the SD card will be extracted, and the recorded footage will be post-processed with tracker software and Matlab to obtain the kinematic parameters.

2.2 Free-Fall Test

The second test will be a free-fall of a full-scale shelter structure from different heights with different angles. The shelter is equipped with a safety chair and a crash test dummy on-board for simulating the human body in this event. The shelter unit will be hung from an overhead crane with a maximum span height of 12 m (Fig. 3). Afterwards, the unit will be released to fall from different heights until it reaches its maximum elevation of 9 m, equivalent to the height of the six-floor building and considered collapse acceleration of 0.5 g (six times the half-floor height). After performing the shaking table test, the considered height and acceleration values may change.

Some details of the safety chair, shock absorber system and the dummy sitting on it are shown in Fig. 4. All relevant kinematic parameters such as the maximum displacement, velocity and acceleration of the chair, maximum impact acceleration on the body, etc. must be investigated. Accordingly, except for the load cell that will be placed under the chair seat as an inertial accelerometer for obtaining the shock force to the hip, pelvis, and the end part of the spinal cord, the remaining sensors (accelerometer and high-speed cameras) will be the same as the ones in the shaking table test with the targets (sticker) and sensors on the crash test dummies, shelter structure and safety chair.

3 Sensors and Data Acquisition

The sensors described for both tests are divided into three categories: high-capacity accelerometers, high-speed cameras, and inertial accelerometers. In both tests, the sensors are mostly similar; however, their differences are related to the feature of the first test aiming at destroying the model and determining the kinematic parameters without repetition and using non-wired sensors; hence, the inertial accelerometers would not be used in the first test. The first sensor type corresponds to four sets of high-capacity wireless accelerometers to measure the acceleration in the three axes with a maximum sampling rate of 1.000 Hz. Each of the triaxial accelerometers sets comprises three Arduino microcontrollers, three analogue output accelerometers, two ADXL377 and one ADXL1004, with the maximum range of ±200 g and ±500 g for two horizontal and vertical directions, respectively. The unit is also provided with three reader/writer modules for SD card, screwed to a C-shape steel profile with 3 mm thickness. The units will be welded on the base plate of half-scaled shelter (Fig. 5). For operating three accelerometers in each set with their maximum data rates, they are wired to the selected Arduino MKR 1010 Wi-Fi model; also, the Wi-Fi option in Arduino makes this controller possible to be exploited remotely. These Arduino boards are connected to a computer with a specific IP address via a Wi-Fi router. The acquired data is stored in a reader/writer module with a 32 GB SD card wired to the Arduino using the Serial Peripheral Interface (SPI) communication protocol for having a higher speed of data transfer. The Arduino and SD card are powered with 5 V provided by an electric circuit including a breadboard and an inserted transistor (level shifter) in the circuit connected to two 9 V batteries; also, the 3 V power for the accelerometer is supplied by Arduino directly.

During several trial impact tests on the four sets of accelerometers using ADXL377 in all axes from different altitudes over lime bags, it was realized that the impact acceleration was near the maximum range of the accelerometer (200 g), and it may exceed this value if a harder impact occurs. Also, it was understood that the battery would stop working for a fraction of a second at the impact instant, leading to the Arduino, SD card reader and accelerometer becoming interrupted. To overcome the first issue, another accelerometer called H3LIS331DL Breakout with a versatile output range equal to 400 g, data rates of 1000 Hz and an I2C or SPI interface option was substituted. However, according to the comparison of the test results between ADXL377 (calibrated with a piezoelectric accelerometer as a reference) and H3LIS331DL Breakout simultaneously, the digital output of the latter using the I2C communication protocol had higher noise at the impact moments; consequently, the analogue accelerometer ADXL1004 with the maximum range of 500 g, similar functionality to the ADXL377 and a smoother output diagram was selected in the vertical direction. The proposed solution for dealing with the second problem is the use of 10 microfarad capacitors for storing some electrical energy and supplying it when the batteries stop working.

Other instruments synchronized with wireless accelerometers are high-speed cameras. Based on their speeds varying between 300 and 1000 frames per second, these sensors will be dedicated to covering less critical to more critical areas of the model. Besides these cameras, a GoPro camera without the intention of using it in post-processing analysis will record the overall scene, including the steel protection structure. Figure 2 shows different camera types, their installation distance from the model (10 m due to the limitations of the coverage area and the barriers in the shaking table lab) and the installed targets on the model; also, in Fig. 6, the covered area of each camera, the close view of the optical target and the details of two installed infrared LEDs as a proposed anti-dust technique is depicted. All allocated computers for camera and accelerometer operation are linked to a central computer to control and synchronize all sensors. The shaking table initiates operating with a 5 V command system from its control room; simultaneously, the Raspberry Pi device receives this command and switches it to the digital output for the central computer of the sensor system. Therefore, when the shaking table starts working, the central computer sends the launching command to all the sensors through the run Matlab scripts in other linked computers. In each computer, there is one frame grabber board connected to a camera paired with specific software, in this case, Streampix for configuring and controlling the camera as well as data acquisition. The recorded video footage will be analysed with Matlab and a user-friendly software called Tracker, having a graphical interface to obtain the studied parameters such position, velocity and acceleration. In the shaking table test, around ninety sets of optical + infrared LEDs targets (LED light has the advantage of passing through dust cloud) will be positioned on the masonry building and the shelter structure.

However, in the free-fall tests, in addition to the targets placed on the crash test dummy and safety chair for analyzing the video to obtain kinematic parameters by the Tracker, the Digital Images Correlation (DIC) is another optical approach with specific post-processing software using high-speed cameras that can be used to

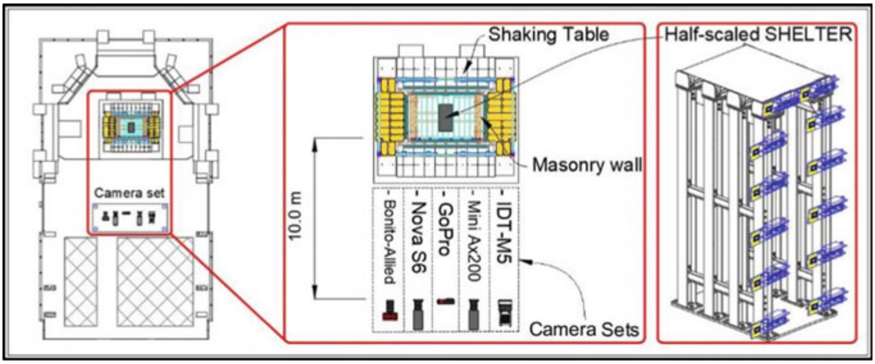

Fig. 2 The plan view of the shaking table laboratory, a close view of the different camera type positions, half-scaled *shelter* and the installed targets over it

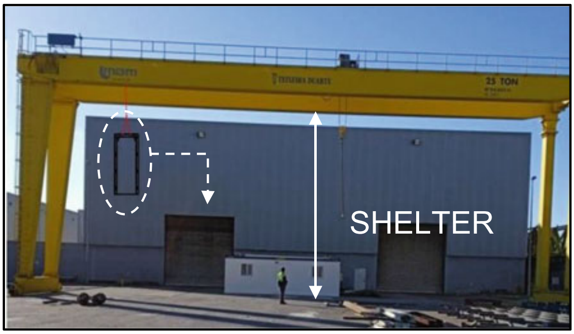

Fig. 3 The overhead crane to be used in the free-fall test in the Teixeira Duarte site and the schematic view of the hanging *shelter*

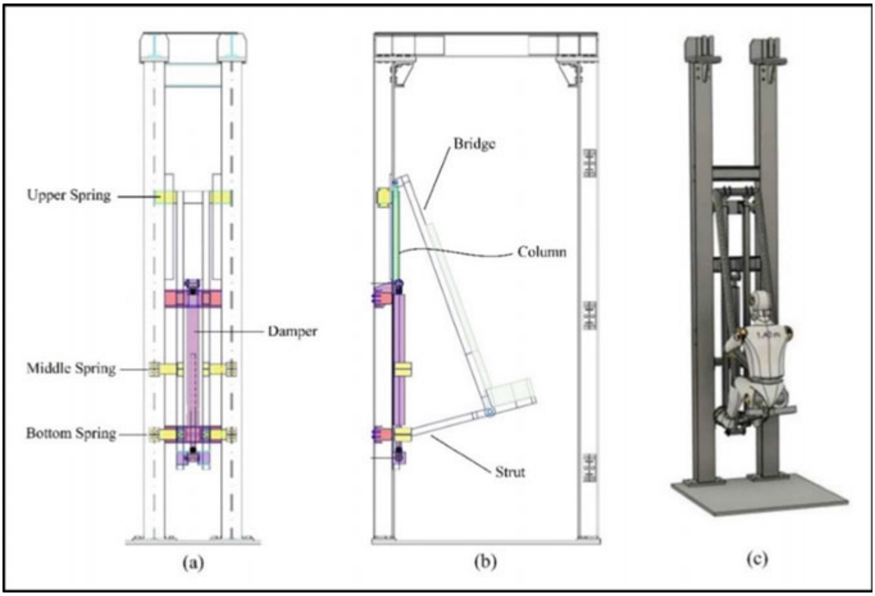

Fig. 4 Three different views of the safety chair and shock absorber system: Front view (**a**); and side view (**b**); of the safety chair with its details; perspective view of the safety chair with a dummy on it (c) [4]

measure displacements and deformation of the safety chair components as well as the dummy. The primary purpose of this test is to evaluate the performance of the chair in regards to the reduction of the impact acceleration on the dummy representing the human body; also, one GoPro camera is dedicated to the recording of the test, and only one camera has been considered for post-processing part of the test so far. Hence, all settings, such as Region of Interest (RoI), resolution, exposure, frame rates, and distance, are limited and configurated according to the primary goal. As these mentioned parameters are crucial for image calibration in DIC techniques and will be modified based on the accuracy of the main studied parameters of the test but not the DIC ones, the possibility of using this technique will be assessed after the test. Nonetheless, this technique was not considered in the preliminary free fall test on the safety chair with the dummy. Also, the free fall test is less destructive, and the use of a wired sensor is practicable' therefore, the Inertial accelerometer comprising the load cell connected to the data acquisition unit and known mass (mass of dummy) will be placed under the safety chair seat during thetest to measure the force on the lower parts of the human body.

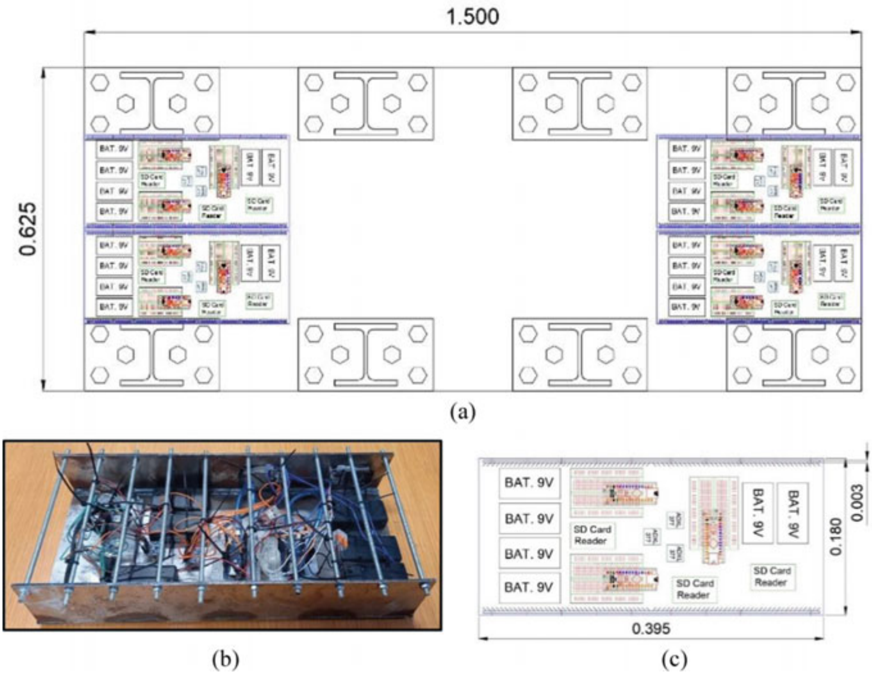

Fig. 5 The schematic plan view of the half-scaled *shelter* base plate with the welded sets of accelerometers (**a**); the real view of one of the assembled sets of triaxial accelerometers (**b**); plan view of an accelerometer schematically (**c**)

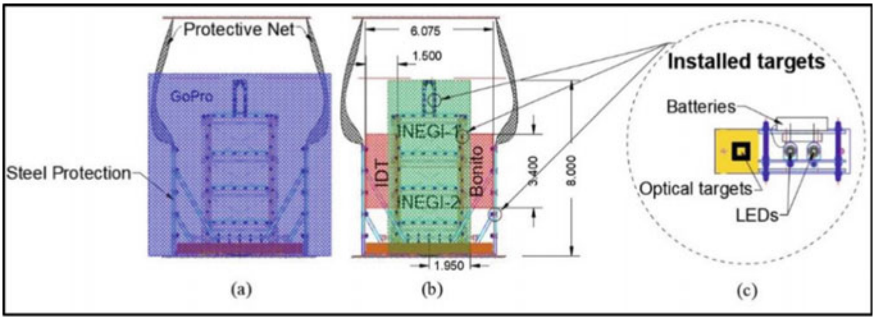

Fig. 6 Different covered areas of the model by each camera: GoPro (**a**); the other cameras (**b**); and the details of the installed target (**c**)

4 Calibration Test—Comparison Between the Result of the High-Speed Camera and Wireless Accelerometers with a Reference Accelerometer

In these tests, the results based on the camera IDT M5 (velocity and acceleration) and on the triple-axis accelerometer with a maximum range of 200 g (ADXL377) were compared to those obtained with an IEPE (Integrated Electronics Piezo-Electric) accelerometer (with cable) belonging to the shaking table laboratory (LNEC), which served as a reference for the calibration process. All mentioned devices and the camera target were connected to the towing wire and hung from an overhead crane hook initially, and they were released from different heights of 4 m, 5 m and 6 m to fall without any contact with the ground. Since one Arduino was used for all axes of the MEMS accelerometer, the data rate of the accelerometer was reduced to 300 Hz instead of 1000 Hz; also, the camera speed in this test with the almost full-HD resolution was 300 frames per second (fps). The reference accelerometer from LNEC was connected with a cable to the data acquisition system in the shaking table control room and functioned with a constant sampling rate of 600 Hz. Due to the maximum capacity of this accelerometer, which was 50 g, it was not possible to let the set of devices hit the ground. Also, the connected towing wire to the crane hook reduced the free-fall acceleration. The selected results of three out of seven tests with a duration of almost 40 s on the target specified with a red circle are presented in Figs. 7, 8 and 9.

5 Conclusion

- The comparison between the result of the wireless accelerometer (MEMS) at 300 Hz sampling rate and the reference LNEC accelerometer at 600 Hz sampling rate showed the efficient performance of the MEMS accelerometer for this acceleration range; moreover, the sampling rate of this accelerometer will be 1 kHz in the main test.
- The IDT camera with the noise tolerance of $\pm$ 10 g had a lower accuracy, with an error up to 5% of the capacity of the Wireless accelerometer. To track the optical target properly with lower noises, the target should not rotate more than 45° relatively to the considered 2D coverer area (canvas); also, to avoid having lost frames or processing cessation due to the target invisibility, this angle should not exceed 80°.
- This test demonstrated the proper performance of the low-cost wireless accelerometer and the benefits and limits of high-speed cameras when compared to the cabled accelerometer (with a higher price) for obtaining kinematic parameters in demanding or destructive test types.

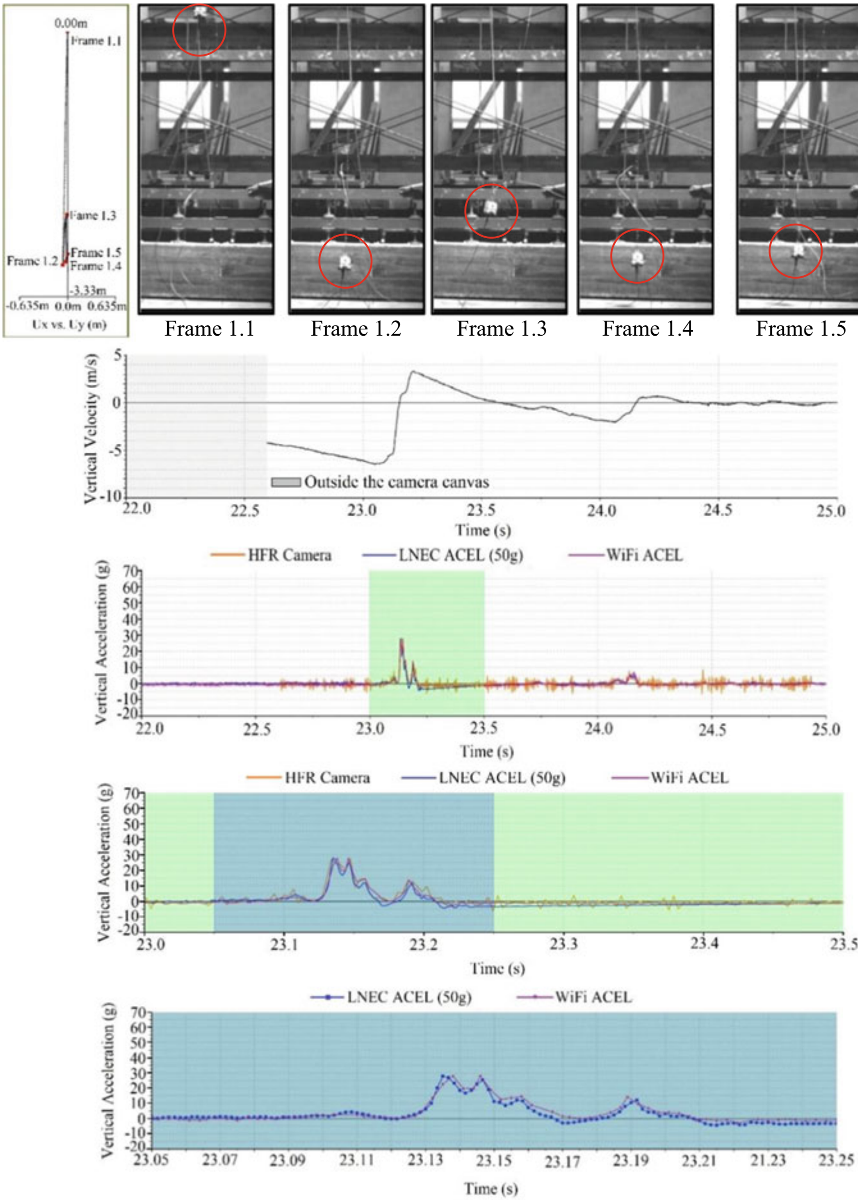

Fig. 7 The result of the 1st impact calibration test with 4 m of falling height

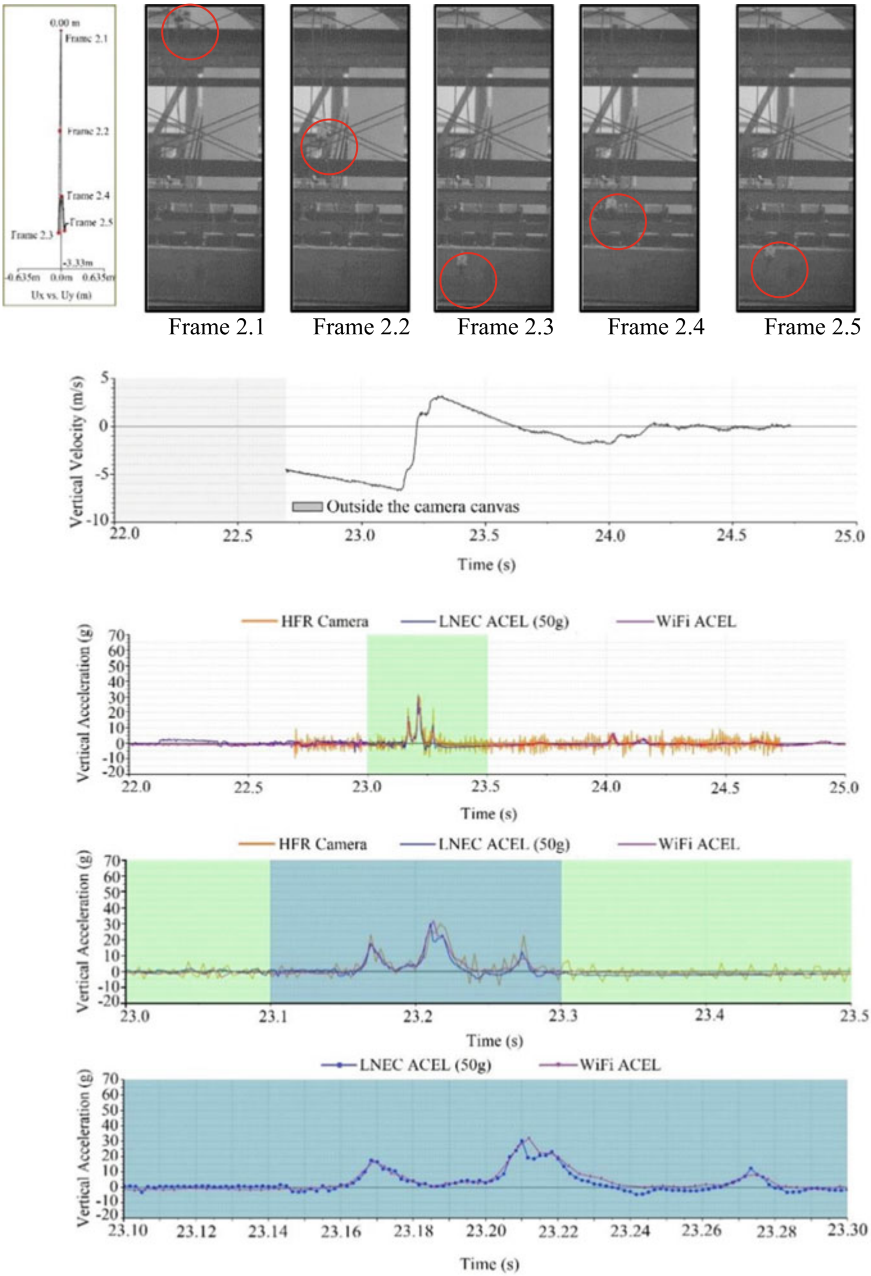

Fig. 8 The result of the 2nd impact calibration test with 5 m of falling height

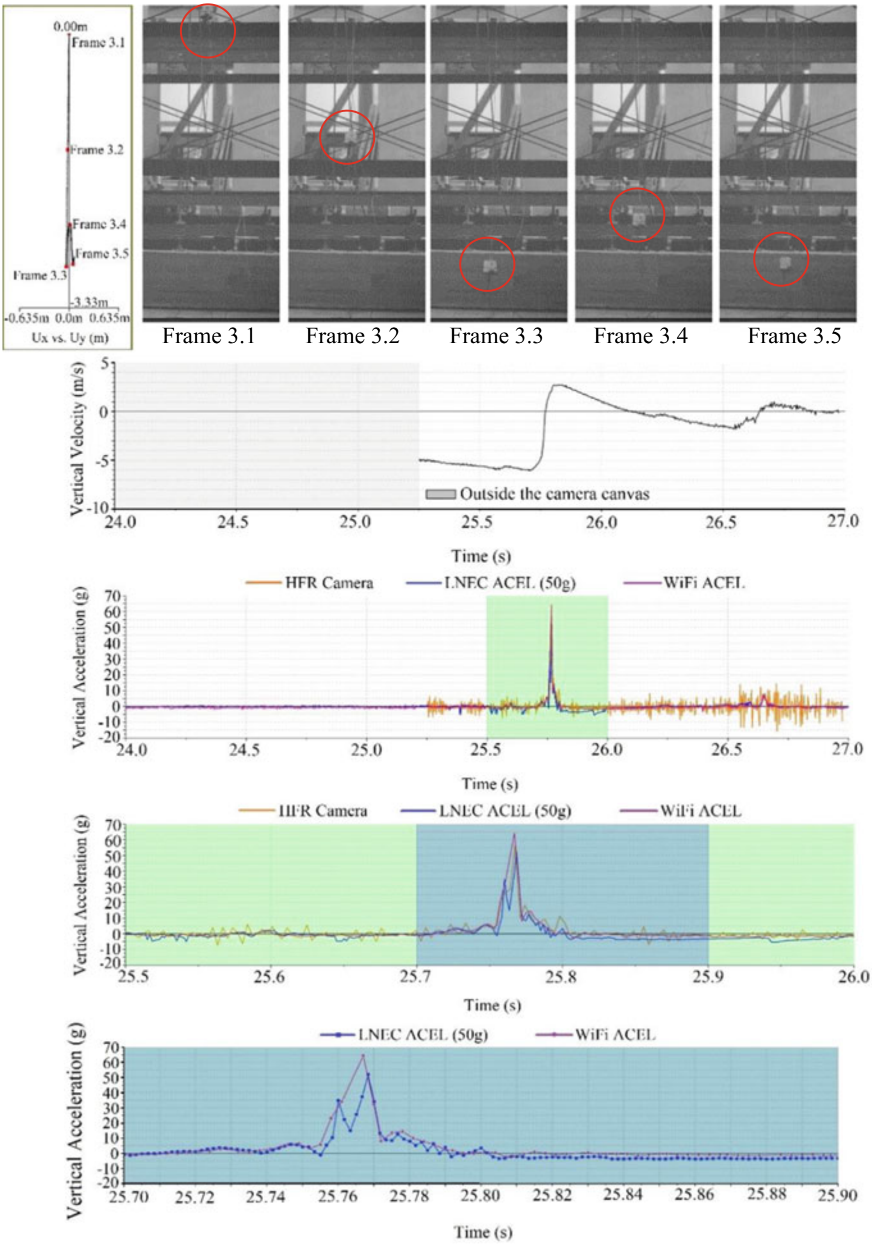

Fig. 9 The result of the 3rd impact calibration test with 6 m of falling height

Acknowledgements CCDRLVT—Comissão de Coordenação e Desenvolvimento Regional de Lisboa e Vale do Tejo, Programa Operacional Regional de Lisboa 2014/2020—Lisboa 2020, and ANI—Agência Nacional de Inovação are all acknowledged by the authors for their financial support regarding project ref. LISBOA-01-0247-FEDER-032854 entitled "SHELTER—Structural Hyper-resisting Element for Life Threatening Earthquake Risk.

LNEC, the National Laboratory of Civil Engineering, is acknowledged for their high competence and availability to host the seismic table test of the SHELTER project.

Finally, our colleagues that have been contributing to the SHELTER project, with fruitful debating, are acknowledge, namely Carlos Sousa Oliveira, Fernando Branco, João Azevedo, (IST), Henrique Nicolau, Nuno Gonçalves and Bernardo Santos (Teixeira Duarte).

References

1. João, G.F., Moura, R., Guerreiro, L., Guerreiro, J.: SHELTER—structural hyper-resisting element for life threatening earthquake risk. an innovative approach for seismic protection. Eng. Struct. **235** (2021). doi:https://doi.org/10.1016/j.engstruct.2021.112012
2. João, G., Ferreira, J.G., Guerreiro, L., Moura, R., Hosseini, S.: The design of a structural Hyper-resisting element for Life Threatening Earthquake risk (SHELTER) for building collapse scenarios: The life-saving capsule. Eng. Struct. **258** (2022). doi:https://doi.org/10.1016/j.engstruct.2022.114151
3. Hosseini, S., Guerreiro, J., Guerreiro, L., Moura, R., Ferreira, J.G.:SHELTER—structural hyper-resisting element for life threatening earthquake risk. Static tests on the *shelter* structure. J. Build. Eng. **47** (2022). doi:https://doi.org/10.1016/j.jobe.2021.103824
4. João, G., Guerreiro, L., Hosseini, S., Moura, R., Ferreira, J.G.: The design of a structural hyper-resisting element for life-threatening earthquake risk (SHELTER) for building collapse scenarios: the safety chairs. Appl. Sci. **12**(9) (2022). doi:https://doi.org/10.3390/app12094103